

Springer Series in Advanced Manufacturing

Jan C. Aurich
Hans Hasse *Editors*

Component Surfaces

Manufacturing-Morphology-Property
Relationships

 Springer

Springer Series in Advanced Manufacturing

Series Editor

Duc Truong Pham, University of Birmingham, Birmingham, UK

The **Springer Series in Advanced Manufacturing** includes advanced textbooks, research monographs, edited works and conference proceedings covering all major subjects in the field of advanced manufacturing.

The following is a non-exclusive list of subjects relevant to the series:

1. Manufacturing processes and operations (material processing; assembly; test and inspection; packaging and shipping).
2. Manufacturing product and process design (product design; product data management; product development; manufacturing system planning).
3. Enterprise management (product life cycle management; production planning and control; quality management).

Emphasis will be placed on novel material of topical interest (for example, books on nanomanufacturing) as well as new treatments of more traditional areas.

As advanced manufacturing usually involves extensive use of information and communication technology (ICT), books dealing with advanced ICT tools for advanced manufacturing are also of interest to the Series.

Springer and Professor Pham welcome book ideas from authors. Potential authors who wish to submit a book proposal should contact Anthony Doyle, Executive Editor, Springer, e-mail: anthony.doyle@springer.com.

INDEXED IN SCOPUS

Jan C. Aurich · Hans Hasse
Editors

Component Surfaces

Manufacturing-Morphology-Property
Relationships

 Springer

Editors

Jan C. Aurich
Institute of Manufacturing Technology
and Production Systems
RPTU Kaiserslautern
Kaiserslautern, Germany

Hans Hasse
Institute of Engineering Thermodynamics
RPTU Kaiserslautern
Kaiserslautern, Germany

ISSN 1860-5168

ISSN 2196-1735 (electronic)

Springer Series in Advanced Manufacturing

ISBN 978-3-031-35574-5

ISBN 978-3-031-35575-2 (eBook)

<https://doi.org/10.1007/978-3-031-35575-2>

© The Editor(s) (if applicable) and The Author(s), under exclusive license to Springer Nature Switzerland AG 2024

This work is subject to copyright. All rights are solely and exclusively licensed by the Publisher, whether the whole or part of the material is concerned, specifically the rights of translation, reprinting, reuse of illustrations, recitation, broadcasting, reproduction on microfilms or in any other physical way, and transmission or information storage and retrieval, electronic adaptation, computer software, or by similar or dissimilar methodology now known or hereafter developed.

The use of general descriptive names, registered names, trademarks, service marks, etc. in this publication does not imply, even in the absence of a specific statement, that such names are exempt from the relevant protective laws and regulations and therefore free for general use.

The publisher, the authors, and the editors are safe to assume that the advice and information in this book are believed to be true and accurate at the date of publication. Neither the publisher nor the authors or the editors give a warranty, expressed or implied, with respect to the material contained herein or for any errors or omissions that may have been made. The publisher remains neutral with regard to jurisdictional claims in published maps and institutional affiliations.

This Springer imprint is published by the registered company Springer Nature Switzerland AG
The registered company address is: Gewerbestrasse 11, 6330 Cham, Switzerland

Preface

This is a book about component surfaces—to the best of our knowledge, it is the first one that is solely dedicated to this important subject. Machines and apparatuses are built from mechanical components, which have to fulfill specific tasks. To make a component work, many issues have to be considered—and many of these are well understood. However, astonishingly, this does not hold for one of the most critical issues: the component's surface. The surface encloses the component just like the skin encloses the human body. It is through the surface that the component interacts with the environment, which is why the surface is often decisive for the functionality and the life time of the component.

Despite this, the research on component surfaces has been limited to individual aspects for a long time, and a comprehensive approach has been lacking. This is not astonishing, as the hurdles for such an endeavor are high: it is inherently interdisciplinary—various fields of engineering and physics have to interact; it requires a multi-scale approach—the interfacial region is small, but its effects are macroscopic; and, last not least: it requires linking fundamental and applied research.

These challenges have been tackled in a coordinated research project funded by Deutsche Forschungsgemeinschaft (DFG) from 2011–2023: the *Collaborative Research Center CRC 926 Microscale Morphology of Component Surfaces (MICOS)*, in which, over the years, more than 100 researchers have co-operated at University of Kaiserslautern, Germany, and affiliated institutes. The scientific results from this endeavor have been published in more than 500 scientific papers in journals from different fields of science and engineering. This book aims at giving an overview of these results. We hope that it will be of interest both for scientists and engineers who deal with the influence of surfaces on macroscopic properties of components and who are interested in designing and manufacturing these surfaces in such a way as to obtain desired component properties. This book is a starting point, it is a guide to

current research, and it describes directions for future research. It is still a long way to establishing a comprehensive theory of component surfaces; here, we are only adding a few pieces to this great work.

Kaiserslautern, Germany
June, 2023

Jan C. Aurich
Hans Hasse

Acknowledgements

This book presents scientific results obtained in an interdisciplinary collaboration of many researchers over 12 years. The authors of this book are those who have provided contributions to the individual chapters, but many more have been involved in the original research. Their names can be found in the original papers cited throughout this book. Here, we want to give explicit credit to the valuable work of: Peter Arrabiyeh, Stephan Basten, Andre Becker, Stefan Becker, Steven Becker, Robert Bischof, Luisa Böhme, Annika Boemke, Martin Bohley, Paul Breuninger, Alexander Brodyanski, Sebastian Buhl, Georgis Bulun, Christoph Burkhart, Felix Diewald, Niklas Erdmann, Daniel Frölich, Yu Gao, Claudia Godard, Jürgen Hartmüller, Michaela Heier, Marius Heintz, Hendrik Hotz, Manuel Huster, Matthias W. Klein, Daniel Kleine, Jörg Lösch, Patrick Mayer, Jerome Meiser, Lucia Morales-Rivas, Christopher Müller, Regina Müller, Ingo G. Reichenbach, Daniel Sappok, Christin Schlegel, Simon Schmidt, Frank Schneider, Robert Skorupski, Binjun Wang, Jana Wolf.

The research on which we report here would not have been possible without the substantial and long-term funding by Deutsche Forschungsgemeinschaft (DFG) under its CRC-program, which provides a perfect frame for free research, defined and organized by the researchers themselves. We gratefully acknowledge not only this funding, but also the continuous support from DFG's head office, in particular from Thomas Münker; as well as the work of all reviewers in the three evaluation rounds of CRC 926.

Thanks are also due to University of Kaiserslautern, which has continuously supported CRC 926 in many ways. Last not least, we want to thank Ilona Stein for running the office of CRC 926 so marvellously for 12 years.

Kaiserslautern, Germany
February 2023

Jan C. Aurich
Hans Hasse

Contents

Manufacturing–Morphology–Property (MMP) Relationships: Concept and Application to Component Surfaces	1
Jan C. Aurich and Hans Hasse	
Fundamentals and Technologies	
Geometrical, Microstructural, and Chemical Characterization	9
Michael Kopnarski, Tilmann Beck, Stella Diederichs, Eberhard Kerscher, Jörg Seewig, and Marek Smaga	
Indentation and Scratching on the Nanoscale	41
Herbert M. Urbassek, Iyad Alabd Alhafez, Hans Hasse, Michael Kopnarski, and Simon Stephan	
Creating Surface Morphologies by Micro Milling and Micro Grinding	67
Jan C. Aurich, Nicolas Altherr, Sonja Kieren-Ehse, Benjamin Kirsch, and Tobias Mayer	
Creating Surface Morphologies by Cryogenic Machining	97
Benjamin Kirsch, Jan C. Aurich, Kevin Gutzeit, Erik von Harbou, Hans Hasse, and Ralf Müller	
Creating Surface Morphologies by Cold Spraying	125
Sergiy Antonyuk, Mustafa Bozoglu, and Siegfried Ripperger	
Creating Surface Morphologies by Additive Manufacturing	147
Georg von Freymann, Julian Hering-Stratemeier, Kristin E. J. Kühl, Thomas Palmer, and Erik H. Waller	
Interactions Between Particles and Surfaces	173
Kristin M. de Payrebrune, Clarissa Schönecker, Sergiy Antonyuk, Raphael Bilz, Fabian Krull, Isabell Noichl, Siegfried Ripperger, and David Strohner	

Adsorption and Wetting of Component Surfaces	203
Hans Hasse, Martin T. Horsch, Michael Kopnarski, Kai Langenbach, Ralf Müller, Simon Stephan, and Herbert M. Urbassek	
Interrelationship of Manufacturing, Surface Morphology, and Properties of Titanium	231
Eberhard Kerscher, Stella Diederichs, Nafiseh Ghavidel, Andrej Keksel, Charlotte Kuhn, Ralf Müller, Jörg Seewig, and Fábio J. P. Sousa	
Influence of Manufacturing and Load Conditions on the Phase Transformation and Fatigue of Austenitic Stainless Steels	257
Tilmann Beck, Marek Smaga, Sergiy Antonyuk, Dietmar Eifler, Ralf Müller, Herbert M. Urbassek, and Tong Zhu	
Influence of Surface Morphology on Fatigue and Tribological Behavior of TRIP/TWIP Steels	289
Marek Smaga, Tilmann Beck, Michael Kopnarski, Rolf Merz, Kristin M. de Payrebrune, and Stefan Wolke	
Applications	
Manufacturing of Areal Material Measures	315
Jörg Seewig, Georg von Freymann, Jan C. Aurich, Matthias Eifler, Julian Hering-Stratemeier, and Katja Klauer-Dobrowolski	
Manufacturing-Morphology-Property Relationships for Rotating Shaft Sealing Systems	349
Stefan Thielen, Sergiy Antonyuk, Jan C. Aurich, Tilmann Beck, Hans Hasse, Michael Kopnarski, Balázs Magyar, Bernd Sauer, and Marek Smaga	
Influence of the Surface Morphology on Rolling Bearing Life Under Mixed Lubrication	369
Bernd Sauer, Tilmann Beck, Bastian Blinn, Flavien Foko Foko, Pascal Ostermayer, and Lukas Rüth	
Manufacturing-Morphology-Property Relationships for Chain Joints	393
Manuel Oehler, Dominik Meffert, and Bernd Sauer	
Manufacturing-Morphology-Property Relationships for Biofilms	411
Roland Ulber, Sergiy Antonyuk, Jan C. Aurich, Tilmann Beck, Mustafa Bozoglu, Georg von Freymann, Sonja Kieren-Ehse, Christine Müller-Renno, Kai Muffler, Andrea Schmeckeber, Clarissa Schönecker, Jörg Seewig, Marek Smaga, Judith Stiefelmaier, Dorina Strieth, Ahmed Zayed, Christiane Ziegler, and Sebastian Zimmermann	

Contributors

Iyad Alabd Alhafez Institute of Computational Material Science, RPTU Kaiserslautern, Kaiserslautern, Germany

Nicolas Altherr Institute of Manufacturing Technology and Production Systems, RPTU Kaiserslautern, Kaiserslautern, Germany

Sergiy Antonyuk Institute of Particle Process Engineering, RPTU Kaiserslautern, Kaiserslautern, Germany

Jan C. Aurich Institute of Manufacturing Technology and Production Systems, RPTU Kaiserslautern, Kaiserslautern, Germany

Tilmann Beck Institute of Materials Science and Engineering, RPTU Kaiserslautern, Kaiserslautern, Germany

Raphael Bilz Institute of Computational Physics in Engineering, RPTU Kaiserslautern, Kaiserslautern, Germany

Bastian Blinn Institute of Materials Science and Engineering, RPTU Kaiserslautern, Kaiserslautern, Germany

Mustafa Bozoglu Institute of Particle Process Engineering, RPTU Kaiserslautern, Kaiserslautern, Germany

Kristin M. de Payrebrune Institute of Computational Physics in Engineering, RPTU Kaiserslautern, Kaiserslautern, Germany

Stella Diederichs Institute of Materials Testing, RPTU Kaiserslautern, Kaiserslautern, Germany

Dietmar Eifler Institute of Materials Science and Engineering, RPTU Kaiserslautern, Kaiserslautern, Germany

Matthias Eifler Institute of Measurement and Sensor Technology, RPTU Kaiserslautern, Kaiserslautern, Germany

Flavien Foko Foko Institute of Machine Elements, Gears and Tribology, RPTU Kaiserslautern, Kaiserslautern, Germany

Nafiseh Ghavidel Institute of Materials Testing, RPTU Kaiserslautern, Kaiserslautern, Germany

Kevin Gutzeit Institute of Manufacturing Technology and Production Systems, RPTU Kaiserslautern, Kaiserslautern, Germany

Hans Hasse Institute of Engineering Thermodynamics, RPTU Kaiserslautern, Kaiserslautern, Germany

Julian Hering-Stratemeier Institute of Optical Technologies and Photonics, RPTU Kaiserslautern, Kaiserslautern, Germany

Martin T. Horsch Institute of Computer Science, Norwegian University of Life Sciences (NMBU), As, Norway

Andrej Keksel Institute of Measurement and Sensor Technology, RPTU Kaiserslautern, Kaiserslautern, Germany

Eberhard Kerscher Institute of Materials Testing, RPTU Kaiserslautern, Kaiserslautern, Germany

Sonja Kieren-Ehse Institute of Manufacturing Technology and Production Systems, RPTU Kaiserslautern, Kaiserslautern, Germany

Benjamin Kirsch Institute of Manufacturing Technology and Production Systems, RPTU Kaiserslautern, Kaiserslautern, Germany

Katja Klauer-Dobrowolski Institute of Manufacturing Technology and Production Systems, RPTU Kaiserslautern, Kaiserslautern, Germany

Michael Kopnarski Institute of Surface and Thin Film Analysis (IFOS), Kaiserslautern, Germany

Fabian Krull Institute of Particle Process Engineering, RPTU Kaiserslautern, Kaiserslautern, Germany

Charlotte Kuhn Faculty of Engineering Design, Production Engineering and Automotive Engineering, Universität Stuttgart, Stuttgart, Germany

Kristin E. J. Kühl Institute of Optical Technologies and Photonics, RPTU Kaiserslautern, Kaiserslautern, Germany

Kai Langenbach Institute of Thermal Process Engineering, University of Innsbruck, Innsbruck, Austria

Balázs Magyar Institute of Sustainable Materials, Processes and Products, University of Paderborn, Paderborn, Germany

Tobias Mayer Institute of Manufacturing Technology and Production Systems, RPTU Kaiserslautern, Kaiserslautern, Germany

Dominik Meffert Institute of Machine Elements, Gears, and Tribology, RPTU Kaiserslautern, Kaiserslautern, Germany

Rolf Merz Institute of Surface and Thin Film Analysis (IFOS), RPTU Kaiserslautern, Kaiserslautern, Germany

Kai Muffler Bingen University of Applied Sciences, Bingen, Germany

Ralf Müller Institute of Mechanics, Technical University of Darmstadt, Darmstadt, Germany

Christine Müller-Renno Institute of Physics and Biophysics of Complex Interfaces, RPTU Kaiserslautern, Kaiserslautern, Germany

Isabell Noichl Institute of Micro Fluid Mechanics, RPTU Kaiserslautern, Kaiserslautern, Germany

Manuel Oehler Institute of Machine Elements, Gears, and Tribology, RPTU Kaiserslautern, Kaiserslautern, Germany

Pascal Ostermayer Institute of Materials Science and Engineering, RPTU Kaiserslautern, Kaiserslautern, Germany

Thomas Palmer Fraunhofer Institute of Industrial Mathematics (ITWM), Kaiserslautern, Germany

Siegfried Ripperger Institute of Particle Process Engineering, RPTU Kaiserslautern, Kaiserslautern, Germany

Lukas Rüth Institute of Machine Elements, Gears and Tribology, RPTU Kaiserslautern, Kaiserslautern, Germany

Bernd Sauer Institute of Machine Elements, Gears and Tribology, RPTU Kaiserslautern, Kaiserslautern, Germany

Andrea Schmecke Institute of Bioprocess Engineering, RPTU Kaiserslautern, Kaiserslautern, Germany

Clarissa Schönecker Institute of Micro Fluid Mechanics, RPTU Kaiserslautern, Kaiserslautern, Germany

Jörg Seewig Institute of Measurement and Sensor Technology, RPTU Kaiserslautern, Kaiserslautern, Germany

Marek Smaga Institute of Materials Science and Engineering, RPTU Kaiserslautern, Kaiserslautern, Germany

Fábio J. P. Sousa Federal University of Rio Grande do Norte, Natal, Brazil

Simon Stephan Institute of Engineering Thermodynamics, RPTU Kaiserslautern, Kaiserslautern, Germany

Judith Stiefelmaier Institute of Bioprocess Engineering, RPTU Kaiserslautern, Kaiserslautern, Germany

Dorina Strieth Institute of Bioprocess Engineering, RPTU Kaiserslautern, Kaiserslautern, Germany

David Strohner Institute of Particle Process Engineering, RPTU Kaiserslautern, Kaiserslautern, Germany

Stefan Thielen Institute of Machine Elements, Gears and Tribology, RPTU Kaiserslautern, Kaiserslautern, Germany

Roland Ulber Institute of Bioprocess Engineering, RPTU Kaiserslautern, Kaiserslautern, Germany

Herbert M. Urbassek Institute of Computational Material Science, RPTU Kaiserslautern, Kaiserslautern, Germany

Georg von Freymann Institute of Optical Technologies and Photonics, RPTU Kaiserslautern, Kaiserslautern, Germany;
Fraunhofer Institute of Industrial Mathematics (ITWM), Kaiserslautern, Germany

Erik von Harbou Institute of Reaction and Fluid Process Engineering, RPTU Kaiserslautern, Kaiserslautern, Germany

Erik H. Waller Institute of Optical Technologies and Photonics, RPTU Kaiserslautern, Kaiserslautern, Germany;
Fraunhofer Institute of Industrial Mathematics (ITWM), Kaiserslautern, Germany

Stefan Wolke Institute of Materials Science and Engineering, RPTU Kaiserslautern, Kaiserslautern, Germany

Ahmed Zayed Institute of Bioprocess Engineering, RPTU Kaiserslautern, Kaiserslautern, Germany

Tong Zhu Institute of Materials Science and Engineering, RPTU Kaiserslautern, Kaiserslautern, Germany

Christiane Ziegler Institute of Physics and Biophysics of Complex Interfaces, RPTU Kaiserslautern, Kaiserslautern, Germany

Sebastian Zimmermann Institute of Micro Fluid Mechanics, RPTU Kaiserslautern, Kaiserslautern, Germany

Manufacturing–Morphology–Property (MMP) Relationships: Concept and Application to Component Surfaces



Jan C. Aurich and Hans Hasse

1 The Concept of MMP Relationships

Manufacturing–Morphology–Property Relationships (MMP) is a broadly applicable concept that has been pioneered, applied, and successfully validated in the research carried out in CRC 926. MMPs combine the complex relationships between the component manufacturing, the component’s morphology, and the component’s behavior into a single coherent concept. Hereby, they address two fundamental problems of mechanical engineering: How can a component with desired properties be designed, and how can it be manufactured?

In an MMP, the link between the manufacturing and the properties of the component is established by the component’s morphology. The term morphology is used in many different ways, often only to refer to the form and shape of an object. We use it in a much broader sense, following ideas of *Fritz Zwicky*, an astrophysicist: according to Zwicky, studying the morphology of an object (usually a complex one) refers to studying diverse properties of that object, and combining the results to a holistic picture, considering also interactions of the object with its environment.

A basic scheme of an MMP is depicted in Fig. 1, where the arrows indicate the relationships, which lead either from the manufacturing to the properties or in the reverse direction, from desired properties to a suitable manufacturing process, i.e., the relationships described by MMPs are bijective. MMPs can be derived from experimental investigations, from modeling and simulation studies, and—of course—from combinations of both. The way in which the description of the relationships is done is thereby left open; it does not need to be mathematical. An MMP does not neces-

J. C. Aurich
Institute of Manufacturing Technology and Production Systems, RPTU Kaiserslautern,
Kaiserslautern, Germany

H. Hasse (✉)
Institute of Engineering Thermodynamics, RPTU Kaiserslautern, Kaiserslautern, Germany
e-mail: hans.hasse@rptu.de



Fig. 1 Scheme of Manufacturing–Morphology–Property Relationships (MMPs) for mechanical components as they are studied in the present book. The arrows indicate the relations, which lead either from the manufacturing to the properties or in the reverse direction, from desired properties to a suitable manufacturing process

sarily claim to represent all existing relationships, the goal is rather to capture the essential relationships for the studied case. This implies that also the morphological features that have to be considered to link both ends of the chain depend on the application—but they do not depend on the direction in which the MMP is used.

There are different types of MMPs: *Specific MMPs* lead from a specific manufacturing process to the properties of a given component (i.e., from left to right in Fig. 1), or, vice versa, from a certain set of property requirements for a component to a suitable manufacturing process (i.e., from right to left in Fig. 1). In the same bidirectional way, *Generalized MMPs* relate classes of manufacturing process to classes of component properties via morphological features. In general, MMPs refer to real-world manufacturing processes, components, and their properties. However, the concept can also be extended to the virtual world, where it refers to models of components, their manufacturing, and their properties.

2 Component Surfaces

In CRC 926, MMPs were applied to component surfaces. Hereby, the term component surface comprises much more than just the geometric surface: it also includes the boundary zones on both sides of the geometric component surface, cf. Fig. 2. The concept of boundary layers is well known from fluid mechanics. The idea behind this concept is to divide the object under scrutiny (the flow field in fluid mechanics) into a region that can be described by established methods (the bulk), and another region that requires special attention (the boundary layer). We adopt this viewpoint here and apply it to both sides of the geometric component surface: in the boundary zone on the component side, the material differs from the bulk. The same holds on the other side, where the component comes into contact with its environment, which is usually a fluid, but could be also another solid body—or both, as it is, e.g., the case in lubricated tribological contacts.

The width of these boundary zones on both sides of the geometric surface depends on the application and is typically on the microscale. This is why microscale phenomena are so important for developing MMPs of component surfaces, and why the microscale is explicitly mentioned in the title of CRC 926. Investigations of microscale phenomena pose special challenges, as on the one side, the area is

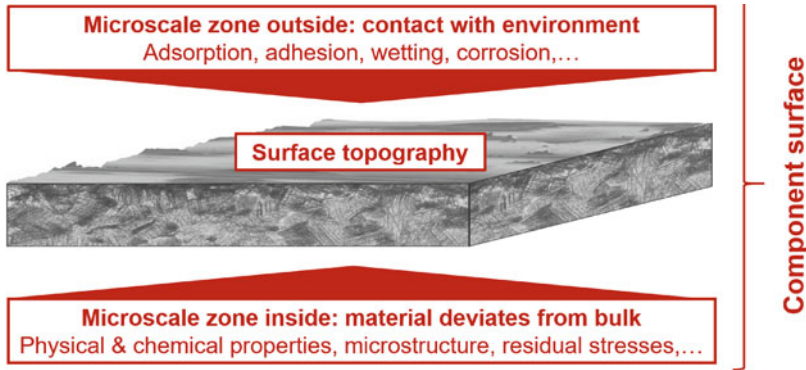


Fig. 2 Scheme illustrating the term component surface as it is used in this book. It includes the microscopic near-surface zones on the inside and outside of the component

generally too large to be studied with atomistic resolution, but, on the other side, lumping, as it is usually done in macroscopic studies, may be an over-simplification.

The morphology of the so-defined component surface (including the adjacent microscopic regions) comprises many highly interrelated features. They obviously include much more than the topography of the surface: on the component side, essential features are the physical and chemical material properties, the microstructure, and the residual stresses, which may all deviate from the bulk values. On the outer side of the component, the morphologic features include adsorption, adhesion, wetting, corrosion, triobologic layers, etc. Together, they define the function-determining properties of the component surface.

3 Studies of MMPs of Component Surfaces in CRC 926

In CRC 926, MMPs that focus on component surfaces were studied—which is particularly challenging, as much less is known on the properties of component surfaces than on their bulk properties. A general scheme of MMPs of component surfaces is shown in Fig. 3. In such MMPs, the microscale morphology of the component surface plays the central role. This is why manufacturing methods that allow to flexibly

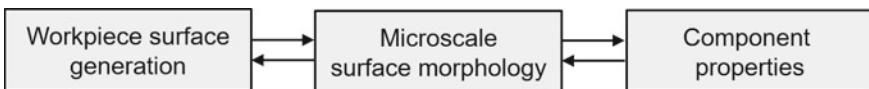


Fig. 3 Scheme of Manufacturing–Morphology–Property Relationships (MMPs) of component surfaces

create desired microscale morphologies of component surfaces were of paramount interest in CRC 926.

For deriving MMPs, in CRC 926 both experimental methods as well as modeling and simulation were applied—and often both approaches were combined. The manufacturing methods that were used, studied, and improved in CRC 926 include additive manufacturing by laser lithography, cold spraying, grinding, milling, lapping, and turning. Also micro-milling and micro-grinding were applied, as well as cryogenic cutting techniques. A variety of methods were used to study the microscale morphology of the manufactured components experimentally, including atomic force microscopy (AFM), coherence scanning interferometry (CSI), confocal microscopy, ellipso height topometry, electron backscatter diffraction (EBSD), nano-indentation, optical coherence tomography (OCT), polarized light microscopy, scanning electron microscopy (SEM), scanning tunneling microscopy (STM), transmission electron microscopy (TEM), X-ray diffraction (XRD), and X-ray photoelectron spectroscopy (XPS). In practically all studies, several of these experimental methods were combined to create a morphologic picture of the component surface. The component properties that were studied in CRC 926 include fatigue behavior (including very-high cycle fatigue, VHCF), friction coefficient, geometric properties, hardness (including cyclic hardening and micro-hardness), monotonic stress–strain behavior, position of crack initiation sites, reaction to particle impact, residual stresses, wear, tensile strength, and wetting properties.

Different levels of modeling and simulation were applied. Thereby, the focus was on the microscopic near-surface regions on both sides of the interface (cf. Fig. 2) but also manufacturing processes and application properties were simulated. The techniques that were used include molecular dynamics (MD), phase-field (PF) modeling, finite element methods (FEM), and computational fluid dynamics (CFD). A wide range of applications was considered, in which component surfaces are of prime importance. Examples stem, among others, from the following application fields: banknote printing, calibration standards, chain joints, film bioreactors, rolling bearings, and rotating shaft sealings.

4 Example: Cryogenic Turning for Improved Component Hardness

Examples of MMPs can be found throughout this book. We therefore limit ourselves here to a brief description of a single MMP that relates the cryogenic turning of austenitic steel to applications of components where the hardness of the component surface is important.

In this MMP, the key is the deformation-induced transformation of the metastable austenitic microstructure in the surface-near zone of a shaft to a martensitic microstructure during cryogenic turning (see Fig. 4). The phase transformation is the result of a deliberate application of high mechanical loads onto the component

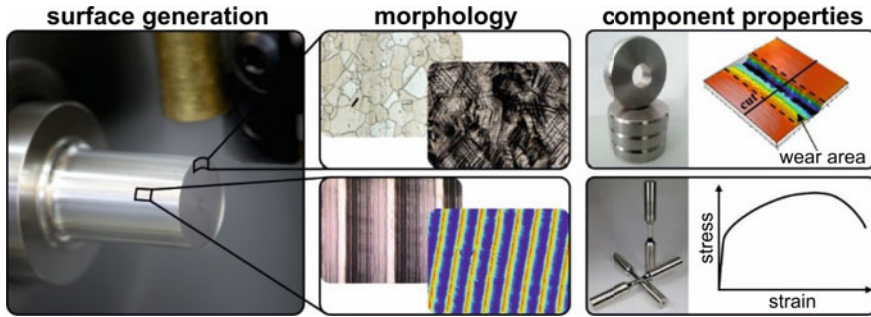


Fig. 4 MMP relating cryogenic turning of austenitic steels to the component hardness. Here, the key element is the microstructure of the surface-near zone, which may change from austenitic to martensitic

surface when turning. As the phase transformation in metastable steels only takes place in a certain low-temperature range, a powerful cooling system is necessary during turning of the components.

As a result of the high mechanical loads during cryogenic turning, a near-surface zone is generated whose morphology is characterized by a partial phase transformation of the soft austenite into significantly harder martensite. This leads to a significant hardening of the near-surface areas of the component and significant changes in the residual stress state.

To achieve a detailed understanding of this process, atomistic simulations, continuum mechanical modeling, and experimental investigations of the austenite–martensite phase transformation have been carried out. Furthermore, suitable process parameters for the generation of deformation-induced martensite during the turning of metastable austenitic steels have been determined and, finally, the influence of martensitically transformed component edge zones on the component properties has been comprehensively evaluated. Using fatigue and wear resistance analyses, the improvement of the mechanical component properties could be quantified. The established MMPs characterize these relationships and will help in future to design the cryogenic turning process according to the required component function.

5 Conclusions

This chapter provides both a brief general introduction to Manufacturing–Morphology–Property Relationships (MMPs) as well as an introduction to the work described in the present book, that focuses on component surfaces, which are crucial for the function and the application behavior of components.

In CRC 926, the relationships between the generation of the component surface, its microscale morphology, and the component properties were investigated. These MMPs of component surfaces have been worked out by an interdisciplinary team

of researchers from mechanical engineering, process engineering, and physics. As a result, many MMPs are now available, which allow a requirement-oriented design of manufacturing processes for a specific component function and describe the component behavior as a function of the manufacturing process. These MMPs are, thus, a means to better understand and design manufacturing processes, components, and in the end, complete products.

The research on which we give report in this book has yielded many building blocks for constructing a systematic theory MMPs of component surfaces—however, it is still a long way to create such a theory. This leaves ample room, and calls, for more research on this important topic. The concept of MMPs has proven to be fruitful throughout the work of CRC 926. MMPs are not only a goal of research but also give guidelines to tackle problems, to organize studies, and to analyze their results—both in scientific research and in applications. With this book, we aim at sharing our positive experience with the concept of MMPs with others.

Fundamentals and Technologies

Geometrical, Microstructural, and Chemical Characterization



Michael Kopnarski, Tilmann Beck, Stella Diederichs, Eberhard Kerscher,
Jörg Seewig, and Marek Smaga

Abstract The chapter presents work on the geometric, structural, and chemical analysis of microscale surface structures. In the first part, the focus is on the technical and methodological developments themselves. Techniques as well as technical and methodological developments for the geometric characterization of surfaces, including the associated measuring instruments, data evaluation, and the characterization methods, are discussed. Furthermore, some special methods for the microstructural analysis of surface morphologies, in particular, with optical methods and by means of X-ray diffraction, are presented. The second part of this chapter deals with the application of microscopic, spectroscopic, and mass spectrometric techniques to characterize surfaces subjected to friction and wear. It is shown which information can be obtained with the methods mentioned and it is shown exemplarily how, on the one hand, technologies that have been developed for analysis can be used to generate defined surface structures. On the other hand, special microscopic surface structures have been developed that can also be used beneficially for the investigation of tribological processes.

M. Kopnarski (✉)
Institute of Surface and Thin Film Analysis (IFOS), Kaiserslautern, Germany
e-mail: kopnarski@ifos.uni-kl.de

T. Beck · M. Smaga
Institute of Materials Science and Engineering, RPTU Kaiserslautern, Kaiserslautern, Germany

S. Diederichs · E. Kerscher
Institute of Materials Testing, RPTU Kaiserslautern, Kaiserslautern, Germany

J. Seewig
Institute of Measurement and Sensor Technology, RPTU Kaiserslautern, Kaiserslautern, Germany

1 Geometrical Characterization Methods for Microscale Surface Morphologies

1.1 Introduction

The surface texture of a component is defined as geometrical irregularities contained in a scale-limited surface [1]. The surface texture has a dominant influence on the functional behavior of a component. Examples investigated in the CRC 926 are: tribologically stressed contact surfaces, such as sealing surfaces or sliding surfaces or the growth of biofilms. However, surface texture characterization can also be used to assess the manufacturing process of a component and its surface, because surface texture is the fingerprint of the manufacturing process. For many decades, the geometric characterization of surfaces has been performed using profile sections. Well-known parameters are R_a , the arithmetic mean height, and R_z , the maximum height, which are used worldwide in development and research. Both are standardized in ISO 21920, Part 2 [1] which has replaced the former ISO 4287 [2]. The information content of surface texture represented by a profile trace is limited. Therefore, areal-based measurements are increasingly being carried out with the aid of optically measuring instruments. Parameters for areal characterization of surface texture are standardized in ISO 25178, Part 2 [3], which includes the well-known “Birmingham 14” (for example, S_a , S_q , S_z) introduced in 1993 as the “Blue Book” [4]. Many parameters have been transferred from the profile case to the areal case without considering the high potential of areal-based measurements.

The measuring chain for both, the profile and areal characterization, is shown in Fig. 1. The measuring chain starts with the measurement of the surface. Both tactile and optical instruments are available. Their properties and calibration are described in the ISO 25178-60X and ISO 25178-70X series. Recently, scanning force microscopes have also been used. Section 1.2 describes optical measurement devices that were analyzed and further developed within the CRC 926. After the measurement, the data set has to be pre-processed. In case of tactile measurements, a morphological erosion is applied. When using optical measuring devices, there are occasionally unmeasured points that have to be interpolated. Reason for the unmeasured points is the complex physical interaction between the surface and the optical measurement principle used. Interpolation algorithms are available. However, for an anisotropic surface texture, the interpolation results are often insufficient.

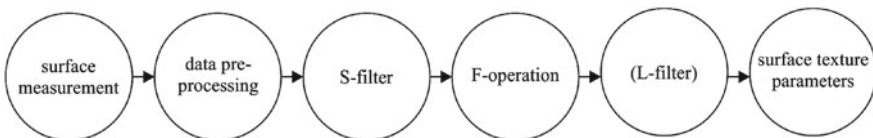


Fig. 1 Measuring chain for the geometrical characterization of surface texture

Therefore, a new interpolation technique was developed in the CRC 926, which is introduced in Sect. 1.3.1. After interpolation, a low-pass S-filter (default is a Gaussian filter according to the ISO 16610 series) ensures that the data set is band-limited (scale-limited) to compensate the different transmission characteristics of different measuring devices. The following F-operation removes the nominal shape of a component from the measured data. Usually, the least-squares method is used to fit the nominal shape to the data set. In the CRC 926, a new approach was taken using Bayes statistics, which is described in Sect. 1.3.2. The fitting algorithm was improved by incorporating prior knowledge into the evaluation procedure. After F-operation, an optional high-pass filter is then applied to extract the surface texture (roughness). For this purpose, the ISO 16610 series provides a toolbox with a wide range of different filters. In a final step, surface texture parameters are calculated. The parameters can be separated into height parameters, hybrid parameters, and structure-oriented parameters. For the latter parameters, a new structure-oriented evaluation method based on the watershed transform was introduced in the CRC 926 to analyze a surface structured with TiO₂ microparticles. Results are shown in Sect. 1.4.1. In addition, a new approach was taken to characterize an abrasive manufacturing process using machine learning which is discussed in Sect. 1.4.2.

1.2 Areal Measuring Instruments

One of the most common measurement techniques for optically measuring three-dimensional topographies of technical surfaces is confocal microscopy. The key of this measuring principle is the prior filtering of out-of-focus light from detection by a pinhole which is located in front of the detector. Surface topography is reconstructed by analyzing the pixel-wise intensity curves extracted from the underlying image stack. In the CRC 926, a new evaluation approach was developed and presented in [5] where the spectrum of the confocal curves is analyzed by applying Fourier transform and thus performing signal processing in the frequency domain. Applying this approach, disturbances in the signal that are identified as high-frequency oscillations can easily be removed and, based on the Fourier transform properties, the shift of the confocal curve and thus the sample surface height value can be determined.

Besides the confocal technique, one of the most popular optical principles for measuring surface topography in the nanometer range is Coherence Scanning Interferometry (CSI) using a broadband light source in combination with the basic principles of interferometry (also known as white light interferometry). By using broadband light, a small coherence length in the sub- to single-digit μm range is obtained. The resulting signal is called a correlogram and can be assigned to the height of the sample surface. One field of application in which CSI systems are frequently used is the measurement of surface roughness. Component surfaces are not always optically cooperative. As a result, measured signals are commonly distorted in reality. In the CRC 926 (see [6]) it is shown that the evaluation of distorted correlograms is challenging as it generally leads to increased uncertainty and can be described by

Cramér–Rao bounds. Therefore, possible improvements of established methods for calculating envelopes using a mathematical measurement model are presented.

Another challenge in CSI is artifacts caused by material contrasts on the surface due to the physical interaction between light and matter. Ellipso-Height-Topometry is based on the principle of white light interferometry, but in addition to the topographic information, it also allows material-specific ellipsometric angles to be measured, with the help of which material-specific artifacts can be compensated. In the CRC 926 (see [7]), the development of the required measurement standards and the calibration strategy for this novel instrument are presented and described in detail. Approaches for calibrating ellipsometric measurements as well as standards with defined material changes are introduced. Later, these standards are applied to verify the height correction of material-specific height distortions. Finally, a standard containing lateral material contrast is developed to characterize the lateral material resolution. Overall, three newly designed calibration standards for material-specific calibration were developed: a plane standard with an aluminum coating, a nanostructured standard with uniform spacing of aluminum on silicon, and a nanostructured standard with aluminum spacing on silicon with decreasing spacing length.

1.3 Data Pre-processing and F-Operation

1.3.1 Interpolation of Non-measured Points by Kriging

The areal measurement of component surfaces is carried out optically due to the fast and non-contact data acquisition with high resolution. Established measurement principles are focus variation, coherent scanning interferometry, and confocal microscopy. The complex interaction between the optical wave front and the component surface is described by the Maxwell's equations. Significant quantities influencing the quality of the topography reconstructed from the optical information are: the surface reflectivity, the complex refraction index of the surface material, and steep slopes of surface structures. Various research projects have dealt or are dealing with the influence of surface structures and the material on the quality of the reconstruction of the topography [8, 9]. Due to the described relationships, non-measured points occur with optically measured component surfaces. An example for non-measured points is shown in Fig. 2 on the left. The topography height is coded as a colormap. In this case, steep edges on the surface topography resulted in non-measured points, which are marked in white. In particular, these areas must be suitably filled for the parameter calculation because the algorithms used require an equidistant measuring grid without missing data points. For the calibration of a measuring device, this step is not necessary. For the filling of the non-measured data interpolation methods are used. The result for such an interpolation is shown in Fig. 2 on the right. Data points have been estimated for the non-measured areas.

A number of different interpolation methods are available: nearest neighbor, Delaunay triangulation, linear polynomial interpolation, spline interpolation, inverse

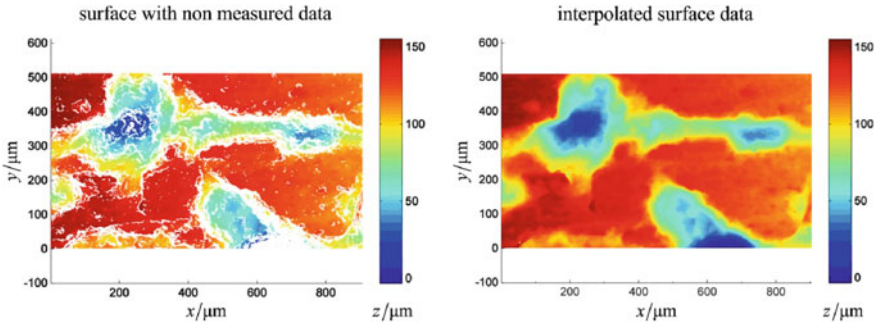


Fig. 2 Interpolation of non-measured data: On the left, data set with non-measured points (white areas). On the right, the interpolated surface data set

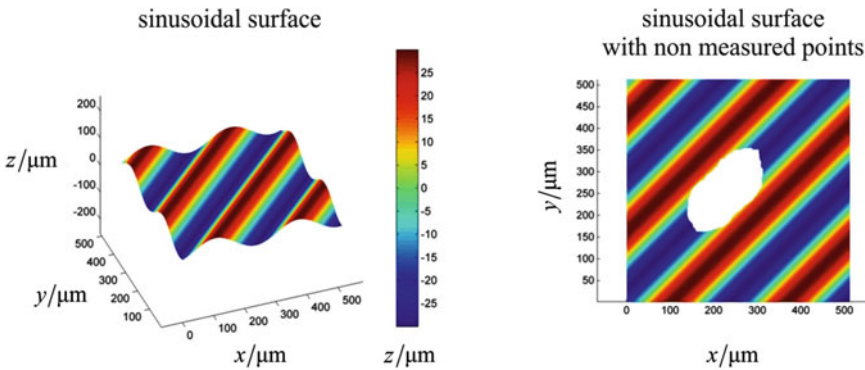


Fig. 3 Simulated sinusoidal surface as an example for an anisotropic structure orientation. Measurement points were removed in the center of the surface (white areas)

distance to a power, radial basis function, etc. Engeln et al. [10] give an overview of the different interpolation methods. One problem of the described algorithms is that certain surface structures, such as grooves, are distorted, for example, by closing the grooves. Interpolation often does not take into account a structure direction on the surface. To overcome this problem, a new interpolation method was introduced in the CRC 926, the Kriging method, which is described in detail by Raid et al. [11]. Figure 3 shows a surface with an anisotropic surface structure simulated by a sinusoidal wave front (see left side of the figure). Measurement points in the center of the surface were removed (see right side of the figure) to demonstrate the advantages of the Kriging method compared to other interpolation methods.

The result of the Kriging interpolation method is shown on the left side of Fig. 4. As can be seen, the wave front structure has been preserved. The result of the inverse distance to a power interpolation method (as an alternative algorithm) is shown on the right side of Fig. 4. This method is not able to take into account a structure direction on the surface. In an environment with radius R of the height to be interpolated,

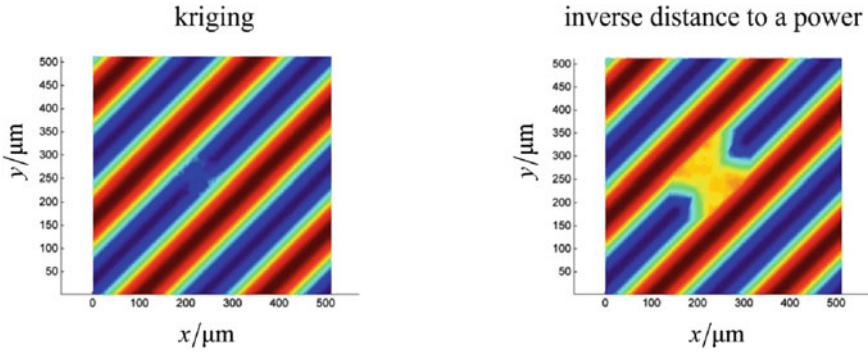


Fig. 4 Interpolation of the simulated sinusoidal surface. On the left, interpolation by Kriging. On the right, interpolation by an inverse distance to a power

a weighted mean is calculated. This results in the structure being interrupted by a material bridge at this point. With the introduced Kriging method, this effect does not occur because the weighting is done depending on the structure direction.

1.3.2 F-operation Based on Bayesian Analysis of Uncertainties in Circle, Straight Line, and Ellipse Fitting Considering A Priori Knowledge

Motivation

Fitting of geometric standard elements such as circles, straight lines, or ellipses into a set of measurement data is routinely used in many technical applications, e.g., in order to quantify form deviations between measured data and an underlying nominal geometry or for applying the F-operation according to ISO for the analysis of surface textures. Thus, the use of geometric fitting algorithms is also common in manufacturing metrology, since consideration and removal of an underlying nominal shape of a measuring object is an indispensable first step in roughness evaluation and thus is included in the corresponding standardization of roughness measurement [12]. Hereby, the most typical nominal shapes to be fitted are straight lines or circles. Typically, the parameters of fitted geometry elements are estimated using least-squares or total-least-squares methods [13]. However, often a priori knowledge from former measurements, of the measuring equipment, or regarding the uncertainty of the parameters to be estimated could be achieved. To this day, this information usually remains unused [13]. This can lead to the fact that tolerances required in production cannot be confirmed on the basis of pure measurement data in some cases and/or manufactured workpieces are incorrectly declared as rejects. One concept to combine fundamentally different types of information, like measurement data and prior knowledge, is by using Bayesian analysis [14–19]. The theory is universally applicable to most measurement data evaluation tasks, including complex nonlinear

adjustments and cases where established least-squares approaches fail [18]. Within the CRC 926 the Bayesian approach was initially investigated in the context of uncertainties that arise when fitting circular segments into (poor) measurement data sets considering a priori knowledge [20]. Afterward, this approach was extended to fit straight lines and ellipses as well in order to generally qualify for being implemented into the F-operation routine in surface texture analysis. The assessment regarding practical suitability of respective approaches is discussed below.

The Bayesian Approach

Bayesian analysis is based on a mathematical relationship that couples fundamentally different categories of information: measurement data and prior knowledge. This coupling is done by modeling several conditional Probability Density Functions (PDF) that can be linked to each other according to Bayes’ theorem [21]:

$$f_{\text{post}}(\theta|\eta) = \frac{f_{\text{like}}(\eta|\theta) \cdot f_{\text{prior}}(\theta)}{\int_{-\infty}^{\infty} f_{\text{like}}(\eta|\theta) \cdot f_{\text{prior}}(\theta) d\theta} = C_{\text{post}} \cdot f_{\text{like}}(\eta|\theta) \cdot f_{\text{prior}}(\theta). \quad (1)$$

By evaluating the **a posteriori** PDF $f_{\text{post}}(\theta|\eta)$, resulting parameter estimates as well as corresponding uncertainties can be determined considering information obtained by measurement data as well as several types of prior knowledge. According to Eq. 1, the a posteriori arises by combining PDFs that are easier to formulate. These PDFs are called **likelihood** and a **priori** PDF. The **likelihood** $f_{\text{like}}(\eta|\theta)$ contains information obtained by measurement data processed in a corresponding measurement model, whereby prior knowledge of the measurands of interest, etc. is contained in the **a priori** PDF $f_{\text{prior}}(\theta)$. Combining likelihood and a priori PDFs leads to the formulation of the a posteriori PDF, wherefore this PDF can be seen as carrier of the entire information available, see Fig. 5.

Here, exemplary models for likelihood and a priori PDFs used in literature [13, 14, 17] are adopted. To model $f_{\text{like}}(\eta|\theta)$, the underlying measurement model must first be defined by formulating a functional relationship between acquired measurement data η , model parameters θ to be fitted, and presumed measurement deviations ξ . A common assumption used here is that the measurement deviation follows a

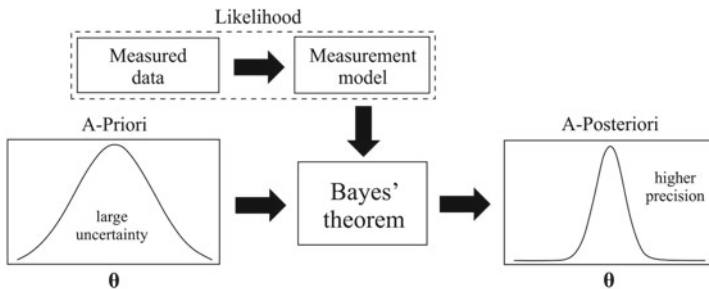


Fig. 5 Relationship of likelihood, a priori and a posteriori PDFs in context of Bayesian analysis

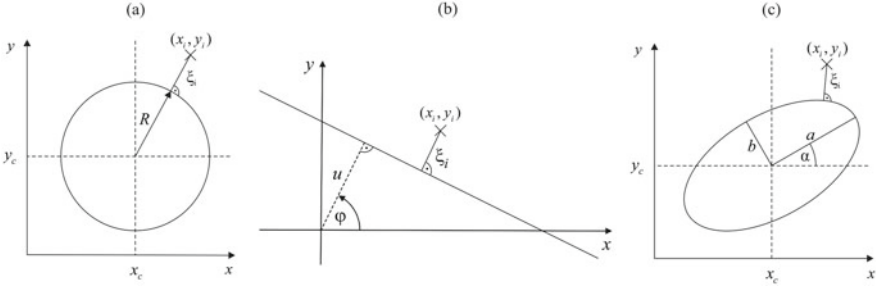


Fig. 6 Relationship of measured data points and ideal **a** circle, **b** straight line, and **c** ellipse to be fitted

multivariate Gaussian distribution $\xi \sim N(0, \sigma^2)$. In order for information from measurement data to be coupled with prior knowledge about the model parameters, in this study, it is exemplary assumed that prior knowledge, expressed as $f_{\text{prior}}(\theta)$ PDF, is Gaussian distributed as well, which is adopted from [13, 14].

Application in Circle, Straight Line, and Ellipse Fitting

The measurement models used for fitting circles, straight lines, and ellipses are based on the orthogonality relationship between measured data points (x_i, y_i) and the ideal geometry to be fitted (see Fig. 6). This modeling approach corresponds to the well-established total-least-squares fitting approach [22].

Since the measurement models are nonlinear, these tasks are not analytically solvable. Thus, numerical methods must be applied to fully evaluate the a posteriori PDF [13, 14]. Numerical methods suitable for evaluation include numerical quadrature or Monte Carlo methods. Quadrature methods are suitable for numerical integration tasks of low order (dimensions $D \leq 3$) [23]. To solve integrals of higher order (dimensions $D \geq 3$) numerically, Monte Carlo methods are usually preferred [23].

To investigate the extent to which potential prior knowledge might influence resulting uncertainties, scattered measurement data sets for different cases were simulated and evaluated using Bayesian analysis. The findings are summarized in Table 1.

Circle: The determined fitting variances strongly depend on the quality and quantity of measurement data. If the measurement data represent just a small circular segment, the variances of the estimated circle parameters grow large. As the measured circular segment increases, the variances decrease sharply. It was shown that prior knowledge in case of evaluating small circular segments has a much greater influence on the determined uncertainty than evaluating measurements of larger circular segments. As a result, large uncertainties can be significantly reduced by including only “little” prior knowledge.

Straight line: Uncertainties in straight line fitting increase with the data basis getting poorer, meaning total segment length and/or number of sample points decreasing. Thus, the influence of prior knowledge applying Bayesian analysis increases with the data basis getting poorer. Further, it was shown that the influence of prior knowledge

Table 1 Summary of methods used and conclusions drawn within this investigation

Metric assessed	Circle	Straight line	Ellipse
Number of parameters to be estimated	3	2	5
Numerical integration method used	Numerical quadrature	Numerical quadrature	5D Metropolis Monte Carlo method
Computational costs	Low/Medium (+ 0)	Low (++)	High (--)
Numerical stability when operating with uncertain data basis	Medium (0)	High (++)	Low (--)
Potential benefit compared to state-of-the-art methods	High (++)	High/Medium (+ 0)	Medium/Low (0 -)

on straight line fitting is only beneficial in cases, where the data basis is very poor and/or strongly scattered.

Ellipse: The determination of ellipse parameter uncertainties requires a multidimensional integration of a 5D PDF. Since numerical quadrature methods are inefficient when solving higher dimensional integrals, the application of alternative methods like Monte Carlo methods is required. Since a circle is a special type of ellipse, the ellipse fitting procedure delivers similar results. The smaller the measured ellipse segment, the more uncertain the fitting results and the greater the potential influence of prior knowledge on the final result. However, in contrast to the circle or straight line fitting procedure, for five ellipse parameters to be evaluated, the computational costs are extremely high and the numerical stability of the evaluation is highly fragile, especially when the measurement data basis is poor and no or just little prior knowledge is available.

In conclusion, Bayesian analysis may offers real benefits compared to the established geometry fitting methods. Since the presented method can also be used in the absence of prior knowledge, it represents an “all-inclusive” method that covers the state-of-the-art method and additionally provides the possibility to include any type of prior knowledge.

1.4 Examples for Surface Texture Characterization Techniques

1.4.1 Structure-Oriented Characterization of TiO₂ Particles

A variety of different parameters are available for the geometrical characterization of component surfaces. They are grouped according to: height parameters, spatial parameters, hybrid parameters, material ratio parameters, parameters for stratified

surfaces, areal material probability parameters, volume parameters, and multi-scale geometric parameters and functions (see ISO 25178-2 [3], Annex F for a comprehensive overview). Examples of applications for this type of evaluation are described, for example, in Leach et al. [24] and the EU project SURFSTAND [25] (which is published as the “Green Book”). In 1996, Paul J. Scott presented a new structure-oriented surface characterization technique [26]. It is based on a method that Wolf used for “for the generalization of the topological structure of topographic surfaces” [27]. The idea was to apply a watershed transform (see Soille [28]) to a measured surface topography to separate hills, saddle points, and dales and to characterize them with regard to their geometric properties (for example, for hills and dales: volume, height, curvature, developed interfacial area ratio, and many more). Weidner et al. [29] extended the methodology to include a marker-based watershed transformation (see Soille [28]). Instead of the measured topography, the authors use the gradient of the topography with the aim to detect the edges of the structural elements on the surface.

With a further adaptation, the evaluation procedure was successfully applied to a component surface investigated in the CRC 926. The surface is structured by a cold spray method in which individual TiO₂ microparticles were dispersed in a stream of nitrogen gas, heated and accelerated through a Laval nozzle to supersonic speeds and hit the surface. This fixes the particles to the surface, as the kinetic energy in the contact zone was converted into heat. A detailed description of this process and the characterization of the particles is given in [30]. This particle-structured surface is shown on the left side of Fig. 7. On the right side of Fig. 7, the extracted TiO₂ microparticles are shown. The following parameters were calculated for the extracted particles: the height, the base area and the volume of the particles, the distance between different particles and the distribution of the particles on the surface. Such a characterization of the surface structures cannot be performed with a standardized evaluation according to ISO 25178-2.

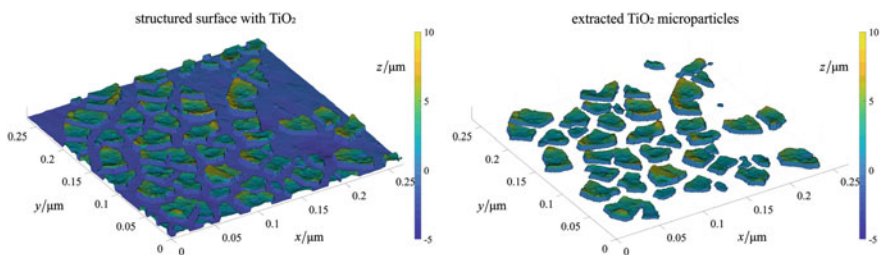


Fig. 7 Left side of the figure: Measured surface structured with TiO₂ microparticles. Right side of the figure: TiO₂ microparticles extracted with the watershed transform

1.4.2 Surface Texture Characterization by Machine Learning

Besides the characterization methods discussed in the section before, also Machine Learning approaches are used to characterize surface morphologies. Rief et al. and Eifler et al. therefore use machine learning approaches to classify manufacturing processes from surface topographies [31, 32]. Based on this research, a case study was conducted in the CRC 926 using a convolutional neural network as a regression model to correlate manufacturing parameters of an abrasive process with the resulting surface topographies [33]. The basic idea of the study is shown in Fig. 8.

For the sample manufacturing, an abrasive process with one layer of dry silicon carbide particles was used, which represents a lapping process without fluid with S235JR steel and 27 different manufacturing parameter combinations. The manufacturing parameters include the grit size of the silicon carbide particles, the normal force, and the feed rate. The samples were measured with a confocal microscope with a $20\times$ magnification, featuring a field of view of $0.8\text{ mm} \times 0.8\text{ mm}$. Multiple measurements are stitched together to form a topography extract with an approximate size of $0.8\text{ mm} \times 13\text{ mm}$.

From these surfaces, profiles are extracted and different representations of these profiles are then used for training. First, profiles from the measured surfaces are used directly. Second, a time series modeling approach, called ARMAse1, is utilized for artificial profile generation from the measured ones. Third, these time-domain data sets are transformed into the frequency domain and used for training the neural network model. Thus, it can be investigated whether the bigger data set size of the artificial surface data set and which of the data representations helps training the model to find nonlinear correlations between the surface topography and the manufacturing parameters.

By comparing the prediction results of the neural networks trained on these different data sets, the authors found that converting the data into their amplitude spectrum

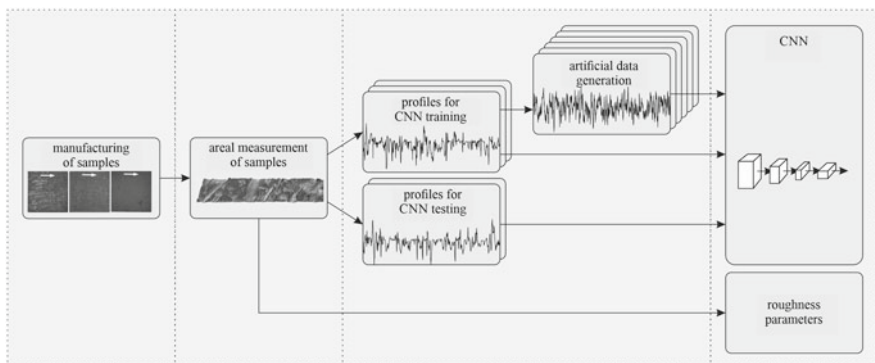


Fig. 8 Convolution neural networks are used for predicting manufacturing parameters of samples. The prediction is compared to a linear correlation between common roughness parameters and the manufacturing parameters. Modified from [33]

for training the neural network helped to better discriminate the grain size parameters and thus predict them better based on surface profiles. Using artificial data for the training did not show a general benefit, but can be beneficial if only sparse data are available.

Finally, the results of the trained neural network models are compared with the linear correlation between commonly used surface roughness parameters and the manufacturing parameters. When the neural network is trained to only predict the grit size, it does it with an accuracy of 91,3 %. When the network is also trained to predict the other two manufacturing parameters, it predicts the grain size with 89 % accuracy, the applied force with 54 %, and the feed rate with 41 %. Compared to the linear correlation of the R-parameters, the neural network could predict the grain size better. The force parameter could only be predicted better with the R_{sm} parameter. The feed rate could not be predicted well with the neural network.

1.5 Summary

As part of the CRC 926, numerous advancements were made in the field of areal optical metrology, including the development of new evaluation strategies, mathematical models, and calibration standards. This section only covers a small selection of the individual sub-projects that were elaborated. An interpolation method was introduced that allows the reconstruction of unmeasured data points considering the direction of the surface structure. Further, a fitting algorithm based on Bayes' theorem was developed to improve the fitting of geometric elements by taking into account a priori knowledge. Based on the watershed method, a new structure-oriented evaluation method for the characterization of particle-structured surfaces was introduced and applied to surfaces with TiO₂ microparticles. Finally, a new machine learning approach for characterizing grinding processes was discussed.

2 Microstructural Characterization Methods for Microscale Surface Morphologies

2.1 Introduction

Metallic materials are composed of individual crystals. Their configurations, such as orientation, phase and size, influence the mechanical properties of the material. For example, a well-known effect is the influence of the grain size on the strength of a material as stated in the Hall–Petch effect [34]. According to which a smaller grain size leads to a higher strength.

The manufacturing of a surface can change the configurations of crystals right below and close to the surface. These changes can subsequently lead to undesired

changes in the material properties and thus the behavior of the part when submitted to different strains, such as fatigue. It is thus crucial to be able to define the crystal configurations to understand and predict certain material behaviors.

In order to define these crystal configurations, different methods are widely used, e.g., etching, light microscopy, Electron Backscatter Diffraction (EBSD), and X-Ray Diffraction (XRD). Polishing and subsequent etching of a sample can be used to determine the grain size. EBSD is used to define the grains' orientations and XRD is used to determine the phase of a crystal.

Within the CRC 926 the above-mentioned methods have been refined and extended in order to explore new applications or to improve previously existing ones. A new application for polarized light microscopy allows to define the crystallographic orientation of α -titanium grains. Moreover, the metallographic preparation method to obtain a cross section of certain steels has been further developed to avoid deformation-induced phase changes. Two XRD methods have been combined for the first time in the CRC 926 to obtain information about the phases in certain steels after a manufacturing process that leads to a nanostructured layer of the material's surface. These new approaches are the subject of this chapter and are explained in detail below.

2.2 Polarized Light Microscopy

To define the crystallographic orientations of grains in a bulk metallic material, Electron Backscatter Diffraction (EBSD) is a well-established method that can be found as an extra detector in an SEM. The characterization of the orientation can be represented by the so-called Euler angles ϕ_1 , Φ , and ϕ_2 [35] that are assigned to each pixel of the EBSD image. So the pixels' and thus the grains' crystallographic orientations with respect to the sample's coordinate system are fully described. However, it is a time-consuming method as it is carried out using an SEM and as it needs a very well-prepared sample surface to work properly. Furthermore, the use of the SEM also limits the sample size and the area that can be analyzed.

The grain orientation in bulk metallic materials with an intrinsic anisotropy in the unit cells, like α -titanium with its hexagonal unit cell, can also be defined using polarized light microscopy by exploiting this anisotropy. In order to do so, a new method has been developed within the CRC 926 to define the orientation of the crystallographic c-axis in commercially pure titanium by combining polarized light images of the material with a subsequent MATLAB code to evaluate the grain orientations.

The phenomenon that can be exploited for this new method is the bireflectance of an incident linearly polarized light beam when reflected from the surface of an optical anisotropic material. After the reflection, the light beam is no longer linearly polarized but elliptically polarized. Depending on the crystallographic orientation and the sample position, the beam is differently elliptically polarized. This is indicated by the different gray values or light intensities when the beam passes through the analyzer which filters the beam again and it becomes once more linearly polarized.

Table 2 Light microscopy settings for PLM; reprinted from [36] with permission from Elsevier

Optical magnification	×2.5
Brightness	10
Exposure time	102.1ms
Gain	×1
Gamma	2.60
Saturation	Auto (1.00)

These different gray values when looked at over the course of a sample rotation reveal enough information about the orientation of the crystallographic c-axis to define the first two Euler angles ϕ_1 and Φ .

Image Acquisition and Gray Value Evolution

For the image acquisition, a Leica DM2700M with a polarizer and an analyzer that can be adjusted separately was used. To obtain a good contrast, the polarizer and analyzer were fixed in a cross position. The further settings used for the image acquisition are summarized in Table 2 [36].

By using gray scale images the individual grains can thus be identified by their different gray values that result from the refraction of the polarized light depending on the grains' orientations. In order to define the orientation of the crystallographic c-axis of the individual grains by polarized light and to define all grain boundaries, the sample has to be rotated from $\gamma = 0^\circ$ to $\gamma = 180^\circ$ in steps of 10° . For each step an image of the area of interest is taken.

The evolution of the gray values for each grain can be identified in the images and can be plotted over the rotation angle of the sample as shown in Fig. 9. The resulting curve can be described by a sine according to Eq. 2 as explained in [36]. In this equation, G_0 describes the average value of the gray value evolution, G_a is the amplitude, and α is the phase shift.

$$G(\gamma) = G_0 + G_a \cdot \sin(2(\gamma - \alpha)). \quad (2)$$

Comparing results obtained by the polarized light method with results from EBSD a correlation between the phase shift α of Eq. 2 and the first Euler angle ϕ_1 and between the amplitude normalized by the average gray value G_a/G_0 and the second Euler angle Φ can be established. These correlations can exemplarily be seen in Fig. 10. They are subsequently used to define the first two Euler angles and thus the orientation of the crystallographic c-axis.

Postprocessing in MATLAB

To identify all grains and the grain boundaries in the area of interest and to define the evolution of the gray values for all grains and thus their orientations, a MATLAB code has been developed. The procedure in this MATLAB code can be summarized in three steps:

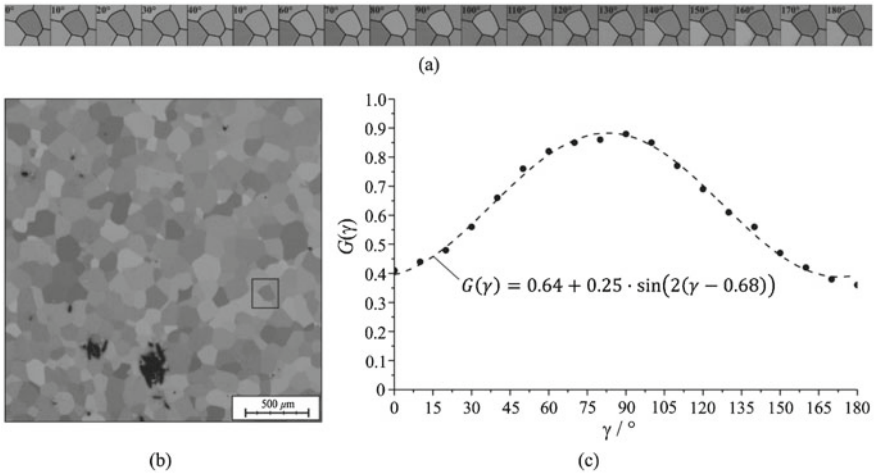


Fig. 9 **a** Change in the gray values of a grain over the sample rotation, **b** position of the grain in the area of interest, and **c** evolution of the gray value plotted over the sample rotation; reprinted from [36] with permission from Elsevier

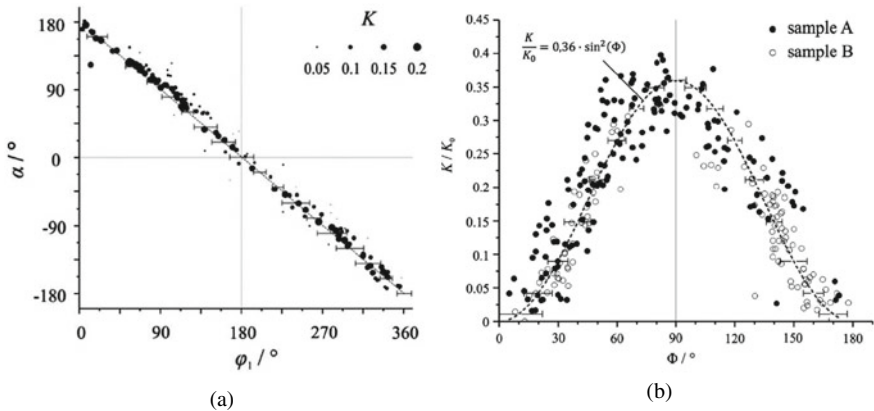


Fig. 10 The first Euler angle correlates with the phase shift **(a)**, the second Euler angle correlates with the normalized intensity **(b)**; reprinted from [36] with permission from Elsevier

1. A superposition of all images that have been taken after virtually rotating all images to $\gamma = 0^\circ$ with a subsequent manual cropping of the area of interest.
2. Definition of the grain boundaries in each individual picture and summing up of all grain boundaries.
3. Calculation of the gray value evolution for each grain in correlation with the sample rotation,

- a. for each grain, where the grains are defined as the areas enclosed by the grain boundaries and
- b. for each pixel in the area of interest.

Summing up the identified grain boundaries from all images as indicated in step two is important to achieve a net of all grain boundaries. As some neighboring grains' gray values may be almost the same in one configuration and different in another configuration, this summing up ensures to identify all grain boundaries.

Whether it is more reasonable to average the gray value evolution over a grains' area or to define the gray value evolution for each pixel, as mentioned in step three, needs to be defined before the process. Both methods offer advantages and disadvantages. Averaging the gray values over a grain reduces, for example, the influence of faulty pixels. Whereas a gray value detection per pixel reduces the influence of not completely recognized grain boundaries.

Eventually the parameters of Eq. 2 can be defined for each grain or pixel and can be correlated to a crystallographic orientation. This is also discussed in further detail in [36].

Results of the Polarized Light Method

With this new method it is thus possible to define the grain boundaries of α -titanium and so identify individual grains [37] and the orientation of the crystallographic c-axis via the first two Euler angles [36].

The polarized light method has been carried out on untextured and textured α -titanium and compared to results from EBSD for the same region [36]. The untextured titanium was also used to calibrate the method with the EBSD results. For both samples, a good agreement between the methods was found as can be seen in Fig. 11. Figure 11 a and b shows the grains' orientations of the untextured α -titanium material from EBSD and PLM, respectively. The sub-images (c) and (d) of Fig. 11 show the results for the textured material for EBSD and PLM, respectively. A good agreement can be found also for the textured materials for both methods. Although for the textured material it was more difficult to define all grain boundaries. This is due to the fact that for textured materials neighboring grains can share similar orientations of the crystallographic c-axis which makes it difficult for them to be separated by the polarized light method.

The polarized light method shows the advantage of a more stable imaging process. Meaning that the quality of the surface does not have such a big influence on the results as it does for EBSD as Morales-Rivas et al. showed in [38].

This new method can thus be used, for example, to easily define grain sizes and texture of hexagonal close packed titanium over larger areas with a relatively low effort. As explained in [38], it should also be possible to define the type of deformation twin occurring in titanium with this new method.

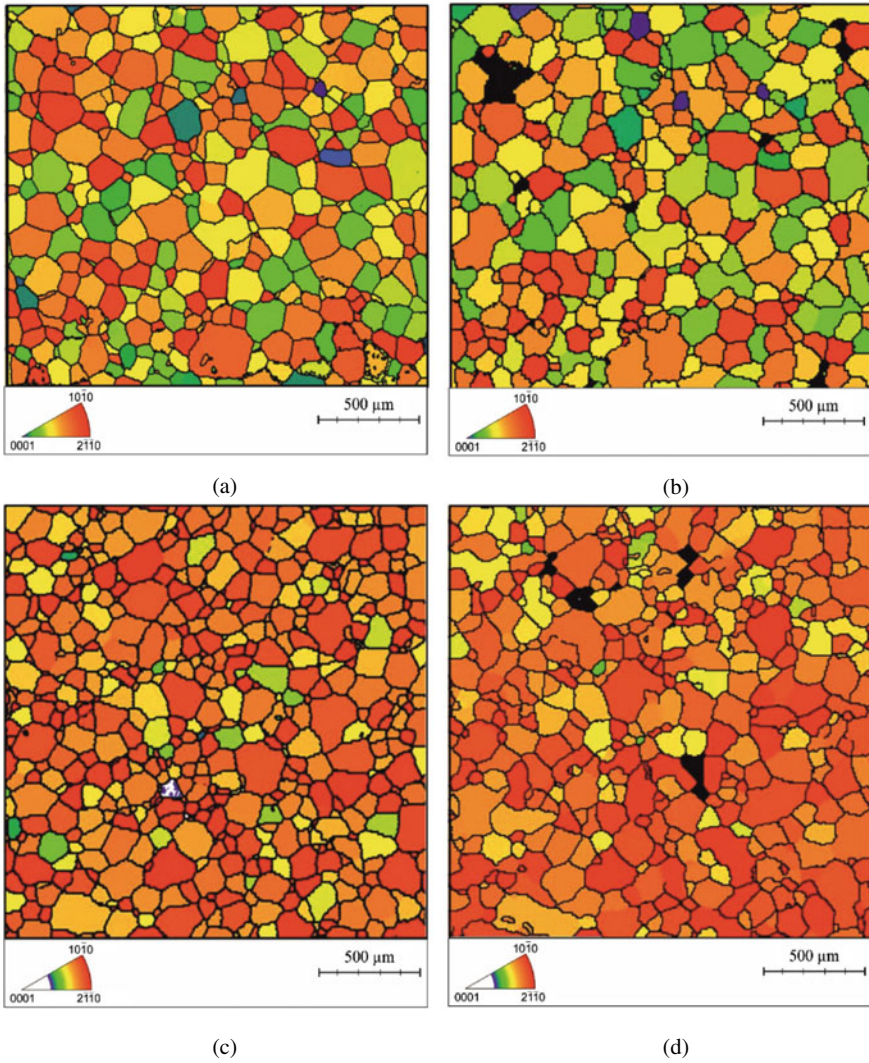


Fig. 11 Color-coded results representing the angle between the crystallographic c-axis of the grains and the rolling direction of the material **a** from EBSD and **b** from PLM for the untextured material and **c** from EBSD and **d** for PLM for the textured material; reprinted from [36] with permission from Elsevier

2.3 Methodology of Metallographic Specimen Preparation for Metastable Austenitic Steels

Metastable austenitic stainless steels (see Chap. 11) and Transformation-Induced Plasticity/TWinning-Induced Plasticity–TRIP/TWIP austenitic steels (see Chap. 12) undergo during mechanical loadings besides conventional deformation mechanism, e.g., the development and glide of dislocations, further changes in the microstructure. In dependence on their chemical compositions, load range and load temperature, formation of stacking faults, twinning and development of new phases: the hexagonal close packed ϵ -martensite and/or the body-centered cubic α' -martensite can take place. Using magnetic measurement, the ferromagnetic α' -martensite can be easily detected because ϵ -martensite and γ -austenite are paramagnetic. However, another body-centered cubic phase, namely, the δ -ferrite, which is also ferromagnetic, can exist in the initial state together with the γ -austenite. Consequently, for a comprehensive quantitative phase analysis several measurement methods have to be combined as well as the preparation/deformation-induced α' -martensite formation must be avoided [39].

Figure 12 shows the microstructure of TRIP steel type X3CrMnNi16-8-3 under the light microscope. During the conventional preparation, the cut surfaces were gradually ground using grinding paper up to a grit of 1200 at ambient temperature with water cooling. Subsequently, mechanical vibratory polishing was performed (120 min, 90 Hz, 950 g). In order to minimize the preparation/deformation-induced phase transformation of γ -austenite to ϵ - and/or α' -martensite, the sample preparation method was modified by the use of boiling water during the grinding process. Therefore, the specimen temperature was increased above the M_{d30} temperature [40] and the deformation-induced martensite formation was inhibited. The light microscope images were acquired after swab etching with diluted Beraha-I etchant under polarized light, making the phases visible [41]. Not only γ -austenite, but also lamellar δ -ferrite can be observed by its color contrast on the micrograph. α' -martensite is visible owing to the darker color, however, ϵ -martensite cannot be identified. The

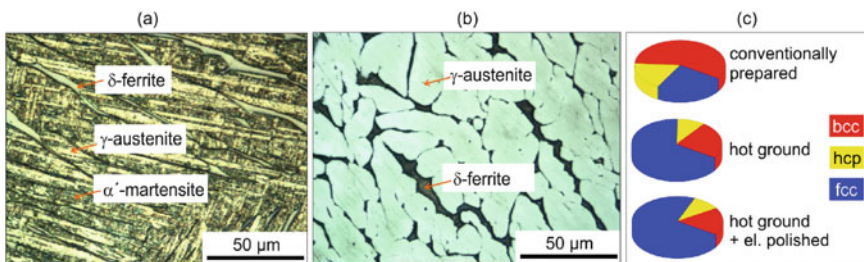


Fig. 12 Microstructure of TRIP steel after conventional preparation (a) and after warm grinding and electrolytic polishing (b) under polarized light after swab etching using diluted Beraha-I etchant as well as phase composition at the sample surface after different preparation methods by X-ray analysis (c) [39]

elevated temperature during the warm grinding process does not entirely suppress the martensite formation at the surface, but considerably reduces it. The quantitative X-ray phase analysis according to Rietveld method [42] showed a 66 vol.% fcc phase fraction, a 10 vol.% hcp phase fraction, and a 24 vol.% bcc phase fraction. For further preparation, the warm ground surface was electrolytically polished without applying force. This process resulted in 72 vol.% fcc, 10 vol.% hcp, and 18 vol.% bcc phase fractions, respectively (Fig. 12c). Compared to the conventional sample preparation, the preparation by warm grinding and subsequent electrolytic polishing results in a significantly reduced phase transformation at the section's surface. Hence, the quantitative phase analysis can be realized using combination of magnetic, light optical microscopy, SEM/EBSD, and XRD method [40].

2.4 XRD Phase Analysis of Textured Metastable Austenitic Steels

Machining of metastable austenite can lead to the phase transformation at the component surface (see Chap. 5). The distribution and amount of γ -austenite, ϵ -martensite, and α' -martensite in the near-surface regime have a significant influence on fatigue (see Chaps. 11 and 12) and wear (see Chap. 13) properties of the material. For a comprehensive understanding of the influences of the surface morphology on the material behavior, quantitative phase analysis is needed. Unfortunately, the machining process usually induces texture and a nanocrystalline layer at the materials surface, which hampered the usability of microscopic methods for the quantitative phase analysis [43]. Here the X-ray diffraction (XRD) method can help, however, the influence of the texture must be taken into consideration. For this so-called wobble scan with five tilted angles ψ in the range from -20° to $+20^\circ$ can be done. The 2θ range has to be enough high to obtain a high amount of diffraction peaks of all phases. For example, using the Cu radiation the successful scanning range is $40^\circ \leq 2\theta \leq 100^\circ$. Due to tilt of the specimens by the ψ angle (see Figure 13a), different oriented grains will be scanned in diffraction condition and the influence of texture can be minimized. Figure 13b shows two diffractograms measured on the cryogenic turned specimen from metastable austenitic stainless steel AISI3471FP at the same places with same parameter sets but at two different tilted angles, $\psi = 0^\circ$ and $\psi = 20^\circ$. The details of measurements parameters were published elsewhere [44, 45]. It is obvious that depending on which both diffractograms will be used for the phase analysis, a different amount of γ -austenite and α' -martensite will be determined. Usually, the quantitative phase analysis for the determination of α' -martensite/ γ -austenite fraction in steels is performed using ASTM standard [46]. However, this method doesn't provide the quantify in the case of three phases materials: α' -martensite, γ -austenite, and ϵ -martensite. Therefore, a Rietveld analysis of X-ray diffractograms must be realized. Figure 13c shows the result of the Rietveld analysis applied on a diffractogram from a wobble scan, with volume fractions of all phases. Using the

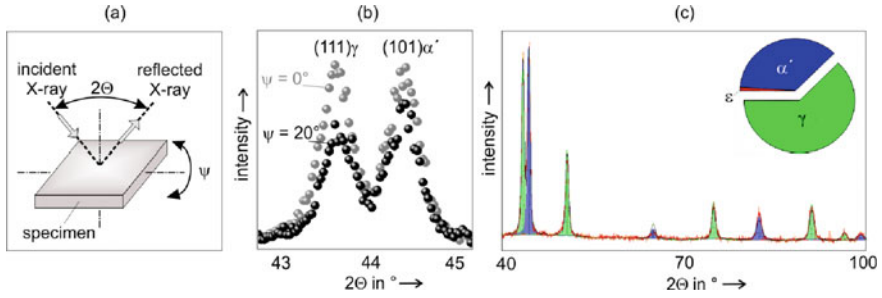


Fig. 13 Measuring principle of wobble scan (a), details of two diffractograms at two different tilt ψ angles (b) and view of Rietveld analysis using X'Pert software based on wobble scan of cryogenically turned AISI3471FP with $v_c = 30$ m/min; $a_p = 0, 2$ mm; $f = 0, 35$ mm/U (c)

wobble scan and Rietveld analysis, systematic XRD investigations were performed to characterize the influences of cryogenic turning process and change in the process parameters on the surface morphology of metastable austenite [47]. Hence, the same methodology was successfully applied for the characterization of surface morphology of milled austenitic stainless steels (see Chap. 11) and TRIP/TWIP steels (see Chap. 12).

2.5 Summary

A new method using polarized light microscopy to determine the crystallographic orientation of α -titanium via the first two Euler angles has been determined in the CRC 926. This method uses the anisotropy of the hexagonal close packed α -titanium and the resulting gray value evolution of the individual grains when the sample is rotated in polarized light.

To eliminate the preparation-induced phase transformation in metastable austenitic steels an elevated temperature grinding process with subsequent forceless electrolytic polishing of the section's surface was established. Furthermore, for the XRD investigations so-called wobble scan strategy was used, which allows a quantitative phase analysis of textured metastable austenitic steels.

3 Characterization of Friction and Wear Properties at Surfaces

3.1 Introduction

The geometry as well as the chemical and structural composition of component surfaces has a significant influence on the friction and wear properties of tribological systems that are equipped with the corresponding components. Parameters are therefore required that are characteristic of the influence that the component surfaces have on friction and wear. The following section focuses on methods for measuring friction values and wear coefficients in the case of dry friction. Adhesive interactions between the surfaces should be excluded as far as possible. Furthermore, it is shown how special surface structures are produced, which can themselves serve as a tool to research basic tribological processes.

3.2 Characterization of Friction on Structured Surfaces

3.2.1 Measurement of Friction Coefficients

The Coefficient of Friction (CoF) is a dimensionless number that is used to characterize the friction behavior of surfaces sliding against one another. The coefficient of friction is defined as the ratio of the lateral (or frictional) force that causes the surfaces to slide and the corresponding normal force that the two surfaces exert on each other. There is almost a large number of tribometers that can be used to measure frictional forces for different materials and in a wide variety of tribological systems. For example, Atomic Force Microscopy (AFM) can be used to measure normal and tangential forces between an AFM tip and a surface, thus studying friction on an atomistic scale. However, for technological questions in connection with the tribological properties of micro-structured surfaces, as shown in Fig. 14, one must consider that friction and the coefficient of friction that describes it is a property of the respective tribological system and not of a specific microstructure alone.

This means that the friction properties of the micro-structured surfaces should be tested under more realistic conditions, in which the surfaces to be examined slide flat over a selected reference surface. It must also be taken into account that

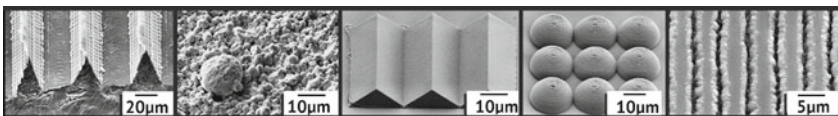


Fig. 14 Micro-structured model surfaces, created by micro-milling, particle structuring, 3D laser lithography, and direct laser structuring

the structures produced on a laboratory scale are often only available on limited surface areas. As with micro-milled titanium surfaces [48], the stress conditions in the few load-bearing tribo-contacts can destroy the structures to be examined during the CoF measurement even under relatively small normal forces. Metallic surfaces that are stochastically equipped with finely dispersed Ti-particles [49–51], three-dimensional laser-lithographically generated silver structures, or directly laser-structured surfaces [50] are further examples of surface structures whose friction behavior is to be characterized reproducibly and quantitatively.

A relatively simple method for this is the principle of an inclined plane on which small test specimens with the surface structure to be examined slide down. The principle is that a high-speed camera records the movement of the specimen accelerated by gravity as it slides down an inclined plane made of the material and structure of the desired counter-body. The system is relatively freely scalable with regard to the possible sample size, the sample geometry, and the normal force used. Even surfaces with only a few defined individual contacts can be examined.

Technically, the system is equipped with a microprocessor-controlled robot hand, which places the sample on the inclined plane in a controlled manner, then releases it and thus triggers the high-speed camera, which is mounted with the line of sight in the plane normal. The angular table of a tool machine allows precise adjustment of the tilting angle of the inclined plane. Guide elements to keep the slide body on track are obsolete. The system balances itself as the friction body hugs the base and slides independently without guidance.

For the measurement of friction values while avoiding adhesion effects, the surface of the inclined plane can be wetted with polyalphaolefin, for example. By the very direct method friction values and wear can be characterized even at low loadings (comparable to nano-scoring tests), which place little stress on the specimens.

During the measurement process, the macroscopic test bodies are accelerated by the difference between the down-hill slope force and the frictional force. The associated displacement–time profile is recorded by the high-speed camera. From this, the acceleration a of the specimen can be determined. With the tilting angle α of the inclined plane and the gravitational acceleration g , the Coefficient of Friction μ_G is calculated according to

$$\mu_G = \tan \alpha - \frac{a}{g \cos \alpha}. \quad (3)$$

The numerical calculation of the acceleration a is done simply by fitting a polynomial of the second degree to the measured displacement versus time data (Fig. 15).

3.2.2 Application of the Method

With the method described, coefficients of friction for differently structured surfaces made of different materials can be measured (Fig. 16). The mean standard deviation of the measured values was in the range of 10% of the measured values.

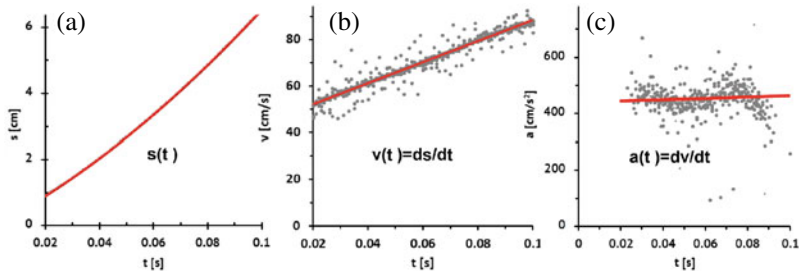


Fig. 15 Experimental values for different motion quantities of a specimen sliding down the inclined plane. Data are derived from the recorded high-speed images. Velocity v (b) and acceleration a (c) calculated by numerical differentiation of the experimental values for the displacement s of the specimen (a) as function of time t are given as gray dots. The results obtained by fitting a second-degree polynomial to the measured $s(t)$ values and analytical differentiation are given as red line

The method can also be used to determine the coefficient of static friction μ_H . This is done by slowly increasing the tilt angle α of the plane until the specimen starts to move. From the according maximum tilt angle α_H , the static friction coefficient is simply calculated via $\mu_H = \tan \alpha_H$.

3.3 Model Asperities as a Tool for the Investigation of Friction and Wear Processes

3.3.1 Manufacturing of Sophistically Designed Model Asperities

A whole range of methods is available today for the chemical and structural characterization of component surfaces on a microscopic and submicroscopic scale. In addition to classic methods of material analysis, such as electron microscopy (scanning electron microscopy (SEM), transmission electron microscopy (TEM)), this

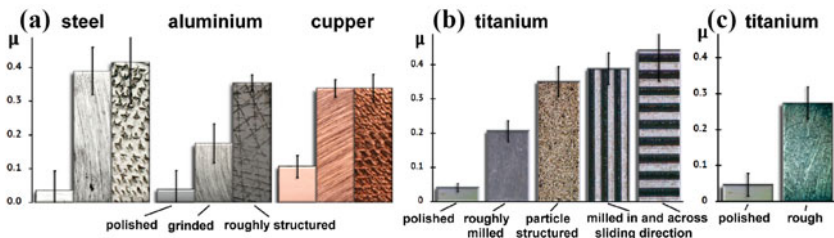


Fig. 16 Friction coefficients for round washers of steel, aluminium, copper, titanium, and of several surface qualities (polished, grinded, roughly structured) sliding on an inclined copper plane (a–b), respectively, perfectly polished silicon wafer (c)

also includes methods that have emerged from modern surface physics, such as electron spectroscopic (AES, ESCA) and mass spectrometric methods (secondary ion mass spectrometry (SIMS), secondary neutral mass spectrometry (SNMS)) or near-field probe—methods such as Atomic Force Microscopy and Scanning Tunneling Microscopy (AFM, STM). The procedures and methods mentioned are also used to analyze component surfaces from real tribological systems. The characterization and tracking of running-in processes and the associated material changes in the actual contact areas is particularly challenging. This is due to the fact that the real contact area of two macroscopic metal surfaces sliding on one another is usually many orders of magnitude smaller than their apparent macroscopic contact area. The real contact area is created by a large number of small touching protuberances, so-called asperities. The representative analysis of the surface then usually represents a statistical averaging over many of such microscopic or submicroscopic contact areas. The tracking of the events and processes on individual asperities, on the other hand, presupposes that the real microcontacts and their position on the surface are known from the beginning of the tribological load. So-called model asperities are to be produced and used for this purpose.

Solid-state friction is generated by asperities, which plough the surface of the counter-body. The geometric shape of the “submerged” asperity tip has a decisive influence on the macroscopically observed coefficient of friction (see Chap. 3). Overall, this results in the following essential requirements for the properties of a surface structure equipped with the desired “Sophisticated Designed Model Asperities” (*SDMAs*):

1. The *SDMAs* should enable a targeted control of the coefficient of friction for the surface equipped with it. This should work largely independently of the respective load, so that a self-similar form of the asperities is desired (see Chap. 3).
2. It must be ensured that the applied *SDMA* tips actually determine the real contact area with the counter-body, i.e., they must represent sufficiently high elevations on the surface equipped with them.
3. The *SDMA* structures must be strong enough to allow a limited number of them to withstand macroscopic load without excessive wear.

With view to the second requirement, the *SDMA* structures could be created on “pedestals” which must be almost perfectly aligned relative to one another. For this purpose, the following approach was taken in a first experiment: first, the surface of a steel pellet (100Cr6) with a diameter of 6mm was milled down, leaving three microscopic areas untouched, whose total surface is about $100 \mu\text{m}^2$. When the pedestals of the specimen come into contact with a flat glass under an additional load of 10g, the contact points on the elevated structures begin to flow plastically and fairly smooth surfaces are created on each pedestal. *SDMAs* could then be attached to these almost perfectly aligned sockets (Fig. 17).

Another concept for the production of a suitable basis for *SDMAs* is a shallowly sloped circular wall from structurally practically unchanged steel, which can be manufactured very precisely as a turned part (Fig. 18).

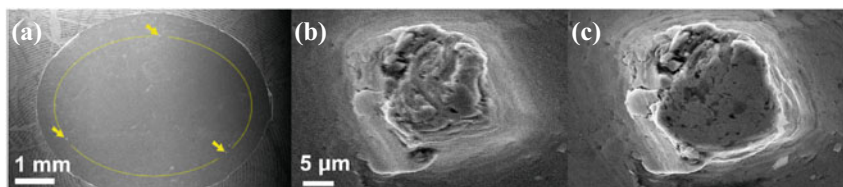


Fig. 17 Manufacturing steps for socket structures (material: 100Cr6) on which *SDMAs* can be built. Positioning of the base structures along a circle with a diameter of 10mm **a** *SDMA* base before **b** and after **c** loading with 10g

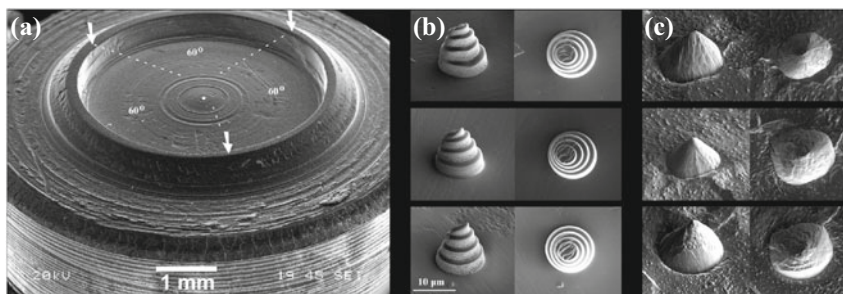


Fig. 18 *SDMA* structures: **a** Ring wall as a base structure for *SDMAs*. **b** Deposited Pt organics as etching masks. **c** *SDMA* cones from intrinsic material with a semi-apex angle of about 40°

SDMAs then are produced with a mask technique using a dry etching process. In a first step, microstructures of an organic platinum compound are deposited on the wall base in a Focused Ion Beam (FIB) instrument as shown in Fig. 18 and serve as sputter masks for the subsequent sputter etching process. A noble gas low-pressure plasma was used for the homogeneous and controlled sputter removal of the entire sample surface with Ar^+ -ions with an energy of 1keV and a current density of about $1\text{mA}/\text{cm}^2$. This removes the mask material, including the surrounding surface (Fig. 19), and after an etching time of a few hours, cone structures are formed on the steel surface, which consist intrinsically of the base material (Fig. 18) and were also subjected to practically no mechanical stress. Since the sputter removal was carried out in the analysis chamber of an SNMS (secondary neutral mass spectrometry) apparatus, the disappearance of the mass spectrometric Pt signal originating from the sputter mask material can be used to precisely switch off the etching process after the mask has been removed.

3.3.2 Application of *SDMAs*

The coefficient of friction of steel samples (100Cr6) whose surface was equipped with the conical *SDMAs* shown in Fig. 18 was tested using the method described in Sect. 3.2.1. Copper, a material with a significantly lower hardness, was chosen as the

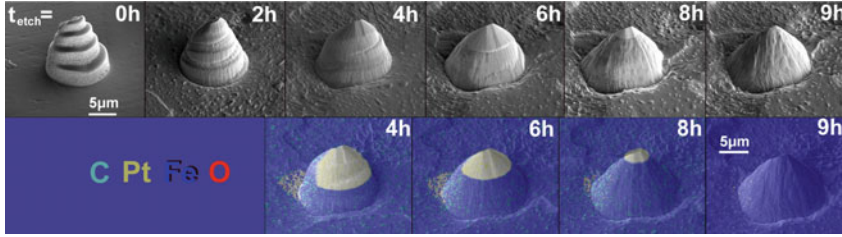


Fig. 19 Evolution of intrinsic *SDMA* structures via ion etching for different etching times t_{etch} . The upper row of images shows SEM images of the generated structures, in the lower row the corresponding three-dimensional color-coded representations for the C, Pt, and Fe distributions measured by means of EDX are superimposed

counter-body. Initially, the measured coefficient of friction $\mu_{exp} = 0.5$ agrees fairly well with the coefficient of friction $\mu_{geo} = 0.53$ calculated theoretically (cf. Chap. 3, Eq. 3.7) for a cone with a semi-apex angle of $\beta = 50^\circ$. However, after a series of friction tests, the coefficient of friction becomes increasingly smaller. The reason for this are progressive wear processes, which change the shape of the *SDMA*s, leading to a rounded profile of the originally conical *SDMA* tips. Using an electron microscope such wear processes can be observed directly on the asperities (Fig. 20). The volume V_W of the worn cone tip is about $40 \mu\text{m}^3$. With the specimen weight $G \approx 15 \text{ mN}$, a running distance of around 100 m and the total of three *SDMA*s ($F_N = G/3$), the mean wear coefficient, defined as the wear volume divided by the normal load F_N and the running distance s , results in a fairly low value of $k_{mean} \approx 1 \cdot 10^{-7} \text{ (mm}^3/\text{Nm)}$. Since the sample can be examined as a whole under the electron microscope and is not destroyed in the process, it is in principle possible to carry out alternating friction and wear measurements. In principle, the course of the coefficient of friction and the associated wear coefficient can then be recorded over the travel distance. At the same time, with the help of energy-dispersive X-ray analysis EDX, the *SDMA*s allow further tribological processes (Fig. 20) to be observed at the individual asperity contacts and tracked over the running time.

The EDX analysis shows the transfer of copper from the counter-body. Cu adhesions are found on the contact surface of the asperity, but copper chips are also detected, which accumulate at the base of the asperity. Oxygen occurs predominantly in association with carbon. Taking into account the information depth of EDX, this indicates that organic impurities, which can also influence the tribological behavior, are enriched in the vicinity of the asperities and that metallic oxide layers, which could be detected using electron spectroscopic techniques, are relatively thin. This is also confirmed by a more detailed analysis of a cross section of the asperity structure (Fig. 21), which was prepared from an *SDMA* using the lift-off technique in a FIB (focused ion beam) device. A change in morphology and the beginning of grain refinement under the contact area of the asperity (see also Chaps. 3 and 12) can also be observed in the ion-induced FIB image. Electron Energy Loss Spectroscopy (EELS) on the electron-transparent TEM cross section shows that a Cu particle with

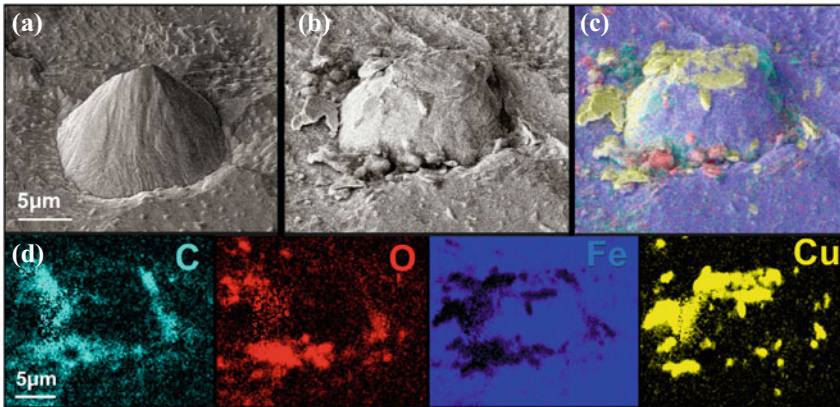


Fig. 20 Electron microscope image of a *SDMA* structure before (a) and after (b) tribological loading (SEM), three-dimensional (c) and lateral (d) representation of the elemental concentrations of Cu (yellow), Fe (blue), O (red) for this *SDMA* after loading (EDX)

an oxidic layer surrounding has penetrated the surface of the asperity and evidently caused wear there.

In order to further close the gap between experiments with a single asperity (indenter) and those with surfaces that are in tribological contact with each other, it will be important for future development to equip surfaces with significantly more *SDMAs* than has been the case so far. The conditions would then come closer to a real rough surface with a large number of statistically distributed asperities. Further areas of application for *SDMA* will also be experiments in a lubricated environment in the future. Here the interaction of the lubricant and its additive components with the asperities is of particular interest and *SDMAs* could be a tool to help clarify the associated reaction pathways.

3.4 Summary

Geometry as well as chemical and structural composition of component surfaces has a significant influence on the friction and wear properties of tribological systems. This opens the possibility to influence friction and wear in a targeted manner by applying a suitable microstructure to the component surface. So artificially created, highly precise, largely wear-resistant, protruding microasperities can be used to force defined microcontacts of the friction partners, in contrast to stochastically distributed roughness peaks with time-varying not predictable microcontacts. These Sophisticated Designed Model Asperities (*SDMAs*) provide an approach to characterize the influence that component surfaces have on friction and wear. Furthermore,

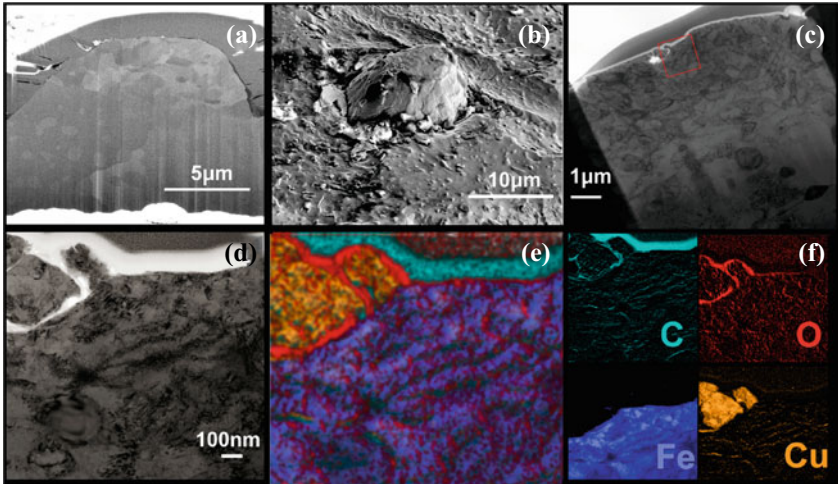


Fig. 21 *SDMA* structures: **a** Ion-induced electron image of a cross section prepared in the FIB (focused ion beam) of the *SDMA* structure shown in Fig. 20 after tribological loading; **b** another *SDMA* structure after tribological loading; **c** lift-off preparation with the Transmission Electron Microscope (TEM) examined section (see rectangular marking); **d** TEM image of the examined area; **e** overlay of the lateral C (blue), O (red), and Fe (blue) distribution measured by Electron Energy Loss Spectroscopy (EELS), **f** lateral element distribution images for C, O, Fe, and Cu (EELS)

the *SDMAs* themselves can serve as an analytical tool to research basic tribological processes.

References

1. En DIN, ISO 21920–2. Geometrische Produktspezifikation (GPS), (2021) Oberflächenbeschaffenheit: Profile-Teil 2: Begriffe und Kenngrößen für die Oberflächenbeschaffenheit. Beuth Verlag, Berlin
2. En DIN, ISO 4287. Geometrische Produktspezifikation (GPS), (2010) Oberflächenbeschaffenheit: Tastschnittverfahren-Benennungen. Beuth Verlag, Berlin, Definitionen und Kenngrößen der Oberflächenbeschaffenheit
3. En DIN, ISO 25178–2. Geometrische Produktspezifikation (GPS), (2012) Oberflächenbeschaffenheit: Flächenhaft-Teil 2: Begriffe und Oberflächen-Kenngrößen. Beuth Verlag, Berlin
4. Stout K (1993) The development of methods for the characterisation of roughness in three dimensions. European Report EUR 15178N
5. Seewig J, Raid I, Wiehr C, George BA (2013) Robust evaluation of intensity curves measured by confocal microscopies. In: Optical measurement systems for industrial inspection VIII, vol 8788. SPIE, pp 200–212. <https://doi.org/10.1117/12.2020551>
6. Seewig J, Böttner T, Broschart D (2011) Uncertainty of height information in coherence scanning interferometry. In: Optical measurement systems for industrial inspection VII, vol 8082. SPIE, pp 269–277. <https://doi.org/10.1117/12.889796>

7. Raid I, Eifler M, Kusnezowa T, Seewig J (2015) Calibration of Ellipso-Height-Topometry with nanoscale gratings of varying materials. In: *Optik* 126, vol 23, pp 4591–4596. <https://doi.org/10.1016/j.ijleo.2015.08.093>
8. BMBF (2014) Anwenderorientierte Assistenzsysteme zum sicheren Einsatz optischer Abstandssensoren
9. EMPIR (2021) Traceable industrial 3D roughness and dimensional measurement using optical 3D microscopy and optical distance sensors
10. Engeln-Müllges G, Uhlig F (2014) *Numerical algorithms with C*. Springer. ISBN: 3642646824
11. Raid I, Kusnezowa T, Seewig J (2013) Application of ordinary kriging for interpolation of micro-structured technical surfaces. *Meas Sci Technol* 24(9). <https://doi.org/10.1088/0957-0233/24/9/095201>
12. ISO 3274 (1996) Geometrical Product Specifications (GPS)-Surface texture: profile method-nominal characteristics of contact (stylus) instruments (ISO 3274: 1996)
13. Seewig J, Ehret G (2011) Unsicherheitsbetrachtungen zur Formmessung an optischen Bauelementen auf der Basis von Bayes. Düsseldorf
14. Elster C (2007) Calculation of uncertainty in the presence of prior knowledge. *Metrologia* 44(2):111–116. ISSN: 0026-1394. <https://doi.org/10.1088/0026-1394/44/2/002>
15. Baum M, Klumpp V, Hanebeck UD (2010) A Novel Bayesian method for fitting a circle to noisy points. In: 2010 13th international conference on information fusion. IEEE, 2010, pp 1–6. ISBN: 978-0-9824438-1-1. <https://doi.org/10.1109/ICIF.2010.5711884>
16. Elster C, Toman B (2011) Bayesian uncertainty analysis for a regression model versus application of GUM supplement 1 to the least-squares estimate. *Metrologia* 48(5):233–240. ISSN: 0026-1394. <https://doi.org/10.1088/0026-1394/48/5/001>
17. Lira I, Wöger W (2001) Bayesian evaluation of the standard uncertainty and coverage probability in a simple measurement model. *Meas Sci Technol* 12(8):1172–1179. ISSN:0957-0233. <https://doi.org/10.1088/0957-0233/12/8/326>
18. Weise K, Woger W (1993) A Bayesian theory of measurement uncertainty. *Meas Sci Technol* 4(1):1–11. ISSN: 0957-0233. <https://doi.org/10.1088/0957-0233/4/1/001>
19. Werman M, Keren D (2001) A Bayesian method for fitting parametric and nonparametric models to noisy data. *IEEE Trans Pattern Anal Mach Intell* 23(5):528–534. ISSN: 01628828. <https://doi.org/10.1109/34.922710>
20. Keksel A, Ströer F, Seewig J (2018) Bayesian approach for circle fitting including prior knowledge. *Surf Topogr Metrol Prop* 6(3):035002. <https://doi.org/10.1088/2051-672X/aad2b4>
21. Bolstad WM (2007) *Introduction to Bayesian statistics*, 2nd edn. Wiley, Hoboken, NJ. 0470141158
22. Ahn SJ, Rauh W, Warnecke H-J (2001) Least-squares orthogonal distances fitting of circle, sphere, ellipse, hyperbola, and parabola. *Pattern Recognit.* 34(12):2283–2303. ISSN: 00313203. [https://doi.org/10.1016/S0031-3203\(00\)00152-7](https://doi.org/10.1016/S0031-3203(00)00152-7)
23. Davis PJ, Rabinowitz P (1984) Approximate integration in two or more dimensions. In: *Methods of numerical integration*. Elsevier, pp 344–417. ISBN: 9780122063602. <https://doi.org/10.1016/B978-0-12-206360-2.50011-X>
24. Leach R (2013) *Characterisation of areal surface texture*. Springer. <https://doi.org/10.1007/978-3-642-36458-7>
25. Blunt L, Jiang X (2003) Advanced techniques for assessment surface topography: development of a basis for 3D surface texture standards “SURFSTAND”. Kogan Page Science, London. <https://doi.org/10.1016/B978-1-903996-11-9.X5000-2>
26. Scott PJ (1996) Recent advances in areal characterization. In: IX. Internationales Oberflächenkolloquium, pp.151–158
27. Wolf GW (1991) A FORTRAN subroutine for cartographic generalization. *Comput Geosci* 17(10):1359–1381. [https://doi.org/10.1016/0098-3004\(91\)90002-U](https://doi.org/10.1016/0098-3004(91)90002-U)
28. Soille P (2004) *Morphological image analysis*. Springer, Berlin Heidelberg. ISBN: 978-3-540-42988-3
29. Weidner A, Seewig J, Reithmeier E (2006) 3D roughness evaluation of cylinder liner surfaces based on structure-oriented parameters. *Meas. Sci. Technol.* 17:477–482. <https://doi.org/10.1088/0957-0233/17/3/S03>

30. Schmidt K, Buhl S, Davoudi N, Godard C, Merz R, Raid I, Kerscher E, Kopnarski M, Müller-Renno C, Ripperger S, Seewig J, Ziegler C, Antonyuk S (2017) Ti surface modification by cold spraying with TiO₂ microparticles. In: Surface and coatings technology, vol 309, pp 749–758. ISSN: 0257-8972. <https://doi.org/10.1016/j.surfcoat.2016.10.091>
31. Rief S, Ströer F, Kieß S, Eifler M, Seewig J (2017) An approach for the simulation of ground and honed technical surfaces for training classifiers. *Technologies* 5(4). ISSN: 2227-7080. <https://doi.org/10.3390/technologies5040066>
32. Eifler M, Ströer F, Rief S, Seewig J (2018) Model selection and quality estimation of time series models for artificial technical surface generation. *Technologies* 6(1). ISSN: 2227-7080. <https://doi.org/10.3390/technologies6010003>
33. Schmidt S, Eifler M, Issel JC, de Payrebrune KM, Ströer F, Karatas A, Seewig J (2022) Parameter identification of an abrasive manufacturing process with machine learning of measured surface topography information. *J Comput Inf Sci Eng* 22(4):041010. ISSN: 1530-9827. <https://doi.org/10.1115/1.4053670>
34. Hall EO (1951) The deformation and ageing of mild steel: III discussion of results. *Proc Phys Soc Sect B* 64(9):747–753. <https://doi.org/10.1088/0370-1301/64/9/303>
35. Bunge HJ (1982) Texture analysis in materials science. mathematical methods. Butterworth-Heinemann. ISBN: 9780408106429. <https://doi.org/10.1016/C2013-0-11769-2>
36. Böhme L, Morales-Rivas L, Diederichs S, Kerscher E (2018) Crystal CAXis mapping of hcp metals by conventional reflected polarized light microscopy: application to untextured and textured cp-titanium. *Mater Charact* 145:573–581. <https://doi.org/10.1016/j.matchar.2018.09.024>
37. Morales-Rivas L, Diederichs S, Böhme L, Gordo E, Hebestreit A, Kerscher E (2018) Method for the detection of grain boundaries in? Ti-based alloys by means of polarized light microscopy and image processing in MATLAB. *Pract Metallogr* 55(10):678–692. <https://doi.org/10.3139/147.110515>
38. Morales-Rivas L, Böhme L, Kerscher E (2020) Orientation mapping of cp-Ti by Reflected Polarized Light Microscopy. In: Villechaise P, Appolaire B, Castany P, Dehmas M, Delaunay C, Delfosse J, Denquin A, Gautier E, Germain L, Gey N, Gloriant T, Hascoët J-Y, Hémerly S, Millet Y, Monceau D, Pettinari-Sturmel F, Piellard M, Prima F, Viguier B (eds) MATEC web of conferences, vol 321, p 11096. <https://doi.org/10.1051/mateconf/202032111096>
39. Klein MW, Krebs F, Smaga M, Beck T (2018) Preparation of polished sections and determination of the phase composition of highly metastable TRIP steel by microscopic and radiographic methods. *Pract Metallogr* 56:106–123
40. Smaga M, Boemke A, Daniel T, Klein MW (2018) Metastability and fatigue behavior of austenitic stainless steels. In: MATEC web conference, vol 165. <https://doi.org/10.1051/mateconf/201816504010>
41. Beraha E, Shpigler B (1977) Color metallography. American society for metals
42. Bish D, Howard S (1988) Quantitative Phase analysis using the rietveld method. *J Appl Cryst* 21:86–91
43. Smaga M, Skorupski R, Eifler D, Beck T (2017) Microstructural characterization of cyclic deformation behavior of metastable austenitic stainless steel AISI 347 with different surface morphology. *J Mater Res* 32:4452–4460
44. Smaga M, Skorupski R, Mayer P, Kirsch B, Aurich JC, Raid I, Seewig J, Man J, Eifler D, Beck T (2017) Influence of Surface Morphology on Fatigue Behavior of Metastable Austenitic Stainless Steel AISI 347 at Ambient Temperature and 300°C. *Proc Struct Integr* 5:989–996
45. Skorupski R (2017) Einfluss der oberflächennahen Martensitbildung auf das LCFund HCF-Ermüdungsverhalten sowie die Verschleißfestigkeit des metastabilen austenitischen Stahls X6CrNiNb1810. Dissertation TU Kaiserslautern,
46. Standard AE (2013) Practice for X-ray determination of retained austenite in Steel with near random crystallographic orientation. ASTM, Conshohocken, PA
47. Mayer P, Kirsch B, Müller C, Hotz H, Müller R, Becker S, Harbou EV, Skorupski R, Boemke A, Smaga M, Eifler D, Beck T, Aurich JC (2018) Deformation induced hardening when cryogenic turning. *CIRP J Manuf Sci Technol* 23:6–19

48. Bohley M, Reichenbach IG, Kieren-Ehse S, Heberger L, Arrabiyeh PA, Merz R, Böhme L, Hering J, Kirsch B, Kopnarski M et al (2018) Coating of ultra-small micro end mills: analysis of performance and suitability of eight different hard-coatings. *J Manuf Mater Process* 2(2):22. <https://doi.org/10.3390/jmmp2020022>
49. Buhl S, Schmidt K, Sappok D, Merz R, Godard C, Kerscher E, Kopnarski M, Sauer B, Antonyuk S, Ripperger S (2015) Surface structuring of case hardened chain pins by cold-sprayed microparticles to modify friction and wear properties. *Particuology* 21:32–40. <https://doi.org/10.1016/j.partic.2014.10.001>
50. Schmidt K, Buhl S, Davoudi N, Godard C, Merz R, Raid I, Kerscher E, Kopnarski M, Müller-Renno C, Ripperger S, Seewig J, Ziegler C, Antonyuk S (2017) Ti surface modification by cold spraying with TiO₂ microparticles. *Surf Coat Technol* 309:749–758. [j.surfcoat.2016.10.091](https://doi.org/10.1016/j.surfcoat.2016.10.091)
51. Breuninger P, Krull F, Buhl S, Binder A, Merz R, Kopnarski M, Sachweh B, Antonyuk S (2019) Microstructuring of titanium surfaces with plasma- modified titanium particles by cold spraying. *Particuology* 44:90–104. <https://doi.org/10.1016/j.partic.2018.08.002>

Indentation and Scratching on the Nanoscale



Herbert M. Urbassek, Iyad Alabd Alhafez, Hans Hasse, Michael Kopnarski, and Simon Stephan

Abstract Indentation and scratching of Fe, as a model of ferritic steels, are studied by atomistic simulation and experiment. The modeling allows to include the effect of lubrication. Selected experiments reveal the relevance of the nanoscopic simulation results to real surface scratching. We study the evolution of plasticity under indentation and scratching, the dependence of scratching on surface orientation and scratch direction, the influence of tip geometry on scratching, the effect of lubrication during scratching, and friction and wear on micro- and nanoscales.

1 Introduction

Indentation and scratching of surfaces are prototypical examples of the machining of workpieces. For metals, they involve plastic deformation of the workpiece, in which material is damaged below the tool and other material is moved onto the surface.

Theoretical methods to model these processes are available for all space and time scales of interest [1]. They range from continuum models of crystal plasticity over mesoscopic models—such as discrete dislocation dynamics or phase fields—to atomistic models based on molecular dynamics (MD).

The major advantage of MD is that all plastic processes as well as material damage are treated on a common basis, namely the interatomic interaction between the workpiece atoms. No further assumptions—such as on dislocation glide, reaction, or cross-slip—need to be introduced. However, the systems treated are of a size extending only over a few 10 nm and the transferability of the results to the micrometer scale and above needs to be validated by comparison to experiment. In addition,

H. M. Urbassek (✉) · I. Alabd Alhafez
Institute of Computational Material Science, RPTU Kaiserslautern, Kaiserslautern, Germany
e-mail: urbassek@rptu.de

H. Hasse · M. Kopnarski · S. Stephan
Institute of Engineering Thermodynamics, RPTU Kaiserslautern, Kaiserslautern, Germany
e-mail: simon.stephan@mv.uni-kl.de

M. Kopnarski
Institute of Surface and Thin Film Analytics (IFOS), Kaiserslautern, Germany

© The Author(s), under exclusive license to Springer Nature Switzerland AG 2024
J. C. Aurich and H. Hasse (eds.), *Component Surfaces*, Springer Series in Advanced Manufacturing, https://doi.org/10.1007/978-3-031-35575-2_3

simulated indent and scratch velocities are in the range of m/s such that movements over nanometers are achieved in times of nanoseconds, while in experiment velocities are several orders of magnitude smaller. This fact also affects the importance of thermally activated processes; these are as a rule suppressed in MD while they may contribute—due to the large timescales available—in microscopic experiments.

In many applications, the contact between tool and workpiece is not dry but lubricated. The effect of lubrication has not been studied as comprehensively as dry contacts, partly because the multitude of lubrication liquids available renders a generalized treatment difficult.

In this chapter, we present several novel insights obtained using MD for dry and lubricated indentation and scratching processes. In addition, selected experimental results are compared with these findings.

2 Simulation Method

In the present chapter, we focus on a workpiece consisting of elemental iron as a model of ferritic steels. The setup of the simulation system is shown schematically in Fig. 1. A block of crystalline bcc Fe is modeled atomistically; it is surrounded by layers in which a thermostat acts to keep the temperature at a constant value and outer layers where the atoms are fixed to prevent the workpiece from any translational movement during indentation and scratch. Often, simulations are performed at low temperature, <1 K, in order to ease the detection of crystal defects, in particular dislocations. Outside the workpiece, there may be vacuum or a lubricating fluid. Further information on the modeling of lubricated machining is provided in Sect. 4.

Fe atoms interact via a many-body potential of the embedded-atom-model type as detailed in Ref. [2]. Such many-body potentials allow to model the physics of metals—including defects, surfaces, and dislocations—realistically.

The tip is usually considered to be made of diamond and is often modeled as a sphere of radius R . Often, when the wear of the tip is not considered, the tip is considered to be rigid. This can be done by an atomistic sphere cut out from a block of diamond. The interaction between the C atoms of the tip and the Fe atoms of the workpiece is as a rule modeled by a purely repulsive potential; this can be simply chosen as a Lennard–Jones potential,

$$\Phi_{\text{LJ}}(r) = 4\epsilon \left[\left(\frac{\sigma}{r} \right)^{12} - \left(\frac{\sigma}{r} \right)^6 \right], \quad (1)$$

cut off at the potential minimum. Here, r denotes the distance between two atoms, ϵ is an energy parameter equal to the bond energy, and σ is a length parameter characterizing the distance where the potential energy vanishes.

An alternative approach [3] uses a non-atomistic tip, modeled as a repulsive sphere,

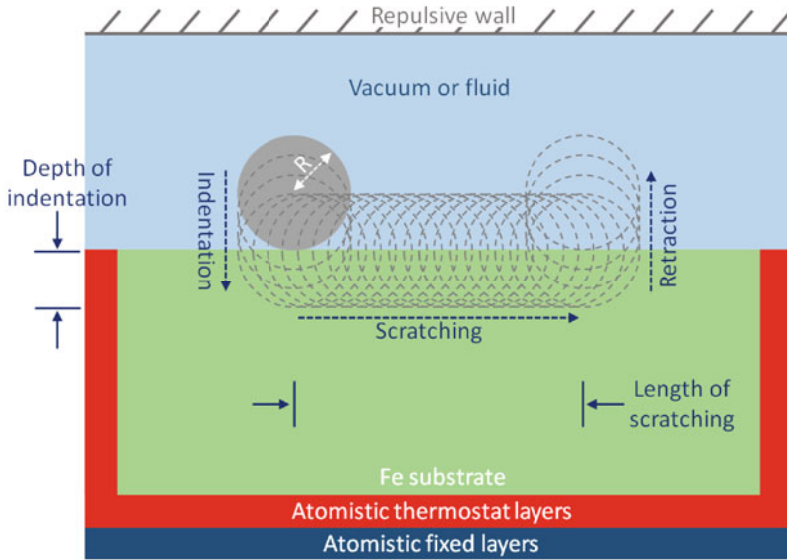


Fig. 1 Setup of the simulation system, illustrating the path of the tip during the processes of indentation, scratching, and retraction

$$V(r) = \begin{cases} k(R - r)^3, & r < R, \\ 0, & r \geq R, \end{cases} \quad (2)$$

where r is the distance of a substrate atom to the center of the indenter. The indenter stiffness has been set to $k = 10 \text{ eV/\AA}^3$. Such a smooth indenter is akin to the concept of a Hertzian indenter as it shows no friction nor roughness. Indentation is described faithfully by smooth indenters [4–6]; however, the roughness of atomistic indenters may influence the dislocation nucleation process.

The tip is initially positioned above the surface, immediately outside the C–Fe interaction. For the indentation simulation, the indenter moves into the substrate up to the final depth of $d = 4 \text{ nm}$. Then the tip moves parallel to the surface up to the total scratch length of $L = 15 \text{ nm}$ and is finally retracted. These steps are indicated in Fig. 1.

The open-source LAMMPS code [7] is used to perform the simulations, and the dislocation extraction algorithm [8] to identify the dislocations and to determine their Burgers vectors. The free software tool OVITO [9] is employed to visualize the atomistic configurations.

3 Dry Indentation and Scratching

3.1 Dislocations

The generation of dislocations is exemplified in Fig. 2. This simulation was run on a block of Fe with a (100) surface and consisting of 22.1×10^6 atoms. The scratch direction is along $[0\bar{1}\bar{1}]$. The final indentation depth amounts to $d = 4$ nm and the scratch length to $L = 15$ nm. The contact radius for full indentation is given by

$$a_c = \sqrt{R^2 - (R - d)^2} \quad (3)$$

and amounts to $a_c = 8$ nm. In all stages, the indenter velocity amounts to 20 m/s.

Dislocations with Burgers vector $\underline{b} = \frac{1}{2}\langle 111 \rangle$ and $\langle 100 \rangle$ are created, which form a dense network adhering to the indent pit. A detailed inspection shows that shear loops are generated in the region of highest shear stress under the indenter; these loops expand with leading dislocation lines of an edge character followed by trailing lines of a screw character. The trailing screw lines annihilate leading to a pinch-off of the shear loop and its emission as a prismatic loop [11], as displayed on the right-hand side of Figure 2b.

As this example shows, the plasticity developing under the tool can be divided into a *plastic zone* proper—consisting of dislocations adherent to the impact or scratch groove—and ejected loops. The ejected loops migrate in the stress field gradient away from the plastic zone but their later fate is not easily modeled by MD due to the boundaries existing in the simulation volume. Eventually, these loops will be pinned by some defects existing in the workpiece far from the indent zone. The plastic zone adherent to the impact pit is of highest interest, since it is this zone that will also be visible in actual microscopy images.

The size of the plastic zone, R_{pl} , may be defined as the largest distance of the adherent dislocations to the center of the contact zone [12, 13]. In experiment, R_{pl} is found to scale with the radius of the contact zone, a_c , Eq. (3), such that the plastic-zone size factor

$$f = \frac{R_{\text{pl}}}{a_c} \quad (4)$$

is of the order of $f = 2\text{--}3$ [14, 15]. MD simulations of nanoindentation in a variety of metals—with hcp, bcc, and fcc crystal structures—show that this behavior also applies to the nanoworld [12, 16].

3.2 Groove and Pile-up

After nanoindentation, the pile-up surrounding the indent pit shows the symmetry of the surface; this happens analogously for the pile-up structure of the scratch groove.

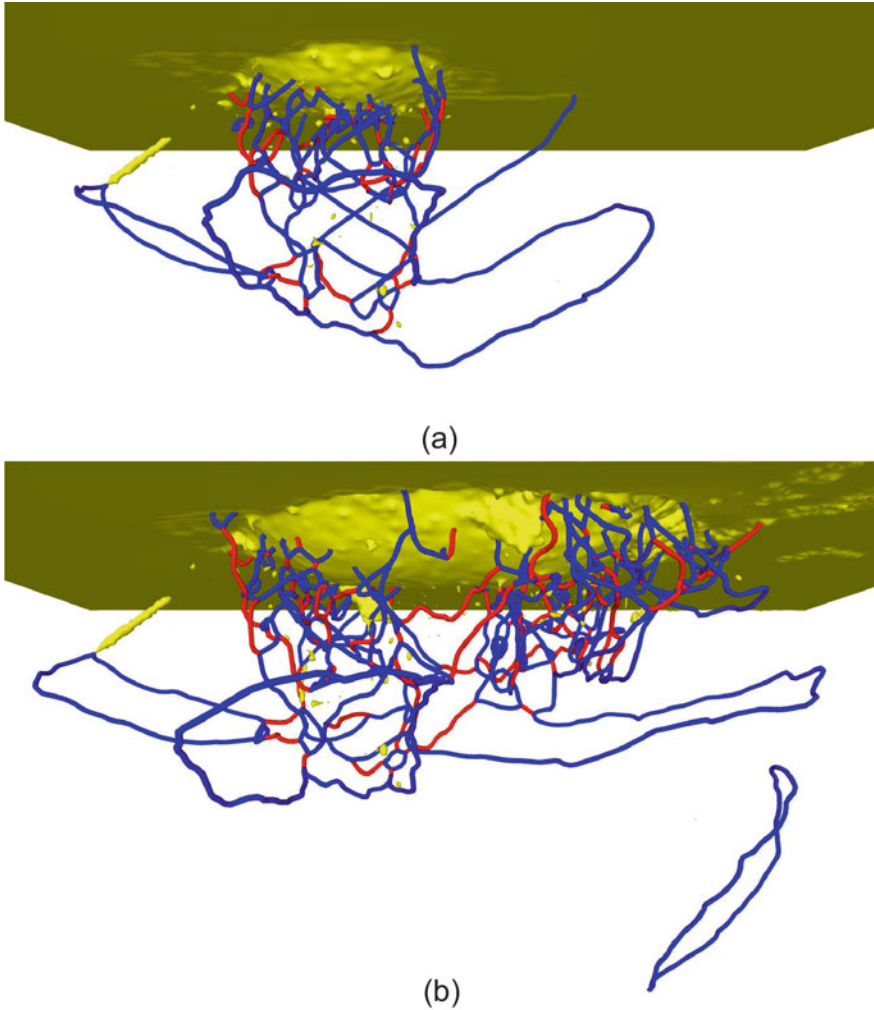


Fig. 2 Dislocation network developing **a** after indent and **b** after scratch. Dislocations are colored according to their Burgers vector b : blue $\frac{1}{2}(111)$ and red (100) . Yellow denotes the surface of the indent pit as well as unidentified defects. The snapshots are at the same scale. Data taken from Ref. [10] under CC BY 3.0

Figure 3 exemplifies this finding for scratching of the (100) , (110) , and (111) surfaces of Fe in several low-index directions. In this simulation, a small tip ($R = 2.1$ nm) was used and correspondingly the indent depth $d = 2.1$ nm and scratch length $L = 5$ nm could be chosen smaller than in the example shown above.

The structure of the pile-up is generated by the anisotropic slip occurring in crystals since pile-up is generated by atoms transported onto the surface along slip directions—identical to the Burgers vector of the relevant dislocation—on a slip

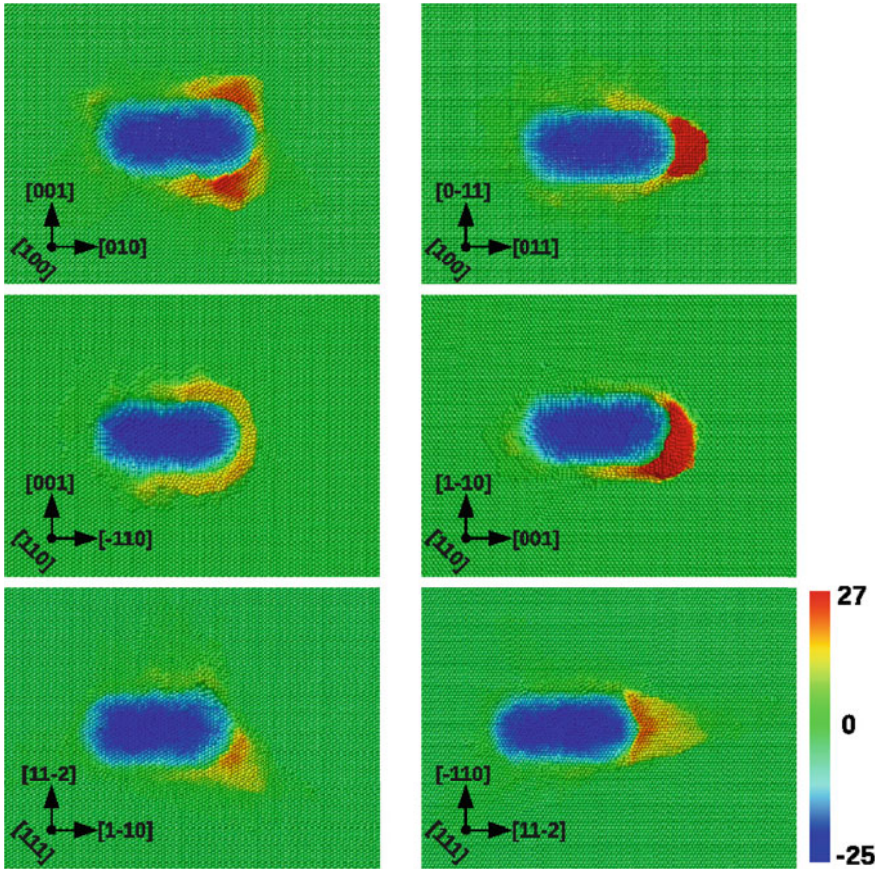


Fig. 3 Synopsis of pile-up formation after scratching and indenter retraction. Color codes height above the surface in Å. Taken with permission from Ref. [17]

plane. In the simplest picture, slip occurs in bcc Fe along the $\langle 111 \rangle$ directions. The relevant glide planes in Fe are the $\{110\}$ and $\{112\}$ planes.

Thus, we expect symmetric pile-ups for the (100) surface, which goes in an oblique direction sideways for scratch in [010] direction—along $[111]$ and $[1\bar{1}\bar{1}]$ —and is predominantly frontal for the [011] scratch direction (along $[111]$); this is corroborated by Fig. 3. A similar analysis gives a (more or less) symmetric pile-up for the (110) surface [17]. Most interesting is the scratch of the (111) surface as it has a three-fold symmetry. Here only scratch along $[11\bar{2}]$ leads to a symmetric pile-up as the relevant slip vector points along the scratch direction. Scratch in $[1\bar{1}\bar{0}]$ direction leads to asymmetric pile-up since only glide along $[11\bar{1}]$ leads to pile-up towards the front while the second activated slip system in $[11\bar{1}]$ direction assembles the pile-up on the lateral side of the groove.

3.3 Hardness and Friction

The determination of the forces acting on the tool is straightforward in an MD simulation; Fig. 4 a gives an example of the forces during scratching specified in Sect. 3.1, cf. Fig. 2. After indentation, the normal force decreases, since less force is required to keep the tip at constant depth d . Simultaneously, the transverse force increases as the tip starts digging its groove sideways. This *onset regime* has a length of 4 nm, roughly equivalent to the tip depth d . Later, the normal force saturates, while the transverse force steadily increases, as the pile-up in front of the tip keeps growing.

The friction coefficient, μ , is defined as the ratio of the transverse force, F_t , to the normal force, F_n ,

$$\mu = \frac{F_t}{F_n}. \tag{5}$$

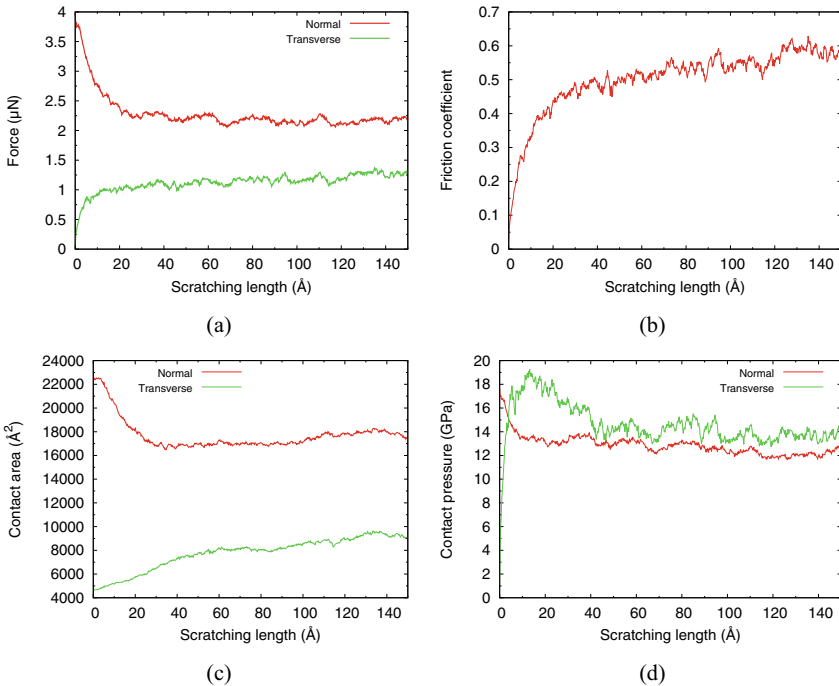


Fig. 4 **a** Forces, **b** friction coefficient, **c** contact areas, and **d** contact pressure during a scratch simulation. Data correspond to the simulation leading to the dislocation pattern in Fig. 2. Data taken from Ref. [10] under CC BY 3.0

It does not saturate, see Fig. 4 b, as the transverse force is constantly growing even after the end of the onset regime; this growth is caused by the constantly growing pile-up in front of the tool, cf. Fig. 3.

The calculation of the contact pressure,

$$p = \frac{F}{A}, \quad (6)$$

requires the determination of the contact area of the tip with the workpiece during the simulation. For the normal contact pressure, the force F_n is divided by the normal contact area, i.e., the projection of the contact area between the tip and the workpiece into the surface plane, $A_n = \pi a_c^2$, see Eq. 3. Analogously, a transverse contact pressure can be defined in which the transverse force is divided by the transverse area, A_t , which is the projection of the contact area between the tip and the workpiece into the plane orthogonal to the scratch direction. In experiments, the projection of the submersed part of the tip is used, while in MD, one may use the position of the atoms contacting the tip to determine these areas [17, 18]. Figure 4 c shows the evolution of these areas with scratch length; the normal area decreases after the onset regime as the rear part of the tip loses contact with the groove bottom, while the transverse area increases due to the growth of the frontal pile-up.

After the onset regime, the contact pressures assume roughly constant values, Fig. 4 d; these are denoted as the (normal or transverse) hardness of the material. Fluctuations occur since, in particular, the force is subject to fluctuations generated by the generation and emission of dislocations in the plastic zone. Such fluctuations will be smeared out for slower processes and larger indenters, i.e., in comparisons with larger-sized experiments. In nanoscopic simulations, hardness is not a material characteristic but depends on the process. Thus, it decreases with increasing indenter size [6] in agreement with the indentation size effect [19, 20] which originates in the decrease of dislocation density—and hence of Taylor hardening—for larger tips [19–21].

Assuming that normal and transverse hardnesses are approximately equal [22], the friction coefficient, Eq. 5, is simply given by the ratio of transverse and normal areas. Using the geometrical areas, this prediction gives a value of $\mu = 0.45$, in rough agreement with the simulation result immediately after the onset regime [10].

3.4 Tip Geometry

Actual tips used for indentation or scratch experiments often have a pyramidal—Berkovich or Vickers—form. However, on a nanoscale, they are rounded at their end, with curvature radii that may be as small as several ten nm. Thus, the simulations described above may be realistic for indentation and scratch depths in the nm range. Nonetheless, it is interesting to study the dependence of the indentation and scratch mechanisms on the shape of the indenter by scaling down the size of

actual indenters to the nanoscale. Such simulations have been performed for conical indenters, Berkovich pyramids, and cube-corner indenters [23, 24].

Figure 5 shows the dislocation network developing under a conical indenter after scratching in dependence of the semi-apex angle, β , of the cone. A strong increase of the network with β can be observed. It is related to the fact that the $\langle 111 \rangle$ slip directions form an angle of 54.7° to the surface normal. Hence, for large semi-apex angles, the cones obstruct slip to the surface leading to complex networks. In agreement with the increase of the dislocation network, also the indentation hardness increases with the semi-apex angle β , see Fig. 6a.

The friction coefficient shows a monotonically decreasing trend with β , Fig. 6b. This can be easily understood from a macroscopic argument. Assuming [22] that normal and tangential hardness during scratch are approximately identical, the friction coefficient, Eq. 5, is given by the ratio of transverse and normal areas, which can be calculated from geometry to give [23]

$$\mu = \frac{2}{\pi \tan \beta}. \quad (7)$$

The close agreement of this law with the MD simulations, Fig. 6b, shows that, in this case, macroscopic ideas on friction hold down to the nanoscale.

Simulations with spherical and pyramidal indenters can be compared to conical indenters using the concept of an *equivalent cone angle* [25]. It is defined by stipulating that the ratio of the normal contact area to the indentation depth d is identical to that of a cone. This gives an equivalent cone angle for the pyramid of $\beta_B = 70.3^\circ$. For a sphere, the equivalent angle depends on the indentation depth; in our case, it is equal to $\beta_s = 63.4^\circ$. Figure 6 exemplifies that this idea of an equivalent cone angle works well for the Berkovich pyramid, since this pyramid is a self-similar structure and β_B does not depend on indentation depth. For the sphere, this concept does not work so well; the sphere shows a smaller hardness and a higher friction coefficient than an equivalent cone. This deviation may be traced back [23] to the fact that the cone has an (atomically) sharp tip, while the sphere is blunt; for small indentations $d \ll R$, it actually appears flat. This finding demonstrates that blunt indenters exhibit a different scratching behavior than sharp indenters. Also, the onset of plasticity during indent occurs considerably later than for sharp indenters.

3.5 Multiple Indentation

Multiple (or cyclic) indentation into the same position on a workpiece has been employed to characterize cumulative plasticity in materials [26, 27]. The repeated indentation cycles are as a rule performed to the same maximum load. Since every indentation changes the state of defects—in particular, the dislocations—inside the material, repeated indentation cycles lead to different material responses.

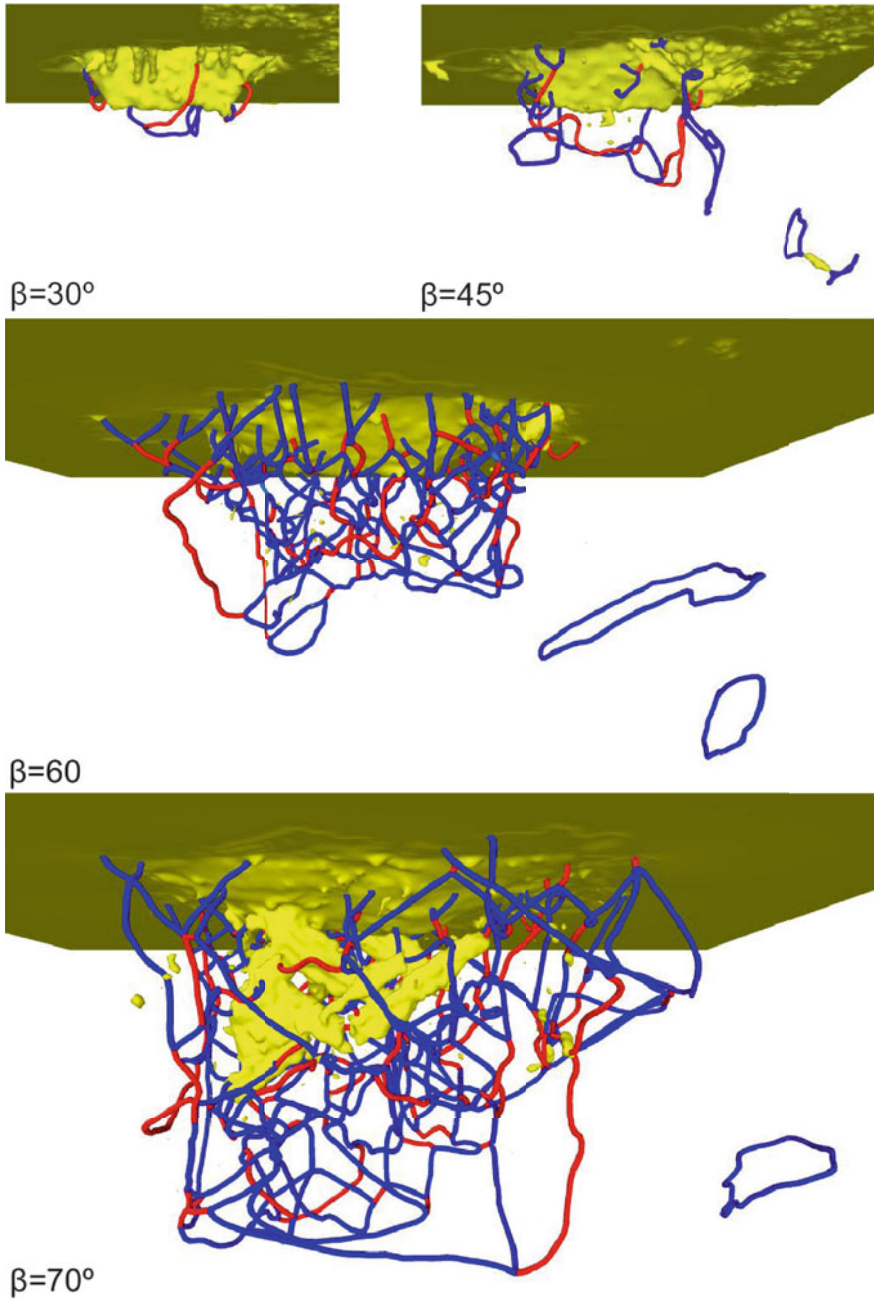


Fig. 5 Dislocation network generated after scratching and retraction of a conical tip with semi-apex angle β as indicated. Dislocations colored as in Fig. 2. The snapshots are at the same scale. Taken with permission from Ref. [23]

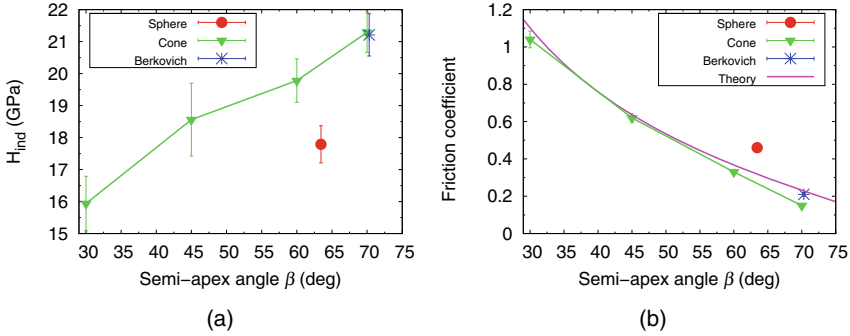


Fig. 6 Dependence of the **a** indentation hardness and **b** friction coefficient on the semi-apex angle β . A (100) Fe surface is scratched in the $[0\bar{1}\bar{1}]$ direction. Data for the spherical indenter and the Berkovich indenter are included at the respective equivalent cone angles. Lines are to guide the eye. The friction results denoted as “Theory” present Eq. 7. Taken with permission from Ref. [23]

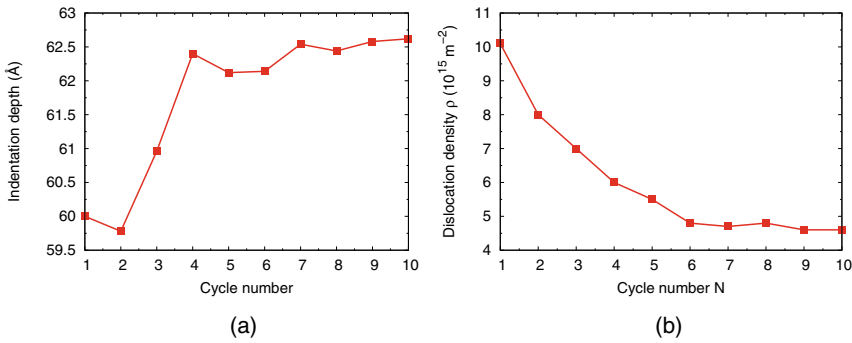


Fig. 7 Multiple indentation: Dependence of the **a** maximum indentation depth and **b** dislocation density in the plastic zone on cycle number. Taken from Ref. [26] under CC BY

Figure 7 illustrates this phenomenon, for example, of an Fe (100) surface. The first indentation—into a defect-free ideal crystal—was performed to a depth of 6 nm and required a maximum force of $4.55 \mu\text{N}$. Repeated indentations with the same maximum force allowed the indenter to penetrate deeper into the material, Fig. 7a. This indicates that the dislocation network generated by the first indent is further modified by subsequent indentations. A detailed inspection [26] of these changes shows that the total length of dislocations was reduced from $1.07 \mu\text{m}$ after the first indent to $0.69 \mu\text{m}$ after the tenth indent. Concomitantly, the size of the plastic zone grew from 36.2 to 40.4 nm. In total, the density of dislocations decreased in the plastic zone by a factor of around 2, see Fig. 7b. These changes reflect the relaxation of the dislocation network under the multiple plastic deformations occurring in a cyclic indentation scenario.

4 Lubrication

Lubrication plays an important role in tribological and machining processes. It serves twofold: On the one hand, lubrication reduces the friction and thus weakens the generation of heat in the contact process. On the other hand, the working fluid cools the solid bodies, acting as a heat sink. Both functionalities were investigated for a nanoscopic scratching process by means of molecular dynamics simulations.

The contact process depicted in Fig. 1 was adapted here using a fluid as lubricant. Two different situations were considered: (1) a simple, yet representative and generic model system [28–31]; (2) specific real substance systems [32, 33]. For the model system, a quasi-two-dimensional setup was used. Hence, the indenter was a cylinder. For the real substance systems, the indenter was a sphere [32] or a spherical cap [33]. As lubricant, in a first study, methane was used [32]; in a second study, both methane and decane were used [33]. The force fields of the real substance fluids, which we have also studied regarding bulk phase properties [34, 35], were taken from an extended version of the MolMod database [36].

Here, the focus is on the lubricated model systems. Results for the lubricated model system are presented and discussed using the Lennard–Jones units system (see Chap. 9 and Ref. [37] for details). The force field settings, simulation parameters, and simulation box configurations applied here were adopted from Refs. [29, 30].

For the model system, the Lennard–Jones truncated & shifted (LJTS) model potential was used for describing all applicable interactions. The LJTS model system has been extensively studied in the literature. Therefore, the relation of many macroscopic properties to the model parameters as well as the thermodynamic state point has been elucidated, e.g., for the vapor–liquid equilibrium [38, 39], the wetting behavior [40, 41], the transport properties [35, 42, 43], and interfacial properties [44, 45]. Details on the LJTS model system are discussed in Chap. 9. Here, the model system was in particular used to systematically study the influence of the solid–fluid interaction energy on the contact process properties.

Figure 8 shows the results for the coefficient of friction (COF) in the scratching process. In the starting phase of the scratching process, the COF is larger in the dry case. Vice versa, in the quasi-stationary phase, the COF is larger in the lubricated case. The presence of a lubricant reduces the COF by about 25% compared to the dry reference case, which is due to the fact that a significant amount of lubricant molecules remain between the indenter and the substrate in the starting phase until they are squeezed out of the gap between the indenter and the substrate. The presence of the lubricant molecules in the gap result in an increased normal force and a slightly decreased tangential force in the starting phase [29]. Once the fluid molecules are squeezed out and the contact is essentially dry with ongoing scratching, the coefficient of friction is increased by the presence of a fluid compared to a dry case by approximately 15%. This is due to the fact that individual fluid molecules are imprinted into the substrate surface, which requires additional work being done by the indenter [32]. The change in the COF by the presence of a fluid is practically independent of the energy of the solid–fluid interaction, cf. Fig. 8-right.

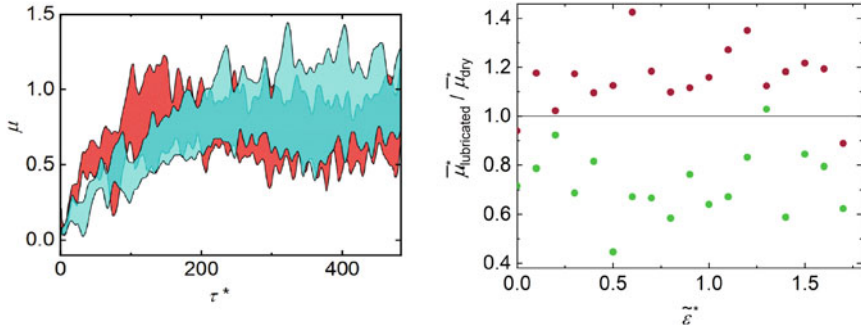


Fig. 8 Coefficient of friction sampled in dry and lubricated simulations. Left: COF as a function of the simulation time during the scratching process for a dry case (red) and a lubricated case (blue). The lubricated case had the solid–fluid interaction energy $\tilde{\epsilon}^* = 0.5$. The shaded areas (red and blue) are bands of the width of the standard deviation obtained from a set of eight simulation replicas around their arithmetic mean. Right: average COF as a function of the reduced solid–fluid interaction energy obtained in the starting phase (brown symbols) and a steady-state phase (green symbols). Data taken from Refs. [29, 30]

Figure 9 shows the temperature field (left) and the thermal balance (right) of the scratching process. For the temperature field, results for a dry case (top) and a lubricated case (bottom) are shown. For the thermal balance, ΔU_S^* and ΔU_F^* indicate the changes in the total energy (kinetic + potential energy) of the substrate and the fluid, respectively. $Q_{\text{thermostat}}^*$ is the total heat removed from the system by the thermostat and W_I^* is the work done by the indenter on the system. All properties of the energy balance W_I^* , ΔU_S^* , ΔU_F^* , and Q_{Th}^* are normalized at each time step during the simulation by the work done by the indenter at the end of the contact process $W_{\text{I,dry}}^*(\tau_{\text{end}}^*)$ in the dry case

$$\Delta E_{\text{norm}}(\tau^*) = \frac{Z(\tau^*)}{W_{\text{I,dry}}^*(\tau_{\text{end}}^*)} \quad \text{with } Z = W_I^*, \Delta U_S^*, \Delta U_F^*, Q_{\text{Th}}^*. \quad (8)$$

The presence of a fluid has a significant influence on the temperature field of the fluid and the energy balance of the process [29]. The fluid in the direct vicinity of the formed chip shows a significantly increased temperature compared to the bulk material, cf. Fig. 9-left. The temperature field moreover reveals that the temperature in the substrate decays much faster than in the fluid. This is due to the fact that the heat conductivity in the substrate is about an order of magnitude higher than that in the fluid. The maximum temperature is found at the tip of the chip.

The heat impact on the substrate is reduced up to 20% by the presence of a lubricant compared to a dry simulation, cf. Fig. 9-right. Two effects contribute to the cooling effect: (a) the fluid reduces the friction during the starting of the scratching and therefore reduces the amount of dissipated energy in the contact zone; (b) a heat flux from the contact zone to the fluid directly cools the contact zone. Moreover, the

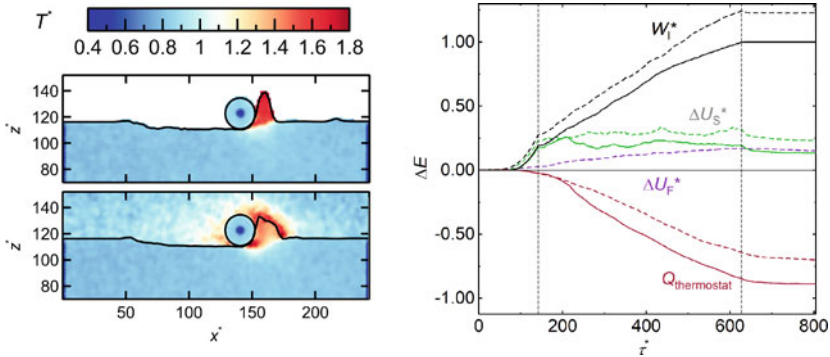


Fig. 9 Temperature field in the simulation box in lubricated simulation (left) for a dry case (top) and a lubricated case (bottom) and thermal balance as a function of the simulation time (right). The lubricated case had the solid–fluid interaction energy $\bar{\epsilon}^* = 0.5$. For the temperature profiles (left), the temperature was averaged over the box length in y -direction. For the thermal balance, solid lines indicate a dry reference case and dashed curves indicate the lubricated case. Details are given in Ref. [29]. Data taken from Refs. [29, 31]

cooling capabilities of the fluid have been found to be dependent on the energy of the solid–fluid interaction, which has been discussed in detail by Stephan et al. [29].

The main part of the work done by the indenter is found to dissipate and is removed from the system via the substrate thermostat, cf. Fig. 9. The potential energy of the substrate fluctuates in the stationary phase of the scratching but does not steadily increase with the ongoing formation of the chip. The energy dissipation dominates the energy balance compared to the energy required for defect generation and plastic deformation.

By performing sets of replicas, the statistical uncertainties of the non-equilibrium MD simulation observables were estimated [30]. The standard deviation of a given observable of a set of replicas, which solely differ in the initial thermal motion is normalized for each observable so that the reliability of the findings derived from different properties can be compared. Most importantly, the statistical uncertainty of all investigated observables was found to quickly converge during the scratching process. Hence, differences among the simulations of a set of replicas do not build up with the simulation time.

5 Relation to Experimental Observations

5.1 Experimental

Experimental results related to the simulations are derived from indentation and scratch tests performed with a nominally conical diamond indenter on an Fe single

crystal surface. The standard indenter with an apex angle of 90° is rounded at its tip. According to the manufacturer's information, the radius of curvature is less than $1\ \mu\text{m}$. In this section, the focus of the investigations will be on scratch experiments in the $[0\bar{1}\bar{1}]$ direction of the (100) surface of the crystal. After the indenter has touched the surface, the load F_n is linearly increased up to a fixed value (indentation) and then moved parallel to the surface for the scratching experiments with an almost constant normal force and a constant speed of $0.1\ \mu\text{m/s}$ (scratching). The lateral force is measured over the scratch length of typically $5\ \mu\text{m}$, then the tip is pulled out of the surface and the topography of the scratch is measured with an atomic force microscope (AFM) in tapping mode (tip radius $< 10\ \text{nm}$). Loading and unloading times are both 15 s for the scratching experiments, while the unloading times for the indentation experiments are only 5 s. Scratch and indentation tests were repeated between 5 and 15 times for each measured value and the results are averaged accordingly. In order to prevent small metal particles adhering to the indenter tip from influencing the results, the indenter was subjected to a special procedure before each series of measurements: In order to remove any metal particles adhering to the indenter tip, 10 indentations are carried out on a fused silica surface with almost the maximum permissible normal force. This procedure is repeated after each measurement series with a maximum of 10–12 scratches. Tests with the smallest and largest loads are carried out twice, at the beginning and at the end of a series. Since there was no significant difference between the results, it is assumed that these were not influenced by adhering metal particles.

5.2 Groove, Pile-up, and Tip Geometry

Figure 10 on the left shows AFM results after an indentation measurement with a load of $F_n = 300\ \mu\text{N}$; on the right, the corresponding 3D representation for the scratched surface is shown. Due to the four $\langle 111 \rangle$ slip directions available in an intact crystal (cf. Sect. 3.2), one expects a four-fold symmetry for material ejection beside the indentation. While the four-fold symmetry is clearly evident for larger loads, due to contaminations and irregularities on the Fe surface, the full four-fold symmetry could not always be observed for $F_n < 500\ \mu\text{N}$. As observed in the simulation (see Fig. 3-top right), for the scratch experiments the pile-up should appear predominantly in the forward direction in front of the scratch. In contrast, the experiments for low loads ($< 300\ \mu\text{N}$) show the ejected material almost exclusively sideways along the scratch track (Fig. 10-right). A possible explanation for this behavior is that during scratching the material originally excavated in front of the indenter tip is transported sideways along the indenter surface, at least for scratch lengths that are significantly longer than in the simulation. Another explanation could also be the effect of so-called subsurface lattice rotations [46], which under certain conditions can reduce long-range stress fields. Since such effects would be relatively slow on the one hand and wide-ranging on the other, it is not expected that they would be noticeable in the MD simulation, but could play a role in the experiment.

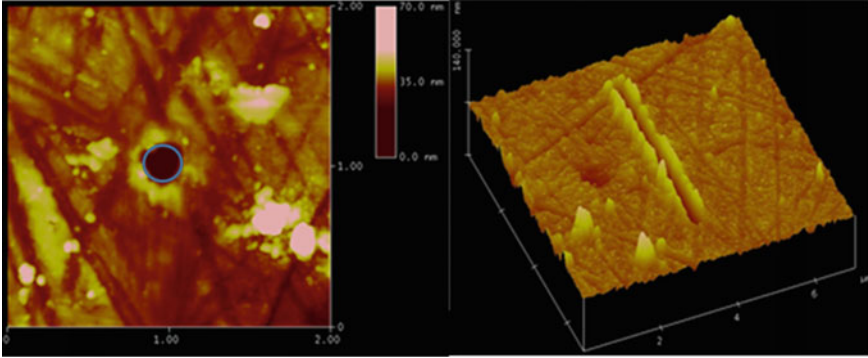


Fig. 10 Two-dimensional representation of an indent on an Fe (100) surface taken at a normal force of $300 \mu\text{N}$ (left side); three-dimensional representation of a scratch in the $[0\bar{1}1]$ direction with the same normal force value (right side)

Since the penetration depth is small enough for low loads, the indentation image can be used to obtain information about the actual radius of curvature at the tip of the indenter. The radius of the circle drawn in Fig. 10 is $a \approx 110 \text{ nm}$, and accordingly, the indentation depth is $d \approx 27 \text{ nm}$. If the shape of the indenter tip for this is still small, the depth d is completely approximated by a sphere and the radius obtained is $R = (a^2 + d^2)/(2d) \approx 240 \text{ nm}$. Hence, the indenter used here can be described by a cone (semi-apex angle $\beta = 45^\circ$) with a sphere of radius R at the tip, the slope of which is chosen also to be β at the transition to the cone.

5.3 Friction and Hardness

As in the simulation, the forces exerted during scratching can be measured relatively easily both in the lateral and in the normal direction, i.e., F_t and F_n , so that the coefficient of friction μ is calculated using Eq. 5. Figure 11 shows on the left experimentally determined coefficients of friction plotted over the length of the scratch, and on the right, results from the simulation [17]. The corresponding loads F_n and the corresponding scratch depth values are also included. The experimental curves represent mean values of relatively large areas and over many individual measurements (5–15) and show therefore a significantly smoother course compared to the friction values obtained from the simulation. In the simulated curves, the onset range of the friction values can be assigned approximately to the radius of the indenter tip (here R is always 2.14 nm), in the experimental curves, it is correlated with the radius of the associated indentation. After that, the coefficients of friction in both cases reach more or less constant values that depend on the respective indentation depth. The reason for this behavior is that the projected tangential submersed indenter area A_t for non-self-similar indenter geometries does not remain constant in relation to the

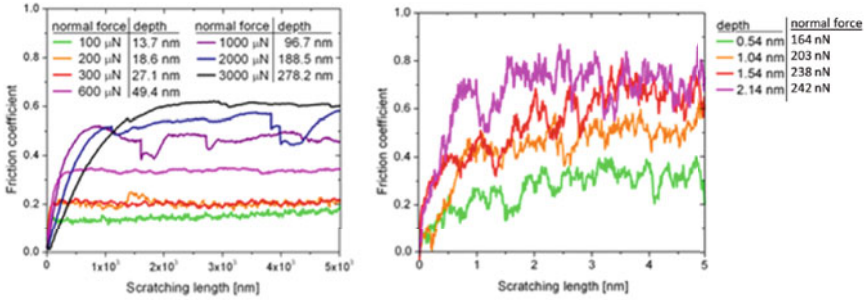


Fig. 11 Evolution of the friction coefficient during scratching of an Fe (100) surface in the $[0\bar{1}\bar{1}]$ direction for various normal loads. The associated penetration depths are also given; experimental data (left side) and simulation results (right side) [17]

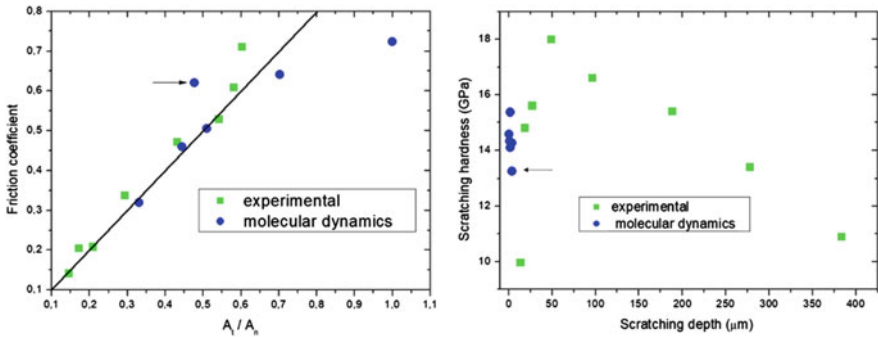


Fig. 12 Comparison of experimental results on friction coefficients (left side) and normal hardness values to molecular dynamic calculations (data from Refs. [17, 23]). The scratch tests were carried out experimentally with a cono-spherical indenter. The molecular dynamic data mainly belong to simulations with a spherical indenter. Results for a conical indenter (same semi-apex angle as in the experiment) are indicated by an arrow. All data are for the same Fe substrate surface and scratching direction as described in the text

normal contact area A_n ; the ratio increases with increasing indentation depth [23]. This can be clearly seen in Fig. 12-left, where experimental and simulated coefficients of friction are plotted against the associated ratio A_t/A_n . Here, A_n is always half of the cross-sectional area of the indenter, since the rear part of the indenter has lost contact with the scratch groove. The plot shows that the measured and simulated coefficients of friction are in good agreement with the theory of Bowden and Tabor [22], which assumes no difference between the scratch hardness in the tangential and normal direction, H_t or H_n respectively, so that μ is determined exclusively by the geometric ratio A_t/A_n . Deviations from this behavior are only indicated for area ratios above 0.5.

For the explicit measurement of the associated hardnesses $H_t = F_t/A_t$ and $H_n = F_n/A_n$, in addition to the forces, the actual respective contact areas A_t and A_n must also be determined. A precise measurement of these areas, which goes

beyond an estimation of the areas alone from the geometric shape of the indenter, as described above, turns out to be particularly difficult both in the simulations and in the experiment. While the actual contact areas cannot be observed in situ during scratching in the experiments, this can still be done in the simulations by determining the contact area occupied by the indenter's contacting substrate atoms [17]. For measuring the associated contact pressures, however, the load transferred with each element of contact area and the role of the resulting pile-up would also have to be taken into account. Figure 12-right shows the progression of the scratch hardness H_n over the respective penetration depth. In the case of the experimental values, the areas A_n are determined from the geometry of the indenter tip, while these were explicitly evaluated in the simulations. In the area of small penetration depths, there is a fair agreement between the molecular dynamic calculations and the experimental values. For greater penetration depths, a drop in hardness values can be observed. This general trend, which is also reflected in the indentation hardnesses, is caused by the indentation size effect [46] which leads to strain hardening of the material with increasing dislocation densities (small penetration depths).

6 Relation to Friction on a Macroscopic Scale

In contrast to the one-time stress on the metal surface in the nanoscratch experiment, a pronounced running-in behavior must be taken into account in the case of recurring stress in a laboratory tribometer used in practice. Here, the metal surface to be tested is moved back and forth on a straight, 10 mm long line segment under a fixed diamond Vickers tip with a maximum relative speed of 10 mm/s. The normal force F_n exerted during the linear reciprocating movement is $F_n = 5$ N. Note that nominally sharp-edged asperity forms, such as the intrinsically self-similar Vickers pyramid, generally have a non-zero radius of curvature at the apex. Even originally sharp-edged asperity profiles can be rounded off by the continued stress when scratching. In practice, the more spherical, i.e., not self-similar, shape of the asperity tip is the rule and decisive for the observed coefficient of friction. In Fig. 13 on the right, experimentally in a laboratory tribometer determined friction coefficient curves for two different orientations of the Vickers tip are distinguished in a double-logarithmic representation, depending on whether the pyramid's "edge" or its "plane" is aligned in the direction of the scratch. It turns out that at the beginning of the experiments, contrary to what is expected for a Vickers pyramid, an influence of the orientation of the Vickers pyramid relative to the direction of the scratch is actually not recognizable. On the other hand, one does find a difference in the coefficients of friction for the two materials used, which in turn is not to be expected for the self-similar shape of a Vickers pyramid. However, both experimentally observed findings are a consequence of the spherical shape of the outermost indenter tip when the scratching tests are carried out with the same normal force on steel samples of different hardness, i.e., case hardening steel 16MnCr5 and an austenitic TWIP steel (HSD600, see Chap. 12), and therefore different penetration depths have to be taken into account. Measuring

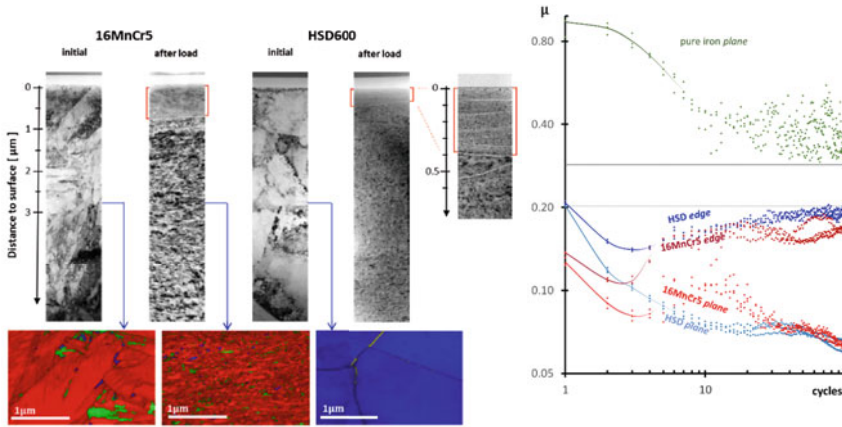


Fig. 13 Surface morphology (left side) and friction coefficient curves (right side) for a case-hardened steel (16MnCr5) and an austenitic HSD steel. Left: EFTEM brightfield and ACOM (Automated Crystal Orientation Mapping) images of cross-sectional areas near the surface, without and after tribological loading with $F_n = 5$ N, Vickers diamond, α -martensite (red), ϵ -martensite (yellow), austenite (blue), and ϵ -carbide phases (green). Right: development of the coefficient of friction for different materials as a function of the number of cycles

the tip profile in an electron microscope results in a value of around $R \leq 50 \mu\text{m}$ for its radius of curvature. With a microhardness that is above 700 HV for the case-hardened steel in the initial state and less than half this value for the HSD steel, the geometric approximation already described in this chapter actually gives friction coefficients μ_{geo} for the spherical indenter tip that is close to the measured values for both steels.

Due to characteristic changes in the morphology of the near-surface areas, the coefficient of friction can change significantly after repeated stress caused by repeated scratching of the same surface area. After about 100 load changes in the tribometer, the coefficients of friction for the two materials can hardly be distinguished, as was the case at the beginning of the tests. However, significant different μ values are now measured depending on the orientation of the Vickers tip. In order to be able to understand the similar values of the friction coefficients for different kinds of steel, the near-surface area in the scratch mark was analyzed in detail using EFTEM (Energy Filtered Transmission Electron Microscopy) (Fig. 13-left). For this purpose, the tests were selected with the pyramid surfaces oriented in the direction of the scratch and the associated cross-sectional lamellae were taken from the bottom of the wear track in a FIB (Focused Ion Beam).

Through the combined application of different analytical techniques, i.e., Selected Area Diffraction (SAD), Electron Precession Diffraction (PED), Energy-Dispersive X-ray spectroscopy (EDX), and Electron Energy Loss Spectroscopy (EELS), it becomes apparent [47] that two structurally clearly distinguishable tribolayers are formed in the 16MnCr5 steel, a fine-grained lower layer mainly of α -iron and a thin,

clearly separated and approximately $0.7 \mu\text{m}$ thick, nanocrystalline layer above it (see red marking in Fig. 13-left) with additional small magnetite (Fe_3O_4) quantities. Like the unstressed base material, both layers have a high martensite content. In the case of the HSD steel, a very fine-grained area that reaches several micrometers into the structure and, clearly separated, a somewhat thinner, nanocrystalline zone of $0.4\text{--}0.6 \mu\text{m}$ is created by grain refinement under tribological stress. The selected area diffraction proves that the predominantly austenitic starting material is almost completely transformed into α -martensite, while a mixture of the austenitic starting phase and the transition phase ϵ -martensite is still found in the fine crystalline zone below (see also Chap. 12). The chemical and structural properties of the near-surface zones of both materials, although clearly different in the initial state, have apparently become much more similar due to tribological stress [47].

As a result of the tribo-induced processes during many friction cycles, a similar nanocrystalline morphology appears in both materials, which offers comparatively less resistance to the lateral movement of the indenter on a solidified, fine-grained base material. With the pyramid orientation of the surface moving in the direction of the scratch, this leads obviously to a decrease in the coefficient of friction down to a value of $\mu = 0.06$, which is the same for both materials. Apparently, a different course is obtained if the Vickers orientation is chosen with the edge first. This probably results in other tribological properties in the relevant surface zone, which lead to different coefficients of friction for the edge orientation compared to the face orientation.

In Fig. 13-right, the course of the coefficients of friction for tests with the Vickers indenter on pure Fe (Fe99) is also given. Since the hardness of pure iron is only around 10% of that of case-hardening steel, the indenter now penetrates so deeply that the tip rounding described above is practically irrelevant. But μ is now even significantly higher than the area ratios calculated from the geometry of a Vickers indenter. The reasons for this are, as the comparatively “noisy” progression of the coefficients of friction indicates, adhesion processes that can be attributed to the known affinity of diamond to iron, as well as the significantly larger contact surface for pure Fe. Only with an increasing number of cycles do oxidation processes in particular [48] ensure that the influence of adhesion decreases again. In practice, the adhesion and affinity of the indenter material to the substrate material can indeed play a dominant role. This is shown, for example, in Fig. 14. An adhesive interaction or even the formation of chemical bonds between the indenter and the carrier material can only be avoided if the experiments are carried out with sufficient humidity so that the pure plowing part of the friction values can be observed. With steel instead of diamond, adhesion effects generally even gain in influence and μ depends strongly on air humidity, surface cleanliness [49] and wetting behavior [50].

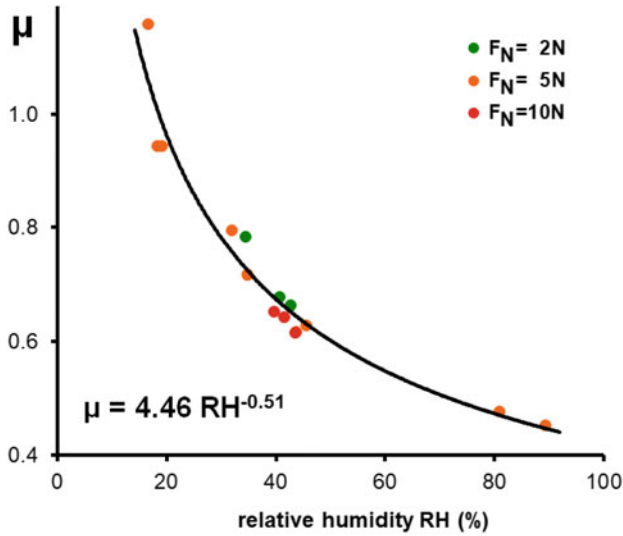


Fig. 14 Coefficient of friction μ as a function of the relative humidity RH for various loads ($F_n = 2, 5,$ and 10 N): The solid line corresponds to a simple exponential dependence $\mu(RH) = 4.46 RH^{-0.51}$. Only for $RH \geq 90\%$, friction is dominated by plowing

7 Summary

MD simulations of indentation and scratching allow to assess the atomistic processes occurring during the plastic deformation of materials. The present review highlighted several of the important findings as follows.

1. The size, R_{pl} , of the plastic zone adherent to the indent pit scales with the radius a_c of the contact zone, $R_{pl} = f a_c$. The plastic-zone size factor f assumes values of the order of 2–3, in agreement with experiments on the microscale.
2. Indentation and scratching of single crystals lead to anisotropic pile-up patterns. The distribution of the pile-up can be understood from a consideration of the activated slip systems that transport atoms onto the surface.
3. The determination of the material hardness requires an assessment of the contact area of the tool with the workpiece. During scratch, this contact area deviates from macroscopic considerations, in particular, because the pile-up generated in front of the scratch tip needs to be taken into account.
4. The friction coefficient during scratch follows the ratio of the transverse to normal contact areas as long as the frontal pile-up is negligible.
5. Tip geometry strongly influences the dislocations generated under the indenter and consequently hardness and friction coefficient. For sharp conical tips, the hardness increases and the friction coefficient decreases with a semi-apex angle.
6. Pyramidal tips follow the behavior of the cones if the pyramid is assigned its equivalent cone angle. Spherical tips behave differently as their shape is not self-

similar; this shows that blunt tips exhibit a different scratching behavior than sharp tips.

7. Multiple or cyclic indentation allows to assess the changes in the dislocation network under the multiple deformations.
8. For lubricated scratching, the coefficient of friction is increased compared to a dry case at the beginning of the scratching process when fluid particles remain in the gap. With ongoing scratching, the fluid particles are squeezed out of the gap and the contact becomes essentially dry. During that phase, the coefficient of friction in a lubricated case is slightly increased compared to a dry case, which is due to the fact that individual fluid particles are imprinted into the substrate surface.
9. The presence of a lubricant has important consequences for the thermal balance of a scratching process, i.e., it reduces the maximum temperature of the substrate and the heat flux into the substrate.

When comparing to experimental data, we find surprisingly good agreement with the calculated friction and hardness data provided by MD calculations. In particular, both MD and experiment find that the hardness on a nanoscale is higher than on a micro- or macroscale. This phenomenon is caused by the indentation size effect which is based on the decrease of dislocation density with tip size. Even in cases, where quantitative deviations occur between simulated and experimentally determined values, atomistic simulations prove to be useful for the interpretation of both individual effects and general trends. Such deviations may be caused not only by the different length and time scales used in the simulations but also by surface contaminations that may occur in experiment, as discussed in Sect. 6.

References

1. Raabe D (1998) Computational materials science. Wiley-VCH, Weinheim
2. Mendeleev MI, Han S, Srolovitz DJ, Ackland GJ, Sun DY, Asta M (2003) Development of new interatomic potentials appropriate for crystalline and liquid iron. *Philos Mag* 83:3977–3994. <https://doi.org/10.1080/14786430310001613264>
3. Kelchner CL, Plimpton SJ, Hamilton JC (1998) Dislocation nucleation and defect structure during surface indentation. *Phys Rev B* 58:11085–11088. <https://doi.org/10.1103/PhysRevB.58.11085>
4. Wagner RJ, Ma L, Tavazza F, Levine LE (2008) Dislocation nucleation during nanoindentation of aluminum. *J Appl Phys* 104:114311. <https://doi.org/10.1063/1.3021305>
5. Luan B, Robbins MO (2005) The breakdown of continuum models for mechanical contacts. *Nature* 435:929. <https://doi.org/10.1038/nature03700>
6. Ruestes CJ, Bringa EM, Gao Y, Urbassek HM (2017) Molecular dynamics modeling of nanoindentation. In: Tiwari A, Natarajan S (eds) Applied nanoindentation in advanced materials. Chapter 14. Wiley, Chichester, UK, pp 313–345. <https://doi.org/10.1002/9781119084501.ch14>
7. Plimpton S (1995) Fast parallel algorithms for short-range molecular dynamics. *J Comput Phys* 117, pp 1–19. <http://lammmps.sandia.gov/>, <https://doi.org/10.1006/jcph.1995.1039>
8. Stukowski A, Albe K (2010) Extracting dislocations and non-dislocation crystal defects from atomistic simulation data. *Model Simul Mater Sci Eng* 18:085001. <https://doi.org/10.1088/0965-0393/18/8/085001>

9. Stukowski A (2010) Visualization and analysis of atomistic simulation data with OVITO—the Open Visualization Tool. *Model Simul Mater Sci Eng* 18:015012. <http://www.ovito.org/>, <https://doi.org/10.1088/0965-0393/18/1/015012>
10. Alabd Alhafez I, Urbassek HM (2019) Influence of tip adhesion on nanoindentation and scratching. *Model Simul Mater Sci Eng* 27(6):065014. <https://doi.org/10.1088/1361-651x/ab27ed>
11. Remington TP, Ruestes CJ, Bringa EM, Remington BA, Lu CH, Kad B, Meyers MA (2014) Plastic deformation in nanoindentation of tantalum: a new mechanism for prismatic loop formation. *Acta Mater* 78:378–393. <https://doi.org/10.1016/j.actamat.2014.06.058>
12. Gao Y, Ruestes CJ, Tramontina DR, Urbassek HM (2015) Comparative simulation study of the structure of the plastic zone produced by nanoindentation. *J Mech Phys Sol* 75:58–75. <https://doi.org/10.1016/j.jmps.2014.11.005>
13. Alabd Alhafez I, Ruestes CJ, Urbassek HM (2018) Size of the plastic zone produced by nanoscratching. *Tribol Lett* 66(1):20. <https://doi.org/10.1007/s11249-017-0967-9>
14. Johnson KL (1985) *Contact mechanics*. Cambridge University Press, Cambridge
15. Durst K, Backes B, Göken M (2005) Indentation size effect in metallic materials: correcting for the size of the plastic zone. *Scr Mater* 52:1093–1097. <https://doi.org/10.1016/j.scriptamat.2005.02.009>
16. Alabd Alhafez I, Ruestes CJ, Gao Y, Urbassek HM (2016) Nanoindentation of hcp metals: a comparative simulation study of the evolution of dislocation networks. *Nanotechnology* 27(4):045706. <https://doi.org/10.1088/0957-4484/27/4/045706>
17. Gao Y, Brodyanski A, Kopnarski M, Urbassek HM (2015) Nanoscratching of iron: a molecular dynamics study of the influence of surface orientation and scratching direction. *Comput Mater Sci* 103:77–89. <https://doi.org/10.1016/j.commatsci.2015.03.011>
18. Ziegenhain G, Urbassek HM, Hartmaier A (2010) Influence of crystal anisotropy on elastic deformation and onset of plasticity in nanoindentation: a simulational study. *J Appl Phys* 107:061807. <https://doi.org/10.1063/1.3340523>
19. Nix WD, Gao H (1998) Indentation size effects in crystalline materials: a law for strain gradient plasticity. *J Mech Phys Sol* 46:411. [https://doi.org/10.1016/S0022-5096\(97\)00086-0](https://doi.org/10.1016/S0022-5096(97)00086-0)
20. Swadener JG, George EP, Pharr GM (2002) The correlation of the indentation size effect measured with indenters of various shapes. *J Mech Phys Sol* 50:681. [https://doi.org/10.1016/S0022-5096\(01\)00103-X](https://doi.org/10.1016/S0022-5096(01)00103-X)
21. Al-Rub RKA, Voyiadjis GZ (2004) Analytical and experimental determination of the material intrinsic length scale of strain gradient plasticity theory from micro- and nano-indentation experiments. *Int J Plast* 20(6):1139–1182. <https://doi.org/10.1016/j.ijplas.2003.10.007>
22. Bowden FP, Tabor D (1966) Friction, lubrication and wear: a survey of work during the last decade. *Brit J Appl Phys* 17:1521–1544. <https://doi.org/10.1088/0508-3443/17/12/301>
23. Alabd Alhafez I, Brodyanski A, Kopnarski M, Urbassek HM (2017) Influence of tip geometry on nanoscratching. *Tribol Lett* 65:26. <https://doi.org/10.1007/s11249-016-0804-6>
24. Zonana MC, Ruestes CJ, Bringa EM, Urbassek HM (2020) Effect of tip roundness on the nanoindentation of Fe crystals. *Tribol Lett* 68(2):56. <https://doi.org/10.1007/s11249-020-01295-9>
25. Fischer-Cripps AC (2004) *Nanoindentation*, 2nd edn. Springer, New York
26. Deldar S, Alabd Alhafez I, Smaga M, Beck T, Urbassek HM (2019) Cyclic indentation of iron: a comparison of experimental and atomistic simulations. *Metals* 9(5):541. <https://doi.org/10.3390/met9050541>
27. Chicot D, Roudet F, Zaoui A, Louis G, Lepingle V (2010) Influence of visco-elasto-plastic properties of magnetite on the elastic modulus: multi cyclic indentation and theoretical studies. *Mater Chem Phys* 119(1):75–81. <https://doi.org/10.1016/j.matchemphys.2009.07.033>
28. Lautenschlaeger MP, Stephan S, Urbassek HM, Kirsch B, Aurich JC, Horsch MT, Hasse H (2017) Effects of lubrication on the friction in nanometric machining processes: a molecular dynamics approach. *Appl Mech Mater* 869:85–93. <https://doi.org/10.4028/www.scientific.net/AMM.869.85>
29. Stephan S, Dyga M, Urbassek HM, Hasse H (2019) The influence of lubrication and the solid-fluid interaction on thermodynamic properties in a nanoscopic scratching process. *Langmuir* 35(51):16948–16960. <https://doi.org/10.1021/acs.langmuir.9b01033>

30. Stephan S, Dyga M, Alabd Alhafez I, Urbassek HM, Hasse H (2021) Reproducibility of atomistic friction computer experiments: a molecular dynamics simulation study. *Mol Simul* 47(18):1509–1521. <https://doi.org/10.1080/08927022.2021.1987430>
31. Schmitt S, Stephan S, Kirsch B, Aurich JC, Kerscher E, Urbassek HM, Hasse H (2021) Molecular simulation study on the influence of the scratching velocity on nanoscopic contact processes. In: Garth C, Aurich JC, Linke B, Müller R, Ravani B, Weber GH, Kirsch B (eds) 2nd international conference on physical modeling for virtual manufacturing (iPMVM 2020), vol 89. Open Access Series in Informatics (OASISs). Schloss Dagstuhl - Leibniz-Zentrum für Informatik, Dagstuhl, Germany, pp 17:1–17:16. <https://doi.org/10.4230/OASISs.iPMVM.2020.17>
32. Stephan S, Lautenschlaeger MP, Alabd Alhafez I, Horsch MT, Urbassek HM, Hasse H (2018) Molecular dynamics simulation study of mechanical effects of lubrication on a nanoscale contact process. *Tribol Lett* 66(4):126. <https://doi.org/10.1007/s11249-018-1076-0>
33. Stephan S, Schmitt S, Hasse H, Urbassek HM (2023) Molecular dynamics simulation of the Stribeck curve: boundary lubrication, mixedlubrication, and hydrodynamic lubrication on the atomistic level. In: *Friction* (2023). in press
34. Schmitt S, Fleckenstein F, Hasse H, Stephan S (2023) Comparison of force fields for the prediction of thermophysical properties of long linear and branched alkanes. *J Phys Chem B* 127(8):1789–1802. <https://doi.org/10.1021/acs.jpcc.2c07997>
35. Fertig D, Hasse H, Stephan S (2022) Transport properties of binary Lennard-Jones mixtures: insights from entropy scaling and conformal solution theory. *J Mol Liq* 367:120401. <https://doi.org/10.1016/j.molliq.2022.120401>
36. Stephan S, Horsch M, Vrabec J, Hasse H (2019) MolMod-an open access database of force fields for molecular simulations of fluids. *Mol Simul* 45(10):806–814. <https://doi.org/10.1080/08927022.2019.1601191>
37. Stephan S, Thol M, Vrabec J, Hasse H (2019) Thermophysical properties of the Lennard-Jones fluid: database and data assessment. *J Chem Inf Model* 59(10):4248–4265. <https://doi.org/10.1021/acs.jcim.9b00620>
38. Vrabec J, Kedia GK, Fuchs G, Hasse H (2006) Comprehensive study of the vapour-liquid coexistence of the truncated and shifted Lennard-Jones fluid including planar and spherical interface properties. *Mol Phys* 104(9):1509. <https://doi.org/10.1080/00268970600556774>
39. Stephan S, Liu J, Langenbach K, Chapman WG, Hasse H (2018) Vapor-liquid interface of the Lennard-Jones truncated and shifted fluid: comparison of molecular simulation, density gradient theory, and density functional theory. *J Phys Chem C* 122(43):24705–24715. <https://doi.org/10.1021/acs.jpcc.8b06332>
40. Becker S, Urbassek HM, Horsch M, Hasse H (2014) Contact angle of sessile drops in Lennard-Jones systems. *Langmuir* 30(45):13606. <https://doi.org/10.1021/la503974z>
41. Heier M, Stephan S, Diewald F, Müller R, Langenbach K, Hasse H (2021) Molecular dynamics study of wetting and adsorption of binary mixtures of the Lennard-Jones truncated and shifted fluid on a planar wall. *Langmuir* 37:7405–7419. <https://doi.org/10.1021/acs.langmuir.1c00780>
42. Diewald F, Lautenschlaeger M, Stephan S, Langenbach K, Kuhn C, Seckler S, Bungartz H-J, Hasse H, Müller R (2020) Molecular dynamics and phase field simulations of droplets on surfaces with wettability gradient. *Comput Methods Appl Mech Eng* 361:112773. <https://doi.org/10.1016/j.cma.2019.112773>
43. Lautenschlaeger MP, Hasse H (2019) Transport properties of the Lennard-Jones truncated and shifted fluid from non-equilibrium molecular dynamics simulations. *Fluid Phase Equilib* 482:38–47. <https://doi.org/10.1016/j.fluid.2018.10.019>
44. Heier M, Diewald F, Horsch MT, Langenbach K, Müller R, Hasse H (2019) Molecular dynamics study of adsorption of the Lennard-Jones truncated and shifted fluid on planar walls. *J Chem Eng Data* 64(2):386–394. <https://doi.org/10.1021/acs.jced.8b00927>
45. Schmitt S, Vo T, Lautenschlaeger MP, Stephan S, Hasse H (2022) Molecular dynamics simulation study of heat transfer across solid-fluid interfaces in a simple model system. *Mol Phys* 120(10):e2057364. <https://doi.org/10.1080/00268976.2022.2057364>
46. Pharr GM, Herbert G, Gao Y (2010) The indentation size effect: a critical examination of experimental observations and mechanistic interpretations. *Annu Rev Mater Res* 40:271. <https://doi.org/10.1146/annurev-matsci-070909-104456>

47. Brodyanski A, Klein MW, Merz R, Smaga M, Beck T, Kopnarski M (2020) Microstructural changes caused by friction loading in high manganese TWIP steel and case-hardened 16MnCr5. *Mater Charact* 163:110231. <https://doi.org/10.1016/j.matchar.2020.110231>
48. Merz R, Brodyanski A, Kopnarski M (2015) On the role of oxidation in tribological contacts under environmental conditions. In: *Conference Papers in Science 2015*, p 515498. <https://doi.org/10.1155/2015/515498>
49. Huttenlochner K, Müller-Renno C, Ziegler C, Merz R, Merz B, Kopnarski M, Chodorski J, Schlegel C, Ulber R (2017) Removing biofilms from stainless steel without changing surface properties relevant for bacterial attachment. *Biointerphases* 12(2):02C404. <https://doi.org/10.1116/1.4982196>
50. Becker S, Merz R, Hasse H, Kopnarski M (2016) Solvent cleaning and wettability of technical steel and titanium surfaces. *Adsorpt Sci Technol* 34(4–5):261–274. <https://doi.org/10.1177/0263617416645110>

Creating Surface Morphologies by Micro Milling and Micro Grinding



Jan C. Aurich, Nicolas Altherr, Sonja Kieren-Ehse, Benjamin Kirsch,
and Tobias Mayer

Abstract Micro cutting and micro abrasive processes are promising techniques to produce microstructured surfaces in a wide range of materials in a short time and in an economic way. However, due to occurring size effects, simply downscaling of known and mastered macro-scaled processes is not readily possible. At the same time, material removal at small scales holds challenges in observing and characterizing the process itself as well as the process results. Our investigations focused on developing methods and implementing measurement techniques to close the knowledge gap in micro milling and micro grinding. This article presents the development of customized machine tools, tools, processes as well as measurement equipment for micro milling with micro end mills with typical diameters of 50 μm . It will be shown how and with which methods the process and its results can be optimized. Regarding micro grinding, special emphasis is on the manufacturing and application of micro pencil grinding tools via electroless plating, a process customized to produce tools with diameters down to 5 μm .

1 Introduction

Micro products and microstructured surfaces become increasingly important in industrial applications. Examples are medical devices [1], the security and safety technology, information technology, and optical devices [2]. Especially microstructuring of surfaces is a promising way to provide unique properties to otherwise standard surfaces [3]. Micro cutting and micro abrasive processes are manufacturing methods to implement such structures in almost any material. Especially for small batches, those manufacturing methods prevail over competing technologies such as laser ablation or etching in terms of economics and productivity [4].

Milling and grinding are well established industrial processes at conventional scales. Early research has shown that those processes cannot be simply downscaled

J. C. Aurich (✉) · N. Altherr · S. Kieren-Ehse · B. Kirsch · T. Mayer
Institute of Manufacturing Technology and Production Systems, RPTU Kaiserslautern,
Kaiserslautern, Germany
e-mail: fbk@mv.rptu.de

to the microscale [5]. The influence of vibrations and run-out, the limited sharpness of the cutting edge, the limited cutting speeds (due to limited spindle speeds of available spindles), and the limited mechanical strength of the tools all contribute to the so-called size effects [6]. Those size effects necessitate adapted tools and processes compared to conventional machining.

In our research within the CRC 926, we developed customized machine tools, tools, and devices to improve micro milling and micro grinding by understanding the process and process results. A key to this understanding was the integration of advanced measurement technologies into the machine tools and the collaboration with other projects located in the CRC 926. This chapter summarizes the main works conducted and the main findings made.

2 Micro Milling

2.1 *High-Precision Desktop Machine Tool with Integrated Measuring Systems*

In micro milling, high-precision machine tools are needed to manufacture and apply the micro end mills. Commercially available machine tools for micro manufacturing require a large installation space and exceed the size of the workpiece by several magnitudes. Therefore, a desktop sized machine tool was developed to produce and use micro end mills. Due to the smaller size, thermal growth and its negative effect on machining are reduced. These small dimensions also improve the eigenfrequency and thus the stiffness of the whole machine tool. Smaller and lighter parts can be used, which further enhances efficiency and dynamic behavior.

The spindle system of the machine tool must provide very low run-out errors at very high spindle speeds, in order to achieve sufficient cutting speeds. The run-out can be reduced if the tool is produced and used without reclamping. The machine tool presented in this section implements this by combining tool manufacture and micro milling on the same machine. The micro milling center (MMC) consists of several modules that allow the manufacturing and application of tools as well as integrated measurements during and after machining.

Figure 1 shows the MMC with the application module, the main spindle module, the AFM module, and the universal module. All modules are mounted on a massive granite machine bed, which is set up on a Newport Vision Isostation M-VIS3648-SG4-325A table that uses passive pneumatic isolators to minimize the influence of external vibrations. The dimension of the granite bed of only 760 mm × 675 mm × 500 mm leads to a coefficient of linear growth of 3.0×10^{-6} mm/K. The precision linear axis (Rexroth TKK15-155 AL) has a length of 600 mm and moves the main spindle to the application module, the AFM module, and the universal module. The machine tool is controlled by an Aerotech A3200 automation system.

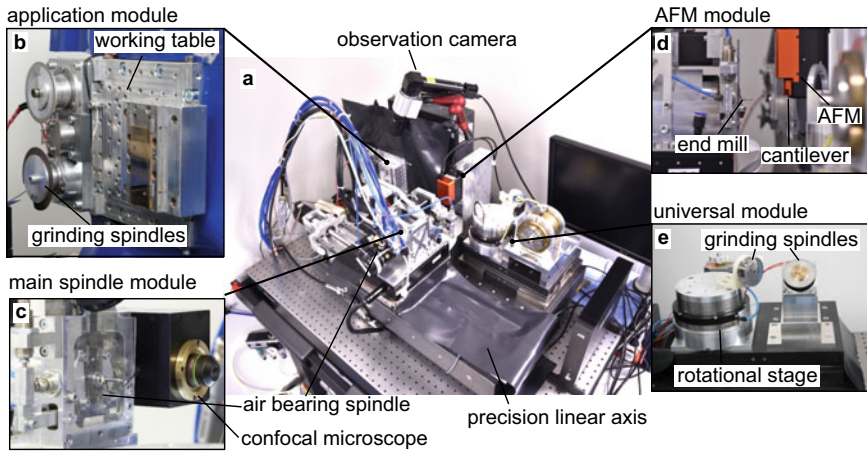


Fig. 1 a Overview of the developed micro milling center, b Application module, c Main spindle module, d AFM module, and e Universal module according to [7]

The application module (Fig. 1b) consists of an Aerotech ANT130-XY-110-Plus linear stage system with a travel range of 110 mm in X- and Y-direction (position accuracy ± 300 nm, minimal step size 1 nm), two grinding spindles for tool manufacturing [8], and a working table for workpiece mounting. This setup can achieve speeds up to 3,200 mm/min with an acceleration of 1 g. A resistance detection system is used to measure the length of the tool.

The main spindle module (Fig. 1c) consists of the main spindle, a spindle positioning system for tool manufacturing, and an Aerotech ANT130-110-Plus axis for movement in the Z-direction. This module is mounted on the precision linear axis, to allow the positioning at the application, universal, or AFM module. An ABL MM125 air-bearing spindle with speeds of up to 125,000 rpm is used as the main spindle. It has no rotary encoder to define the spindle position. For tool manufacturing, an external positioning system is used. To define and hold the specific rotational position of the spindle rotor, the positioning system consists of a stepper motor, a drive belt, and three pneumatic cylinders. The spindle has a total indicated run-out error lower than $4 \mu\text{m}$ at 45,000 rpm and the spindle and spindle mount are water-cooled with a hysteresis of ± 0.2 K. For further information on spindle run-out measurement we refer to [7].

The universal module (Fig. 1e) allows components to be mounted for various applications such as additional grinding wheels or an air bearing rotational stage. For more information on the universal unit, we refer to [7].

Confocal Microscope Integration

To further improve the performance and versatility of the MMC, additional measurement equipment was added to the machine tool. Only in-situ measuring is suitable, due to the reclamping error when using different machines for measuring and

manufacturing. A confocal microscope was added to the MMC's spindle module. A nanofocus confocal microscope (weight 4 kg, length 430 mm, width 66 mm, and height 100 mm) was chosen. It has a resolution of 2 nm in the Z-direction and uses a 1200 × 1200 ppi camera. The resolution in X- and Y-direction depends on the equipped objective. To allow fast mounting (<1 min) with high accuracy (<2 μm), a 3R chuck system was used. The microscope was positioned next to the main spindle and 5 mm in front of the micro end mill so that neither the micro end mill nor the workpiece does need to be removed when measuring. The confocal microscope software can communicate with the MMC's machine control via TCP/IP-Ethernet to move to the desired measurement area or to stitch measurements together. Thus, it is possible to take measurements during machining and to automatically return to machining after measuring [9].

AFM Integration

In micro milling, tool wear has a critical influence on the machining process as the cutting edge radius increases due to wear. High cutting edge radii in the same order as the chip thickness lead to ploughing instead of cutting the material. The characterization of the cutting edge radius is therefore of high interest. Reclamping caused by off-machine measurements is not possible as the tool spindle system is influenced by the reclamping, which can introduce a change in the system's run-out and the Z-offset. An atomic force microscope (AFM) was integrated into the MMC (Fig. 1). A NaniteAFM by Nanosurf is used for integration in the MMC due to its small dimensions (86 mm × 45 mm × 61 mm), low Z-measurement noise level of typically 90 pm (RMS, dynamic mode), and sufficiently large scan area of 110 μm × 110 μm × 20 μm. A mounting device made of aluminum is used to attach the AFM to the MMC. For fast installation and removal of the AFM, a quick mounting plate on the mounting device is used. Figure 1d shows the side view of the main spindle module and the AFM. The AFM is mounted in a way that the tool axis is positioned in the middle of the travel of the AFM axis so that the tool clamped in the spindle can be measured. This integration method offers a characterization of the cutting edge geometry of micro end mills including the cutting edge radii. Also, in situ tool characterization after tool manufacturing and process intermittent wear analysis without unclamping of the tool can be realized. The cutting edge is scanned line per line, with each line perpendicular to the cutting edge. After measuring, the precision linear axis is used to move the main spindle back to the application module, where the milling process is continued. In that way, it is possible to characterize tool wear with respect to the tool life. Figure 2c shows the measurement results of an uncoated micro end mill. The micro end mill is made from cemented carbide with a grain size of 0.2 μm. A 5 μm × 5 μm image in tapping mode was taken and the measurement area was placed right below the corner of the cutting edge (see scanning electron microscope (SEM) image in Fig. 2a). The AFM image resolves individual grains. To determine the cutting edge radius, the software MountainsSPIP Premium V8 was used. A 2 μm sectional cut perpendicular to the cutting edge was used to extract a single profile of the cutting edge which is used to determine the cutting edge radius and the wedge angle (see Fig. 2d). The cutting edge radii measured are typically in

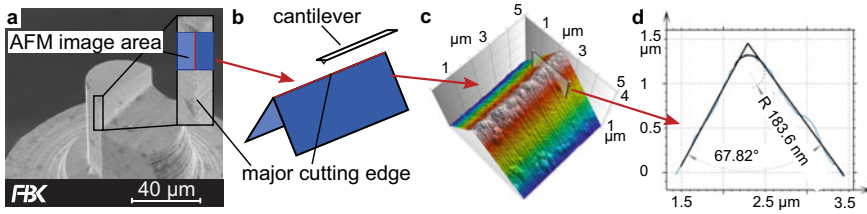


Fig. 2 a + b Alignment of the cutting edge for AFM measurement, c Measurement results of a cutting edge as 3D view, d Sectional cut of the AFM image according to [10]

a range of 100 μm–200 μm. Placing the sectional cut at different locations leads to deviations in the resulting cutting edge radii of up to 50 %. This effect is caused by the shape of the individual grains that form the cutting edge. Also, grain pullouts and defects introduced during the tool grinding process highly influence the cutting edges [10].

A Python-based algorithm is implemented that automatically processes the datasets from the AFM measurements to compute the mean cutting edge radius and variance (see Ref. [11]).

2.2 Micro End Mill Development

2.2.1 Tool Geometry

The micro end mill tool design needs to fulfill several requirements:

- good chip formation and chip removal.
- sharp cutting edge to minimize uncut chip thickness and cutting force.
- flank geometry that prohibits contact to the workpiece at the side walls.
- economical manufacturing in a robust and fast process.

To achieve these requirements, single-edged micro end mills made of cemented carbide are very well suited, as they are capable of machining different kinds of workpiece materials [4]. The developed main geometrical characteristics are shown in Fig. 3a. To avoid contact between the tool and the sidewalls of the workpiece, the radii of the radial flank face are smaller than the effective cutting edge radius r . A positive minor cutting edge angle χ'_r is used to prohibit contact between the tool and the bottom surface. The zero axial and radial rake angles γ are distinct characteristics of the tools. The micro end mills can be manufactured with different helix angles λ . An FEA analysis of the total deformation and total stress for tools was carried out in [12] to find the parameters with the best load distribution. For micro end mill manufacturing of these tools, a three-step grinding process was developed, see [12] for further details. For a micro end mill with a diameter of 20 μm (Fig. 3b), the total manufacturing time is below 20 min, while achieving cutting edge radii r_β of about 0.1 μm–0.2 μm [12].

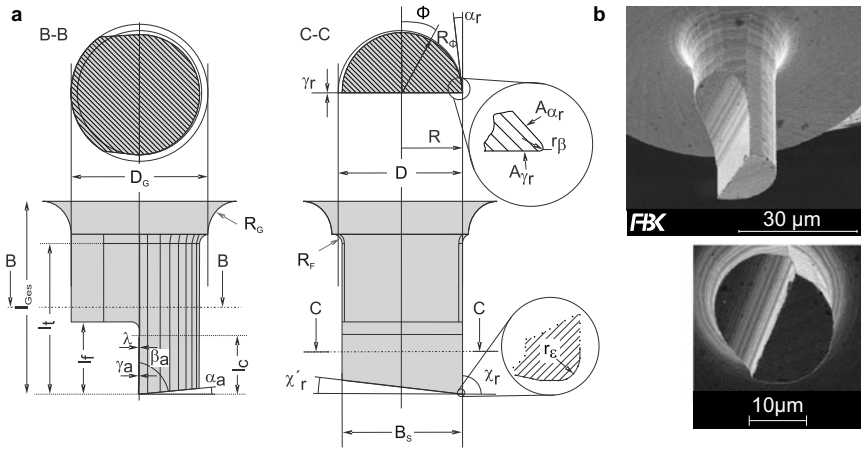


Fig. 3 a Single-edge micro end mill, b SEM image of micro end mill [12]

2.2.2 Effect of Tool Substrate Specification on Tool Quality

The specification of the tool substrate has a large impact on the tool’s performance. This influence was investigated by manufacturing tools made from ultrafine-grained, finest grained, and coarse-grained cemented carbide. With decreasing grain size the tool geometry improved, and a more homogeneous and smooth cutting edge geometry was produced. This is also evident for the cutting forces of these tools when machining cp-titanium (Fig. 4): The highest force values were recorded for the coarse- and finest grained tools, with tool failures after about 42.5 mm and 1,600 mm, respectively. The ultrafine-grained tool reached 16,000 mm feed travel without failure. Thus, it can be concluded that the finer the grain size, the longer the achievable feed travel and the smaller the process forces [13].

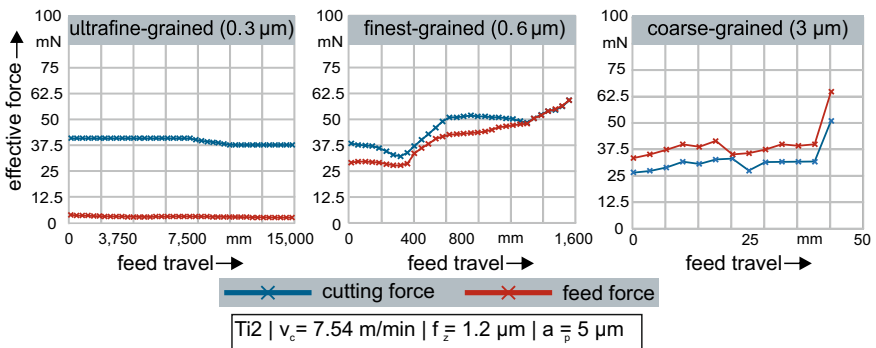


Fig. 4 Forces in dependence of the cemented carbide specification when micro milling according to [13]

2.2.3 All-Ceramic Micro End Mills

Technical ceramics offer good mechanical properties and fine grain sizes, but are not widely utilized for ultra-small micro end mills (USMs). We tested the three oxide ceramics aluminum oxide (alumina/ Al_2O_3), yttria stabilized tetragonal zirconia polycrystal (zirconia/Y-TZP), zirconia toughened alumina (ZTA), and the non-oxide ceramic silicon nitride (Si_3N_4) on their suitability as tool substrates. Figure 5 shows a ground micro end mill for each substrate. The Y-TZP tool has a very sharp cutting edge and no grain pullouts. Si_3N_4 shows less sharp, chamfered cutting edges due to smaller grain pullouts. Both these substrates' tools match the target geometry. That is not the case for the alumina-based ceramics: They show severe grain pullouts and dull cutting edges, and thus the target geometry could not be matched. The increase in grain pullouts visible in the SEM images correlates with the decrease in the ceramics' fracture toughness. Due to the low tool quality of the other substrates, only zirconia is suitable for the manufacture of micro end mills, likely owing to its low grain size and its transformation hardening mechanism [14].

2.2.4 Coating of Micro End Mills

Tool coatings can be applied to micro end mills to improve their wear behavior and milled structure quality. The coating process itself is challenging due to the tool size: The coating has to be thin and evenly distributed, with a high adhesion strength. The thickness of the coating increases the cutting edge radius and, accordingly, the cutting forces, which could lead to tool breakage and low cutting performance. Therefore, the coating layer needs to be fine and dense to increase the cutting edge radius as little as possible.

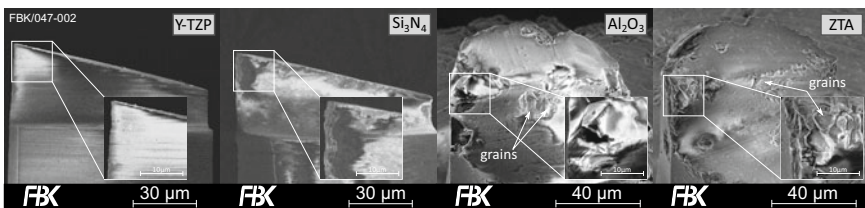


Fig. 5 SEM-images of the ground all-ceramic micro end mills [14]

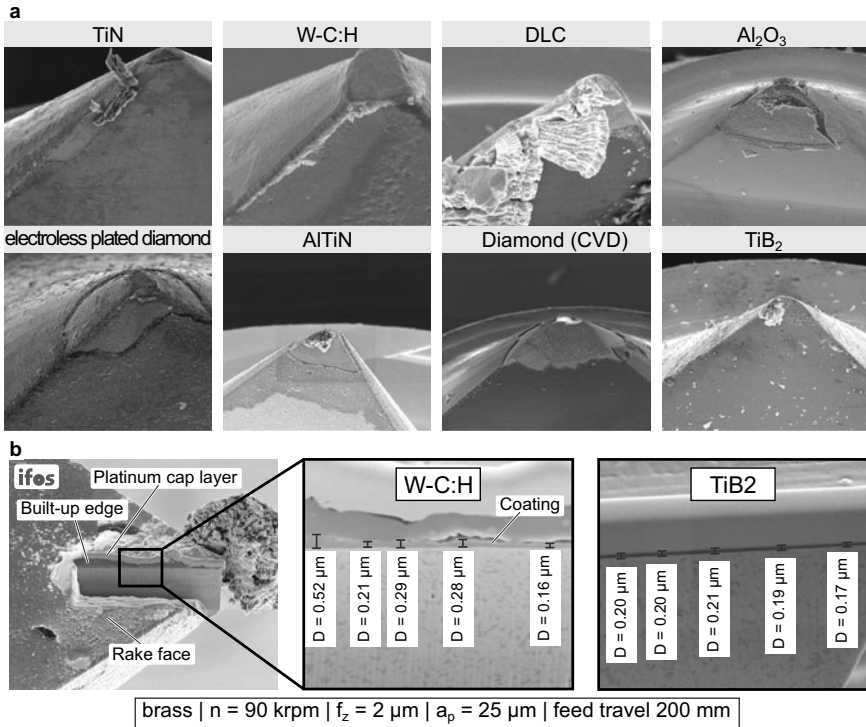


Fig. 6 **a** Coated micro end mills, **b** FIB cut at the tip of the micro end mill, coated with W-C:H (middle) and TiB₂ (right) according to [15]

Comparison of Different Coating Systems

To study suitable coating systems, eight different coatings were applied and evaluated for tapered micro end mills with a diameter of < 40 μm. The applied coatings were TiN, AlTiN, Al₂O₃, TiB₂, DLC (diamond like carbon), W-C:H, electroless plated diamond, and CVD-diamond. Figure 6 a shows the micro end mills after deployment [15].

TiN and W-C:H provide adequate adhesion on the cemented carbide micro end mill, but are not hard enough and show abrasive wear at the cutting edge and on the rake face. For the DLC, Al₂O₃, electroless plated diamond, and TiAlN-coated tools, immediate flake off is seen due to low adhesion to the tool. The CVD-diamond coated tool shows the same behavior, but additionally, the tip of the tool broke off. The TiB₂ coating as the thinnest coating performs the best, with almost no wear and no flaking off. Figure 6 b shows an SEM image with a focused ion beam (FIB) cut of the TiB₂ coating’s cross section, and W-C:H as a comparison. For W-C:H, an inhomogeneous layer thickness of the coating is visible, varying from 0.16 μm to 0.52μm (1.3 μm initial thickness). In contrast, TiB₂ has a very consistent layer thickness in the range of 0.17 μm and 0.21 μm (unworn layer thickness about 0.2 μm), verifying the low

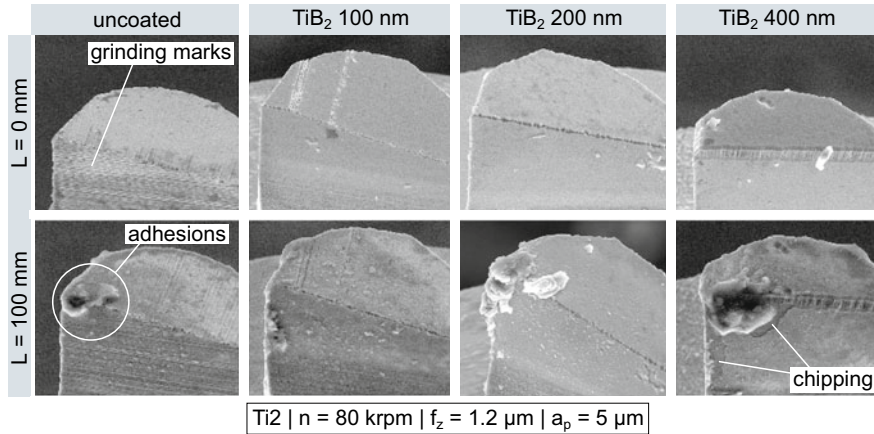


Fig. 7 Micro end mills before and after machining according to [16]

wear observed in the SEM images. The results show that conventional coatings are not applicable for small diameter tools: They are too thick, reducing the tool’s cutting capabilities, or too soft to prohibit abrasive wear on the cutting edge. The only exception to this is TiB₂. With its high hardness, low thickness and good surface adhesion, it can be successfully applied to USMs and further investigations on TiB₂ were carried out [15].

Variation of TiB₂ Layer Thickness

The coating thickness of the TiB₂ coating was varied to find its optimum. The uncoated tool shows sharp cutting edges before milling, and small adhesions and little abrasive wear with a built-up edge (BUE) afterward (Fig. 7). The coating with 100 nm thickness is very homogeneous and shows adhesions and small BUEs after machining, with no abrasive wear. The coating with 200 nm thickness is also homogeneous with small adhesions and BUEs. No abrasive wear or delamination of coating layers is visible. In contrast, the 400 nm coating shows layer delamination at the cutting edges before milling. After milling BUEs are visible and the coating is flaking off the tool [16].

The values of the surface roughness at the slot bottoms machined with the coated tools are higher than those of uncoated tools. However, they have less fluctuating roughness values than the uncoated ones. These fluctuations of the uncoated micro end mills indicate BUE formation. The 200 nm coating shows the smallest cutting forces. The cutting performance of this coating thickness in combination with the SEM images and the roughness values therefore supersedes the other two tested thicknesses, reducing the formation of BUEs and lowering abrasive tool wear the most [16].

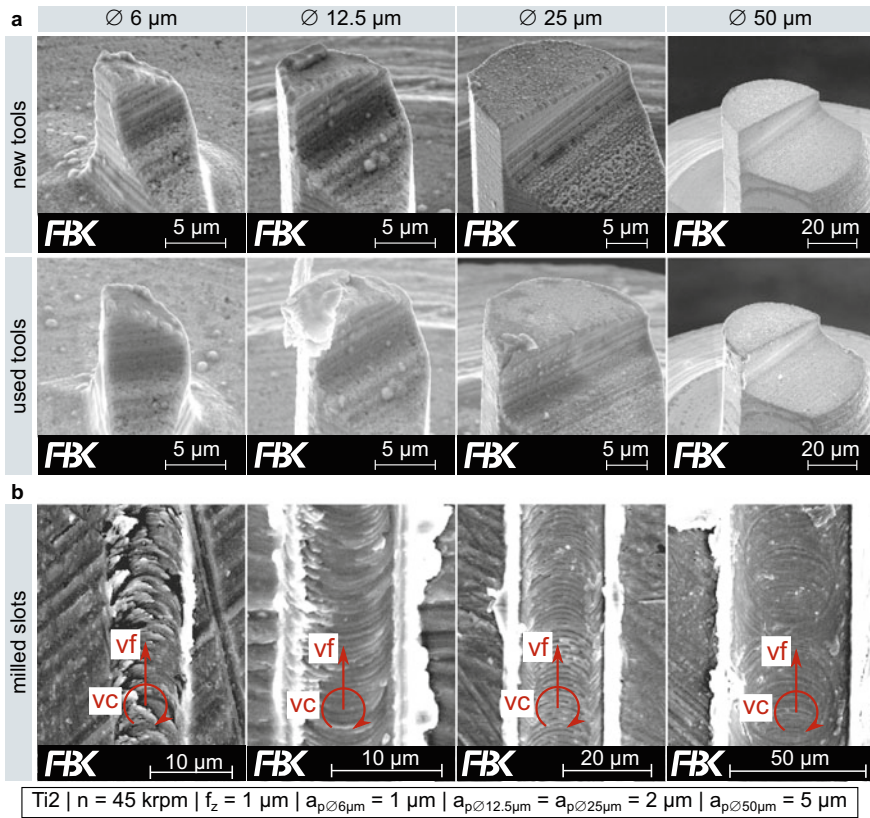


Fig. 8 **a** Micro end mills, **b** SEM images of the micro milled slots according to [17]

Application for TiB₂ Coated USMs with Diameters Down to 6 μm

Micro end mills with diameters of 6, 12.5, 25, and 50 μm were produced and coated with a TiB₂ layer thicknesses of 200 nm. SEM images of the tools after deployment are shown in Fig. 8a, and the micro milled slots in Fig. 8b [17].

No signs of wear and only little adhesions can be seen for the 25 μm and 50 μm micro end mill. Adhesions were found on the 12.5 μm micro end mill, covering the flank face and about half of the micro end mill. The 6 μm tool shows no signs of wear, though the measured slot bottom roughness (not shown) suggests high friction and ploughing resulting from the slow cutting speed and low depth of cut. Also, Fig. 8 shows a nearly burr free structure for the 6 μm tool: The squeezed material stays at the slot bottom and is not formed into a burr, as seen in the resulting uneven slot geometry. The minimum chip thickness seems not to be reached. However, it was shown that all tools, down to a diameter of 6 μm , can be coated with the TiB₂ coating. Coating adhesion was high enough to withstand the high amount of friction, heat, and abrasive wear in the micro milling processes. The 6 μm tool seems to be the

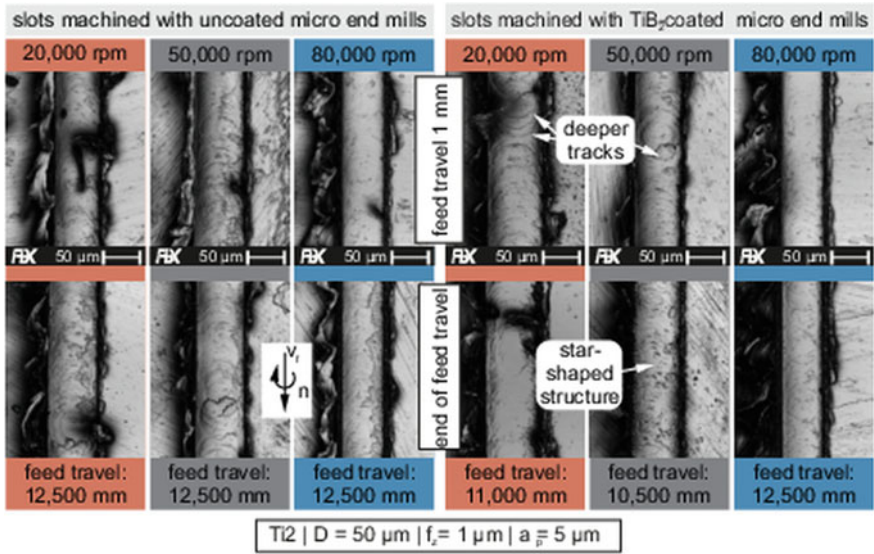


Fig. 9 Slot bottom topography and tool wear depending on spindle speed and tool coating for micro end mills with a diameter of 50 μm according to [18]

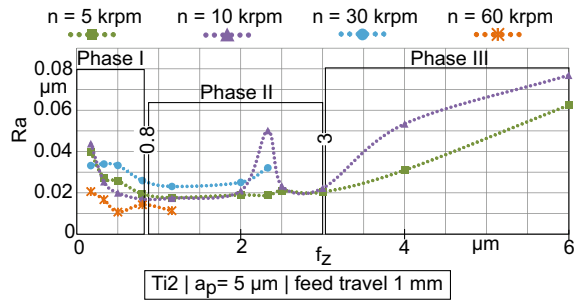
limit for coated tools, since at this diameter the machined surface is getting irregular due to squeezing material instead of cutting. Higher cutting speeds or a higher depth of cut are needed to improve the cutting conditions. However, these adaptations and the higher cutting edge radius from the coating lead to higher process forces, that the smaller tools aren't able to withstand [17].

Improvements of Tool Life and Surface Quality when Using TiB₂ Coated USMs

The effects of the TiB₂ coating on tool life and the surface quality of the milled structures heavily depend on the cutting speed: With a larger tool diameter (50 μm and 25 μm), coated tools are only advantageous at higher cutting or spindle speeds (above 80,000 rpm). Figure 9 shows the wear behavior for 50 μm coated and uncoated tools at three spindle speeds, with the corresponding slot bottoms [18].

However, the lower the tool diameter (12.5 μm and 6 μm), the higher the tool life of the coated tools at lower cutting or spindle speeds (20,000 rpm and 50,000 rpm). Overall, with tool diameters as low as 12.5 μm and 6 μm, coating leads to significantly longer tool life by enhancing the tools' mechanical strength. This and the additional friction reduction compensates for the higher cutting edge radius, resulting in a longer tool life [18].

Fig. 10 Influence of the feed per tooth on the arithmetic mean roughness Ra according to [19]



2.3 Micro End Mill Application and Performance

2.3.1 Cutting Parameters and Tool Workpiece Interactions

Feed per Tooth

The cutting parameters (spindle speed n , feed per tooth f_z , depth of cut a_p , and the spindle tilt angle ρ) can have a major influence on the cutting process in micro milling. The influence of the feed per tooth on the arithmetic mean roughness R_a was investigated at different spindle speeds, see Fig. 10. Three distinct phases can be observed: In phase I, R_a seems to fall with rising f_z , while in phase II, the roughness is independent from spindle speed n and f_z . In phase III, R_a increases with rising feed per tooth. Also, a higher spindle speed leads to smaller roughness values [19].

Spindle Tilt Angle

The influence of the spindle tilt angle was evaluated by tilting the spindle parallel to the X-axis. ‘Milling stars’ with variable angular relation to the X-axis were machined. To avoid the influence of the axial run-out of the spindle, the tilt angle must be large enough to ensure enough clearance under the micro end mill. However, to avoid shape deviations, the tilt angle needs to be kept as small as possible. As such, tilt angles of -1.5° , 0° and 1.5° were used to enable front and back cutting. Figure 11 shows the machined ‘milling stars’, the influence of the relative angle between feed direction and spindle tilt on burr formation is clearly visible. In addition, the slots milled with tilt angle feature lower burrs in comparison to the non-tilted slots, which can be attributed to the cutting effect of the tilt angle: It acts like a milling tool with a helix angle. This can be exploited on 5-axis machine tools, where the tilt angle can be adjusted to the feed direction [20].

Spindle/Cutting Speed

To achieve a higher productivity, higher feed rates are needed, requiring higher spindle speeds to reach an acceptable feed per tooth. Investigating spindle speeds up to 330,000 rpm, three different resulting slot bottom surface types were identified. Figure 12a classifies these into I, II, and III according to their topography [21].

Type I is characterized by C- and D-tracks on the slot bottom and appears primarily at low spindle speeds (30 krpm – 50 krpm). The kinematics of the cutting process are clearly visible and no BUE formation occurs. Type II shows adhesions, especially at the side walls and holes in the slot bottom that are smaller than the tool diameter. These holes result from BUEs at the minor cutting edge. For type II, BUEs seem to form and collapse periodically, leading to unregular, nonpredictable slot bottoms. Type III is also influenced by BUEs, showing regular but undefined structures and a comparably flat slot bottom surface. This is caused by large BUEs at both the minor and major cutting edge. A correlation between the arithmetic mean height Sa and the slot bottom types exists, too: For type III, the Sa values are lower than for

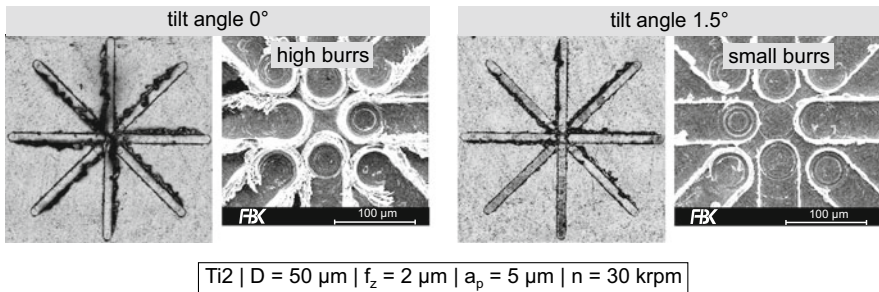


Fig. 11 Burr formation of the micro milled structure according to [20]

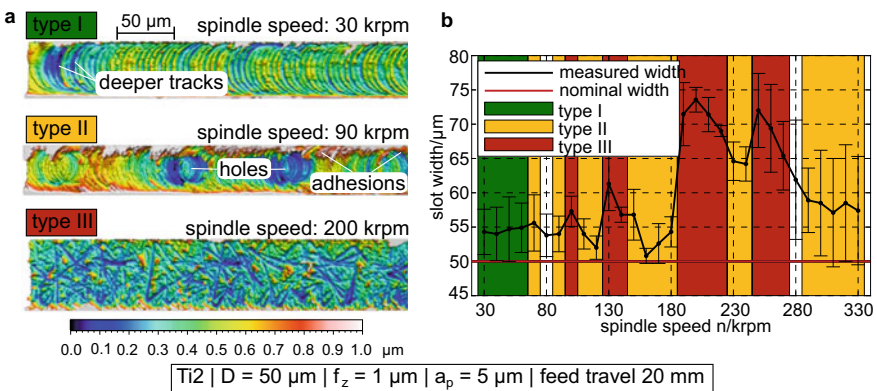


Fig. 12 a) One example of each of the three types of slot bottom topography that have occurred during micro milling at different spindle speeds, b) Slot width depending on the spindle speed according to [21]

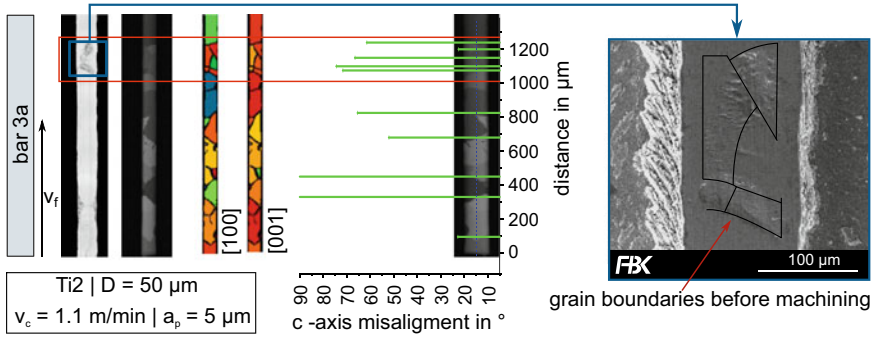


Fig. 13 Visualization of the correlation between ripped out workpiece and c-axis misalignment by surface topography, polarized light microscopy images and orientation maps, c-axis orientation maps, and SEM and FIB images according to [22]

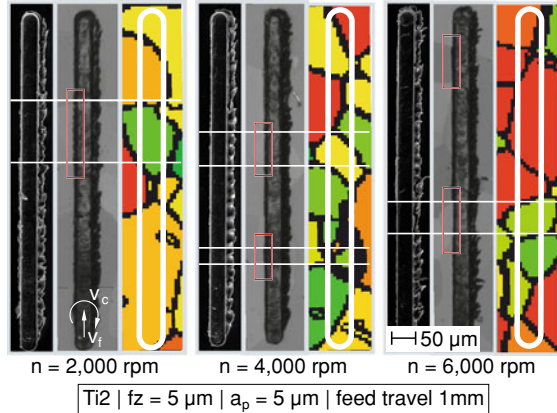
type II. This is caused by the adhesions next to the side walls of type II. Ra values are not affected. The occurrence of the surface types is depicted in Fig. 12b, together with the measured width of the micro milled slot. Narrow slots are found for type I, medium slots for type II, and very wide slots for type III. This behavior stems from the formation of BUEs, resulting in larger effective tool diameters leading to very wide slots [21].

Crystallographic Orientation of the Workpiece Material

In micromachining, the grain size of the workpiece material and the uncut chip thickness are in the same order of magnitude, and the cutting process takes place inside individual crystallographic grains. To quantify the influence of the crystallographic orientation, orthogonal cutting, and micro milling tests were conducted in cp-titanium. The grain orientation and grain boundaries of the workpiece were analyzed before machining. For detailed information on the specimen preparation, analysis, and the setup and tools used, see [22]. In orthogonal cutting, the workpiece surface shows areas where material is ripped out. These areas often correspond to the position of the grain boundaries, identified before machining, as seen for bar 3a in Fig. 13. This also occurs at regions where the c-axis alignment of two consecutive grains is different [22].

This also results in serpentines on the surface (shown in Ref. [22]), that always originate from the grain boundaries. The different orientations of the c-axis in comparison to the feed movement result in the turning points. Only sliding on the main slip plain is suspected, as there is no supporting effect by neighboring workpiece material. Additionally, the cutting forces (shown in Ref. [22]) are influenced by the orientation of the grains. When the grains' slip planes are aligned with the feed vector, less force is required for material separation. Micro milling adds a circular cutting motion to the linear feed, leading to less clear results than orthogonal cutting. The process forces were not influenced by the grain orientation, but the burr formation was at low spindle speeds (1–6 krpm). Figure 14 shows the burr width and shape

Fig. 14 Burr formation depending on the grain orientation and the spindle speed (SEM images, polarized light microscopy images and [001]-orientation maps) according to [22]



in relation to the grain orientation. The change of the burr always occurs on the up-milling side when entering or leaving a grain (red boxes) [22].

2.3.2 Metalworking Fluid Application in Micro Milling

Influence of Different Metalworking Fluids

Metalworking fluids (MWF) are applied to reduce friction and heat generation when machining. As conventional minimum quantity lubrication (MQL) systems provide unnecessary high oil flow rates over a large area (relative to the tool diameter), MQL systems with very low flow rates and concentrated spray mists were utilized to investigate the influence of very small amounts of MWF. Three different MWF types were investigated using MQL: Isopropanol, sodium dodecylsulfate (SDS), and cutting oil as well as dry machining as a reference. For more information on the MQL setup and the MWFs, we refer to [23]. Compared to dry machining, the MWFs are able to prevent BUE formation, effectively reducing tool wear (not shown). The surface morphology is improved as well, see Fig. 15. Dry machining leads to many adhesions at the slot bottom and a high amount of burr on the down-milling side. The surface is rough and irregular in general. Using isopropanol, slight adhesion occurs at the slot bottom, and only small burrs are formed on the up- and down-milling side. For SDS, no adhesions occur, but a continuously occurring pattern is present, and a lot of burrs are visible. The slots milled with cutting oil lubrication show no adhesions, regular structures, and very little burr formation. Cutting oil provides a lubricating effect, reducing friction and thus generating a more uniform surface. In addition, standard deviations of Ra and the process forces (not shown) are much lower [23].

Influence of Metalworking Fluid Quantity

Flow rates of 0.7 ml/h, 1.5 ml/h and 6 ml/h were investigated, with dry machining (0 ml/h) as reference. As MWF cutting oil was used. Further details on the MQL system can be found in [24]. The influence of MQL quantity on tool wear is clearly visible in Fig. 16a: Dry machining leads to BUEs, while micro milling with 0.7 ml/h shows only slight adhesions and abrasive wear but no BUEs. The higher flow rates 1.5 ml/h and 6 ml/h then lead to increasing BUE formation again [24].

Figure 16b shows the machined slot bottoms, showing indications of BUE formation and adhesions for 0 ml/h, especially at the slot sides. 0.7 ml/h leads to an evenly distributed surface roughness with D-marks, while 1.5 ml/h results in C- and D-marks, indicating changing cutting conditions. The slot bottom machined with 6 ml/h shows adhesions, caused by BUEs. The lower surface quality with increasing oil flow rate can be explained by a higher influence of the oil’s surface tension, which reduces the amount of oil in the contact zone [24].

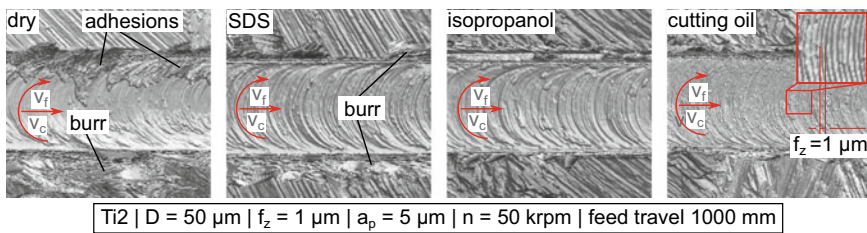


Fig. 15 Surface morphology of the slot bottom according to [23]

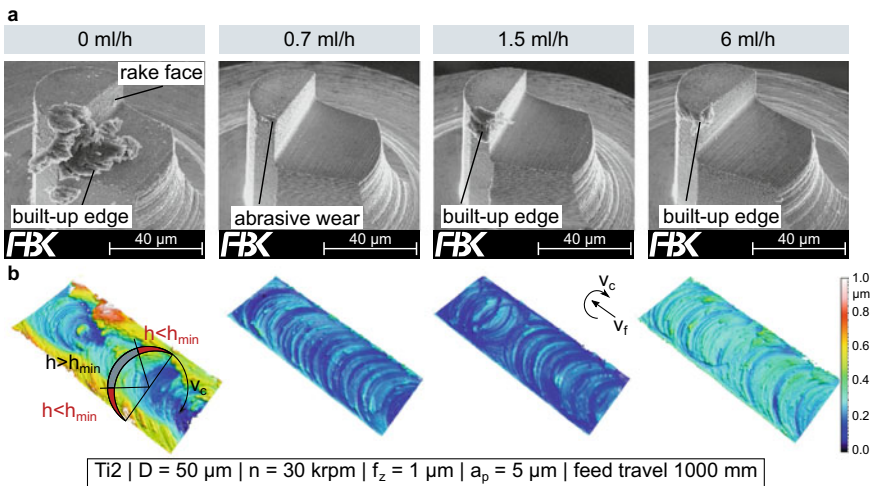
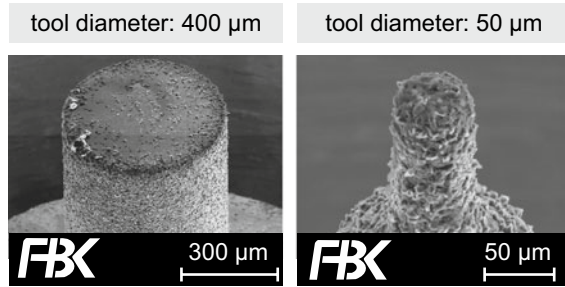


Fig. 16 a) Wear of micro end mills, b) Slot bottom topography after a feed travel of 1,000 mm according to [24]

Fig. 17 Example for a micro pencil grinding tool with a nominal diameter of **a** 400 μm and **b** 50 μm



3 Micro Grinding

3.1 Development of Micro Grinding Tools

For microstructuring of hard and brittle materials, micro pencil grinding tools (MPGTs) were developed, including the manufacturing of the tool blanks and the following plating process. Examples of MPGTs with two different tool diameters are given in Fig. 17.

3.1.1 Electroless Plating of Micro Grinding Tools

Suitable blanks for the MPGTs can be made of cemented carbide or high-speed steel. Machining of the blanks was done with a high accuracy desktop grinding machine [25] in order to realize the basic tool geometry [26]. Detailed information about this process is given in [27]. Before the actual plating process, which creates the abrasive body of the tool, a pretreatment of the blanks was performed to prepare the blank surface, and to provide an initial nickel coating. First, the blanks were deburred, as described in [27]. The tool shaft (apart from the tool tip) was masked with shrinking tubes [25] to avoid oxidation effects on the shaft areas, which should not be plated. Following this, chemical processes were used to degrease and clean the blank surfaces as described in [26, 27]. A galvanic process was applied to rough up the blank surface for better adhesion of the abrasive layer [27]. In the third step, the blank surface was treated in hydrochloric acid to neutralize alkaline residuals [26]. In a last step, an initial thin nickel layer was deposited via electroplating, as described in [28].

For the generation of the abrasive body of the tools, the electroless plating process was developed. It generates a more uniform coating than electroplating, and is independent of the blank geometry [26]. As with electroplating a metallic layer is deposited, but without applying an electrical potential difference [26]. Instead, a chemical reduction reaction is used to provide a nickel-phosphorous compound on the blank surface [29]. An overview of the plating process is depicted in Fig. 18. The

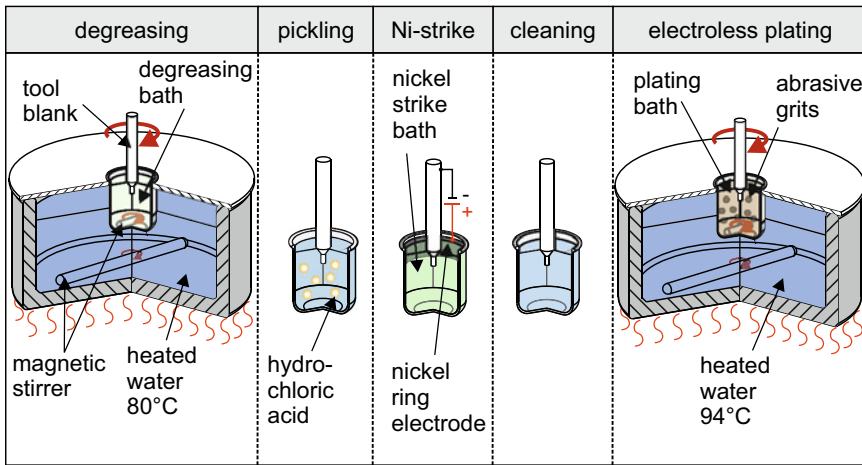


Fig. 18 Schematic principle of the electroless plating process according to [25]

chemical components of the plating solution are given in Table 1 [26], with Nickel Sulfate and Sodium Hypophosphite being the main components. We found that stable temperatures and pH values are essential for successful plating processes (see [28, 29] for more details). As the plating solution would decompose after 1–2 h, the deposition rate should be maximized [13]. In our evaluations, we found Thiourea to be a suitable stabilizing agent [28]. With a concentration of 0.4 mg/l, the deposition rate could be maximized to 21 $\mu\text{m/h}$ [26]. Plating thicknesses of 50 %–70 % of the average grit size were achieved [13].

Two important tool properties for their applicability are the grit concentration and the grit protrusion height. These were controlled by the grit concentration within the plating solution. However, it was found that the concentration had to be adjusted to the respective grit size and the tool diameter. The final step was the grit embedding process directly after the main plating step. With embedding, the bond of the grits was improved. To achieve this, the rotation of the stirrer inside the plating solution was turned off, stopping the abrasive grit motion. Consequently, gravity pulled the

Table 1 Components of the electroless plating bath [26]

Component	Concentration in g/l
Nickel sulfate ($\text{NiSO}_4 \cdot 6\text{H}_2\text{O}$)	30
Sodium hypophosphite (NaH_2PO_2)	20
Sodium acetate ($\text{C}_2\text{H}_3\text{NaO}_2$)	20
Thiourea ($\text{CH}_4\text{N}_2\text{S}$)	0–0.0011
Hydrochloric acid HCl	Adapted to pH-value
Abrasive grits	0–10

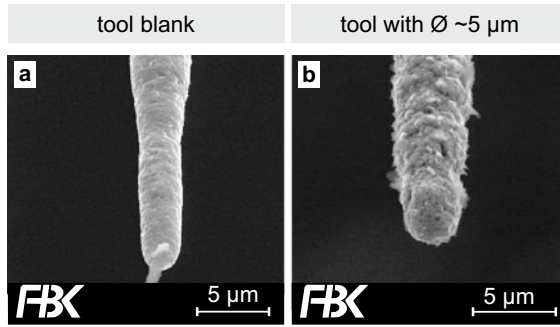


Fig. 19 MPGTs with a diameter below $5 \mu\text{m}$. **a** tool blank, **b** coated tool according to [29]

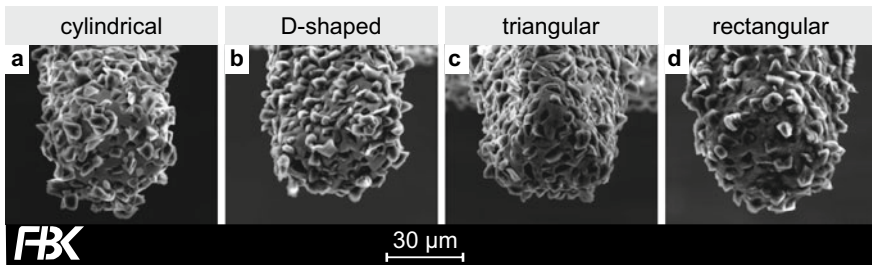


Fig. 20 MPGTs with special cross sections: **a** cylindrical, **b** D-shaped, **c** triangular, **d** rectangular according to [30]

grits down to the bottom of the bath preventing more grits from being embedded on the tool. Then, further nickel-phosphorous was deposited on the tool surface which improved the form fitting of the grits [13].

With the electroless plating process it was possible to manufacture tools with a diameter down to about $5 \mu\text{m}$, as shown in Fig. 19. For such tools, blanks with $2 \mu\text{m}$ – $3 \mu\text{m}$ in diameter and cBN grit sizes of $0.5 \mu\text{m}$ – $1 \mu\text{m}$ were used [29].

In addition to the manufacturing of very small grinding tools, the electroless plating process can be used to manufacture grinding tools with special geometries: Aside from the cylindrical shape, tools with D-shaped, rectangular, and triangular cross sections were investigated, see Fig. 20. The modified cross sections of the tools create larger areas, in which additional metalworking fluid can accumulate and be transported to the grinding zone [30]. This changed the wear behavior of the MPGTs due to the interrupted tool engagement caused by the modified tool shapes and influenced the bottom surface topography of the ground slots [30].

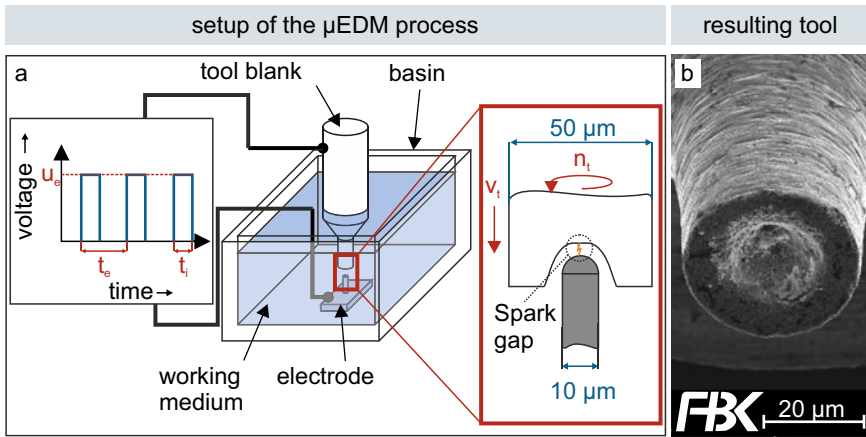


Fig. 21 a Schematic setup of the μEDM process and the signal shape of the electrical pulse, b Example for an optimized tool according to [31]

3.1.2 Optimization of Micro Grinding Tools

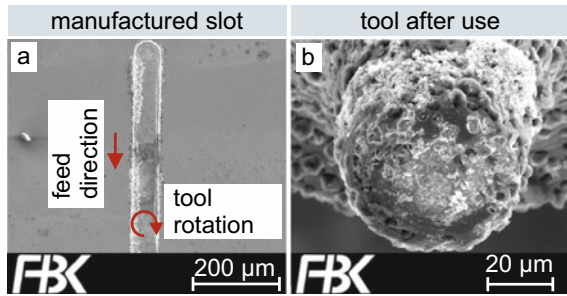
The micro pencil grinding tools were optimized by modifying the tool face: As the cutting speed in the middle of the tool face equals zero, material adhesions occur. This was solved by manufacturing a cavity in the center point of the tool to prevent contact of the grits with the workpiece. For this, we used microelectrical discharge machining (μEDM). The tool blanks were used as anode, moving axially towards an electrode in a nonconductive dielectricum to form material removing electrical arcs. A schematic representation of the process and an exemplary optimized tool blank is shown in Fig. 21 [31].

The μEDM -process was investigated for MPGTs with $50\ \mu\text{m}$ in diameter. It was performed by using special cemented carbide electrodes with a round and pointed shape for efficient material removal. This electrode had a diameter of $10\ \mu\text{m}$ and was set inside distilled water as dielectric working fluid. The process is characterized by the signal shape of the electrical pulse as depicted in Fig. 21. The influence of the discharge voltage u_e and the pulse duration t_i on the spark gap during μEDM were investigated. It was found that a voltage of $45\ \text{V}$, a pulse duration of $0.25\ \mu\text{s}$, and a feed rate of $2\ \mu\text{m}/\text{min}$ resulted in a stable manufacturing process [31].

Table 2 Process parameters [25]

Parameter	Value
Feed rate	0.1 mm/min
Spindle speed	95,000 rpm
Depth of cut	$10\ \mu\text{m}$

Fig. 22 **a** Slot manufactured with a MPGT, **b** Tool after the machining process according to [25]



3.2 Application of Tools in Micro Grinding

The application of the electroless plated MPGTs has been investigated in numerous studies [25, 29, 30]. In this chapter, the results and findings from these investigations are summarized.

3.2.1 Process Parameters for Micro Grinding

Micro grinding experiments were performed on a desktop sized machine tool. The workpiece material was 16MnCr5 with a hardness of 650 HV30. For the 50 μm tools, rectangular slots with a length of 500 μm were machined in dry condition [25]. The micro grinding process was performed using the parameters in Table 2.

During the machining process, the abrasive layer of the MPGT face broke off, caused by the decreasing cutting speed towards the tool's center point. Besides, chips remained on the used tool as can be seen in Fig. 22, even though the tool was cleaned with cleaning dough and in an ultrasonic bath. We concluded that the loss of the bond on the tool face was caused by temperatures in the process, that are high enough to melt the bond material [25].

To reduce the temperatures, metalworking fluid was applied. Hence, in further investigations, an MQL system was used. Additionally, the axial depth of cut was reduced to 5 μm , the spindle speed was varied between 30,000 rpm and 50,000 rpm, and the feed rate was set between 0.1 mm/min and 0.2 mm/min. Suitable parameters were determined by analyzing the influence on the tool life. It was found that a lower spindle speed and a smaller value for the feed rate were preferable to reduce the temperatures within the process and increase tool life. Using higher feed rates between 1 mm/min and 4 mm/min was possible when applying abrasive grit sizes of 5 μm –10 μm . In this case, the largest feed travel was achieved when using a feed rate of 2 mm/min. With these parameters, a slot with a length of 35.4 mm was machined which is large considering the tool diameter of 50 μm [32].

More productive process parameters can be applied when the slot is produced via a pendulum grinding process with 0.5 μm depth of cut: The feed rate could be increased up to 240 mm/min in combination with a spindle speed of 120,000 rpm

to machine slots with a length of 5 mm. However, smaller values for spindle speeds were preferable for tool life, too [33].

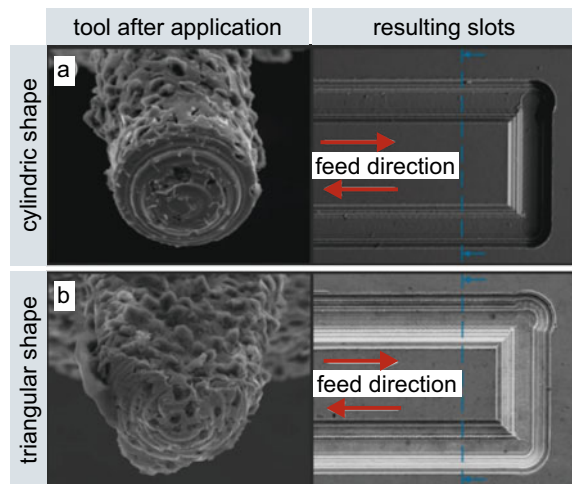
In further investigations, it was found that due to the different heights of the grits at the tool face, stepped surface topographies were generated during machining of the slots. This effect was caused by the different protrusion heights of the grits on the tool face near to the tool's center point. This can be prevented by setting a tilt angle between workpiece surface and tool axis. Tilt angles of two degrees are sufficient to remove almost all of the stepped topography [31].

Another approach to reduce the step shape was to apply the tools optimized via the μ EDM process. Since they did not have active grits at the center point of the tool face, an additional tilt angle was not necessary. When using the optimized tools, the amount of steps on the topography decreased. Adhesions occurred with the optimized tools, but they were only located inside the cavity, leaving the active grits of the tool uncovered [31].

3.2.2 Application of MPGTs with Diameters of $\sim 5 \mu\text{m}$

A special case for a micro grinding process was using MPGTs with diameters of about $5 \mu\text{m}$ to machine-hardened 16MnCr5. Due to the small diameter, a spindle speed of 30,000 rpm results in a low cutting speed. However, it was found that higher spindle speeds led to reduced tool life. Regarding the feed rate, experiments were performed to determine suitable values. For all experiments, the axial depth of cut was set to $2 \mu\text{m}$. In our experiments, a feed rate of $50 \mu\text{m}/\text{min}$ produced the best results and tool life. Slots with a length of about $500 \mu\text{m}$ and a surface roughness R_a of 12.5 nm could be achieved [29].

Fig. 23 Machining results using MPGTs with different shapes of cross sections according to [30]



3.2.3 Application of MPGTs with Special Geometries

Experiments with special geometry tools (see Fig. 20) were performed with a spindle speed of 150,000 rpm, a feed rate of 50 mm/min, and an axial depth of cut of 0.5 μm . The workpieces were made of hardened 16MnCr5. Cross sections of the resulting microslots and SEM images of the worn tools are given in Fig. 23. All tools had clear signs of wear. The additional transport of metalworking fluid due to the large areas created by the modified cross sections did not result in reduced tool wear. Instead, it seems that the reduced amount of active grits led to increased tool wear. Only the wear of the D-shaped tool was comparable to the standard cylindrical tools. In conclusion, the tools did not provide improvements and are not suitable for the machining process [30].

3.2.4 Wear of MPGT

The influence of the feed rate, the spindle speed as well as grit size on the wear of the MPGTs was investigated. Experiments were performed using tool diameters of about 50 μm . We found that small grit sizes led to severe wear and poor tool performance [13]. Larger grits only had a minor influence on the surface quality but they significantly improved tool life [32].

Increasing the feed rate led to higher loads on the abrasive body of the MPGT due to rubbing and ploughing of the grits in the center of the tool face, again resulting in poor performance. When applying high feed rates and high spindle speeds, tools with a grit size between 1 μm –2 μm were subjected to severe wear due to high grit loads. Higher feed rates and spindle speeds led to lower chip thicknesses, which resulted in smaller roughness of the machined slots as depicted in Fig. 24. Also, larger grit sizes led to better surface qualities, which can be explained by the ploughing-dominated material removal mechanism of smaller grit sizes and chip spaces. Overall, smaller grits are not to be preferred, since tools tended to clog due to smaller chip spaces [13].

3.2.5 Influence of MWF and MWF Supply

The application of MWFs is essential in micro grinding to achieve suitable tool life, as dry machining of steel workpieces results in clogging of the tools [34]. In general, three different MWF supply strategies are conceivable for the process: submerged grinding, MQL, and flood lubrication, shown in Fig. 25. A comparison between the strategies is given in [34, 35]. In our experiments submerged grinding achieved the best results and the highest feed travels, because a constant supply of MWF was guaranteed, and, thus, should be preferred. However, when the workpiece is tilted during the machining process, MQL should be preferred [34].

Apart from the supply strategy, different MWFs are suitable for micro grinding. In general, the use of MWFs decreased surface roughness and burr formation, and

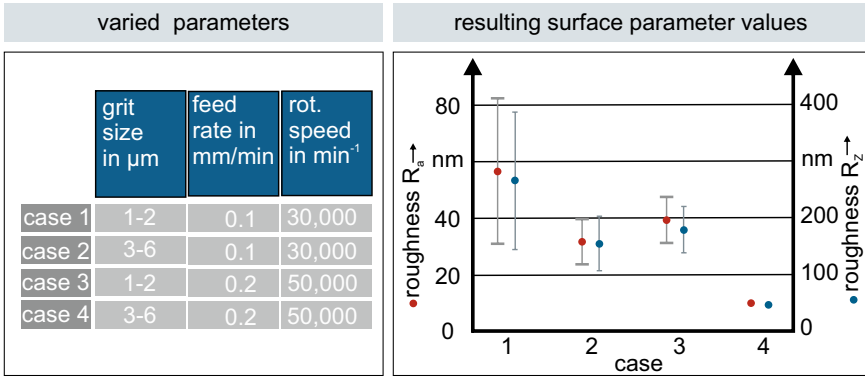


Fig. 24 Surface Ra and Rz for different combinations of grit size, feed rate, and spindle speed according to [13]

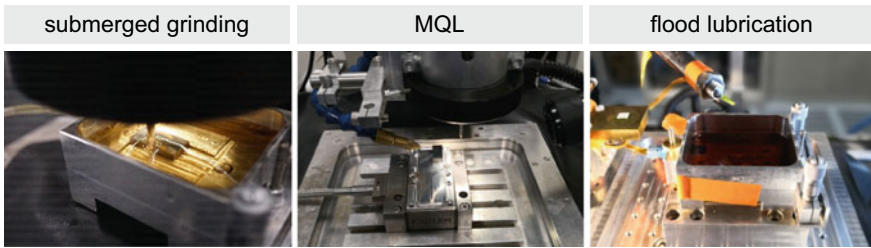


Fig. 25 Comparison of MWF supply strategies

led to a more stable grinding process. Even the usage of distilled water as MWF could slightly improve the process results compared to dry machining [35].

We performed a comparison between seven different MWFs in submerged grinding of microslots; and found that plant-based MWFs with higher viscosity significantly reduced adhesions on the tool. The higher lubricity and pressure absorption capacity proved beneficial. Pure canola oil, mineral, and synthetic MWFs led to worse results in comparison to plant based MWFs or resulted in partial tool failure [34]. As an alternative to oils, sodium dodecyl sulfate as a cost-effective lubricant can be used as MWF: In our tests, the tool life was increased, and the surface roughness of the machined workpieces reduced [35]. Furthermore, lesser concentrations of Sodium Dodecyl Sulfate are preferable, since they led to less adhesions on the tool [34]. In comparison to the application of plant-based MWFs, using Sodium Dodecyl Sulfate resulted in more adhesions on the worn tool [34].

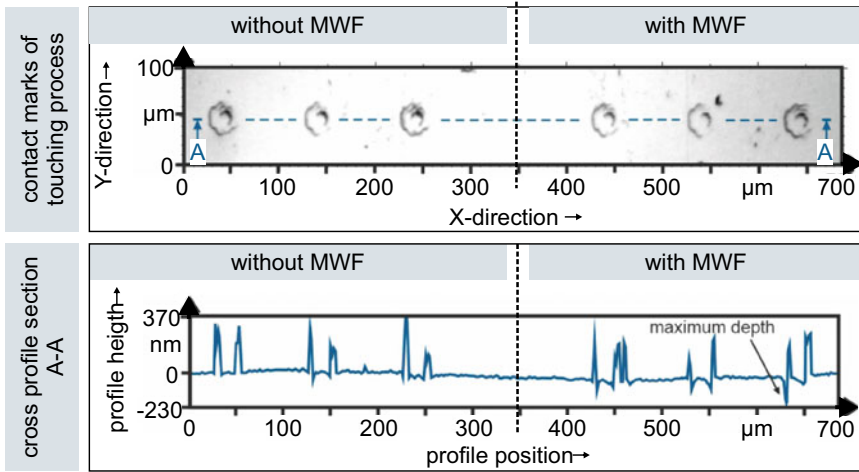


Fig. 26 Contact marks and corresponding cross sections received with and without applying MWF according to [36]

3.2.6 Wear Compensation Via Acoustic Tool-Workpiece Contact Detection

To reduce the influence of tool wear on the machining accuracy, change in tool length due to wear had to be compensated within the process. For this purpose, the position of the tool tip relative to the workpiece surface had to be determined regularly after defined time steps. This was done by repeating the touching process. To avoid errors due to manual touching by the operator, an automated process was developed. Thus, tool-workpiece contact was automatically detected via an acoustic sensor, which was mounted below the workpiece. This system can be applied for dry machining as well as for submerged grinding. As it is shown in Fig. 26 the contact mark had a depth below or equal to 230 nm which is a higher accuracy as it would be possibly due to manual touching. Even if the touching accuracy for wet machining processes was not as high as for dry conditions, the acoustic detection system is suitable for grinding processes with and without MWF [36].

3.3 Possibilities and Limitations of Micro Grinding

With the electroless plating process it was possible to manufacture MPGTs with high quality of the abrasive body. The process delivered high contour fidelity which made it suitable to coat even non-cylindrical tools with sharp edges on the peripheral surface [30]. Although electroless plating was applied to produce tools with a diameter of 5 μm, the process was limited by the manufacturing accuracy of the tool blanks [29].

The abrasive grit sizes of the tool had a large influence on the performance and the process results, as described in the previous sections. However, even if large grit sizes were preferable regarding the process results, the maximum grit size was limited by the plating process. Large grits are difficult to embed on the tool blank due to their own weight in connection with the rotation of the plating solution [13].

Another limitation caused by the grits is that the produced slots did not have an ideal rectangular shape. Different protrusion heights of the abrasive grits led to a step shaped slot bottom surface [31]. Using optimized tools reduced the depth of the steps, however, a complete prevention was not possible [33].

Within the grinding process, high temperatures occur, which can melt the abrasive layer. Hence, the application of MWFs was essential for sufficient tool life [25].

When applying MWF, MPGTs with a nominal diameter of 50 μm were suitable to machine slots up to a length of 35.4 mm in hardened steel [32]. It was possible to machine complex two-dimensional structures, characterized by many changes in the feed direction [33]. As an example of microstructuring of larger surface areas, text was engraved on a workpiece as it is shown in Fig. 27 [33].

Besides machining of hardened steel, also workpieces made of glass were ground using the MPGTs. In general, sufficient tool life was received when using low feed rates and low spindle speeds [33]. Due to this fact, the speed of the machining process was limited.

4 Summary

In this chapter, we presented the work conducted in the CRC 926 regarding the manufacture of microstructures via micro milling and grinding. The desktop machine and its integrated measurement system developed within the CRC were presented. The capability to measure the tool wear of ultra-small micro end mills (USMs) process-intermittent was proven. The development of the USM geometry, as well as the research regarding tool substrates and coatings, were shown. Investigations concerning the cutting parameters and metalworking fluid application during micro milling helped to improve the process and its understanding.

For micro grinding, one main focus was the coating process of the abrasive layer and the impact of the tool shape. The other main research topic was their application and the reduction of tool wear: The process parameters and MWF supply strategies with different MWFs were researched. The automated wear compensation via acoustic emission and the possibilities and limitations of the micro grinding process were discussed.



Fig. 27 Text engraved in a workpiece made of 16MnCr5 using six MPGTs in a micro grinding process according to [33]

References

1. Dornfeld D, Min S, Takeuchi Y (2006) Recent advances in mechanical micromilling. CIRP Ann 55(2):745–768. <https://doi.org/10.1016/j.cirp.2006.10.006>
2. Masuzawa T (2000) State of the art of micromachining. CIRP Ann 49(2):473–488. [https://doi.org/10.1016/S0007-8506\(07\)63451-9](https://doi.org/10.1016/S0007-8506(07)63451-9)
3. Aurich JC, Kirsch B, Setti D, Axinte D, Beaucamp A, Butler-Smith P, Yamaguchi H (2019) Abrasive processes for micro parts and structures. CIRP Ann 68(2):653–676. <https://doi.org/10.1016/j.cirp.2019.05.006>
4. Chae J, Park SS, Freiheit T (2006) Investigation of micro-cutting operations. Int J Mach Tools Manuf 46:313–332. <https://doi.org/10.1016/j.ijmactools.2005.05.015>
5. Ikawa N, Donaldson RR, Komanduri R, König W, Aachen TH, McKeown PA, Moriwaki T, Stowers IF (1991) Ultraprecision metal cutting-the past, the present and the future. CIRP Ann 40(2):587–594. [https://doi.org/10.1016/S0007-8506\(07\)61134-2](https://doi.org/10.1016/S0007-8506(07)61134-2)
6. Vollertsen F, Biermann D, Hansen HN, Jawahir IS, Kuzman K (2009) Size effects in manufacturing of metallic components. CIRP Ann 58(2):566–587. <https://doi.org/10.1016/j.cirp.2009.09.002>
7. Bohley M, Reichenbach IG, Müller C, Aurich JC (2016) Development of a desktop machine tool for integrated ultra-small micro end mill production and application. In: 11th international conference on micro manufacturing (2016)

8. Bohley M, Reichenbach IG, Müller C, Kirsch B, Aurich JC (2016) Compact hydrodynamic spindle module for micromachining applications. In: Proceedings of the 16th euspen international conference
9. Bohley M, Müller C, Kirsch B, Aurich JC (2017) Integration of a confocal microscope in a desktop machine tool for in situ process control. In: Proceedings of the 17th euspen international conference, pp 122–123
10. Kieren-Ehse S, Mayer T, Kirsch B, Aurich JC (2021) Atomic force microscope for in situ micro end mill characterization-Part I: integration into a desktop sized machine tool. In: Proceedings of the 21st euspen international conference, pp 463–466
11. Mayer T, Kieren-Ehse S, Kirsch B, Aurich JC (2021) Atomic force microscope for in situ micro end mill characterization-Part II: development of an algorithm to characterize the cutting edge radius of micro end mills. In: Proceedings of the 21st euspen international conference, pp 493–496
12. Aurich JC, Reichenbach IG, Schöler GM (2012) Manufacture and application of ultra-small micro end mills. *CIRP Ann* 61(1):83–86. <https://doi.org/10.1016/j.cirp.2012.03.012>
13. Kirsch B, Bohley M, Arrabiyeh PA, Aurich JC (2017) Application of ultra-small micro grinding and micro milling tools: possibilities and limitations. *Micromachines* 8(9):261–279. <https://doi.org/10.3390/mi8090261>
14. Mayer T, Kieren-Ehse S, Heintz M, Kirsch B, Aurich JC (2020) Manufacture of novel all-ceramic micro end mills. In: Proceedings of the 20th euspen international conference, pp 113–114
15. Bohley M, Reichenbach IG, Kieren-Ehse S, Heberger L, Arrabiyeh PA, Merz R, Böhme L, Hering J, Kirsch B, Kopnarski M, Kersch E, von Freymann G, Aurich JC (2018) Coating of ultra-small micro end mills: analysis of performance and suitability of eight different hard-coatings. *J Manuf Mater Process* 2(2). <https://doi.org/10.3390/jmmp2020022>
16. Bohley M, Heberger L, Kirsch B, Aurich JC (2017) Untersuchung des Verschleißverhaltens von TiB₂-beschichteten Mikrofräswerkzeugen. *ZWF* 112(9):598–601. <https://doi.org/10.3139/104.111766>
17. Bohley M, Kieren-Ehse S, Heberger L, Kirsch B, Aurich JC (2018) Size limitations and wear behavior of TiB₂ coated micro end mills ($\varnothing < 50\mu\text{m}$) when machining cp-titanium. In: *Procedia CIRP 71-Proceedings of the 4th CIRP conference on surface integrity* 71:187–191. <https://doi.org/10.1016/j.procir.2018.05.095>
18. Aurich JC, Kieren-Ehse S, Mayer T, Bohley M, Kirsch B (2022) An investigation of the influence of the coating on the tool lifetime and surface quality for ultra-small micro end mills with different diameters. *CIRP J Manuf Sci Technol* 37:92–102. <https://doi.org/10.1016/j.cirpj.2022.01.004>
19. Reichenbach IG, Bohley M (2013) Micromachining of cp-titanium on a desktop machine-study on bottom surface quality in micro end milling. *Adv Mater Res* 769:53–60. <https://doi.org/10.4028/www.scientific.net/AMR.769.53>
20. Aurich JC, Bohley M, Reichenbach IG, Kirsch B (2017) Surface quality in micro milling: influences of spindle and cutting parameters. *CIRP Ann* 66(1):101–104. <https://doi.org/10.1016/j.cirp.2017.04.029>
21. Kieren-Ehse S, Bohley M, Mayer T, Kirsch B, Aurich JC (2020) Effect of high spindle speeds on micro end milling of commercially pure titanium. In: Proceedings of the 20th euspen international conference, pp 63–66
22. Kieren-Ehse S, Böhme L, Morales-Rivas L, Lösch J, Kirsch B, Kersch E, Kopnarski M, Aurich JC (2021) The influence of the crystallographic orientation when micro machining commercially pure titanium: a size effect. *Precis Eng* 72:158–171. <https://doi.org/10.1016/j.precisioneng.2021.04.007>
23. Kieren-Ehse S, Bohley M, Arrabiyeh PA, Kirsch B, Aurich JC (2018) Influence of different metal working fluids when micro machining cp-titanium with 50 μm diameter micro end mills. In: *Procedia CIRP 71-Proceedings of the 4th CIRP conference on surface integrity, vol 71*, pp 198–202. <https://doi.org/10.1016/j.procir.2018.05.097>

24. Kieren-Ehse S, Bohley M, Kirsch B, Aurich JC (2019) Influence of the metal working fluid quantity on process results when micro milling cp-titanium with 50 μm diameter micro end mills. In: Proceedings of the 19th euspen international conference, pp 400–401
25. Arrabiyeh PA, Raval V, Kirsch B, Bohley M, Aurich JC (2016) Electroless plating of micro pencil grinding tools with 5–10 μm sized cBN grits. *Adv Mater Res* 1140:133–140. <https://doi.org/10.4028/www.scientific.net/AMR.1140.133>
26. Arrabiyeh PA, Kirsch B, Aurich JC (2017) Development of micro pencil grinding tools via an electroless plating process. *J Micro Nano-Manuf* 5(1). <https://doi.org/10.1115/1.4034645>
27. Heintz M, Arrabiyeh PA, Kirsch B, Aurich JC (2020) Herstellung von Schleifwerkzeugen für die Mikrobearbeitung mithilfe eines chemischen Nickel-Phosphor-Dispersions-Beschichtungsverfahrens. *Jahrbuch Schleifen, Honen, Läppen und Polieren-Verfahren und Maschinen* 69:16–25
28. Arrabiyeh PA, Kirsch B, Aurich JC (2016) Development of micro pencil grinding tools via an electroless plating process. In: Proceedings of the 2016 manufacturing science and engineering conference
29. Arrabiyeh PA, Kirsch B, Aurich JC (2018) Electroless plating and application of micro pencil grinding tools with a diameter of $\sim 5 \mu\text{m}$. In: Proceedings of the 18th euspen international conference, pp 309–310
30. Heintz M, Kirsch B, Aurich JC (2021) Experimental investigations of modified base body geometries of micro pencil grinding tools applied in 16MnCr5. In: Proceedings of the 21st euspen international conference, pp 127–130
31. Arrabiyeh PA, Dethloff M, Müller C, Kirsch B, Aurich JC (2019) Optimization of micropencil grinding tools via electrical discharge machining. *J Manuf Sci Eng* 141. <https://doi.org/10.1115/1.4042110>
32. Arrabiyeh PA, Setti D, Basten S, Kirsch B, Aurich JC (2019) Micro grinding 16MnCr5 hardened steel using micro pencil grinding tools with diameters $\sim 50 \mu\text{m}$. *CIRP J Manuf Sci Technol* 27:1–10. <https://doi.org/10.1016/j.cirpj.2019.10.002>
33. Arrabiyeh PA (2021) Electroless plated micro pencil grinding tools: conception, manufacturing, and application. Als Manuskript gedruckt. Vol. 2021, Band 02. Produktionstechnische Berichte aus dem FBK. Kaiserslautern: Technische Universität Kaiserslautern, 2021. ISBN: 978-3-95974-158-3
34. Arrabiyeh PA, Heintz M, Kieren-Ehse S, Bohley M, Kirsch B, Aurich JC (2020) Submerged micro grinding: a metalworking fluid application study. *Int J Adv Manuf Technol* 107(9–10):3807–3815. <https://doi.org/10.1007/s00170-020-05240-x>
35. Arrabiyeh PA, Bohley M, Ströer F, Kirsch B, Seewig J, Aurich JC (2017) Experimental analysis for the use of sodium dodecyl sulfate as a soluble metal cutting fluid for micromachining with electroless-plated micropencil grinding tools. *Inventions* 2(4). <https://doi.org/10.3390/inventions2040029>
36. Heintz M, Mayer T, Kirsch B, Aurich JC (2020) Tool/workpiece contact detection via acoustic emission in micro grinding. In: Proceedings of the 20th euspen international conference, pp 587–588

Creating Surface Morphologies by Cryogenic Machining



Benjamin Kirsch, Jan C. Aurich, Kevin Gutzeit, Erik von Harbou, Hans Hasse, and Ralf Müller

Abstract Cryogenic machining offers the potential to improve the surface morphology within a single process step by substituting the surface hardening into the form-shaping process. To realize a sufficient surface hardening, low temperatures and high mechanical loads have to be provided by the cryogenic machining process. Within this chapter, facilities and processes are presented aiming to optimize the surface morphology via cryogenic turning and milling. Cryogenic cooling strategies aim to achieve the necessary low thermal loads. The thermal loads are characterized via cutting experiments and temperature field simulations. The machining operations are designed in terms of cutting parameters and tool properties to provide favorable thermo-mechanical loads and consequently an optimized surface morphology. For both a metastable austenitic steel and a difficult-to-cut titanium alloy, an optimization of the surface morphology is realized. In addition, a novel, sub-zero cooling approach is presented and compared with the application of cryogenic coolants and conventional cooling approaches.

1 Introduction

The performance of technical components regarding their wear resistance or fatigue life is highly impacted by their respective surface morphology. The surface morphology is often characterized by the surface topography as well as the mechanical and

B. Kirsch (✉) · J. C. Aurich · K. Gutzeit
Institute of Manufacturing Technology and Production Systems, RPTU Kaiserslautern,
Kaiserslautern, Germany
e-mail: benjamin.kirsch@rptu.de

E. von Harbou
Institute of Reaction and Fluid Process Engineering, RPTU Kaiserslautern, Kaiserslautern,
Germany

H. Hasse
Institute of Engineering Thermodynamics, RPTU Kaiserslautern, Kaiserslautern, Germany

R. Müller
Institute of Mechanics, Technical University of Darmstadt, Darmstadt, Germany

© The Author(s), under exclusive license to Springer Nature Switzerland AG 2024
J. C. Aurich and H. Hasse (eds.), *Component Surfaces*, Springer Series in Advanced
Manufacturing, https://doi.org/10.1007/978-3-031-35575-2_5

metallurgical properties inside the workpiece surface layer [1]. To realize a favorable surface morphology and therefore a positive application behavior, a low roughness and a strengthened surface layer are highly desirable [2].

The surface morphology of machined components is often improved by additional finishing processes. Surface hardening is commonly realized via heat treatment which is characterized as a time and energy-intensive process [3]. Consequently, efforts to substitute this expensive process were made by establishing mechanical hardening processes like deep rolling or shot peening [4]. Here, the increased hardness is attributed to strain hardening mechanisms which are promoted by a high amount of plastic deformation leading to grain refinement, twinning, and an increased dislocation density within the workpiece surface layer [5, 6]. In addition, low temperatures further promote strain hardening, since the dynamic recrystallization is hindered during the process [7]. These mechanical hardening processes are easy to integrate into the process chain and can reduce time and energy in comparison to a heat treatment. However, thermal hardening still outperforms the mechanical hardening processes when regarding the maximum hardness achievable within the workpiece surface layer [8].

Consequently, the approach to combine thermal and mechanical surface hardening within one process is of high interest in order to design an efficient process. Especially the combination of cryogenic cooling strategies and mechanical surface hardening offers potential to further improve the surface morphology. Cryogenic cooling often refers to the usage of liquid nitrogen (LN_2) and carbon dioxide (CO_2), since these are the most established cryogenic coolants due to the comparably easy handling and the sufficiently low supply temperatures [9]. When applying these cryogenic coolants during surface hardening processes, the significantly decreased process temperatures promote strain hardening mechanisms which results in improved hardness of the surface layer [10, 11].

Cryogenic machining offers great potential to design a favorable surface morphology by creating the surface topography and simultaneously increasing the hardness in the workpiece surface layer via strain hardening. This integration of the surface hardening into the form-shaping machining process is highly desirable as it shortens the process chain saving costs and resources (Fig. 1) [12].

Within the presented research, the aim is to investigate and describe the causal relations between the cryogenic cutting processes, the occurring thermal and mechanical loads and the resulting surface morphologies. Within this research, the influence of the cutting process on the surface morphology is studied in terms of cutting parameters and cutting-edge geometry for both turning and milling operations. Additionally, the influence of different cryogenic cooling strategies and the newly developed sub-zero cooling approaches are investigated.

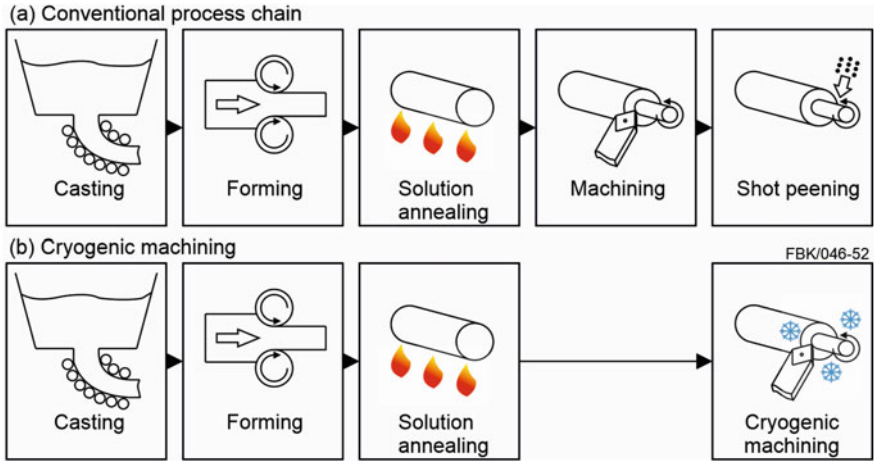


Fig. 1 Process chains for manufacturing components with a hardened surface layer adapted from [12]

2 Facilities for Cryogenic and Sub-zero Machining

2.1 Cryogenic Machining with CO₂ and LN₂

A depiction for the experimental setups used for the turning and milling operations is given in Fig. 2. All turning experiments were conducted on a CNC lathe (Boehringer NG 200¹). A three-component dynamometer (Kistler Type 9129 AA¹) was used to measure the occurring forces and characterize the mechanical loads (Fig. 2a).

A five-axis machining center (DMU 70 eVolution) was used for the milling operations. To measure the occurring forces during milling, a rotating dynamometer (Kistler Type 9123C) was installed between the spindle and the tool (Fig. 2b).

Within the presented investigations, LN₂ and CO₂ were utilized as cryogenic coolants. Regarding the LN₂ cooling, the cryogenic coolant was transported to the cutting zone via super-insulated tubes. At an atmospheric pressure, LN₂ boils at a temperature of 77 K. To ensure that the LN₂ was applied at liquid state, a phase separation was applied before starting each test. The description of the setup regarding the LN₂-cooling is further specified by Mayer et al. [15] and Basten et al. [16].

For the CO₂ cooling strategy, the cryogenic coolant was stored at ambient temperature and at a pressure of roughly 60 bar in a siphoned gas cylinder. Via pressure-insulated tubes, the CO₂ was transported to the nozzle outlet, where it expanded due to the drop toward the ambient pressure. Because of the Joule–Thomson effect, this expansion leads to a decrease in temperature toward roughly 195 K [17]. As a result,

¹ Naming of specific manufacturers is done solely for the sake of completeness and does not necessarily imply an endorsement of the named companies nor that the products are necessarily the best for the purpose.

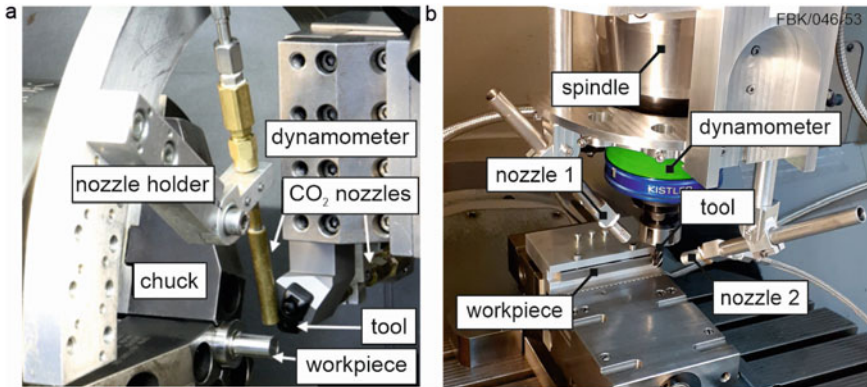


Fig. 2 Experimental setup for **a** turning according to [13] and for **b** milling according to [14] with cryogenic coolants

the CO₂ was supplied to the cutting zone as a solid-gas mixture. A detailed depiction of the cryogenic CO₂ cooling strategy is given by Mayer et al. [15] for turning and Gutzeit et al. [18] for milling. The mass flow of the respective cooling strategies was calculated by measuring the weight loss of the storage tanks when cutting.

2.2 Sub-zero Machining

While the application of cryogenic cooling strategies with LN₂ and CO₂ can reduce the temperatures during cutting significantly, there are also some disadvantages regarding those cryogenic coolants. During cryogenic machining, the high cooling effects are achieved due to the low supply temperature of the cryogenics. However, a sufficient cooling effect is also promoted by a favorable heat transfer coefficient. In this regard, LN₂ tends to film boiling (Leidenfrost effect) forming a gaseous boundary layer and therefore reducing the heat transfer coefficient [19]. Since CO₂ is applied as a solid gaseous two-phase mixture, the heat transfer is mainly achieved by convection of the cold gaseous CO₂ and sublimation of the solid particles [20]. As a result, the heat transfer coefficient as well as lubrication effects when using LN₂ and CO₂ are relatively low compared to a media supplied at liquid state [16]. Besides that, these cryogenics are applied by single use and therefore at low mass flows which can only be varied with considerable effort [9].

In contrast, conventional metalworking fluids (MWF) are applied cost-effectively in circulation systems at high mass flows and ambient temperature. Good lubrication effects and a high heat transfer coefficient are achieved due to the beneficial wetting of the liquid MWF. However, these MWF are limited to supply temperatures above 273 K.

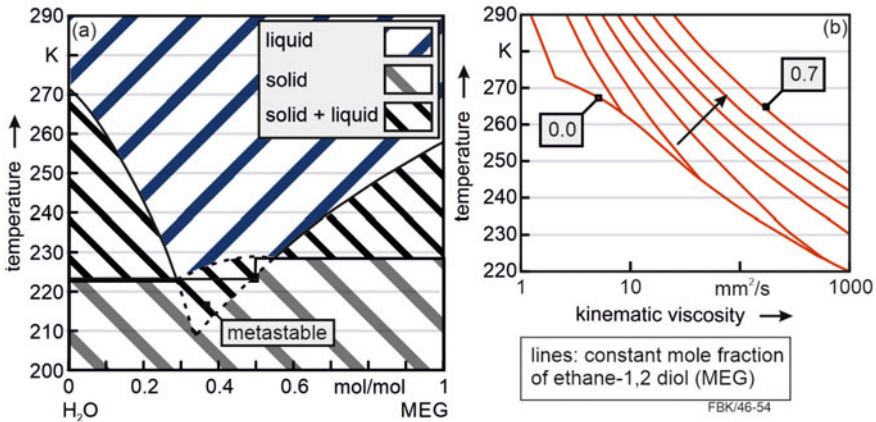


Fig. 3 Phase diagram **a** and kinematic viscosity **b** of mixtures of ethane-1,2 diol (MEG) and water (H₂O) according to [21, 22]

To combine the advantages of the cooling strategies using conventional MWF and cryogenic coolants, a novel cooling approach which utilizes sub-zero MWF was developed within the CRC 926. These sub-zero MWF are a mixture of polyhydric alcohols (e.g., ethane-1,2 diol (MEG)) and water which can be applied to the cutting zone at liquid state at supply temperatures as low as 224 K (Fig. 3) [21]. As a result, high cooling capacities are possible due to low supply temperatures and a beneficial heat transfer coefficient. Additionally, favorable lubrication in comparison to conventional cryogenics is achieved, and additives can be used to further improve the performance of the sub-zero MWF. The influence of additives regarding the performance of the sub-zero MWF is described in detail by Basten et al. [22]. Within the presented investigations, a mixture of water and MEG with a mass ratio of $\zeta_{\text{MEG,water}} = 1.72 \text{ g/g}$ was used as a sub-zero MWF. Na₂SiO₃ was used a corrosion inhibitor with a concentration of 3.7 g per 1 kg of sub-zero MWF. As anti-wear agent 14 g of C₁₂H₂₇O₄P was added per 1 kg of sub-zero MWF.

To apply these sub-zero MWF when machining, new cooling systems were developed and integrated in the experimental setup for milling and turning operations. When turning, a cooling system was developed allowing a maximum mass flow of 110 l/min and supply pressures up to 50 bar. A detailed description of the developed setup is given by Basten et al. [23]. A second and more resource efficient setup was developed which is described by Gutzeit et al. [24]. Here the sub-zero MWF can be applied with volume flow rates up to 8 l/min and a maximum supply pressure of 30 bar.

3 Simulation of the Temperature Field

To better understand the temperature distribution and history of parts during machining under cryogenic conditions, simulations were performed. In the bulk material, the simulations take heat conduction due to inhomogeneous temperature fields and advection due to the turning workpiece into account. The latter requires an upwind Petrov–Galerkin stabilization. For details, the reader is referred to [25]. A typical temperature distribution is shown in Fig. 4. In Fig. 4a no cooling is considered leading to high temperatures, while with cryogenic turning condition in place, the temperatures are significantly lower, see Fig. 4b.

The bulk parameters are well known and can be taken from the literature, see [26]. However, the influence of thermal boundary conditions becomes significant for the simulation. The cutting tool is represented as a heat flux into the workpiece, while the rest of the surface is treated as a convection surface. The natural convection by the surrounding air and the forced convection by the cooling with CO₂ are considered. Details on the thermal boundary value problem and the material data can be found in [25].

The parameters, for example, heat flux Q_{in} and heat transfer coefficient α_{CO_2} are identified with the help of three measuring points (MP) in the workpiece. The different parameters are identified by separate experiments, such as dry cutting including cooling on air and cooling with the coolant CO₂. Different process parameters, such as different feed rates ($f = 0.15$ mm/rev and $f = 0.35$ mm/rev), are resulting in different values for heat flux Q_{in} and heat transfer coefficient α_{CO_2} . Details of the parameter identification procedure and the experimental setup can be found in [25].

Using these identified parameters predictive runs are calculated, by simulating a cutting process with coolant. The comparison is reported in Fig. 5. It can be seen that the strategy of identifying the individual parameters from separate experiments already provides certain agreement. But, measuring point 1 (MP1) has larger deviations. If all parameters are identified on the cutting process with cooling directly a much more accurate agreement between experiment and simulation can be obtained. The fact that the parameters for the heat flux Q_{in} and the heat transfer coefficient

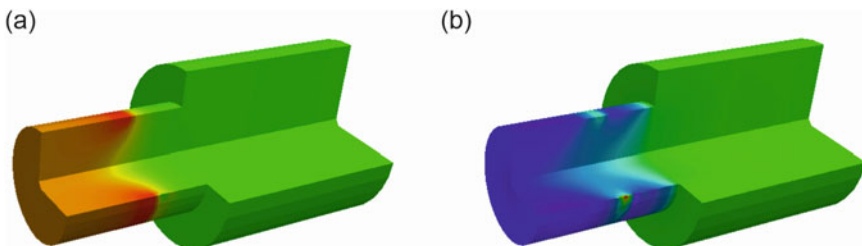


Fig. 4 Simulation of temperature distribution during turning without cooling **a** and with a CO₂ cooling **b** according to [25]

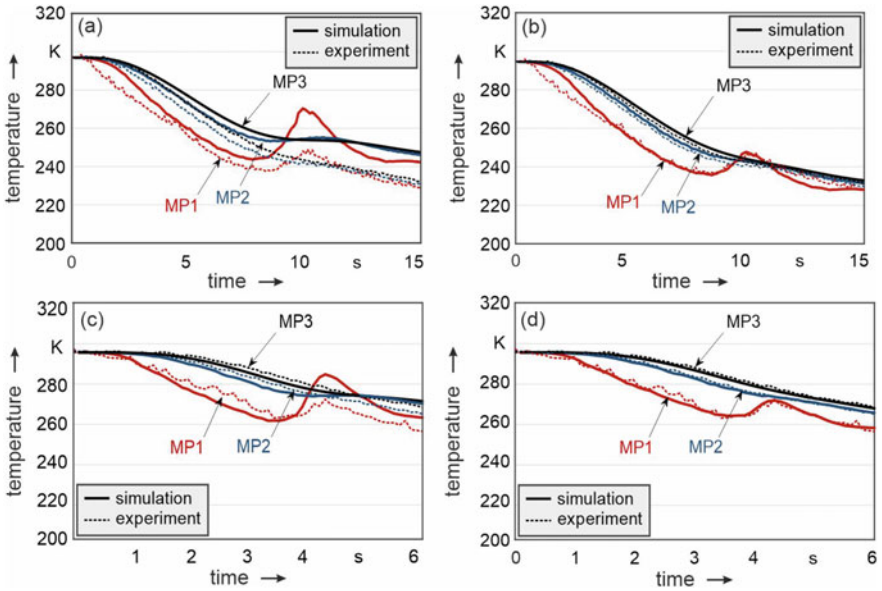


Fig. 5 Predictive temperature history using identified parameters for **a** $f = 0.15$ mm/rev and **b** $f = 0.35$ mm/rev and optimized temperature history using identified parameters for **c** $f = 0.15$ mm/rev and **d** $f = 0.35$ mm/rev. according to [26]

α_{CO_2} cannot be identified from separate experiments indicates the strong nonlinearity and coupling of the problem.

The values identified from dry turning including cooling on air and cryogenic cooling are reported in Fig. 6, left diagrams. The optimized values for cryogenic turning are reported in Fig. 6, right diagrams. It is apparent that the value for the heat transfer coefficient α_{CO_2} is rather not influenced by the setup of the boundary value

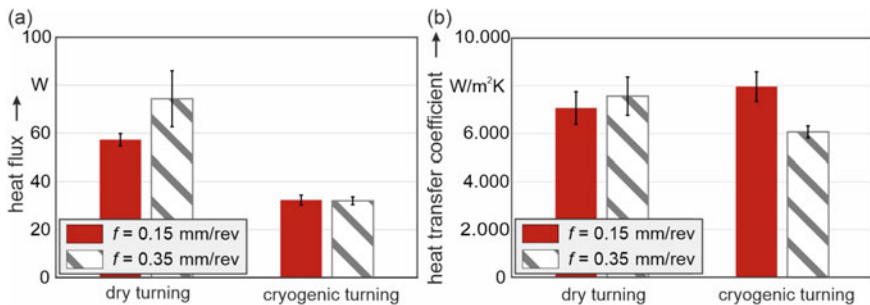


Fig. 6 Mean values regarding the heat flux Q_{in} **a** and the heat transfer coefficient α_{CO_2} **b** in dependence of the cooling strategy during turning according to [26]

problem. As expected, the heat flux into the workpiece by the tool Q_{in} is strongly influenced by the cryogenic turning and needs to be identified properly.

4 Cryogenic Machining of Metastable Austenite

Due to their excellent corrosion resistance as well as their favorable combination of strength and ductility, metastable austenitic steels are widely used in industry. If these steels are cryogenically machined, a deformation-induced phase transformation from the metastable γ -austenite into ε - and α' -martensite can occur [1, 27]. This martensitic phase inhibits a higher microhardness than the initial austenitic one. The increase in microhardness resulting from the deformation-induced phase transformation can be superimposed with the increase in microhardness via strain hardening, which is why cryogenic machining offers high potential for a pronounced surface hardening [28]. The phase transformation from γ -austenite into ε - and α' -martensite is promoted by a high deformation in the workpiece surface layer and a sufficient cooling. The reason is given in Fig. 7a where a thermodynamic explanation of the phase transformation is depicted. The metastable austenitic steel is characterized by the fact that the martensitic state (G_α) offers an energetically favorable state compared to the austenitic one (G_γ) below the temperature T_0 . As a result, a phase transformation from austenite to martensite is possible, if the minimum difference of free energy ΔG_{min} is provided. At the martensite start temperature M_s this amount of free energy is given due to a sufficient decrease in temperature, resulting in a thermally induced phase transformation. At temperatures above M_s but below T_0 , additional free energy is necessary to induce the phase transformation. Applying stress results in an increase of the mechanical free energy ΔG_{mech} , which can be utilized to reach the minimum free energy ΔG_{min} in superposition with the thermal free energy ΔG_{therm} . A detailed description of the phase transformation from γ -austenite into ε - and α' -and martensite is given by Hotz et al. [27] and Kirsch et al. [29].

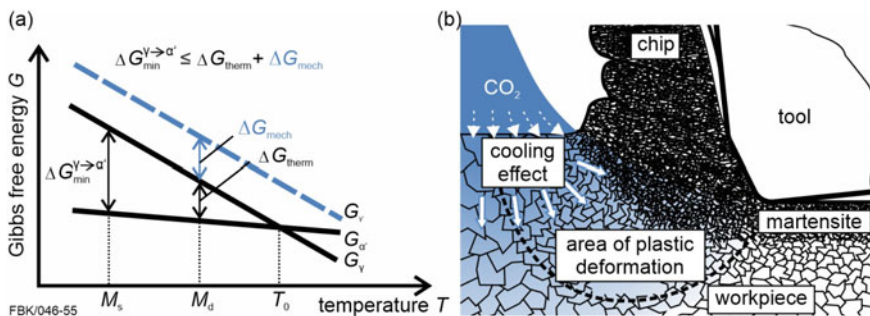


Fig. 7 a Correlation between Gibbs energy and temperature according to [30, 31] b Schematic view of the deformation-induced phase transformation when cryogenic machining according to [32]

This thermodynamical background can be utilized to design the surface conditioning via cryogenic machining which is depicted in Fig. 7b. It is evident that a sufficient cooling has to be applied, decreasing the temperature, and therefore promoting higher thermal free energy ΔG_{therm} . Moreover, the cutting process has to favor a high amount of plastic deformation in the workpiece surface layer increasing the mechanical free energy ΔG_{mech} [32].

The martensitic phase transformation is not solely influenced by the occurring thermo-mechanical load. The chemical composition of the respective batch also has a decisive influence on the phase transformation. For example, the martensitic start temperature is highly dependent on the chemical composition which can be calculated by Eq. (1) according to Eichelmann [33]. Nevertheless, *Kirsch et al.* proved that a deformation-induced phase transformation and the resulting surface hardening via cryogenic machining are possible regardless of the investigated batch [29].

$$M_s = 1350 - 1665(C + N) - 28Si - 33Mn - 42Cr - 61Ni. \quad (1)$$

Within the investigations presented, the martensite content in the workpiece surface layer was measured using a magnetic sensor (Feritscope FMP30¹). Consequently, only the amount of α' -martensite is measured, while the magnet sensor did not allow a measurement of the paramagnetic ε -martensite.

4.1 Influence of the Cryogenic Cooling Strategy

As a first step, investigations were conducted to identify a suitable cooling system configuration in order to reduce the temperatures and the respective thermal load during cutting. Four different cryogenic cooling setups, see Fig. 8, were investigated and compared to dry cutting when turning the metastable austenitic steel.

The influence of the applied cooling strategies on the thermo-mechanical load and on the resulting surface morphology is depicted in Fig. 9. For the mechanical load (Fig. 9a) only the passive forces are depicted here, since this force component is the crucial factor influencing the mechanical load in the workpiece surface layer [3]. However, no distinct influence on the passive force is observed when varying the cooling system, as can be expected.

In Fig. 9b, the impact of the cooling system is depicted regarding the thermal load. Here a reduced temperature is achieved for every cryogenic cooling strategy in comparison to dry cutting. When being compared with the internal cooling system, the usage of an external supply results in lower temperatures since the workpiece surface is cooled directly. Lower temperatures are measured when using LN₂ instead of CO₂. However, when applying LN₂ externally, a cold gas layer is formed at the workpiece surface due to the enormous temperature difference. This layer reduces the cooling capacity and influences the infrared thermography that was used to measure the temperatures here. Consequently, the real temperatures at the workpiece surface are expected to be higher. The best cooling effect is observed when combining the

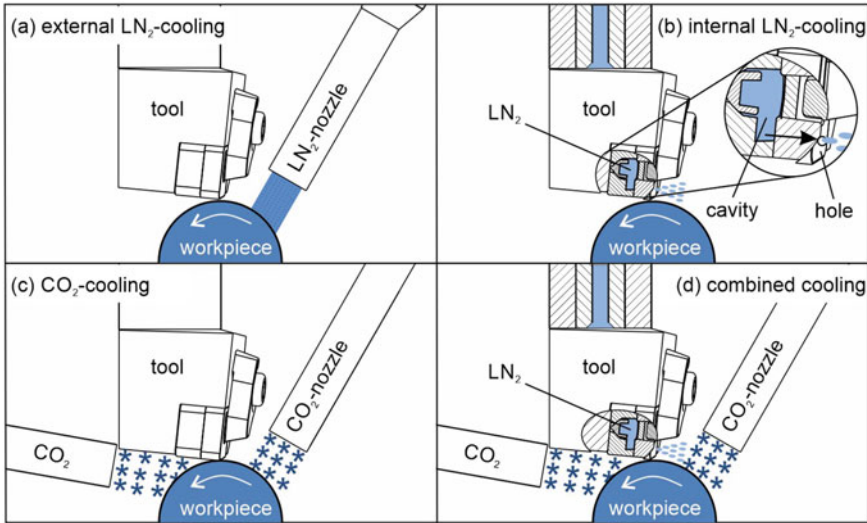


Fig. 8 Cooling strategies investigated when cryogenic turning adapted from [15]

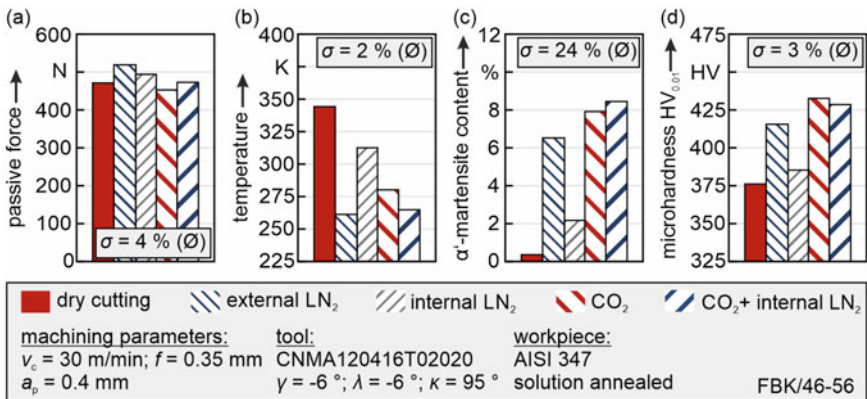


Fig. 9 Passive force (a), workpiece temperature (b), α' -martensite content (c), and microhardness d in dependence of the cooling strategy when cryogenic turning adapted from [15]

CO₂-cooling in superposition with the internal LN₂ cooling. However, a bad dimensional accuracy resulted when using the internal LN₂ cooling, since the extremely low temperatures led to a thermally induced shrinkage of the tool holder and the tool.

The content of α' -martensite measured in the workpiece surface layer in dependence of the cooling system used is depicted in Fig. 9c. A significant amount of α' -martensite is observed when the external cooling systems are applied since the reduced thermal loads promote the phase transformation. Due to a higher thermal load, the α' -martensite content is significantly lower for dry cutting and the internal

LN₂-cooling. A higher content of α' -martensite is achieved when using CO₂ instead of LN₂ despite the higher temperatures measured here. This supports the aforementioned assumption that the real temperatures during cryogenic turning with LN₂ were higher than the ones measured via thermography.

In Fig. 9d, the maximum microhardness measured is depicted in dependence of the five cooling systems investigated. Within the bulk of the workpiece a core microhardness of 231 HV0.01 is measured. Consequently, a surface hardening is achieved for every specimen, regardless of the cooling system. Since almost no α' -martensite content is measured for dry cutting, the increased microhardness can be attributed to strain hardening. However, if a promoted phase transformation is achieved, a significant increase of the microhardness can be observed, which was the case when applying external coolant. A more detailed observation regarding the influence of the cooling system is given by Mayer et al. [15].

From these results, it can be concluded that the usage of an external CO₂-cooling is most suitable to improve the surface morphology when cryogenic machining metastable austenitic steels. Consequently, the influence of an external CO₂-cooling was characterized in more detail to further optimize the cooling strategy. Therefore, the influence of the CO₂ mass flow on the occurring temperature and the resulting content of α' -martensite was investigated. Within this investigation, the opening of a valve used to limit the mass flow was systematically varied. Here, a valve opening of 100% corresponds to a CO₂ mass flow of 3.5 kg/min. The results are given in Fig. 10. A clear tendency is observed, depicting higher temperatures with decreasing mass flows. As the process parameters and therefore the process time were kept constant, less CO₂ is applied during cutting when the mass flow is lowered. This in term results in a reduced cooling capacity and therefore higher temperatures.

With decreasing mass flows and therefore rising temperatures a less promoted phase transformation is observed. Note that the passive forces measured were of equal magnitude, resulting in a minor influence of the mass flow on the mechanical loads. Consequently, differences regarding the α' -martensite content can only be led back to a promoted phase transformation due to different thermal loads. It can

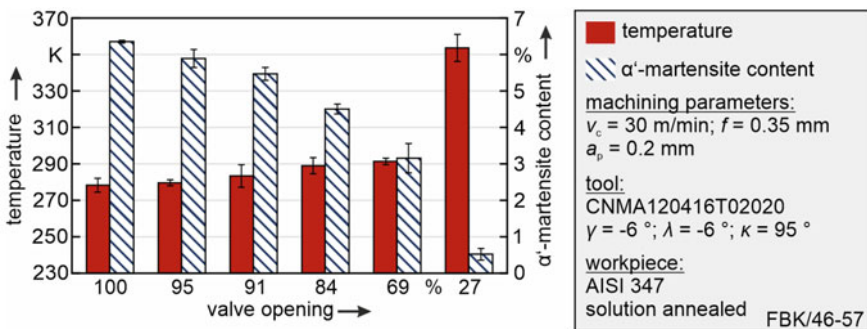


Fig. 10 Workpiece temperature and volume content of α' -martensite in dependence of the valve opening and the respective mass flow adapted from [30]

therefore be concluded that a maximum mass flow has to be applied in order to achieve a maximum amount of α' -martensite content in order to optimize the surface morphology. A detailed investigation regarding the optimization of the CO₂-cooling strategy is given by Mayer et al. [30].

4.2 Influence of the Cutting Process

As a second step, the influence of the cutting process was investigated. Within the investigations presented, a constant depth of cut was chosen. While a higher depth of cut favors a martensitic phase transformation due to an increased amount of plastic deformation, a bigger part of the hardened workpiece surface layer is also removed. The influence of the depth of cut is described by Mayer et al. [32] in detail. The influence of the cutting speed and the feed regarding the occurring thermo-mechanical load and the resulting surface morphology is depicted in Fig. 11. Increasing the feed results in higher passive forces as the cross section of the undeformed chip and therefore the material removal is increased. A decreasing passive force is observed at higher cutting speeds. This can be attributed to higher amounts of heat being generated at elevated cutting speeds resulting in thermal softening. This assumption is supported by the temperature measurements depicted in Fig. 11b, since higher thermal loads are observed at higher cutting speeds. When the feed is increased, the temperatures increase as well, due to a reduced cooling time and a higher amount of friction.

Regarding the content of α' -martensite (Fig. 11c), an increased cutting speed reduces the α' -martensite content. This can be explained by the increasing temperature hindering the phase transformation. In contrast, an increased feed promotes the

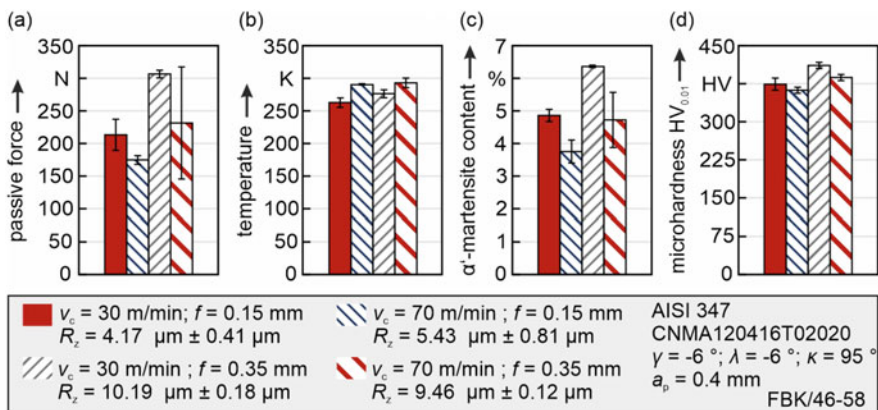


Fig. 11 Passive force (a), temperature (b), martensite content (c), and microhardness (d) in dependence of the cutting parameters according to [15]

phase transformation; a higher α' -martensite content is measured here. Despite the increasing thermal loads at higher feeds, the significant increase of the passive forces seems to be more beneficial regarding a promoted martensitic phase transformation.

The microhardness in the workpiece surface layer correlates with the content of α' -martensite measured. Consequently, the highest increase in microhardness is achieved when choosing a low cutting speed and a high feed (Fig. 11d).

However, when regarding the surface topography, a higher feed results in a significantly decreased surface quality, due to an increased kinematic roughness. In comparison, the cutting speed has a minor influence on the surface roughness. The influence of the cutting parameters during cryogenic machining metastable austenitic steels is further described by Hotz et al. [27] as well as Mayer et al. [15, 32] for turning and by Gutzeit et al. [34] for milling.

Aside from the cooling strategy and the cutting parameters, the tool properties have a decisive impact on the thermo-mechanical load and the surface morphology. Consequently, the influence of the tool properties was investigated to further optimize the surface conditioning of metastable austenitic steels via cryogenic machining. The results presented here focus on the cutting-edge preparation regarding the cutting-edge radius and chamfered cutting edges. An in-depth investigation of the tool properties including additional influences of the corner radius and various coating architecture is given by Hotz et al. [35, 36].

In Fig. 12, the thermo-mechanical load as well as the α' -martensite content and the surface roughness are depicted as a function of the varied cutting-edge radius and the chamfer angle. Increasing the cutting-edge radius results in higher occurring passive forces since the cutting edge decreases in sharpness favoring ploughing effects and friction (Fig. 12a). In comparison to the cutting-edge radius, higher chamfer angles lead to a more significant increase of the passive forces. Due to stronger negative rake angles the amount of plastic deformation within the cutting zone increases which leads to higher passive forces. Regarding the process temperature, only a minor increase is detected at higher cutting-edge radii despite the increased amount of friction and heat being generated. This can be explained by a counteracting effect, since the heat dissipation is also promoted due to the larger surface [37]. When using chamfered cutting edges, only a chamfer angle of 60° leads to a significant increase of the thermal load. This could be explained by the high amount of mechanical work that is converted to heat as a result of the extremely high passive forces.

With a bigger cutting-edge radius, the mechanical load rises while the thermal load does not change significantly. This favorable thermo-mechanical load promotes a martensitic phase transformation resulting in a higher content of α' -martensite measured (Fig. 12c). An increase of the α' -martensite content is also observed for chamfered cutting edges up to a chamfer angle of 40° due to the favorable thermo-mechanical load. A further increase of the chamfer angle not only leads to drastically higher passive forces but also to higher temperatures. The highly increased thermal load inhibits the phase transformation resulting in a drop of the α' -martensite content. Regarding the surface topography (Fig. 12d), a slightly higher surface roughness is measured at higher cutting-edge radii due to promoted ploughing effects. When using greater chamfer angles a significant decrease of the surface quality is observed result-

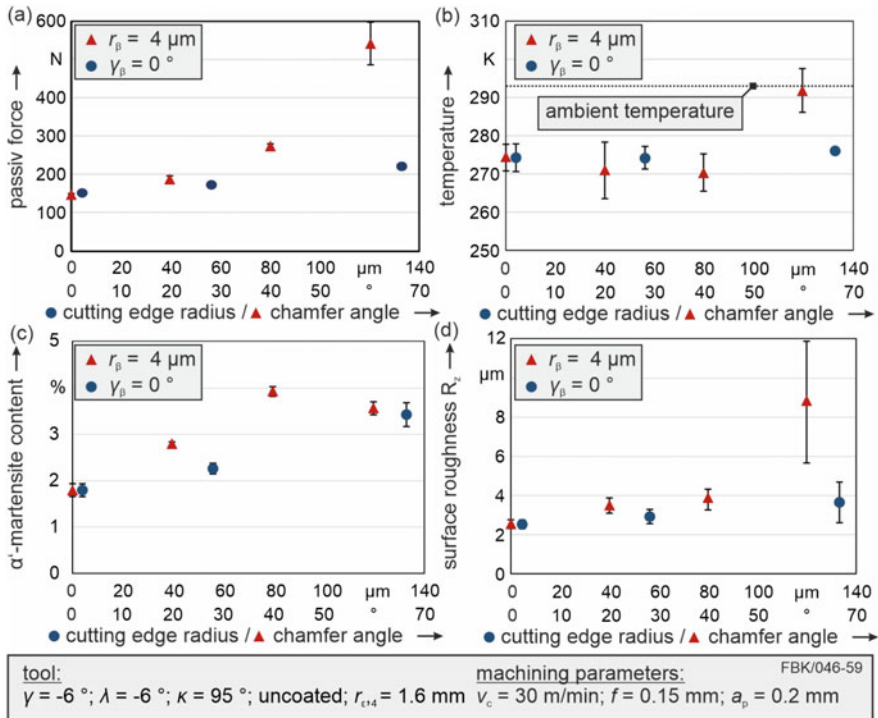


Fig. 12 Passive force (a), temperature (b), martensite content (c), and surface roughness (d) in dependence of the cutting-edge preparation to [35]

ing from severe adhesions at the workpiece surface. These adhesions are promoted due to the negative effective rake angle favoring built-up edges and the high passive forces pressing the material in front of the cutting edge into the newly generated workpiece surface.

To characterize the influence of the cutting-edge preparation on the microhardness, three representative microhardness profiles are given in Fig. 13a. The corresponding micrographs depicting the martensite content in the surface layer are depicted in Fig. 13b.

The increase of the cutting-edge radius leads to an increased maximum microhardness and hardness penetration depth. This results from the higher content of α' -martensite and promoted strain hardening due to the higher mechanical loads. When using the chamfered cutting edge, the hardness penetration depth increases significantly which can be led back to a higher transformation depth of the α' -martensite (Fig. 13b). Additionally, a pronounced nanocrystalline surface layer is found here, due to severe plastic deformation during the cutting process.

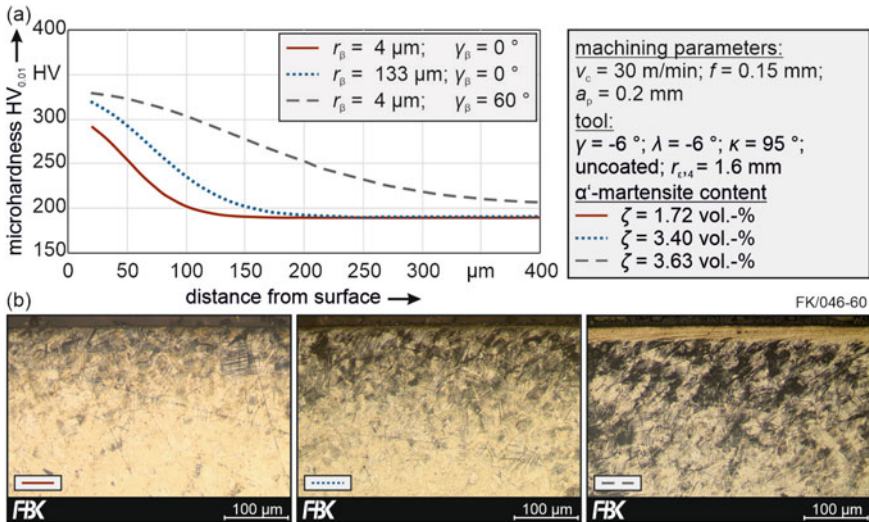


Fig. 13 Microhardness (a) and distribution of martensite (b) in the workpiece subsurface in dependence of the cutting-edge geometry according to [35]

4.3 Development of a Two-Step Turning Process

It was demonstrated that especially high feeds and bigger chamfer angles promote a surface hardening and improve the mechanical and metallurgical properties of the surface morphology significantly. However, increasing these parameters also results in a decreasing surface quality, generating a conflict between a sufficient surface hardening and an adequate surface topography.

Thus, a two-step turning process was developed to produce an optimized surface morphology which combines a significantly hardened surface layer and a low roughness topography. The first process step aimed at a maximum content of deformation-induced martensite to increase the hardness in the workpiece surface layer. To achieve this, a high feed and a chamfered cutting edge were used. Additionally, a precooling of the workpiece was conducted in order to achieve a favorable thermal load. In the second process step, the final surface topography was generated while maintaining the highest possible martensite content that had been generated by the first process step. Consequently, a very low depth of cut, a low feed, and a high cutting speed as well as a sharp tool were utilized.

In Fig. 14, the resulting thermo-mechanical loads and the achieved surface morphologies are depicted for both process steps and for a referential single-step turning process. High passive forces are achieved during the first process step (Fig. 14a), mainly because of the large undeformed chip cross section and the distinct negative effective rake angle. During the second process step a significantly lower passive forces is measured due to the lower depth of cut and the sharp cutting edge of the

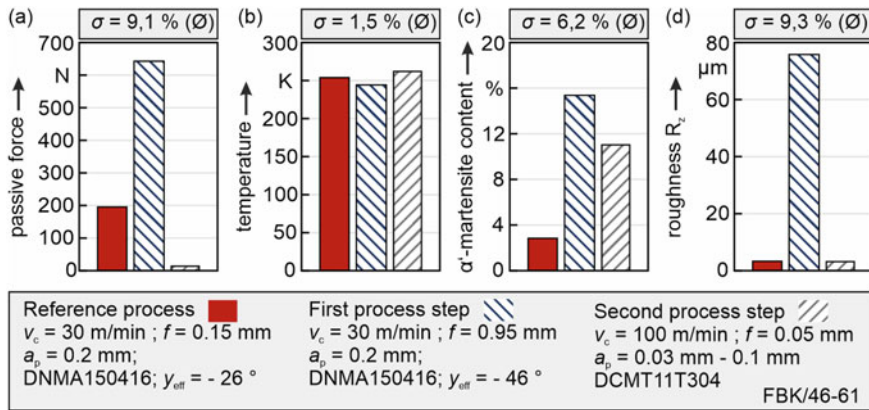


Fig. 14 Passive force (a), temperature (b), martensite content (c), and roughness (d) for the reference workpiece and the two-step turning process according to [35, 38]

tool used. The workpiece temperature (Fig. 14b) is at a similar level for all cutting steps. Note that an equal amount of CO_2 was used for the first process step and the referential cut. While a precooling was used during the first process step, the higher feed also reduced the process time decreasing the amount of CO_2 used.

The content of α' -martensite is significantly higher after the first process step in comparison to the referential cut (Fig. 14c). This promoted phase transformation results from the favorable thermo-mechanical load due to the higher passive forces. After the second process step, the α' -martensite content is reduced since a layer of martensite was removed during cutting. Regarding the surface topography (Fig. 14d), a significant improvement is observed after the second process step. As a result, the measured roughness is within the same magnitude as the roughness measured for the referential cut. Additionally, less chatter marks and adhesions are observed on the workpiece surface after the two-step turning process.

The martensite distribution and the hardness profiles within the workpiece surface layer after the two-step process and the referential cut are depicted in Fig. 15. In comparison to the initial hardness, a significant increase is achieved for both turning processes. However, a higher maximum microhardness as well as a deeper penetration depth is generated with the two-step turning process. This is achieved because of the higher α' -martensite content and promoted strain hardening introduced due to the significantly higher mechanical loads.

To conclude, the two-step turning process can improve the overall surface morphology regarding the hardness within the workpiece surface layer and the surface topography. A detailed investigation of the two-step turning process is given by Hotz et al. [38, 39].

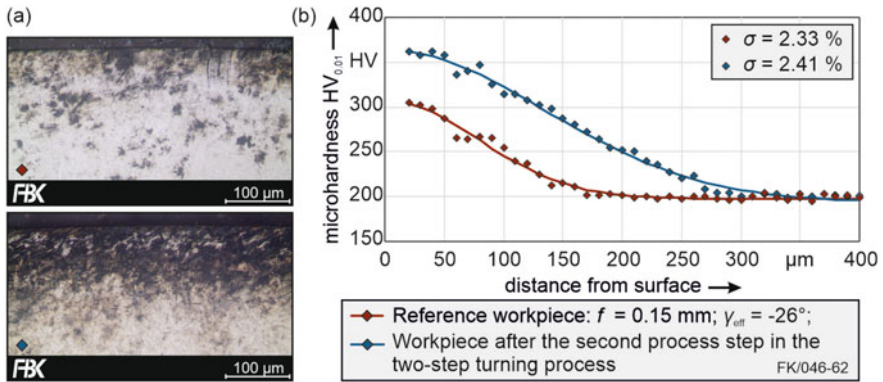


Fig. 15 Distribution of martensite (a) and microhardness (b) in the workpiece subsurface of the reference workpiece and after the two-step turning process according to [38]

5 Cryogenic and Sub-zero Machining of Titanium Alloys

Due to an excellent ratio of low density to high strength as well as a strong corrosion resistance, the titanium alloy Ti-6Al-4V is widely used in industrial applications, especially in the aerospace industry [40]. However, the high strength, the low thermal conductivity, and the promoted chemical reactivity especially at elevated temperatures of Ti-6Al-4V result into high mechanical, thermal and chemical loads when machining it, classifying this titanium alloy as a difficult-to-cut material [41].

When machining Ti-6Al-4V, an efficient reduction of the thermal load is desirable in order to prevent thermo-chemical-induced tool wear. Common methods are the reduction of the cutting speed, yet limiting the process efficiency, or coatings and cutting-edge preparations which increase tool costs significantly [42, 43].

Another, more efficient approach to reduce the thermal load is the application of suitable cooling strategies. Within this chapter, the application of cryogenic cooling strategies is investigated when turning and milling Ti-6Al-4V. Additionally, the novel sub-zero cooling approach, developed within the CRC 926, is examined and compared with the performance of conventional cryogenic coolants.

5.1 Impact of Cryogenic and Sub-zero Cooling Strategies When Turning Titanium Alloy

When turning Ti-6Al-4V, six different cooling strategies were investigated, for details we refer to Kirsch et al. [44]. Dry cutting as well as the usage of a conventional MWF (MWF_c) and the application of cryogenic coolants (CO₂, LN₂) were investigated. Additionally, the use of a sub-zero MWF applied at a supply temperatures of 293 K (MWF₂₀) and 243 K (MWF₋₃₀) was examined. The influence of the cooling strategies

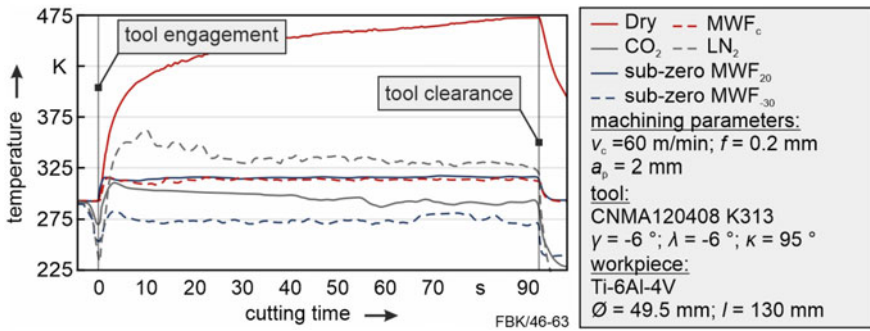


Fig. 16 Tool temperature as a function of the cutting time in dependence of the cooling strategy applied according to [44]

on the tool temperature, standing for the thermal load, is depicted in Fig. 16 for a representative cut. Here, the tool temperature is given as a function of the cutting time when external cylindrical turning Ti-6Al-4V. Before the tool engagement, a precooling is observed when applying coolants at a supply temperature below the ambient temperature. The lowest temperature before tool engagement is observed for LN₂, while the sub-zero MWF₋₃₀ leads to lower temperatures than CO₂ despite higher supply temperatures but due to a better heat conductivity and wettability.

After the tool engagement, the tool temperature rises for every tool because of the heat that is introduced during cutting. Since no cooling is applied, dry cutting leads to the highest tool temperature measured. The second highest tool temperature is observed when using LN₂ as a coolant. Despite the lowest supply temperature, film boiling causes a very poor heat transfer, resulting in higher temperatures during cutting. For the conventional MWF_c and the sub-zero MWF₂₀, similar temperature curves are observed. The lowest tool temperature and consequently the best cooling effect are achieved when using the sub-zero MWF₋₃₀. This is achieved due to the low supply temperatures in addition to the favorable wetting behavior and better heat transfer of the liquid MWF (Fig. 16).

The influence of the cooling strategies investigated regarding tool wear is depicted in Fig. 17 in dependence of the cutting time. As no significant influence was observed regarding the flank wear of the tool, only the crater wear is depicted here. Due to the high thermal loads, dry cutting results in the shortest tool life which is reached after a cutting time of 254 seconds. Applying cryogenic coolants improves tool life in comparison to the MWF applied at an ambient temperature. The longest tool life is achieved when using the sub-zero MWF₋₃₀, as the lowest thermal load is provided. As a result, the tool life criterion of a crater ratio $K = 0.2 \mu\text{m}/\mu\text{m}$ was not reached after a cutting time of 383 seconds for sub-zero turning with a supply temperature of 243 K. Consequently, the thermo-chemical-induced tool wear progress is efficiently hindered due to a sufficient reduction of the thermal load when turning Ti-6Al-4V.

In general, during turning of Ti-6Al-4V, the titanium alloy tends to produce unfavorably long chips. This characteristic chip formation leads to a difficult handling

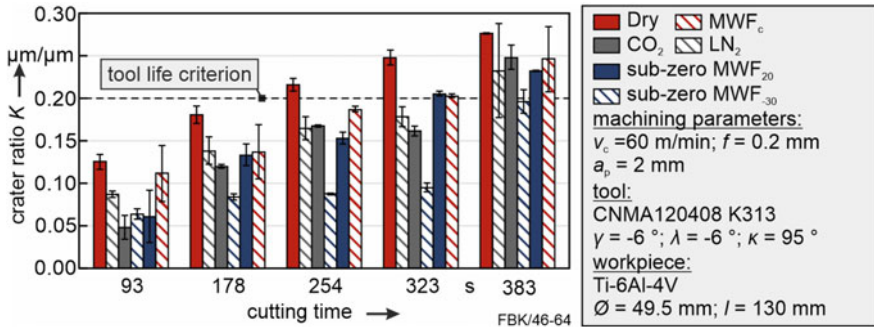


Fig. 17 Crater ratio as a function of the cutting time in dependence of the cooling strategy according to [44]

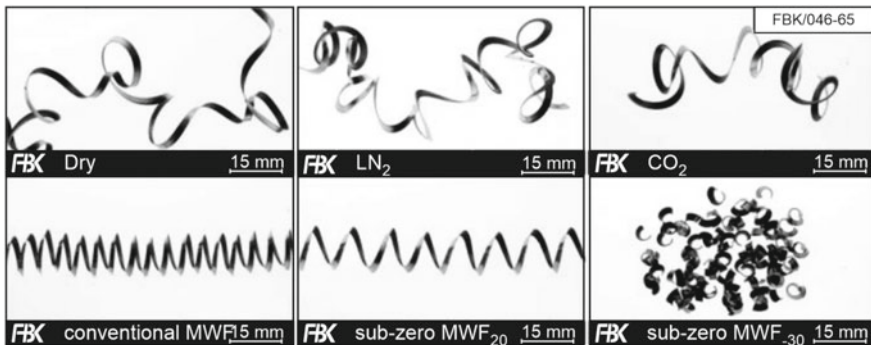


Fig. 18 Depiction of generated chips in dependence of the cooling strategy according to [44]

and high disposal costs, especially in automated processes, making chip formation a big issue. In Fig. 18, the chips produced when turning Ti-6Al-4V are depicted in dependence of the cooling strategy applied.

Cylindrical helical chips are formed when the conventional MWF_c and the sub-zero MWF₂₀ are applied. However, these chips still exhibit a highly unfavorable chip volume ratio, just like the chips produced during dry and cryogenic turning. When the sub-zero MWF₋₃₀ is applied, the chip formation changes significantly. Favorable chips with a low chip volume ratio are produced which are easy to dispose and do not damage the workpiece surface. The change in chip formation is explained by high thermal stresses within the chips. These are a result from the big temperature differences at the top and bottom of the chips caused by the high cooling efficiency of the sub-zero MWF₋₃₀. This highly effective cooling generally decreases the temperature within the chips, which results in an embrittlement further promoting chip breakage. The results presented for sub-zero turning of Ti-6Al-4V are described in a higher detail by Kirsch et al. [44]. Additionally, the influence of different supplying

techniques during sub-zero turning was investigated by Basten et al. [45], confirming the superior cooling efficiency of this novel cooling approach.

5.2 *Impact of the Cryogenic and Sub-zero Cooling Strategies When Milling Titanium Alloy*

The cutting speed and the feed per tooth were systematically varied when milling the titanium alloy Ti-6Al-4V with CO₂ cooling while examining the occurring thermo-mechanical load and the resulting surface morphology. The results are depicted in Fig. 19 as a function of the feed velocity v_f , which is influenced by the cutting speed v_c and the feed f and the number of teeth z according to Eq. (2). As a consequence, the influence of the cutting speed is given implicitly when increasing the feed velocity at a constant feed per tooth f_z .

$$v_f = f_z z n = f_z z v_c 1,000 / D \pi. \quad (2)$$

At higher feed velocities, the workpiece temperature rises due to a less effective cooling as the amount of CO₂ applied during the process is reduced. Higher feeds further increase the temperature, as more material is removed per cut resulting in more heat being generated. Additionally, higher temperatures are observed at higher cutting speeds. This is explained by an increased cutting power and higher strain rates within the deformation zone, which are promoted at higher cutting speeds.

Regarding the mechanical load (Fig. 19b), significantly higher forces are observed at an increased feed per tooth. Because of the higher undeformed chip cross section at a higher feed per tooth, more material is removed per cut, which results in higher forces. When being compared with the feed, the influence of the cutting speed on the process forces is rather low. However, at an elevated feed per tooth, a slight increase of the resulting forces is observed with rising cutting speeds. This can be explained by alterations of the tool geometry due to promoted adhesions at the cutting edge.

The microhardness measured in the near-surface layer at a distance of 20 μm to the final machined surface is given in Fig. 19c in dependence of the feed velocity. In comparison to the core microhardness, a surface hardening is observed for all parameter variations investigated with the exception of one. When increasing the cutting speed at a constant feed, the microhardness decreases for all cases investigated due to the elevated thermal load. At a constant cutting speed, the lowest microhardness is measured at a feed per tooth of $f_z = 0.08 \text{ mm}$. This is explained by the opposing effects of the feed regarding the occurring forces and temperatures within the workpiece surface layer. While a higher feed favors the plastic deformation, the thermal load is decreased at lower feeds. Since the highest microhardness is measured at the lowest feed investigated, the most favorable thermo-mechanical load did occur here.

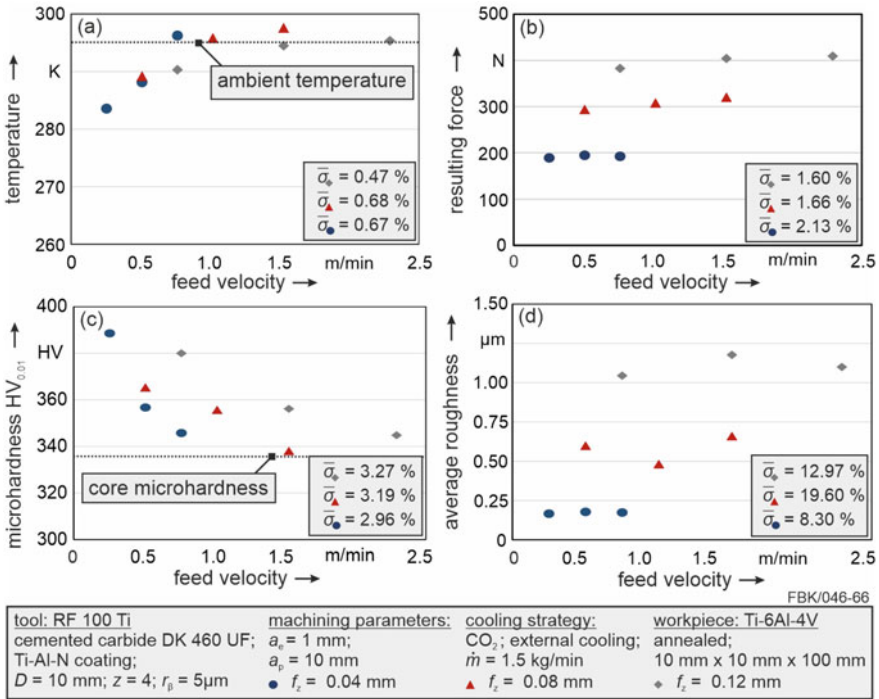


Fig. 19 Workpiece temperature (a), resulting force (b), microhardness (c), and average roughness (d) in dependence of the cutting parameters during cryogenic milling according to [46]

Consequently, the reduction of the thermal load does seem to have a higher impact in comparison to the mechanical load when cryogenically milling Ti-6Al-4V.

The influence of the cutting parameters on the surface roughness is depicted in Fig. 19d. It is observed that the roughness significantly increases at higher feeds, due to an increase of the kinematic roughness of the milling process. When varying the cutting speed at a constant feed per tooth, no major impact regarding the surface roughness is found.

Consequently, it can be deduced that choosing a low feed per tooth as well as a low cutting speed is most beneficial in order to improve the surface morphology of Ti-6Al-4V during cryogenic milling. A detailed investigation regarding the influence of the cutting parameters for cryogenic milling is given by Gutzeit et al. [14].

To further improve the surface morphology when milling, the application of the novel sub-zero cooling approach was investigated. The sub-zero MWF was applied at three different supply temperatures when milling Ti-6Al-4V at constant process parameters. The performance of the sub-zero cooling regarding the thermo-mechanical load and the resulting microhardness is compared to dry and cryogenic milling within Fig. 20.

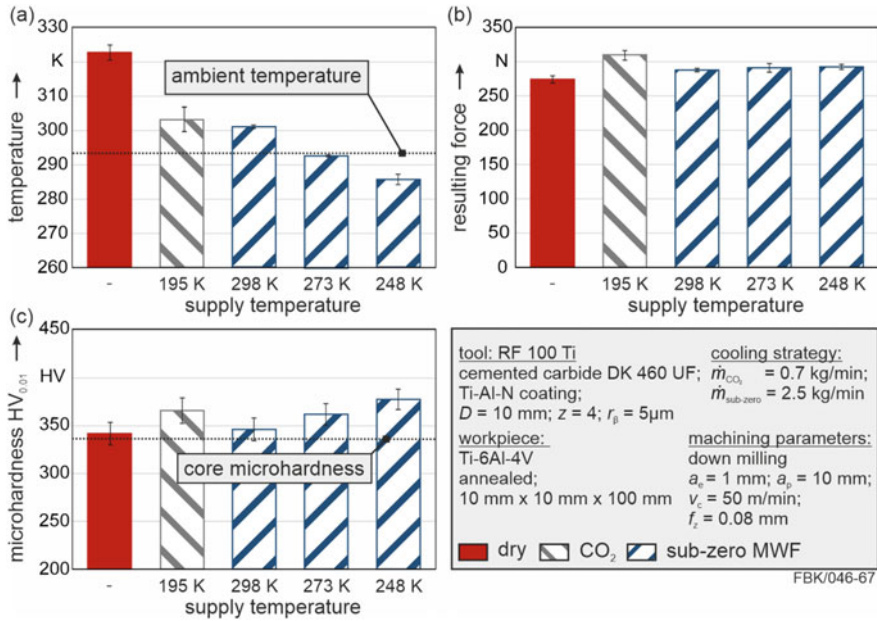


Fig. 20 Influence of the cooling strategy on the workpiece temperature (a), the resulting force (b), and the microhardness (c) when milling Ti-6Al-4V according to [46]

Since no cooling was applied during dry milling (Fig. 20a), the highest workpiece temperature is measured here. The second highest thermal load is found when applying the cryogenic CO₂ cooling. Sub-zero milling results in the lowest thermal load which further decreases when lower supply temperatures are used. As a result, the lowest thermal load is achieved during sub-zero milling with a supply temperature of $T_{supply} = 248$ K. While the supply temperature is still higher in comparison to the cryogenic CO₂ cooling strategy, the sub-zero MWF provides a sufficient cooling effect due to a better heat transfer coefficient and wetting behavior. Additionally, a promoted lubrication reduces friction and therefore the amount of heat being generated during cutting. The highest occurring forces (Fig. 20b) are measured when using the cryogenic cooling strategy. This is attributed to the lack of lubrication leading to more friction and consequently higher forces. While a higher amount of friction is also expected for dry milling, the lowest forces are observed here. In this case, a more significant influence regarding thermal softening is expected, due to the higher temperatures measured here. For sub-zero milling, a slight increase of the forces is observed with decreasing supply temperatures, which can also be attributed to thermal softening. However, this increase of the resulting forces is comparatively low.

The influence of the investigated cooling strategies on the microhardness is depicted in Fig. 20c. For dry milling, no significant surface hardening is observed, as the high thermal load favors the dynamic recrystallization and counteracts strain

hardening. At decreasing supply temperatures an increasing microhardness is observed after sub-zero milling. Since the thermal load decreases at lower supply temperatures, the dynamic recrystallization is suppressed which favors strain hardening and therefore a higher microhardness. A higher microhardness is also observed after cryogenic milling. However, the highest microhardness is observed for sub-zero milling with the lowest supply temperature, since the most favorable thermo-mechanical load is achieved.

The surface roughness has also been examined. However, since the process parameters were identical for all tests conducted, the measured roughness parameters are within the same order of magnitude. Despite that, less ploughing effects and adhesions were observed for sub-zero milling which is attributed to the favorable lubrication effects. The results shown are explained in greater detail by Gutzeit et al. [46].

The potential of the novel sub-zero cooling strategy in comparison to dry cutting and cryogenic cooling was also examined regarding tool wear when milling Ti-6Al-4V. In Fig. 21, the resulting tool life is depicted in dependence of the cooling strategy applied. Additionally, the influence of different cutting-edge radii is given. Increasing the cutting-edge radius results in an increased tool life, regardless of the cooling strategies applied. This is explained by the increased strength of the cutting edge which in turn prevents cutting-edge chipping. The lowest tool life is observed for cryogenic milling with CO₂ as a coolant, despite lower thermal loads in comparison to dry milling. This is explained by fatigue effects resulting from cyclic thermal loads during cutting as a consequence of the interrupted cut when milling. When applying the sub-zero cooling strategy, the longest tool life is achieved regardless of the cutting-edge radius. This is explained by the highly efficient cooling capacity resulting in a reduced thermal load and thermally induced tool wear. Despite the high cooling efficiency, no fatigue failure is observed for sub-zero milling. It is therefore assumed that the thermal cyclic load is less pronounced in comparison to

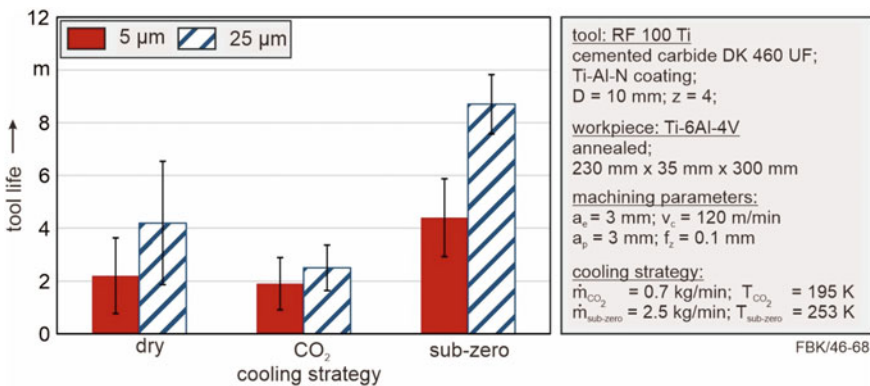


Fig. 21 Influence of the cooling strategy and the cutting-edge preparation on the tool life when milling Ti-6Al-4V according to [47]

the cryogenic cooling. This is attributed to the higher supply temperatures and the reduced heat generation in the cutting zone due to beneficial lubrication effects. A detailed study on the effects on tool wear when milling Ti-6Al-4V using cryogenic and sub-zero cooling strategies is given by Gutzeit et al. [47].

6 Summary

In this chapter, facilities and processes were presented to improve the surface morphology via cryogenic machining. The improvement of the surface morphology was realized by increasing the surface quality and the microhardness within the workpiece surface layer. A sufficient surface hardening was promoted by providing high mechanical loads and low thermal loads during cutting. A temperature field simulation was developed to deepen the understanding of the thermal loads.

When cryogenically machining the metastable austenitic steel, a deformation-induced martensitic phase transformation could be utilized to increase the microhardness in superposition with the introduction of strain hardening mechanisms. By using an external CO₂ cooling, the lowest thermal loads were achieved during cutting. As a result, the highest amount of martensite was measured leading to a promoted increase of the microhardness in the workpiece surface layer. Increasing the mass flow of the CO₂ also reduced the thermal load and favored the martensitic phase transformation. The increased microhardness is likely to promote the application behavior, especially when regarding fatigue failure. These causal relations will be discussed within Chap. 11.

Choosing high feeds and low cutting speeds resulted in a favorable thermo-mechanical load promoting the martensitic phase transformation, further improving the surface hardening. Regarding the tool, chamfered cutting edges provided high mechanical loads due to high negative effective rake angles which were beneficial for the surface hardening. However, if the rake angle exceeded a critical value, the thermal load increased drastically which inhibited the martensitic phase transformation and therefore the optimization of the surface morphology. Furthermore, choosing high feeds and high chamfer angles resulted in a decrease of the surface quality. This led to a conflict of interest between a promoted surface hardening and a sufficient surface quality. As a consequence, a two-step turning process was developed which allowed an optimization of the surface morphology regarding the microhardness within the workpiece surface layer and the surface quality.

In addition to the application of conventional cryogenic cooling strategies, a novel sub-zero cooling approach was developed and applied when machining the difficult-to-cut titanium alloy Ti-6Al-4V. Regarding turning operations, the usage of a sub-zero MWF with a supply temperature of $T_{\text{supply}} = 243 \text{ K}$ offered the best cooling capacity due to a high heat transfer coefficient as well as favorable lubrication and wetting effects. As a result, the sub-zero cooling strategy outperformed the usage of cryogenic coolants and conventional MWF in terms of tool wear. Furthermore, a

beneficial chip generation was observed when applying a sub-zero cooling strategy during turning of Ti-6Al-4V.

Regarding milling, the application of a sub-zero cooling strategy also outperformed cryogenic coolants in terms of a better surface morphology and a longer tool life. As a result, the application of this novel sub-zero cooling approach offers a great potential for future applications, especially in terms of conditioning the surface morphology and the machining of difficult-to-cut materials.

References

1. Aurich JC, Mayer P, Kirsch B, Eifler D, Smaga M, Skorupski R (2014) Characterization of deformation induced surface hardening during cryogenic turning of AISI 347. *CIRP Ann* 63:1, 65–68. ISSN:00078506. <https://doi.org/10.1016/j.cirp.2014.03.079>
2. Jawahir IS, Brinksmeier E, M'Saoubi R, Aspinwall DK, Outeiro JC, Meyer D, Umbrello D, Jayal AD (2011) Surface integrity in material removal processes: recent advances. *CIRP Ann* 60, 2:603–626. ISSN: 00078506. <https://doi.org/10.1016/j.cirp.2011.05.002>
3. Brinksmeier E, Garbrecht M, Meyer D, Dong J (2008) Surface hardening by strain induced martensitic transformation. *Prod Eng* 2, 2:109–116. ISSN: 0944-6524. <https://doi.org/10.1007/s11740-007-0060-6>
4. Thielen S, Breuninger P, Hotz H, Burkhart C, Schollmayer T, Sauer B, Antonyuk S, Kirsch B, Aurich JC (2021) Improving the tribological properties of radial shaft seal countersurfaces using experimental micro peening and classical shot peening processes. *Tribol Int* 155:106764. ISSN: 0301679X. <https://doi.org/10.1016/j.triboint.2020.106764>
5. Venkatesh BD, Chen DL, Bhole SD (2009) Effect of heat treatment on mechanical properties of Ti-6Al-4V ELI alloy. *Mater Sci Eng: A* 506, 1–2:117–124. ISSN: 09215093. <https://doi.org/10.1016/j.msea.2008.11.018>
6. Rotella G, Umbrello D (2014) Finite element modeling of microstructural changes in dry and cryogenic cutting of Ti6Al4V alloy. *CIRP Ann* 63, 1:69-72. ISSN: 00078506. <https://doi.org/10.1016/j.cirp.2014.03.074>
7. Pu Z, Umbrello D, Dillon OW, Lu T, Puleo DA, Jawahir IS (2014) Finite element modeling of microstructural changes in dry and cryogenic machining of AZ31B magnesium alloy. *J Manuf Proc* 16, 2:335–343. ISSN: 15266125. <https://doi.org/10.1016/j.jmapro.2014.02.002>
8. Brinksmeier E, Garbrecht M, Meyer D (2008) Cold surface hardening. *CIRP Ann* 57, 1:541–544. ISSN: 00078506. <https://doi.org/10.1016/j.cirp.2008.03.100>
9. Jawahir IS, Attia H, Biermann D, Duflou J, Klocke F, Meyer D, Newman ST, Pusavec F, Putz M, Rech J, Schulze V, Umbrello D (2016) Cryogenic manufacturing processes. *CIRP Ann* 65, 2:713–736. ISSN: 00078506. <https://doi.org/10.1016/j.cirp.2016.06.007>
10. Novelli M, Fundenberger J-J, Bocher P, Grosdidier T (2016) On the effectiveness of surface severe plastic deformation by shot peening at cryogenic temperature. *Appl Surf Sci* 389:1169–1174. ISSN: 01694332. <https://doi.org/10.1016/j.apsusc.2016.08.009>
11. Caudill J, Huang B, Arvin C, Schoop J, Meyer K, Jawahir IS (2014) Enhancing the surface integrity of Ti-6Al-4V alloy through cryogenic burnishing. *Procedia CIRP* 13:243–248. ISSN: 22128271. <https://doi.org/10.1016/j.procir.2014.04.042>
12. Hotz H, Kirsch B, Becker S, Müller R, Aurich JC (2019) Combination of cold drawing and cryogenic turning for modifying surface morphology of metastable austenitic AISI 347 steel. *J Iron Steel Res Int* 26, 11:1188–1198. ISSN: 1006-706X. <https://doi.org/10.1007/s42243-019-00306-x>
13. Hotz H, Kirsch B, Mayer P, Becker S, von Harbou E, Boemke A, Skorupski R, Smaga M, Müller R, Beck T, Aurich CJ (2017) Surface integrity of cryogenic turned austenitic stainless steels AISI 347 and AISI 904L. In: *Production at the leading edge of technology—Proceedings*

- of the 7th congress of the German academic association for production technology (WGP), pp 473–480
14. Gutzeit K, Weber D, Basten S, Kirsch B, Aurich JC (2021) Improving the surface morphology by adjusting the cutting parameters during cryogenic milling of Ti-6Al-4V. In: Proceedings of the 21th machining innovations conference for aerospace industry, pp 24–31. <https://doi.org/10.2139/ssrn.3934248>
 15. Mayer P, Skorupski R, Smaga M, Eifler D, Aurich JC (2014) Deformation induced surface hardening when turning metastable austenitic steel AISI 347 with different cryogenic cooling strategies. In: Procedia CIRP 14:101–106. ISSN: 22128271. <https://doi.org/10.1016/j.procir.2014.03.097>
 16. Basten S, Kirsch B, Merz R, Kopnarski M, Hasse H, Aurich JC (2020) Adsorption and reaction layers when turning AISI 304 using various cooling strategies. Procedia CIRP 87:125–130. ISSN: 22128271. <https://doi.org/10.1016/j.procir.2020.02.100>
 17. Barber CR (1966) The sublimation temperature of carbon dioxide. Br. J Appl Phys 17, 3:391–397
 18. Gutzeit K, Hotz H, Kirsch B, Aurich JC (2020) Influence of nozzle position during cryogenic milling of Ti-6Al-4V. In: Production at the leading edge of technology—Proceedings of the 10th congress of the German academic association for production technology (WGP) 10:284–293. <https://doi.org/10.1007/978-3-662-62138-7>
 19. Hribersek M, Sajin V, Pusavec F, Rech J, Kopac J (2017) The procedure of solving the inverse problem for determining surface heat transfer coefficient between liquefied Nitrogen and Inconel 718 workpiece in cryogenic machining. In: Procedia CIRP 58:617–622. ISSN: 22128271. <https://doi.org/10.1016/j.procir.2017.03.227>
 20. Zhang X-R, Yamaguchi H (2011) An experimental study on heat transfer of CO₂ solid-gas two phase flow with dry ICE sublimation. Int J Therm Sci 50, 11:2228–2234. ISSN: 12900729. <https://doi.org/10.1016/j.ijthermalsci.2011.05.019>
 21. Ott J (1972) Solid-liquid phase equilibria in Water + Ethylene Glycol. J Chem Thermodyn 4, 1:123–126
 22. Basten S, Kirsch B, Hasse H, Aurich JC (2020) Formulation of sub-zero metalworking fluids for cutting processes: influence of additives. CIRP J Manuf Sci Technol 31:25–33. ISSN: 17555817. <https://doi.org/10.1016/j.cirpj.2020.09.006>
 23. Basten S, Kirsch B, Hasse H, Aurich CJ (2017) Neue kryogene Kühlstrategie für die Zerspanung. MM Maschinenmarkt 13:24–28
 24. Gutzeit K, Berndt M, Schulz J, Müller D, Kirsch B, von Harbou E, Aurich JC (2022) Optimization of the cooling strategy when applying a sub-zero metalworking fluid. Prod Eng. ISSN: 0944-6524
 25. Becker S, Hotz H, Kirsch B, Aurich JC, Harbou EV, Müller R (2018) A finite element approach to calculate temperatures arising during cryogenic turning of metastable austenitic steel AISI 347. J Manuf Sci Eng 140, 10. ISSN: 1087-1357. <https://doi.org/10.1115/1.4040778>
 26. Becker S, Mayer P, Kirsch B, Aurich JC, Harbou EV, Müller R (2016) Transient finite element simulation of the temperature field during cryogenic turning of metastable austenitic steel AISI 347. In: PAMM, vol 16, 1, pp 303–304. ISSN: 16177061. <https://doi.org/10.1002/pamm.201610140>
 27. Hotz H, Kirsch B, Aurich JC (2021) Impact of the thermomechanical load on subsurface phase transformations during cryogenic turning of metastable austenitic steels. J Intell Manuf 32, 3:877–894. ISSN: 0956-5515. <https://doi.org/10.1007/s10845-020-01626-6>
 28. Zhang W, Wang X, Hu Y, Wang S (2018) Predictive modelling of microstructure changes, micro-hardness and residual stress in machining of 304 austenitic stainless steel. Int J Mach Tools Manuf 130–131:36–48. ISSN: 08906955. <https://doi.org/10.1016/j.ijmachtools.2018.03.008>
 29. Kirsch B, Hotz H, Müller R, Becker S, Boemke A, Smaga M, Beck T, Aurich JC (2019) Generation of deformation-induced martensite when cryogenic turning various batches of the metastable austenitic steel AISI 347. Prod Eng 13, 3–4:343–350. ISSN: 0944-6524. <https://doi.org/10.1007/s11740-018-00873-0>

30. Mayer P, Kirsch B, Aurich JC (2014) Investigations on cryogenic turning to achieve surface hardening of metastable austenitic steel AISI 347. *Adv Mater Res* 1018:153–160. <https://doi.org/10.4028/www.scientific.net/AMR.1018.153>
31. Wayman CM, Bhadeshia HKDH (1996) Phase transformations, nondiffusive. *Phys Metall* 4:1507–1554
32. Mayer P, Kirsch B, Müller C, Hotz H, Müller R, Becker S, von Harbou E, Skorupski R, Boemke A, Smaga M, Eifler D, Beck T, Aurich JC (2018) Deformation induced hardening when cryogenic turning. *CIRP J Manuf Sci Technol* 23:6–19. ISSN: 17555817. <https://doi.org/10.1016/j.cirpj.2018.10.003>
33. Eichelmann GC, Hull TC (1953) The effect of composition on the temperature of spontaneous transformation of austenite to martensite in 18–8 type stainless steel. *Trans Am Soc Metals* 45:165–174
34. Gutzeit K, Basten S, Kirsch B, Aurich CJ (2021) Cryogenic milling of metastable austenitic stainless steel AISI 347. *MM Sci J* 5:4962–4969
35. Hotz H, Kirsch B (2020) Influence of tool properties on thermomechanical load and surface morphology when cryogenically turning metastable austenitic steel AISI 347. *J Manuf Proc* 52:120–131. ISSN: 15266125. <https://doi.org/10.1016/j.jmappro.2020.01.043>
36. Hotz H, Kirsch B, Aurich JC (2020) Estimation of process forces when turning with varying chamfer angles at different feed rates. *Procedia CIRP* 88:300–305. ISSN: 22128271. <https://doi.org/10.1016/j.procir.2020.05.052>
37. Denkena B, Biermann D (2014) Cutting edge geometries. *CIRP Ann* 63, 2:631–653. ISSN: 00078506. <https://doi.org/10.1016/j.cirp.2014.05.009>
38. Hotz H, Kirsch, Becker S, von Harbou E, Müller R, Aurich JC (2018) Improving the surface morphology of metastable austenitic steel AISI 347 in a two-step turning process. *Procedia CIRP* 71:160–165. ISSN: 22128271. <https://doi.org/10.1016/j.procir.2018.05.090>
39. Hotz H, Smaga M, Kirsch B, Zhu T, Beck T, Aurich JC (2020) Characterization of the subsurface properties of metastable austenitic stainless steel AISI 347 manufactured in a two-step turning process. *Procedia CIRP* 87:35–40. ISSN: 22128271. <https://doi.org/10.1016/j.procir.2020.02.012>
40. Leyens C, Peters M (2010) Titanium and titanium alloys: fundamentals and applications. Weinheim and Chichester: Wiley-VCH. ISBN: 9783527305346
41. Cotterell M, Byrne G (2008) Dynamics of chip formation during orthogonal cutting of titanium alloy Ti-6Al-4V. *CIRP Ann* 57, 1:93–96. ISSN: 00078506. <https://doi.org/10.1016/j.cirp.2008.03.007>
42. Wyen C-F, Wegener K (2010) Influence of cutting edge radius on cutting forces in machining titanium. *CIRP Ann* 59, 1:93–96. ISSN: 00078506. <https://doi.org/10.1016/j.cirp.2010.03.056>
43. Chowdhury M, Chowdhury S, Yamamoto K, Beake BD, Bose B, Elfizy A, Cavelli D, Dosbaeva G, Aramesh M, Fox-Rabinovich GS, Veldhuis SC (2017) Wear behaviour of coated carbide tools during machining of Ti6Al4V aerospace alloy associated with strong built up edge formation. *Surf Coat Technol* 313:319–327. ISSN: 02578972. <https://doi.org/10.1016/j.surfcoat.2017.01.115>
44. Kirsch B, Basten S, Hasse H, Aurich JC (2018) Sub-zero cooling: a novel strategy for high performance cutting. *CIRP Ann* 67, 1:95–98. ISSN: 00078506. <https://doi.org/10.1016/j.cirp.2018.04.060>
45. Basten S, Kirsch B, Gutzeit K, Hasse H, Aurich JC (2020) Influence of the supplying technique of a sub-zero metalworking fluid on the performance of face turning of Ti-6Al-4V titanium alloy. *SSRN Electron J*. <https://doi.org/10.2139/ssrn.3724124>
46. Gutzeit K, Bulun G, Stelzer G, Kirsch B, Seewig J, Aurich JC (2022) Investigation of the surface integrity when cryogenic milling of Ti-6Al-4V using a sub-zero metalworking fluid. *Procedia CIRP* 108:25–30. ISSN: 22128271. <https://doi.org/10.1016/j.procir.2022.03.010>
47. Gutzeit K, Müller D, Kirsch B, Aurich CJ (2022) Influence of the cutting edge radius on tool wear during cryogenic machining with cemented carbide end mills. In: Proceedings of the 20th plansee seminar: international conference on refractory metals and hard materials, pp 1–12

Creating Surface Morphologies by Cold Spraying



Sergiy Antonyuk, Mustafa Bozoglu, and Siegfried Ripperger

Abstract This chapter presents the method for the microstructuring of component surfaces by the cold spray process with fine particles. Depending on the process parameters the collision phenomena of particles with the substrate surface by this method can lead to different surface morphologies. The focus of this work is on the investigation of the manufacturing–morphology–property relationship. The mechanisms of cold spraying are explained and the investigated surfaces are discussed in detail. From CFD simulations, the velocities and temperatures of the particle before collision were obtained from the overall velocity and temperature of the gas stream. The impact phenomena were studied by FEM simulations. The microstructured surfaces were used for applications like biofilm growth or friction improvements.

1 Introduction

Cold spraying is a well-known thermal spraying method to create coatings for different applications or to repair damaged equipment surfaces of apparatuses. The principle of this process is based on the acceleration of fine particles in gas within a Laval nozzle to supersonic velocities as can be seen in (Fig. 1a). The gas-particle stream is directed onto the surface to cause impact of particles. A strong plastic deformation, mechanical interlocking, and bonding of particle will occur if the particle collision velocity reaches a critical value, which depends on the deformation behavior and temperatures of contact partners (particle and surface) as can be seen in Fig. 1b.

The most common particle feedstock materials used in cold spraying are copper and aluminum [1, 2]. Such soft metals are easy to handle in cold spraying because they can undergo plastic deformation even at lower collision energies and temperatures. Stainless steel or harder particles can be used as well but, because of a high yield strength, they need a higher kinetic energy to create a dense coating [3]. The name cold spraying is derived from the fact that the process temperature is below the

S. Antonyuk (✉) · M. Bozoglu · S. Ripperger
Institute of Particle Process Engineering, RPTU Kaiserslautern, Kaiserslautern, Germany
e-mail: sergiy.antonyuk@mv.rptu.de

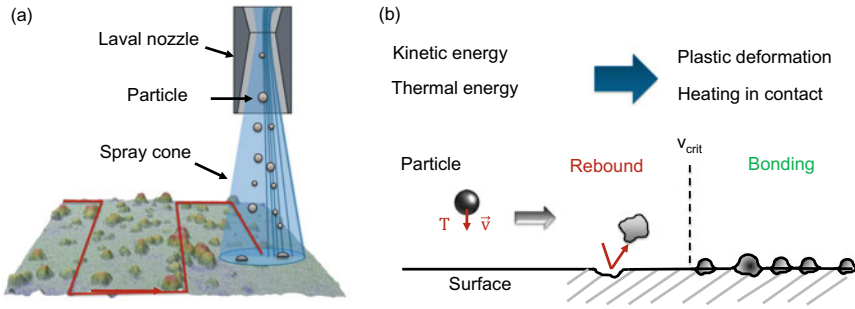


Fig. 1 **a** Scheme of cold spraying and **b** principle of surface morphology creation

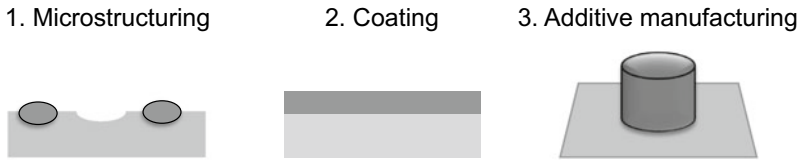


Fig. 2 Possible surfaces created by cold spraying

melting temperature of the materials. Therefore, particles as well as the substrate remain in solid state. Due to the use of an inert carrier gas, no chemical changes in the particle and substrate materials occur. This is especially necessary to prevent oxidization. Due to these advantages, the cold spraying method is well established in the aerospace and automotive industry. In this work, the cold spray method is especially adapted for the microstructuring of surfaces. During conventional use of cold spraying for coating and additive manufacturing (Fig. 2), the particle impact velocity is about 1.5–2 times higher than the critical velocity for particle bonding. Here, the aim is to achieve dense structures with low porosities, good adhesion, and high deposition efficiencies. In contrast to this, the process parameters for surface microstructuring are set to reach a particle impact velocity which is lower or slightly larger than the critical velocity. The collisions of the particles result corresponding to these conditions in the rebounds and formation of a surface microstructure with craters or in bonding of partially deformed particles which create a hill-like surface microstructure.

The understanding of the collision and bonding mechanisms is a key essential for the optimization process. Although intensive research has been conducted in the field of cold spraying since the 1990s, the particle bonding mechanisms have not been fully described. The main reason for this issue is the high particle velocity in the gas stream accelerated by the Laval nozzle [4]. The particle deformation during impact on the substrate occurs very quickly up to 100 ns. The bigger the particle size the higher the time for penetration. *Aleksieieva et al.* showed that particles with a size of 2 μm tend to penetrate into the substrate in 2.1 ns, while 50 μm need 56 ns [5]. The most important mechanisms identified in the last decades from experimental and

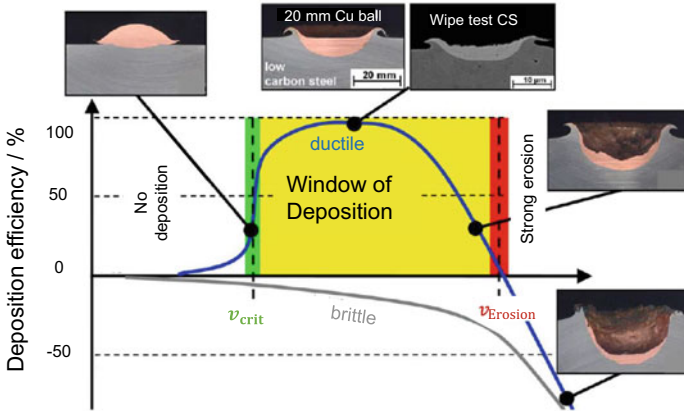


Fig. 3 Window of deposition in cold spraying [2]

numerical studies are mechanical interlocking, adiabatic shear instability (ASI) and localized melting [1, 6, 7]. Depending on the process parameters, the material (e.g., metal, oxides, etc.) and particle size one of the mechanisms may be more dominant. For example, for oxides mechanical interlocking may be the main mechanism while for metal and alloys ASI is assumed to result in a bonding between particle and substrate. However, recent investigations performed by Hassani-Gangaraj et al. [8] and Dowding et al. [9] question the adoption of ASI. From real-time observations of single particle impacts of copper and aluminum they showed that bonding is caused by high hydrodynamic stress that exceeds the flow strength of the material. A generalized parameter window for successful bonding during cold spraying was developed by Schmidt et al. which is shown in Fig. 3 [2]. It describes the deposition efficiency depending on the particle impact velocity. The critical impact velocity is the minimal impact velocity to reach a deposition efficiency of 50%.

Therefore, it determines the lower range of the deposition window. At smaller impact velocities the particles will rebound from the surface. In further studies of Schmidt [10] it was shown that the optimum coating can be achieved if the ratio of the impact velocity to the critical velocity is around 1.5. At the ratios higher than 2, erosion of the surface is observed. These observations were only valid for ductile materials because this material group showed good deformation behavior to fully bond on the surface. Therefore, many investigations were mainly limited to particle–substrate combination with soft metals like copper and aluminum. With the development of the high-pressure cold spraying, it was possible to coat harder materials such as titanium and steel with high deposition efficiencies [3, 11]. The critical velocity is given by the equation according to Schmidt et al. [12]:

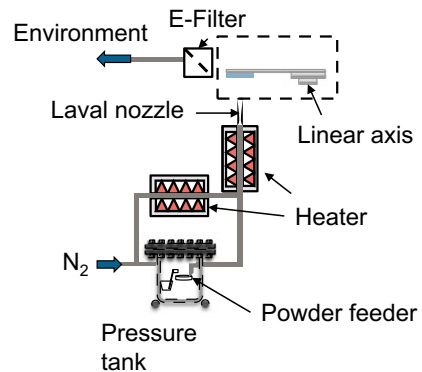
$$v_{crit} = \sqrt{F_1 \cdot \frac{4}{\rho} \cdot \sigma_{TS} \cdot \left(1 - \frac{T_{imp} - T_{ref}}{T_{mel} - T_{ref}}\right) + F_2 \cdot c_p \cdot (T_{mel} - T_{imp})} \quad (1)$$

Here, c_p is the specific heat capacity, ρ is the particle density, σ_{TS} is the tensile strength, and F_1 and F_2 are empirical coefficients. T_{ref} , T_{mel} , and T_{imp} are the reference (20°C), impact and melting temperatures, respectively. Equation (1) takes the plastic deformation and the heat dissipation during the impact into account. The main disadvantage of this equation, however, is that it can only be applied when the particle and substrate material are identical and the temperature is the same. At the time when *Schmidt et al.* developed the diagram, it was believed that brittle materials can not adhere due to the fracture behavior during impact. In recent research, it was shown that they can bond on the surface like TiO_2 [13]. Even if there are some empirical equations to estimate the critical velocity, they do not show a high accuracy which leads to further investigations in this field.

2 Experimental Setup for Cold Spraying for Microstructuring of Component Surfaces

The experimental setup developed for the microstructuring process is shown in Fig. 4. The carrier gas is nitrogen (Air Liquide, 99.8%) that can be pressurized up to 0.9 MPa. The main flow stream is divided in two, where one is pre-heated in a tube furnace while the second stream is loaded with the powder by a powder disperser (Topas SAG 409, Topas, Germany), adapted to work under pressure conditions. The dosage rate can be set up to 12 g/h. Both gas streams are mixed again in the mixing/heating chamber and are heated up to nozzle temperatures of 500°C. The Laval nozzle is fixed below the component surface. This configuration allows the successful structuring of the sample with fine particles because clogging of the nozzle is avoided. As can be seen from Fig. 4, for microstructuring of the component surface the substrate is mounted on an XY linear stage. The linear stage is used to set the speed and line distance. The speed can be varied up to 10 mm/s, and the line distance can be set in a range from 50 to 1000 μm . The structuring is performed by moving the substrate

Fig. 4 Cold spray setup for microstructuring of component surfaces [14]



in a grid pattern over the nozzle orifice at the predetermined speed and line distance. The stand-off distance is set up to 5 mm and can be changed by a linear axes that is height adjustable.

Titanium (grade 2) and 316Ti stainless steel samples were used as substrates for cold spraying experiments with a maximum size of $30 \times 30 \text{ mm}^2$ and a thickness of 2 mm. The samples were polished in three steps with diamond paste in the grain size of 6, 3, and $1 \text{ }\mu\text{m}$. After polishing, they were subsequently cleaned with isopropanol in an ultrasonic bath for 10 min. As particle feedstock material, titanium (grade) and stainless steel (316L) were used. For the investigations of titanium, square-edged particles (Alfa Aesar by Fisher Scientific, Karlsruhe, Germany; -325 mesh, 99.5% metals basis) and spherical particles (ECKART TLS GmbH, grade 2) were used. Both particle systems had a median size of around $d_{50,3} = 15 \text{ }\mu\text{m}$ and a particle size range of $4\text{--}39 \text{ }\mu\text{m}$. The 316L particle system was produced by Goodfellow (Hamburg, Germany). They had a mean diameter of $3.1 \text{ }\mu\text{m}$, while all present sizes were in the range from 1 to $10 \text{ }\mu\text{m}$ [14]. The particle distributions of the powder systems were obtained by a laser diffraction spectroscopy (Horiba LA-950, Retsch, Haan, Germany).

3 Particle Acceleration and Heating in Supersonic Flow

The microstructuring process is influenced mainly by the gas properties (temperature, pressure), particle properties (size, density, hardness), and nozzle geometry (shape, length). The main component in the self-developed cold spray setup is a specially designed nozzle. The shape of the nozzle and its length was designed especially for particles with sizes in the range of $1\text{--}10 \text{ }\mu\text{m}$ [15–17]. The overall length from inlet to outlet of the nozzle is 30 mm, while the converged part having a length of 4.5 mm (Fig. 5). The diameters of the inlet, minimum diameter, and outlet diameter are 8 mm, 0.8 mm, and 1.5 mm, respectively. The expansion ratio for the nozzle is 3.58 and allows to reach a Mach number up to 2.4. For the description of particle deposition, the distributions of velocities and temperatures of particles before colli-

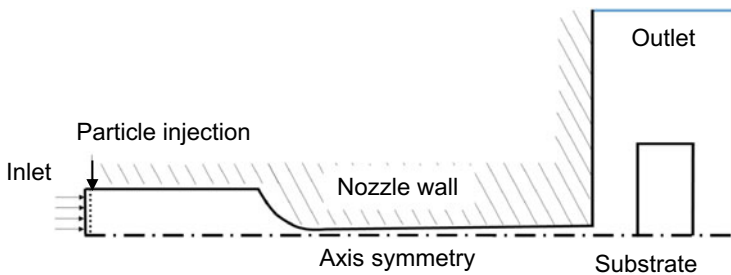


Fig. 5 2D model for CFD simulations [20]

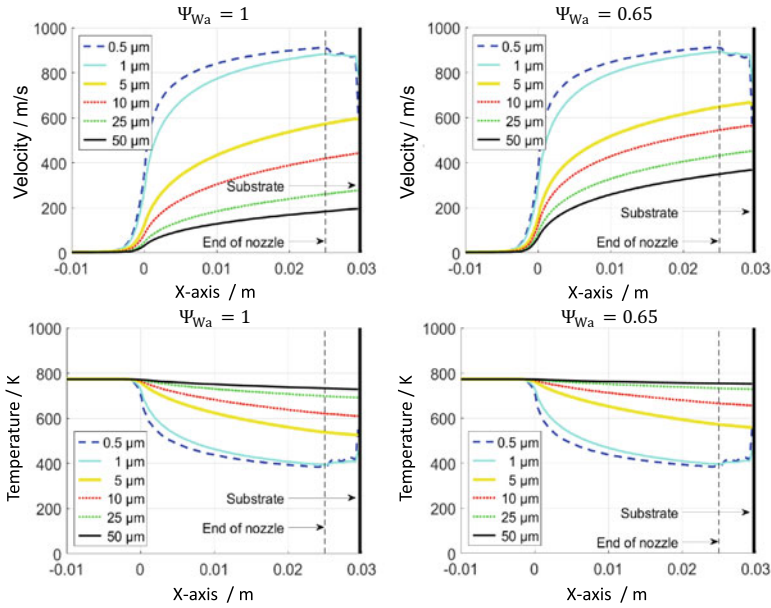


Fig. 6 Velocity and temperature of titanium particles with different sizes within the nozzle and jet obtained by CFD simulation [22]. Simulations are performed at a nozzle inlet temperature of 500 °C and an inlet pressure of 9 bar

sion are needed. These parameters can be predicted by the numerical simulation of the flow and particle movement with Computational Fluid Dynamics (CFD) using Lagrangian approach. A one-way coupling was applied and the drag force is estimated according to Morsi and Alexander [18]. The $k-\omega$ SST turbulence model was used in the performed simulation. To simplify the system, simulations are performed in steady state and the geometry is defined as axis-symmetric. At the nozzle inlet, the temperature and pressure conditions are defined and varied. The outlet boundary conditions are equal to the ambient environment. Nitrogen is assumed to be an ideal gas and the fluid viscosity was calculated according to the model of Sutherland [19].

Figure 6 shows the obtained velocities of titanium particles during the movement in the nozzle and the jet. The size and shape of the particles were varied. The influence of the particle shape on the drag force is described by sphericity factor ψ_{Wa} according to Wadell, which is defined as the ratio of the surface area of an ideal sphere with the same volume of the real particle as the real particle surface [21]. Due to the higher inertia, the bigger particles have lower acceleration and impact velocities. For small particles, the velocity firstly increases but it decreases strongly when approaching to the surface in the stagnation region. In comparison to the spherical particles, the irregular shaped particles ($\psi_{Wa} = 0.65$) reach higher velocities, which is particularly significant for the particle sizes larger than 5 μm . This is a result of the higher drag forces on irregular shaped particles. The temperature of particles with sizes bigger

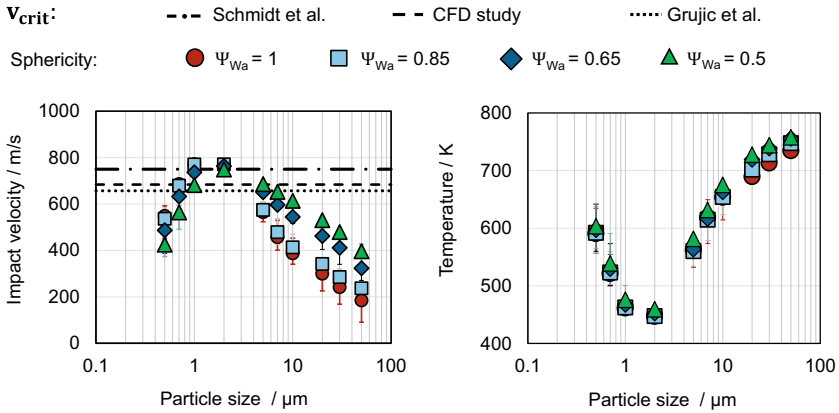


Fig. 7 Impact velocities and temperatures of titanium particles obtained by CFD simulations at a nozzle inlet pressure of 9 bar, an inlet gas temperature of 500 °C and a stand-off distance of 5 mm [22]. Dotted lines indicate the calculated critical velocity

than 1 μm decreases from the nozzle to the substrate surface. Particles equal to 1 μm or lower show a significant decrease of temperature as well in the gas stream at the nozzle outlet but temperature increases at the substrate surface again. This is a result of the stagnation zone where the gas velocity drops while its temperature increases. The small particles tend to adopt the gas temperature due to a high surface-to-volume ratio that improves heat transfer. Therefore, particles with sizes of 0.5 and 1 μm have the same temperature as the gas flow and the particle temperature decreases within the nozzle and the outlet, while it increases at the surface. For irregular-shaped particles, the temperature is slightly higher than the spherical particles because of the improved heat transfer at the higher velocity.

In Fig. 7, the impact velocities depending on the particle size with different shape factors are compared. The dotted lines show critical velocity calculated according to the models of Schmidt et al. [12] (Eq. (1)) and Grujic et al. [23]. Impact velocities below these dotted lines will result in particle rebound on the surface, while impact velocities equal or higher will lead to bonding at the surface. It can be seen that particle sizes in the range of 0.7–2 μm (spherical) and 0.8–5 μm (sphericities of 0.5 and 0.65) can bond successfully on the surface. Smaller and bigger particles will result in rebound and therefore to surfaces with microcrater. Bonded particles will create a valley-like surface.

Next to titanium, cold spraying of stainless steel particles on a stainless steel substrates was investigated. Figure 8 shows the trajectories of particles with the size of 1 and 3 μm, which were simulated for four different start positions at the nozzle inlet. The collision velocity of the smaller particles is much higher compared to 3 μm particles. Smaller particles tend to follow the gas stream compared to bigger particles. As a result, smaller particles are focused in the core of the stream leading to

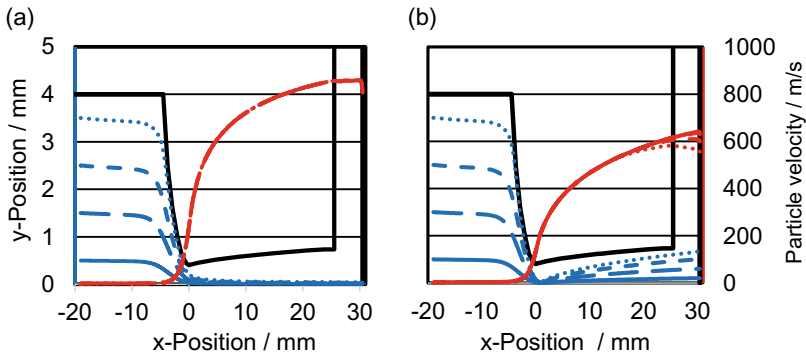


Fig. 8 Particle trajectories and local velocities of stainless spherical steel particles with sizes of 1 μm (a) and 3 μm (b) for different starting position in the inlet cross section. CFD simulation at a nozzle inlet pressure of 9 bar, an inlet gas temperature of 500 $^{\circ}\text{C}$ and a stand-off distance of 5 mm [14]

a focused particle stream that impacts the substrate. The highest velocity is 800 m/s which is above the critical velocity according to the model of Schmidt et al. [12].

For the 3 μm the higher inertia leads to lower particle velocities. Here, the highest collision velocity is 650 m/s. Next to this, particles no longer follow the core flow but start to spread at the divergent part of the nozzle. The jet that hits the sample surface thus becomes wider. The width of this jet in the substrate area is 1.3 mm. In this case, the starting position of particles affects significantly the resulting collision velocity. The farther the particles start from the center of the nozzle, the lower its impact velocity. Figure 9 deviation bars show the range of minimum and maximum impact velocities for each particle size obtained by varying the initial position in the radial direction in the nozzle inlet. The nozzle temperature was set to 400 $^{\circ}\text{C}$ and 500 $^{\circ}\text{C}$ and the pressure to 9 bar. The dashed lines indicate the calculated critical velocity according to Eq. (1), which includes the particle impact temperature as a function of particle size.

Particles with a size near to 1 μm have the highest impact velocities and the lowest scattering. For larger particle sizes, the impact velocity quickly decreases again. The trend of both curves is identical with the difference that for an inlet temperature of 400 $^{\circ}\text{C}$, smaller particle velocities and temperatures are obtained during impact. For particle sizes below 1 μm , the stainless steel particles show higher impact velocities of 10–90 m/s as compared to titanium. This is due to the fact that the stainless steel particles have a higher inertia which leads to a lower deceleration. If the stainless steel particles are bigger than 1 μm than the impact velocity is lower compared to titanium due to slower acceleration along the nozzle exit. The difference can be up to 50 m/s. The temperature differs as well which can be attributed to the impact velocity and the heat capacity of the particle material. Due to the different inertia, the position of impact can be influenced as well. The particle impact velocity and temperature

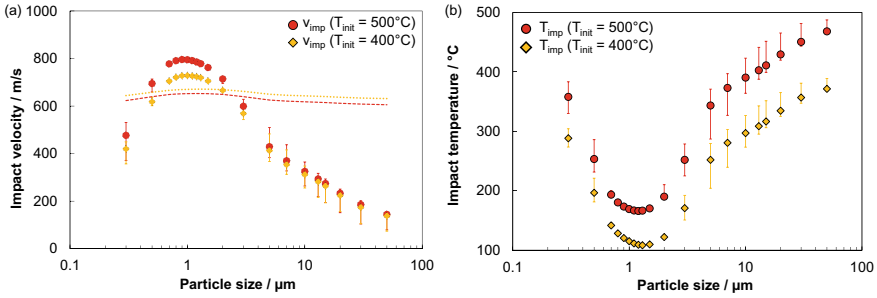
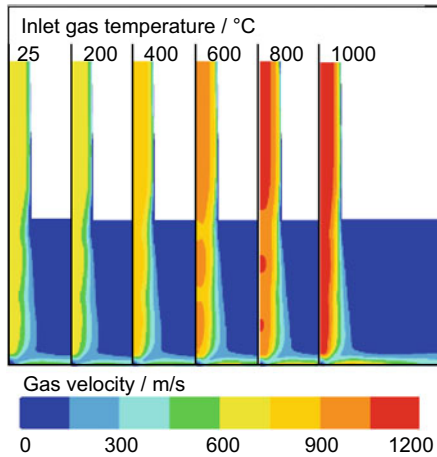


Fig. 9 Averaged particle velocities (a) and temperatures (b) of stainless steel particles obtained with CFD simulation at a nozzle inlet pressure of 9 bar, an inlet gas temperature of 500 °C and a stand-off distance of 5 mm [14]

Fig. 10 Influence of the nozzle inlet temperature on the gas velocity at an inlet pressure of 9 bar and a stand-off distance of 5 mm [20]



can be increased in cold spraying with the increase of the process temperature. The gas velocities obtained in a case CFD study by the variation of gas inlet temperature in a range of 25–1000 °C are shown in Fig. 10. The process pressure in the inlet is set to 9 bar for each case. The higher the gas temperature the higher the gas velocity will be.

The influence of the gas temperature on the simulated impact velocities and temperatures for stainless steel particles can be observed from Fig. 11. In general, with increasing gas velocity and temperature the impact velocity and temperature of particles increase. For particles with sizes of 0.5 and 1 μm, an increase in gas temperature of 100 °C will lead to an increase of the impact velocity of 50 m/s.

Particles bigger than 5 μm show only a slight increase of about 80 m/s in the entire temperature range. Particle sizes of 25 μm show a neglectable increase in impact velocity. The impact temperature increases strongly with the increase of gas temperature for particle sizes from 5 to 25 μm. Smaller particles show an increase as

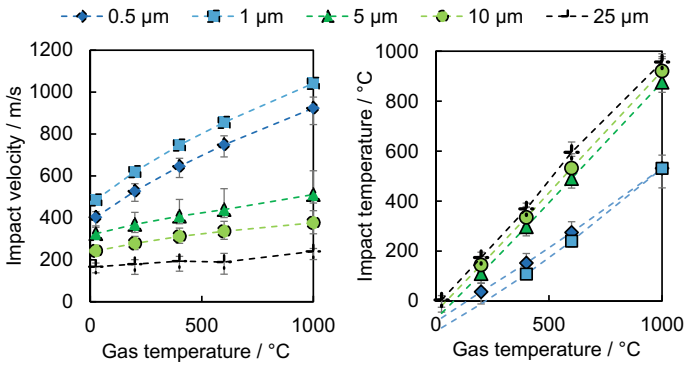


Fig. 11 **a** Impact velocity and **b** temperature of 316L particles depending on the gas temperature in the inlet of the nozzle at an inlet pressure of 9 bar [20]

well in impact temperature but with a smaller slope compared to the bigger particles. However, the higher temperature of big particles is a result of delayed heat exchange due to the smaller specific area. If the particle velocity is high enough, an increase in the gas temperature always leads to increased deposition rates due to the higher impact velocity and the temperatures of the particles and the surface. With the increase of velocity, the necessary kinetic energy is reached to allow bonding on the surface. The high-temperature results in the softening of the material and increasing plastic deformation. In addition to the temperature, the gas pressure is the second parameter of the flow that can be varied in cold spray process. The expansion of the gas in the nozzle (Fig. 12a) results in a pressure minimum before the pressure builds up again in front of the substrate surface in a stagnation area. Slight pressure fluctuations occur which are dependent on process parameters like temperature and the type of the carrier gas. However, they have no significant influence on the particle impact velocity. A variation of the inlet pressure from 0.4 to 1.2 MPa at constant inlet temperature leads to a shift of the position and even to a change in the number of these areas. An increase in the inlet pressure also leads to an increase in the width of the spray area. As a result, the increase of particle velocity with the increase of the pressure will be slower after 5 bar and the particle impact velocity remains constant.

The influence of the pressure on the particle impact velocity is shown in Fig. 12b. Due to the increase of gas velocity, there is an increase of the particle velocity as well. The inlet gas temperature was constant at 500 °C for all simulated pressures. It can be seen that the impact temperature is decreasing with an increase in the pressure due to enhanced heat convection. Another important process parameter is the stand-off distance. The influence of the stand-off distance on the gas velocity is shown in Fig. 13. After leaving the nozzle, the jet with a high gas velocity has a length of 10 mm until it slows down. At shorter working distances, the jet is compressed and widens. The particles can be accelerated by a smaller working distance in a slightly wider spray cone. Due to the compression, a very sharp boundary between supersonic and subsonic velocity is created up to a working distance of 5 mm. Since this boundary is

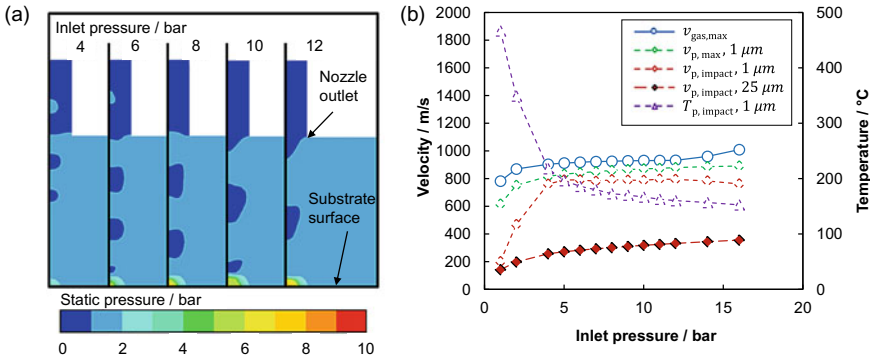
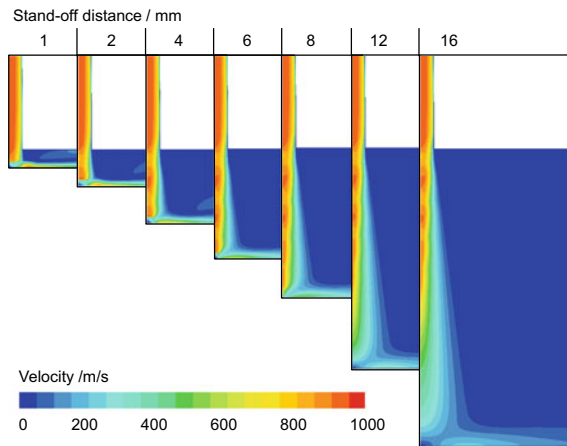


Fig. 12 a Static pressure distribution in the jet area depending on the inlet pressure and b gas velocity and particle velocity and temperature influenced by the gas pressure [20]

Fig. 13 Gas velocity influenced by stand-off distance at an nozzle inlet temperature of 500 °C and an inlet pressure of 9 bar [20]



created parallel to the substrate surface, all particles passing through this boundary are decelerated equally.

Comparing the surface temperature depending on the stand-off distance (Fig. 14) it can be seen that at small working distances the heat cannot dissipate. A high amount of kinetic energy of the gas is converted into heat that increases the substrate temperature.

The resulting impact velocity and temperature show for distances between 1 and 8 mm the change is not significant. At larger working distances, the maximum particle velocity decreases progressively, with the maximum impact velocity shifting towards slightly larger particles (Fig. 15). In general, the impact temperature reacts less sensitively to an increase in the working distance beyond 8 mm. Only at working distances above 10 mm a significant change in the impact conditions occurs. As shown in Fig. 15 smaller distances lead to lower heat dissipation and therefore cause a higher surface substrate temperature. This favors plastic deformation and also par-

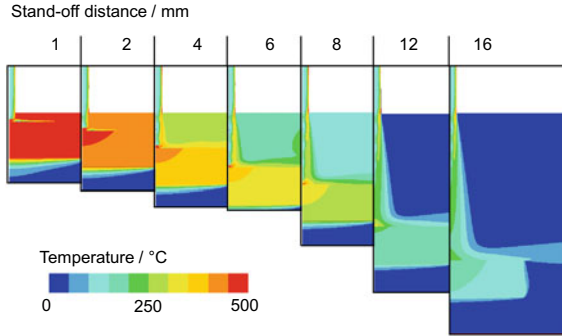


Fig. 14 Surface temperature depending on the stand-off distance at a nozzle inlet temperature of 500 °C and an inlet pressure of 9 bar [20]

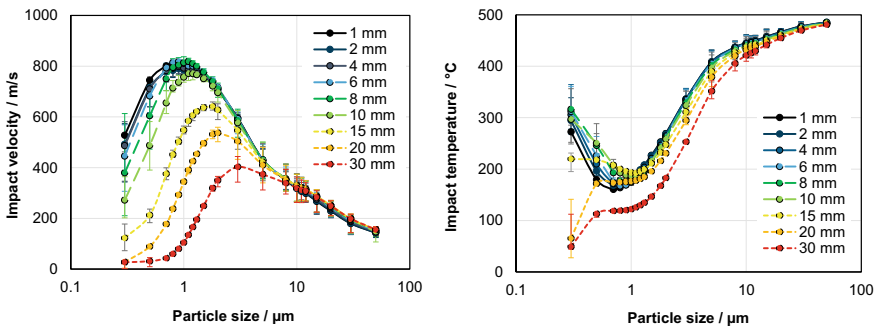


Fig. 15 Impact velocity and temperature influenced by stand-off distance at a nozzle inlet temperature of 500 °C and an inlet pressure of 9 bar [20]

ticle adhesion. Thus, a working distance smaller than 8 mm for all particle sizes is to be aimed for. This is consistent with experimental observations, which have shown that spray quality decreases at larger distances.

4 Particle Impact Simulation

An important aspect of cold spraying is the mechanical property of the materials. Particles have different sizes, forms, and structures (pores, roughness) that can affect the stiffness and yield strength. Figure 16 shows the experimentally derived Young’s modulus of stainless steel particles (316L) according to the Hertzian law [24, 25]. Here, a nanoindentation device equipped with a flat punch indenter was used. The dashed lines are limit values for bulk stainless steel [26].

It can be seen that the results are in good agreement with the bulk material but some show higher or lower values. The particles investigated were produced by gas

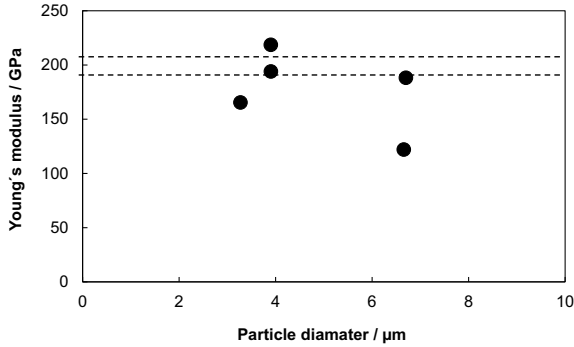


Fig. 16 Young’s modulus of spherical stainless steel (316L) particles obtained by nanoindentation measurement

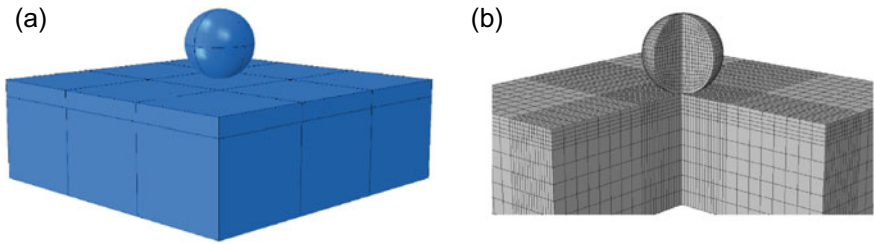


Fig. 17 **a** 3D model for simulation of particle impact and **b** sliced model with mesh refinement in the contact area [20]

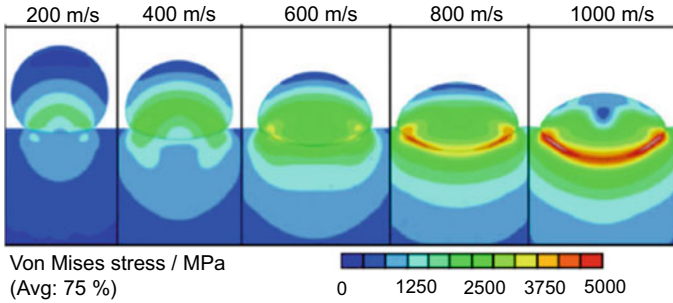
atomization of melted alloys. This process can lead to porosity within the particles or other alloy phases that can affect the mechanical properties [27]. Therefore, it is important to investigate particle feedstock material because the production process may affect the product properties. To predict the conditions for particle bonding and the morphology of microstructured component surfaces, it is necessary to simulate the deformation behavior during the impact. Therefore, an FEM simulation can be performed. In the beginning of the collision simulation, a particle is placed upon the substrate. The particle impact velocity is set as an initial boundary condition to study its effect. The three-dimensional model of a spherical particle and the substrate in this study is shown in Fig. 17.

Due to the fact that in cold spraying high temperatures and strain rates occur during the impact, the flow stress is well predictable with the model according to Johnson and Cook (JC) [28]:

$$\bar{\sigma} = \left(A + B (\bar{\epsilon}^{pl})^n \right) \cdot \left[1 + C \ln \left(\frac{\dot{\bar{\epsilon}}^{pl}}{\bar{\epsilon}_0^{pl}} \right) \right] \cdot \left(1 - \left(\frac{T - T_r}{T_m - T_r} \right)^m \right) \quad (2)$$

Table 1 Parameter sets for impact simulation of steel (1.4404) [29]

Set	A/MPa	B/MPa	C/–	n/–	m/–	$\dot{\epsilon}_0/s^{-1}$
M1	305	1161	0.01	0.61	0.517	1
M2	305	441	0.057	0.1	1.041	1
M3	301	1472	0.09	0.807	0.623	0.001
M4	280	1750	0.1	0.8	0.85	200
M5	514	514	0.042	0.508	0.533	0.001

**Fig. 18** Deformation and von Mises stresses during impact of a 2 μm 316L stainless steel particle with M4 parameter set (Table 1) with an impact velocity between 200 and 1000 m/s at 1.9 ns seconds after initial contact [20]

Here, A is the quasi-steady-state yield stress, B is the power law pre-exponential factor, C is the strain rate pre-exponential factor, n describes the strain hardening exponent, and m is the thermal softening exponent. T is the actual temperature, T_m is the melting temperature, and T_r is the reference temperature. For a given material, the parameters can be derived from experimental investigations with the Split-Hopkins Pressure Bar (SPHB), nanoindentation or an inverse FEM analysis [29–31]. The impact process and the resulting stresses depend strongly on the kinetic energy of the particles. In Fig. 18, the impact of the 2 μm particles is shown for different impact velocities derived from the material properties M4 according to Umbrello et al. [29].

For an impact velocity of less than 600 m/s, only very small stresses occur in the contact zone. A higher velocity of 800 m/s results in von Mises stresses of 5 GPa. It occurs in an annular contact region that spreads toward the edge and south pole of the particle as the impact velocity increases. The shape of the particle changes drastically with increasing velocity. At low velocity, the spherical shape is clearly preserved; as the velocity increases, the particle shape changes from a hemispherical shape to a very flat dome shape. Due to the combination of penetration and shear loading, the highest internal stresses in an annular ring occur in the contact zone.

The simulation results are in agreement with the theoretical considerations and experimental observations of [11, 32]. In cold spraying experiments, it was shown that impact velocities at 600 m/s are below the critical impact velocity and will lead to a crater on the surface [14]. To investigate the influence of the JC material parameters,

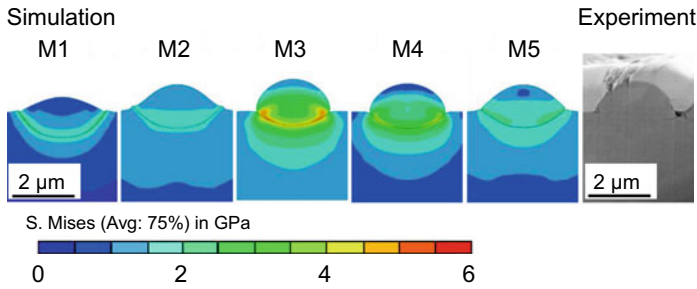


Fig. 19 Particle impact of a 2 μm stainless steel particle with different JC constants with an impact velocity of 800 m/s [20]

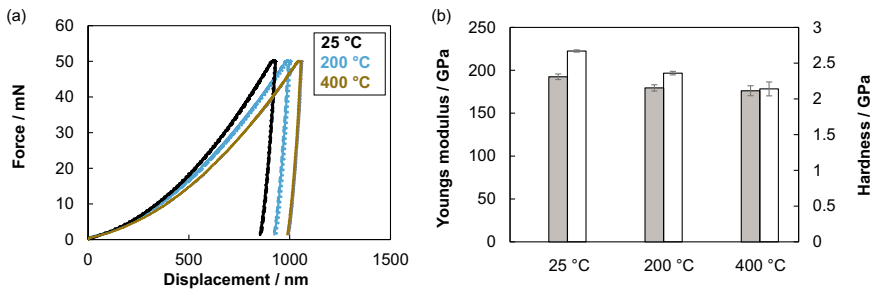


Fig. 20 Results of **a** force–displacement curves and **b** Young’s modulus (gray bar) and hardness (white bar) obtained by nanoindentation of 316Ti substrate at elevated temperatures

a set of different constants were investigated. The parameter sets are derived from analytical and experimental methodology. The numerical results are compared with the cross section of a deposited particle from cold spraying experiments as can be seen in Fig. 19. The shape of the particles shows that the deformation on the upper side is most likely represented by the material constants M3 and M4, while the deformation in the area of the jet is similar to the calculation result with M2 or M5. However, it must be taken into account that deviations arise in the experiment due to the significant flattening of the particles on the bottom.

To obtain the mechanical properties of 316Ti substrate under the experimental conditions, nanoindentation experiments (TI Premier, Hysitron) with a diamond Berkovich tip were performed. The results are shown in Fig. 20. Here, a high-temperature stage was used to set the temperature of the sample in a range from room temperature to 400 °C.

With higher temperatures the force–displacement curves are shifted to the right and show a higher penetration depth of the indenter. The derived Young’s modulus and hardness decrease with an increase in temperature which is a result of thermal softening. These results are in agreement with the literature data of stainless steel bulk materials [33]. From the conducted nanoindentation experiments, it is possible to obtain JC parameters by using the method according to Dao et al. [31]. Here,

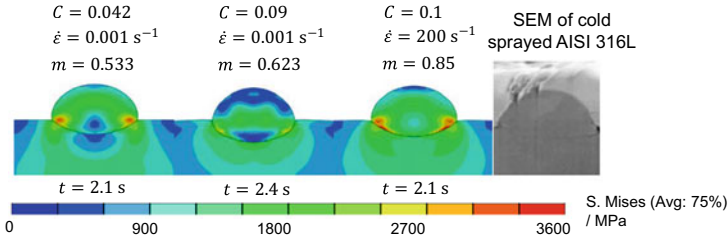


Fig. 21 FEM simulation of particle impact with different JC parameters compared with the performed experiment of a cold sprayed 316L particle (2 μm) at an impact velocity of 800 m/s

additional FEM simulations of 2D nanoindentation with the used Berkovich shape are performed to obtain the strain rate pre-exponential factor C . Because particles with sizes of 2 μm showed an impact temperature of 200 $^{\circ}\text{C}$, indentations at 200 $^{\circ}\text{C}$ were performed for the derivation of the model parameters. The results of the FEM simulations from the derived parameters are shown in Fig. 21. The parameters A , B , n from Eq. (2) were kept constant while C , $\dot{\epsilon}_0$ and m were varied. The deformation determined by simulation shows a good agreement (1–5% deviation) with the cross section of a deposited stainless steel particle obtained by SEM.

5 Investigation of the Formed Surface Morphology

5.1 Microstructuring of Titanium Samples

Depending on the particle velocity two phenomena occur during impact, which affects the morphology of the surface: rebound or binding. Particles with low velocity bounce off the surface and create a crater structure, while at high velocities a bond can occur due to strong deformation (Fig. 22).

Successful particle binding results in hills that deviate from an ideal spherical shape due to deformation. Because a whole stream of particles hits the surface at the same time, several impacts at the same spot influence the generation of microstructures significantly. At higher concentrations, a slow spray velocity, or when scanning several times, impacts on the same spot become increasingly likely and lead to higher roughnesses. At one point it can happen that particles will attach to the surface due to mechanical interlocking if it hits at or near a cavity [5].

In Fig. 23, a microstructured titanium (grade 1) surface is shown. As a particle feedstock material, titanium particles were used with sizes in the range between 5 and 35 μm . The SEM images show the morphology when the line distance is varied. The dimensionless factor p is defined as the ratio of maximum wide (600 μm) that was observed from experiments to the spray wide.

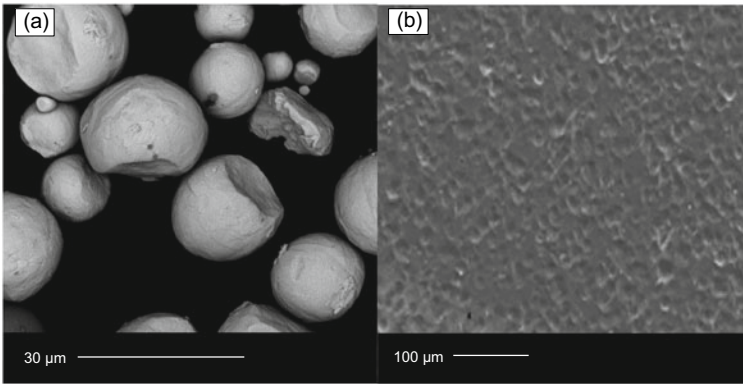
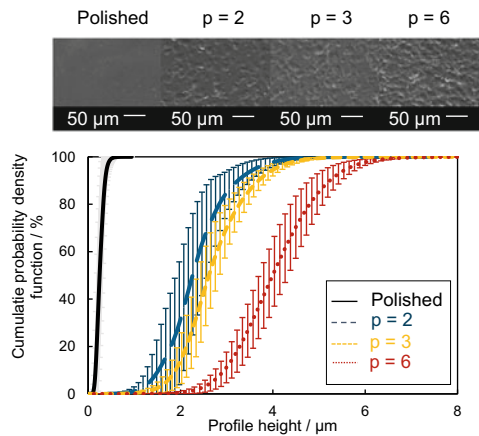


Fig. 22 **a** Rebounded titanium particles and **b** micro-structured titanium surface with craters

Fig. 23 Material proportion curves of structured titanium surfaces. $T = 500^\circ\text{C}$, $\Delta p = 8$ bar, stand-off distance of 5 mm [20]



The images clearly show that at a track width of 300 μm (corresponding to $p = 2$), there are still predominantly polished surfaces between the craters, which are about 3 μm deep. If the number of passages is increased, the polished areas decrease. At a track width of 100 μm , the structural elements are very dense and overlap several times. The structure was created by multiple particle collisions at the same site. The material proportion curves show a decreasing slope of the curve with increasing passage number. While the standard deviations of $p = 2$ and 3 still slightly overlap, the polished and the highly textured ($p = 6$) differ strongly from these. The number of passages is well suited for comparing the properties of surfaces of different structuring parameters or even of different plants, since it is a measure of how often a specific spot on the substrate passes the nozzle. With reduction of the line spacing by 100 μm each, the arithmetic mean S_a and root mean square S_q of roughness increase by about 20% (Fig. 24). The low error bars of the standard deviation indicate a uniform spray quality and high reproducibility of the microstructuring. The right image shows

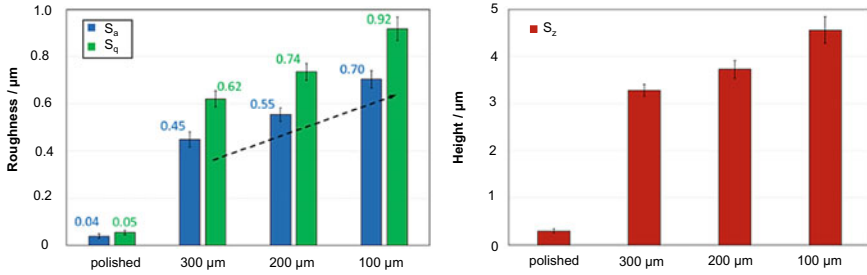


Fig. 24 Surface roughness in track spacing as well as overall height of microstructures created [20]

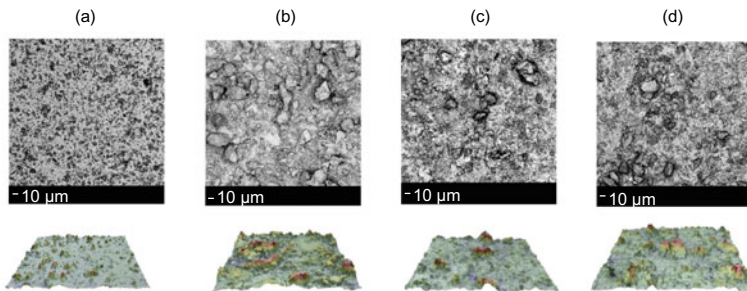


Fig. 25 3D scanning electron microscope images of micro-structured titanium surfaces with **a** non modified particles, and particles modified with **b** Ar, **c** Ar-C₂H₂, and **d** N₂ plasmas [22]

the height of the generated structure from the highest peak to the lowest valley S_z . As the number of passages increases, this value increases because the increased number of passages causes the substrate to heat up. Therefore, during collision, the substrate deforms more easily. In addition, structures are deeper due to multiple collisions of particles. The higher structure density creates craters in other craters and there is also increased material throw-up between two neighboring craters.

In academic research and industrial applications, mainly metals and alloys are used as a powder feedstock material in cold spraying. The research with materials that consists of interesting chemical properties like surface functionality is new and not fully clarified. Here, the square-edged particles were functionalized via a chemical vapor deposition (CVD) plasma process. For the plasma-modified particles, a significant increase in bonded particles was observed, especially for large particle sizes above 20 μm. This is attributed to the surface modification in the plasma process. The surface modification results in significantly more and significantly larger particles being deposited on the surface. This can be seen in Fig. 25 and (Table 2).

Table 2 Roughness values for structured titanium surfaces with non- and modified titanium particles [22]

Roughness/ μm	Initial titanium	Ar	Ar-C ₂ H ₂	N ₂
S_a	1.0 \pm 0.1	4.4 \pm 1.8	3.3 \pm 0.7	2.7 \pm 1.2
S_q	1.4 \pm 0.1	5.6 \pm 2.2	4.9 \pm 1.1	3.6 \pm 1.7
S_z	13.9 \pm 1.4	33.7 \pm 8.2	34.8 \pm 6.1	30.0 \pm 12.7

5.2 Microstructured Steel Surfaces

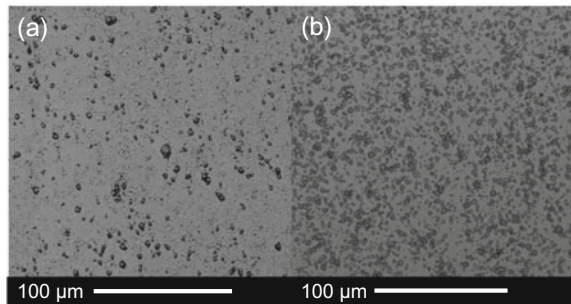
The dominant process parameter that affects the impact velocity the most is the gas temperature. An example is shown in Fig. 26 where 316L particles were sprayed on stainless steel substrates. At higher temperatures of 500 °C (Fig. 26b), a higher amount of deposited particles can be seen. The higher deposition rate is reached by the higher particle velocity and the thermal softening.

The variation of the structure concentration under the same process parameters (temperature and pressure) can be obtained by changing the amount of spray lines, the particle mass flow, the line distance, and the speed of the XY linear stage. For the structuring of stainless steel, SEM images of a polished surface and two cold sprayed substrates are shown (Fig. 27). By decreasing the line distance from 80 to 40 μm , an increase in particle loading can be observed.

In general, a decrease in the line distance leads to a higher amount of particle impacts and an increase in temperature of the surface. These two conditions increase the deposition efficiency. Additionally, due to more rebounded particles, it is possible to form craters that improve particle attachment by mechanical interlocking. A higher surface roughness is observed with lower line distance (Table 3).

The increase in the roughness is mainly caused by the aggregated structures. The value of S_{mr} decreases with higher particle concentration due to the higher amount of peaks on the surface.

Fig. 26 SEM images of microstructured stainless steel samples with 316L particles at initial gas temperatures of 400 (a) and 500 °C (b) with a nozzle inlet pressure of 9 bar [14]



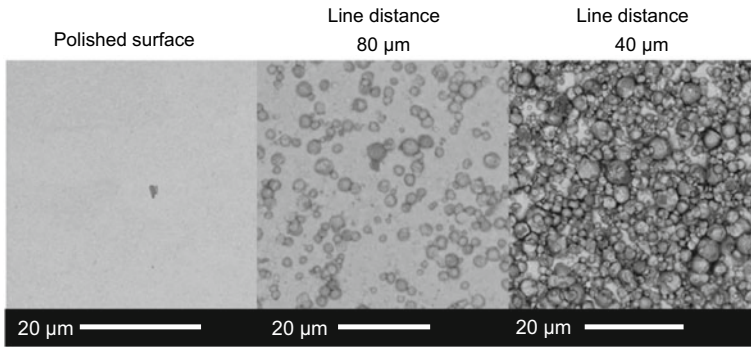


Fig. 27 SEM images of microstructured 316Ti substrates with 316L particles. The particles were sprayed onto the sample surface at two different line distances [14]

Table 3 Surface roughness of microstructured 316Ti samples [14]

	Polished	80 μm	40 μm
S_a/nm	2.8 ± 0.5	166.7 ± 9.7	372.7 ± 13.0
S_q/nm	8.6 ± 3.0	225.0 ± 16.4	461.7 ± 18.7
$S_z/\mu\text{m}$	0.36 ± 0.06	1.76 ± 0.1	3.26 ± 0.2
$S_{mr}/\%$	100 ± 0.0	57.1 ± 21.0	14.1 ± 5.5

6 Conclusion and Future Work

Within this work microstructured surfaces were produced by cold spraying of fine particles. As feedstocks materials titanium and stainless steel particles were used. They showed different characteristics like functionality, hardness, and shape, for example. The effect of process parameters on the critical velocity was investigated by CFD simulations. It showed that the temperature is the main parameter to change the velocity. The deformation of the particle during impact was simulated using FEM. It was possible to estimate the shape of the deformation with good accuracy using the Johnson–Cook plasticity model with material parameters derived from experimental investigations. The structured surfaces showed different morphologies. It was possible to produce morphologies with craters and hills depending on the process parameters. For future work, the CFD simulations have to be validated by experimentally measured particle velocities. For a better understanding, the simulation of the impact has to be done with models derived from particle compression test.

References

1. Raelison RN, Verdy C, Liao H (2017) Cold gas dynamic spray additive manufacturing today: deposit possibilities, technological solutions and viable applications. *Mater Des* 133:266–287. ISSN: 02613069. <https://doi.org/10.1016/j.matdes.2017.07.067>
2. Schmidt T, Assadi H, Gärtner F, Richter H, Stoltenhoff T, Kreye H, Klassen T (2009) From particle acceleration to impact and bonding in cold spraying. *J Thermal Spray Technol* 18, 5–6:794–808. ISSN: 1059-9630. <https://doi.org/10.1007/s11666-009-9357-7>
3. Bagherifard S, Kondas J, Monti S, Cizek J, Perego F, Kovarik O, Lukac F, Gaertner F, Guagliano M (2021) Tailoring cold spray additive manufacturing of steel 316 L for static and cyclic load-bearing applications. *Mater Des* 203:109575. ISSN: 02641275. <https://doi.org/10.1016/j.matdes.2021.109575>
4. Hassani-Gangaraj M, Veysset D, Nelson KA, Schuh CA (2018) In-situ observations of single micro-particle impact bonding. *Scripta Materialia* 145:9–13. ISSN: 13596462. <https://doi.org/10.1016/j.scriptamat.2017.09.042>
5. Aleksieieva O, Dereviankina L, Breuninger P, Bozoglu M, Tretiakov P, Toporov A, Antonyuk S (2022) Simulation of particle interaction with surface microdefects during cold gas-dynamic spraying. *Coatings* 12, 9:1297. <https://doi.org/10.3390/coatings12091297>
6. Rokni MR, Nutt SR, Widener CA, Champagne VK, Hrabec RH (2017) Review of relationship between particle deformation, coating microstructure, and properties in high-pressure cold spray. *J Thermal Spray Technol* 26, 6:1308–1355. ISSN: 1059-9630. <https://doi.org/10.1007/s11666-017-0575-0>
7. Assadi H, Gärtner F, Stoltenhoff T, Kreye H (2003) Bonding mechanism in cold gas spraying. *Acta Materialia* 51, 15:4379–4394. ISSN: 13596454. [https://doi.org/10.1016/S1359-6454\(03\)00274-X](https://doi.org/10.1016/S1359-6454(03)00274-X)
8. Hassani-Gangaraj M, Veysset D, Champagne VK, Nelson KA, Schuh CA (2018) Adiabatic shear instability is not necessary for adhesion in cold spray. *Acta Materialia* 158:430–439. ISSN: 13596454. <https://doi.org/10.1016/j.actamat.2018.07.065>
9. Dowding I, Hassani M, Sun Y, Veysset D, Nelson KA, Schuh CA (2020) Particle size effects in metallic microparticle impact-bonding. *Acta Materialia* 194:40–48. ISSN: 13596454. <https://doi.org/10.1016/j.actamat.2020.04.044>
10. Assadi H, Schmidt T, Richter H, Kliemann J-O, Binder K, Gärtner F, Klassen T, Kreye H (2011) On parameter selection in cold spraying. *J Thermal Spray Technol* 20, 6:1161–1176. ISSN: 1059-9630. <https://doi.org/10.1007/s11666-011-9662-9>
11. King PC, Busch C, Kittel-Sherri T, Jahedi M, Gulizia S (2014) Interface melding in cold spray titanium particle impact. *Surf Coat Technol* 239:191–199. ISSN: 02578972. <https://doi.org/10.1016/j.surfcoat.2013.11.039>
12. Schmidt T, Gärtner F, Assadi H, Kreye H (2006) Development of a generalized parameter window for cold spray deposition. *Acta Materialia* 5, 3:729–742. ISSN: 13596454. <https://doi.org/10.1016/j.actamat.2005.10.005>
13. Schmidt K, Buhl S, Davoudi N, Godard C, Merz R, Raid I, Kerscher E, Kopnarski M, Mäller-Renno C, Ripperger S, Seewig J, Ziegler C, Antonyuk S (2017) Ti surface modification by cold spraying with TiO₂ microparticles. *Surf Coat Technol* 309:749–758. ISSN: 02578972. <https://doi.org/10.1016/j.surfcoat.2016.10.091>
14. Breuninger P, Krull F, Huttenlochner K, Mäller-Reno C, Ziegler C, Merz R, Kopnarski M, Antonyuk S (2019) Microstructuring of steel surfaces via cold spraying with 316L particles for studying the particle-wall collision behavior. *Surf Coat Technol* 379:125054. ISSN: 02578972. <https://doi.org/10.1016/j.surfcoat.2019.125054>
15. Buhl S (2018) Mikrostrukturierung von Bauteiloberflächen mittels Kaltgasspritzen. Dissertation Kaiserslautern: TU Kaiserslautern. <https://doi.org/10.1002/cite.201450318>
16. Buhl S, Breuninger P, Antonyuk S (2018) Optimization of a laval nozzle for energy-efficient cold spraying of microparticles. *Mater Manuf Proc* 33, 2:115–122. ISSN: 1042-6914. <https://doi.org/10.1080/10426914.2017.1279322>

17. Buhl S, Schmidt K, Sappok D, Merz R, Godard C, Kerscher E, Kopnarski M, Sauer B, Antonyuk S, Ripperger S (2015) Surface structuring of case hardened chain pins by cold-sprayed microparticles to modify friction and wear properties. *Particuology* 21:32–40. ISSN: 16742001. <https://doi.org/10.1016/j.partic.2014.10.001>
18. Morsi SA, Alexander AJ (1972) An investigation of particle trajectories in two-phase flow systems. *J Fluid Mech* 55, 02:193. <https://doi.org/10.1017/S0022112072001806>
19. Sutherland W (1893) LII. The viscosity of gases and molecular force. *Philos Mag* 36:507–531. <https://doi.org/10.1080/14786449308620508>
20. Breuninger P (2021) Mikrostrukturierung von Stahl- und Titanoberflächen mit feindispersen Partikeln mit einem Kaltgasverfahren. Dissertation. Kaiserslautern: Kaiserslautern
21. Wadell H (1934) The coefficient of resistance as a function of Reynolds number for solids of various shapes. *J Frankl Inst* 217, 4:459–490
22. Breuninger P, Krull F, Buhl S, Binder A, Merz R, Kopnarski M, Sachweh B, Antonyuk S (2019) Microstructuring of titanium surfaces with plasmamodified titanium particles by cold spraying. *Particuology* 44:90–104. ISSN: 16742001. <https://doi.org/10.1016/j.partic.2018.08.002>
23. Grujicic M, Zhao C, DeRosset W, Helfrich D (2004) Adiabatic shear instability based mechanism for particles/substrate bonding in the cold-gas dynamic-spray process. *Mater Des* 25, 8:681–688. ISSN: 02613069. <https://doi.org/10.1016/j.matdes.2004.03.008>
24. Hertz H, über die Berührung fester elastischer Körper, 156. *J für die reine und angewandte Mathematik* 92:156–171
25. Antonyuk S, Heinrich S, Tomas J, Deen NG, van Buijtenen MS, Kuipers JAM (2010) Energy absorption during compression and impact of dry elastic-plastic spherical granules. *Granular Matter* 12, 1:15–47. ISSN: 1434–5021. <https://doi.org/10.1007/s10035-009-0161-3>
26. METALCOR GmbH. Datasheet: 1.4404 (AISI 316 L), S31603 | METALCOR
27. Sousa BC, Gleason MA, Haddad B, Champagne VK, Nardi AT, Cote DL (2020) Nanomechanical characterization for cold spray: from feedstock to consolidated material properties. *Metals* 10, 9:1195. <https://doi.org/10.3390/met10091195>
28. Johnson GR, Cook WH (1985) Fracture characteristics of three metals subjected to various strains, strain rates, temperatures and pressures. *Eng Fract Mech* 21, 1:31–48. ISSN: 00137944. [https://doi.org/10.1016/0013-7944\(85\)90052-9](https://doi.org/10.1016/0013-7944(85)90052-9)
29. Umbrello D, M'Saoubi R, Outeiro JC (2007) The influence of Johnson-Cook material constants on finite element simulation of machining of AISI 316L steel. *Int J Mach Tools Manuf* 47, 3–4:462–470. ISSN: 08906955. <https://doi.org/10.1016/j.ijmactools.2006.06.006>
30. Assadi H, Gärtner F (2020) Particle compression test: a key step towards tailoring of feedstock powder for cold spraying. *Coatings* 10, 5:458. <https://doi.org/10.3390/coatings10050458>
31. Dao M, Chollacoop N, van Vliet KJ, Venkatesh TA, Suresh S (2001) Computational modeling of the forward and reverse problems in instrumented sharp indentation. *Acta Materialia* 49, 19:3899–3918. ISSN: 13596454. [https://doi.org/10.1016/S1359-6454\(01\)00295-6](https://doi.org/10.1016/S1359-6454(01)00295-6)
32. Schmidt T, Gaertner F, Kreye H (2006) New developments in cold spray based on higher gas and particle temperatures. *J Thermal Spray Technol* 15, 4:488–494. ISSN: 10599630. <https://doi.org/10.1361/105996306X147144>
33. Hangen U, Chen C-L, Richter A (2015) Mechanical characterization of pm2000 oxide-dispersion-strengthened alloy by high temperature nanoindentation. *Adv Eng Mater* 17, 11:1683–1690. ISSN: 14381656. <https://doi.org/10.1002/adem.201500095>

Creating Surface Morphologies by Additive Manufacturing



Georg von Freymann, Julian Hering-Stratemeier, Kristin E. J. Kühl,
Thomas Palmer, and Erik H. Waller

Abstract Additive manufacturing on the micron-scale allows for unprecedented control of surface morphologies. With the smallest feature sizes in the range of 50 nm, surface roughness in the order of 10 nm, and with no observable damage to the underlying substrate material, additive manufacturing is an ideal choice if the influence of surface topography as part of the morphology is to be studied. While the highest surface definition is achieved with polymer-based materials, first, promising steps towards additive manufacturing of metals on the micron-scale have been recently made. To reach as small as possible deviations between the designed structure and the manufactured one, dimensional accuracy is crucial. To reach high dimensional accuracy, the fabrication processes for polymeric as well as metallic materials are to be understood in detail via numerical simulations. In this chapter, we review the underlying physical principles, discuss the numerical models employed, and provide an overview over common materials.

1 Introduction to Additive Manufacturing on the Micron-Scale

Additive manufacturing on the macro-scale is industrially established and accelerates prototyping processes, enables the fabrication of spare parts, reduces the complexity of assembly, and allows the creation of multi-material parts unachievable with conventional subtractive fabrication technology. Since the foundation of maker communities sharing designs via the internet and the availability of low-cost 3D printers for private use, additive manufacturing has made its way from the scientific community into society.

The two most common additive manufacturing technologies for the macro-scale are fused filament fabrication (FFF) and selective laser sintering (SLS). While both

G. von Freymann (✉) · J. Hering-Stratemeier · K. E. J. Kühl · E. H. Waller
Institute of Optical Technologies and Photonics, RPTU Kaiserslautern, Kaiserslautern, Germany
e-mail: georg.frey mann@rptu.de

G. von Freymann · T. Palmer · E. H. Waller
Fraunhofer Institute of Industrial Mathematics (ITWM), Kaiserslautern, Germany

© The Author(s), under exclusive license to Springer Nature Switzerland AG 2024
J. C. Aurich and H. Hasse (eds.), *Component Surfaces*, Springer Series in Advanced
Manufacturing, https://doi.org/10.1007/978-3-031-35575-2_7

techniques are truly mature, they cannot reach down to the micron-scale as required for studying surface morphologies on this scale. In FFF, a precursor material is fed to a heated nozzle, in which the material is heated close to its melting point. A small aperture in the nozzle defines the dimension and shape of the viscous material extruded through the nozzle and deposited to the substrate, where it quickly cools down and hardens. The smallest aperture diameters are defined by the achievable pressure to extrude the precursor and typically reach down to the order of 50–100 μm . Combined with the precision of the stages moving the print head in the x - and y -directions and the substrate in the z -direction, the smallest features to be realized are on the order of few 100 μm . Due to the movement of the massive print head and stage, the achievable fabrication speed is limited.

Using one or several scanning laser beams, SLS is a much faster and more precise additive manufacturing technology. Here, the material is provided as a solid powder with grain sizes down to few 10 μm . On top of the building platform, a layer of powder is mechanically prepared. The laser beam locally heats and melts the powder. Scanning the laser beam connects the melt pools, thus forming a solid structure after hardening of the melt. After depositing another powder layer this process starts again, fabricating the overall structure in a succession of single layers. The smallest features are defined by roughly the grain size of the powder and cannot reach down to the micron-scale. Reducing the grain size in the powder is not easily possible, as smaller grains tend to agglomerate, hindering the deposition of smooth powder layers. Furthermore, to prevent oxidization of the materials SLS has to be performed under protective gas atmosphere.

Hence, scaling down additive manufacturing from the macro-scale to the micron-scale is not readily possible and requires a different approach. The most established approach is three-dimensional laser lithography based on two-photon polymerization (2PP). In contrast to the above two methods, the material is neither extruded nor provided in layers. For 2PP, the whole volume to be printed is deposited once and a scanning laser beam introduces local chemical changes inside the volume to define the final structure. Using nonlinear optical processes, the material is only modified in the very focal volume of the laser beam, creating single building blocks (so-called volume pixels or voxels) with dimensions on the scale of the laser focus. A subsequent development step removes the material afterwards, which does not belong to the desired structure.

Comparing the different additive manufacturing approaches with respect to fabrication speed measured in voxels per second, 2PP is leading the comparison while providing the smallest features sizes (see Fig. 1). In this chapter, we provide an overview over the optical setup, the most common materials used in 2PP as well as oversimulation and measurement approaches to understand and optimize the surface morphologies fabricates using 2PP.

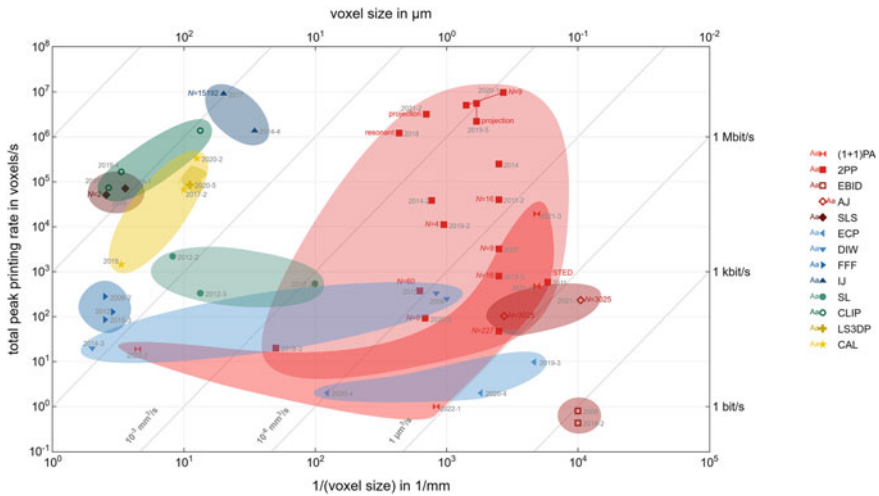


Fig. 1 Overview of various 3D additive manufacturing methods. The respective voxel size of each method is plotted (upper logarithmic horizontal scale) versus the total peak printing rate (left logarithmic vertical scale). The lower scale gives the inverse of the voxel size, which is loosely associated with the resolution. On the right scale, the total peak printing rate is expressed in terms of bits per second. References for the individual data points are given in the original publication. (1+1)PA: (1+1)-Photon Absorption, 2PP: Two-Photon Printing, EBID: Electron Induced Deposition, AJ: Aerosol Jet 3D Nanoprinting, SLS: Selective Laser Sintering, ECP: Electrochemical Printing, DIW: Direct Ink Writing, FFF: Fused Filament Fabrication, IJ: Inkjet Printing, SL: (Projection Micro-)Stereolithography, CLIP: Continuous Liquid Interphase Printing, LS3DP: Light-Sheet 3D Printing, CAL: Computed Axial Lithography. Figure and caption adapted from [1]. Changes have been made with respect to the original document. An updated version can be found <https://3dprintingspeed.com/>. Figure reproduced from the website under CC-BY license

2 Additive Manufacturing via Two-photon Polymerization

Additive manufacturing based on two-photon polymerization, also known as three-dimensional μ -printing, three-dimensional laser lithography or direct laser writing (DLW) was first reported by *Maruo* in 1997 [2]. In the past 25 years the technology developed from a scientific curiosity to a commercially available tool. As this development has been covered by numerous review articles (see e.g., [3–5]), we here briefly report on the common optical setup, which can still be found in most of the DLW devices around the world. An ultrafast laser with pulse durations in the range of 50–250 fs, a pulse repetition rate in the range of 40–100 MHz, and a center-wavelength in the range of 780–800 nm emits a laser beam which is expanded to fill the entrance pupil of a high-numerical aperture (NA 1.4) oil-immersion microscope objective. The microscope objective tightly focuses the laser light into the focal volume to reach intensities high enough to enable two-photon absorption. In the most simple model assumption, the photosensitive material shows a step-like threshold behavior: the material polymerizes or crosslinks in all regions with an intensity

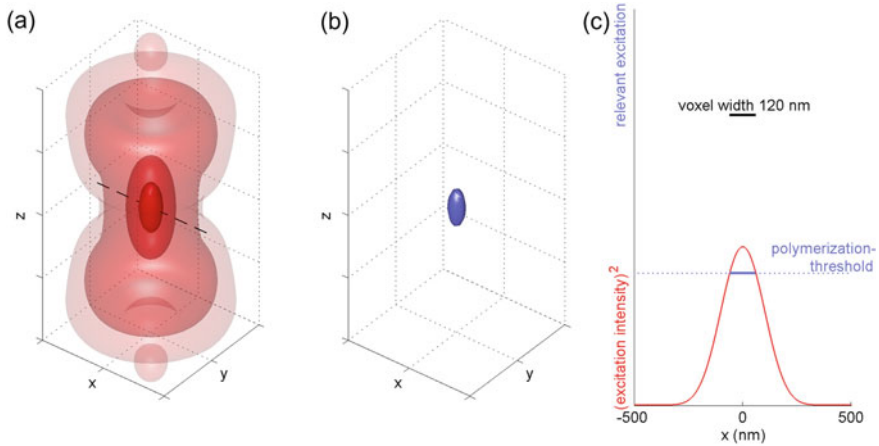


Fig. 2 **a** Intensity distribution inside the focal volume of a laser beam at 800 nm wavelength focused with an oil-immersion objective with $NA = 1.4$. **b** Resulting voxel defined by an isointensity surface defined by the threshold of the material. **c** Cross section along the dashed line in **(a)** to show the resulting intensity distribution (red curve) and the threshold intensity of the material defining the voxel (blue curve)

above the threshold, while it stays chemically unmodified in all other regions. This is exemplified in Fig. 2a–c: While in a, some isointensity surfaces inside the focal volume are shown; in b, the defining isointensity surface is depicted for which the intensity crosses the threshold value. The cross section in c demonstrates this threshold (dotted line). After removing the unaltered material, only the blue ellipsoid, the voxel, would remain. Moving the focus through the material joins different voxels to a connected three-dimensional structure.

While in the early days, the sample moved relatively to the focus, in more modern systems galvanometric mirrors are added between laser and objective to allow for fast scanning of the laser beam. Furthermore, an acousto-optical modulator is added to the beam, to allow for quick intensity adjustments to control the voxel size while scanning. Another important piece of optics is a quarter-wave plate, which ensures that the light reaching the material is circularly polarized to avoid anisotropies found in the voxel under focusing with high numerical aperture objectives.

Each individual optical element added to the beam path introduces a slight amount of aberrations, which lead to a deviation of the intensity distribution in the focal volume reducing the reachable feature size and resolution. To characterize these deviations, a small gold nanoparticle (diameter roughly 80 nm) is scanned through the focal volume, and the scattered intensity is mapped for each position. Corresponding focal intensity distributions are depicted in Fig. 3 in the center column. Compared with the desired intensity distribution shown in the left column, deviations are clearly visible.

To correct these deviations, another element is added to the optical path, a so-called spatial light modulator (SLM), which allows to manipulate the phase and, hence, the

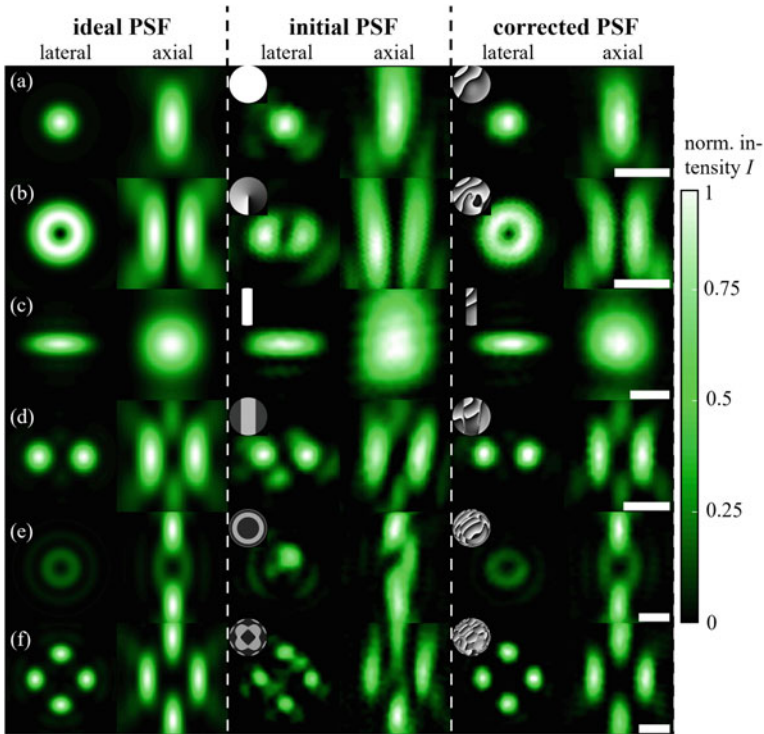


Fig. 3 **a** Major aberrations present in a TEM_{00} mode, **b** a doughnut mode, **c** a slit mode, **d** a lateral-double-spot mode, **e** an axial-double-spot mode, and **f** a six-spots mode can be compensated by using a spatial light modulator. The respective phase patterns used are shown in the upper left corner of each laser mode. The scale bars correspond to 500 nm, respectively. Adapted with permission from [6]

aberrations [7]. Applying a modified iterative Gerchberg–Saxton algorithm [8] to calculate the required phase correction, one removes almost all deviations from the beam [6]. The results after this aberration corrections are shown in the right column of Fig. 3. Compared with the design in the left column almost no deviations can be observed. The corrected phase pattern required to remove the aberration is shown as a small inset in all columns from Fig. 3a–f in the top-left corner. The ideal phase distribution can be seen in the center column and it is obvious that quite some correction has to be applied to reach the desired distribution in the real setup.

2.1 Dimensional Accuracy

Structure formation in additive manufacturing using three-dimensional laser lithography is a complex process in which the optical and chemical processes are

intertwined. While the optical part of three-dimensional laser lithography is very well understood and controlled (see the above section), the photochemical side starting from the excitation mechanism of the photoinitiator, the subsequent polymerization, and the sample behavior under the development process strongly depend on the chosen material, the writing strategy, and the sample geometry to be printed itself to name the most important parts.

To quickly get an overview, of which structural features can be printed with a certain set of writing parameters (e.g., scan speed and laser power), we define a test structure, which contains all relevant feature sizes and allows for detecting anisotropic behavior for different writing directions. The circular surface of this structure is modulated by a linear chirp function $z(r)$:

$$z(r) = \frac{H}{2} \sin \left(\Phi_0 + 2\pi r \left(f_0 - \frac{\Delta f}{2R} r \right) \right), \quad (1)$$

where H is the feature height, R the radius of the outer border of the pattern, f_0 the initial topographic frequency, and Δf the bandwidth of the structure. Scanning the surface of the printed structure with an atomic force microscope (AFM), the topography is reliably measured. These measurements along different angles are then compared to the desired design defined by Eq. (1). To define a single numerical value allowing for comparison of different samples, we define the achievable dimensional accuracy by the geometrical wavelength of the printed profile for which the gain of its Fourier transform dropped to -6 dB. At this spatial wavelength, the printed feature drops to half of the designed amplitude. This is illustrated in Fig. 4 and described in much deeper detail in [9]. For the two exemplary evaluated curves in the figure, the dimensional accuracy reaches 0.83 μm and 0.67 μm , respectively. Of course, much smaller features can still be printed, but the deviations to the initial design are then too large. Thus, the here-defined dimensional accuracy delivers an objective criterion for comparison and thus allows for optimization of the printing parameters.

3 Polymer-Based Materials

Within this section, we will focus on the partially name-giving and probably still the most used material in two-photon polymerization: polymer-based photo resins. Since photopolymerization serves as research focus for several tens of years, there is a huge variety of resins, chemical processes, applications, and related literature – see e.g., these textbooks [10–14] for detailed information.

For photopolymerization, one typically distinguishes between the so-called positive tone and negative tone photo resins. The latter are characterized by a light-induced hardening behavior, whereas positive tone resins contrarily are getting soluble to specific solvents after exposure [12]. Both types of resins can be further classified into the free radical and the ionic mechanism, respectively, due to their fundamental routes for the polymerization initiation [13, 15].

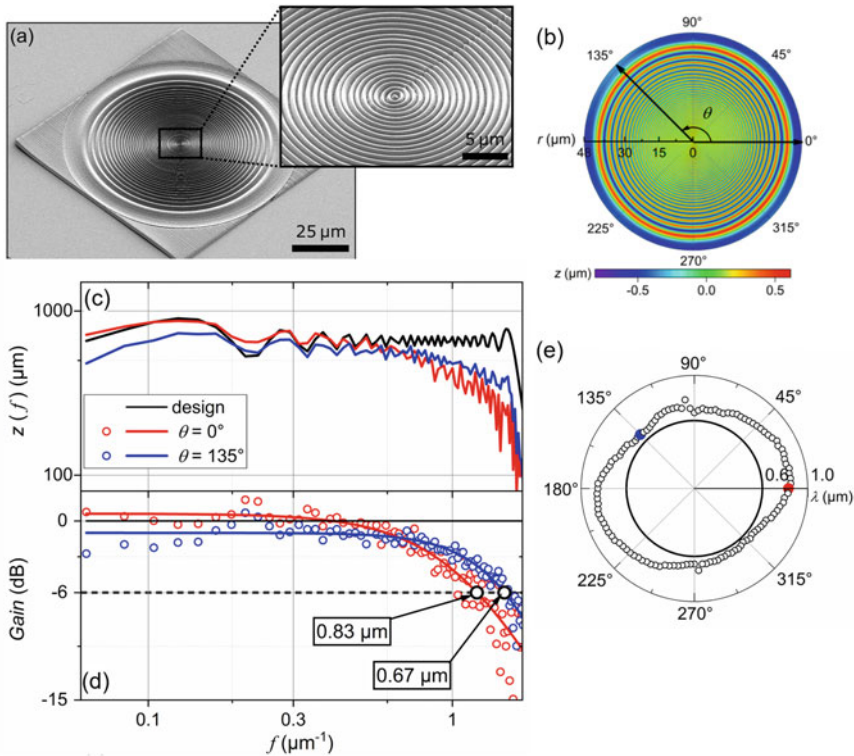


Fig. 4 **a** Electron micrograph of a circular chirped structure used to define a measure for the dimensional accuracy. **b** Atomic force microscopy (AFM) image of the structure in **(a)**. **c** Amplitude curves calculated by Fourier transformation of the AFM cross-sections along two different directions (blue and red curve) and comparison with the design (black curve). **d** Evaluated (open circles) and fitted (solid lines) instrument transfer functions of the curves in **(c)**. The dashed line marks the -6 dB line, which defines the reachable dimensional accuracy. **e** Dimensional accuracy values plotted along the different directions clearly showing an anisotropy of the structure not directly visible in **(a)** or **(b)**

A very prominent and one of today’s highest resolution commercial photo resins for two-photon polymerization is *Nanoscribe GmbH & Co. KG*’s negative tone, free radical IP-L [17], which will be discussed here as a representative example for research and application of the CRC 926. IP-L’s photoinitiator 7-diethylamino-3-thenoylcoumarin (DETC) is a so-called type-II photoinitiator [18], which generates radicals via a bimolecular process [19]. In contrast, a type-I photoinitiator, such as the widely used Irgacure 369, is characterized by a photo-induced decay into radicals without another molecule. Consequently, this is called a Norrish type-I reaction [20]. For IP-L, analogously, the Norrish type-II reaction shown in Fig. 5 applies. First, the photon energy of the laser focus $2\hbar\omega$ is absorbed by the ketone carbonyl group ($C = O$) between the thiophene and naphthalene backbone [10] and the photoinitiator

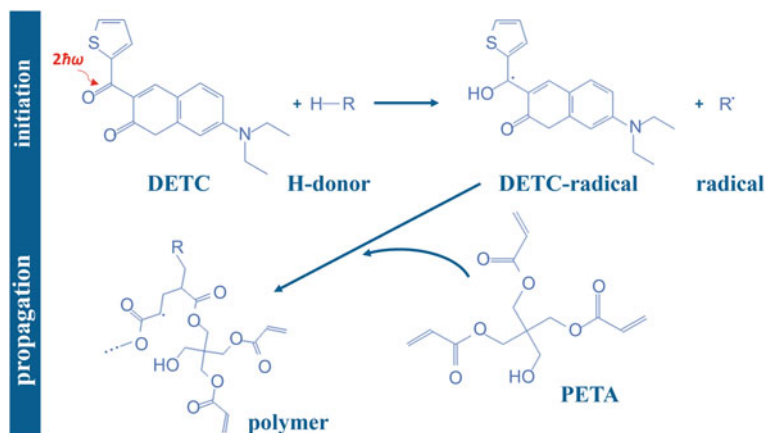


Fig. 5 Type-II photoinitiator-based cross-linking of triacrylate monomers during two-photon polymerization. DETC: 7-diethylamino-3-thenoylcoumarin, PETA: pentaerythritol triacrylate. Adapted with permission from [16]

molecule is thus raised into an electronically excited state. However, this does not yet cause a direct bond break as in the case of type-I photo initiators, since the surrounding CO-aryl bond energies are too strong (roughly 335–377 kJ/mol [21]). For this reason, a hydrogen donor, usually tertiary amines [21], is needed as co-initiator. This co-initiator reacts with the excited photoinitiator molecule, resulting in a free radical R^\bullet , and, hence, initiating the subsequent polymerization. The radical binds to the vinyl group (CH_2) of IP-L's monomer pentaerythritol triacrylate (PETA) so that the shell of the carbon atom of the resulting CH group is incompletely occupied [22]. Another PETA molecule can then bind to this site, which in turn generates another reactive carbon atom. Consequently, this concatenation of several monomers to oligomers finally results in a highly cross-linked polymer network. The cross linking propagates until no further monomers are available to the active part of the network, called trapping, or until the propagation is terminated by another radical. This can be either a second excited photoinitiator molecule or a second propagating polymer chain. In addition, inhibitory molecules, such as oxygen, can stop the polymerization [11]. This inhibition is done intentionally in most commercial photo resins by the addition of inhibitors to increase the shelf life of the product. So-called quenching, on the other hand, involves additional, sometimes undesirable terminations, which often occur due to the respective laboratory conditions such as, e.g., temperature and humidity.

All polymer-based fabricated structures during the period of CRC 926 followed this free radical, negative tone behavior. Nevertheless, the aforementioned alternative polymerization mechanisms are of course worth mentioning, too: the majority of ionic photo polymerization is assigned to cationic mechanisms, since anionic photoinitiators are considerably less investigated [23]. In contrast to the free radical mechanism, both, homolytic cleavage and dissociation of a counter anion take place for the cationic mechanism subsequently to the light-induced excitation of the

photoinitiator. This directly leads to the generation of a cationic radical, an aryl radical, as well as an unaltered counter anion. Due to the abstraction of a Lewis acid by the cationic radical, a weakly bound hydrogen and a free radical are produced, from where the acid is further deprotonated by the anion in solution. This leads to a Lewis acid with the starting anion as counter ion. The polymerization is finally initiated by the generated acid proton and follows an analogue propagation mechanism as for the free radical polymerization, described above [24]. The probably most common cationic (negative tone) resin is SU-8 [17].

In total contrast to the negative tone resins described so far, positive tone resins such as most of the AZ resins [17] and the commonly used (DNQ-) Novolac resins [25], are not getting insoluble, but soluble to specific solvents due to light exposure. Therefore, one typically has to treat the resin by temperature prior to the exposure (pre-bake), allowing the resin's solvents to evaporate. Hence, the resin hardens prior to the structuring process. The photo active component within the resin now breaks the chemical bonds when being exposed to light, consequently becoming soluble at the exposed areas. After development and some resin-specific post-treatments, only the unexposed areas remain on the substrate [12].

All these different ways of polymerization and their respective materials come up with different advantages and disadvantages, such as more or less out-of-focus polymerization, different resolution capabilities, varying requirements on overall purity, pre- and post-treatment or toxicity. Hence, one has to balance all those aspects carefully for each individual two-photon polymerization application.

3.1 *Materials Properties*

Although two-photon polymerization has been investigated for more than 25 years, there are still many challenges in how to experimentally receive the exactly desired 3D printed structures. Regarding voluminous structures, e.g., micro-optics or calibration measures, one can observe deviations from the respective designs as shrinkage or bulging. Regarding the fabrication of features in close proximity, e.g., line gratings with periods below a few hundreds of nanometers, undesired effects like line-width broadening, tiny sporadic connections, and bending occur [5]. These undesired effects as well as the aforementioned bulging of greater structures are commonly summarized by the term proximity effect [26]. In 2016, Waller *et al.* [27] investigated this phenomena for the very first time in an accurate, time- and spatially resolved way. They created two excitation foci with a precisely defined distance to each other with the help of a spatial light modulator and fabricated single lines with just as precisely defined fabrication speed. Varying the speed and the spatial distance in a series of experiments allowed for exploring the spatio-temporal influence of the first written line onto the second and vice versa, leading to the line-broadening b :

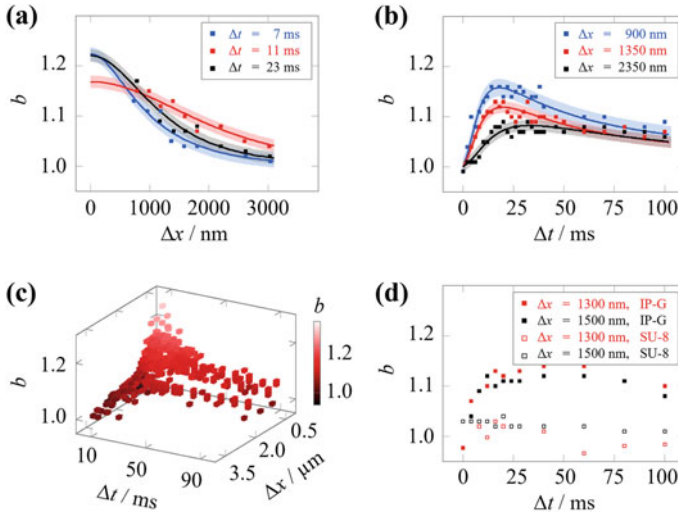


Fig. 6 The dots indicate the measurement data, the solid lines represent the respective model fit and the underlay illustrates the corresponding mean squared error. **a** Spatial characteristics of the broadening b for exemplary delays Δt , **b** temporal characteristics of b for exemplary separations in x direction Δx , **c** spatio-temporal characteristics of b , **a–c** illustrate the behavior for IP-L, **d** comparison of temporal characteristics of b in SU-8 (opened dots) and IP-G (filled dots) for exemplary values of Δx . Adapted with permission from [27]

$$b = \sqrt{\frac{1 + \beta R_{\text{diff}}^{l_1 \rightarrow l_2}}{1 + \beta R_{\text{diff}}^{l_2 \rightarrow l_1}}}. \quad (2)$$

Here, $l_1 \rightarrow l_2$ is the contribution of the first written line to the radical generation rate of the second line ($l_2 \rightarrow l_1$ vice versa) and β is a constant fit parameter. The diffusion-related radical generation rates are

$$R_{\text{diff}}^{l_1 \rightarrow l_2} \propto \int_0^{t_w} \frac{1}{4\sqrt{\pi D t'}^3} \exp\left[-\frac{d^2 + (\Delta y - vt')^2}{4Dt'}\right] dt', \quad (3)$$

$$R_{\text{diff}}^{l_2 \rightarrow l_1} \propto \int_{\Delta t}^{t_w} \frac{1}{4\sqrt{\pi D t'}^3} \exp\left[-\frac{d^2 + (vt')^2}{4Dt'}\right] dt', \quad (4)$$

with D being the effective diffusion constant, d the lateral distance between the two lines, v the fabrication speed, t' the time difference from $t = 0$ over Δt as starting time of the second line to t_w as end time, as well as $\Delta y = v\Delta t$ being the distance along the fabrication direction. The respective experimental and model results are exemplary shown for the IP-L resin in Fig. 6a–c, and an additional comparison between IP-G and SU-8 is given in Fig. 6d. One can nicely conclude that the diffusion of radicals (or oxygen) strongly affects the final structures for two-photon

polymerization. This does not only explain the aforementioned undesired effects (line-width broadening, sporadic connections between individual features, etc.) but also the observable bulging of voluminous structures. The mutual influence extends well beyond the focal region on a spatial scale of several micrometers and over several hundreds of milliseconds [27].

The image of radical and oxygen diffusion also explains the three-regime behavior of photo resins, discovered by *Yang et al.* in 2019 [28]. Since two-photon polymerization requires a minimal exposure dose to start the polymerization reaction [29], *Yang et al.* meticulously investigated this threshold behavior for different photo resins over seven orders of magnitude in exposure time (from 1 μ s to 10s). The so-called Schwarzschild effect states in contrast to the reciprocal law, that the required light intensity is not entirely inversely proportional to the exposure time for a constant lithographic (or originally photographic) process [30]: even for extremely long exposure times, no polymerization occurs for intensities below a certain threshold. Now, *Yang et al.* identified this Schwarzschild behavior in two-photon polymerization as regime II, appearing on intermediate exposure times, roughly between 1 ms and 100 ms. For lower exposure times (regime I), the reciprocal law of intensity and exposure time holds true, whereas, for large exposure times (regime III), a significant Schwarzschild behavior deviation is observed due to the diffusion of radicals and oxygen [28].

Moreover, two-photon polymerized structures are characterized by another, mostly undesired property: they shrink during and subsequent to the fabrication process. This is getting obvious when looking at the resin's density $\rho = m/V$. Assuming that the mass m is conserved, there must be a loss in volume V due to polymerization, since the density of an unpolymerized negative tone photo resin is smaller than that of its polymerized state [31]. Thereby, the shrinkage strongly depends on the degree of polymerization, hence, on the product of the laser intensity and the exposure time (within regimes I and III [28]). However, shrinkage occurs not only during the writing process but also during the subsequent development of the samples. Here, soluble components of the resin, such as unpolymerized monomers or unreacted photoinitiators, simply dissolve [32]. Furthermore, developers generally induce some kind of swelling in a slight amount. The resulting capillary effects lead to another shrinkage of the structures [33], which has been found to be the most prominent contribution [34]. All in all, deviations of up to 30% are not rare [5, 35] and need to be considered for designing structures for two-photon polymerization.

The mechanical properties of the finally created structures strongly depend on the respective photo resin, the exposure dose while fabricating, as well as on the post-treatment. For instance, a post-print UV curing increases Young's modulus by more than 50% for Nanoscribe's IP-Dip photo resin [36]. Typically, Young's modulus of two-photon polymerized polymeric photo resins lies in the range of some few GPa, the refractive indices are about 1.5 and the Poisson's ratios are roughly 0.3 [17].

Investigating the polymeric structure's properties is still today's research work, likewise the specific design and modification.

3.2 Modeling of the Fabrication Process

Modeling approaches of the final two-photon polymerized structures reach back to first considerations about the width of a single line in 2013 [5], as well as voxel and pillar dimensions in 2019 [38]. In 2022, *Pingali and Saha* took the reaction–diffusion during polymerization into account, which dramatically complicated the modeling—even for very simple lines [39]. It was only possible to predict the line widths in a reliable way, but not their heights or aspect ratios. An alternative way was already presented by *Guney and Fedder* in 2016 by a semi-empirical analytic model through simulations and fitting for estimating widths and heights of single lines [40]. Limited to rather simple structures as well, this approach cannot be easily transferred to voluminous structures with a footprint of several tens or hundreds of microns. A very promising work was recently published by *Adão et al.* in 2022 [41], establishing an algorithm to spatially predict the resulting exposure dose for fabricating waveguide structures, based on experimental parameters like scan speed, laser power, and numerical aperture. Unfortunately, the shrinkage behavior was not taken into account, hence, still showing deviations from their target structures. Moreover, no reliable statement about predicting other structures than waveguides has been given.

Within the period of CRC 926, we came up with a very first model for predicting voluminous structures, additionally including shrinkage effects [37]. The procedure is schematically shown in Fig. 7 and starts with the structure to be printed as point

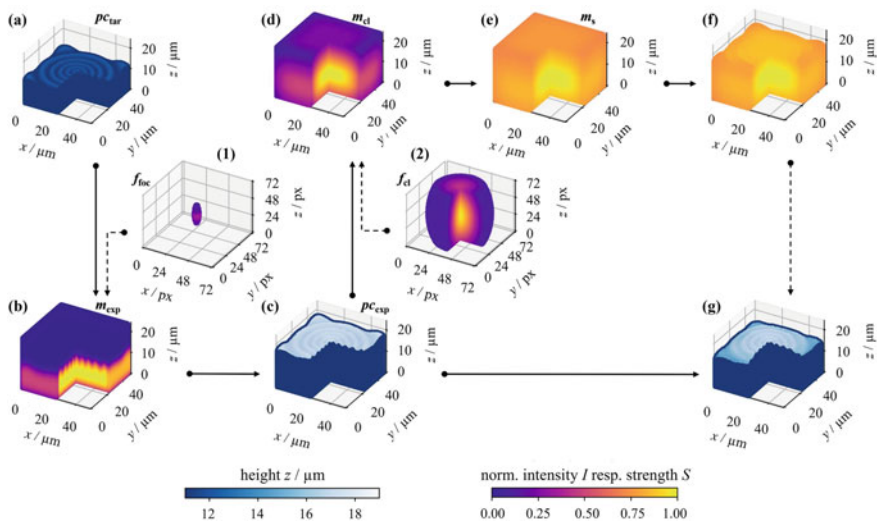


Fig. 7 All relevant steps of the prediction algorithm are schematically shown for a radially chirped topography. The two-photon polymerization predicted structure is represented by (g). Adapted with permission from [37]

cloud $pc_{\text{tar}}(x, y, z)$. For modeling the exposure in two-photon polymerization, this target point cloud is convoluted with a 3D Gaussian distribution $f_{\text{foc}}(x, y, z)$, representing the laser focus with its experimentally proven spatial extensions. A subsequent binarization based on values beyond and below a certain threshold, takes the threshold model into account (compare Sect. 3.1). The thus achieved exposure point cloud pc_{exp} is then convoluted with another 3D Gaussian function, representing the cross-linking distribution f_{cl} . Its spatial extensions are inspired by Waller *et al.*, being on the micrometer range [27]. The linear mapping operation, represented by Eq. 5, transfers the previously obtained cross-linking matrix $m_{\text{cl}} = pc_{\text{exp}} \otimes f_{\text{cl}}$ into a shrinkage matrix m_{s} , ascribing every point of the cross-linking matrix a specific shrinkage factor κ :

$$m_{\text{s}} = \frac{\kappa_{\text{max}} - \kappa_{\text{min}}}{\max(m_{\text{cl}}) - \min(m_{\text{cl}})} \cdot m_{\text{cl}} + \kappa_{\text{min}}, \quad (5)$$

with κ_{max} and κ_{min} being the maximal and minimal shrinkage factors, respectively. Next, the values of m_{s} are averaged along the z -direction to retrieve a 2D matrix which is multiplied by the 2D version of exposure point cloud (sum of all layers times the slicing distance). This gives the final two-photon polymerization prediction of the structure to be printed and is shown as point cloud in Fig. 7g.

Whereas most of the prediction parameters are given by the experiment, such as hatching & slicing distance or the laser power and are therefore fixed, some others are not specifically accessible. For instance, the spatial extent of the cross-linking distribution depends on the discretization of the structure, as well as on the structure itself. We found seven non-accessible parameters to be optimized individually for high-quality predictions. Fortunately, these seven parameters represent real physical quantities whose range of values can be roughly identified by other experiments. For example, the lateral and axial extensions of the exposed volume σ_{xy}^{exp} , σ_z^{exp} can be estimated by fabricating and measuring single voxels. Besides of those two parameters, the polymerization threshold P_{thresh} , the lateral and axial extensions of the cross-linking distribution σ_{xy}^{cl} , σ_z^{cl} , as well as the minimal and maximal shrinkage factors κ_{min} , κ_{max} have to be optimized. Based on the fabrication and measurement of the unmodified structures, we use a Downhill–Simplex algorithm [42] to perform this parameter optimization. In the end, this can lead to the prediction results exemplary shown in Fig. 8 for a radially symmetric chirped and an areal irregular surface topography. There, the overall conformity in terms of root-mean-square error (*rmse*) between the 3D prints (Fig. 8b and e) and their modeled predictions (Fig. 8c and f) is below 1 μm [37].

Thinking ahead, one can use this promising prediction model to pre-compensate for the deviations to be expected in two-photon polymerization. After only two correction iterations, again exemplary used a radially symmetric chirped topography, is in striking resemblance to its original target, as illustrated in Fig. 9. There, the *rmse* reduces from more than 4 μm between the unmodified 3D print (Fig. 9b) and its target

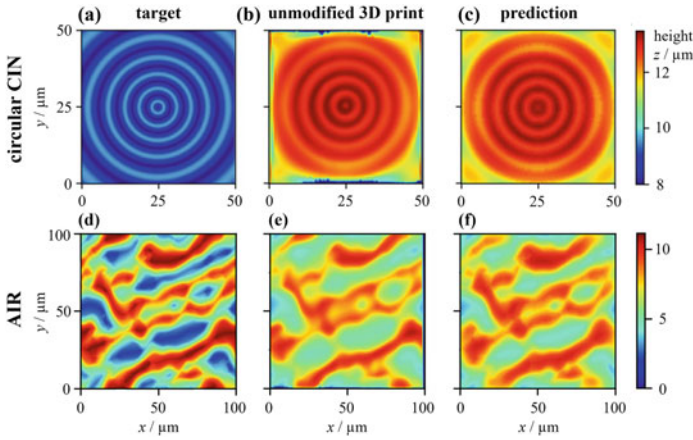


Fig. 8 A radially symmetric chirped (CIN, a–c) and an areal roughness (AIR, d–f) μ -structure serve as examples. The respective targets are shown in the first column, the unmodified printed and measured topographies are shown in the second column and their respective predictions are shown in the third column. Adapted with permission from [37]

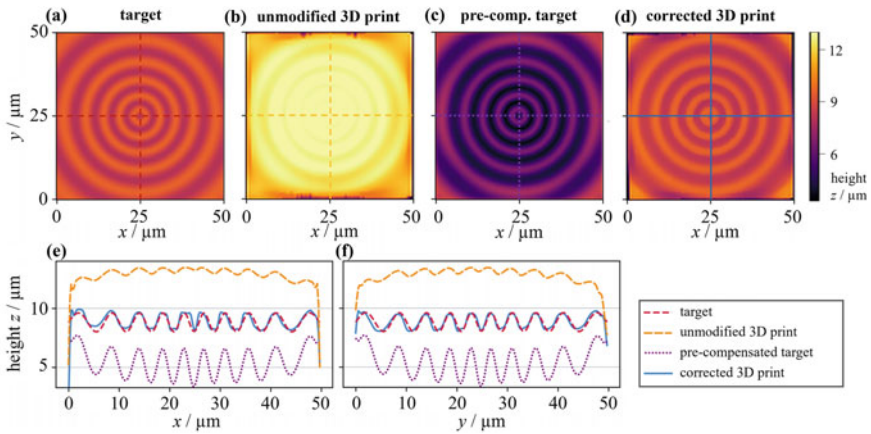


Fig. 9 The radially symmetric chirped (CIN) topography serves as an example for correcting the two-photon polymerization process, where (a) and (b) are equal to Fig. 8. Based on the prediction, one can modify the target structure in such a way (c), that its printed topography (d) strongly resembles the original target (a). Respective profiles are given in (e and f). Adapted with permission from [37]

(Fig. 9a) down to roughly 300 nm for the second correction iteration (Fig. 9d) [37]. This is evidently confirmed by the respective profiles, given in Fig. 9e, f and holds true for other structures with different dimensions as well.

4 Metallic Materials

Two routes have been followed in the past to fabricate metal microstructures using direct laser writing: 1. direct laser writing of polymeric template structures that are subsequently filled using galvanic growth (see, e.g., [43]); 2. direct laser writing of metallic structures using photoreductive [44] processes. The first is a well-known process and has led to 3D microstructures of extremely high-quality rivaling the quality of direct laser written polymer structures. However, this technique limits the freedom of structure design due to the bottom-up and area-dependent growth process. The second extends the concept of exploiting multi-photon-initiated chemical reactions for additive manufacturing to the fabrication of metallic microstructures [45–48]. The chemical reactions leading to metal microstructures and the structure formation process, however, differ fundamentally from polymerization presented in Sect. 3 and are thus reviewed here.

The structure formation process can be decomposed into five steps (see Fig. 10a for a scheme):

1. multi-photon excitation of a photoreducing agent,
2. electron transfer to a metal ion and reduction,
3. nucleation of metal atoms,
4. growth of metal nanoparticles, and
5. coalescence or agglomeration of nanoparticles to form the voxel.

A typical composition used for metal fabrication contains a solvent, a photoreducing agent, a metal precursor, and potentially a surfactant that allows control of the growth step. For example, to fabricate the silver structure in Fig. 10b, silver perchlorate was employed as the metal source, water as the solvent, and gelatin as the stabilizer and photoreducing agent. The photoreducing agent plays an important role. The challenge is to find a photoreducing agent that has an excited state reduction

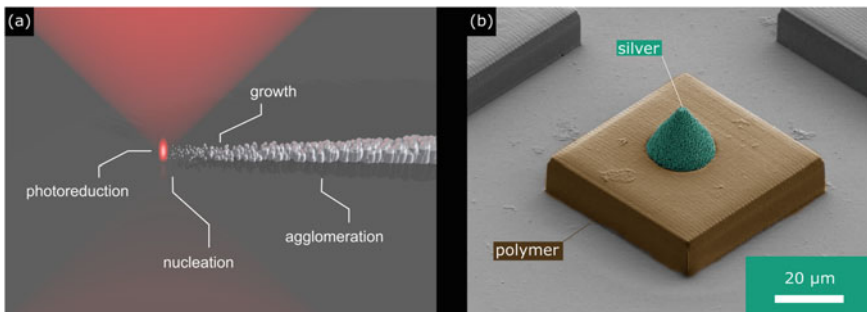


Fig. 10 **a** Scheme of the metal microstructure formation process: After multi-photon excitation the photoreducing agent reduces metal ions, the metal atoms nucleate, the nanoparticles grow, and finally, agglomerate to form the fundamental building block of the metal microstructure. **b** SEM image of a thus fabricated sample microstructure made of silver on top of a polymer cube

potential lower than the reduction potential of the metal ion to be reduced (e.g., the Ag^+ ion has a reduction potential of 0.8 V versus the standard hydrogen reference electrode). At the same time its ground state reduction potential needs to be higher than the reduction potential of the metal ion plus its two-photon absorption cross-section needs to be sufficiently large to photoinitiate the reaction (alternatively two-photon sensitizers are an option). Clearly, due to their higher reduction potential noble metals are more easily photoreduced compared to non-noble metals such as titanium or nickel.

Besides the challenge of selecting the right photoreducing agent, fabrication of metallic microstructures via multi-photon reduction is a slow process compared to fabrication via two-photon polymerization: While two-photon initiated polymerization takes place on the order of a few microseconds [8, 49], formation of a metallic voxel via nucleation, growth, and agglomeration requires several hundreds of milliseconds [50]. Since voxel formation efficiency strongly depends on optical forces to avoid diffusion of particles (see Sect. 4.2), voxel formation cannot happen in the dark. In direct consequence, the fabrication speed is reduced by several orders of magnitude compared to the fabrication speed via two-photon polymerization. In principle, the laser power could be increased to improve voxel formation efficiency and thus enable higher fabrication speeds. However, strong laser-matter-interaction sets very close limits to this option (Sect. 4.2).

Not surprisingly, most groups that have employed this method circumvented this issue by limiting themselves to planar silver [51], gold [52] and titania [53] microstructures. Others turned away from pure metal structures by combining polymerization of a host matrix and photoreduction of metal seeds leading to 3D polymer-nickel [54] or polymer-gold [55, 56] composite structures.

Only a few groups have fabricated true 3D pure metallic microstructures via the photoreduction method. One of those few reports on the fabrication of pure silver 3D microstructures is by *Tanaka et al.* where they directly reduced silver nitrate in water without a known photoreducing agent [45]. The thus obtained structure had a minimum feature size of 2 μm and very high surface roughness. In a follow-up publication, they included coumarin 440 as a photoreducing agent, which did not, however, lead to any visual improvement of fabricated 3D structures [57]. A reduction of feature size down to a few hundreds of nanometers and reduced surface roughness was obtained by the same group by using *n*-decanoylsarcosine sodium as a surfactant [58], however, design fidelity remained an issue. Finally, in 2021 we presented the already mentioned gelatin-based composition [48]. Due to high structural quality (see Sect. 4.1) with this composition, it was possible to fabricate 3D photonic components working in the mid-infrared. Besides silver, no other metal has up to now been directly printed in 3D in a one-step process via the photoreduction scheme.

4.1 Materials Properties

Materials suitable for the application of metallic direct laser writing are very sensitive, especially to the interaction with light, and therefore require very specific material properties. As mentioned in Sect. 4, the photosensitive material typically contains a solvent, a photoreducing agent, and a metal precursor. Furthermore, it may contain a surfactant that can be used to control the growth of the metallic structure.

The metal precursor is the component that provides the metal ion that is reduced to the desired material during the photoreaction process. Metal salts, e.g. silver perchlorate [48] or titanium lactate [59], are often suitable for this application.

In the process of direct laser writing, the photosensitive material is exposed to focused laser light, which triggers the reduction of the precursor and thus the formation of the metallic material. Responsible for initiating this process is the photoreducing agent, which must be chosen to be excited by multiphoton excitation in the laser focus. The laser we used was a femtosecond Ti:Sa laser pulsed at 80 MHz (Chameleon Ultra VIS, Coherent) with a tunable wavelength. Commercially available DLW systems operate at a central wavelength of 780 nm [48], so it stands to reason that photoreducing agents must be able to perform two-photon absorption at this wavelength. Another requirement for the choice of the photoreduction agent is that its reduction potential in the excited state must be lower than the reduction potential of the metal ion contained in the precursor, while its reduction potential in the ground state must be higher than the reduction potential of the metal ion. Possible photoreducing agents are, e.g., photoreduced dyes like methylene blue and proflavine [59].

Unlike the photoreducing agent and the metal precursor, no surfactant is necessarily required for the chemical redox process. Instead, surfactants like sodium hypophosphite or hexadecyltrimethylammonium bromide affect the properties of the growing metal structure, such as the formation of pores or grain sizes [60, 61]. It is therefore advisable to consider them on a more deferred basis. They offer an opportunity to subsequently improve previously discovered materials that function for the additive manufacturing of metal structures.

Figure 11 shows some three dimensional silver structures fabricated by direct laser writing using the gelatin-based material composition proposed in Sect. 4. These structures were analyzed in some of their properties. The smallest reproducible helix pitch was 2 μm leading to the conclusion that the resist supports an axial resolution of 500 lines/mm [48]. From the close-up view of the toppled helix in Fig. 11d it is found that the lateral and axial feature sizes both were approximately 760 nm. This result suggests the assumption of a spherical voxel which is probably caused by the deteriorating effect of the evolving structure in the focal field [48]. The deviation of the diameter of the helices from the mean diameter was determined as a measure for contour accuracy and found to be in the order of ± 100 nm with a mean roughness of approximately ± 30 nm [48].

While the helices in Fig. 11a, d and the right-angle structure in Fig. 11b were fabricated in single lines, the structures in Fig. 11c, e were fabricated using a

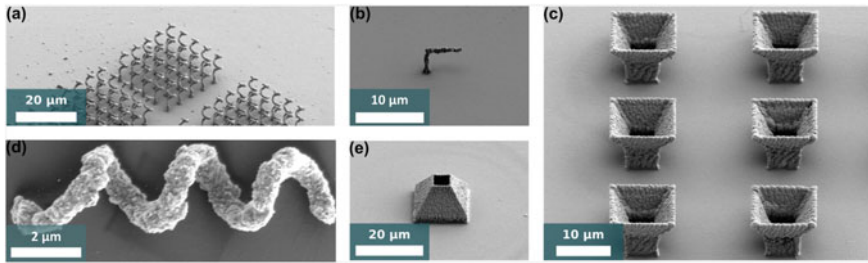


Fig. 11 3D silver structures fabricated via direct laser writing. **a** Arrays of filigree helices. **b** A right-angled structure. **c** An array of miniature horn antennas. **d** A toppled helix. **e** A hollow pyramid. Adapted with permission from [48]

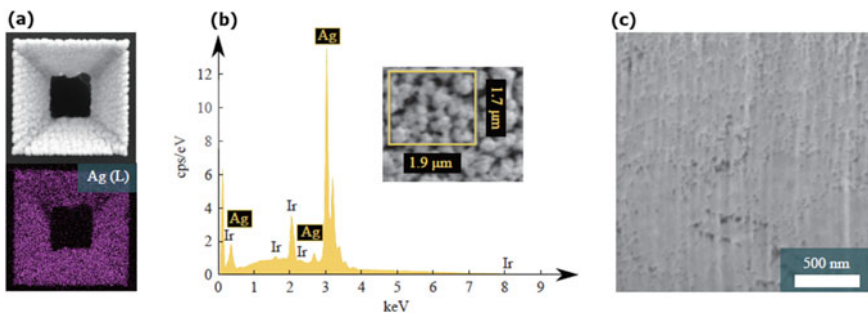


Fig. 12 **a** SEM images and EDX silver-count map of a 3D sample structure. **b** Electron diffraction X-ray spectrograph of a freshly fabricated 3D sample structure. The iridium peaks are due to post-fabrication sputtering of a 10 nm iridium layer that reduces charging effects during SEM. The inset shows the region where the spectrum was acquired. **c** SEM image of a focused-ion-beam-milled cross-section of a 3D sample structure showing a high material density and small average pore size. Adapted with permission from [48]

layer-by-layer approach. This results in a periodic, wave-like topography with an average pitch of approximately 670 nm [48]. This is possibly due to the same mechanism responsible for the formation of laser-induced periodic surface structures [62], where the incident light interferes with scattered or diffracted light near the surface of the structure. This factor leads to a peak-to-valley deviation of the flat surface of approximately ± 150 nm and obviously reduces the contour accuracy compared to that determined from the helix [48].

To determine the silver content of the additively fabricated structures, the sample was examined using a scanning electron microscope (SEM) capable of electron diffraction X-ray (EDX) spectroscopy. An acceleration voltage of 10 kV was used for the measurement, corresponding to an approximate probing depth of 300 nm [48]. The EDX silver count map and spectrum of analysis can be found in Fig. 12a, b. In addition, Fig. 12b shows an inset visualizing the region where the spectrum was acquired. While the count map proves that silver was found exactly in the area of the structure, the spectrum proves that the structure consists of almost 100 wt%

silver at the examined surface. The only other element present in this analysis is iridium which is sputtered onto the sample before SEM to avoid charging effects [48]. Figure 12c shows an SEM image of a cross-section of such structures, which was revealed by focused ion beam milling. An EDX analysis of this cross section revealed approximately 99 wt% silver with some traces of calcium, lead, and sulfur [48]. Also, from this cross section the material density was determined. The average material density was 95% with an average pore diameter of 27 nm [48].

Another important property of silver microstructures for their application as conductive functional components is their conductivity. The high purity and material density of the structures in Fig. 11 promise a good conductivity like bulk silver. For this purpose, 3D wires with a length of 90 μm and a diameter of 1 μm were fabricated and investigated. Thus, the specific resistivity of the additive manufactured material was found to be in the order of $3.3 \times 10^{-5} \Omega\text{m}$, while for bulk silver it was $1.6 \times 10^{-8} \Omega\text{m}$ [48]. Since gelatin melts at moderate temperatures, heating the material to 50 $^{\circ}\text{C}$ for 3 hours leads to a drop of the specific resistivity to $6.7 \times 10^{-6} \Omega$, which is comparable to that of directly written conductive polymers which only supported 2D structures [48, 63].

In summary, with the materials described in Sect. 4 and their properties described in Sect. 4.1, an important step has been made towards the development of novel materials for the application of additive manufacturing of metallic microstructures with properties suitable for a wide range of applications.

4.2 Modelling of the Fabrication Process

As explained above in Sect. 4, the fabrication rate is limited by nucleation and growth of the silver particles. Thus, in order to maximize the fabrication speed, optimal utilization of the nuclei produced is central. This means that it must be ensured that the nuclei do not diffuse out of the laser focus but continue to grow there and aggregate to form the structure to be fabricated. The optical forces exerted by the laser on nanoparticles can have a supporting effect here. This phenomenon is also commonly known as optical tweezers [64, 65] and has also been studied and modeled theoretically [66, 67]. At the same time, however, nanoparticles very efficiently absorb the irradiated laser power [68] and can thus cause the photoresist to boil. The resulting gas bubbles usually damage the structure to be fabricated and are therefore also referred to as “microexplosions” in the jargon.

As part of CRC 926, we have developed and published a simulation model for the interaction of nanoparticles and lasers in the fabrication process [69]. We omit photochemistry and instead assume an idealized particle source, which produces nanoparticles at a defined rate, at the laser focus. Our simulations depict the influence of the optical forces of the laser on the diffusion and deposition of the particles. Furthermore, the heating as well as the dynamics of the photoresist induced by this is taken into account. With such simulations, we investigate the effects of optical

configuration and scanning speed on the deposition of the particles and characterize the relative importance of the different phenomena involved in the process.

The key element of this model is the transport equation for the local concentration c of the nanoparticles. In a reference frame moving with the laser focus, this equation reads

$$\frac{\partial c}{\partial t} + \nabla \cdot \{(\mathbf{u} + \gamma^{-1}\mathbf{F}_{\text{opt}})c\} = -\nabla \cdot (D\nabla c) + S_c, \quad (6)$$

where D denotes the diffusion constant and γ the Stokes friction coefficient (cf. [70]). Here, the term $(\mathbf{u} + \gamma^{-1}\mathbf{F}_{\text{opt}})c$ accounts for the advection of the particles due to the laser scanning and flow of the photoresist as well as the optical forces \mathbf{F}_{opt} of the laser. S_c denotes the source density of particle production, where the production rate is determined by comparison with experiment. The extent of this source is assumed to correspond to the intensity square of the laser.

The temperature evolution in the photoresist is described by a heat conduction equation. Since the photoresist is essentially transparent to the irradiated laser, we assume the nanoparticles to be the only heat source. With their absorption cross section σ_{abs} and local light intensity I , this heat source is given by $cI\sigma_{\text{abs}}$.

Our simulations show that the optical forces of the laser always significantly outweigh the influence of the convection of the photoresist. Consequently, even adding a second laser would not destabilize the fabrication process by increasing convection. Rather, the potential laser power is limited by the evaporation of the photoresist when heated too much. The laser powers at which damage to the written structures is reproducibly visible in experiments are similar to the laser powers for which our simulations predict photoresist boiling. In this context, we find that the largest particles present are responsible for this phenomenon, since they are highly concentrated at the focus due to their strong polarizability and offer particularly large absorption cross sections to the irradiated light.

Furthermore, we investigate the influence of process parameters such as scanning speed, laser power, and laser focusing on the deposition of the growing nanoparticles. For this purpose, we determine the fraction q of particles adsorbing on a line to be written. This deposition efficiency q is approximately halved by increasing the scanning speed from 10 μm to 100 $\mu\text{m/s}$ (see Fig. 13) for the particle sizes of 30...60 nm which are typical for the experiment. In contrast, q is maximized by the highest possible laser power and focusing (NA); at a particle diameter of 60 nm and moderate scanning speeds, $q \approx 1$ (see Fig. 14).

Complementary to these simulations, silver lines with varying scanning speed and numerical aperture were produced in the experiment. Atomic force microscopy (AFM) was used to measure the cross-sections of the lines and their roughness. Thus, we obtained realistic values for the particle production S_c and were able to compare the velocity dependence of the deposition of simulation and experiment. Here, our data support the assumption that in the experiment, some of the particles grow directly on the substrate and are therefore less sensitive to an increase in traverse speed. We could not prove a suspected correlation between the parameter-dependent deposition efficiency of large particles in our simulations and the roughness of the fabricated

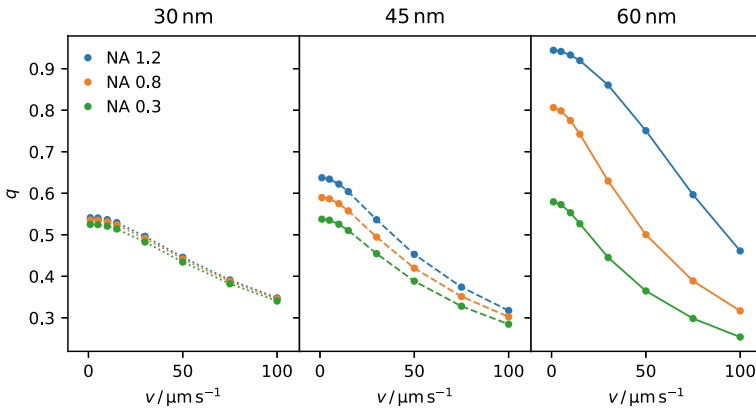


Fig. 13 Deposition efficiency as a function of scanning speed (after [69]) for three exemplary numerical apertures (NA) and particle diameters 30...60 nm (left to right). Laser power 6 mW, wavelength 780 nm. Towards higher scanning speeds, the deposition efficiency decreases, especially markedly for larger particles. Smaller particles are less affected by NA or scanning speed because their behavior is dominated by diffusion. Larger NAs generally improve the deposition of large particles

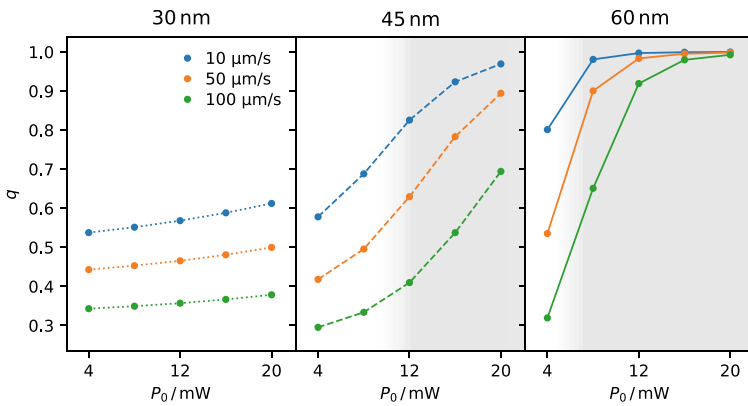


Fig. 14 Deposition efficiency as a function of laser power (after [69]) at three exemplary scanning speeds (10, 50, 100 $\mu\text{m/s}$ and particle diameters 30...60 nm (left to right). Wavelength 780 nm, NA = 1.2. The gray shaded areas indicate powers at which photoresist boiling is to be expected for the respective particle diameter. For larger particles, increasing the power causes a significant improvement in deposition

structures; apart from the trapping effect of the laser, other factors favor the growth of large particles in the experiment.

5 Summary

During the funding period of CRC 926, two-photon laser lithography has been established as one of the most suitable additive manufacturing tools for creating surface morphologies. Complex test structures on the micron-scale have been implemented to deliver an objective criterion for comparison of different manufacturing devices. Moreover, fundamental improvements in the fabrication have been achieved, such as an automated aberration correction algorithm for high numerical aperture systems. More importantly, the crucial step from polymeric structures towards metallic 3D micro-printing has been taken successfully and widens the field of application, e.g., to more demanding micro-electromechanical systems (MEMS) or magnetic implementations. As a decisive condition for that, a deeper understanding of the chemical processes during the fabrication has to be named. Here, numerical simulation approaches for metallic, as well as polymeric materials have made a significant contribution and, furthermore, have led to the computational prediction and correction of two-photon laser lithographically manufactured microstructures.

References

1. Hahn V, Kiefer P, Frenzel T, Qu J, Blasco E, Barner-Kowollik C, Wegener M (2020) Rapid assembly of small materials building blocks (Voxels) into large functional 3D metamaterials. *Adv Funct Mater* 2020:1907795. <https://doi.org/10.1002/adfm.201907795>
2. Maruo S, Nakamura O, Kawata S (1997) Three-dimensional microfabrication with two-photon-absorbed photopolymerization. *Opt Lett* 22, 2:132–134. <https://doi.org/10.1364/OL.22.000132>
3. von Freymann G, Ledermann A, Thiel M, Staude I, Essig S, Busch K, Wegener M (2010) Three-dimensional nanostructures for photonics. *Adv Funct Mater* 20:1038. <https://doi.org/10.1002/adfm.200901838>
4. Hohmann JK, Renner M, Waller EH, von Freymann G (2015) Three-dimensional?-Printing: an enabling technology. *Adv Optical Mater* 3:1488. <https://doi.org/10.1002/adom.201500328>
5. Fischer J, Wegener M (2013) Three-dimensional optical laser lithography beyond the diffraction limit. *Laser Photon Rev* 7, 1:22–44. <https://doi.org/10.1002/lpor.201100046>
6. Hering J, Waller EH, von Freymann G (2016) Automated aberration correction of arbitrary laser modes in high numerical aperture systems. *Opt Express* 24:28500–28508. <https://doi.org/10.1364/OE.24.028500>
7. Waller E, Renner M, von Freymann G (2012) Active aberration- and point-spread-function control in direct laser writing. *Opt Exp* 20:24949. <https://doi.org/10.1364/OE.20.024949>
8. Waller EH, von Freymann G (2015) Multi foci with diffraction limited resolution. *Opt Exp* 21:21708. <https://doi.org/10.1364/OE.21.021708>
9. Dai G, Hu X, Hering J, Eifer M, Seewig J, von Freymann G (2021) Define and measure the dimensional accuracy of two-photon laser lithography based on its instrument transfer function. *J Phys: Photon* 3:034002. <https://doi.org/10.1088/2515-7647/abfaa7>

10. Guillet J (1985) *Polymer photophysics and photochemistry*. Cambridge University Press, New York, NY
11. Odian G (2004) *Principles of polymerization*. Wiley
12. Sun H-B, Kawata S (2004) Two-Photon photopolymerization and 3D lithographic microfabrication. In: *NMR o 3D analysis o photopolymerization*. Springer, Berlin, Heidelberg. <https://doi.org/10.1007/b94405>
13. Ravve A (2006) *Light-associated reactions of synthetic polymers*. Springer
14. Sadasivuni KK, Chen D, Almaadeed MA (2020) 3D and 4D printing of polymer nanocomposite materials: processes, applications and challenges. Elsevier
15. Crivello JV, Reichmanis E (2014) Photopolymer materials and processes for advanced technologies. *Chem Mater* 26, 1:533–548. <https://doi.org/10.1021/cm402262g>
16. Hering J (2020) Von der STED inspirierten Zwei-Photonen Laserlithographie zur industriellen Metrologie. PhD thesis. Technische Universität Kaiserslautern
17. Nanoscribe GmbH & Co KG NanoGuide. Nanoscribe GmbH & Co KG, 12 Aug 2022. Germany
18. Baldacchini T (2015) Three-dimensional microfabrication using two-photon polymerization: fundamentals, technology, and applications. William Andrew
19. Wolf TJ (2012) *Ultrafast photophysics and photochemistry of radical precursors in solution*. KIT Scientific Publishing
20. Norrish RG, Kirkbride FW (1932) 204. Primary photochemical processes. Part I. The decomposition of formaldehyde. *J Chem Soc (Resumed)* 1518–1530. <https://doi.org/10.1039/JR9320001518>
21. Frick E (2016) Mechanistic investigation of photoinitiation processes via PLPESI-MS. PhD thesis. Karlsruher Institut für Technologie
22. Decker C (1996) Photoinitiated crosslinking polymerisation. *Prog Polym Sci* 21, 4:593–650. [https://doi.org/10.1016/0079-6700\(95\)00027-5](https://doi.org/10.1016/0079-6700(95)00027-5)
23. Fouassier J-P, Lalevère J (2012) *Photoinitiators for polymer synthesis: scope, reactivity, and efficiency*. Wiley
24. Zhdankin VV (2013) *Hypervalent iodine chemistry: preparation, structure, and synthetic applications of polyvalent iodine compounds*. Wiley
25. Dammel R (1993) *Diazonaphthoquinone-based resists*, vol 11. SPIE Press
26. Chang T (1975) Proximity effect in electron-beam lithography. *J Vac Sci Technol* 12, 6:1271–1275. <https://doi.org/10.1116/1.568515>
27. Waller EH, von Freymann G (2016) Spatio-Temporal proximity characteristics in 3D-printing via multi-photon absorption. *Polymers* 8, 8:297. <https://doi.org/10.3390/polym8080297>
28. Yang L, Münchinger A, Kadic M, Hahn V, Mayer F, Blasco E, Barner-Kowollik C, Wegener M (2019) On the schwarzschild effect in 3D two-photon laser lithography. *Adv Opt Mater* 7, 22:1901040. <https://doi.org/10.1002/adom.201901040>
29. Jiang LJ, Zhou YS, Xiong W, Gao Y, Huang X, Jiang L, Baldacchini T, Silvain J-F, Lu YF (2014) Two-Photon polymerization: investigation of chemical and mechanical properties of resins using raman microspectroscopy. *Opt Lett* 39, 10:3034–3037. <https://doi.org/10.1364/OL.39.003034>
30. Schwarzschild K (1900) On the deviations from the law of reciprocity for bromide of Silver Gelatine. *Astrophys J* 11:89. <https://doi.org/10.1086/140669>
31. Zhou X, Hou Y, Lin J (2015) A review on the processing accuracy of two-photon polymerization. *Aip Adv* 5, 3:030701. <https://doi.org/10.1063/1.4916886>
32. Denning RG, Blanford CF, Urban H, Bharaj H, Sharp DN, Turberfield AJ (2011) The control of shrinkage and thermal instability in SU-8 photoresists for holographic lithography. *Adv Funct Mater* 21, 9:1593–1601. <https://doi.org/10.1002/adfm.201002653>
33. Meisel DC, Diem M, Deubel M, Pérez-Willard F, Linden S, Gerthsen D, Busch K, Wegener M (2006) Shrinkage precompensation of holographic three-dimensional photonic-crystal templates. *Adv Mater* 18, 22:2964–2968. <https://doi.org/10.1002/adma.200600412>
34. Sun Q, Ueno K, Misawa H (2012) In Situ investigation of the shrinkage of photopolymerized micro/nanostructures: the effect of the drying process. *Opt Lett* 37, 4:710–712. <https://doi.org/10.1364/OL.37.000710>

35. Purto J, Verch A, Rogin P, Hensel R (2018) Improved development procedure to enhance the stability of microstructures created by two-photon polymerization. *Microelectron Eng* 194:45–50. <https://doi.org/10.1016/J.MEE.2018.03.009>
36. Oakdale JS, Ye J, Smith WL, Biener J (2016) Post-Print UV curing method for improving the mechanical properties of prototypes derived from two-photon lithography. *Opt Exp* 24, 24:27077–27086. <https://doi.org/10.1364/OE.24.027077>
37. Lang N, Enns S, Hering J, von Freymann G (2022) Towards efficient structure prediction and pre-compensation in multi-photon lithography. *Opt Exp* 30, 16:28805–28816. <https://doi.org/10.1364/OE.462775>
38. Purto J, Rogin P, Verch A, Johansen VE, Hensel R (2019) Nanopillar diffraction gratings by two-photon lithography. *Nanomaterials* 9, 10:1495. <https://doi.org/10.3390/nano9101495>
39. Pingali R, Saha SK (2022) Reaction-Diffusion modeling of photopolymerization during femtosecond projection two-photon lithography. *J Manuf Sci Eng* 144, 2. <https://doi.org/10.1115/msec2021-60255>
40. Guney M, Fedder G (2016) Estimation of line dimensions in 3D direct laser writing lithography. *J Micromech Microeng* 26, 10:105011. <https://doi.org/10.1088/0960-1317/26/10/105011>
41. Adão RM, Alves TL, Maibohm C, Romeira B, Nieder JB (2022) Two-Photon polymerization simulation and fabrication of 3d microprinted suspended waveguides for on-chip optical interconnects. *Opti Exp* 30, 6:9623–9642. <https://doi.org/10.1364/oe.449641>
42. Nelder JA, Mead R (1965) A simplex method for function minimization. *Comput J* 7, 4:308–313. <https://doi.org/10.1093/COMJNL/7.4.308>
43. Gansel J, Thiel M, Rill M, Decker M, Bade K, Saile V, von Freymann G, Linden S, Wegener M (2009) Gold helix photonic metamaterial as broadband circular polarizer. *Science* 325, 5947:1513–1515. <https://doi.org/10.1126/science.1177031>
44. Tabrizi S, Cao Y, Lin H, Jia B (2017) Two-Photon reduction: a cost-effective method for fabrication of functional metallic nanostructures. *Sci China-Phys Mech Astron* 60:034201. <https://doi.org/10.1007/S11433-016-0447-6>
45. Tanaka T, Ishikawa A, Kawata S (2006) Two-Photon-Induced reduction of metal ions for fabricating three-dimensional electrically conductive metallic microstructure. *Appl Phys Lett* 88:081107. <https://doi.org/10.1063/1.2177636>
46. Waller E, von Freymann G (2018) From photoinduced electron transfer to 3D metal microstructures via direct laser writing. *Nanophotonics* 7, 7:1259–1277. <https://doi.org/10.1515/nanoph-2017-0134>
47. Waller E, Dix S, Gutsche J, Widera A, von Freymann G (2019) Functional metallic micro-components via liquid-phase multiphoton direct laser writing: a review. *Micromachines* 10, 12:827. <https://doi.org/10.3390/mi10120827>
48. Waller E, Karst J, von Freymann G (2021) Photosensitive material enabling direct fabrication of filigree 3D silver microstructures via laser-induced photoreduction. *Light: Adv Manuf* 2, 8. <https://doi.org/10.37188/LAM.2021.008>
49. Mueller J, Fischer J, Mayer F, Kadic M, Wegener M (2014) Polymerization kinetics in three-dimensional direct laser writing. *Adv Mater* 26, 38:6566–6571. <https://doi.org/10.1002/adma.201402366>
50. Yang L, Rahimzadegan A, Hahn V, Blasco E, Rockstuhl C, Wegener M (2022) In Situ diagnostics and role of light-induced forces in metal laser nanoprinting. *Laser Photonics Rev* 16, 3:2100411. <https://doi.org/10.1002/lpor.202100411>
51. Saha SK, Au B, Oakdale JS (2019) High-Speed direct laser writing of silver nanostructures via two-photon reduction. *Adv Eng Mater* 21, 9:1900583. <https://doi.org/10.1002/adem.201900583>
52. Lu W, Zhang Y, Zheng M, Jia Y, Liu J, Dong X, Zhao Z, Li C, Xia Y, Ye T, Duan X (2013) Femtosecond direct laser writing of gold nanostructures by ionic liquid assisted multiphoton photoreduction. *Opt Mater Exp* 3:1660–1673. <https://doi.org/10.1364/OME.3.001660>
53. Yu S, Schrodj G, Mougin K, Dentzer J, Malval J, Zan H, Soppera O, Spangenberg A (2018) Direct laser writing of crystallized TiO₂ and TiO₂/Carbon microstructures with tunable conductive properties. *Adv Mater* 30:1805093. <https://doi.org/10.1002/adma.201805093>

54. Vyatskikh A, Delalande S, Kudo A, Zhang X, Portela C, Greer J (2018) Additive manufacturing of 3D nano-architected metals. *Nat Commun* 9, 593. <https://doi.org/10.1038/s41467-018-03071-9>
55. Shukla S, Furlani P, Vidal X, Swihart M, Prasad P (2010) Two-Photon lithography of sub-wavelength metallic structures in a polymer matrix. *Adv Mater* 22, 33:3695–3699. <https://doi.org/10.1002/adma.201000059>
56. Blasco E, Müller P, Trouillet V, Schön M, Scherer T, Barner-Kowollik C, Wegener M (2016) Fabrication of conductive 3D gold-containing microstructures via direct laser writing. *Adv Mater* 28, 18:3592–3395. <https://doi.org/10.1002/adma.201506126>
57. Ishikawa A, Tanaka T, Kawata S (2006) Improvement in the reduction of silver ions in aqueous solution using two-photon sensitive dye. *Appl Phys Lett* 89:113102. <https://doi.org/10.1063/1.2345601>
58. Cao Y, Takeyasu N, Tanaka T, Duan X, Kawata S (2009) 3D metallic nanostructure fabrication by surfactant-assisted multiphoton-induced reduction. *Small* 5, 10:1144–1148. <https://doi.org/10.1002/smll.200801179>
59. Oster G, Oster G (1959) Photoreduction of metal ions by visible light1. *J Am Chem Soc* 81, 21:5543–5545. <https://doi.org/10.1021/JA01530A007>
60. Chen B-H, Hong L, Ma Y, Ko T-M (2002) Effects of surfactants in an electroless nickel-plating bath on the properties of Ni-P Alloy deposits. *Ind Eng Chem Res* 41, 11:2668–2678. <https://doi.org/10.1021/IE0105831>
61. Guo C, Zuo Y, Zhao X, Zhao J, Xiong J (2008) Effects of surfactants on electrodeposition of nickel-carbon nanotubes composite coatings. *Surf Coat Technol* 202, 14:3385–3390. <https://doi.org/10.1016/J.SURFCOAT.2007.12.005>
62. Barton P, Mukherjee S, Prabha J, Boudouris BW, Pan L, Xu X (2017) Fabrication of silver nanostructures using femtosecond laser-induced photoreduction. *Nanotechnology* 28, 50:505302. <https://doi.org/10.1088/1361-6528/aa977b>
63. Luo Z, Liu Y, Liu Z, Wang D, Gan Z, Xie C (2020) Direct laser writing of nanoscale undoped conductive polymer. *Nanotechnology* 31, 25:255301. <https://doi.org/10.1088/1361-6528/ab7de4>
64. Ashkin A (1970) Acceleration and trapping of particles by radiation pressure. *Phys Rev Lett* 24, 4:156–159. <https://doi.org/10.1103/physrevlett.24.156>
65. Ashkin A (2000) History of optical trapping and manipulation of small-neutral particle, atoms, and molecules. *IEEE J Sel Top Quantum Electron* 6, 6:841–856. <https://doi.org/10.1109/2944.902132>
66. Nieminen TA, Loke VLY, Stilgoe AB, Knöner G, Brańczyk AM, Heckenberg NR, Rubinsztein-Dunlop H (2007) Optical tweezers computational toolbox. *J Opt A: Pure Appl Opt* 9, 8:S196–S203. <https://doi.org/10.1088/1464-4258/9/8/s12>
67. Nieminen TA, du Preez-Wilkinson N, Stilgoe AB, Loke VL, Bui AA, Rubinsztein-Dunlop H (2014) Optical tweezers: theory and modelling. *J Quant Spectrosc Radiat Trans* 146:59–80. <https://doi.org/10.1016/j.jqsrt.2014.04.003>
68. Baffou G, Rigneault H (2011) Femtosecond-Pulsed optical heating of gold nanoparticles. *Phys Rev B* 84, 3, 035415:035415. <https://doi.org/10.1103/physrevb.84.035415>
69. Palmer T, Waller EH, Andrä H, Steiner K, von Freymann G (2021) Simulation model for direct laser writing of metallic microstructures composed of silver nanoparticles. *ACS Appl Nano Mater* 4, 9:8872–8879. <https://doi.org/10.1021/acsanm.1c01514>
70. Gillespie DT, Seitaridou E (2012) Simple brownian diffusion. Oxford University Press. <https://doi.org/10.1093/acprof:oso/9780199664504.001.0001>

Interactions Between Particles and Surfaces



Kristin M. de Payrebrune, Clarissa Schönecker, Sergiy Antonyuk, Raphael Bilz, Fabian Krull, Isabell Noichl, Siegfried Ripperger, and David Strohner

Abstract Interactions between particles and surfaces play a significant role in many technical systems. To better understand the impact of particles on the overall behavior, the interactions between particles and surfaces are investigated experimentally and numerically for three generalized systems. The systems are chosen such that they differ in the number, mechanical properties, and kinematics of the particles, in the applied surrounding fluid, and in the spacial and temporal scales. In system one, the topography resulting from the interaction of abrasive particles being in contact with surfaces is analyzed. Depending on particle size and wetting conditions, the resulting topography varies from uniformly scattered to single local indentations. System two represents impacting particles on surfaces. The rebound behavior varies strongly depending on the local structure of the surface and the wetting conditions, which can cause additional adhesive forces. System three investigates particles moving in a liquid close to a surface. Though not being in direct contact with the surface, the liquid mediates interactions between the particles and the surface. The particle's trajectory depends strongly on its elastic modulus. These three systems are used to

K. M. de Payrebrune and C. Schönecker have contributed equally.

K. M. de Payrebrune (✉) · R. Bilz
Institute for Computational Physics in Engineering, RPTU Kaiserslautern, Kaiserslautern, Germany
e-mail: kristin.payrebrune@mv.rptu.de

C. Schönecker (✉) · I. Noichl
Institute of Micro Fluid Mechanics, RPTU Kaiserslautern, Kaiserslautern, Germany
e-mail: c.schoenecker@mv.rptu.de

S. Antonyuk · F. Krull · S. Ripperger · D. Strohner
Institute of Particle Process Engineering, RPTU Kaiserslautern, Kaiserslautern, Germany

© The Author(s), under exclusive license to Springer Nature Switzerland AG 2024
J. C. Aurich and H. Hasse (eds.), *Component Surfaces*, Springer Series in Advanced Manufacturing, https://doi.org/10.1007/978-3-031-35575-2_8

analyze special particle surface interactions independently. However, the results can also be used to characterize real applications, in which these interactions may occur in combination.

1 Introduction

Particles influence the behavior of many technical applications and have a considerable impact on the system dynamics, the tribological behavior of the components in contact (lubrication, friction, and surface wear), and thus also on their service life and efficiency.

In order to analyze the interaction through experiments and to model the contact phenomena, the various influences and effects must be precisely identified and described. In the following, the most important influences for the investigation shown here are explained for three-body contact, ref. Fig. 1a, two-body contact, ref. Fig. 1b, and fluid-contact, ref. Fig. 1c. Thereby, the effects can take place on different time scales (impact/quasi-static), length scales (nano-, meso-, or microscale) and are dependent on the particle itself (amount, size, shape, and stiffness), and its kinematics (rolling, sliding, and floating).

In three-body contact (Fig. 1a), the particles are in contact with both mating bodies, the so-called “first” bodies [1], between which they are located. When it comes to a permanent interaction between a layer of abrasive particles and a surface in a three-body contact with relative tangential motion, as investigated in Sect. 2, the kinematics play an important role in friction and wear. Due to the elastic or plastic deformation of the softer body during contact or adhesive bonds, a tangential force needs to be overcome for motion. This tangential force additionally depends on the type of motion, as rolling, spinning, sliding, or a combination of them. For each type of motion, a different ratio of tangential force F_t to normal force F_n results that is defined as kinetic coefficient of friction μ_k in Coulomb’s friction law $F_t = \mu_k F_n$. Only in the case of sticking the relation changes to $F_t \leq |\mu_s F_n|$, with the coefficient of static friction $\mu_s > \mu_k$. Even though more complex friction models exist, which account for effects due to wetting or lubrication, Coulomb’s friction law is the most common one.

Contact and friction are always accompanied by wear, which leads to material removal of one or both “first” bodies. For the investigated three-body contact the

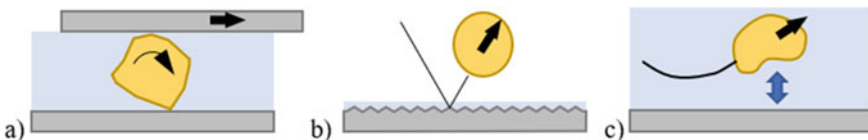


Fig. 1 Different types of particles interacting with their environment: **a** three-body contact, **b** two-body contact during impact, and **c** fluid-mediated contact of an immersed particle

material loss due to abrasion is most dominant, when the harder particle penetrates the softer “first” bodies [2].

In contrast, during a two-body impact of a particle with a structured or wetted surface (Fig. 1b), as described in Sect. 3, especially the energy dissipation during rebound is of particular interest. The coefficient of restitution e summarizes energy dissipating effects due to plastic deformation, adhesion, or friction, which results in slower rebounds compared to the impacts of the particles. The coefficient of restitution is a ratio of the kinetic energy before and after rebound with $\Delta E_{\text{kin}} = \frac{m_1 \cdot m_2}{2(m_1 + m_2)} (v_1 - v_2)^2 \cdot (1 - e^2)$. If no change of mass by agglomeration or breakage is happening, e can be simplified to a ratio of velocities. Typical values range from $e = 0$ for perfectly inelastic collision to $e = 1$ for perfectly elastic collision. The coefficient of restitution can also be divided into a normal and tangential component, accounting for friction effects during oblique collisions that lead to rotations of the particle. Impacts on wetted surfaces are affected by the viscosity and surface tension of the fluid. The viscosity leads to a viscous drag force contrary to the velocity acting on the particle, which increases with smaller distances. Depending on the surface tension and wettability, forces act on a particle through liquid bridges.

In the case of fluid mediated contact (Fig. 1c), the particle does not touch the surface directly, but the contact is mediated by a fluid in between. Through the fluid, the particle is subjected to influences from the surface, such as an increased drag or an induced rotation. An important class of particles are soft particles, e.g., bioparticles, microplastics, emulsions in food processing, etc. For such soft particles, the pressure between the particle and the surface may deform the particle, which in turn creates forces on the particles that alter the particle trajectories. The effect of these elasticity-induced lift forces are investigated in Sect. 4.

2 Contact Phenomena of Abrasive Particles at Surfaces

In order to adequately model a tribological three-body system, both the accuracy of the results of interest and the computational performance must be within an acceptable range. In different tribological three-body systems, different phenomena may be of importance, also depending on the desired results. Therefore, we follow a modular design of the model so that new effects can be additionally integrated into the model if required.

In a three-body system with a layer of hard particles, wear is distinguished on the basis of the particles' motion. If the particles are permanently embedded in one of the two bodies, the wear is called two-body abrasive wear; if the particles roll and slide intermittently, the wear is called three-body abrasive wear [3]. Hard, abrasive particles often have an irregular, angular shape, which influences the dynamics of the tribological system [4] on the one hand and the resulting surface morphology [5] on the other hand.

Both the dynamic behavior and the resulting surface topographies of the first bodies are two very important aspects of tribological three-body systems. The dynamics

of the tribological three-body system strongly interacts with its environment. This can be seen, for example, in the fact that the nature of the applied load can cause a significant change in the dynamic behavior even at the same mean load, especially at increased relative tangential velocities [4, 6]. The resulting surface topography of a first body can influence its subsequent application behavior, e.g., the load carrying capacity of hydrodynamic plain bearings [7], the sealing effect of static seals [8] or hydrodynamic seals [9].

There already exist some specialized models to describe selected tribological three-body systems. For example, some models describing lapping processes can be found in [10]. However, these models do not focus on the dynamics of the first bodies. In contrast, the model proposed in Sect. 2.2 is designed to explicitly capture physical interactions time-resolved.

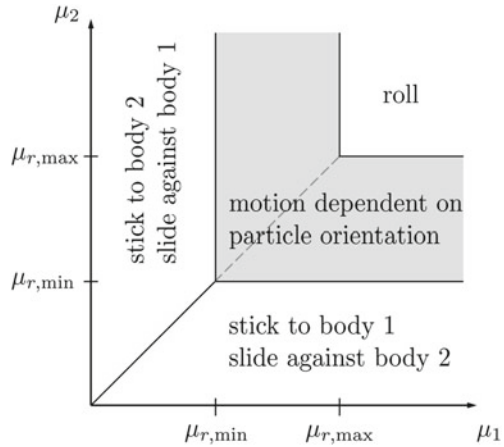
2.1 Phenomena in Tribological Three-Body Systems

Section 2 addresses various issues related to tribological three-body systems consisting of two first bodies that are loaded against each other with abrasive particles in between. In Fig. 1a an example of this kind of tribological system is sketched. Such tribological systems can be found, for example, in gearboxes in sandy environments [11] or in lapping processes [12].

To cause a particle to roll between the two first bodies, a certain ratio of tangential force to normal force must be transmitted in the two contacts between the particle and the respective first body, which depends on the particle shape and its orientation. If the actual coefficients of friction μ_1 and μ_2 in the two contacts are at least as large as the required ratio of tangential force to normal force, the particle rolls; otherwise, the particle slides in contact with the lower coefficient of friction. In Fig. 2, the types of motion of a particle are sketched in the μ_1 - μ_2 diagram. Assuming constant coefficient of frictions μ_1 between the particle and the lower first body (body 1) and μ_2 between the particle and the upper first body (body 2), the conditions can be used to describe the types of motion of a particle in a tribological three-body system. If one of the two coefficients of friction μ_1 or μ_2 is lower than the minimum ratio of tangential and normal force $\mu_{r,\min}$ required for rolling, the particles will always slide. In case both coefficient of frictions μ_1 or μ_2 are larger than the maximum ratio $\mu_{r,\max}$ of tangential to normal force required for rolling, the particles will always roll. Otherwise, rolling and sliding may occur intermittently, depending on the current orientation of the particle in the gap between the first bodies. For example, a coefficient of friction $\mu = 1$ is required for a lying cube to roll over the edges, but a coefficient of friction of $\mu_{r,\max} = \sqrt{2}$ is required for a cube to roll over its diagonal [13].

Rolling particles can decisively influence the system dynamics. Hard, non-spherical particles cause the behavior of the tribological system to depend on the tangential relative velocity of the two first bodies. When the tangential relative velocity exceeds a certain velocity limit v_{lim} , the contact between the first bodies

Fig. 2 Limiting cases and transition range of particle motions rolling and sliding in the μ_1 - μ_2 -diagram when the force ratio required for rolling is between $\mu_{r,min}$ and $\mu_{r,max}$ depending on the particle orientation



and the particles is not permanent anymore but temporarily interrupted. This effect depends primarily on the particle size, the particle shape, the type of load application, and the inertias of the first bodies. Furthermore, the velocity limit is also influenced by the deformation (shift v_{lim} upwards). Therefore, a tribological system can behave similar when replacing the method of load application (e.g., using a spring instead of deadweight) for low velocities, but may differ substantially for high velocities [4, 6].

When also fluid is present between the two first bodies, it affects the tribological system in several ways. Fluids in narrow gaps have a damping effect [14]. If the distance between the two first bodies changes, fluid is either pushed out of the gap or pulled into it. For simple geometries, analytical solutions exist to describe the fluid force, e.g., in [2]. In addition, fluids can cause a velocity-dependent separation of the first bodies up to a certain load limit, as is known from hydrodynamic bearings [15]. The lubricant film thickness increases with increasing speed, increasing viscosity, and decreasing load [10]. If the lubricant film thickness exceeds the particle size, the indentation of the particles into the first bodies is even completely prevented [12].

However, the fluid also directly influences the particle movement. Vortices in the fluid can raise flat-lying particles so that they indent the first bodies [12]. The fluid also has an effect on the contact between the particle and the respective first body, for example, on the coefficient of friction.

A fluid can also influence directly wear resistance of first bodies' surface materials. It has been observed that silica glass wears more when water is present, because water can enter cracks and lower the energy required for further crack growth [16]. In addition, hydraulic pressure crack propagation can occur [3]. However, even increasing humidity usually strongly influences wear rates. In some tribological systems, an increasing humidity causes also increasing wear rates, in others it causes decreasing wear rates. In some tribological systems, humidity even has the opposite effect on the wear rate for three-body wear as opposed to two-body wear [3].

The phenomena mentioned here represent only a small selection of what can occur in tribological systems. However, this section clearly shows how strongly the individual components of a tribological system can influence each other. The subsequent Sect. 2.2 presents a model for tribological three-body contacts that includes the properties of individual components and selected interactions.

2.2 Proposed Modeling of Tribological Three-Body Systems

The model for tribological three-body systems presented in the following is explained in more detail in [17] and extended here by a fluid force model according to [14], both preceding publications of the authors. The model is modular and allows the calculation of the time-resolved dynamics and the resulting topography. The overall model combines the particle force model, the fluid force model, the dynamics model, and the topography evolution model, as shown in Fig. 3.

The particle force model is based on single indentation processes of the particles into the first bodies' surfaces evaluated using finite element simulations. Subsequently, the simulation results are used to calculate the force as a function of the distance between the two first bodies for specific particle orientations (i.e., local minima, maxima, and saddle points of the orientation-dependent particle height). Barycentric coordinates are used to interpolate the relationships for arbitrary orientations between the known results of the finite element simulations. The fluid force model is based on a substitute model previously published in [14]. For different scenarios, the pressure field of the fluid between the two first bodies is simulated using the Reynolds equation and the reaction force is determined from this. The calculated scenarios are used as sampling points for interpolation. Both the particle force model and the fluid force model are created independently. Subsequently, the generated force models are used in simulations of the dynamics model. The dynamics model defines the tribological system in mechanical terms. This definition includes geometry, prescribed motion, initial conditions, and degrees of freedom of the first

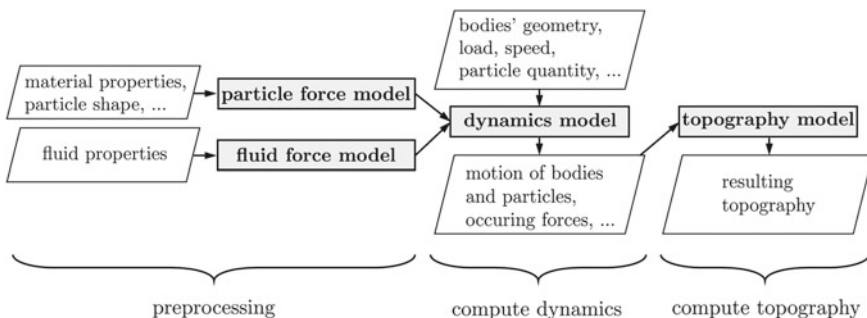


Fig. 3 Overview of data and submodels unified to model tribological three-body systems

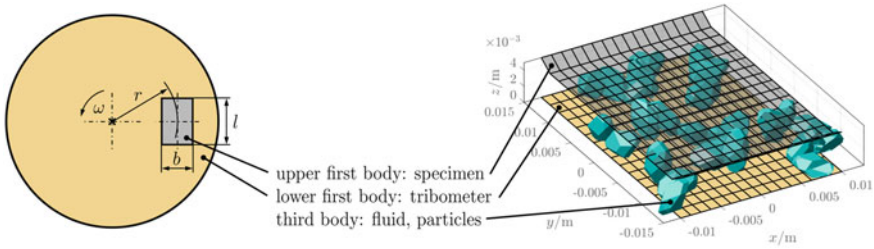


Fig. 4 Tribometer model (left) and sketch of the tribological system including particles (right)

bodies, load, and method of load application (e.g., using deadweight or spring), gravity, fluid, and the choice and initial distribution of particles between the two first bodies. In this study, a tribometer is modeled as shown in Fig. 4. The tribometer disc (lower first body) rotates at a constant angular velocity about its vertical axis of symmetry and is otherwise fixed. The specimen (upper first body) is placed onto the tribometer disc so that the center of the specimen is located at $r = 100$ mm from the center of the tribometer disc. The specimen is a chamfered ($1.2 \text{ mm} \times 30^\circ$ at particle inlet and outlet) flat specimen with dimensions $l = 30$ mm and $b = 20$ mm. It can only move vertically and is loaded by the constant gravitational force $F_g = m_2 g$ acting on its mass m_2 with $g = 9.81 \frac{\text{m}}{\text{s}^2}$. Between the sample and the tribometer disc, there are several particles with random initial position and orientation and optionally fluid. An ordinary differential equations solver iteratively calculates the vertical motion of the specimen for a given time period. During the simulation, the time-dependent variables such as particle positions, individual particle loads, and the fluid force are stored. Formation of surface topography is modeled based on the particle indentations encountered in the simulation, taking into account the particle shape.

2.3 Parameter Study of Velocity and Fluid Viscosity

In this section, simulation results are presented using the model proposed in Sect. 2.2. The test series A resp. B listed in Table 1 comprise 30 large resp. 300 small particles and are performed firstly without fluid, secondly with fluid of dynamic viscosity $\eta_1 = 1 \text{ mPa s}$, and thirdly with fluid of dynamic viscosity $\eta_2 = 1 \text{ Pa s}$. All fluids are Newtonian and incompressible and have a vapor pressure $p_v = 0 \text{ Pa}$. In test series A, 30 large particles with a diameter of $2.12 \text{ mm} \lesssim d \lesssim 4.90 \text{ mm}$ (depending on their orientation) are used [17]. In test series B, 300 small particles of the same shape as in test series A are used, but reduced in size by a factor of 100 so that the diameter is $21.2 \mu\text{m} \lesssim d \lesssim 49.0 \mu\text{m}$. In all tests, the sliding distance under the specimen center is $s = 100$ mm. The specimen is made of 16MnCr5 and the tribometer disc material is copper [17].

Table 1 Test series A and B

Test series	A					B				
Particles	Large					Small				
Number of particles	30					300				
F_g/N	300					30				
Test #	1	2	3	4	5	1	2	3	4	5
$v_T/\frac{m}{s}$	0.04	0.08	0.12	0.16	0.20	0.04	0.08	0.12	0.16	0.20

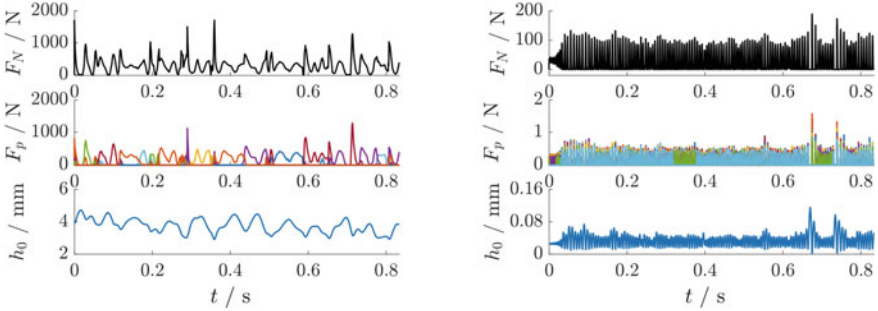
**Fig. 5** Time history of the total normal force F_N , the individual particle forces F_p and the gap height h_0 of test #3 without fluid for test series A (left) and for test series B (right)

Figure 5 shows the time history of some quantities for test #3 (no fluid); on the left for test series A (large particles) and on the right for test series B (small particles). The total normal force F_N transmitted between the two first bodies, the individual particle loads F_p , and the gap height h_0 are shown. Even though test series A and B are not directly comparable with each other due to the different parameter sets, fundamental differences between the system behavior are obvious. In test series A, the individual particle loads F_p and F_N are of similar magnitude, while, in test series B, the individual loads are significantly lower than the occurring total loads. Additionally, quantities shown oscillate at a much higher frequency in test series B than in test series A.

Regarding the dynamics, the fluids had no significant effects in any of the tests with large particles (test series A). This is because the reaction force of a fluid increases sharply with decreasing gap height, and the large particles act as spacers between the specimen and the tribometer disc. Thus, the largest reaction forces of the fluid $|F_{fl}|$ occurred across all experiments of test series A were $|F_{fl}| \leq 0.03 F_g$. Thus, only the observed effects of the fluid in test series B are discussed in more detail at this point. In Fig. 6, the distributions of total normal force F_N , individual particle force F_p , and fluid reaction force F_{fl} versus velocity are shown for no fluid, $\eta_1 = 1 \text{ mPa s}$ and $\eta_2 = 1 \text{ Pa s}$. Minima and maxima are marked by error bars and the time-weighted mean value is marked by a black circle. To the right of the error bars estimated probability density functions (from the 1st to the 99th percentile) are attached. Even

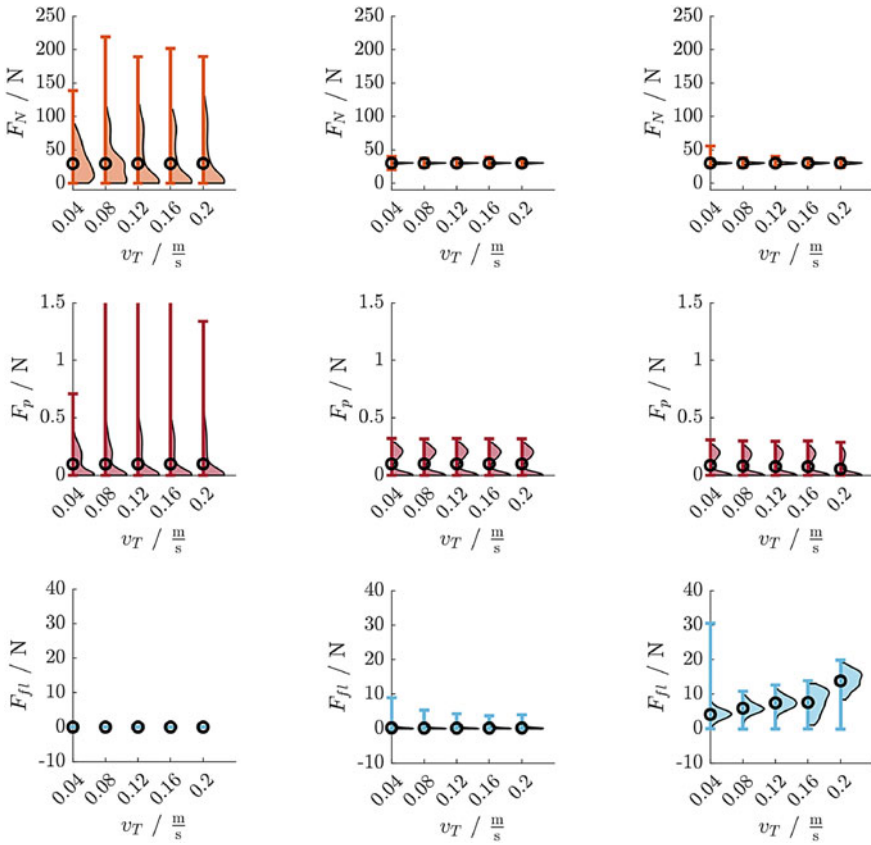


Fig. 6 Influence of velocity v_T on normal force F_N (top), individual particle forces F_p (middle), and fluid force F_{fl} (bottom) in test series B, if no fluid (left), fluid with viscosity $\eta_1 = 1 \text{ mPa s}$ (center), and fluid with viscosity $\eta_2 = 1 \text{ Pa s}$ (right) is present

a low viscosity fluid ($\eta_1 = 1 \text{ mPa s}$) provides a very narrow F_N distribution. In fact, this is an interesting result considering that on average the fluid carries only a fraction of less than 1% of F_g . In addition, the individual particle loadings F_p are distributed more compactly if a fluid is present. Given a viscosity of $\eta_2 = 1 \text{ Pa s}$, one observes a decrease in the average particle load F_p as the velocity increases, while the average fluid force increases substantially. In this case, the fluid shows a load-carrying effect and contributes about 40% of the gravitational force F_g for $v_T = 0.2 \frac{\text{m}}{\text{s}}$. However, the results for $\eta_2 = 1 \text{ Pa s}$ cannot be easily compared, because due to the very high viscosity, these tests (unlike all other tests) never reached a steady state. Except for some tests, where a short upward movement occurred at the beginning, caused by the initially randomly distributed particles, the specimen performs a continuous slow downward movement, which is strongly decelerated by the squeeze flow of the fluid.

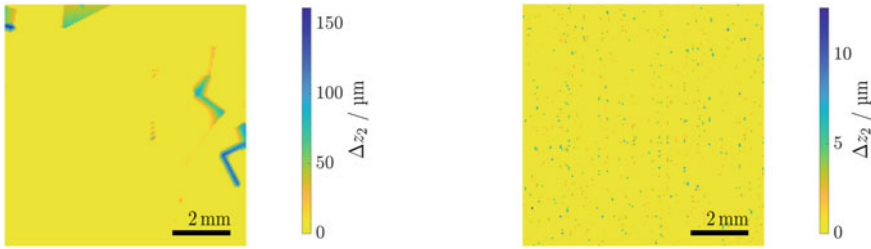


Fig. 7 8 mm \times 8 mm clip of surface topography, test #3, no fluid, test series A (left) and test series B (right)

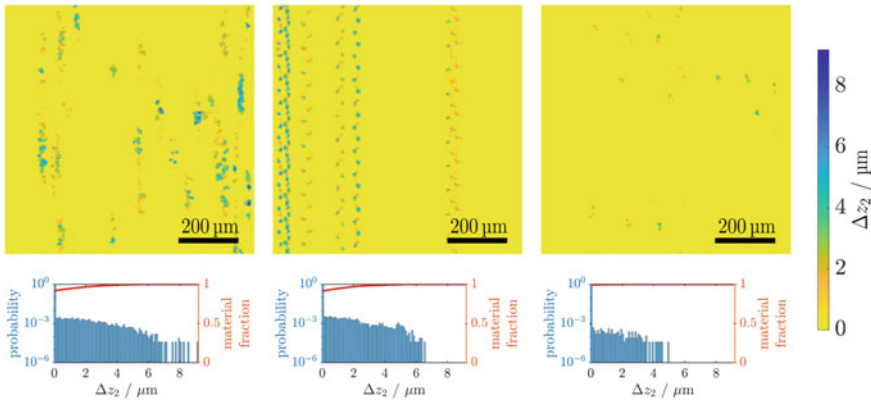


Fig. 8 Influence of velocity v_T on resulting surface topography and surface height distributions in test series B, test #3 for no fluid (left), fluid with viscosity $\eta_1 = 1$ mPa s (center), and fluid with viscosity $\eta_2 = 1$ Pa s (right)

In Fig. 7, sections of 8 mm \times 8 mm of the resulting surface topography at the center of the specimen are shown for test #3, without fluid for large particles (test series A) on the left and small particles (test series B) on the right. Each topography shown is resolved by a 160×160 grid. The topography on the left shows short traces left by the individual large particles on the sample surface. No overarching pattern can be discerned from this small excerpt. In contrast, the topography shown on the right side appears to be representative for the whole specimen surface. However, to adequately resolve the shape of the particle indentations, finer resolution is needed.

In test series B, the fluid influences not only the dynamics but also the specimen surface topography. Figure 8 shows the topography for no fluid, a fluid with $\eta_1 = 1$ mPa s and $\eta_2 = 1$ Pa s of a 0.8 mm \times 0.8 mm section with a resolution of 160×160 . The shape of the indentations is resolved much more precisely and clear differences between the three topographies shown can be observed. With no fluid, there are short traces randomly distributed on the surface in the direction of particle motion (i.e. from bottom to top). Also, the shape of the individual traces differs strongly from each other. In contrast, the indentations for $\eta_1 = 1$ mPa s are more nar-

row and show a regular pattern. The vertical motion is damped by the fluid strongly enough to allow a continuous rolling motion of the particles, which leaves these regular patterns. For a high viscosity fluid ($\eta_2 = 1 \text{ Pa s}$), there are only very few scattered indentations. The carrying effect of the fluid causes the two first bodies to separate and the particles to penetrate less deeply into the surfaces of the first bodies. This is also reflected in the distributions of the depth values, which were determined from the depicted topography sections. With increasing viscosity, the probability distribution shifts towards lower values, and for $\eta_2 = 1 \text{ Pa s}$, the fraction of the processed area also decreases to below 1% compared to 8–9% in the other two cases.

Although the parameter ranges investigated in this study were selected more from an academic point of view, basic properties of a tribological system, such as the dynamics and the resulting topography, can be modeled. The qualitative nature of the observed effects of the interplay of particles and fluid on both dynamic quantities and the resulting surface topography are in line with previously mentioned effects in Sect. 2.1.

2.4 Summary

In tribological three-body systems, particles cause time- and location-dependent loads on the surfaces of the first bodies. Local phenomena such as particle kinematics (rolling or sliding), as well as global phenomena (e.g., the total load or the motion of the first bodies), play a role. The proposed model is suitable for mapping the dynamics and subsequent estimation of the emerging topography of tribological three-body systems. The study shows that some quantities, such as the gap height, particle forces, as well as transmitted total normal force, are time-dependent quantities and that this time dependency can have a serious impact. For example, the comparison of the tests with small particles (test series B) with fluid and without fluid clearly demonstrates this. Although the mean fluid force is negligible, both the total normal forces and the individual particle forces are distributed completely differently. The resulting topographies also differ significantly from each other, although the mean total normal load is the same in both cases.

3 Interaction of Solid Particles with Structured Surfaces

The morphology of component surfaces plays an important role during the interaction of particles with these surfaces. This includes the direct contact of particle and surface, adhesion effects, and also the surrounding fluid. For gaining a better understanding of particle dynamics in contact with micro-structured surfaces, these aspects must be considered. In this section, methods for the simulation of particles are described in combination with experimental methods to validate these simulations and determine important influence parameters.

3.1 Simulation Methods for Interaction of Particles on Surfaces

For the simulation of particle dynamics the Discrete Element Method (DEM) is well established since it was introduced by Cundall and Strack [18]. Each particle in the simulated domain is described as a discrete element which follows the equations of motion. The equations are solved numerically for small time steps. During each timestep particle–particle and particle–wall contacts are detected and the contact forces are calculated and added to the equation of motion. For resolving the contact, different approaches exist. Either a hard-sphere model is used and the rebound is calculated only using the coefficient of restitution to account for energy losses or a soft sphere model is used to account for deformation through an overlap of the contact partners [19, 20].

To describe the interaction of a particle with the surrounding fluid, the DEM is extended by force models describing the influence of the fluid or it can be coupled to computational fluid dynamics (CFD) for which the Navier–Stokes equations are solved [21]. For an exact modeling of the interaction between single particles and the fluid, it is necessary to directly calculate the fluid forces acting on the particle by resolving the flow around the particle. The movement of the particle can be accounted for by the use of overset CFD meshes [21]. In this method, two meshes are used to describe the simulation domain. One is discretizing the background of the fluid domain and the other one moving in that domain discretizing the flow region around the particle. Both meshes are connected by an interpolation at the boundary of the moving mesh. For the simulation of particle collisions on wet surfaces, a third phase needs to be integrated. This is done with the Volume of Fluid Method (VOF) [22] which uses averaged fluid parameters of the involved fluids and geometrically reconstructs the interface between them.

The influence of liquid bridges can also be modeled separately without fully resolving the fluid behavior using the Young–Laplace equation [23, 24]. It describes a pressure difference over the interface between two fluids. This capillary pressure is caused by the surface tension of the fluid–fluid interface and can be calculated using the mean curvature of the interface. For the particle–wall contact, this curvature is defined by the geometry of the liquid bridge using two radii. By adding the surface force along the three-phase contact line the force acting on the particle by a liquid bridge can be estimated [24].

3.2 Experimental Methods

The collision of a particle with the surface can be investigated by a three-dimensional analysis with high-speed cameras. At least two cameras are needed recording the particle–wall collision from the front and the side to reconstruct a three-dimensional trajectory of the particle [25]. The particle movement is realized by a free-fall setup

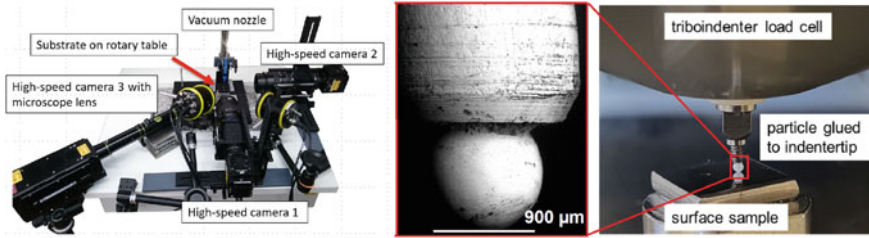


Fig. 9 High-speed camera setup (left), indenter setup for the direct measurement of forces on particles (center and right)

using a vacuum pump to place the particle on a dosage needle over the substrate. By turning off the vacuum pump, the particle falls on the substrate, while impact and rebound are recorded by the high-speed cameras. Via image processing of the recordings, the particle velocity, collision angles, and energy dissipation can be analyzed. The shown rotary table in Fig. 9 can be tilted and adjusted to an intended angle for experiments with oblique collisions [25]. Placing the substrate inside a frame allows to add liquid or a liquid layer with a specified height to investigate the collision on a wet surface. For the measurement of the layer height, the setup is extended by a confocal sensor. It measures the thickness of the layer analyzing the reflected wavelengths of a monochromatic light beam.

At lower velocities, the particle surface interaction is investigated via triboindentation. As the used triboindenter (Bruker Ti Premier) is capable to measure wide force ranges from 1 μN up to 2.5 N, it can be used to directly measure forces on a particle during the interaction with a surface. Therefore, special indenters were manufactured using zirconium oxide particles with sizes from 100 μm up to 900 μm as a tip (cf. Fig. 9). By scratching the particle tip over the substrate, the friction is measured as a tangential force at a predefined constant normal force. This allows to measure the sliding friction coefficients of a particle–substrate pairing in specific contact situation over a wide range of normal forces. Another application for the nanoindenter is the determination of viscous forces caused by a fluid. During the approach of a particle to a wall, the liquid in the gap is squeezed out. This leads to high pressure and shear forces. Adding a micro-stage to the setup enables the direct measurement of these forces by approaching the particle with the surface through the movement of the stage.

For the morphology characterization of surface and particle surface scanning probe microscopy (SPM) can be used. The substrate is scanned with a Berkovich indenter tip to determine x -, y -, and z -position of the surface. This data can be used to calculate the roughness. SPM imaging is also used to generate artificial copies of the surface for the implementation in simulation tools [25].

A measurement method for the adhesion of bulk material is the vibration method. Particles are placed on a substrate attached to a vibration exciter. The particles are accelerated and will detach from the substrate at the highest amplitude of the vibration

movement if the acceleration by the vibration overcomes the adhesion forces. This can be observed with a microscope and evaluated by image processing. With the amplitude z_{max} , the frequency f_{vib} of the vibration and the mass of the particle m_p it is possible to calculate an acceleration $a_{vib} = (2\pi f_{vib})^2 z_{max}$ which corresponds to the detachment force $F_{det} = m_p \cdot a_{vib}$ [26].

3.3 Relationships as a Result of Experiments and Simulation of Particle Interaction with Surfaces

The vibration method described in the preceding chapter was used to measure adhesion forces between particles and different surfaces. Small glass beads (10–80 μm) and an untreated titanium surface were used to compare the experiments to models of van der Waals forces. A well-known model is the one by Hamaker [27]. For the interaction of a sphere and a plate, it can be simplified to $F = -A_H \cdot R / (6 \cdot a_0^2)$. A_H is the material-dependent Hamaker constant and a_0 the contact distance. To account for the deformation of roughness asperities, a modified contact area model can be applied to describe the contact area resulting from the deformation. This area $A_c = 2\pi R^2(1 - \sqrt{1 - f^2})$ can be determined from the particle radius R and the function f which is derived from the deformation depth in combination with the geometry of the deformed asperity [26].

For a mean value of 56 nm for the radius of the contact area A_c , the modified model was able to qualitatively describe the adhesion measured in the experiments, as shown in Fig. 10. The deviation can be explained by different contact situations as well as multiple asperity contacts. Additional experiments were done using micro-milled surfaces with micro-structures in the form of grooves, pores, and a grid structure (Chap. 4). Glass beads with a mean size of 70 μm were used to compare the adhesion of the different surface morphology. These substrates showed the same adhesion

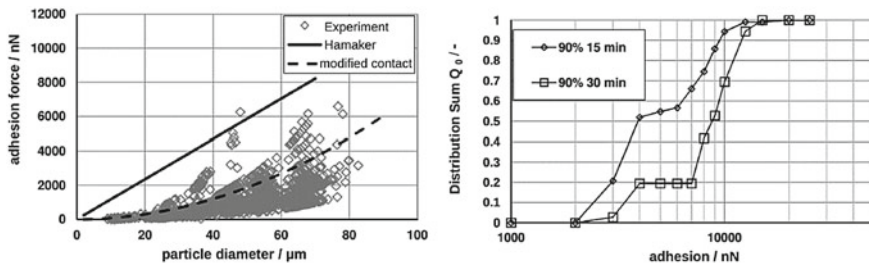


Fig. 10 Adhesion force between glass particles ($d = 10 - 80 \mu\text{m}$) and stainless steel substrate measured by the vibration method compared to the Hamaker model and a modified contact area model [26] (left) and adhesion by liquid bridges after different exposure times to highly humid air (right) [26]

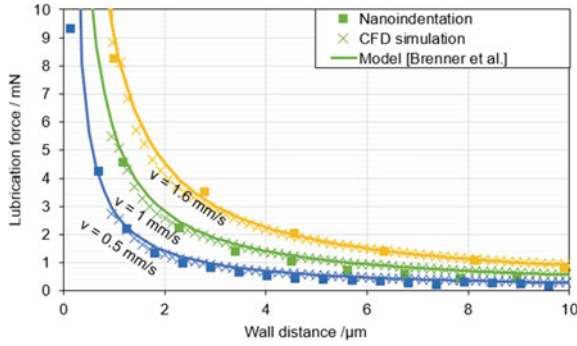


Fig. 11 Lubrication force during the approach of zirconium oxide particles ($d = 900 \mu\text{m}$) on a smooth titanium surface. Comparison between measurement, simulation, and analytical solution at different approach velocities of 0.5 mm/s (blue), 1.0 mm/s (green), and 1.6 mm/s (yellow) in glycerol with a viscosity of 1.48 Pa s

distribution independent of the structure shape. This states that adhesion force is not affected by surface topology on this size scale [26].

For the measurement of capillary forces, the setup was extended by a climatic chamber to control the humidity. The adhesion was measured after different exposure times of samples with particles on polished titanium surfaces in a moist air environment in the chamber. Figure 10 shows the adhesion after the humidity was held at 90% and 30 min indicating an increase in adhesion force. As liquid bridge forces exceed van der Waals forces, the longer exposure time to humid air is leading to a formation of a higher number of liquid bridges by condensation. This shows the importance of the environmental conditions in terms of adhesion.

The lubrication force during the particle approach to the wall was measured with a nanoindentation setup described in Sect. 3.2 at three velocities of 0.5, 1.0, and 1.6 mm/s and compared to the analytical solution by Brenner et al. [28]. Zirconium oxide particles with a diameter of about $900 \mu\text{m}$ were investigated on a polished titanium surface to neglect surface roughness in comparison to the analytical calculation. The experiment was done completely immersed in glycerol with a viscosity of 1.48 Pa s. The results of the experiments were in good agreement with the analytical solution showing increasing forces with lower distance as well as with higher velocity, see Fig. 11. The figure also shows resolved CFD simulations which were performed with the overset-mesh method that are in good agreement with the analytical solution. With reasonable computational expense, it was possible to resolve the lubrication force up to $1 \mu\text{m}$ distance to the wall. A dynamic case will show the influence of different surface morphology on the lubrication forces in a later part of the section.

For the determination of sliding friction between particles and surfaces, the quasi-static setup using the triboindenter was compared to a dynamic method using oblique collisions captured by high-speed cameras described in Sect. 3.2 [25]. Different-sized zirconium oxide particles from $280 \mu\text{m}$ to $912 \mu\text{m}$ were used on a stainless-steel

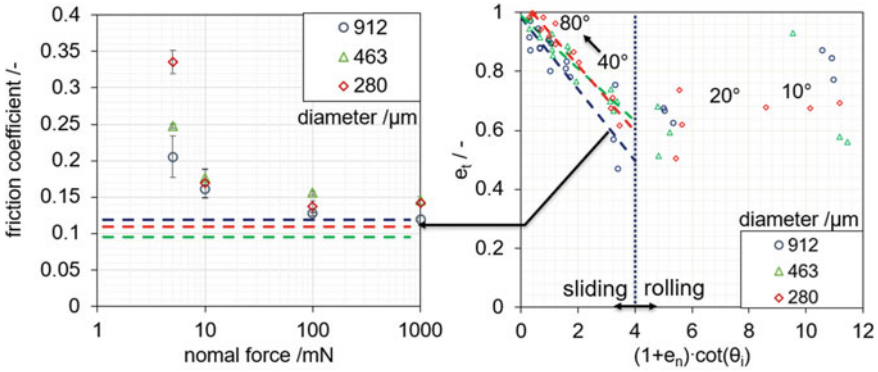


Fig. 12 Coefficient of friction for different-sized zirconium oxide particles with direct measurement and rigid body theory of an oblique collision

substrate ($r_q = 0.27 \mu\text{m}$). While the triboindentation determines the friction coefficient μ from the measured normal and tangential loads, the dynamic method uses a correlation from the rigid body theory [29, 30] with the normal e_n , the tangential e_t coefficient of restitution and the impact angle θ to account for energy losses caused by the short sliding moment during the collision with

$$e_t = 1 - \mu \cdot (1 + e_n) \cdot \cot(\theta_{\text{impact}}). \tag{1}$$

These parameters resulted of investigations oblique collisions with the high-speed cameras. The correlation is valid for impact angles bigger than about 30° where the sliding is dominant. Smaller angles will lead to micro sticking and rolling. Figure 12 compares results obtained with different approaches. On the left diagram, the measured coefficient of friction from the triboindentation is displayed for different normal forces. The particles of all sizes show increasing friction with smaller normal forces ($<100\text{mN}$). This was already described by other authors [31], who found this to be an effect resulting of the small contact area, which highly influences the interaction of different friction mechanisms. Low normal forces lead to only elastic deformation of the asperities. During the tangential movement higher tangential forces are needed as the asperities are interlocking. With higher normal forces the asperities will be deformed plastically leading to lower friction coefficients which are independent of the normal force with increasing load. On the right diagram, the friction is determined by the linear regression of the displayed values using the rigid body. The resulting friction coefficient is between 0.092 for the 463 μm particles and 0.121 for the 912 μm particles. The friction is similar to the measured friction by the triboindenter at higher normal loads. The lower friction of the smaller particles is probably caused by slight amounts of initial rotation which was observed for the smaller particles as well as higher roughness for the 463 μm fraction which was measured by Krull et al. [32]. This might lead to increased proportion of rolling during the collision, affect-

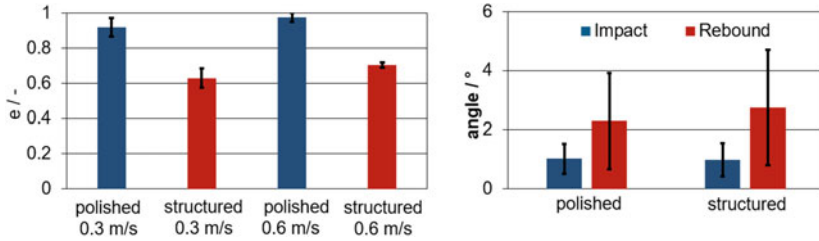


Fig. 13 Coefficient of restitution and collision angles of polystyrene particles ($d = 665 \mu\text{m}$) on polished and micro-structured surfaces, coefficient of restitution (left) and rebound angle (right) [25]

ing the determined friction coefficient. As the maximum normal force that occurs during the collisions (at 0.3 m/s) would be comparable to the lower measured normal forces that were studied with nanoindentation ($<10 \text{ mN}$) the observed additional friction in the measurement at lower forces seems to be a result of the quasi-static experiment. For the oblique collisions, inertial effects might exceed the additional friction mechanisms.

For the investigation of the collision behavior on micro-structured surfaces in normal direction, free fall experiments with polystyrene particles (mean diameter $665 \mu\text{m}$) were executed [25]. The high-speed camera setup described in Sect. 3.2 was used to determine rebound angles and the coefficient of restitution on stainless steel substrates at different velocities (0.3 m/s and 0.6 m/s). Substrates with a polished surface and a cold sprayed surface (Chap. 6) were used. The results showed a rise of energy dissipation caused by the microstructured surface, cf. Fig. 13. This is probably caused by asperities penetrating into the softer particle leading to plastic deformation due to high local stresses. Regarding the rebound angle, a slight increase was observed. Yet this was no significant effect, as the standard deviation was relatively high compared to the increase.

The investigated micro-structure ($r_q = 0.31 \mu\text{m}$) was also analyzed with SPM imaging to create a CAD model of it. This model was used as a wall boundary for a DEM simulation of the particle collision with the structure. For use in the simulation, the surface model was triangulated with two meshes having different resolution – a coarse mesh with 4000 faces and a fine mesh with 150000 faces on a $1 \text{ mm} \times 1 \text{ mm}$ area. The simulation was done with a particle velocity of 0.6 m/s at different points of the implemented surface. The fine mesh showed a good agreement with the experimental data regarding the coefficient of restitution, while both meshes were able to predict the rebound angle, see, Fig. 14. It can be concluded that a sufficiently fine mesh is needed to resolve the contacts occurring during the collision, yet the method using SPM imaging is a good tool for the simulation of the particle contact with micro-structures.

The influence of fluid during the particle–wall contact was investigated with collision experiments in air and water over Stokes numbers ranging from 10 to 9000 [32]. Zirconium oxide particles with a size range of $280 \mu\text{m}$ – $912 \mu\text{m}$ were used. They

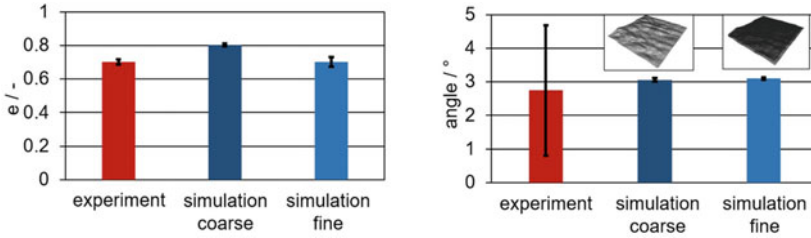


Fig. 14 Comparison of DEM simulation to experiment of single particle collision with polystyrene particles ($d = 665 \mu\text{m}$) on a cold sprayed micro-structure, coefficient of restitution (left) and rebound angle (right) [25]

were investigated on polished and untreated titanium surfaces to see the influence of surface morphology in different environment. It can be observed in Fig. 15 that the experiments in air result in a higher coefficient of restitution on the polished surface due to higher roughness asperities that are plastically deformed. At low Stokes numbers, another effect was observed because of the viscous forces acting in the near wall region. These forces decrease with increasing roughness values, which were already described by Barnocky and Davis [33] who introduced a model for the restitution coefficient on a wet surface $e_{\text{wet}} = e_{\text{dry}} + \frac{1+e_{\text{dry}}}{St} \ln\left(\frac{x_c}{x_0}\right)$. The model uses the dry coefficient of restitution e_{dry} and the Stokes number in combination with a ratio of wall distance x_0 and a critical distance parameter x_c which they related to the roughness. Equivalent roughness parameters (s_{RMS} and s_a) of both contact partners were calculated by different models and implemented for critical distance in this equation. Both parameters and averaging methods were able to make a qualitative prediction of the curve, the model by Rabinovich [34] showed the best agreement for the polished surface and the geometric model [32] was the best suitable for the untreated surface, as obvious from Fig. 15.

Collision experiments with different heights of water layers were performed using the high-speed cameras described in Sect. 3.2. Zirconium oxide particles with a mean size of $912 \mu\text{m}$ were used for this case. In Fig. 16 it can be seen that the polished surface has a higher coefficient of restitution for each experiment than the untreated surface. This is probably resulting of plastic deformation of the roughness asperities. Compared to experiments completely immersed in fluid the effect of decreasing lubrication force is not exceeding the energy loss by the asperity deformation. Also the differences are in the range of standard deviation. An additional micro-structured surface was investigated which was micro-milled (Chap. 4) with a pyramid stump structure. With a maximum height of $60 \mu\text{m}$ the pyramid stumps were relatively high compared to common roughness asperities. This resulted in a scatter of the coefficient of restitution with high standard deviations. From Fig. 16 it can be observed that the average value of the dry experiment ($0 \mu\text{m}$) is lower for the micro-milled surface. An explanation for this is the more complex contact situation as the asperities of the micro structure are big enough for the particles to impact between two or more

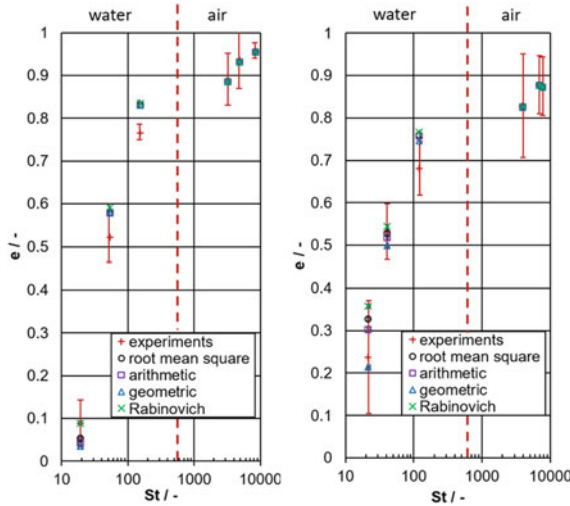


Fig. 15 Coefficient of restitution of ZrO₂ particles over Stokes number ($St = \frac{v_{impact} \cdot d_p \cdot \rho_p}{\nu \cdot \rho_f}$) for collisions on a polished (left) and untreated (right) titanium surface [32] which were performed in air and water—compared to modified model from Barnocky and Davis [33]

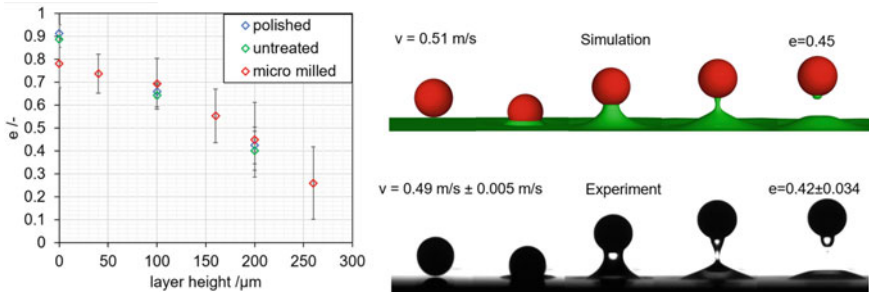


Fig. 16 Coefficient of restitution during impact on different surface structures with varied heights of liquid layers (left), comparison of experiment and simulation of the collision on a 200 μm layer (right)

asperities. That lead to increased contact areas and friction. With the added water layer the coefficient of restitution of the micro-milled surface exceeds those of the other surfaces with same layer heights. This might be due to collisions on asperities where the effective layer height is lower than on flat surfaces. Also, the viscous lubrication force near the wall is affected as the fluid can evade through the structure instead of being compressed between the particle and the flat wall. The high standard deviation during the experiments indicates, that the particle collision on the micro structure is highly dependent on the exact contact situation.

For the polished surface with a 200 μm water layer a resolved simulation was executed using a hard sphere model coupled to the VOF method described in Sect. 3.1,

cf. Fig. 16. The simulation shows a good agreement for the liquid bridge formation, as well as the resulting coefficient of restitution, still it is not completely possible to resolve the lubrication force in the last micrometers before the wall without an excessive use of computational resources.

3.4 Summary

It was shown that the surface morphology affects the particle dynamics during different stages of a collision, which can be regarded separately with varying approaches of which some were considered here. The main effects are caused by the direct solid-solid contact and the surrounding fluids. During solid-solid contact a higher number of asperity contacts compared to a flat wall can have significant influences on the dissipated energy due to friction and plastic deformation. The roughness of a surface can also influence the viscous force acting on a particle near the wall or adhesion effects. Regarding the size of the micro-structure, there is also a dependence of the particle behavior to the specific contact situation leading to higher uncertainty for coarser structures. The simulation of the implemented surface using SPM imaging showed good results for the simulation of a micro-structured surface, while the hard-sphere model coupled to VOF was able to depict the fluid interaction on a flat wall. A combination of both is numerically complicated and expensive. Better applicable is the approach to describe different effects with separate models that can be implemented in DEM to include influences like adhesion [26] or viscous forces [32] depending on the effects that considerably have the biggest impact.

4 Interaction of Elastic Particles with Surfaces

The transport of particles to a component surface followed by adhesion is one of the crucial steps in numerous processes and applications, e.g., in biotechnology. For example, it determines how efficiently bioparticles are transported to a surface, where they can start to grow a biofilm.

4.1 Fundamental Forces on Suspended Particles Close to Surfaces

Nonbuoyant microparticles suspended in a fluid usually follow the streamlines of the flow over the component surface (cf. Sect. 3, Chap. 17) as long as the particles are far enough away from the surface. In this case, the particle–fluid flow corresponds to an *unbounded fluid flow*, where influences resulting from the presence of the walls

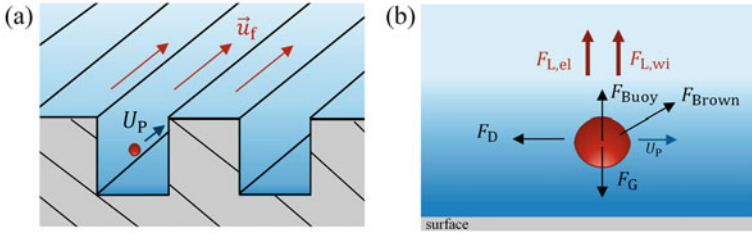


Fig. 17 **a** Microparticle flowing inside a rectangular microchannel; **b** Forces acting on a particle in close vicinity of a component surface

usually do not play a role. If, on the other hand, the particles flow in close vicinity of a component surface, they interact both with the fluid and the component surface, which leads to additional forces acting on the particles. In the case of micro-structured rectangular channels, as for example shown in Fig. 17a, the particle interacts with at least three walls surrounding the particle when flowing inside such a channel. The influence due to the walls is no longer negligible. General forces acting on a suspended particle flowing with velocity \underline{U}_p near a wall are shown in Fig. 17b.

Mass forces, such as gravity and buoyancy, act on particles in quiescent fluids as well as in fluid flows. These mass forces cause the particles to settle by sedimentation either when there is enough time to overflow a surface or when the particles enter undisturbed fluid regions. For particles with a diameter of approx. $D_p < 1 \mu\text{m}$, additional diffusive forces in the form of Brownian forces have to be considered [35]. Furthermore, a particle translating in a fluid experiences a drag force \underline{F}_D . The drag depends on the shape of the particle's surface and on the distance between the particle and the wall [36]. If a particle translates steadily along a wall, drag exerted on the sphere is increased, and furthermore, the particle experiences an additional force perpendicular to the wall, which drives the particle away from the wall. This force is called the *wall-induced (hydrodynamic) lift force* $\underline{F}_{L,wi}$ and was first treated by Faxén in 1922 [37, 38]. Other examples of induced lift forces are the shear-induced Saffman lift force or the rotation-induced Magnus lift force [39, 40]. A combined effect of shear-induced and wall-induced lift forces is the Segré-Silberberg effect, in which particles suspended in a Poiseuille flow collect on certain tube radii depending on their diameter [41]. All these effects are sufficiently well described for rigid particles, both analytically and experimentally, or empirically, respectively. In numerous applications, however, elastic and deformable interaction partners can be found. An example is the flow of biological cells, which are supposed to grow on a surface to form productive biofilms (cf. Chap. 17). In the direct region of influence of the component surface (Fig. 17b), the deformability of one of the interaction partners plays a decisive role, since the deformation of either the surface or the particle leads to another lift force, the *elastohydrodynamic lift* $\underline{F}_{L,el}$ [42, 43]. However, the relation between deformation, or elasticity respectively, of the particle and the fluid is not completely understood so far. Even supposedly simple particle dynamics such as sedimentation (i.e., the motion of an elastic particle in a quiescent

fluid due to gravity) in an unbounded fluid domain is only described in a rudimentary way [44].

When a rigid, spherical particle with radius R , volume V_P and density ρ_P sediments due to gravitational acceleration g with velocity U_P in an unbounded fluid, the equation of motion can be described with the Basset-Boussinesq-Oseen (BBO) equation. The BBO equation is valid for particles classified as non-heavy particles, i.e., the particle-to-fluid density ratio is $\gamma = \rho_P/\rho \rightarrow 1^+$ (quasi neutrally buoyant particles). The BBO equation results from the force balance around the particle with $\underline{F}_I + \underline{F}_G + \underline{F}_{\text{Buoy}} + \underline{F}_{\text{St}} + \underline{F}_{\text{AM}} + \underline{F}_B = 0$. The differential equation for the particle velocity U_P in direction of the gravitational acceleration reads as [45]

$$\rho_P V_P \frac{dU_P}{dt} = (\rho_P - \rho)g V_P - 6\pi\eta R U_P - \frac{1}{2}\rho V_P \frac{dU_P}{dt} - 6R^2\sqrt{\rho\pi\eta} \int_0^t \frac{\dot{U}(s)}{\sqrt{t-s}} ds. \quad (2)$$

The overdot denotes a time-derivate and s is a dummy time variable for integration. The fluid density is ρ and the fluid dynamic viscosity is η . Furthermore, the particle starts from rest at $t = 0$ s and, initially, the fluid velocity field around the particle is $|\underline{u}_f| = 0$ m/s. In the stationary state the particle sediments in the Stokes regime with the particle Reynolds number $Re_P = 2U_P R \rho \eta^{-1} \ll 1$. The term on the left side of Eq. 2 is the inertial force F_I . The inertial force is equaled by the gravitational force F_G and the buoyancy F_{Buoy} . F_{St} denotes the drag force resulting from Stokes's law [46]. The third term on the right is the added mass force F_{AM} which arises because the acceleration of the particle requires acceleration of the fluid surrounding it. The last term F_B is the Basset history force, which includes past acceleration and represents the effect of the diffusion of vorticity around the sphere due the temporal delay in boundary layer development. In the steady state ($\frac{dU_P}{dt} = 0$), where the gravitational force and buoyancy balance the drag and the acceleration forces vanish, Eq. 2 results in the terminal Stokes velocity

$$U_{\text{St}} = \frac{2R^2 \Delta\rho g}{9\eta}. \quad (3)$$

However, when a rigid particle settles in the vicinity of walls, the wall-bounded drag force F_D is higher than Stokes's drag, which leads to a decrease in velocity ($U_P/U_{\text{St}} = F_{\text{St}}/F_D < 1$). Numerous drag corrections are available for single plane walls and also for two parallel plane walls [36–38]. On the other hand, only few correlations for the sedimentation of particles in the low Reynolds number regime are available for four plane walls like in closed rectangular channels [47].

With respect to soft, deformable particles, *Noichl and Schönecker* performed sedimentation experiments in a rectangular tank [48]. The following manufacturing-morphology-property relation is covered: elastic polydimethylsiloxane model particles were manufactured by casting in such a way that various elastic moduli were obtained. The altered morphological material and surface characteristics of the soft model particles lead to completely different dynamical properties during sedimentation in a bounded fluid domain compared to those of rigid particles in the vicinity

of surfaces. It is expected, that there exists a coupled relation between the particle velocity, and hence, the drag and lift forces acting on particles, and the elastic deformation due to the presence of the surface.

4.2 Sedimentation Experiments with Symmetric Wall Influence

Sedimentation was performed with rigid ($E_1 = 2.9$ GPa) and elastic spheres ($E_2 = 1712$ kPa, $E_3 = 936$ kPa and $E_4 = 135$ kPa) with a radius of 6 mm in the center of a rectangular duct at low Reynolds numbers, see Fig. 18 [48].

For this purpose, a glass tank with dimensions of $0.14\text{ m} \times 0.14\text{ m} \times 0.5\text{ m}$ ($W \times D \times H$) was filled with highly viscous silicone oil ($\eta = 980$ mPa s). The choice of the

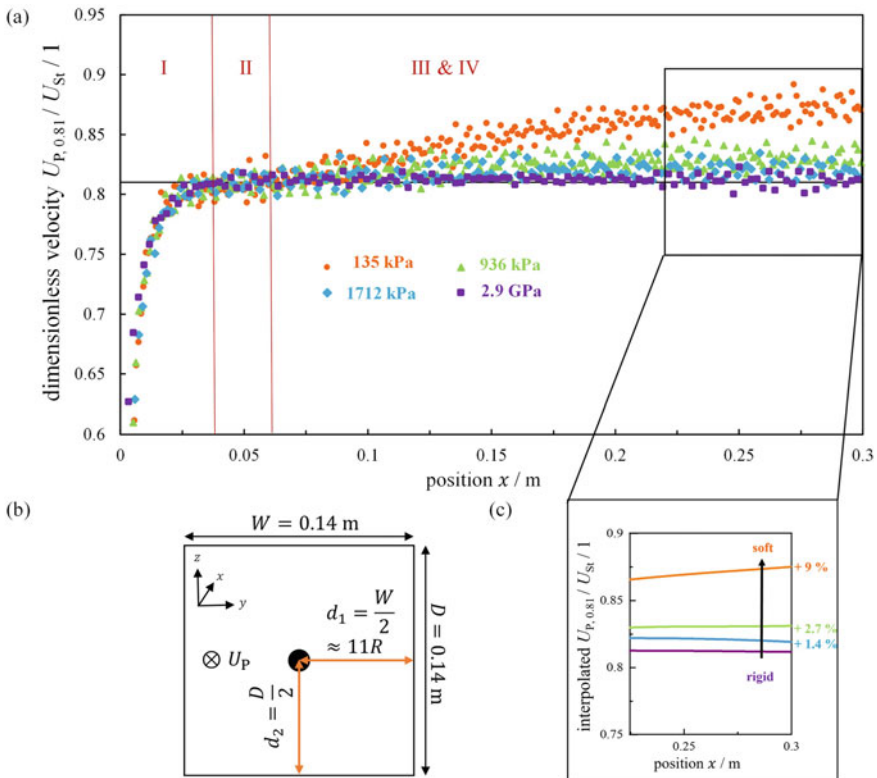


Fig. 18 Sedimentation experiments of rigid (purple) and elastic spheres (blue, green, orange) in the center of a rectangular tank: **a** dimensionless velocity U_P/U_{St} plotted against the position x (direction of gravity g); **b** 2-D sketch of the tank dimensions; **c** extract from terminal velocity range at the end of sedimentation (interpolated data of U_P/U_{St})

model particle size together with the choice of a high viscosity liquid ensured that $Re_p \ll 1$. This condition allowed to investigate the same conditions as small, elastic microparticles would experience in aqueous liquids. Trajectories were optically recorded and the velocities were evaluated from displacement measurements.

Sedimentation dynamics of rigid spheres was as expected. Velocities of $\sim 81\%$ of the Stokes velocity were measured for the rigid spheres, which is in good agreement with existing data from literature, and reflects the influence of the walls. The experiments with the elastic model particles showed a completely different velocity-time behavior, and velocity-displacement behavior respectively, than rigid particles. It appears that elastic effects kick in at a comparatively large time scale, such that the sedimentation of elastic spheres could be described by four phases instead of two phases as for solid particles. The first phase showed a transient acceleration and the second phase a first velocity plateau that corresponds to the dimensionless velocity of the rigid spheres. Thereafter, for all elastic spheres, a second acceleration began after a distance of about $10R$. From this characteristic time on, the elasticity has a significant influence on the sedimentation of elastic spheres in the bounded fluid. The third phase of sedimentation showed further acceleration that depends strongly on the Young's modulus. The more deformable the spheres were, the longer the second acceleration lasted and the further the distance was until the terminal velocity of the second plateau was reached. The measured percentage increase compared to the rigid velocity plateau was found to be up to 9%. It is assumed that small, undetectable deformations lead to a reduction of the drag forces, which only become apparent with a time delay after a distance of $\sim 10R$. The four side walls initially seem to increase the drag over this distance for all particle specimens. In the longer term, however, deformations of the elastic spheres lead to a reduction in drag again. Conceivable is the deformation into a prolate spheroid, as suggested by *Murata* in 1980 for the sedimentation in an unbounded fluid [44].

4.3 Sedimentation Experiments with Asymmetric Wall Influence

Sedimentation in the center of a rectangular tank leads to symmetric influences of the surrounding walls on the particle. However, in close vicinity of one wall, as depicted in Fig. 19b, the influence of the walls becomes asymmetric. Sedimentation dynamics differ fundamentally from those in the center, see Fig. 19a.

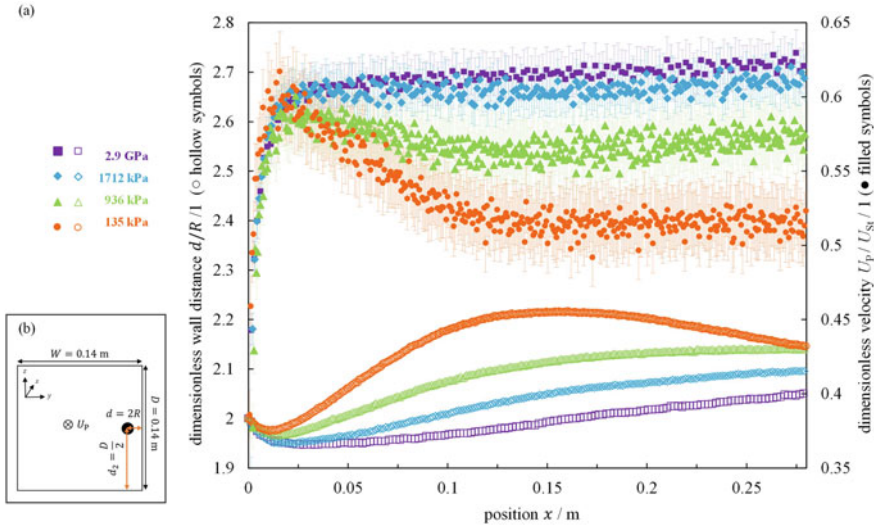


Fig. 19 Sedimentation experiments of rigid (purple) and elastic spheres (blue, green, orange) in the near wall region of a rectangular tank (asymmetric sedimentation): **a** trajectories presented as dimensionless wall distance d/R plotted against the position x (left axis, hollow symbols) and (dimensionless velocity U_P/U_{St}) plotted against the position x (right axis, filled symbols); **b** 2-D sketch of tank dimensions and positioning of the sphere in the near wall region

In close vicinity of a wall (dimensionless wall distance $d/R \approx 2$), no steady sedimentation conditions were reached, as the wall-induced normal forces lead to a continuous change in the wall distance and hence in drag. Under the large influence of the near wall and the large increase in drag, both rigid and elastic spheres initially accelerate to a velocity of only $\sim 60\%$ of the Stokes velocity U_{St} . According to Faxén (Eq. 4), the presence of one plane wall at this wall distance would reduce the velocity of the sphere to $\sim 72\%$ of U_{St} [37].

$$\frac{U_P}{U_{St}} = 1 - \frac{9}{16} \left(\frac{R}{d}\right) + \frac{1}{8} \left(\frac{R}{d}\right)^3 - \frac{45}{256} \left(\frac{R}{d}\right)^4 - \frac{1}{16} \left(\frac{R}{d}\right)^5. \quad (4)$$

A further reduction by the other two walls which were located at a distance of $d_2 = 11R$ away from the sphere therefore is reasonable.

As in the symmetric case, the rigid spheres behave as expected. The trajectories of rigid spheres show a linear migration away from the wall with $x \sim d/R$. This is due to the action of the wall-induced lift force $F_{L,wi}$, which is directed perpendicular to the wall. Furthermore, the measured migration velocity perpendicular to the wall ($U_{P,y}$) is small ($\sim 0.2\%$ of U_{St}), and was constant in all rigid sphere experiments. Consistently, the wall-induced lift force leads to a gradual increase in velocity in direction of gravity (U_P) due to the increase in gap size, see Fig. 19a filled purple velocity curve.

In contrast, the elastic spheres behave again completely different. The trajectories differ the more from linearity, the softer the spheres are ($x \sim (d/R)^n$). After the first acceleration phase, elastic spheres show a significant increase in gap size. This might be related to an elasto-hydrodynamic lift force. However the softest spheres later reduce the distance again resulting in a wave-like trajectory. With these trajectories observed, the measured velocities of the elastic spheres appear all the more unexpected. Although the wall-distance increases with $\max(U_{P,y})$, the overall settling velocity decreases. In fact, this behavior is counterintuitive since all existing drag models predict a reduction of the drag force (and consequently increase in velocity) when the gap size is increased. The observations suggest that a non-linear force coupled with the hydrodynamics, i.e., the elasto-hydrodynamic lift force $F_{L,el}$, is acting on the particles. Furthermore, the more deformable the spheres were, the lower was the measured velocity. This is completely opposite to the symmetric case of sedimentation in the center of the tank.

4.4 Summary

These two examples of sedimentation at different container positions already show that the dynamics of elastic particles near walls at $Re \ll 1$ differ fundamentally from the dynamics of rigid particles. In particular, with respect to applications involving the attachment of deformable particles to component surfaces, elasto-hydrodynamic forces should be considered. The results from these and other experimental and numerical investigations concerning this topic (e.g., more variations of wall distances, deformable surfaces, different particle shapes etc.) suggest that elasto-hydrodynamic interactions cannot be neglected when modeling particle-laden flows near surfaces. With the help of the experimental data of these experiments and the characteristic quantities obtained so far, it is already possible to make some easy-to-calculate statements about the expected velocity of elastic (micro-)particles under wall influence. Regardless, modeling the observed non-linear coupled forces will be one of the major challenges in the future in this area of particle–fluid dynamics.

5 Conclusions

Particles can undergo a variety of interactions with surfaces. They depend on the type of contact between the interaction partners. This means whether the interaction partners are in direct contact, such as in tribological three-body and two-body systems, whether a fluid is present, or whether the interaction is indirectly mediated by an in-between fluid.

With respect to three-body contacts, we presented a new process simulation model for tribotechnical systems. This model can be applied to technical processes such as lapping. It relates the micro-morphology of the particles, such as their geometry and

force-indentation relationship to the macroscopic property abrasion. It also includes manufacturing process parameters (kinematics, velocity, normal force).

Regarding two-body contacts, new methods of collision phenomena of microparticles with surfaces have been shown. Both in DEM simulations, the influence of the surface morphology was included, as well as the effects were characterized in experiments of particles impacting on dry and wetted substrates. Relations have been set up between the particle and liquid properties and the collision dynamics of the particles. Especially the coefficient of restitution could be described depending on the surface morphology and liquid properties.

For fluid-mediated interactions, new effects of elastic surface interactions on the kinematics of particles have been demonstrated. Particle speed and acceleration are related to their elastic modulus, which determines their elastic deformation. It was shown that elastic particles behave entirely different from rigid ones, which is especially relevant for understanding and controlling the kinematics of bioparticles.

References

1. Denape J (2015) Third body concept and wear particle behavior in dry friction sliding conditions. *Key Eng Mater* 640:1–12. <https://doi.org/10.4028/www.scientific.net/kem.640.1>
2. Popov VL (2016) *Kontaktmechanik und Reibung*. Springer, Berlin, Heidelberg, 12 Jan 2016. ISBN: 3662459752. <https://doi.org/10.1007/978-3-662-45975-1>
3. Stachowiak GW (2014) *Engineering tribology*. Elsevier, Oxford. ISBN: 9780123970473. <https://doi.org/10.1016/c2011-0-07515-4>
4. Bilz R, de Payrebrune KM (2021) Investigation of the influence of velocity in a tribological three-body system containing a single layer of rolling hard particles from a mechanical point of view. In: *Tribology international*, p 106948. <https://doi.org/10.1016/j.triboint.2021.106948>
5. Stachowiak G, Stachowiak G (2001) The effects of particle characteristics on three-body abrasive wear. In: *Wear*, vol 249, 3–4, pp 201–207, May 2001. [https://doi.org/10.1016/s0043-1648\(01\)00557-9](https://doi.org/10.1016/s0043-1648(01)00557-9)
6. Bilz R, Sridhar P, de Payrebrune KM (2021) Parameter identification aspects of tribological systems containing hard particles. In: *PAMM*, vol 21, 1, Dec 2021. <https://doi.org/10.1002/pamm.202100018>
7. Bartel D (2010) *Simulation von Tribosystemen*. Vieweg+Teubner Verlag, 188 pp, 24 Feb 2010. ISBN: 3834812412. <https://doi.org/10.1007/978-3-8348-9656-8>
8. Shao Y, Yin Y, Du S, Xia T, Xi L (2018) Leakage monitoring in static sealing interface based on three dimensional surface topography indicator. *J Manuf Sci Eng* 140, 10. <https://doi.org/10.1115/1.4040620>
9. Hao M-M, Wang Y-l, Li Z-T, Sun X-H (2018) Effects of surface topography on hydrodynamic performance of liquid film seals considering cavitation. *Ind Lubr Tribol* 70, 6:984–992. <https://doi.org/10.1108/ilt-12-2016-0321>
10. Marinescu I, Uhlmann E, Doi T (2007) *Handbook of lapping and polishing*. CRC Press. <https://doi.org/10.1201/9781420017632>
11. Woldman M (2014) *An experimental and theoretical investigation into threebody abrasive wear*. PhD thesis. University of Twente. <https://doi.org/10.3990/1.9789036536219>
12. Klocke F (2017) *Fertigungsverfahren 2*, vol 448, pp 15. Springer GmbH, Nov 2017. ISBN: 9783662533109
13. Bilz R, de Payrebrune KM (2019) Analytical investigation of the motion of lapping particles. In: *PAMM*, vol 19, 1, Nov 2019. <https://doi.org/10.1002/pamm.201900076>

14. Bilz R, de Payrebrune KM (2023) Development of a simple substitute model to describe the normal force of fluids in narrow gaps. In: PAMM, vol 22, 1. <https://doi.org/10.1002/pamm.202200062>
15. Papadopoulos CI, Kaiktsis L, Fillon M (2013) Computational fluid dynamics thermohydrodynamic analysis of three-dimensional sector-pad thrustbearings with rectangular dimples. *J Tribol* 136, 1. <https://doi.org/10.1115/1.4025245>
16. Belkhir N, Bouzid D, Herold V (2009) Surface behavior during abrasive grain action in the glass lapping process. *Appl Surf Sci* 255, 18:7951–7958. <https://doi.org/10.1016/j.apsusc.2009.04.178>
17. Bilz R, de Payrebrune KM (2022) Simulation of non-spherical particles in tribological three-body systems. In: 8th European congress on computational methods in applied sciences and engineering. CIMNE. <https://doi.org/10.23967/eccomas.2022.249>
18. Cundall PA, Strack ODL (1979) A discrete numerical model for granular assemblies. In: *Géotechnique*, vol 29, 1, pp 47–65. <https://doi.org/10.1680/geot.1979.29.1.47>
19. Hesse R, Krull F, Antonyuk S (2020) Experimentally calibrated CFD-DEM study of air impairment during powder discharge for varying hopper configurations. *Powder Technol* 372:404–419. <https://doi.org/10.1016/j.powtec.2020.05.113>
20. Weis D, Krull F, Mathy J, Evers M, Thommes M, Antonyuk S (2019) A contact model for the deformation behaviour of pharmaceutical pellets under cyclic loading. *Adv Powder Technol* 30, 11:2492–2502. <https://doi.org/10.1016/j.apt.2019.07.026>
21. Ferziger J, Peri M, Street R (2019) *Computational methods for fluid dynamics*. Springer International Publishing. ISBN: 9783319996936
22. Hirt C, Nichols B (1981) Volume of fluid (VOF) method for the dynamics of free boundaries. *J Computat Phys* 39, 1:201–225. [https://doi.org/10.1016/0021-9991\(81\)90145-5](https://doi.org/10.1016/0021-9991(81)90145-5)
23. Young T (1805) III. An essay on the cohesion of fluids. In: *Philosophical transactions of the royal society of London*, vol 95, pp 65–87. <https://doi.org/10.1098/rstl.1805.0005>
24. Grohn P, Oesau T, Heinrich S, Antonyuk S (2022) Investigation of the influence of wetting on the particle dynamics in a fluidized bed rotor granulator by MPT measurements and CFD-DEM simulations. In: *Powder technology*, vol 408, p 117736. ISSN: 0032-5910. <https://doi.org/10.1016/j.powtec.2022.117736>
25. Krull F, Hesse R, Breuninger P, Antonyuk S (2018) Impact behaviour of microparticles with microstructured surfaces: experimental study and DEM simulation. *Chem Eng Res Des* 135:175–184. <https://doi.org/10.1016/j.cherd.2018.05.033>
26. Hartmüller J (2017) *Theoretische und experimentelle Untersuchung von Partikelhaftkräften an Oberflächen*. ger. Fortschritt-Berichte Band 14. Kaiserslautern: Technische Universität. ISBN: 9783959740449
27. Hamaker HC (1937) The London-van der Waals attraction between spherical particles. In: *Physica*, vol 4, 10, pp 1058–1072, Oct 1937. [https://doi.org/10.1016/S0031-8914\(37\)80203-7](https://doi.org/10.1016/S0031-8914(37)80203-7)
28. Brenner H (1961) The slow motion of a sphere through a viscous fluid towards a plane surface. *Chem Eng Sci* 16, 3:242–251. ISSN: 0009-2509. [https://doi.org/10.1016/0009-2509\(61\)80035-3](https://doi.org/10.1016/0009-2509(61)80035-3)
29. Sondergaard R, Chaney K, Brennen CE (1990) Measurements of solid spheres bouncing off flat plates. *J Appl Mech* 57, 3:694–699. ISSN: 0021-8936. <https://doi.org/10.1115/1.2897079>
30. Mueller P, Antonyuk S, Stasiak M, Tomas J, Heinrich S (2011) The normal and oblique impact of three types of wet granules. *Granular Matter* 13:455–463. <https://doi.org/10.1007/s10035-011-0256-5>
31. Rymuza Z, Pytko S (2012) The effect of scale in tribological testing. *J Mater Res Technol* 1, 1:13–20. [https://doi.org/10.1016/S2238-7854\(12\)70004-2](https://doi.org/10.1016/S2238-7854(12)70004-2)
32. Krull F, Mathy J, Breuninger P, Antonyuk S (2021) Influence of the surface roughness on the collision behavior of fine particles in ambient fluids. *Powder Technol* 392:58–68. <https://doi.org/10.1016/j.powtec.2021.06.051>
33. Barnocky G, Davis RH (1988) Elastohydrodynamic collision and rebound of spheres: experimental verification. In: *The physics of fluids*, vol 31, 6:1324–1329. <https://doi.org/10.1063/1.866725>

34. Rabinovich YI, Adler JJ, Ata A, Singh RK, Moudgil BM (2000) Adhesion between nanoscale rough surfaces: I. Role of asperity geometry. *J Colloid Int Sci* 232, 1:10–16. ISSN:0021-9797. <https://doi.org/10.1006/jcis.2000.7167>
35. Einstein A (1905) Über die von der molekularinetischen Theorie der Wärme geforderte Bewegung von in ruhenden Flüssigkeiten suspendierten Teilchen. In: *Annalen der Physik*, vol 322, 8, pp 549–560, Jan 1905. <https://doi.org/10.1002/andp.19053220806>
36. Happel J, Brenner H (1983) *Low Reynolds number hydrodynamics: with special applications to particulate media. Mechanics of fluids and transport processes.* Springer Netherlands. ISBN: 9789024728770
37. Faxén H (1922) Der Widerstand gegen die Bewegung einer starren Kugel in einer zähen Flüssigkeit, die zwischen zwei parallelen ebenen Wänden eingeschlossen ist. *Annalen der Physik* 373:89–119
38. Ekanayake NI, Berry JD, Harvie DJ (2021) Lift and drag forces acting on a particle moving in the presence of slip and shear near a wall. *J Fluid Mech* 915. ISSN: 0022-1120. <https://doi.org/10.1017/jfm.2021.138>
39. Saffman PG (1965) The lift on a small sphere in a slow shear flow. *J Fluid Mech* 22, 2:385–400. <https://doi.org/10.1017/S0022112065000824>
40. Seifert J (2012) A review of the Magnus effect in aeronautics. In: *Progress in aerospace sciences*, vol 55, pp 17–45. ISSN: 0376-0421. <https://doi.org/10.1016/j.paerosci.2012.07.001>
41. Segré G, Silberberg A (1961) Radial particle displacements in poiseuille flow of suspensions. In: *Nature*, vol 189, 4760, pp 209–210, Jan 1961. <https://doi.org/10.1038/189209a0>
42. Urzay J, Llewellyn Smith SG, Glover BJ (2007) The elasto-hydrodynamic force on a sphere near a soft wall. In: *Physics of fluids*, vol 19, 10, p 103106. ISSN: 1070-6631. <https://doi.org/10.1063/1.2799148>
43. Rallabandi B, Saintyves B, Jules T, Salez T, Schönecker C, Mahadevan L, Stone HA, Rotation of an immersed cylinder sliding near a thin elastic coating. *Phys Rev Fluids* 2 (7):074102. <https://doi.org/10.1103/PhysRevFluids.2.074102>
44. Murata T (1980) On the deformation of an elastic particle falling in a viscous fluid. *J Phys Soc Jpn* 48 (5):1738–1745. <https://doi.org/10.1143/JPSJ.48.1738>
45. Clift R, Grace J, Weber MB (1978) *Drops, and particles.* Academic Press, New York. ISBN: 9780121769505
46. Stokes GG (1851) On the effect of the internal friction of fluids on the motion of pendulums. *Trans Camb Phil Soc* 9:8–106. <https://doi.org/10.1017/CBO9780511702266.002>
47. Tashibana M, Kitasho K (1976) The Motion of a falling sphere in a viscous fluid and the effects of side walls. In: *Memoirs of the Faculty of Engineering Fukui University*, vol 24(2)
48. Noichl I, Schönecker C (2022) Dynamics of elastic, nonheavy spheres sedimenting in a rectangular duct. In: *Soft matter*, vol 18, 12, pp 2462–2472. <https://doi.org/10.1039/D1SM01789F>

Adsorption and Wetting of Component Surfaces



Hans Hasse, Martin T. Horsch, Michael Kopnarski, Kai Langenbach, Ralf Müller, Simon Stephan, and Herbert M. Urbassek

Abstract The wetting properties of component surfaces are important in many technical applications. They depend on the wetting liquid and the morphology of the component surface, including the adsorption layer, which is always present on technical surfaces. Both wetting and adsorption are governed by the same molecular interactions, and it is highly interesting to study the influence of these interactions on macroscopic wetting and adsorption behavior. This was done here in a scale-bridging approach by coupling molecular dynamics simulations with phase field simulations in a consistent way by a molecular-based equation of state. Systematic studies of wetting and adsorption in dispersive model systems were carried out, which, however, exhibit basically all phenomena observed in real systems. These simulation studies were complemented by experiments, in which contact angle measurements were combined with X-ray photoelectron spectroscopy (XPS) surface analytics. The results demonstrate that the wetting of technical surfaces is dominated by the adsorption layer. The substrate's role is only indirect: It influences the morphology of the surface layer.

H. Hasse (✉) · S. Stephan

Institute of Engineering Thermodynamics, RPTU Kaiserslautern, Kaiserslautern, Germany
e-mail: hans.hasse@rptu.de

M. T. Horsch

Institute of Computer Science, Norwegian University of Life Sciences (NMBU), As, Norway

M. Kopnarski

Institute of Surface and Thin Film Analytics (IFOS), Kaiserslautern, Germany

K. Langenbach

Institute of Thermal Process Engineering, University of Innsbruck, Innsbruck, Austria

R. Müller (✉)

Institute of Mechanics, Technical University of Darmstadt, Darmstadt, Germany
e-mail: ralf.mueller@mechanik.tu-darmstadt.de

H. M. Urbassek

Institute of Computational Material Science, RPTU Kaiserslautern, Kaiserslautern, Germany

1 Introduction

Wetting of surfaces plays an important role in many technical processes. For an ideal surface, the *Young equation* establishes a link between the contact angle Θ of a droplet resting on the surface with the interfacial free energies which arise from the atomistic interactions of the involved components [1–4]. For a liquid droplet on a planar solid surface, the *Young equation* can be written as

$$\cos \Theta = \frac{\gamma_{SV} - \gamma_{SL}}{\gamma_{LV}}, \quad (1)$$

where γ_{SV} , γ_{SL} , and γ_{LV} indicate the surface tension of the solid–vapor, the solid–liquid, and liquid–vapor interface, respectively. However, technical surfaces do not fulfill the prerequisites of the *Young equation* as they exhibit topographical and chemical heterogeneities which lead to complex wetting phenomena [5–7]. Thereby, adsorption layers on the surface play a central role [2, 3, 8].

The wetting of component surfaces and the formation of adsorption layers on these surfaces are determined by the same molecular interactions. Hence, it should be possible to model these phenomena consistently based on the knowledge of these interactions. We have followed this route in our research in the CRC 926 using molecular dynamics simulations. These simulations are, however, strongly limited in both the length scale and the time scale that can be observed. To overcome these limitations, phase field modeling was used and connected in a consistent way to the molecular simulations, in a scale-bridging approach, in which a molecular-based equation of state is used for describing the free energy in the phase field model. Not only equilibrium properties of the molecular model are inherited, but also transport properties. This multiscale simulation paradigm is graphically represented in Fig. 1.

These simulation studies described here are limited to model systems, in which the attractive interactions are dispersive. While this could be seen as an important restriction of the scope, it turns out that even these simple systems contain basically all relevant features of adsorption and wetting of real systems—but have the advantage of being simple enough to enable systematic studies of the influence of the molecular parameters on the macroscopic behavior, which is our main focus.

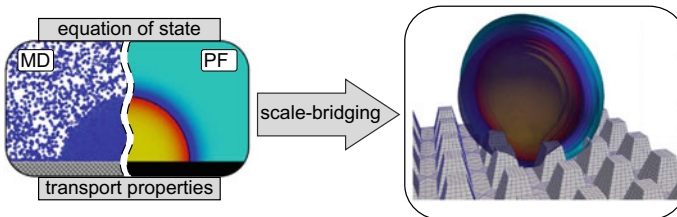


Fig. 1 Simulation paradigm illustrating the bridging of scales in wetting simulations by connecting atomistic molecular dynamics (MD) simulations and macroscopic phase field (PF) simulations

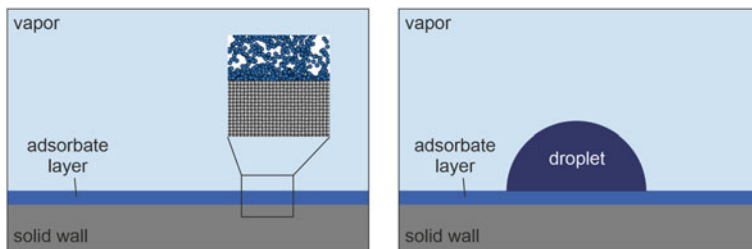


Fig. 2 Scheme of both studied simulation setups: Adsorption of a vapor phase on a solid wall (left) and wetting of a liquid phase droplet that is in equilibrium with a vapor phase on a solid wall (right)

The present chapter gives an overview of the results from simulation studies, in which both static and dynamic wetting with pure fluids and mixtures on smooth and rough surfaces were studied.

In molecular simulations, wetting and adsorption are intrinsically coupled: There are no molecular simulations of wetting in which there is not also adsorption (cf. Fig. 2). If the fluid in these simulations is a mixture, the adsorption layer will generally have a composition that differs from that of the droplets [1–3]. In many cases, the droplet sitting on top of the adsorption layer will only “see” this layer, and not the solid material below (the particles in the droplet will basically only interact with those in the adsorption layer and not with those in the solid). Then, the influence of the solid on the droplet formation is only an indirect one: It determines the composition and thickness of the adsorption layer, which, in turn, influences the droplet formation.

In the second part of this chapter, we give experimental evidence for this, that was obtained from studies of wetting of surfaces of different materials, that were machined in different ways and afterward cleaned by different procedures. Contact angles of water on these surfaces were measured and the thickness and composition of the adsorption layers were determined by X-ray photoelectron spectroscopy (XPS) measurements.

2 Simulation Studies

2.1 Studied Dispersive Model Systems

We report here on studies of wetting and adsorption in model systems. The aim is to establish a direct link between the properties on the atomistic scale and the macroscopic phenomena. This is achieved by systematic studies, in which the parameters describing the molecular interactions are systematically varied and the results are observed in a multiscale approach.

We limit ourselves to systems, in which the attractive interactions are dispersive. Despite the seeming simplicity of such systems, they exhibit the essential features of

real systems and basically all phenomena of interest in adsorption and wetting of real surfaces can be observed and analyzed as a function of relatively few parameters on the molecular scale. Their variation enables obtaining insights into the macroscopic behavior that are difficult to obtain otherwise.

On the molecular level, dispersive systems are commonly described by the Lennard–Jones (LJ) potential. The LJ potential (in its different variants) is probably the most frequently used model potential in computational physics and chemistry. It describes both repulsive and dispersive interactions between a pair of particles. A particularly convenient form of the LJ potential is the Lennard–Jones truncated and shifted (LJTS) potential with a cut-off at 2.5σ , where σ indicates the particle size. The LJTS potential is computationally cheap, but still gives a reasonable picture of the behavior of simple materials—in particular simple fluids [9]. Therefore, the LJTS potential is an excellent candidate for systematic studies on the relation between nanoscopic and macroscopic properties.

The LJTS potential u_{LJTS} is

$$u_{\text{LJ}}(r) = 4\varepsilon \left[\left(\frac{\sigma}{r} \right)^{12} - \left(\frac{\sigma}{r} \right)^6 \right] \quad \text{and} \quad (2)$$

$$u_{\text{LJTS}}(r) = \begin{cases} u_{\text{LJ}}(r) - u_{\text{LJ}}(r_c) & r \leq r_c \\ 0 & r > r_c, \end{cases} \quad (3)$$

with u_{LJ} being the full LJ potential, ε and σ being the energy and size parameter of the particles, respectively. The distance between two particles is r . The truncation radius r_c of the potential is set to 2.5σ throughout the present work, and “LJTS” always refers to that cut-off radius.

Throughout the present work, all physical properties are reported with respect to the LJ potential parameters of the fluid ε_{FF} and σ_{FF} , the mass of the fluid particles M_{F} , and the Boltzmann constant k_{B} .

Here, the LJTS potential was used to describe all three interaction types, i.e., fluid–fluid, solid–solid, and solid–fluid. The size parameter σ and the particle mass M of all fluids and the solid wall particles were the same. The energy parameter ε describing the fluid–fluid, solid–solid, and solid–fluid interactions were systematically varied.

In this work, for the fluid, both the pure LJTS component and mixtures of LJTS fluids were studied. In the latter case, binary mixtures consisting of a high-boiling component 1 and a low-boiling component 2 were considered. The high-boiling component was the same in all mixtures and can be considered as the reference fluid. The low-boiling character of component 2 is obtained by decreasing its dispersion energy with respect to component 1, i.e. $\varepsilon_{\text{FF},2}/\varepsilon_{\text{FF},1}$. The cross interactions between the fluid particles of components 1 and 2 were modeled using the modified Lorentz–Berthelot combination rules [10, 11]

$$\sigma_{\text{FF},12} = \frac{\sigma_{\text{FF},1} + \sigma_{\text{FF},2}}{2}, \quad (4)$$

$$\varepsilon_{\text{FF},12} = \xi \sqrt{\varepsilon_{\text{FF},11} \varepsilon_{\text{FF},22}}, \quad (5)$$

where ξ is a state-independent parameter characterizing the cross affinity of the two components.

The solid–fluid interaction energy ε_{SF} has an important influence on the adsorption and wetting behavior. Here, ε_{SF} was modeled as

$$\varepsilon_{\text{SF}} = \zeta \varepsilon_{\text{FF}}, \quad (6)$$

where ζ is also a state-independent parameter characterizing the attraction of the fluid particles on the solid wall. The solid–fluid interaction size parameter was the same as the fluid–fluid interaction size parameter—in all cases.

Systematic studies on the influence of the atomistic interaction parameters and the thermodynamic conditions on the macroscopic behavior of the system were carried out. Namely, the adsorption of both the pure LJTS component as well as of binary mixtures on solid walls was studied [12–15]. Moreover, the wetting of droplets of the pure LJTS component as well as of binary mixtures on solid walls was studied [16, 17]. While the aforementioned studies were carried out using equilibrium conditions and an atomistically flat solid wall, also more complex scenarios were studied, e.g., the wetting of droplets on structured walls [18–20], the dynamic behavior of droplets on walls with a wettability gradient and transport properties [21, 22] as well as the wetting behavior in microstructures [21, 23].

Within this work, also more complex model systems were studied such as the two-center Lennard–Jones plus dipole (2CLJD) [24] and the two-center Lennard–Jones plus quadrupole (2CLJQ) fluid [25] as well as the generalized LJ fluid, i.e., the Mie fluid [26]. Also, for studying heterogeneous systems by MD simulations using the named model types, new methods had to be developed for considering long-range interactions and finite size effects at interfaces [27–29].

2.2 Simulation Techniques

2.2.1 Molecular Dynamics

MD simulations of heterogeneous systems were carried out with the massively parallel code `ls1 mardyn` [30] (which presently holds the world record for the largest MD simulation [31]). The simulations were carried out in the NVT ensemble using classical velocity scaling for thermostating. Periodic boundary conditions were applied in all directions. The number of fluid particles was at least 8,000 for the adsorption simulations and 15,000 for the droplet simulations. Both, the equilibration time and the production time were at least 2.5 million time steps. The parallelization was accomplished by spatial domain decomposition based on a linked cell data structure. Newton’s equations of motion were integrated using the Verlet leapfrog algorithm with a time step of $\delta\tau = 0.0005 (M_{\text{F}}/\varepsilon_{\text{FF}})^{1/2} \sigma_{\text{FF}}$.

The wall was represented by particles arranged on a face-centered cubic (fcc) lattice with the (100) surface exposed to the fluid. To maintain solid state of the

wall, its energy parameter ε_{SS} of the solid (S) is related to that of the fluid (F) by $\varepsilon_{SS} = 100 \varepsilon_{FF}$. With the size parameter of the solid $\sigma_{SS} = \sigma_{FF}$, the lattice constant of the solid phase is $a = 1.55 \sigma_{SS}$ and the particle density is $\rho_{\text{wall}} = 1.07 \sigma_{SS}^{-3}$.

The sampling of the density profiles was carried out bin-wise. For the adsorption simulations, all three Cartesian coordinates were discretized to equally spaced rectangular bins. For the droplet simulations, a cylindrical coordinate system was used. Statistical uncertainties were estimated using the block-averaging method. Further simulation details on the heterogeneous wetting and adsorption simulations can be found in Refs. [12, 14, 16–18].

Moreover, simulations of homogeneous systems were carried out using the MD/MC code *ms2* [32–35]. Thereby, systematic studies on bulk phase properties of the studied LJTS systems were carried out regarding the pVT -behavior [36], the gas solubility [37], and transport properties [22, 38, 39].

2.2.2 PeTS Equation of State

The perturbed truncated and shifted (PeTS) equation of state (EOS) was developed in this work to model the thermodynamic properties of the LJTS fluid [36] and LJTS fluid mixtures [40]. The PeTS EOS is based on the perturbation theory of *Barker and Henderson*, which splits the Helmholtz energy per particle a into the ideal gas contribution a_{id} , the free energy of a hard sphere potential a_{hs} , and a perturbation a_{pert} contribution due to dispersion, i.e.,

$$a = a_{\text{id}} + a_{\text{hs}} + a_{\text{pert}}. \quad (7)$$

The perturbation contribution is modeled as a sum of a first-order and second-order contribution, i.e., $a_{\text{pert}} = a_1 + a_2$, which are developed in a Taylor series as functions of the packing fraction η . The parameters of the PeTS EOS were fitted to vapor–liquid equilibrium data of the LJTS fluid and describe the vapor pressure and the saturated densities well [36]. The PeTS EOS has been extended to mixtures [40] using van der Waals one-fluid theory. The PeTS EOS was, moreover, validated using homogeneous pVT data at stable and metastable states as well as phase equilibrium data for mixtures and good agreement was found [36, 37, 40]. It is also known that the PeTS EOS gives a realistic description of the region between the binodals, i.e., a single van der Waals loop [36]. For the modeling of mixtures, the PeTS EOS also uses the modified combination rules of Lorentz and Berthelot, cf. Eqs. (4) and (5).

Figure 3 shows the results from the PeTS EOS for the vapor–liquid equilibrium (VLE) of the LJTS fluid in comparison to computer experiment data taken from the literature [41]. The results from the PeTS EOS are in excellent agreement with the MD reference data. This also holds for the prediction of mixture VLE and homogeneous state properties [22, 40, 42].

The PeTS EOS has been used in conjunction with density gradient theory (DGT) and density functional theory (DFT) for modeling both solid–fluid and fluid–fluid interfacial properties. Details are given in Refs. [13, 36, 43]. Moreover, the PeTS

EOS was used in the phase field (PF) approach as a free energy functional, which is described in the following. Thereby, the predictions from the mesoscopic models PF, DGT, and DFT, are thermodynamically consistent with the predictions from MD. Hence, the PeTS EOS establishes the link between the two modeling approaches, MD on one side and PF, DGT, and DFT on the other side.

2.2.3 Phase Field Modeling

Phase Field Modeling for Static Properties

The main ingredient of a phase field is the potential that drives the system. For static wetting simulations, an *Allen-Cahn* approach is taken to reach a stationary solution. The particle density ρ is chosen as the order parameter and the total potential of the system is given by

$$F[\rho, \nabla\rho, \lambda] = \int_B (\psi(\rho, \nabla\rho) + \tilde{\rho}gz) dV + \lambda \left(\int_B \rho dV - N \right), \quad (8)$$

where ψ is the specific energy density and the gradient dependency on $\nabla\rho$ is introduced to take the vapor–liquid interface into account, and $\tilde{\rho}$ is the mass density. The Lagrange multiplier λ introduces a constraint on the number of particles N within the simulation volume. Furthermore, the potential energy of gravity g is taken into account. The field equations can be obtained from the potential Eq. (8) by the calculus of variations. The particle density ρ follows a time-dependent *Ginzburg–Landau* equation [44]

$$\dot{\rho} = -K \frac{\delta F}{\delta \rho} \quad \text{with} \quad \frac{\delta F}{\delta \rho} = \frac{\partial(\rho\psi)}{\partial \rho} - \nabla \cdot \frac{\partial(\rho\psi)}{\partial \nabla \rho} + Mg z + \lambda, \quad (9)$$

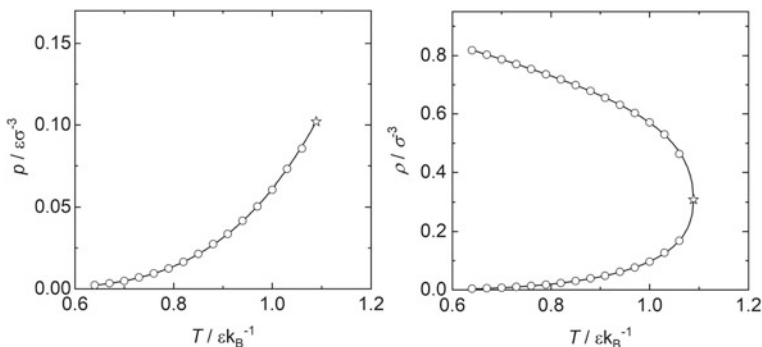


Fig. 3 Vapor–liquid equilibrium of the LJTS fluid: Vapor pressure (left), saturated densities (right). Solid lines indicate PeTS EOS [36]; symbols indicate MD results from *Vrabec et al.* [41]

where K is a mobility constant and M is the molar mass. The variation with respect to λ renders the constraint on the number of particles N . Once the rate $\dot{\rho}$ falls below a preset tolerance, a static version of Eq. (9) is solved, by setting the left-hand side to zero. This strategy allows a robust solution with a *Newton–Raphson* procedure in every time step. The discretization in space is done by bi-linear elements in 2D and tri-linear elements in 3D. Furthermore, the contact to the solid is incorporated in the simulation by special interface elements (line elements in 2D and surface elements in 3D) by an energy contribution [45]. This establishes *Young’s* equation and determines the contact angle. Details on the implementation can be found in Refs. [19, 46].

In order to integrate information from MD simulations of the LJTS model system into the phase field model, the PeTS equation of state [36] is used for modeling the thermodynamic behavior of the fluid in the system as

$$\psi(\rho, \nabla\rho) = \rho a(\rho) + \frac{1}{2}\kappa|\nabla\rho|^2. \tag{10}$$

The results obtained from the term ρa are depicted in Fig. 4-left. It is noted that in the simulation, the excess energy ω , see Fig. 4-right is used. In the excess energy, the phase contrast between the vapor density ρ'' and the liquid density ρ' is more pronounced. Details can be found in Ref. [47].

The good agreement between the results obtained from the phase field model and those obtained directly from molecular simulations is illustrated by Fig. 5 for a planar interface of an LJTS fluid.

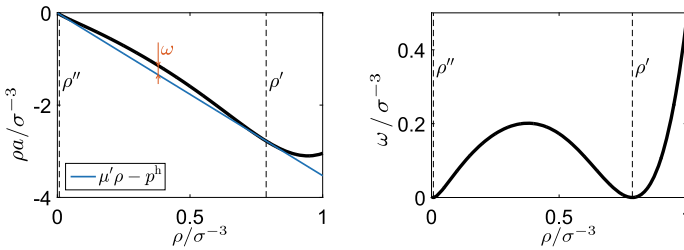


Fig. 4 Left: Helmholtz energy ρa^{PeTS} as a function of the density. Right: excess free energy ω , vapor density ρ'' , liquid density ρ'

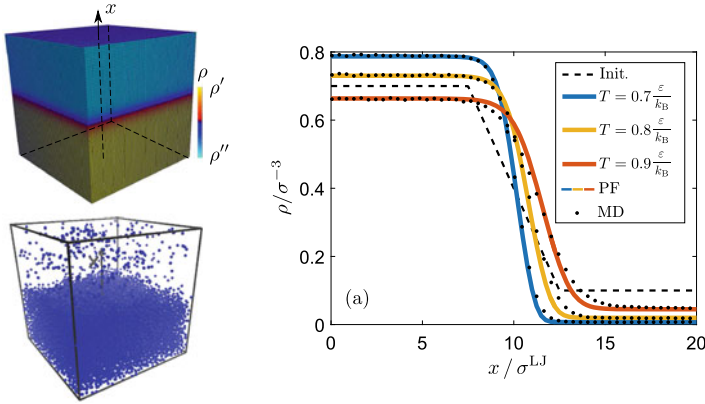
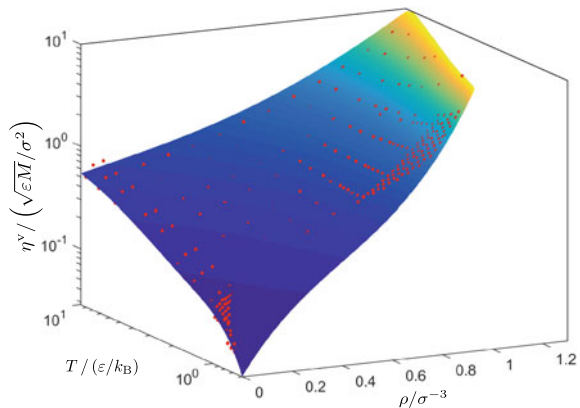


Fig. 5 Comparison of MD simulation and phase field calculation for the stationary planar vapor-liquid interface of the LJTS fluid

Fig. 6 Viscosity of the LJTS fluid as a function of the temperature T and density ρ [21]. Red dots indicate MD simulation results. The colored surface indicates the empirical model fitted to the MD data



Phase Field Modeling for Dynamic Properties

To be able to address more complex, and especially instationary scenarios, a dynamic phase field model was developed [23, 48]. Again, the density is taken as order parameter. Parts of the stress tensor are obtained from the equation of state (that is derived from the MD simulation data). The dissipative stresses are computed using a viscosity model that was developed based on MD data [38].

The dependency of the viscosity of the LJTS fluid on density and temperature is depicted in Fig. 6. For most data points, the empirical model describes the MD data within its statistical uncertainty. MD data in unstable temperature T -density ρ regions were extrapolated to provide data, e.g., the interface transition zone between two bulk phases. For details, the reader is referred to Ref. [21].

The constraint from the static phase field model was replaced for the modeling of dynamic scenarios by the mass balance, given in its local form by

$$\frac{\partial \tilde{\rho}}{\partial t} + \operatorname{div}(\tilde{\rho} \underline{v}) = 0. \quad (11)$$

The equation of motion, or the balance of linear momentum, completes the balance laws of the system, which resembles the compressible *Navier–Stokes* equations [20, 49]

$$\tilde{\rho} \frac{\partial \underline{v}}{\partial t} + \tilde{\rho} \nabla \underline{v} \underline{v} = \operatorname{div} \underline{\underline{\sigma}} + \tilde{\rho} g \underline{e}_z, \quad (12)$$

where \underline{e}_z is the unit vector pointing in the direction of gravity. Thereby, the stress tensor $\underline{\underline{\sigma}}$ incorporates viscous and surface energy effects via the so-called *Navier–Korteweg* tensor. As in Eq. (8), the gradient of the density ρ enters this term.

$$\underline{\underline{\sigma}} = \underline{\underline{\sigma}}^v + \underline{\underline{\sigma}}^K \quad (13)$$

$$\underline{\underline{\sigma}}^v = 2\eta \left[\frac{1}{2} (\nabla \underline{v} + (\nabla \underline{v})^T) - \frac{1}{3} \operatorname{tr}(\underline{v}) \underline{\underline{1}} \right] \quad (14)$$

$$\underline{\underline{\sigma}}^K = -(\rho\mu - \psi) \underline{\underline{1}} - \left(\frac{\partial \psi}{\partial \nabla \rho} \otimes \nabla \rho \right). \quad (15)$$

Due to the almost incompressible behavior in the liquid phase, a mixed finite element formulation is used, taking the velocity vector \underline{v} , the mass density $\tilde{\rho}$, and the chemical potential μ as independent fields. Since the implementation is written in reduced units, the values of the particle density and the mass density are equal. In the finite element discretization, the velocities \underline{v} are interpolated quadratically, while the mass density $\tilde{\rho}$, and chemical potential μ are linearly interpolated. This interpolation scheme is motivated by the *Babuska–Brezzi* condition for mixed finite elements [50].

2.3 Results and Discussion

2.3.1 Nanoscopic Properties

Figure 7 shows the structure of the fluid at different types of interfaces, as predicted by molecular simulation and theory. Results are shown for a solid–vapor (SV) interface [13] (left), a solid–liquid (SL) interface, as it is found for the contact of a droplet with the solid [17] (middle), and a vapor–liquid (VL) interface [40] (right). For the SV interface and the VL interface, results for a binary fluid mixture are depicted, while, for the SV interface, results for a pure component fluid are shown.

The structure of the fluid at the interface depends on many parameters, such as the solid–fluid interaction, described here by the factor ζ (cf. Eq. (6)) [12–17], the density of the solid wall [12, 16], the temperature and bulk fluid density, and, eventually, the composition of the fluid [12–14, 16, 17, 40, 43]. The influence of these parameters on the interface structure has been systematically studied [12–17, 40, 43].

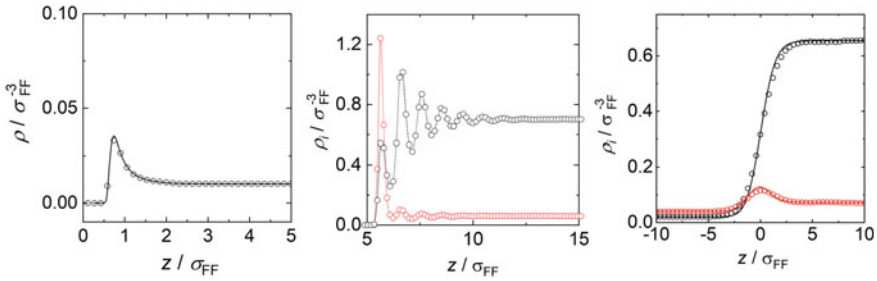


Fig. 7 Density profiles at different types of interfaces: Solid–vapor interface (left), cf. Fig. 2-left; Solid–liquid interface (middle) of a liquid droplet on a solid wall, cf. Fig. 2-right; Vapor–liquid interface (right) between a liquid droplet and a vapor phase, cf. Fig. 2-right. The solid phase was a solid wall of LJTS particles. Left: Symbols are MD results; Solid lines are DFT results [13]. Results for $\epsilon_{SF} = 0.3\epsilon_{FF}$, $T = 0.88 \epsilon_{FF}k_B^{-1}$, and a fluid bulk phase density of $\rho_F = 0.0102 \sigma^{-3}$. Middle: Symbols are MD results; Lines are a guide for the eye [17]. Black indicates component 1 and red indicates component 2—both having identical ϵ_{FF} and $\xi = 1$. Results for $\epsilon_{SF} = 0.3\epsilon_{FF}$, $T = 0.75 \epsilon_{FF}k_B^{-1}$, and a fluid bulk phase density of $\rho_F = 0.079 \sigma^{-3}$. Right: Symbols are MD results; Solid lines are DGT results [40]. Results for $\epsilon_{FF,2}/\epsilon_{FF,1} = 0.9$, $\xi = 0.85$, $T = 0.77 \epsilon_{FF}k_B^{-1}$, and a liquid bulk phase density of $\rho_F = 0.728 \sigma^{-3}$

The three types of interfaces shown in Fig. 7 exhibit distinctly different features. The interfacial thickness is about 10σ in the case of the VL interfaces and the SL interfaces, whereas the thickness is significantly smaller for the SV interface (about 1σ). This is due to the fact that the total difference between the bulk phase densities is significantly larger for the SV interface than for the two other interfaces. The atomistic structuring is most pronounced in the case of the SL interface (cf. Fig. 7-middle), where several adsorption layers can be observed, whereas only one adsorption layer is formed at the SV interface (cf. Fig. 7-left). The atomistic layering has a wavelength of about 1σ , which is as expected. For the VL interface depicted in Fig. 7-right, no atomistic layering is observed. Nevertheless, it was shown in an earlier work of our group that atomistic layering at VL interfaces exists also for the LJTS model system [43]; yet the amplitude is about two orders of magnitude smaller compared to that observed for the SL interface. In the case of the VL interface, an additional phenomenon is observed: the low-boiling component accumulates at the interface, which is called *enrichment* [17, 51]. The enrichment peak has a width of about $\delta z = 5\sigma$ and is, therefore, not related to a geometrically driven layer formation, but rather a thermodynamic phenomenon [42, 51].

For the SV interface and VL interface, results from both computer experiments and a theory (DFT in the case of the SVE interface and DGT in the case of the VLE interface) are depicted in Fig. 7. The predictions from the two simulation methods are in excellent agreement. Details on the comparison of the two methods can be found elsewhere [13, 40, 43, 47].

2.3.2 Macroscopic Properties

The adsorption and wetting behavior of the LJTS model system (cf. Sect. 2.1) was predicted using on the one hand classical molecular simulation computer experiments and, on the other hand, theoretical methods such as PF, DGT, and DFT. The theoretical methods are consistent with each other as well as consistent with the molecular simulation predictions by using the PeTS equation of state for modeling the thermodynamic properties of the LJTS fluid and fluid mixtures.

Adsorption

The adsorption of the LJTS model system has been studied comprehensively for both pure components [12, 13, 15, 43, 52, 53] and binary mixtures [14, 17, 40, 42]. Also, the adsorption at different types of interfaces was considered, i.e., the adsorption of a vapor phase on a planar solid wall [12, 13, 15], the adsorption of a liquid phase on a planar solid wall [17, 52, 53], and the adsorption of components at vapor–liquid interfaces [40, 42, 43].

Figure 8 shows results for the adsorption isotherms of a pure component LJTS fluid on a solid wall (left) [13] and a binary mixture vapor–liquid system (right) [42]. The adsorption Γ (for the pure component system) and $\Gamma_2^{(1)}$ (for the binary mixture system) indicate the amount of fluid particles at the interface per surface area of the interface. Hence, it characterizes the deviation between the interface density (and ev. composition) from the bulk phase values.

For the pure component system, results from MD and DFT are shown. For the binary mixture system, results from MD and DGT are shown. In all cases, the predictions from the computer experiments and the theory are in good agreement. Only in the VLE system, at very large adsorption $\Gamma_2^{(1)}$ of the low-boiling component 2 at the interface, some deviations between the results from the methods are observed.

For both the vapor–solid system and the vapor–liquid system, the adsorption at the interface decreases with increasing temperature. For the vapor–solid system, the adsorption at the interface increases with increasing bulk phase pressure (which corresponds to an increasing bulk phase density). For the vapor–liquid system, the adsorption at the interface first increases with increasing liquid phase concentration x_2' , reaches a maximum, and then decreases to zero upon approaching a critical point in the mixture.

Both systems depicted in Fig. 8 exhibit a wetting transition at a given temperature. A liquid droplet nucleates at the vapor–solid interface (Fig. 8-left) as the vapor pressure is reached at approximately $p^s(T = 0.88 \varepsilon_{\text{FF}} k_{\text{B}}^{-1}) = 0.23 \varepsilon_{\text{FF}} \sigma_{\text{FF}}^{-3}$. This wetting transition corresponds to the steep increase of the adsorption isotherm of $T = 0.88 \varepsilon_{\text{FF}} k_{\text{B}}^{-1}$. In the binary mixture vapor–liquid system (Fig. 8-right), a droplet of a second liquid phase nucleates at the vapor–liquid interface as the state point reaches the vapor–liquid–liquid equilibrium of the system at $T = 0.66 \varepsilon_{\text{FF}} k_{\text{B}}^{-1}$. The liquid phase concentration of the vapor–liquid–liquid equilibrium is at approximately $x_{2,\text{VLE}}'(T = 0.66 \varepsilon_{\text{FF}} k_{\text{B}}^{-1}) = 0.12 \text{ mol mol}^{-1}$.

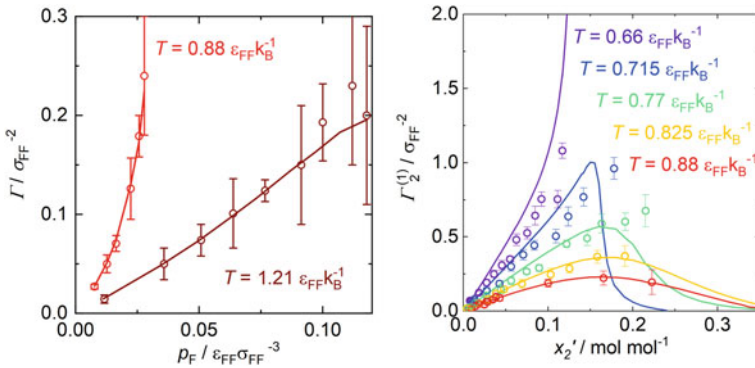


Fig. 8 Adsorption isotherms for a pure LJTS fluid on a solid wall as a function of the bulk fluid pressure p_F (left [13]) and for a binary LJTS vapor–liquid interface as a function of the liquid phase concentration x_2' (right [42]). Symbols indicate MD results; lines indicate theory (DFT for the vapor–solid adsorption (left) and DGT for the vapor–liquid adsorption (right)). The temperature is color-coded. The solid–fluid interaction energy was $\epsilon_{SF} = 0.5\epsilon_{FF}$ (left). The vapor–liquid system (right) is characterized by $\epsilon_{FF,2}/\epsilon_{FF,1} = 0.6$ and $\xi = 0.85$

Wetting

The wetting behavior of the LJTS model system has been studied systematically using both molecular simulation and the phase field model in conjunction with the PeTS EOS. The wetting behavior has been studied for simple planar walls [15, 16, 46] as well as structured walls [18–20, 45] of pure component LJTS fluid systems and also for binary mixture LJTS fluid systems [17, 42]. Also, dynamic wetting scenarios have been studied based on the LJTS model system [21, 23, 48].

Figure 9 shows the MD results for the wetting of binary fluid mixture droplets on a planar wall. Results for three different mixtures are shown. The solid–fluid interaction parameter was different for the two components: $\zeta_1 = 1$ and $\zeta_2 = 0.35$. In the case of pure component droplets, these solid–fluid interaction energies yield total wetting for the LJTS component 1 ($\Theta_A = 0^\circ$) and partial wetting for component 2 ($\Theta_A = 123.8^\circ$) [16]. For the results depicted in Fig. 9, the two fluid components had the same dispersion energy $\epsilon_1 = \epsilon_2$.

For the mixture $\xi = 1$ (cf. Fig. 9-middle), the only difference between component 1 and component 2 is the different strength of the solid–fluid interaction. The strong preference of component 1 for the solid wall particles leads to high local concentrations of component 1 in the first adsorbate layer at the surface and to a depletion of component 2 in this layer. Hence, the droplet sits on an adsorption layer that has a composition that significantly differs from the liquid bulk phase composition. Thereby, the contact angle is significantly decreased compared to the pure component 2. Moreover, the influence of the composition on the contact angle was studied [17]. It was thereby found that, depending on the composition of the fluid, different wetting cases are obtained: For high concentrations of component 2, partial

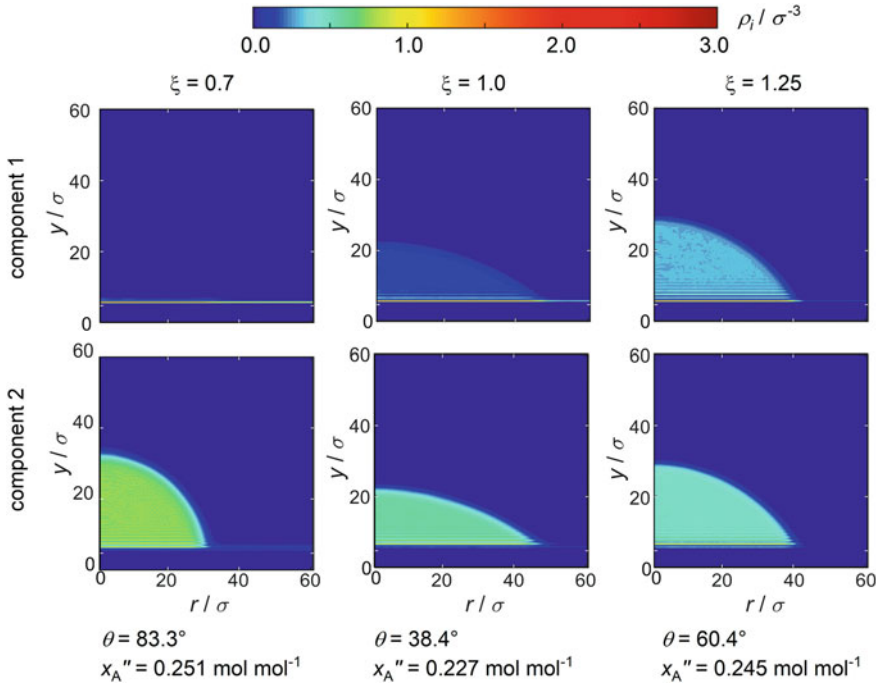


Fig. 9 Density field obtained from MD for droplets on a planar wall. The fluid was a binary mixture of two LJTS fluids: Component 1 (top row) and component 2 (bottom row). Results for three mixtures with different binary interaction parameter $\xi = 0.7$ (left), $\xi = 1$ (middle), and $\xi = 1.25$ (right). The solid–fluid interaction parameter was different for the two components: $\zeta_1 = 1$ and $\zeta_2 = 0.35$. The temperature was $T = 0.75 \varepsilon_{\text{FF},1} k_B^{-1}$ in all cases. Data taken from Ref. [17]

wetting prevails, while for high concentrations of component 1, total wetting prevails. This behavior is in line with a transition between the pure component contact angle values.

Also for the mixture with $\xi = 0.7$ (cf. Fig. 9-left), component 1 has a higher affinity to the surface than component 2, but in addition, the unlike fluid–fluid interaction is unfavorable. Therefore, the phenomenology of the observed wetting behavior differs significantly from that observed for the mixture with $\xi = 1$. Basically, a drop consisting solely of component 2 particles is sitting on an adsorbate layer of component 1 particles.

For the mixture with $\xi = 1.25$ (cf. Fig. 9-right), the high affinity of both fluid components in this mixture leads to an increased homogeneity of the fluid. Therefore, component 1 has a smaller influence on the wetting behavior compared to the mixtures with $\xi = 0.7$ and $\xi = 1$.

Also, the influence of the adsorbate layer on the wetting was studied: For a sufficiently thick adsorbate layer, the influence of the wall and the solid–fluid interaction energy on the wetting behavior vanishes, which is then only determined by the adsor-

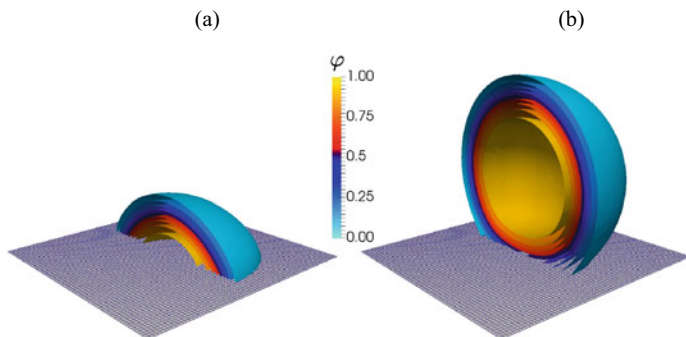


Fig. 10 Droplets on a planar surface computed by the phase field model in combination with the PeTS EOS: (a) contact angle 60° , (b) contact angle 150° . The temperature was $T = 0.7 \varepsilon_{\text{FF}} k_{\text{B}}^{-1}$

bate layer and the interactions between the adsorbate layer particles and the droplet particles. In the studied cases, the strong attraction of component 1 particles on the solid wall results in a shielding of component 2 particles from the solid.

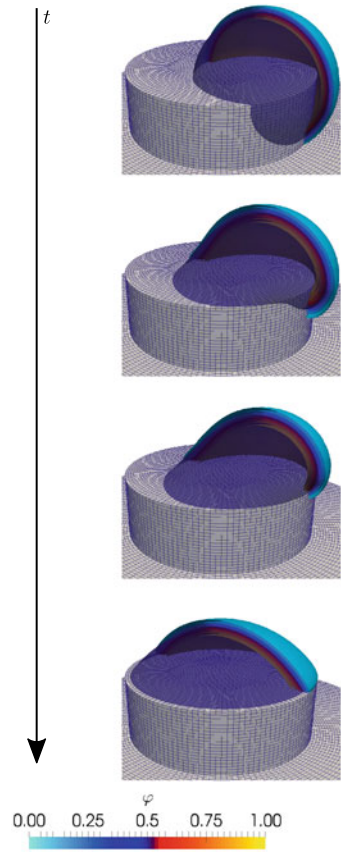
The wetting behavior of LJTS systems was also studied systematically using the phase field method. Figure 10 shows PF results for droplets on a plane surface for different contact angles.

A direct comparison between MD simulations and phase field calculations was carried out to ensure that the energetic properties as well as the interfacial properties are the same. The interfacial properties are mainly represented by the gradient term in Eq. (10), see also Fig. 11a. It is worth mentioning that not only the bulk properties such as the vapor and liquid density ρ'' and ρ' , respectively, are in good agreement with predictions from MD, also the transition zone width is well described [43, 47].

Using data from the MD simulations, a droplet on a cylindrical pedestal was analyzed [19]. Initializing the droplet in an overarching situation, the forces due to the contact angles move the droplet upward into a symmetric position on the pedestal, see Fig. 11. The pseudomotion in that scenario is due to the regularization time in Eq. (9). In the final equilibrium state, the finite element system matrix can be used to analyze the stability of the droplet shape. Such an investigation shows that the symmetric position on the pedestal is the stable configuration. Overarching situations that were observed in MD simulations are unstable situations. They only occur due to dynamic character of the MD simulations and are most likely not long-term stable. The details of such stability analyses are given in [46].

Figure 12b shows the impact of a falling droplet on a structured surface. In the left column, the contact angle was prescribed as 90° resulting in a “sink in” of the resting droplet. It can be observed that the structured surface influences the wetting mechanism leading to a sequential filling of the surface pockets. For a high contact angle of 150° , the droplet does not penetrate into the structure and finally rests on top of the structured surface. It can be seen that, at the first and second intermediate steps, the liquid partly fills the pockets, but cannot fill them completely. During the

Fig. 11 Droplet of a pure LJTS fluid on a solid wall pedestal at temperature $T = 0.7 \varepsilon_{\text{FF}} k_{\text{B}}^{-1}$: The droplet is initialized in an energetically unfavorable position (top) and as time t evolves, the droplet moves in the energetically most favorable position (bottom). The color scale indicates the order parameter φ which corresponds to the density of the system: $\varphi = 1$ indicates the liquid phase; $\varphi = 0$ indicates the vapor phase



process, the droplet even leaves the surface again (snapshot three, on the right). In the stationary state, the high contact angle retreats the liquid from the pockets.

Due to the high importance of the contact angle, also surfaces with varying contact angles, i.e., surface energy between solid and fluid, were studied by both MD and phase field simulations. Therefore, a wettability gradient $\partial\zeta/\partial x$ was prescribed as a boundary condition. The results are reported in Fig. 13. The surface energy decreases towards the center of the simulation domain. For a droplet not located in the center of the domain, the different contact angles on both sides of the droplet result in an overall force pulling the droplet into the center, where the contact angles on both sides are equal resulting in a vanishing overall force. Figure 13 shows that the results from the two independent methods are in excellent agreement.

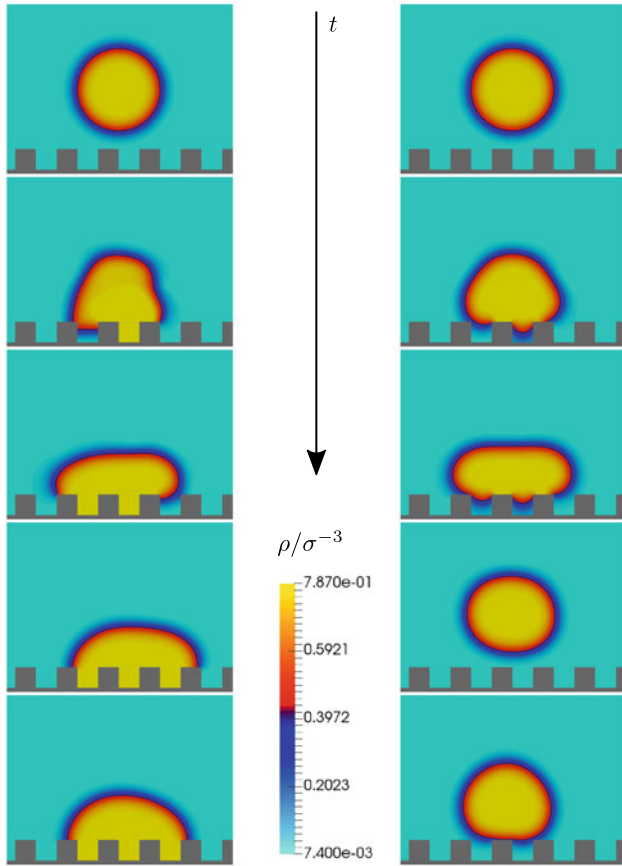


Fig. 12 Impact of a droplet on a structured surface as a function of the time t from top to bottom. Left: Contact angle 90° ; Right: Contact angle 150° . The temperature was $T = 0.7 \epsilon_{FF} k_B^{-1}$

3 Experimental Studies

3.1 Manufacturing–Morphology–Property Relationships for Wetting

The experimental study described here aimed at establishing manufacturing–morphology–property relationships for the field of wetting of component surfaces. As wetting properties are of interest, in the first step of this chain, the manufacturing, not only the material and the way it is machined are important but also the way the component is cleaned, handled, and stored. The features of the morphology of the surface that are relevant for the wetting properties are not only the component

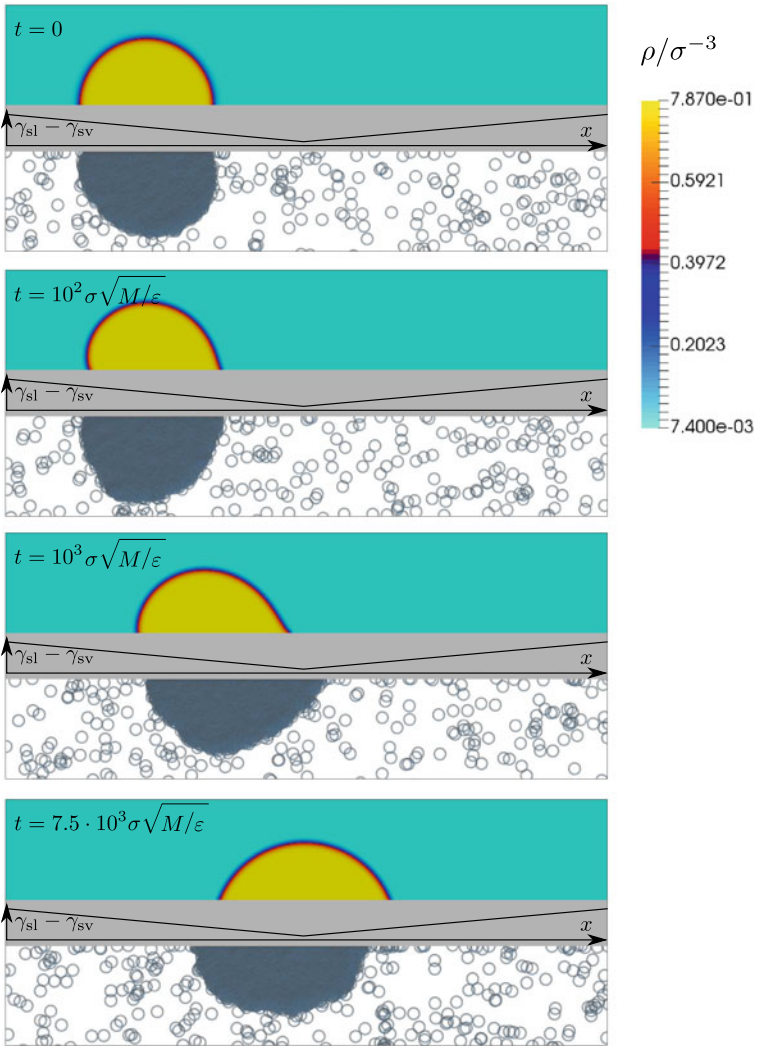


Fig. 13 Moving droplet on the surface with contact angle gradient: PF contour plots (top in each row) and MD results (bottom in each row). The MD results are represented as mirror images. The temperature was $T = 0.7 \varepsilon_{FF} k_B^{-1}$. Results for different times t are shown. Each particle of the MD simulation is represented by a bubble. The first plot shows the initialization state at $t = 0$. The last plot is a snapshot from the equilibrium state of the PF simulations

material and the surface geometry. The results obtained in the present study show that the adsorption layer on the surface plays an essential role.

Such adsorption layers are basically always present on technical surfaces. To study surfaces without such layers, one would have to create them, e.g., by sputtering in ultra-high vacuum. Cleaning of the surface does not remove the adsorption layer, it basically alters it. Hence, characterizing the surface morphology does not only mean to determine the surface geometry but also the adsorption layer needs to be characterized. This was done here using X-ray photoelectron spectroscopy (XPS). The property of interest which was studied here was the contact angle of water droplets on the component surface.

3.2 *Materials and Methods*

3.2.1 **Sample Preparation**

The experimental studies described in this section were carried out with probes made from different materials, machined with different techniques, and cleaned in different ways.

In a first series of studies [54], samples made of steel 16MnCr5 (1.7131) and titanium grade 2 (Thyssen Krupp) were used. The samples were grinded discs with a diameter of 20 mm. For comparison, in a second series of experiments [55] probes with gold surfaces were investigated. These were obtained by sputtering silicon wafers first with chromium and then with a 100 nm thick layer of gold.

3.2.2 **Treatment and Cleaning**

The probes were divided into two sets. One set was exposed to oil (synthetic polyalpha-olefin PAO) the other set was not. The probes from both sets were first cleaned with a cloth and then put in an ultrasonic bath filled with a solvent. The cleaning in the ultrasonic bath was repeated with fresh solvent three times before drying the samples in the air. As a reference, also probes without cleaning in the ultrasonic bath were studied (no cleaning). Three different solvents were used for the triple cleaning in the bath: Acetone, cyclohexane, and isopropanol. For more details, see Refs. [54, 55].

3.2.3 **Surface Topography**

Surface topography maps were obtained by white light interferometry. The root mean squared roughness of the surfaces found from these studies were: 2 nm (gold), 10 nm (steel), and 40 nm (titanium). This corresponds to *Wenzel* roughness factors [6] r of 1.00 (gold), 1.01 (steel), and 1.08 (titanium), where r relates the apparent

contact angle θ_{app} to the contact angle on an ideally flat surface θ according to *Wenzel's* equation

$$\cos(\theta_{\text{app}}) = r \cos(\theta) . \quad (16)$$

The differences between θ_{app} and θ are basically within the experimental uncertainty of the contact angle measurement, even for the titanium surfaces.

3.2.4 Adsorption Layer

The analysis of the surface layer was done by X-ray photoelectron spectroscopy (XPS) as described in detail in Refs. [54, 55]. The main results are the thickness of the adsorption layer δ and atom number fractions x_i of constituents of the adsorption layer. The constituents that could be distinguished based on the available spectral information were: Oxygen (O), carbon in polar groups (C-P), and carbon in unpolar groups (C-NP). Hence, the composition of the adsorbate layer as determined by XPS can be represented in a Gibbs triangular diagram.

3.2.5 Contact Angle

Water contact angles were measured with a drop shape analysis system as described in detail in [54, 55]. The reproducibility of the contact angle measurements was found to be of the order of 5° , which is taken as the error in the contact angle measurements in the present study. The contact angle measurement was carried out a few hours after the XPS analysis. For storage and transport, the samples were wrapped in aluminum foil. All experiments were carried out at room temperature.

3.3 Results and Discussion

The results for the composition of the surface layer for all experiments described in the previous sections are summarized in the Gibbs triangular diagram shown Fig. 14-left. Despite the variation of the substrates (steel, titanium, and gold), the treatment (oil, no oil), and the cleaning (cyclohexane, acetone, isopropanol, and no cleaning), the results fall basically on a single line in the diagram in Fig. 14-right.

The adsorbate layers on the gold samples always showed high concentrations of non-polar carbon (C-NP). The affinity of steel and titanium for non-polar carbon was found to be clearly weaker. As expected, for a given solid material, the adsorbate layer contained more non-polar carbon for the samples that were exposed to oil than for the samples that were kept clean. For a more comprehensive discussion, see Ref. [14].

The amount of data as well as the resolution of the spectroscopic method is not sufficient to establish general relations between the solid material, its treatment, and

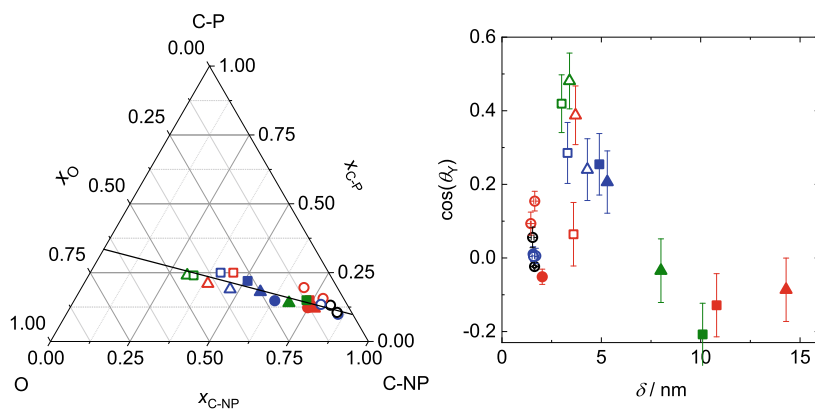


Fig. 14 Left: Atom number fractions of oxygen x_{O} , polar carbon $x_{\text{C-P}}$, and nonpolar carbon $x_{\text{C-NP}}$ in the adsorbate layer. Right: Cosine of water contact angle $\cos \Theta_{\text{Y}}$ as a function of adsorbate layer thickness δ . Colors and symbols have same code in the left and right plots. Results for different substrates: Gold (circles) [14], steel (triangles), and titanium (squares) [54]. Pre-treatment: No-oil (open symbols); with oil (filled symbols). Cleaning: Cyclohexane (blue), acetone (red), isopropanol (green), and no cleaning (black). The black solid line indicates the empirical correlation proposed by Heier et al. [14]

the composition of the surface layer, but it becomes clear that XPS is a valuable method for such studies and that meaningful relations can be established.

Figure 14-right shows the results for the thickness δ of the adsorbate layer together with the results obtained for the contact angle. The adsorbate layers on the gold samples were found to be only about 2 nm thick, and, hence, thinner than those on the steel and titanium samples, for which the thickness varied between about 4 nm and 14 nm. For the latter materials, the exposure to oil led to thicker adsorbate layers, as might have been expected.

The results show that the variation of the contact angle cannot be explained by the adsorbate layer thickness alone: The contact angles measured on the gold surfaces vary, whereas the adsorbate layer thickness is almost constant, similar findings were obtained in the measurements with the steel and titanium probes that were not exposed to oil. Hence, it must be assumed that the contact angles depend on the composition of the adsorbate layer. To test this hypothesis, the results for the contact angle were plotted as a function of the ratio of the atom concentrations of polar to non-polar carbon $x_{\text{C-P}}/x_{\text{C-NP}}$, i.e., along the line shown in Fig. 14-left. The result is shown in Fig. 15. Despite the simplicity of the approach, a fair correlation of the results for the contact angle with the composition of the surface layer quantified by $x_{\text{C-P}}/x_{\text{C-NP}}$ was obtained. There are only three outliers, all of them are results for titanium samples cleaned with polar solvents. Two are for samples treated with oil and show an exceptionally high adsorbate layer thickness of more than 10 nm (cf. Fig. 14-right). It can be speculated that the adsorbate layer on these substrates is inhomogeneous.

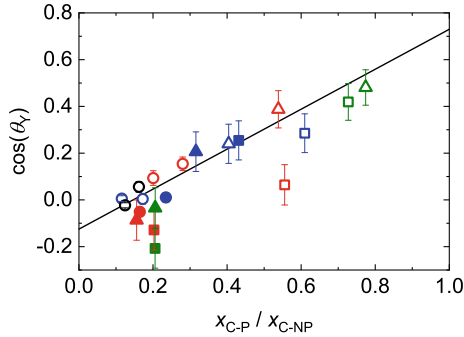


Fig. 15 Cosine of water contact angle $\cos \Theta_Y$ as function of adsorbate layer composition represented as x_{C-P}/x_{C-NP} . Results for different substrates: Gold (circles) [55], steel (triangles), and titanium (squares) [54]. Pre-treatment: No-oil (open symbols); with oil (filled symbols). Cleaning solvent: Cyclohexane (blue), acetone (red), isopropanol (green), and no cleaning (black). Black line indicates empirical correlation for water contact angle $\cos \Theta_Y = -0.125 + 0.855 \frac{x_{C-P}}{x_{C-NP}}$

Furthermore, the roughness of the titanium substrates was larger than that of the other substrates, see Sect. 3.2.3.

Within this work, also studies on the adsorption and the surface tension of vapor–liquid interfaces of binary mixtures were carried out. This was done using both theoretical methods (MD and DGT+EOS) as well as experimental pendant drop measurements. Details are given in Refs. [56–59]. Thereby, the relation between the enrichment of components at vapor–liquid interfaces [51] and the relative adsorption was elucidated, which also plays an important role for the vapor–liquid interface of droplets on surfaces, cf. Fig. 2.

4 Conclusions

Wetting properties of component surfaces are important in many applications. The comprehensive experimental and simulation results discussed in the present chapter contribute to establishing Manufacturing–Morphology–Property Relationships for wetting in several ways:

The wetting properties of a surface are determined by its morphology, which is not only characterized by the material of the solid and its topology, but also by the adsorption layer, which is always present on technical surfaces. This adsorption layer cannot be removed by conventional cleaning; in fact, cleaning rather modifies the adsorption layer than removes it.

The adsorption layer can also change simply upon storing the workpiece in ambient air. A wetting liquid usually does not “see” much of the solid surface. The adsorption layers found in the experiments from the present work were between about 2 nm and 10 nm thick. The size of typical adsorbing molecules, such as carbon dioxide, is

about an order of magnitude lower, i.e., there are many layers of molecules adsorbed on the surface. The adsorbed molecules shield direct interactions between the solid and the wetting liquid. Hence, the wetting is rather dominated by the interactions between the fluid and the adsorbate layer than by those between the fluid and the solid.

However, the solid, together with the way it is treated, determines the nature of the adsorption layer, and, thereby also the wetting, albeit only in an indirect way. All this explains why wetting properties are known to be poorly reproducible and difficult to predict. XPS surface analytics are a suitable way to study the thickness and composition of the adsorption layer. The combination of XPS analytics with contact angle measurements, that was introduced in the experimental studies described here, is well suited elucidating the Manufacturing–Morphology–Property Relationships for wetting.

Also, the simulation studies presented here contribute to establishing Manufacturing–Morphology–Property Relationships for wetting—albeit virtual ones. The analog to the “manufacturing of the component” in the virtual world is the modeling of the solid, i.e., the specification of its nature and topology. The “application” studied here is the wetting of the component. Hence, in the simulation, also the nature of the fluid and its interactions with the solid need to be defined. Given this and the specification of an application scenario (static wetting, dynamic wetting, etc.), molecular simulations yield predictions of the studied wetting phenomena, e.g., static or dynamic contact angles. The predictions also include details of the morphology of the fluid near the surface, such as the adsorption layer and the three-phase contact.

However, molecular simulations are strongly limited both in space and in time: The current limits (for molecular dynamic simulations) are at the lower end of the micrometer scale and the microsecond scale, respectively [31]. To overcome these limitations, a scale-bridging approach was developed in the present work. It relates the (particle-based) molecular simulations in a consistent way to (continuum) phase field modeling. The key element in this is a molecular-based equation of the state of the free energy. The phase field model enables extending both the length scale and the time scale that can be studied in the simulations substantially.

A second challenge is the modeling of real systems. While there is plenty of experience in developing molecular models of fluids [9, 60–65] and solids [66–68], meaningful modeling for the fluid–solid contact is still in its infancy. Experimental data are needed to calibrate these interaction models. Experimental data on contact angles lend themselves for this purpose; however, their determination is often compromised by adsorption layers, as we have demonstrated here. Hence, modeling solid–fluid interactions in real systems remains an interesting and important open field of research.

For systems with dispersive interactions, quantitative relations between the strength of the molecular interactions and the morphology of the region near the surface as well as application properties, such as the contact angle, have been established in the present work. While extensive results were obtained for wetting with pure fluids, much remains to be done for mixtures, namely regarding the formation

of the adsorption layer and its relation to the wetting. The first studies carried out here show that molecular simulations are a good method to gain insights into the complex phenomena in this field. The phase field modeling is an effective tool for extending the scope of this approach, but also here, further work needs to be done before wetting and adsorption of mixtures can be described routinely.

References

1. Rowlinson JS, Widom B (1982) *Molecular theory of capillarity*. Dover Publications, New York
2. De Gennes P-G, Brochard-Wyart F, Quéré D (2013) *Capillarity and wetting phenomena: drops, bubbles, pearls, waves*. Springer Science & Business Media, New York
3. Defay R, Prigogine I, Bellmans A, Everett DH (1966) *Surface tension and adsorption*. Longmans, London
4. Cahn JW, Hilliard JE (1958) Free energy of a nonuniform system. I. Interfacial free energy. *J Chem Phys* 28(2):258. <https://doi.org/10.1063/1.1744102>
5. Quéré D (2008) Wetting and roughness. *Ann Rev Mater Res* 38(1):71-99. <https://doi.org/10.1146/annurev.matsci.38.060407.132434>
6. Israelachvili JN, Gee ML (1989) Contact angles on chemically heterogeneous surfaces. *Langmuir* 5(1):288-289. <https://doi.org/10.1021/la00085a059>
7. Cahn JW (1977) Critical point wetting. *J Chem Phys* 66(8):3667-3672. <https://doi.org/10.1063/1.434402>
8. Bangham DH, Razouk RI (1937) Adsorption and the wettability of solid surfaces. *Trans Faraday Soc* 33:1459-1463. <https://doi.org/10.1039/TF9373301459>
9. Stephan S, Horsch M, Vrabec J, Hasse H (2019) MolMod - an open access database of force fields for molecular simulations of fluids. *Mol Simul* 45(10):806-814. <https://doi.org/10.1080/08927022.2019.1601191>
10. Lorentz HA (1881) Über die Anwendung des Satzes vom Virial in der kinetischen Theorie der Gase. *Ann Phys* 248:127-136. <https://doi.org/10.1002/andp.18812480110>
11. Berthelot D (1898) Sur le mélange des gaz. *C R Hebd Seances Acad Sci* 126:1703-1706
12. Heier M, Diewald F, Horsch MT, Langenbach K, Müller R, Hasse H (2019) Molecular dynamics study of adsorption of the Lennard-Jones truncated and shifted fluid on planar walls. *J Chem Eng Data* 64(2):386-394. <https://doi.org/10.1021/acs.jced.8b00927>
13. Liu J, Heier M, Chapman WG, Langenbach K (2020) Adsorption in purely dispersive systems from molecular simulation, density gradient theory, and density functional theory. *J Chem Eng Data* 65(3):1222-1233. <https://doi.org/10.1021/acs.jced.9b00585>
14. Heier M, Diewald F, Müller R, Langenbach K, Hasse H (2021) Adsorption of binary mixtures of the Lennard-Jones truncated and shifted fluid on planar walls. *J Chem Eng Data* 66(10):3722-3734. <https://doi.org/10.1021/acs.jced.1c00350>
15. Wolf J, Diewald F, Heier M, Staubach J, Langenbach K, Hasse H, Müller R (2021) Adsorption in a phase field model for wetting. *PAMM* 21(1):e202100145. <https://doi.org/10.1002/pamm.202100145>
16. Becker S, Urbassek HM, Horsch M, Hasse H (2014) Contact angle of sessile drops in Lennard-Jones systems. *Langmuir* 30(45):13606. <https://doi.org/10.1021/la503974z>
17. Heier M, Stephan S, Diewald F, Müller R, Langenbach K, Hasse H (2021) Molecular dynamics study of wetting and adsorption of binary mixtures of the Lennard-Jones truncated and shifted fluid on a planar wall. *Langmuir* 37:7405-7419. <https://doi.org/10.1021/acs.langmuir.1c00780>
18. Becker S, Kohns M, Urbassek HM, Horsch M, Hasse H (2017) Static and dynamic wetting behavior of drops on impregnated structured walls by molecular dynamics simulation. *J Phys Chem C* 121(23):12669-12683. <https://doi.org/10.1021/acs.jpcc.6b12741>

19. Diewald F, Kuhn C, Heier M, Horsch M, Langenbach K, Hasse H, Müller R (2017) Surface wetting with droplets: a phase field approach. *Proc Appl Math Mech* 17(1):501–502. <https://doi.org/10.1002/pamm.201710220>
20. Diewald F, Heier M, Lautenschläger M, Horsch M, Kuhn C, Langenbach K, Hasse H, Müller R (2019) A Navier-Stokes-Korteweg model for dynamic wetting based on the PeTS equation of state. *Proc Appl Math Mech* 19(1):e201900091. <https://doi.org/10.1002/pamm.201900091>
21. Diewald F, Lautenschläger M, Stephan S, Langenbach K, Kuhn C, Seckler S, Bungartz H-J, Hasse H, Müller R (2020) Molecular dynamics and phase field simulations of droplets on surfaces with wettability gradient. *Comput Methods Appl Mech Eng* 361:112773. <https://doi.org/10.1016/j.cma.2019.112773>
22. Fertig D, Hasse H, Stephan S (2022) Transport properties of binary Lennard-Jones mixtures: insights from entropy scaling and conformal solution theory. *J Mol Liquids* 367:120401. <https://doi.org/10.1016/j.molliq.2022.120401>
23. Diewald F, Wolf J, Heier M, Lautenschläger M, Stephan S, Kuhn C, Langenbach K, Hasse H, Müller R (2021) Phase field modeling of dynamic surface wetting informed by molecular simulations. *Proc Appl Math Mech* 21(1):e202100051. <https://doi.org/10.1002/pamm.202100051>
24. Werth S, Horsch M, Hasse H (2016) Surface tension of the two center Lennard-Jones plus point dipole fluid. *J Chem Phys* 144(5):054702. <https://doi.org/10.1063/1.4940966>
25. Werth S, Horsch M, Hasse H (2015) Surface tension of the two center Lennard-Jones plus quadrupole model fluid. *Fluid Phase Equilib* 392:12–18. <https://doi.org/10.1016/j.fluid.2015.02.003>
26. Werth S, Stöbener K, Horsch M, Hasse H (2017) Simultaneous description of bulk and interfacial properties of fluids by the Mie potential. *Mol Phys* 115(9–12):1017–1030. <https://doi.org/10.1080/00268976.2016.1206218>
27. Werth S, Rutkai G, Vrabec J, Horsch M, Hasse H (2014) Long-range correction for multi-site Lennard-Jones models and planar interfaces. *Mol Phys* 112(17):2227–2234. <https://doi.org/10.1080/00268976.2013.861086>
28. Werth S, Horsch M, Hasse H (2015) Long-range correction for dipolar fluids at planar interfaces. *Mol Phys* 113(23):3750–3756. <https://doi.org/10.1080/00268976.2015.1061151>
29. Werth S, Lishchuk SV, Hasse H (2013) The influence of the liquid slab thickness on the planar vapor-liquid interfacial tension. *Physica A* 392(10):2359. <https://doi.org/10.1016/j.physa.2013.01.048>
30. Niethammer C, Becker S, Bernreuther M, Buchholz M, Eckhardt W, Heinecke A, Werth S, Bungartz H-J, Glass CW, Hasse H, Vrabec J, Horsch M (2014) ls1 mardyn: the massively parallel molecular dynamics code for large systems. *J Chem Theory Comput* 10(10):4455. <https://doi.org/10.1021/ct500169q>
31. Tchipev N, Seckler S, Heinen M, Vrabec J, Gratl F, Horsch M, Bernreuther M, Glass CW, Niethammer C, Hammer N, Krischok B, Resch M, Kranzlmüller D, Hasse H, Bungartz H-J, Neumann P (2019) TweTriS: twentytrillion-atom simulation. *Int J High Perform Comput Appl* 33(5):838–854. <https://doi.org/10.1177/1094342018819741>
32. Deublein S, Eckl B, Stoll J, Lishchuk SV, Guevara-Carrion G, Glass CW, Merker T, Bernreuther M, Hasse H, Vrabec J (2011) ms2: A molecular simulation tool for thermodynamic properties. *Comput Phys Commun* 182(11):2350–2367. <https://doi.org/10.1016/j.cpc.2011.04.026>
33. Glass CW, Reiser S, Rutkai G, Deublein S, Köster A, Guevara-Carrion G, Wafai A, Horsch M, Bernreuther M, Windmann T, Hasse H, Vrabec J (2014) ms2: a molecular simulation tool for thermodynamic properties, new version release. *Comput Phys Commun* 185(12):3302–3306. <https://doi.org/10.1016/j.cpc.2014.07.012>
34. Rutkai G, Köster A, Guevara-Carrion G, Janzen T, Schappals M, Glass CW, Bernreuther M, Wafai A, Stephan A, Kohns M, Reiser S, Deublein S, Horsch M, Hasse H, Vrabec J (2017) ms2: a molecular simulation tool for thermodynamic properties, release 3.0. *Comput Phys Commun* 221:343–351. <https://doi.org/10.1016/j.cpc.2017.07.025>
35. Fingerhut R, Guevara-Carrion G, Nitzke I, Saric D, Marx J, Langenbach K, Prokopev S, Celný D, Bernreuther M, Stephan S, Kohns M, Hasse H, Vrabec J (2021) ms2: a molecular simulation tool for thermodynamic properties, release 4.0. *Comput Phys Commun* 262:107860. <https://doi.org/10.1016/j.cpc.2021.107860>

36. Heier M, Stephan S, Liu J, Chapman WG, Hasse H, Langenbach K (2018) Equation of state for the Lennard-Jones truncated and shifted fluid with a cut-off radius of 2.5σ based on perturbation theory and its applications to interfacial thermodynamics. *Mol Phys* 116(15):2083–2094. <https://doi.org/10.1080/00268976.2018.1447153>
37. Stephan S, Hasse H (2020) Influence of dispersive long-range interactions on properties of vapour-liquid equilibria and interfaces of binary Lennard-Jones mixtures. *Mol Phys* 118(9-10):e1699185. <https://doi.org/10.1080/00268976.2019.1699185>
38. Lautenschlaeger MP, Hasse H (2019) Transport properties of the Lennard-Jones truncated and shifted fluid from non-equilibrium molecular dynamics simulations. *Fluid Phase Equilib* 482:38–47. <https://doi.org/10.1016/j.fluid.2018.10.019>
39. Fertig D, Stephan S (2023) Influence of dispersive long-range interactions on transport and excess properties of simple mixtures. *Mol Phys* e2162993. <https://doi.org/10.1080/00268976.2022.2162993>
40. Stephan S, Langenbach K, Hasse H (2019) Interfacial properties of binary Lennard-Jones mixtures by molecular simulations and density gradient theory. *J Chem Phys* 150(17):174704. <https://doi.org/10.1063/1.5093603>
41. Vrabec J, Kedia GK, Fuchs G, Hasse H (2006) Comprehensive study of the vapour-liquid coexistence of the truncated and shifted Lennard-Jones fluid including planar and spherical interface properties. *Mol Phys* 104(9):1509. <https://doi.org/10.1080/00268970600556774>
42. Stephan S, Hasse H (2020) Interfacial properties of binary mixtures of simple fluids and their relation to the phase diagram. *Phys Chem Chem Phys* 22(22):12544–12564. <https://doi.org/10.1039/d0cp01411g>
43. Stephan S, Liu J, Langenbach K, Chapman WG, Hasse H (2018) Vaporliquid interface of the Lennard-Jones truncated and shifted fluid: comparison of molecular simulation, density gradient theory, and density functional theory. *J Phys Chem C* 122(43):24705–24715. <https://doi.org/10.1021/acs.jpcc.8b06332>
44. Aranson IS, Kramer L (2002) The world of the complex Ginzburg-Landau equation. *Rev Mod Phys* 74(1):99. <https://doi.org/10.1103/RevModPhys.74.99>
45. Diewald F, Kuhn C, Blauwhoff R, Heier M, Becker S, Werth S, Horsch M, Hasse H, Müller R (2016) Simulation of surface wetting by droplets using a phase field model. *Proc Appl Math Mech* 16(1):519–520. <https://doi.org/10.1002/pamm.201610248>
46. Diewald F, Kuhn C, Heier M, Langenbach K, Horsch M, Hasse H, Müller R (2018) Investigating the stability of the phase field solution of equilibrium droplet configurations by eigenvalues and eigenvectors. *Comput Mater Sci* 141:185–192. <https://doi.org/10.1016/j.commatsci.2017.08.029>
47. Diewald F, Heier M, Horsch M, Kuhn C, Langenbach K, Hasse H, Müller R (2018) Three-dimensional phase field modeling of inhomogeneous gasliquid systems using the PeTS equation of state. *J Chem Phys* 149(6):064701. <https://doi.org/10.1063/1.5035495>
48. Diewald F, Heier M, Lautenschläger M, Kuhn C, Langenbach K, Hasse H, Müller R (2021) Phase field simulations of wetting based on molecular simulations. *Proc Appl Math Mech* 20(1):e202000035. <https://doi.org/10.1002/pamm.202000035>
49. Anderson DM, McFadden GB, Wheeler AA (1998) Diffuse-interface methods in fluid mechanics. *Ann Rev Fluid Mech* 30(1):139–165. <https://doi.org/10.1146/annurev.fluid.30.1.139>
50. Brezzi F, Fortin M (2012) Mixed and hybrid finite element methods, vol 15. Springer series in computational mathematics. Springer, News York
51. Stephan S, Hasse H (2020) Enrichment at vapour-liquid interfaces of mixtures: establishing a link between nanoscopic and macroscopic properties. *Int Rev Phys Chem* 39(3):319–349. <https://doi.org/10.1080/0144235X.2020.1777705>
52. Stephan S, Dyga M, Urbassek HM, Hasse H (2019) The influence of lubrication and the solid-fluid interaction on thermodynamic properties in a nanoscopic scratching process. *Langmuir* 35(51):16948–16960. <https://doi.org/10.1021/acs.langmuir.9b01033>
53. Schmitt S, Vo T, Lautenschlaeger MP, Stephan S, Hasse H (2022) Molecular dynamics simulation study of heat transfer across solid-fluid interfaces in a simple model system. *Mol Phys* 120(10):e2057364. <https://doi.org/10.1080/00268976.2022.2057364>

54. Becker S, Merz R, Hasse H, Kopnarski M (2016) Solvent cleaning and wettability of technical steel and titanium surfaces. *Adsorp Sci Technol* 34(4–5):261–274. <https://doi.org/10.1177/02636174166645110>
55. Heier M, Merz R, Becker S, Langenbach L, Kopnarski M, Hasse H (2021) Experimental study of the influence of the adsorbate layer composition on the wetting of different substrates with water. *Adsorp Sci Technol* 6663989. <https://doi.org/10.1155/2021/6663989>
56. Werth S, Kohns M, Langenbach K, Heilig M, Horsch M, Hasse H (2016) Interfacial and bulk properties of vapor-liquid equilibria in the system toluene+hydrogen chloride+carbon dioxide by molecular simulation and density gradient theory + PC-SAFT. *Fluid Phase Equil* 427:219. issn: 0378-3812. <https://doi.org/10.1016/j.fluid.2016.07.016>
57. Becker S, Werth S, Horsch M, Langenbach K, Hasse H (2016) Interfacial tension and adsorption in the binary system ethanol and carbon dioxide: experiments, molecular simulation and density gradient theory. *Fluid Phase Equilib* 427:476. <https://doi.org/10.1016/j.fluid.2016.08.007>
58. Stephan S, Becker S, Langenbach K, Hasse H (2020) Vapor-liquid interfacial properties of the binary system cyclohexane + CO₂: experiment, molecular simulation and density gradient theory. *Fluid Phase Equilib* 518:112583. <https://doi.org/10.1016/j.fluid.2020.112583>
59. Werth S, Horsch M, Hasse H (2017) Molecular simulation of the surface tension of 33 multi-site models for real fluids. *J Mol Liq* 235:126–134. <https://doi.org/10.1016/j.molliq.2016.12.062>
60. Vrabec J, Stoll J, Hasse H (2001) A set of molecular models for symmetric quadrupolar fluids. *J Phys Chem B* 105(48):12126–12133. <https://doi.org/10.1021/jp012542o>
61. Stoll J, Vrabec J, Hasse H (2003) A set of molecular models for carbon monoxide and halogenated hydrocarbons. *J Chem Phys* 119(21):11396–11407. <https://doi.org/10.1063/1.1623475>
62. Huang Y-L, Merker T, Heilig M, Hasse H, Vrabec J (2012) Molecular modelling and simulation of vapor-liquid equilibria of ethylene oxide, ethylene glycol, and water as well as their binary mixtures. *Ind Eng Chem Res* 51(21):7428–7440. <https://doi.org/10.1021/ie300248z>
63. Merker T, Engin C, Vrabec J, Hasse H (2010) Molecular model for carbon dioxide optimized to vapor-liquid equilibria. *J Chem Phys* 132(23):234512. <https://doi.org/10.1063/1.3434530>
64. Werth S, Stöbener K, Klein P, Küfer K-H, Horsch M, Hasse H (2015) Molecular modelling and simulation of the surface tension of real quadrupolar fluids. *Chem Eng Sci* 121:110–117. <https://doi.org/10.1016/j.ces.2014.08.035>
65. Kulkarni A, Garcia EJ, Damone A, Schappals M, Stephan S, Kohns M, Hasse H (2020) A force field for poly(oxyethylene) dimethyl ethers (OMEn). *J Chem Theory Comput* 16(4):2517–2528. <https://doi.org/10.1021/acs.jctc.9b01106>
66. Zhen S, Davies GJ (1983) Calculation of the Lennard-Jones n-m potential energy parameters for metals. *Phys Status Solidi (a)* 78(2):595–605. <https://doi.org/10.1002/pssa.2210780226>
67. Tersoff J (1989) Modeling solid-state chemistry: interatomic potentials for multicomponent systems. *Phys Rev B* 39(8):5566–5568. <https://doi.org/10.1103/physrevb.39.5566>
68. Mendelev MI, Han S, Srolovitz DJ, Ackland GJ, Sun DY, Asta M (2003) Development of new interatomic potentials appropriate for crystalline and liquid iron. *Philos Mag* 83(35):3977–3994. <https://doi.org/10.1080/14786430310001613264>

Interrelationship of Manufacturing, Surface Morphology, and Properties of Titanium



Eberhard Kerscher, Stella Diederichs, Nafiseh Ghavidel, Andrej Keksel, Charlotte Kuhn, Ralf Müller, Jörg Seewig, and Fábio J. P. Sousa

Abstract Manufacturing of titanium parts modifies the surface morphology mostly with the goal of a functionalization like grooves to change the wettability or to act as reservoirs for lubricants, for instance. While the function of the surface is adapted to special efforts, it must be considered how the new surface morphology acts on mechanical properties like the fatigue limit. Therefore, it is necessary to know which hardening mechanisms are activated during the change of the morphology. To do so, we analyzed the processes during manufacturing and measured the modified morphology of the surface with classical and new methods. The main influence on the fatigue limit is given by the changed roughness or newly introduced notches at the surface. These imperfections must be taken into account when calculating the consequences on the fatigue limit. Thereby, it is of high relevance to be aware of the interaction between the size of the imperfection and the governing microstructural dimensions, i.e., the grain size in titanium because the same imperfection can reduce the fatigue limit in a fine-grained metal while it has no influence on the fatigue limit in a coarse-grained metal.

E. Kerscher (✉) · S. Diederichs · N. Ghavidel
Institute of Materials Testing, RPTU Kaiserslautern, Kaiserslautern, Germany
e-mail: e.kerscher@rptu.de

A. Keksel · J. Seewig
Institute of Measurement and Sensor Technology, RPTU Kaiserslautern, Kaiserslautern, Germany

R. Müller
Institute of Mechanics, Technical University of Darmstadt, Darmstadt, Germany

C. Kuhn
Faculty of Engineering Design, Production Engineering and Automotive Engineering, Universität Stuttgart, Stuttgart, Germany

F. J. P. Sousa
Federal University of Rio Grande do Norte, Natal, Brazil

1 Introduction

Titanium is one of the most interesting candidates for advanced parts due to excellent combination of strength and density as well as corrosion resistivity. Therefore, it is of high relevance how different manufacturing technologies modify the surface of titanium and, in consequence, the properties of the surface structured parts. This chapter discusses the influence of micro milling of commercially pure (cp-)titanium of grade 2 and grade 4 on the surface morphology and mechanical properties. The focus is on the influence of the modified surface morphology on the fatigue limit. It is well known that notches at the surface of parts reduce the fatigue limit significantly due to the increased local stress at the notch root, which causes a higher probability for local plastic deformation and, as a consequence, local fatigue crack initiation [1]. Due to the stress field within the notched area, this fatigue crack can grow and lead to failure at a reduced fatigue limit σ_{th} compared to the fatigue limit σ_0 of the unnotched surface state.

While the above-mentioned findings are usually observed for macroscopic notches in parts, the question remains, whether the same findings are valid for micronotches whose size is smaller than that of the governing microstructure of a material [2]. Within the CRC 926, there are manufacturing technologies available modifying the surface of parts only in very small dimensions of about 30 nm to 30 μm making it possible to investigate if these modifications have an impact on the fatigue limit of the parts. To better understand the competing mechanisms of fatigue crack initiation for notched and unnotched parts, Fig. 1 gives an idea about the possible interactions between the microstructure and the surface state: A perfectly flat surface state is schematically shown in Fig. 1a. The microstructure consists of differently oriented grains beneath the surface. The different surface structuring techniques of the CRC 926 enable the modification of the surface at a dimension of the grains size, schematically shown in Fig. 1b with a notch of a width of w and a depth of d_D . In the case of an unnotched surface, fatigue crack initiation usually happens after some time due to localized plastic deformation within one grain which has the most favorably oriented grain and the highest Schmid factor [3] leading to a shear stress distribution causing dislocation movement on the main glide planes. The movement of dislocations concentrates within persistent slip bands producing intrusions and extrusions at the surface [4]. These intrusions act as fatigue crack initiation sites. The fatigue limit is determined by the possibility of the fatigue crack (represented as a red line in Fig. 1c) to overcome the first grain boundary (this is the transition between the light blue and the green grain in Fig. 1c): if the crack is just not able to overcome the barrier of the grain boundary, the applied stress amplitude is the fatigue limit σ_0 [5]. The production of surface structured parts changes the situation significantly: While the light blue grain in Fig. 1d is still the most favorably oriented grain for fatigue crack initiation, there is an additional possible crack initiation site at the root of the introduced notch which acts as a local stress raiser. In Fig. 1d in the corner of the notch with the green grain, a possible fatigue crack initiation site is represented by the broken red line. Obviously, there is now a competition between the most favorably

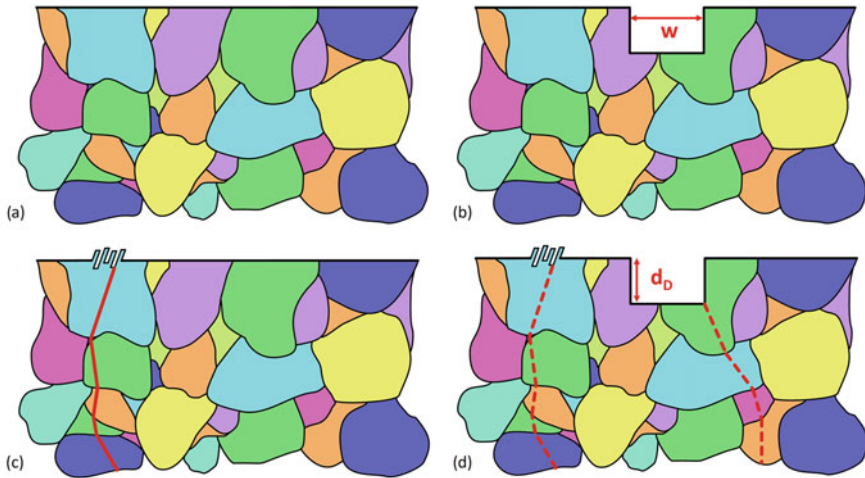


Fig. 1 **a** Schematic side view of a surface and the first few grains beneath the surface. Different colors symbolize different grain orientations; **b** the same surface as in **a** with an additional notch due to surface manufacturing; **c** fatigue crack initiation from an intrusion at the surface; and **d** competition between crack initiation at the original surface and at a notch

oriented grain and the stress raiser due to the notch leading to two possible crack initiation sites for fatigue cracks (shown as broken red lines).

Before CRC 926 it was unknown at which size of the notch, given by its width w and its depth d_D , the fatigue crack will initiate at the notch. Therefore, a goal of the current chapter is to take a closer look at the governing parameters causing a fatigue crack to initiate at the surface or at the notch. Beside the relation between size of the notch and the grain size, an additional factor is a possible modification of the material's microstructure during surface modification. Any changes in the hardening mechanisms due to manufacturing which might change the local resistance against fatigue crack initiation must be taken into account. Consequently, the following chapter focuses on the manufacturing of the grooves in Sect. 2, the changes of the morphology by manufacturing in Sect. 3, the interaction of surface morphologies and properties in Sect. 4, and finally the conclusions and an outlook in Sect. 5.

2 Manufacturing of Different Surface States

There are a lot of manufacturing processes to modify the material's surface as shown in previous chapters. Micro milling is one of the most flexible mechanical microproduction processes, as a large range of workpiece materials can be utilized, and a great variety of geometries can be produced. For detailed information about experimental micro milling, we refer to Chap. 4. Here, we discuss the multi-scale modeling and

simulation of microcutting, the simulation of the process using a crystal plasticity model, and the modification of a surface in dependence on the original grain structure in Sects. 2.1, 2.2, and 2.3, respectively.

2.1 Multiscale Modeling and Simulation of Microcutting

This section looks at the microstructuring of functional surfaces of titanium alloys, to be adapted in a myriad of components for tribological [6] and biological applications [7]. The basic idea is to provide the literature with some fundamental aspects of the ultra-precision cutting process, from which more comprehensive models can be conceived. The experimental results include the manufacturing and preparation of microcutting tools, up to the analysis of the resulting surface [8, 9].

Besides, the manufacturing of microcutting tools was also taken into account [10]. The structuring of functional surfaces offers the possibility of increasing the amount of free surface with a higher level of surface integrity [8]. From a technological point of view, this is made possible by ultra-precision machining. However, in contrast to conventional machining processes, ultra-precision machining is severely affected by the scale factor [11]. Such a size effect results from the mechanical responses of the workpiece's material, due to the presence of inhomogeneities and anisotropy, as well as from the ratio between the radius of the cutting edge of the tool and the depth of cut [12]. In all investigations, the workpiece was a cylindrical bar composed of cp-titanium (grade 2). The workpiece was aligned and clamped into an ultra-precision turning lathe. To assure a nearly pure cutting process, the kinematics was simplified to an orthogonal cutting process, and low values of cutting speed and cutting depth were adopted. In addition, separated peripheral ridges disposed in multiple parallel sections were prepared along the longitudinal axis of the cylinder, as can be seen in Fig. 2. These ridges were approximately 100 μm wide, chosen to be similar to the mean value of the grain size observed in the workpiece. By adopting all of these strategies, a very fundamental model of the cutting process could be experimentally tested so that the influence of the uncut chip thickness under different cutting conditions could be obtained from nano- to microscale [8–10]. To achieve small values of undeformed chip thickness, ranging from 0.1 μm up to 10 μm , microcutting tools containing a monocrystalline diamond tip fixed to a cemented carbide substrate were used. Accordingly, a factor of 100 in the range of scale variation was achieved by this approach. In addition, cutting edges with three different geometries were prepared and used in the experiments: sharp, rounded, and chamfered using a tip of tungsten carbide. The surface integrity in ultra-precision cutting of cp-titanium was investigated by analyzing the process of chip formation, the resulting burrs, and the final texture [8, 9]. Up to then, the investigations of chip formation of titanium available in the literature were mostly focused on titanium alloys, such as Ti–6Al–4V, and on conventional cutting conditions [13, 14]. Finally, a new preparation method for the rounding of microcutting tools was introduced.

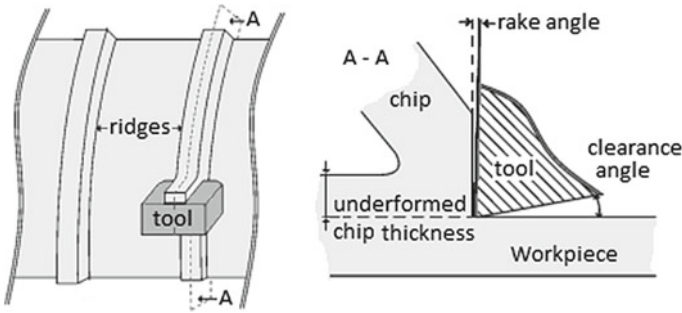


Fig. 2 Geometry, adapted from [9]

The influence of this manufacturing process on the tool’s life was also analyzed, as well as the impact of the tool wear on the surface topography [15].

2.2 Simulation of Microcutting by Crystal Plasticity

The simulation of microcutting uses the concept of crystal plasticity within a finite deformation context. The essential part of finite crystal plasticity is the multiplicative split of the deformation gradient [16] into an elastic and plastic part:

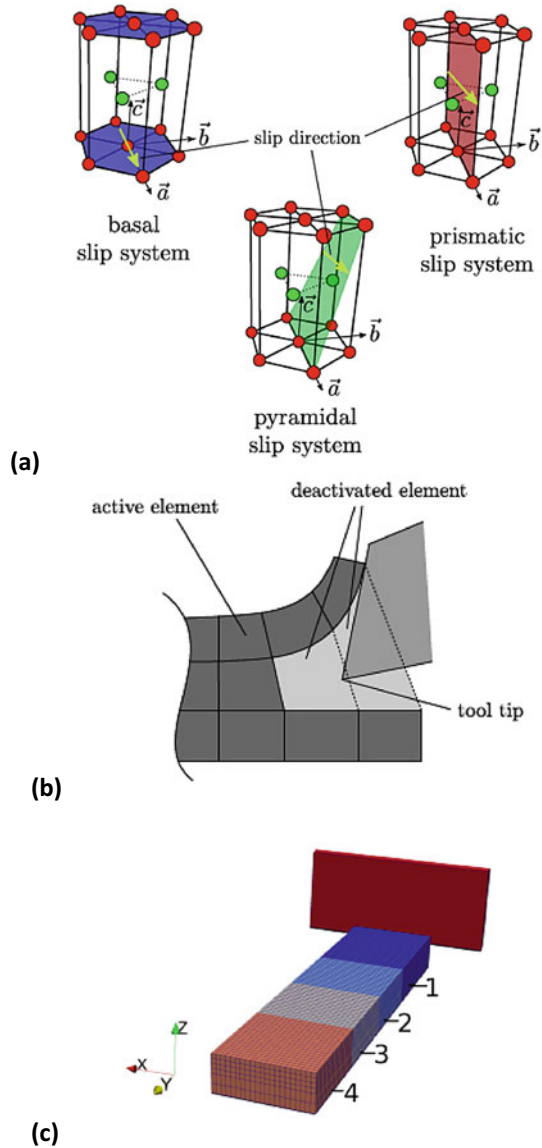
$$\underline{\underline{F}} = \underline{\underline{F}}^e \underline{\underline{F}}^p \tag{1}$$

The plastic part F^P is constructed by the slip in the individual slip systems. Due to the hexagonal structure of titanium, the primal slip systems, which include the basal as well as prismatic slip systems need to be included, see Fig. 3a. The pyramidal slip system is not considered in detail, as the deformation can be obtained from a combination of basal and primal slip systems. In the simulation, only the 12 main slip systems are accounted for. The plastic deformation in one slip system influences not only the hardening in the considered slip system but also the hardening in all other slip systems. These phenomena are referred to as self and latent hardening.

The finite element implementation is done in the current configuration. As the plastic deformation is volume-conserving a, so-called F-bar technique was used, see [17]. The plastic material law is integrated by using a predictor–corrector scheme. Crucial in the implementation is an active set search to determine the active slip systems. In this context, a procedure proposed by [18] is employed.

Using the above-described implementation of the material law, microcutting processes are simulated. The material separation is modeled by deactivating elements that are penetrated by the tool, see Fig. 3b. Therefore, the cut is driven through the grain boundary without any special consideration. An illustrative three-dimensional setup with four different crystal orientations is depicted in Fig. 3c. To simplify the

Fig. 3 a Slip systems in hexagonal titanium, b deactivating elements, c setup of cutting through four crystals with different orientation, indicated by different colors



numerical treatment, the contact between tool and material is assumed to be frictionless.

As can be seen from Fig. 4a, the crystal orientation has a significant influence on the formation of the chip. In simulations 1, 2, and 3, different crystal orientations are assigned to the differently colored blocks. Not only the deformation in machining direction is influenced by different orientations of the crystals but also a deformation

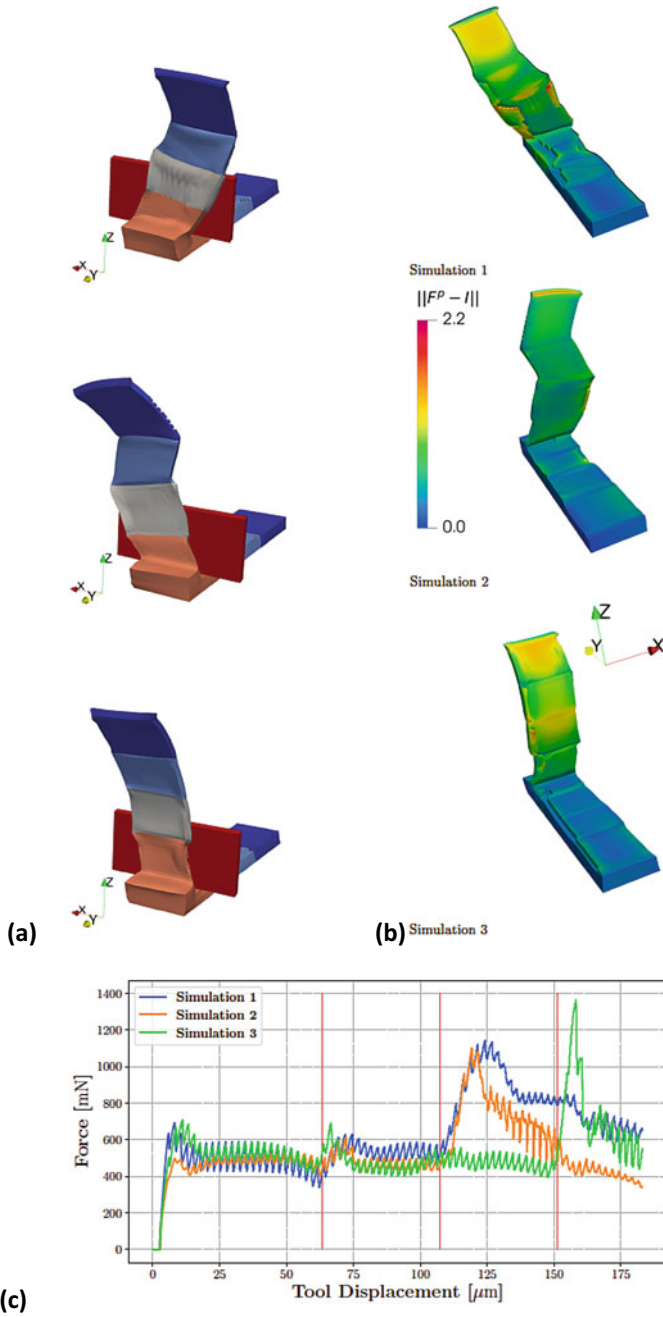


Fig. 4 **a** Influence of crystal orientation **a** on chip formation, **b** on plastic deformation, and **c** on cutting force

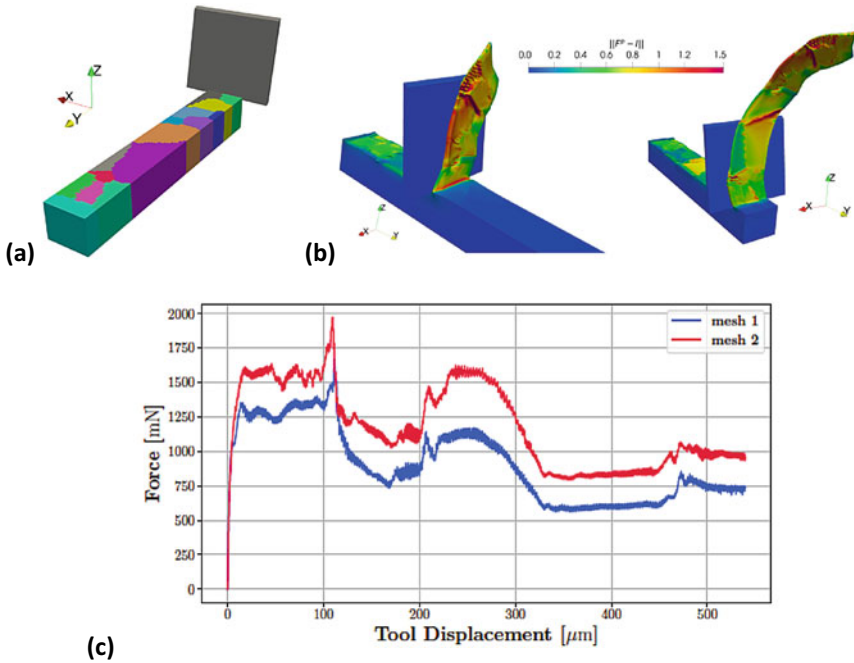


Fig. 5 Simulation based on EBSD data: **a** simulation model, **b** chip formation during cutting progress, and **c** cutting force

perpendicular to the cutting direction occurs. The different crystal orientations lead to locally varying plastic flow during the advancement of the tool. Also, different plastic deformations occur, that influence the deformation and creation of the surface, see Fig. 4b, which shows the chip for two different positions of the cutting tool. The different grain boundaries are clearly visible as the deformation mechanism changes in differently oriented grains. The influence of the complex deformation mechanisms leads to fluctuating forces on the tool. The cutting force is plotted in Fig. 4c. While the small wiggles originate from the continuous deactivation of elements, the different force levels are caused by the different crystal orientations.

In a further simulation setup measured crystal orientations from an electron backscattered (EBSD) image were chosen to incorporate the heterogeneity of the problem, see Fig. 5a. Although the structure is more random than in the first setup, the influence of the grains on the deformation and formation of the chip is clearly observable, see Fig. 5b. Due to the special crystal arrangement in this example, the chip bends forward and to the side. One can also observe that the plastic deformation is not uniformly distributed in the chip. Large plastic deformations are typically found at grain boundaries. Again, the cutting force is strongly influenced by the heterogeneity of the material, see Fig. 5c. The fluctuation of the cutting force during tool advancement can reach factors up to 2 depending on the relative crystal orientations.

In Fig. 5c, also the influence of different discretizations is investigated. Mesh 1 has about 210,000 degrees of freedom, while Mesh 2 is refined and has approximately 387,000 degrees of freedom. Although there is some influence of the discretization on the value of the cutting force, the dependency of the cutting force fluctuation on the crystal orientation is almost identical for both meshes.

2.3 Influence of Grain Orientation on Micromachining Forces

Usually, the tool size in milling processes is much larger than the average grain size of the machined polycrystalline material. In the case of micro milling, the tool size is in the order of magnitude of the average grain size, so the material can no longer be considered as homogeneous and isotropic. Therefore, it must be expected that the individual grain size and orientation have an influence on the cutting process resulting in fluctuating process forces and modified chip geometries during cutting of differently orientated grains, as already shown in the previous subsection. Up to now, it was often experimentally impossible to directly correlate the grain orientation, the surface topography, the process forces, and the chip formation for polycrystalline materials. The newly developed technique to detect the individual grain orientations by polarized light microscopy (PLM, see Sect. 2.2.2) enables the possibility to observe the surface directly before a cutting process and to correlate it with the machined surface at the same position. Two cutting processes, namely orthogonal cutting and micro milling, were carried out after characterizing the grain morphology of the original surface by PLM and EBSD. While machining the process, forces were measured and after machining the topography of the residual surface was analyzed. Thereby, very significant influences of differently oriented grains and their boundaries are visible in the force signals during the cutting process, leading to a rougher local surface after cutting. In contrast, the influence of the grain orientation on the processing forces and the resulting surface during micro milling is not as significant if the spindle turning speed is fast enough (for details see [19]). With the results of this study, it is possible to compensate for the influence of the grain orientation on the process results and to enhance the efficiency and the resulting surface quality of micromachining processes.

3 Surface Morphology After Manufacturing

The manufacturing of surfaces causes changes in geometry, which is usually the goal due to functionalizing attempts, as well as changes in the microstructure like increased dislocation density, twinning, or grain refinement, which all act as hardening mechanisms [20]. The challenge to characterize a functionalized surface after

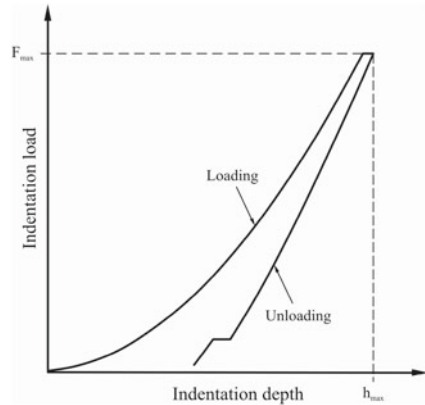
manufacturing is that the hardening mechanisms could be estimated by local hardness measurements, but therefore the surface has to be polished to avoid misinterpretation of the hardness indents. This is obviously not possible if the measurement should give information of the consequence of the manufacturing of functionalized surfaces if these surfaces are polished afterwards. Therefore, Sect. 3.1 presents a new method to reproducibly measure the surface hardness of functionalized surfaces. Of course, a second possibility to characterize the changes in the surface microstructure morphology is to prepare microsections perpendicular to the functionalized surface and observe them in a light microscope (Sect. 3.2). In these metallographic sections, it is even possible to measure the hardness distribution. Results of this method will be shown in Sect. 3.3.

3.1 New Method for Microhardness Testing on Rough Functional Surfaces

Microhardness determination on rough surfaces is a topic of interest, e.g., in industrial applications where the component surface is of functional relevance. However, in general, instrumented indentation tests are performed on polished sample surfaces to ensure comparability of measurements across several samples. One approach of referencing hardness values measured on rough surfaces is by assigning profile roughness parameters (like Ra) to respective measurements. The utility of this approach, however, is quite limited. Extending hardness measurement routines by surface topography measurements provides the potential to derive more accurate referencing of measured indentation hardness on arbitrary surfaces and thus taking the investigations to another level. In this subsection, we use pre- and post-indentation surface topography data to correlate traditionally measured and evaluated hardness values on rough surfaces with local surface states. The obtained results provide a first step toward combining optical imaging techniques like confocal microscopy and indentation testing equipment to improve measurement routines and to broaden the field of application.

Surface machining processes can be used to produce component surfaces featuring particular characteristics such as enhanced strength or wear resistance. Surface hardness, along with topography (roughness, etc.), are the main characteristics of component surfaces and therefore important elements of the surface morphology. The so-called instrumented indentation testing or nano-indentation technique extends traditional hardness testing to much smaller indenter tips which enable investigations of individual phases or extremely localized changes in surface hardness. In both cases, measurements are usually conducted on specially prepared, polished, and flat samples, since any microtopography affects and thus falsifies traditionally measured hardness values [21–23]. The surface preparation procedure ensures the comparability of hardness testing results across different samples and therefore marks a central requirement. At the same time, the measurement of microhardness on structured

Fig. 6 Schematic illustration of the F - d curve from an instrumented indentation experiment according to [26, 27]



topography may be of particular interest in cases where the microtopography is of functional relevance [24]. If such components were polished to remove a microtopography to ensure comparability, the characteristic to be examined would be lost. Within this study, the influence of structured surface topographies on nano-indentation testing is investigated with the superior goal to potentially adjust the standardized evaluation routine by combining surface topography and microhardness measurements. Using topography data at the location of indentation, microhardness measurements on rough surfaces are correlated with characteristic topography parameters, allowing for a better and more precise interpretation and evaluation of the obtained strongly scattering results. Note that the findings presented below are part of the investigation elaborated in more detail in [25].

The basic principle of instrumented indentation testing is that a geometrically well-defined indenter is pressed into the sample surface with controlled loading speed until a given maximum load is reached. Figure 6 schematically illustrates the resulting indentation load and depth curve (F - d curve). Materials of higher strength generally show a steeper increase in the loading segment. Afterwards, indentation hardness values can be calculated considering the known indenter geometry [26, 27].

The indentation tests were performed on samples of titanium stabilized austenitic stainless steel 1.4571 (X6CrNiMoTi17-12-2, or AISI 316Ti) featuring three different surface conditions produced by face milling with feed rates per tooth of 5, 7, and 9 μm . The F - d curves resulting from the applied standardized testing procedure (DIN 14577 [28]) were obtained by 49 instrumented indentation tests per sample.

To potentially overcome the reliance on the type of topography and the necessity of a large number of measurements to average, the relationship between local surface topography parameters at indented positions, measured F - d curves, and the resulting local indentation hardness are investigated. To do so, the local surface topography at a respective location needs to be evaluated by comparing the local surface pre- and post-indentation. By subtracting the topography pre-indentation from the measured topography post-indentation, it is possible to isolate the indentation mark and thus to determine an estimate for the actual depth of the indentation mark, the displaced

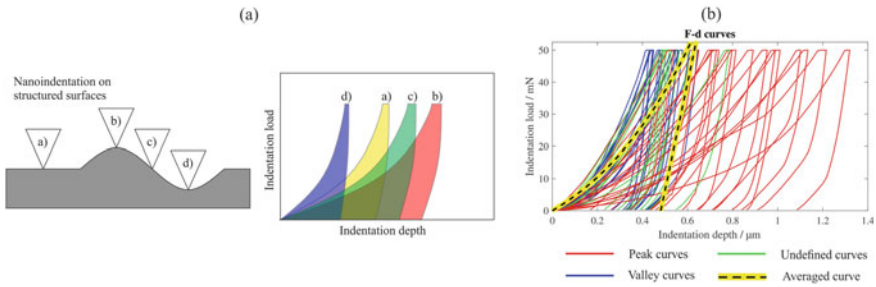


Fig. 7 **a** Illustration of the possible different surface curvatures at the position of the indenter and the resulting indentation curves when indenting on rough surfaces; **b** Set of F–d curves measured on face-milled sample surface; used with permission of IOP Publishing Ltd from [25], permission conveyed through Copyright Clearance Center, Inc

volume, etc. Further, the local surface curvature (smoothed by a second-order polynomial fit) indicates whether the indentation occurred at a local peak, a valley, or in between (see Indent (b), (d), or (c), respectively, in Fig. 7a). We define positive and negative curvatures for concave and convex surfaces, respectively. A combined surface topography and microhardness measuring device could use this information to provide proper and/or to exclude improper indentation locations in advance of indentation testing.

The F–d curves obtained by measurements on the face-milled samples show a significantly large scatter (see Fig. 7b) although the values of the actual material hardness should be in a narrow interval range [22]. Figure 7a illustrates this issue: when indented into a valley, the material appears harder and when indented into a peak, it appears softer. Subjectively classifying the local microscopic character of the topography with the aid of topography measurements, the dependency between local surface topography and measured F–d curve is shown qualitatively by color-coding the single F–d curves according to the underlying topographic characteristic.

To further indicate more specific correlations between local topographic properties and obtained hardness, respective measured indentation hardness values of one of the face-milled samples are plotted against the evaluated indentation depth, displaced volume, and the maximum curvature of the local pre-indentation surface topography (see Fig. 8). The horizontal line represents the averaged measured indentation hardness of the sample. At this level, tendencies of separation of valley and peak indentation can be identified, further pointing out a strong correlation between local surface topography and measured indentation hardness, which is the first step toward an adjusted evaluation routine of microhardness on rough surfaces using a measuring device combining surface topography and hardness measurements.

The investigations show that the topography of a rough surface significantly affects the indentation testing result in a partial systematic manner. Therefore, a synergistic use of hardness and surface topography measurements can open the door for reliable non-destructive hardness measurements on functional surfaces of arbitrary geometry.

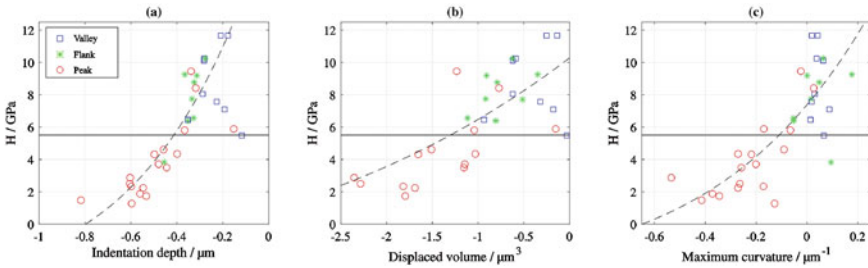


Fig. 8 Measured indentation hardness plotted against determined **a** indentation depth, **b** displaced volume and **c** maximum surface curvature; used with permission of IOP Publishing Ltd from [25], permission conveyed through Copyright Clearance Center, Inc

This is a necessary requirement in industrial applications where the sample surface is of functional relevance.

3.2 Near-Surface Microstructure

As already stated in the introduction of the current chapter, the microstructure, i.e., the size and orientation of the individual crystals or grains, plays an important role in the fatigue behavior and for other mechanical properties of the metallic material. In Section 2.2.2, polarized light microscopy (PLM) has been introduced as a new method to determine the grain size and the grain orientation [29, 30]. For α -titanium, PLM can also be used to identify the individual grains in a cross section without etching the grain boundaries. This is due to the optical anisotropy of α -titanium.

To apply either of the aforementioned methods the sample has to be prepared accordingly. This preparation includes the grinding and polishing of the surface. The quality of the surface, i.e., a low roughness, is crucial, especially for EBSD [31]. In order to get a good surface quality for the α -titanium samples used for the investigations in the current chapter, the preparation steps as indicated in Table 1 were applied.

After preparing the sample as indicated in Table 1, the characteristics of interest of the sample can be explored. As shown in Fig. 9 and mentioned before, the individual grains of α -titanium can be seen by applying PLM. In Fig. 9a, the different shades of gray represent individual grains of the bulk material. On the top of Fig. 9a a micro-milled notch can be seen. Figure 9b is a detailed view of this notch.

Looking at the notch more closely, it is now possible to see that no obvious material deformations such as deformation twins are found in the notch ground. As opposed to the specimen's surface where many deformation twins in the first grains below the surface appear. For this specimen, first, a face milling process was carried out on the whole surface before applying the notch by micro milling. According to the images of the cross section, the face milling process seems to have an influence on

Table 1 Preparation steps for α -Titanium

Step	Grinding 1	Grinding 2	Polishing*
Base	SiC paper, grit size 1200	SiC paper, grit size 2000	Polishing Cloth
Abrasive	SiC	SiC	Oxide Polishing Suspension (particle size 0.05 μ m) and 35% H ₂ O, ratio 80:20
Lubricant	Water	Water	–
Force/N	15	20	10
Time/s	60	90	600

*If needed this step can be repeated until the desired surface quality is achieved

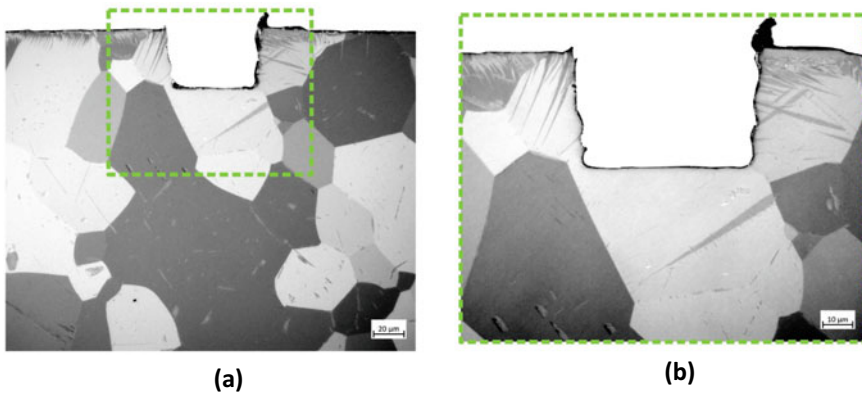


Fig. 9 Cross sections prepared according to the steps of Table 1 of a notched α -titanium specimen: **a** overview and **b** detail of the notch

the microstructure leading to deformation twins, whereas the micro milling seems to not introduce any changes in the microstructure except the notch geometry.

3.3 Near-Surface Hardness Distribution

Surface topography is an important factor for the mechanical properties of a component. Micromachining is a relatively new manufacturing technique, used to precisely adjust the specific surface morphology characteristics. Considering that fatigue crack initiation generally occurs on the surface of a material, it is important to investigate the influence of machining processes on the near-surface properties. The current study aims to investigate the effect of different surface machining processes, which are explained in detail in the previous chapters, on the near-surface properties using instrumented indentation tests. The light microscope images of the cross sections after

the indentation test are shown in Fig. 10, in which the color of each indentation point indicates the calculated hardness value (HIT) (for experimental details see [32]). The results show that for three surface machining processes (polishing, micro milling, and lapping) the influence of the machining process on the near-surface hardness is negligible. While for the other machining processes (conventional milling, finish milling, grinding, microturning, laser machining, and cold spraying) an increase can be detected in the hardness near the surfaces of the samples, and the magnitude of the affected area depends on the machining process. The probable mechanisms of increasing hardness due to surface machining are work hardening, twin formation, and grain boundary strengthening. In the images of “conventional milling”, and “micro turning” samples, narrow twin planes can be detected which act as obstacles for dislocation gliding leading to higher hardness. For those samples with an increase in hardness after surface machining and without twin planes in the images, high hardness values are attributed to work hardening (e.g., “grinding”, “lapping”). In the laser-machined notch sample, the applied high thermal energy can cause a fine-grained area formation below the notch during the local melting and re-solidification of the material during the process.

4 Interaction of Surface Morphologies and Fatigue Properties

In this chapter, we focus on the influence of the structured surface on the fatigue properties, namely the crack initiation site, the lifetime, and the fatigue limit. The influence on other mechanical properties, such as quasi-static properties derived from tensile tests, can be found in [31, 33, 34].

4.1 Fatigue Limit of Surface Structured Specimens

The fatigue limit of cp-titanium specimens with different grain sizes and surface conditions was investigated in load-controlled fatigue tests and evaluated according to the staircase method [35]. For these experiments, flat miniature specimens were cut from different cp-titanium material states with average grain sizes of $2\ \mu\text{m}$ ($\mu 2$), $47\ \mu\text{m}$ ($\mu 47$), and $130\ \mu\text{m}$ ($\mu 130$) [30]. Material states $\mu 47$ and $\mu 130$ are grade 2 materials and $\mu 2$ is grade 4 material. The investigated surface states for these specimens were polished, face-milled, and notched. R_z was used to determine the roughness of the surface after face milling. For the three material states $\mu 2$, $\mu 47$, and $\mu 130$ an average roughness of $R_z = 2, 0\ \mu\text{m}$, $R_z = 1, 8\ \mu\text{m}$, and $R_z = 2, 9\ \mu\text{m}$ was measured, respectively. The three investigated notch geometries were introduced by micro milling and have a width of $50\ \mu\text{m}$ and a depth of $10\ \mu\text{m}$, $20\ \mu\text{m}$, and $30\ \mu\text{m}$, respectively [36]. In this way, the influence of the grain size, surface roughness, and

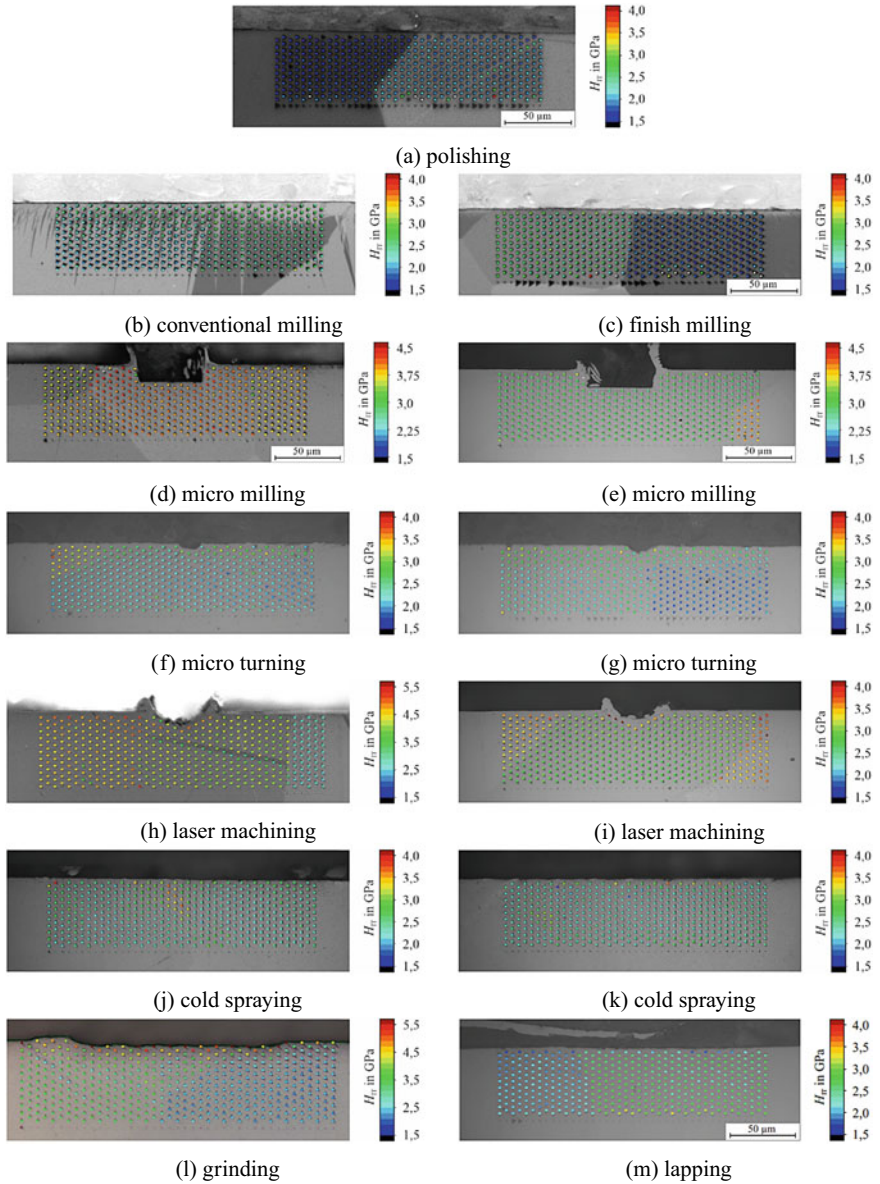
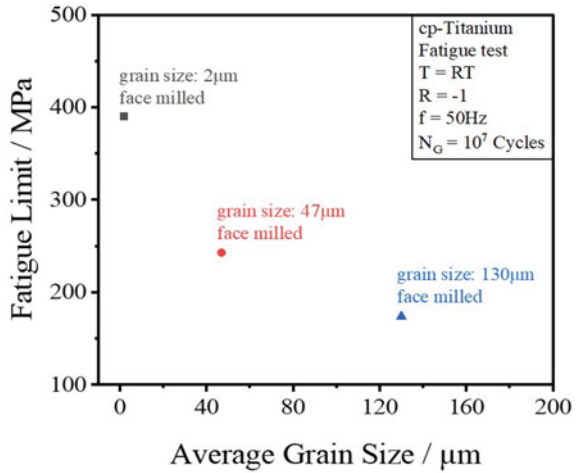


Fig. 10 Measurement areas and indentation hardness of samples after **a** polishing, **b** conventional milling, **c** finish milling, **d**, **e** micro milling, **f**, **g** microturning, **h**, **i** laser machining, **j**, **k** cold spraying, **l** grinding, and **m** lapping

surface structure on the fatigue limit was examined. The fatigue limits of the face-milled surfaces, which have a very similar average roughness, follow the Hall–Petch

Fig. 11 Fatigue limit of cp-Titanium specimens with different grain sizes (T is temperature, RT is room temperature, R is the load ratio, f is the testing frequency, and N_G is the ultimate number of cycles)



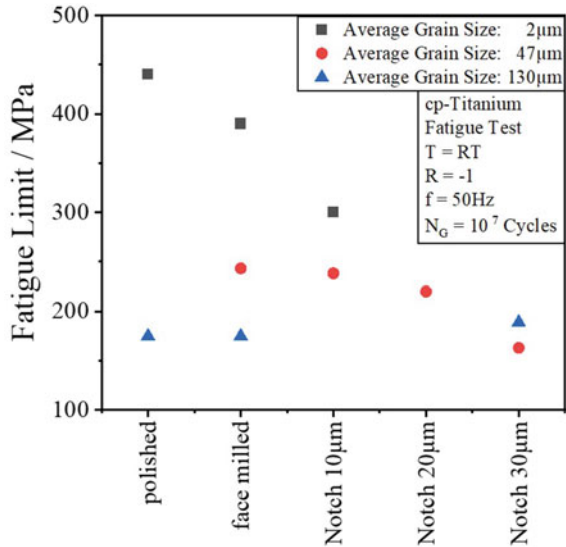
relationship, so the smallest grain size causes the highest fatigue limit, while the largest grain size leads to the lowest fatigue limit, see Fig. 11.

We introduced notches into the surface of the $\mu 47$ material state varying the depth in three steps of $d_D = 10 \mu\text{m}$, $d_D = 20 \mu\text{m}$, and $d_D = 30 \mu\text{m}$ while keeping the width constant at $w = 50 \mu\text{m}$. The fatigue test showed the same fatigue limit and fatigue lifetime for the face-milled and the $d_D = 10 \mu\text{m}$ notched state. Failure of the specimen started mostly (80%) at the face-milled surface, usually at one of the edges of the rectangular gauge length, while 20% of the specimen failed from the notch ground. In contrast, all failed specimens with $d_D = 30 \mu\text{m}$ showed fatigue cracks starting from the ground of the notch and leading to significantly reduced lifetime of the broken specimen and low-stress amplitude of the run-out specimen. At the notch depth in between ($d_D = 20 \mu\text{m}$) failure from the notch ground as well as from the face-milled surface occurred with same probability, while lifetime and fatigue limit are reduced compared to the state with $d_D = 10 \mu\text{m}$ [37]. This observation proves that there is a strong effect of the relationship between notch size and grain size on the crack initiation site, as hypothesized in this chapter.

To check the interrelation between grain size and notch size the $\mu 2$ state was tested with face-milled and micromilled surface states. The notch had a width of $w = 50 \mu\text{m}$ and a depth of $d_D = 10 \mu\text{m}$. This size of the notch, which had no significant influence on lifetime and fatigue limit in the $\mu 47$ state, significantly reduces the lifetime and the fatigue limit of $\mu 2$ state. To further check an influence of the grain size on the fatigue limit, we polished the $\mu 2$ state and found a higher fatigue limit of the polished state compared to the face-milled state. Taking into account that the average roughness of the face-milled $\mu 2$ state is $R_z = 2.0 \mu\text{m}$ and thus it is of the same size as the grain size, leading to reduced fatigue lifetime and fatigue limit.

If our hypothesis is correct we would expect no influence of the polishing as well as of a notch of $d_D = 30 \mu\text{m}$ for a material state with larger grains, like tested in the

Fig. 12 Fatigue limit of different surface states and roughnesses (T is temperature, RT is the room temperature, R is the load ratio, f is the testing frequency, and N_G is the ultimate number of cycles)



$\mu 130$ state. Indeed, there is no difference in lifetime and fatigue limit between the different $\mu 130$ states.

The discussed influence of the roughness and the surface structure such as a notch depth obviously depends on the grain size of the material. This is summarized in Fig. 12. For example, a notch of 10 μm depth and 50 μm width lowers the fatigue limit of cp-Titanium with an average grain size of 2 μm significantly compared to a face-milled surface from 390 MPa to 300 MPa, whereas the same notch geometry decreases the fatigue limit for the cp-Titanium with an average grain size of 47 μm only slightly from 243 MPa to 238 MPa. For example, a notch of 10 μm depth decreases the fatigue limit of the material $\mu 2$ by 90 MPa compared to the face-milled state. It is worth mentioning that the manufacturing and the geometry of the notch were the same for the $\mu 2$, $\mu 47$, and $\mu 130$ state, so a classical calculation of a stress concentration factor of the notch K_t would lead to nearly the same value for the different states, because the most important influencing factor is the radius at the root of the notch, which is practically independent of the grain size and only determined by the milling tool geometry. Although K_t does not differ, the same notches show significantly differing K_f -values depending on the grain size.

A similar behavior can be found when comparing the polished and face-milled states for the cp-Titanium materials $\mu 2$ and $\mu 130$.

Although the roughness of the face-milled states for both materials is comparable the decrease in the fatigue limit is not. Whereas for the $\mu 2$ material a drop of 50 MPa between the fatigue limit of the polished state and the face-milled state can be found, there is no decrease in the fatigue limit for the $\mu 130$ material between these two states.

Hence, considering all results, the assumption can be made that the geometrical defect size, e.g., roughness or notch depth, needs to be above a certain ratio compared to the average grain size of the material for the fatigue limit to be decreased [30, 36, 38].

In order to define this ratio, *Murakami's* $\sqrt{\text{area}}$ concept is applied to the average grain size as a microstructural defect and to the roughness and notches as geometrical defects [39]. The defect size of the microstructural defect is estimated to a circular area with the diameter being the average grain size for each material state. As the cracks initiate always on an edge of the sample, the $\sqrt{\text{area}}$ values for the roughness and the notches are calculated according to Eq. (2), where S_d is the size of the defect and is equal to R_z or the depth of the notch d_D for the face-milled and micromilled surface states, respectively.

$$\sqrt{\text{area}} = \sqrt{\frac{1}{4}\pi(S_d)^2} \tag{2}$$

The $\sqrt{\text{area}}$ values calculated in this way can subsequently be used to define the ratio between the defect size due to the surface geometry to the defect size due to the microstructure. Figure 13 shows a transition from failure due to the microstructure to failure due to the surface geometry at a ratio of about 0.3 for the investigated material states and surface states. This finding could be used in future to only introduce notches with sizes below about 30% of the grain size of a material to avoid decreasing fatigue limits due to the notch.

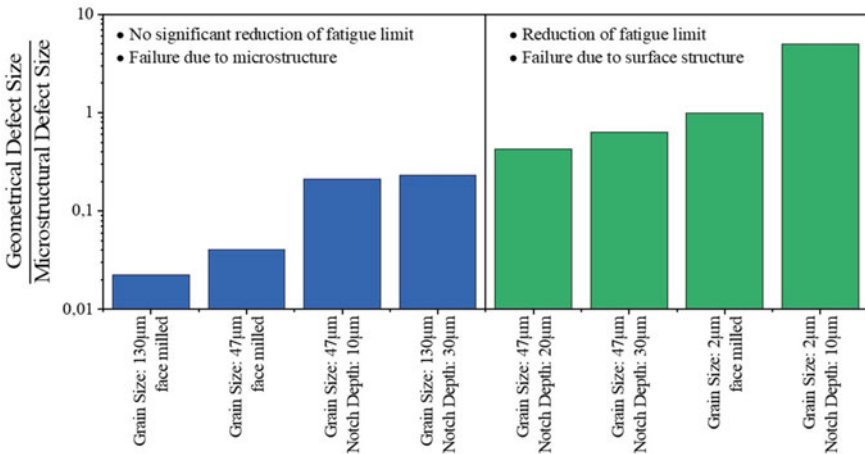


Fig. 13 Ratios of the defect size due to the surface geometry to the defect size due to the microstructure for the examined material and surface states

4.2 Prediction of Fatigue Crack Initiation Site by Using the Morphology of Manufactured Surfaces

In the previous chapter, we derived a critical ratio between a defect size and a grain size to decrease the fatigue limit. The question arises if it is possible to predict the individual crack initiation site of a manufactured surface even before the fatigue test. Therefore, we tried to analyze the surface morphology, to predict with it the crack initiation site, and to compare with the real crack initiation site of the same specimen.

The morphology of the specimen's surface plays a significant role in the failure of the specimen during fatigue loading. This is due to the localized stress concentration induced by the surface morphology which can lead to a crack initiation. Especially areas with a valley, meaning a reduction of the cross section because of the surface morphology, are of interest. In an effort to be able to predict the crack initiation site by observing the specimen's surface morphology, a computer-aided method was developed. This method, which is described in detail in [30], can be divided into three main steps:

1. Acquisition of the topography data by means of confocal microscopy
2. Extraction of the data of the surface roughness or the notch for example
3. Determination of critical locations.

For the acquisition of the surface data a confocal microscope μ surf from NanoFocus was used. With this microscope, the 3D topography of the specimen can be measured. After eliminating any underlying shapes, the material ratio curve can be calculated according to [40]. Using this curve, all valleys on the specimen's surface can be defined and extracted. Critical locations can subsequently be determined by interpreting the resulting height data curves in the x- and y-directions of the specimen. To extract the data of the surface roughness and to determine the critical locations a MATLAB code has been written and implemented.

In order to compare the critical locations with the real fatigue crack initiation sites, the digital image correlation (DIC) system Q400 from Limes was used during the fatigue tests, and the fractured specimens were investigated to determine the fracture initiation site. With this system and the following processing of the data using the software Istra4D, it is possible to visualize and calculate the deformations of the specimen during the test as well as to define the crack initiation site.

After evaluating the data of the critical locations, the fracture surfaces, and the results of the DIC process, the predicted crack initiation site can be compared to the real crack initiation site. This process has been applied to the specimens of the material μ 47 with surface states as-received, face-milled, and with a $10\ \mu\text{m}$ notch, material μ 2 with surface states face-milled and with a $10\ \mu\text{m}$ notch, and to the material μ 130 with a face-milled surface state and with a $30\ \mu\text{m}$ notch.

Figure 14 presents the results of the surface analysis (first line) and the real crack initiation site (second line) for material μ 130 with a notch with $d = 30\ \mu\text{m}$ and face-milled state in Fig. 14a, b, respectively. While most of the μ 130 specimens did not fail from notches, in the here shown case it did.

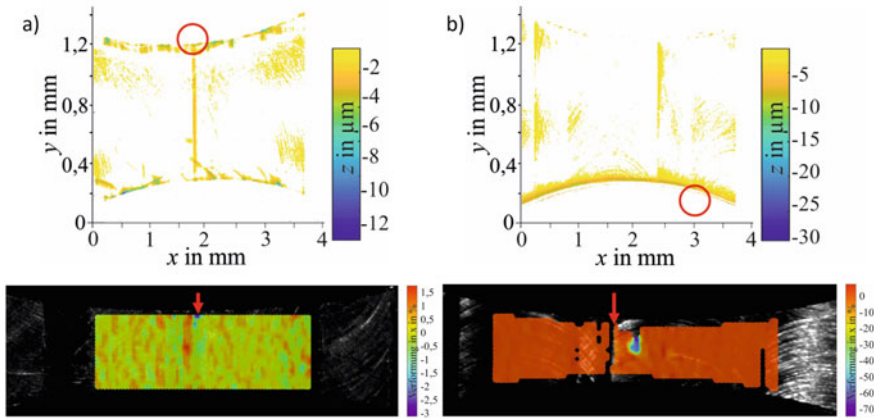


Fig. 14 Results of surface analysis (first line) and the real crack initiation site (second line) (compare [30])

Table 2 Comparison of the predicted and real crack initiation sites

Material	Surface state	Match	No match
$\mu 2$	Face-milled	X	
$\mu 2$	10 μm notch	X	
$\mu 47$	as-received		X
$\mu 47$	Face-milled		X
$\mu 47$	10 μm notch		X
$\mu 130$	Face-milled		X
$\mu 130$	30 μm notch	X	

Table 2 gives an overview of the material and surface states to which the prediction of the crack initiation site has been applied and whether a match with the real crack initiation site was found or not. Matches for the predicted and real crack initiation sites were found for the $\mu 2$ material with face-milled and 10 μm notch surface states and for the $\mu 130$ material with the 30 μm notch surface states. For the other material and surface state combinations, no matches were encountered.

The procedure for the prediction of the crack initiation site was not yet established for the fatigue tests of material $\mu 47$ with notches of 20 μm and 30 μm . For the notch depth of 20 μm the cracks originated mostly in the notch, and for the 30 μm notch the crack always originated in the notch. It can thus be assumed that a prediction of the crack initiation site via the deepest valleys could also be successful for these states. Comparing the results listed in Table 2 to the results shown in Fig. 13 a correlation between the success of the prediction of the crack initiation site and the ratio of the defect size can be assumed. Further investigations must be carried out in order to confirm this assumption.

5 Conclusions and Outlook

The investigations prove that there is an interrelation between the material's microstructure and the size of defect or notches which can lead to a reduction of the fatigue limit: In our cases, the defect size must not exceed 30 % of the grain size to guarantee the fatigue limit according to the Hall–Petch relationship. Otherwise, the fatigue limit can be decreased by defects/notches due to an increase of the stress in the notch ground promoting crack initiation and crack growth until failure. Therefore, all techniques applied to functionalize the surface must avoid to do so by introducing defects/notches larger than the above-mentioned size to ensure that the fatigue limit is not decreased due to the defect/notch.

By the way, any modification of the surface morphology to achieve a functionalization is called a defect here, because of its impact on the fatigue crack initiation. If it is not possible to avoid larger defects, there is a need to either control the position of the induced defect at the surface or to apply an additional treatment to increase the local resistance against fatigue crack initiation at the defect. For the first case, it is necessary to be able to identify areas at the surface which are less critical for crack initiation from defects: this could be a single large grain, if it is significantly larger than the proposed defect to stop a fatigue crack starting at the defect at its grain boundary, or it could be a local arrangement of oriented grains which have a high Schmid factor to reduce the local shear stress. Anyway, it is necessary to identify the local microstructure before manufacturing the defect. Therefore, several advanced techniques are available, see for instance, Chap. 2. Furthermore, an additional treatment after manufacturing the functionalized surface could be applied to increase the fatigue limit, which might be reduced due to defects from manufacturing. Two possible strategies are presented in the following section.

5.1 *Strategies to Increase the Strength of Manufactured Surfaces*

The strategy to increase the fatigue life of micro-notched specimens is to find a thermomechanical treatment to avoid the observed reduction in micromilled and structured surfaces. To this end, two potential pretreatment procedures have been identified to modify the component's surface areas which are critical to fatigue crack initiation. In this way, the fatigue strength is to be raised to the level before geometric microstructuring. One of the thermomechanical treatments is in the temperature range of maximum dynamic strain aging. In other words, a cyclic mechanical loading in the temperature range of dynamic strain aging will be applied to produce a more stable microstructure by stabilizing dislocations around the notches. Dynamic strain aging (DSA) is a strengthening mechanism that involves the interaction of moving dislocations and diffusing solute atoms or point defects. In the case of cyclic loading, sufficient plastic deformation increases the dislocation density, then subsequent

anchoring processes by diffusing solute atoms to the dislocation core stabilize the dislocation structure by increasing the resistance to further movement of dislocations. Thereby a microstructure is generated which may resist higher fatigue loadings in a later room temperature application. The method works for steels showing fatigue failure from defects, i.e., non-metallic inclusions, which act in a similar way as the micronotches at the surface [41, 42].

The other potential thermomechanical pre-treatment is the introduction of deformation twins into the material. Twinning is a mechanism to accommodate deformation, for example, in materials like the hexagonal close-packed α -Titanium which do not have enough independent slip systems to allow a deformation in all directions by dislocation movement. Deformation twinning is mainly influenced by three parameters: strain, strain rate, and temperature [43, 44], where an increase of the first two parameters leads to more deformation twinning. For the temperature, the inverse case takes place, so deformation at lower temperatures leads to more twins. Twinning planes between the deformation twins and the matrix material act as obstacles for dislocations similar to grain boundaries and increase thus the strength of a material [45]. Investigations to verify whether the introduction of deformation twins or the stabilization of the dislocation structure by dynamic strain aging of the notched α -Titanium specimens lead to a better fatigue result are to be carried out.

References

1. Kerscher E (2014) Influence of Microstructure and Micro Notches on the Fatigue Limit. *Proc Eng* 14:210–217. <https://doi.org/10.1016/j.proeng.2014.06.251>
2. Rögner J, Kerscher E, Schulze V, Löhe D (2008) Mechanical properties of primary shaped notched micro specimens made of aluminum bronze. *Adv Eng Mater* 10(6):529–533. <https://doi.org/10.1002/adem.200800032>
3. Schmid E, Boas W (1935) *Kristallplastizität mit besonderer Berücksichtigung der Metalle*. Springer, Berlin
4. Man J, Obrtlík K, Polák D (2009) Extrusions and intrusions in fatigued metals. Part 1. State of the art and history. *Philos Mag* 89(16):1295–1336. <https://doi.org/10.1080/14786430902917616>
5. Navarro A, Rios ERDL (1988) An alternative model of blocking of dislocations at grain boundaries. *Philos Mag A* 57(1):37–42. <https://doi.org/10.1080/01418618808204497>
6. Bruzzone A, Costa H, Lonardo P, Lucca D (2008) Advances in engineered surfaces for functional performance. *CIRP Ann* 57(2):750–769. <https://doi.org/10.1016/j.cirp.2008.09.003>
7. Whitehead KA, Colligon J, Verran J (2005) Retention of microbial cells in substratum surface features of micrometer and sub-micrometer dimensions. *Colloids Surf B: Biointerfaces* 41(2–3):129–138. <https://doi.org/10.1016/j.colsurfb.2004.11.010>
8. Schneider F, Lohkamp R, Sousa F, Müller R, Aurich J (2013) Investigation of the resulting surface in ultra-precision turning of crystalline titanium. In: *Proceedings of the 13th EUSPEN international conference*. Berlin, Germany, pp 72–75
9. Schneider F, Lohkamp R, Sousa F, Müller R, Aurich J (2014) Analysis of the surface integrity in ultra-precision Cutting of Cp-titanium by investigating the chip formation. *Proc CIRP* 13:55–60. <https://doi.org/10.1016/j.procir.2014.04.010>
10. Schneider F, Bohley M, Lohkamp R, Sousa F, Müller R, Aurich J (2014) Development of a quick-stop-device to investigate chip formation in micro and nanomachining. In: *Proceedings*

- of the 14th international conference of the European society for precision engineering and nanotechnology (EUSPEN). Dubrovnik, Croatia
11. Dornfeld D, Min S, Takeuchi Y (2006) Recent advances in mechanical micromachining. *CIRP Ann* 55(2):745–768. <https://doi.org/10.1016/j.cirp.2006.10.006>
 12. Vollertsen F (2008) Categories of size effects. *Prod Eng* 2(4):377–383. <https://doi.org/10.1007/s11740-008-0127-z>
 13. Cotterell M, Byrne G (2008) Characterisation of chip formation during orthogonal cutting of titanium alloy Ti-6Al-4V. *CIRP J Manuf Sci Technol* 1(2):81–85. <https://doi.org/10.1016/j.cirpj.2008.09.017>
 14. Cedergren S, Petti G, Sjöberg G (2013) On the influence of work material microstructure on chip formation, cutting forces and acoustic emission when machining Ti-6Al-4V. *Proc CIRP* 12:55–60. <https://doi.org/10.1016/j.procir.2013.09.011>
 15. Schneider F, Effgen C, Kirsch B, Aurich JC (2019) Manufacturing and preparation of micro cutting tools: influence on chip formation and surface topography when micro cutting titanium. *Prod Eng* 13(6):731–741. <https://doi.org/10.1007/s11740-019-00927-x>
 16. Lee EH (1969) Elastic-plastic deformation at finite strains
 17. de Souza Neto E, Peri? D, Dutko M, Owen D (1996) Design of simple low order finite elements for large strain analysis of nearly incompressible solids. *Int J Solids Struct* 33(20–22):3277–3296
 18. Fischer A (1992) Optimization. A special Newton-type optimization method. 24(3–4):269–284
 19. Kieren-Ehse S, Böhme L, Morales-Rivas L, Lösch J, Kirsch B, Kerscher E, Kopnarski M, Aurich JC (2021) The influence of the crystallographic orientation when micro machining commercially pure titanium: a size effect. *Precis Eng* 72:158–171. <https://doi.org/10.1016/j.precisioneng.2021.04.007>
 20. Löhe D, Vöhringer O (2000) Metallic structural materials: design of microstructure. In: Grabowski H, Rude S, Grein G (eds) *Universal design theory*, pp 147–167
 21. Grau P, Ullner C, Behncke H-H (1997) Uncertainty of depth sensing hardness. *Mater Testing* 39(9):362–367. <https://doi.org/10.1515/mt-1997-390909>
 22. Laurent-Brocq M, Béjanin E, Champion Y (2015) Influence of roughness and tilt on nanoindentation measurements: a quantitative model. *Scanning* 37(5):350–360. <https://doi.org/10.1002/sca.21220>
 23. Qasmi M, Delobelle P (2006) Influence of the average roughness $R_c < B$ on the precision of the young's modulus and hardness determination using nanoindentation technique with a Berkovich indenter. *Surf Coatings Technol* 201(3–4):1191–1199. <https://doi.org/10.1016/j.surfcoat.2006.01.058>
 24. Bohley M, Reichenbach I, Kieren-Ehse S, Heberger L, Arrabiyeh P, Merz R, Böhme L, Hering J, Kirsch B, Kopnarski M, Kerscher E, von Freymann G, Aurich J (2018) Coating of ultra-small micro end mills: analysis of performance and suitability of eight different hard-coatings. *J Manuf Mater Process* 2(2):22. <https://doi.org/10.3390/jmmp2020022>
 25. Böhme L, Kessel A, Ströer F, Bohley M, Kieren-Ehse S, Kirsch B, Aurich JC, Seewig J, Kerscher E (2019) Micro hardness determination on a rough surface by using combined indentation and topography measurements. *Surf Topogr: Metrol Prop* 7(4):045021. <https://doi.org/10.1088/2051-672x/ab518a>
 26. Meyer E (1908) Untersuchungen über Härteprüfung und Härt. In: *Zeitsch. d. Ver. d. Ing.*
 27. Oliver W, Pharr G (1992) An improved technique for determining hardness and elastic modulus using load and displacement sensing indentation experiments. *J Mater Res* 7(6):1564–1583. <https://doi.org/10.1557/jmr.1992.1564>
 28. DIN EN ISO 14577-2 (2015) Metallic materials - instrumented indentation test for hardness and materials parameters: Part 2: verification and calibration of testing machines
 29. Böhme L, Morales-Rivas L, Diederichs S, Kerscher E (2018) Crystal CAxis mapping of hcp metals by conventional reflected polarized light microscopy: application to untextured and textured cp-titanium. *Mater Charact* 145:573–581. <https://doi.org/10.1016/j.matchar.2018.09.024>

30. Bähme L, Ströer F, Keksel A, Seewig J, Kerscher E (2020) Forecast of the Fatigue Crack Initiation Site of Commercially Pure Titanium Miniature Specimens with Local Surface Topography Data. In: Villechaise P, Appolaire B, Castany P, Dehmas M, Delaunay C, Delfosse J, Denquin A, Gautier E, Germain L, Gey N, Gloriant T, Hascoët J-Y, Hémerly S, Millet Y, Monceau D, Pettinari-Sturmel F, Piellard M, Prima F, Viguier B (eds) MATEC web of conferences, vol 321. p 11008. <https://doi.org/10.1051/mateconf/202032111008>
31. Godard C, Klement U, Kerscher E (2017) Electron backscatter diffraction- analysis of deformed micro-milled commercially pure-titanium specimens at different strain values. *Int J Mater Res* 108(10):798–807. <https://doi.org/10.3139/146.111539>
32. Godard C, Klingler A, Junker T, Kerscher E (2015) The applicability of nanoindentation for the examination of microstructured areas in CP titanium samples. *Pract Metallogr* 52(6):314–322. <https://doi.org/10.3139/147.110342>
33. Ruffing C, Grad P, Klassen M, Müller R, Kerscher E (2013) Experimental and numerical investigation of the microstructural influence on the deformation behavior of notched cp-titanium specimens. *Int J Mater Res* 104(6):535–541. <https://doi.org/10.3139/146.110902>
34. Godard C, Bohley M, Aurich JC, Kerscher E (2015) Deformation behaviour of micro-milled cp-titanium specimens under tensile loading. *Int J Mater Res* 106(6):572–579. <https://doi.org/10.3139/146.111233>
35. DIN 50100:2016-12, Schwingfestigkeitsversuch_–Durchführung und Auswertung von zyklischen Versuchen mit konstanter Lastamplitude für metallische Werkstoffproben und Bauteile. <https://doi.org/10.31030/2580844>
36. Böhme L, Godard C, Kerscher E (2016) Influence of engineered surfaces and microstructure on the fatigue limit of titanium. In: Proceedings of 30th international conference on surface modification technologies
37. Godard C, Kerscher E (2014) Characterization of the Fracture morphology of commercially pure (cp)-titanium micro specimens tested by tension compression fatigue tests. *Proc Mater Sci* 3:440–446. <https://doi.org/10.1016/j.mspro.2014.06.074>
38. Kühn C, Kerscher E (2013) Consequences of micro-milled and laser structured surfaces of cp-titanium on tension-compression fatigue behaviour. *Mater Sci Forum* 765:653–657. <https://doi.org/10.4028/www.scientific.net/msf.765.653>
39. Murakami Y (2019) Metal Fatigue: effects of small defects and nonmetallic inclusions. Effects of small defects and nonmetallic inclusions. Elsevier Science & Technology. ISBN: 9780128138762. <https://doi.org/10.1016/C2016-0-05272-5>
40. DIN EN ISO 13565-2:1998-04, Geometrische Produktspezifikationen (GPS) - Oberflächenbeschaffenheit: Tastschnittverfahren - Oberflächen mit plateauartigen funktionsrelevanten Eigenschaften - Teil 2: Beschreibung der Höhe mittels linearer Darstellung der Materialanteilkurve (ISO 13565-2:1996); Deutsche Fassung EN ISO 13565-2:1997. <https://doi.org/10.31030/7434139>
41. Kerscher E, Lang K-H, Vöhringer O, Löhe D (2008) Increasing the fatigue limit of a bearing steel by dynamic strain ageing. *Int J Fatigue* 30:1838–1842. <https://doi.org/10.1016/j.ijfatigue.2008.02.003>
42. Khayatizadeh A, Sippel J, Guth S, Lang K-H, Kerscher E (2022) Influence of a thermo-mechanical treatment on the fatigue lifetime and crack initiation behavior of a quenched and tempered steel. *Metals* 12(2):204. <https://doi.org/10.3390/met12020204>
43. Chichili DR, Ramesh KT, Hemker KJ (1998) The high-strain-rate response of alpha-titanium: experiments, deformation mechanisms and modeling. *Acta Mater* 46(3):1025–1043. [https://doi.org/10.1016/s1359-6454\(97\)00287-5](https://doi.org/10.1016/s1359-6454(97)00287-5)
44. Gray GT (1997) Influence of strain rate and temperature on the structure. Property behavior of high-purity titanium. *Le Journal de Physique IV* 07(C3):C3-423–C3-428. <https://doi.org/10.1051/jp4:1997373>
45. Salem AA, Kalidindi SR, Doherty RD (2002) Strain hardening regime and microstructure evolution during large strain compression of high purity titanium. *Script Mater* 46(6):419–423. [https://doi.org/10.1016/s1359-6462\(02\)00005-2](https://doi.org/10.1016/s1359-6462(02)00005-2)

Influence of Manufacturing and Load Conditions on the Phase Transformation and Fatigue of Austenitic Stainless Steels



Tilman Beck, Marek Smaga, Sergiy Antonyuk, Dietmar Eifler, Ralf Müller, Herbert M. Urbassek, and Tong Zhu

Abstract The passivity and, hence, “stainlessness” as well as a very good combination of material strength and ductility was the main scope in the development of high alloyed chromium–nickel austenitic stainless steels. However, the chemical composition strongly influences not only the chemical passivity, but also the microstructural metastability, since deformation-induced martensite transformation takes place in a huge number of austenitic stainless steels. In this work, the phase transformation behavior was investigated under different loading conditions, using molecular dynamics simulation on the atomistic scale as well as phase field modeling on the microscale. To comprehensively assess the metastability of the investigated materials, a new method was developed and compared with the conventional metastability parameters in the literature. Furthermore, experimental work focusing on the detailed characterization of the surface morphology after different manufacturing processes, i.e., cryogenic turning, conventional milling, ultrasonic surface modification as well as micro-shot peening, is shown. The resulting surface morphologies and their influences on the fatigue properties were investigated from the low cycle fatigue, over the high cycle fatigue to the very high cycle fatigue regime, under uniaxial fully reversed tension–compression loading conditions. Additionally, the fatigue life of austenitic stainless steels with different metastabilities and surface morphologies was investigated in four-point bending fatigue tests.

T. Beck (✉) · M. Smaga (✉) · D. Eifler · T. Zhu
Institute of Materials Science and Engineering, RPTU Kaiserslautern, Kaiserslautern, Germany
e-mail: t.beck@mv.rptu.de

M. Smaga
e-mail: m.smaga@mv.rptu.de

S. Antonyuk
Institute of Particle Process Engineering, RPTU Kaiserslautern, Kaiserslautern, Germany

R. Müller
Institute of Mechanics, Technical University of Darmstadt, Darmstadt, Germany

H. M. Urbassek
Institute of Computational Material Science, RPTU Kaiserslautern, Kaiserslautern, Germany

1 Introduction

With a global market share of more than 80%, Austenitic Stainless Steels (ASSs) are the most common and familiar types of stainless steel. Besides an excellent corrosion resistance, ASSs also demonstrate a good combination of mechanical properties and formability from cryogenic temperatures up to about 700 °C [1, 2].

Due to the addition of austenite-stabilizing alloy elements like Ni, C, and N, ASSs consist of a face-centered cubic (fcc) γ -austenitic lattice structure and are paramagnetic. However, a low content of body-centered cubic (bcc) δ -ferrite can sometimes be found in conventional ASS grades as a consequence of the ferrite-stabilizing alloy elements like Cr, Mo, and Si. The δ -ferrite is ferromagnetic and has a positive effect on the weldability [3]. Generally, in solution-annealed condition, the austenitic grades have a relatively low 0.2% offset yield strength ($200 < R_{p0.2} < 300$ MPa) but high tensile strength ($500 < \sigma_{UTS} < 700$ MPa) and high fracture strain ($33 < \varepsilon_f < 45\%$) at ambient temperature. They can be work-hardened and/or precipitation-hardened, but are barely heat-treatable [1, 2].

According to the stability of the austenitic structure, ASSs can be divided into two grades: stable and metastable [1]. Most ASSs are used in the metastable state [2]. In this case, the phase transformation from paramagnetic γ -austenite into paramagnetic ε -martensite and/or into ferromagnetic α' -martensite with lower free energy is thermodynamically possible, but the driving force is insufficient to activate martensitic transformation thermally. However, since this phase transformation is achieved by a diffusionless shear mechanism, it can also be driven mechanically by external strains and/or stresses [2]. As an important intrinsic parameter, the Stacking Fault Energy (SFE) can be used to predict the microstructural mechanisms in metastable austenite. A low SFE ≤ 20 mJ/m² favors the α' -martensitic transformation either directly or indirectly via ε -martensite [4]. Deformation twinning is preferred in an intermediate SFE range of 20–45 mJ/m². With even higher SFE > 50 mJ/m², the dislocations are barely dissociated, which disables the above-mentioned microstructural mechanisms and makes only dislocation glide possible [4]. The SFE is usually reported to be strongly influenced by the chemical composition and temperature. At room temperature, it can be estimated according to the following equation [5]:

$$\text{SFE in } \frac{\text{mJ}}{\text{m}^2} = 2.2 + 1.9\text{Ni} - 0.9\text{Cr} - 1.2\text{Mn} + 410\text{C} - 77\text{N} - 13\text{Si}. \quad (1)$$

For industrial production, the M_{d30} temperature is used as a common indicator of austenite stability. M_{d30} is the temperature at which 50% of the austenite would be transformed into Deformation-Induced Martensite (DIM) during deformation to 30% true plastic strain. Consequently, a higher M_{d30} represents a higher metastability of the ASSs. An empirical estimate for the M_{d30} -temperature was given according to the following equation [6]:

$$M_{d30} \text{ in } ^\circ\text{C} = 413 - 462(\text{C+N}) - 13.7\text{Cr} - 9.5\text{Ni} - 8.1\text{Mn} - 18.5\text{Mo} - 9.2\text{Si}. \quad (2)$$

However, both empirical equations are based on regression analyses of merely the chemical composition. Since the metastability can be influenced by other factors such as the grain size, dislocation arrangement and density as well as chemical inhomogeneities, etc., the calculated values can sometimes lead to an inappropriate estimation of the metastability, cf. Sect. 4 [7].

In the following sections, both simulations and experimental works are presented to determine the surface Manufacturing–Morphology–Property (MMP) Relationships of stable and metastable ASSs. The phase transformation behavior of metastable ASSs was simulated on the atomistic as well as the microscale, via molecular dynamics simulation (Sect. 2) and phase field modeling (Sect. 3), respectively. Besides conventional mechanical characterization, the metastability of the investigated ASSs was also studied in Sect. 4. In Sects. 5 and 6, a systematic characterization of fatigue specimens in different surface morphologies after various manufacturing and/or post-processing methods is shown, in order to reveal the influence of surface morphologies on the fatigue behavior of ASSs. A conclusion and outlook are given in Sect. 7.

2 Molecular Dynamics Simulation

Molecular dynamics simulation allows to model the structure and dynamics of materials on an atomistic level. It is based on evaluating the forces between atoms that are derived from the interatomic potentials. For metals, these are of a many-body nature. Among the potentials available for iron, the Meyer–Entel potential [8] was proven [9] to be most appropriate to model the α - γ phase transformation between the bcc and fcc phases. It will be used exclusively in this study.

2.1 Free Energy

Figure 1a shows the evolution of the free-energy difference between the fcc and bcc phases with temperature (at zero pressure). It demonstrates that at low temperatures, the bcc phase is thermodynamically stable and at high temperatures the fcc phase is stable, as observed in experiments. The transition temperature is at $T_c = 487$ K. This value is considerably smaller than in reality ($T_c = 1184$ K); molecular dynamics temperatures have therefore to be set in relation to the transition temperature.

The path that atoms take during the transformation is complex and still under discussion. An idealized framework considers the simultaneous and concerted motion of all atoms. A particularly simple path is the Bain path that involves the tetragonal distortion of a bcc unit cell to evolve to an fcc unit cell. Figure 1b shows the evolution of the free energy along that path. The existence of an energy barrier between the bcc and fcc phases is the most remarkable result; this barrier kinetically hinders the

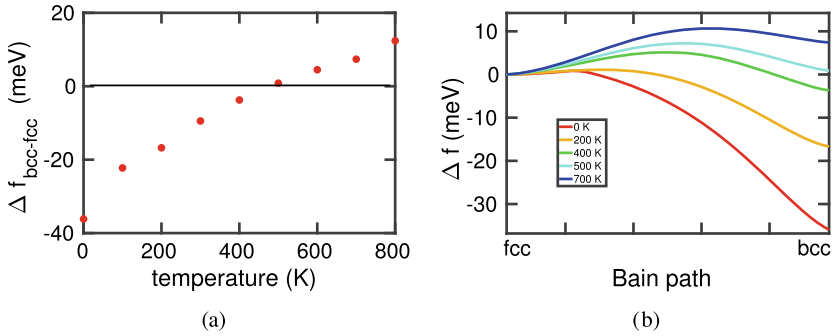


Fig. 1 Dependence of the free-energy difference between fcc and bcc phases on temperature (a). Evolution of the free-energy difference along the Bain path for various temperatures (b). Data evaluated for the Meyer–Entel potential. Taken from Ref. [9] by CC BY

transformation. At low temperatures, it strongly decreases, allowing the martensitic transformation to proceed almost spontaneously.

It could be shown that the evolution of the free energy along a more realistic path, the Nishiyama–Wassermann path, closely agrees with that on the Bain path [10].

2.2 Phase Boundary

The structure of an fcc/bcc phase boundary is subject of intense research, see, e.g., [11]. Figure 2 visualizes the structure of a simple planar phase boundary, characteristic of the Nishiyama–Wassermann orientation relationship: $(111)_{\text{fcc}} \parallel (011)_{\text{bcc}}$. Figure 2a shows all atoms on the bcc side of the interface that are not on ideal bcc positions; the emergence of a misfit dislocation as well as a broadening of the interface region itself is noticeable. Figure 2b colors the interface atoms according to their potential energy and shows the emerging substructure within the interface, which is caused by the misfit.

The data on the interface structure and energetics obtained by such simulations, as well as the thermophysical data provided above, can be used as input parameters in mesoscopic models, see Sect. 3.

2.3 Martensitic Transformation

Cooling of an fcc structure will induce a martensitic transformation to the bcc structure. In simulations, this transformation is kinetically delayed unless defects (phase or grain boundaries, dislocations, precipitates, free surfaces, etc.) are available. Some examples of the transformation are presented in the following.

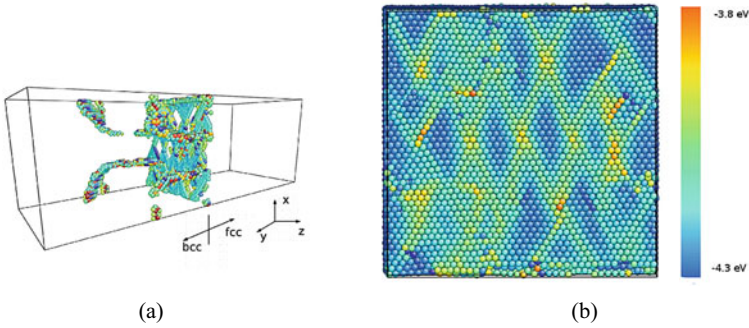


Fig. 2 Three-dimensional view of defective atoms on the bcc side of the phase boundary (a). View on the interface plane (b). Atoms have been colored according to their potential energy, see color bar. Taken with permission from Ref. [12]

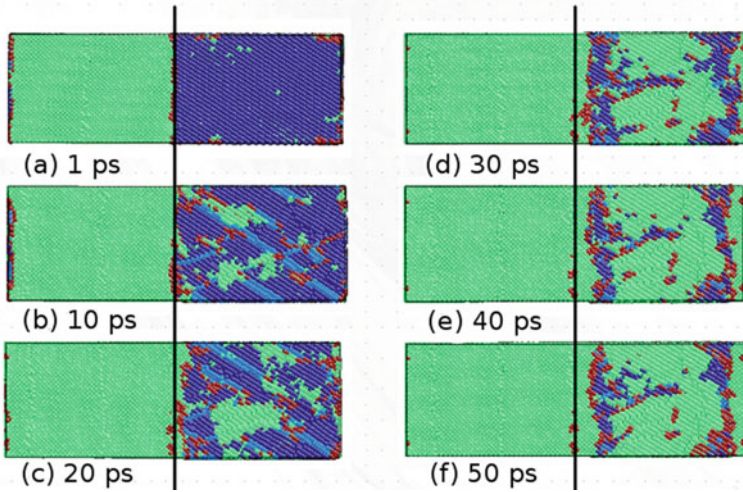


Fig. 3 Snapshots showing the time evolution of the fcc–bcc biphasic system at a temperature of 100 K. The colors denote the local crystal structure. Green: bcc; dark blue: fcc; light blue: hcp; red: unknown. The original position of the interface is marked by a black line. Taken with permission from Ref. [12]

Figure 3 shows the evolution of the biphasic system whose phase boundary was depicted in Fig. 2. When the system is suddenly cooled to 100 K—considerably below the transition temperature—the martensitic transition sets in almost instantaneously, in agreement with the nearly vanishing energy barrier between the phases, Fig. 1b. Remarkably, two growth modes of the bcc phase are observed: (i) homogeneous nucleation, in which the bcc phase nucleates within the fcc grain; (ii) heterogeneous growth by migration of the interface.

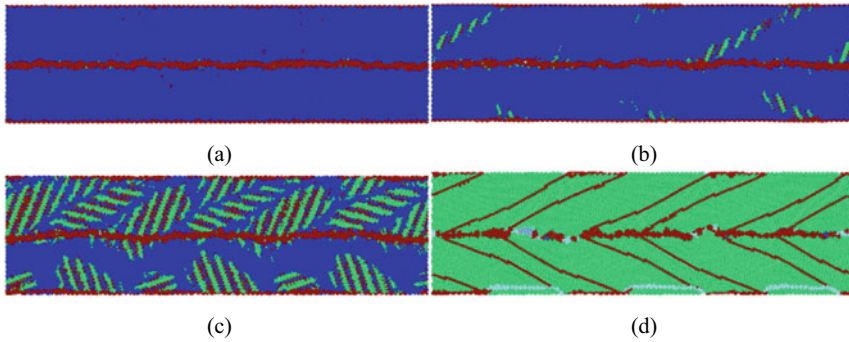


Fig. 4 Snapshots showing the martensitic phase transformation at a $\Sigma 5$ (310) grain boundary. Initial configuration (a), nucleation of the new phase (b), and its propagation in the form of martensitic lamellae (c). Final configuration (d). Colors denote local lattice structure as in Fig. 3. Taken with permission from Ref. [14]

Grain boundaries provide an example of defects, at which the new phase can easily nucleate, since here free atomic volume is available to ease atomic motion during the transition. Figure 4 gives a representative example of the evolution of the martensitic phase transformation occurring when cooling an fcc crystal from 800 K with fixed cooling rate of 0.33 K/ps. The new phase nucleates at the grain boundary at a temperature of 56 K and then expands into the volume. The resulting lamellar structure of the martensite is caused by the simultaneous occurrence of multiple nucleation centers. A similar study [13] shows that also free surfaces strongly influence the martensitic transformation, allowing for heterogeneous nucleation of the bcc phase.

Another prominent example of the influence of defects on the martensitic transformation is provided in Fig. 5. Here, a single-crystalline fcc thin film with (100) free surfaces is steadily cooled down from 1000 K with a cooling rate of 1 K/ps. In the absence of dislocations, no transformation occurred during the simulation time of around 1 ns. However, the presence of dislocations induces the martensitic transformation, see Fig. 5. The transformation starts at the dislocations such that multiple bcc nuclei are created. The nuclei grow, leading to a fine-grained structure. However, the grains eventually coalesce, leading to a simplified microstructure characterized by a few columnar grains, separated by twin boundaries. The snapshots shown in Fig. 5 span the temperature interval of around 140–155 K. The dislocation density becomes strongly reduced during the transformation.

2.4 Martensitic Transformation Induced by Nanoindentation

Besides temperature, also stresses and/or strains may help induce the phase transformation. Figure 6 gives an example of how nanoindentation triggers and influences the transformation. In this example, the sample is an fcc Fe single crystal with a

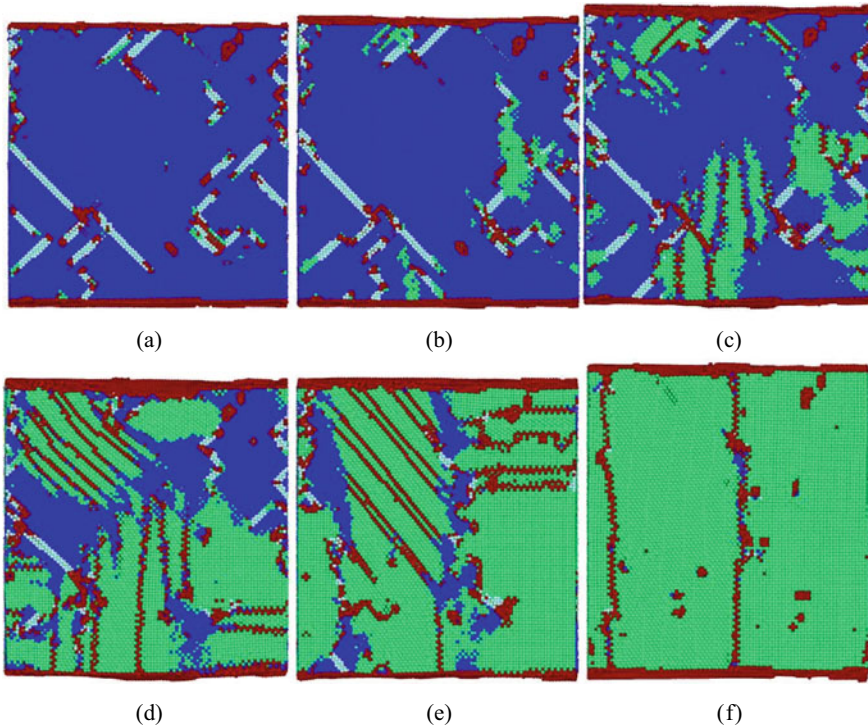


Fig. 5 Martensitic transformation in a thin film with a dislocation density of $\rho = 10.34 \cdot 10^{12} \text{ cm}^{-2}$ during cooling of the sample. Colors denote local lattice structure as in Fig. 3. Taken from Ref. [15] by CC BY

(100) surface. It is indented by a spherical indenter of radius 5 nm to a depth of 5 nm. Figure 6 shows the final state of the sample after indentation at various temperatures.

We observe that indentation induces the phase transformation of the fcc to the bcc phase: (i) At low temperatures, the indentation triggers the transformation which then rapidly proceeds throughout the sample. (ii) At higher temperatures, around the equilibrium transformation temperature T_c , the crystal transforms only in the vicinity of the indent pit. (iii) At intermediate temperatures, the indentation induces a partial transformation.

3 Phase Field Modeling

3.1 Monotonic and Cyclic Loading

Phase field modeling of martensitic transformations was done by using an Allen–Cahn-type model. This model requires three major ingredients. First, appropriate

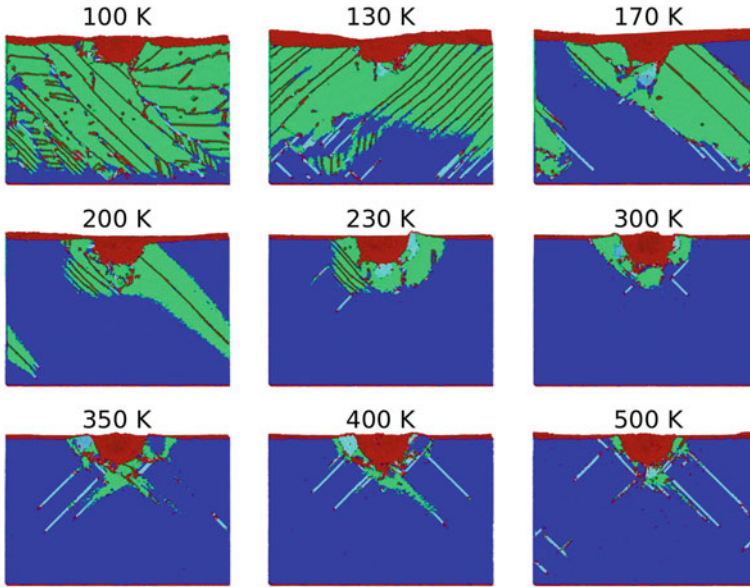


Fig. 6 Final state of the indented sample, showing the crystal structure for various temperatures. Colors denote local lattice structure as in Fig. 3. Taken from Ref. [16] by CC BY

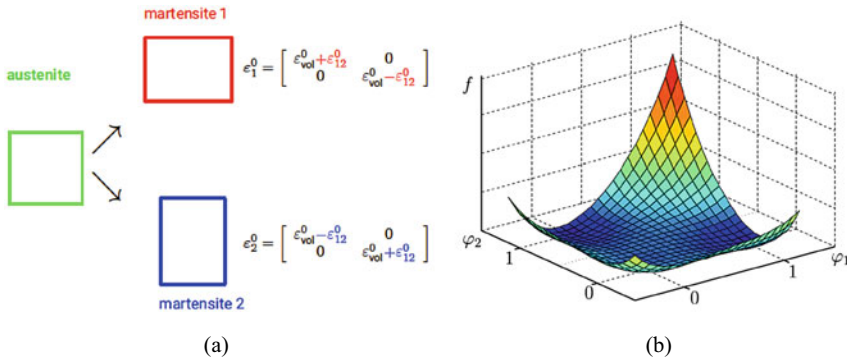


Fig. 7 Martensitic orientation variants and associated transformation strains (a), order parameter-dependent separation energy (b)

phase field parameters have to be chosen. One phase field parameter ϕ_i is chosen for each i orientation variant of martensite. The value of 0 is associated with austenite, while a phase field value of 1 indicates the respective martensite variant. The transformation strains are modeled by inelastic eigenstrains that contain a volumetric as well as a deviatoric part, see Fig. 7a. The potential energy density of the system is then given by Eq. (3).

$$\begin{aligned}
\psi(\underline{\underline{\varepsilon}}, \varphi_i, \nabla \varphi_i) &= \psi^{\text{sep}}(\varphi_i) + \psi^{\text{grad}}(\nabla \varphi_i) + W(\underline{\underline{\varepsilon}}, \varphi_i) \text{ with} \\
\psi^{\text{sep}}(\varphi_i) &= K_{\text{sep}} \frac{G}{L} f(\varphi_i) \text{ (see Fig. 11.7b),} \\
\psi^{\text{grad}}(\nabla \varphi_i) &= \frac{1}{2} K_{\text{grad}} GL \sum_{i=1}^2 |\nabla \varphi_i|^2, \\
W(\underline{\underline{\varepsilon}}, \varphi_i) &= \frac{1}{2} [\underline{\underline{\varepsilon}} - \underline{\underline{\varepsilon}}^0(\varphi_i)] : \underline{\underline{\mathbb{C}}}(\varphi_i) [\underline{\underline{\varepsilon}} - \underline{\underline{\varepsilon}}^0(\varphi_i)] \text{ where} \\
\underline{\underline{\varepsilon}}^0(\varphi_i) &= \sum_{i=1}^2 \varphi_i \underline{\underline{\varepsilon}}_i^0, \quad \underline{\underline{\mathbb{C}}}(\varphi_i) = \underline{\underline{\mathbb{C}}}^A + \sum_{i=1}^2 \varphi_i (\underline{\underline{\mathbb{C}}}^{M_i} - \underline{\underline{\mathbb{C}}}^A).
\end{aligned} \tag{3}$$

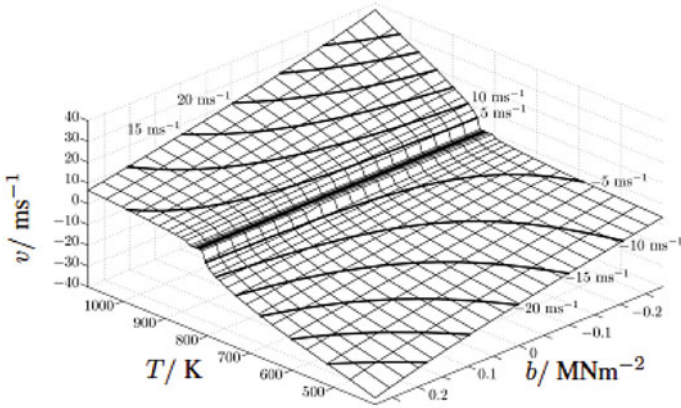
The parameters K_{sep} and K_{grad} are chosen such that G and L describe the interface energy and interface width. The elastic properties are given by $\underline{\underline{\mathbb{C}}}^A$ and $\underline{\underline{\mathbb{C}}}^{M_i}$ for the austenite and martensite variants, respectively. Note that no distinction is made between the different martensite orientations with respect to the elastic properties. The evolution of the martensite is driven by time-dependent Ginzburg–Landau equations

$$\dot{\varphi}_i = -M \frac{\delta \psi}{\delta \varphi_i} \text{ where } \frac{\delta \psi}{\delta \varphi_i} = \frac{\partial \psi}{\partial \varphi_i} - \nabla \cdot \frac{\partial \psi}{\partial \nabla \varphi_i} \tag{4}$$

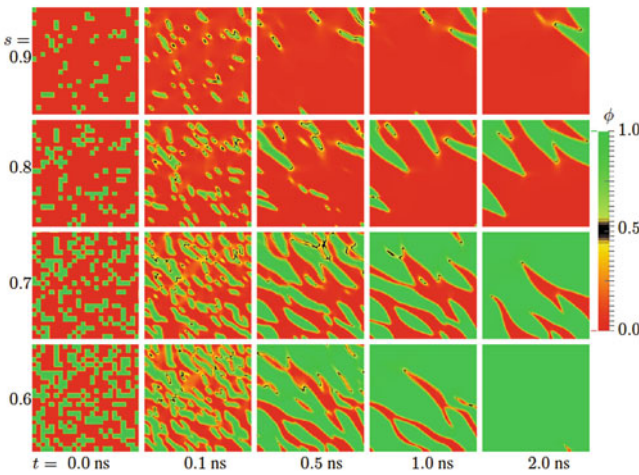
in conjunction with the equilibrium condition,

$$\text{div } \underline{\underline{\sigma}} = \underline{\underline{0}} \text{ where } \underline{\underline{\sigma}} = \frac{\partial \psi}{\partial \underline{\underline{\varepsilon}}} = \underline{\underline{\mathbb{C}}}(\varphi_i) (\underline{\underline{\varepsilon}} - \underline{\underline{\varepsilon}}^0(\varphi_i)). \tag{5}$$

M is the mobility constant. The parameters in Eqs. (3) and (4) are determined from molecular dynamics simulations [17]. Equations (4) and (5) were solved by a monolithic scheme. Discretization in two-dimensional space was done with bilinear finite elements and the time integration is performed by an implicit first-order Euler method. A crucial parameter for the phase transformation is the temperature. Temperature-dependent separation energies were determined, see [18]. It was found that a proper determination of the separation energy renders the mobility constant M to be almost temperature independent. In order to include nonhomogeneous and nonstationary temperature fields, the heat conduction was introduced in the model, see [18] for details. As the velocity of the phase transition is much larger than the characteristic velocity of the temperature evolution, only the spatial temperature distribution has a significant impact on the microstructure evolution. The velocity of individual phase boundaries was analyzed as a function of temperature as well as an applied external load, see [18, 19] and Fig. 8. The phase field model with more than one orientation variant of martensite allows for the simulation of the autocatalytic effect. In Fig. 9, the formation of the two orientation variants of martensite from a random orientation is shown. The color coding is the same as in Fig. 7a (austenite: green, martensite 1: red, martensite 2: blue). Under an applied tensile displacement loading a lath-like, twinned martensite structure is formed. The martensite is stress



(a)



(b)

Fig. 8 Interface velocity as a function of temperature T and applied load b (a), martensite (green) evolution in an inhomogeneous temperature field as a function of nucleation sites s (b)

induced, as the formation of martensite relaxes the stresses induced by the external load, because an overall inelastic deformation is created by the phase transition. The phase transformations lower the elastic energy W and the separation energy ψ^{sep} contribution to the total energy, but they increase the contribution of ψ^{grad} , as interfaces are formed. Nevertheless, the total energy decreases and drives the phase transformation. As can be seen from Fig. 9, the formation of a lath-like microstructure of martensite can be induced by a constant or a cyclic loading.

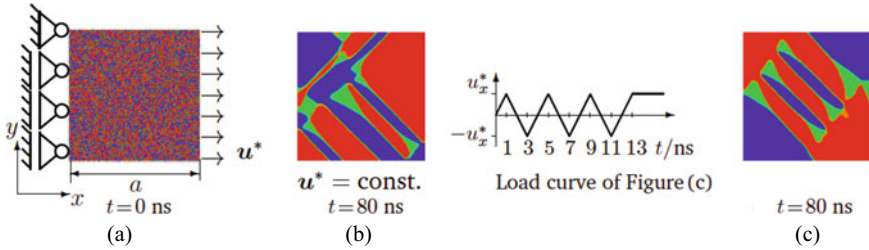


Fig. 9 Stress-induced martensite formation: Initial random distribution (a), constant initial load (b), cyclic loading (c)

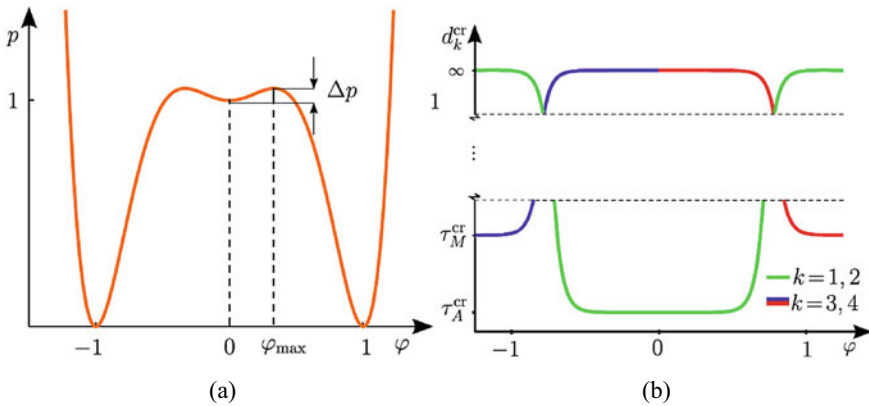


Fig. 10 Separation potential to model austenite, martensite 1, and martensite 2 in a single separation function (a), critical resolved shear stress as a function of the order parameter (b)

3.2 Phase Transformations, Plastic Deformation, and Cryogenic Turning

To also take plastic effects into account the phase field model is coupled to a crystal plasticity model. The numerical effort is reduced by introducing only one phase field variable φ to model austenite $\varphi = 0$ and two martensitic orientation variants $\varphi = \pm 1$, see Fig. 10 a for details. Furthermore, a two-dimensional situation is assumed, where the relevant slip systems of fcc and bcc fall by the projection in the same directions, thus identical slip systems are used for all phases. To distinguish between martensitic and austenitic phases the critical resolved shear stress d_{cr} is assumed to be different in martensite and austenite. This was modeled by a special dependency of d_{cr} on φ , for details see Fig. 10b. The model is numerically very complex, as it couples a stationary equilibrium condition (Eq. 5), with an evolution equation for phase transformation (Eq. 4 for one order parameter) and an evolution equation for the plastic slip γ^k . From the slip γ^k the plastic strain can be computed via

$$\underline{\underline{\varepsilon}}^P = \sum_k^N \gamma^k \underline{\underline{P}}^k, \tag{6}$$

where $\underline{\underline{P}}^k$ represents the geometry of the k^{th} of the N slip systems. Details of the model as well as the numerical treatment can be found in [20, 21]. Including plastic deformation by slip deformation on the crystal level is crucial to model deformation-induced phase transformations as there is a strong interaction between the two inelastic processes—phase transition and plasticity. When the yield limit, i.e., the local critical Schmid stresses are exceeded, both inelastic processes occur. Especially in manufacturing processes this is the case. It was observed experimentally in [22] that a strong passive force (pressure on the surface) facilitates the martensitic transformation during cryogenic turning. To capture these effects, a traveling load of magnitude equivalent to the passive force measured in cryogenic turning (feed rate 0.35 mm/rev) in [22] was considered on an initially purely austenitic workpiece of idealized dimensions $a \times a \mu\text{m}$, see Fig. 11. Three different simulation scenarios were studied: In the elastic model, the transformation only occurs directly under the load and significant back transformation appears, Fig. 12a. The combination with crystal plastic deformation improves the situation only slightly, if the plastic deformations are not inherited from the austenite to the martensite, see Fig. 12b and c.

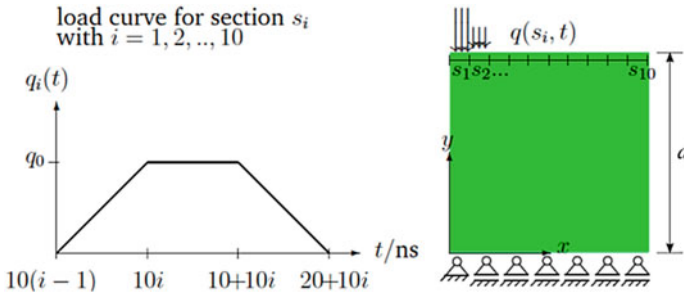


Fig. 11 Traveling load on a surface of an austenitic material

In a final example, the model is used to explain the depth distribution of martensite during cryogenic turning. The model uses an inheritance of the plasticity as well as modified boundary conditions in lateral direction to mimic a long extension in horizontal, i.e., machining direction. A traveling load, similar to the previous example, is applied on the model setup shown in Fig. 13a. The snapshots of the resulted microstructures are given in Fig. 13b–d. The final microstructure is also compared with the data of martensite volume fraction versus the depth, obtained from an experimental investigation of cryogenic turned (feed rate 0.35 mm/rev) austenitic steel (AISI 347) performed in [22], see Fig. 14. To exclude boundary effects that are associated with the lateral boundary conditions, the martensite volume fraction from the

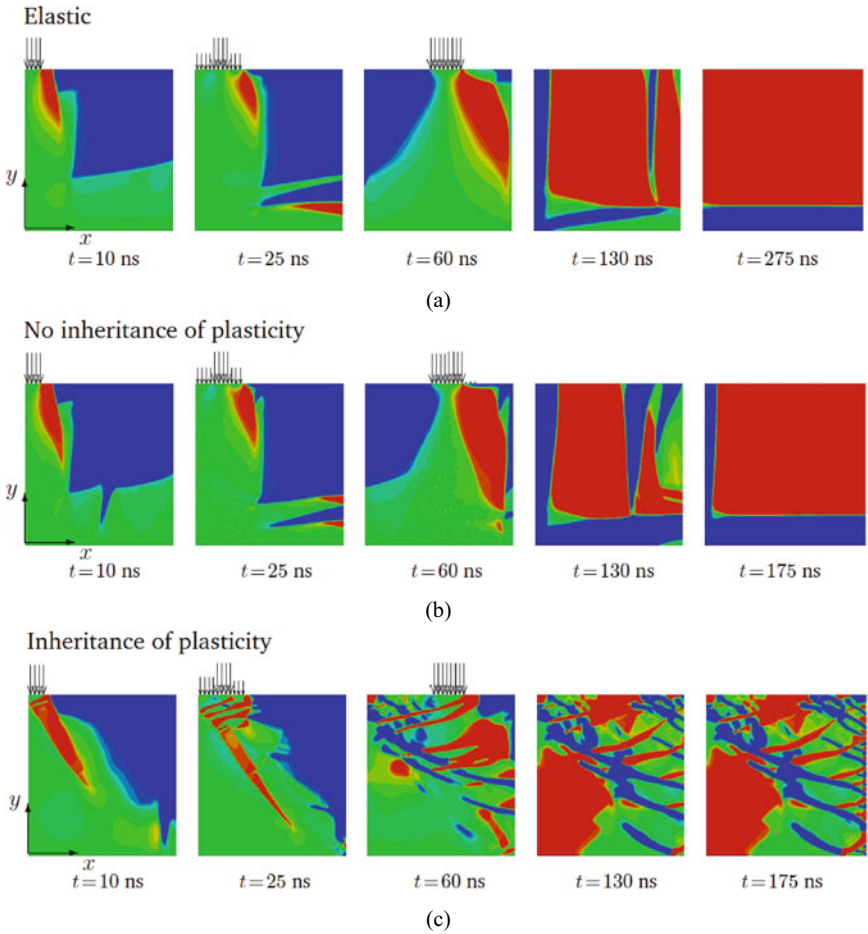


Fig. 12 Evolution of martensite under a traveling load, elastic model (a), crystal plastic model without inheritance of plastic deformation (b), crystal plastic model with inheritance of plastic deformations (c)

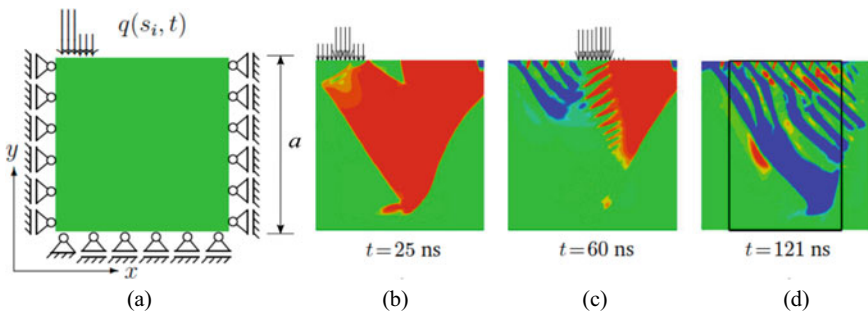


Fig. 13 Depth-dependent distribution of martensite

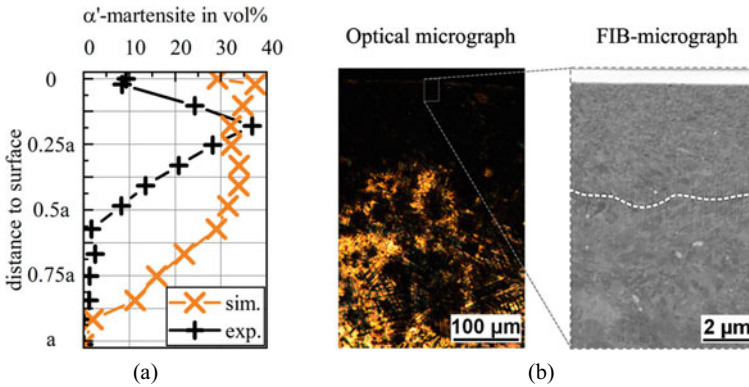


Fig. 14 Comparison of the martensite volume fraction in the near-surface region after cryogenic turning from experimental and simulation data (a), cross-sectional micrograph, and FIB-image taken in the near-surface region (b)

model, considered for comparison, is only averaged over area indicated in black in Fig. 13d.

As can be seen from Fig. 14a, the martensite content directly below the surface is not the highest. Within a certain depth of about 0.25a the martensite volume fraction reaches its maximum and then decays. This is a strong indication that the surface plays an important role, as stress and deformation states are different at the surface and in the bulk. However, far away from the boundary the stresses due to the load (passive turning force) decay and thus lesser martensitic transformation occurs there. The findings of the phase field model are in good qualitative as well as to a certain degree quantitative agreement with experiments. The different decay behavior of the martensite volume fraction with large depth may be explained by the two-dimensional character of the model. In two dimensions, the decay behavior of stresses from a loaded surface is less pronounced than in three dimensions. A three-dimensional extension of the model is possible, but computationally much more expensive. For an extension of the model the reader is referred to [23]. Figure 14b shows the microstructure in the near-surface region of the metastable austenitic steel AISI 347^{IFP} after cryogenic turning taken by optical and scanning electron microscopy [22, 24–28]. Besides the martensite formation, changes in the grain size of the austenite take place. All this together led to the change in the local stress–strain distribution in the near-surface region and consequently to the differences in the phase transformation. In the following sections of this chapter, the microstructure, metastability, surface morphology, and fatigue behavior of several austenitic stainless steels with different surface morphologies are described.

4 Materials

Five commercial austenitic stainless steels: AISI 303, AISI 316L, AISI 316Ti, AISI 347, and AISI 904L were investigated in different batches, which were named in accordance with the Funding Period (FP) number in CRC 926. The chemical compositions were determined by spectral analysis, see Table 1. All investigated materials were solution-annealed except the AISI 316Ti^{3FP}, which was additionally cold drawn to increase the 0.2% offset yield strength and hardness. The mechanical properties as well as characteristic metastability parameters are summarized in Table 2.

According to the SFE, the investigated materials can be well assigned to the three dominant microstructural mechanisms: martensite formation, twinning, and dislocation slip. However, neither the SFE nor the M_{d30} were able to distinguish the metastabilities among the different batches of AISI 347. From a scientific point of view, usage of the experimentally determined magnetic parameter ΔI_{ξ} is strongly recommended, which not only describes the actual metastability more precisely, but is also easy to be obtained: Based on the different magnetic properties of deformation-induced α' -martensite (ferromagnetic) and initial γ -austenite (paramagnetic), the metastability

Table 1 Chemical composition of the investigated ASSs in wt%

AISI ^{batch}	C	Si	Mn	Cr	Mo	Ni	Ti	N	Cu	Nb
303 ^{3FP}	0.03	0.41	1.95	17.44	0.39	8.32	0.01	0.03	0.39	0.01
316L ^{3FP}	0.02	0.40	1.63	16.68	2.04	10.51	0.01	0.04	0.53	0.06
316Ti ^{3FP}	0.02	0.44	1.74	16.68	2.13	10.60	0.17	0.02	0.45	0.02
347 ^{1FP}	0.02	0.63	1.55	17.29	0.19	9.25	0.02	0.02	0.21	0.41
347 ^{2FP}	0.02	0.59	1.55	17.19	0.23	9.44	0.01	0.02	0.11	0.38
347 ^{3FP}	0.04	0.44	0.85	17.31	0.34	9.14	0.01	0.02	0.29	0.55
904L ^{2FP}	0.03	0.55	0.95	19.92	4.22	24.34	0.02	0.06	1.42	0.03
904L ^{3FP}	0.01	0.38	1.74	19.41	4.14	24.64	0.01	0.03	1.23	0.01

Table 2 Parameters of the metastability, mechanical properties, and hardness

AISI ^{batch}	SFE (mJ/m ²)	M_{d30} (°C)	ΔI_{ξ} (FE%)	$R_{p0.2}$ (MPa)	σ_{UTS} (MPa)	ϵ_f (%)	HV
303 ^{3FP}	19	41	0.7	370	680	38	217
316L ^{3FP}	24	4	0.0	336	584	57	180
316Ti ^{3FP}	24	6	0.3	389	613	48	225
347 ^{1FP}	19	46	1.9	220	621	51	152
347 ^{2FP}	20	46	1.6	225	603	53	151
347 ^{3FP}	20	43	1.7	330	653	49	182
904L ^{2FP}	51	-220	0.0	307	631	46	183
904L ^{3FP}	52	-202	0.0	342	649	43	175

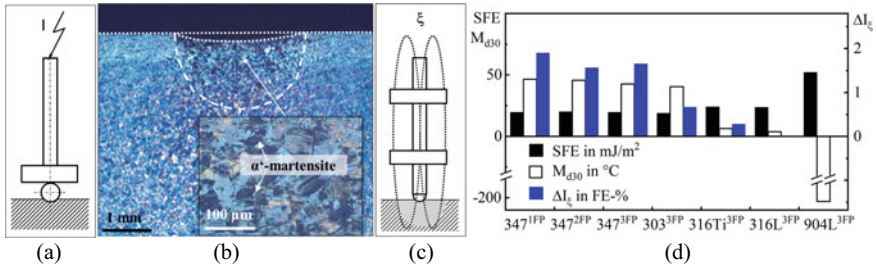


Fig. 15 Plastic deformation after local impact loading shown schematically in (a), optical micrograph with α' -martensite in metastable austenite matrix (b), FeritscopeTM measurements principle (c), and summary of metastability parameters (d)

of ASSs can be evaluated by impact loading followed by magnetic measurements [7]. Thereby, the so-called I_ξ value is measured by a magnetic FeritscopeTM sensor, to obtain the material's susceptibility to α' -martensite formation. Different to the experimental setup in [7], the impact loading in this work was applied by using a “Baumannhammer” with a constant maximum force of 4.75 kN. Besides, due to the possible existence of δ -ferrite in the commercial stainless steel, which is also ferromagnetic, the changes of magnetic value (ΔI_ξ) can represent the increment of deformation-induced α' -martensite. Figure 15d gives an overview of the empirically calculated and experimentally determined metastability parameters of several commercial ASSs: SFE, M_{d30} and ΔI_ξ . The AISI 347 in different batches as well as the AISI 303^{3FP} was supposed to have similar metastabilities according to both empirical calculations, which was experimentally proven to be wrong. Obviously, the experimental parameter ΔI_ξ is more reliable and can be used as a criterion of metastability for ASSs [7].

4.1 Stable ASSs

The stable austenitic stainless steel AISI 904L was investigated as a reference material. With an extremely high nickel content of ~ 24 wt%, the austenitic structure stays stable under plastic deformation at either ambient or cryogenic temperature. The purely austenitic grains can be seen in the micrographs of both AISI 904L^{2FP} and 904L^{3FP} reference samples, see Fig. 16.

4.2 Metastable ASSs

The metastable AISI 347 was investigated in three batches, which have different metastability, see Table 2. Due to the high niobium content, the AISI 347^{1FP} and

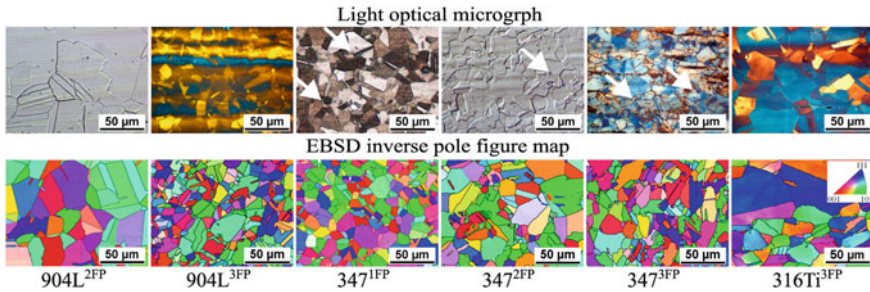


Fig. 16 Microstructure of investigated ASSs

AISI 347^{2FP} consist of an austenitic matrix with niobium carbides (white arrow in Fig. 16) either in linear or locally dotted arrangement. A small number of δ -ferrite strings was observed only in the AISI 347^{3FP}. For the less metastable AISI 316Ti^{3FP}, the addition of titanium led to the formation of titanium carbides. Few δ -ferrite can be seen locally on the micrograph, which was barely detectable by magnetic measurements.

5 Surface Morphology

Aiming at the surface MMP relations of stable and metastable ASSs, different surface morphologies were produced by various manufacturing methods and parameters. Figure 17 summarizes the investigated surface morphologies on the example of AISI 347 (details of the batches are given in the legend of the figure). On the one hand, the research was carried out on round specimens [26, 29], which were turned conventionally and cryogenically. Depending on the turning parameters, the maximum roughness height of the round specimens varied from $1 < S_z < 12 \mu\text{m}$ [25]. To eliminate the influences of surface topography on the fatigue behavior, the turned specimens were mechanically and electrolytically polished and defined as the reference state, see Fig. 17(top). On the other hand, the study was focused on milled flat specimens and their modifications, including Ultrasonic Modification (USM) and Micro-Shot Peening (MSP), respectively, Fig. 17(bottom). An overview of investigated surface morphology characteristics in this work is given in Table 3. Besides the surface texture parameters, the microstructure as well as residual stress states can also be tailored by adjusting the manufacture/modification strategies, which have a significant influence on the performance characteristics of machine elements [24, 26, 29, 30].

To obtain a reference state for the fatigue tests, the respective specimens were first conventionally turned with a cutting speed of $v_c = 30 \text{ mm/min}$, a feed rate of $f = 0.15 \text{ mm/rev}$, and a cutting depth of $a_p = 0.2 \text{ mm}$, and then mechanically and electrolytically polished. With an extremely low surface roughness of $S_z = 1.7 \mu\text{m}$,

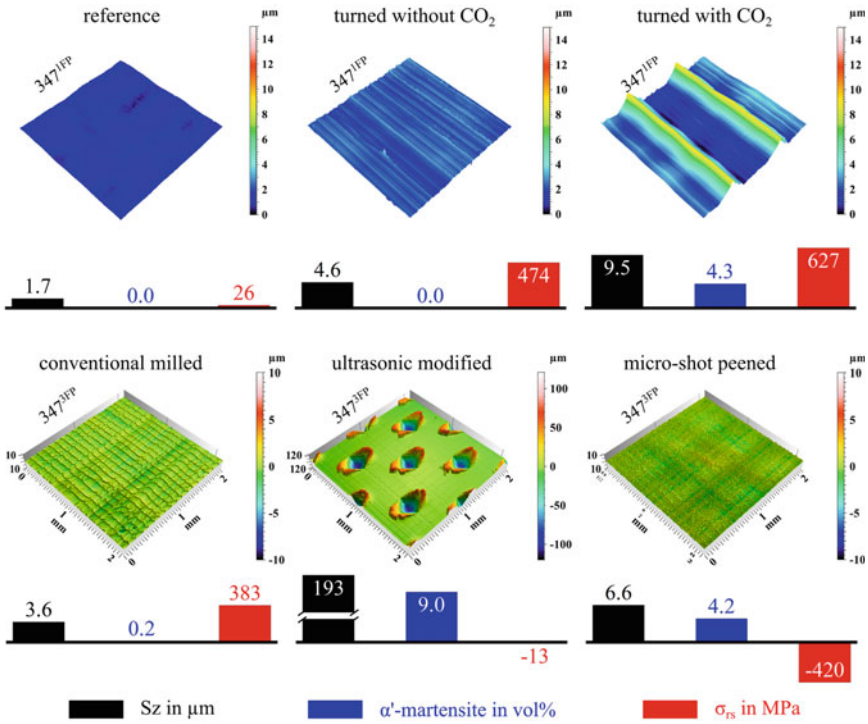


Fig. 17 Exemplary surface morphologies on AISI 347

the reference surface was proven to be martensite-free with neglectable residual stress. Without polishing, the conventionally turned specimen surface had also a low surface roughness of $S_z = 4.6 \mu\text{m}$ and a fully austenitic microstructure, which stays stable due to the high working temperature, that can reach up to 780°C shown for a similar ASS in [31]. A high tensile residual stress of $\sigma_{rs} = 474 \text{ MPa}$ can be determined on the sample surface, due to the high passive force between the cutting edge and turned specimen. The same cutting parameters, but with CO_2 snow cooling—so-called cryogenic turning (see chapter “Creating Surface Morphologies by Cryogenic Machining”)—were used to manufacture the specimen surface with martensitic layer. Additionally, a higher feed rate of $f = 0.35 \text{ mm/rev}$ was used to generate a higher value content of α' -martensite, which also led to a significantly rougher surface with $S_z = 9.5 \mu\text{m}$. Due to the higher thermo-mechanical loadings, a higher tensile residual stress of $\sigma_{rs} = 627 \text{ MPa}$ was induced on the cryogenic turned surface. Moreover, the unique thermo-mechanical conditions during turning led to an unusual phase distribution up to $200 \mu\text{m}$ depth: only 4 vol% of α' -martensite are generated directly in the near-surface regime and a higher volume fraction of 32 vol% was obtained at around $32 \mu\text{m}$ depth [26]. By further optimization to a two-step turning strategy, a higher α' -martensite volume content up to 87 vol% can be achieved

on the sample surface as reported in [32]. For the flat specimens, a two-step down-milling process without CO₂ snow coolant was used to produce a reference state for the further modification using USM and MSP. The cutting depth of the last milling step was kept the same as in the turning process ($a_p = 0.2 \mu\text{m}$) to avoid the DIM from the former milling step on metastable ASSs. With a high cutting speed of $v_c = 94 \text{ m/min}$ and a feed rate $f = 200 \text{ mm/min}$, the milled samples had a low surface roughness of $S_z = 3.6 \mu\text{m}$. Similar like the turned specimen, a high tensile residual stress was detected on the milled surface due to the thermo-mechanical loading. Regarding the low content of δ -ferrite strings in AISI 347^{3FP} as well as the results of quantitative X-ray diffraction (XRD) phase analysis [24, 26, 33], it can be inferred that no DIM was generated on the milled surface due to the unfavorable thermal conditions. Due to the limited hardening possibilities of ASSs, the ultrasonic technologies, such as the Ultrasonic Surface Mechanical Attrition Treatment (SMAT) [34, 35], the Ultrasonic Nanocrystal Surface Modification (UNSM) [36–38], and the Surface Ultrasonic Rolling Processing (SURP) [39], were investigated in the last decades because of their well-known grain refinement effect and favorable residual stress state. With additional surface hardening by DIM, the ultrasonic surface modification has a further potential to improve the fatigue properties of metastable ASSs. On the foreground of this promising work outlined in literature, in the study presented here the following approach for US surface modification was applied: based on the high working frequency of $f = 20 \text{ kHz}$, a short working time of $t = 0.2 \text{ s}$ as well as a low working force of $F \approx 140 \text{ N}$ was chosen to prevent the local overheating. Considering the positive effect of multiaxial loading conditions on the phase transformation [40], the working force was positioned perpendicular to the vibration direction. The profiled surface was generated due to the contour of the ultrasonic sonotrode. The XRD analysis has shown that the tensile stress in the reference surface was strongly reduced by ultrasonic modification. Since the ultrasonic modified surface area was only a small part of the measuring spot of XRD, the deformation-induced α' -martensite can be locally much higher than the average value of 9.4 vol% determinate using the Rietveld analysis [41]. In industrial applications, shot peening is an effective and common post-processing method for metastable ASSs due to a good combination of strain hardening, DIM-transformation, and residual stress state [42]. With a smaller pellet size in the range of 0.02–0.2 mm, the MSP process is able to further improve both surface morphology and fatigue life [38]. For the metastable ASSs, a similar effect was reported for AISI 304 by [43]. Based on the study presented in chapter “Creating Surface Morphologies by Cold Spraying”, MSP was carried out on ASSs with different metastabilities. With a two-step shot peening strategy at $T = 100 \text{ }^\circ\text{C}$, 4.2 vol% of DIM was induced directly on the sample surface. Compared to the USM process, the MSP processed surface showed a lower surface roughness as well as stronger compressive residual stress.

Table 3 Surface morphology characteristics of investigated materials

	AISI 347 ^{1FP} LCF/HCF				AISI 347 ^{2FP} VHCF				
	ASLp	MSLp	MSL _{t015}	MSL _{t035}	ASLp	MSLp	MSL _{t015}	MSL _{t035}	MSL _{dt035}
Sz in μm	1.7	2.0	4.6	9.5	3.0	N/A	12.4	14.2	19.7
α' in vol%	0.0	17.6	17.2	4.3	0.0	26.8	26.3	5.4	23.0
σ_{rs} in MPa	474	439	402	627	-29	-152	396	504	595
	AISI 904L ^{2FP} HCF			AISI 904L ^{2FP} VHCF					
	SSLp	SSL _{t015}	SSL _{t035}	SSLp	SSL _{t015}	SSL _{t035}			
Sz in μm	2.2	9.2	13.5	4.0	10.3	13.6			
α' in vol%	0.0	0.0	0.0	0.0	0.0	0.0			
σ_{rs} in MPa	N/A	N/A	N/A	-13	576	533			
	AISI 347 ^{3FP}			AISI 316Ti ^{3FP}			AISI 904L ^{3FP}		
	ref.	MSP	USM	ref.	MSP	USM	ref.	MSP	USM
Sz in μm	3.6	6.6	193.0	5.5	6.6	149.7	5.1	4.8	199.7
α' in vol%	0.2	4.2	9.4	0.1	0.0	2.1	0.0	0.0	0.0
σ_{rs} in MPa	383	-445	-13	449	-403	114	325	-473	-172

6 Fatigue Behavior

DIM formation at the component surface results in surface hardening [27]. Therefore, the cryogenic turning process (see chapter “Creating Surface Morphologies by Cryogenic Machining”) can increase the fatigue strength of metastable ASSs. The fatigue behavior of ASS specimens with different surface morphology under uniaxial as well as bending tension–compression loading at ambient temperature is described below for low cycle fatigue (LCF), high cycle fatigue (HCF), and very high cycle fatigue (VHCF) regime.

6.1 Tension–Compression Loading

The tension–compression loading was applied on cylindrical specimens with a load ratio $R = -1$ in a servo-hydraulic testing system, and frequencies of $f = 0.01$ Hz and 5 Hz were used for LCF and HCF, respectively. For the VHCF loading, an Ultrasonic Fatigue Testing (USFT) system built up at the authors’ institute was used. The

working frequency in these tests was ~ 20 kHz, which is generated by an ultrasonic generator and transformed in a mechanical oscillation of specimen [29], as shown in Fig. 22a.

6.1.1 LCF Regime

The influence of surface morphology on the cyclic deformation and phase transformation behavior as well as resulting fatigue life of ASSs in the LCF regime can be well visualized by comparing the following two specimens: (i) with a purely Austenitic Surface Layer after polishing (ASL_p) and (ii) with Martensitic Surface Layer after polishing (MSL_p), fatigued at the same total strain amplitude of $\epsilon_{a,t} = 1.0\%$.

Figure 18 shows the development of stress amplitude σ_a and α' -martensite content versus the number of cycles. Since the α' -martensite is ferromagnetic, its formation during fatigue was measured in situ using a magnetic-based Feritscope™ device and plotted as ξ -value in the original sensor measurement unit, i.e., in FE-% [7]. The cyclic deformation behavior of both specimens is characterized by significant cyclic hardening, which leads to a stress level even higher than the $\sigma_{UTS} = 621$ MPa of the investigated material in the solution-annealed state. Due to the initial α' -martensite fraction in the surface layer of the MSL_p specimen, the stress amplitude in the first cycle is about 10% higher than the stress amplitude of the ASL_p specimen. Besides the above-mentioned mechanical data (σ_a) as well as magnetic data (ξ), which characterize the microstructural changes in the bulk material, the change of the electrical resistance (ΔR) and temperature (ΔT) were also measured (Fig. 18b). In both specimens, the deformation-induced changes in specimen temperature were very small, i.e., below 1 K, which had no influence of the deformation-induced α' -martensite formation during the fatigue tests. Furthermore, the ΔR - N -curves showed

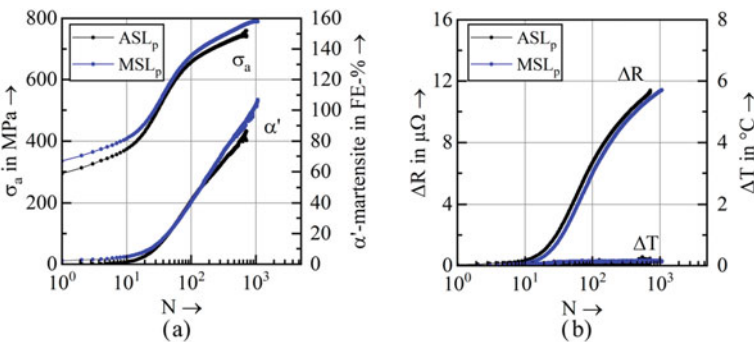


Fig. 18 Development of stress amplitude and fatigue-induced α' -martensite (a) as well as the change in electrical resistance (ΔR) and in the specimen temperature (ΔT) (b) during single step tests, $\epsilon_{a,t} = 1.0\%$, $R = -1$, $f = 0.01$ Hz, AISI 347^{IFP}

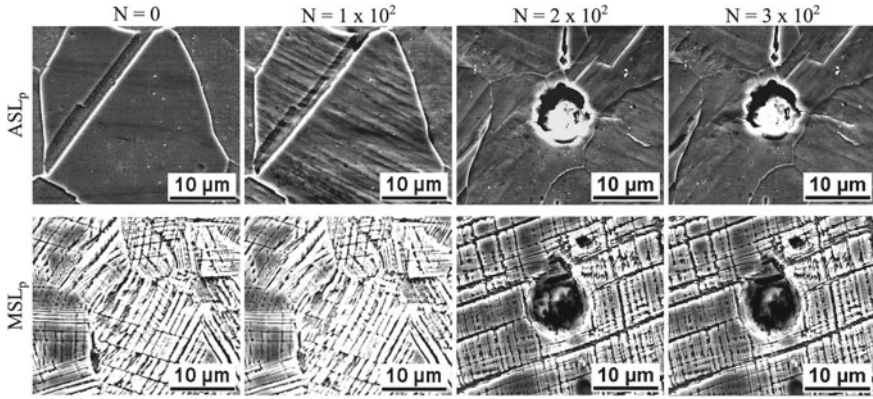


Fig. 19 Development of fatigue-induced surface reliefs in the austenitic surface layer ASL_p and in the martensitic surface layer MSL_p , $\varepsilon_{a,t} = 1.0\%$, $R = -1$, $f = 0.01$ Hz, AISI 347^{1FP}

a similar trend as the σ_a - N -curves for both specimens. The change in electrical resistance correlates with the increase in dislocation density, phase transformation as well as the crack initiation and propagation. Failure of the ASL_p specimen occurred at $N = 718$, while the MSL_p specimen achieved a higher $N = 1071$.

To illustrate the influences of surface morphology on the fatigue-induced surface relief, Scanning Electron Microscopy (SEM) investigations of the initial state ($N = 0$) as well as at defined fatigue states ($N = 1 \times 10^2$, 2×10^2 , 3×10^2) were carried out (cf. Fig. 19). The specimen surface was etched with V2A-etchant to visualize the microstructure. The difference in the surface morphology of ASL_p and MSL_p specimens is clearly visible. Note that besides the martensite induced by cryogenic turning, a considerable amount of austenite exists in the surface of the MSL_p specimen (see Fig. 19). A cyclic loading up to 1×10^2 cycles initiated a higher number of slip bands at the surface of the ASL_p specimens. At the same number of cycles, no change was observed in the surface topography of MSL_p specimen. Further loading until $N = 2 \times 10^2$ led to crack initiation in the ASL_p specimen due to the local stress concentration at a niobium carbide. A similar microstructural notch caused no crack initiation in the MSL_p specimen, when it is embedded in a martensitic area. Further cyclic loading up to $N = 3 \times 10^2$ led to the micro-crack propagation in ASL_p . At this number of cycles, no changes in MSL_p were observed. Generally, crack initiation in both specimens took place only in the areas of austenitic phase. For MSL_p , it was more pronounced at the niobium carbides and along slip bands [28]. In summary, the morphology MSL_p has a positive influence on the fatigue life even at very high load amplitudes in the LCF regime. However, due to pronounced cyclic hardening caused by the martensite formation in the specimen volume for both ASL_p and MSL_p specimens, the fatigue life is strongly determined by this effect, especially in total strain-controlled tests [24]. A positive influence of martensite formation on fatigue life can be especially observed in stress-controlled fatigue tests

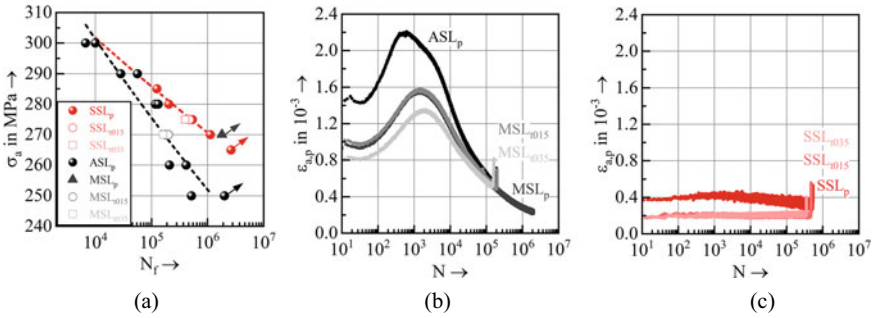


Fig. 20 S-N curves of AISI 347^{1FP} and AISI 904L^{2FP} in reference state with fatigue life of specimen with different morphologies (a), cyclic deformation curves of AISI 347^{1FP} (b), and AISI 904L^{2FP} (c)

where austenite–martensite transformation causes cyclic hardening, which reduces the plastic strain amplitude by a factor of 2 or even more [24].

6.1.2 HCF Regime

Because of the strong influence of surface morphology on the fatigue behavior, especially in the HCF regime, its influence on the cyclic deformation behavior and fatigue life of the investigated metastable austenitic steel AISI 347^{1FP} and stable AISI 904L^{2FP} with different surface morphologies was investigated in detail. The surface morphologies produced by conventional turning and subsequent polishing were named SSL_p (stable surface layer polished) for AISI 904L^{2FP} and ASL_p (austenitic surface layer polished) for AISI 347^{1FP}. To vary the surface morphologies of AISI 347^{2FP} generated by cryogenic turning, two different feed rates, i.e., $f = 0.15$ mm/rev and $f = 0.35$ mm/rev were selected to produce the fatigue specimens with Martensitic Surface Layer after turning (MSL_t) using a CO₂ snow-cooling system with a constant cutting speed of $v_c = 30$ m/min and a depth of cut $a_p = 0.2$ mm. Furthermore, specimens of the type MSL_{t015} were additionally polished mechanically and electrolytically (MSL_p) to eliminate the turning-induced surface roughness. During polishing a layer with about 25–35 μm thickness was removed. The diameter of each specimen was thus carefully measured using an optical system with a resolution of 1 μm before the fatigue tests. The same manufacturing parameters were used for AISI 904L^{2FP} and two surface morphologies called Stable Surface Layer turned (SSL_t) were produced. In summary, seven morphologies were investigated in the HCF regime, which are indicated in the diagram’s legend as: ASL_p, MSL_p, MSL_{t015}, MSL_{t035}, SSL_p, SSL_{t015}, SSL_{t035}.

Figure 20 shows the fatigue life (S-N) curves of fully austenitic specimens with polished surface for both materials in the reference state (SSL_p, ASL_p). At the beginning of the tests, these specimens had a purely austenitic microstructure in

the volume as well as in the near-surface area with a smooth surface in the gauge length. In general, the reference specimens of the batch AISI 904L^{2FP} have a higher fatigue strength than AISI 347^{1FP}, which is related to their higher monotonic strength, see Table 2. However, due to the surface modification by cryogenic turning, the AISI 347^{1FP} with MSL_p morphology can be cyclically loaded with a stress amplitude of 270 MPa without failure, at which the SSL_p sample already failed at 10⁶ cycles. This phenomenon can be explained by the influence of the surface morphology: The cyclic deformation behavior of metastable AISI 347^{1FP} is characterized by initial cyclic softening followed by pronounced cyclic hardening (Fig. 20b), while the stable AISI 904L^{2FP} shows a neutral cyclic deformation behavior (Fig. 20c). Hence, due to the near-surface microstructure, which consists of γ -austenite, α' -martensite, and ε -martensite as well as nanocrystalline layers, the specimens with MSL morphologies show a significantly smaller plastic strain amplitude ($\varepsilon_{a,p}$) than the ASL_p, which only consists of γ -austenite [24]. Consequently, the higher $\varepsilon_{a,p}$ in ASL_p indicates a higher and more pronounced development of slip bands (see Fig. 19), which finally led to micro-crack initiation, propagation, and failure. The smaller $\varepsilon_{a,p}$ in specimen with MSL morphology suppressed the slip band formation and extended the fatigue life to the region where the α' -martensite formation in the specimen volume is more pronounced and leads to a significant reduction of plastic strain amplitude. Note in this context that the turned specimen had a higher surface roughness than the polished ones.

Figure 21 shows the number of cycles to failure as a function of maximum roughness height (Sz). As expected, the polished specimen variants MSL_p and martensite-free ASL_p have a similar surface quality (Sz < 3 μm), while considerable roughness was seen in the turned specimens. Based on this fact, the benefit of the martensitic surface layer on fatigue properties can be clearly seen: The MSL_p specimen achieved the ultimate number of cycles $N_u = 2 \times 10^6$ without failure while the ASL_p specimen with a similar surface roughness (Fig. 21a), but turned without CO₂ snow cooling, i.e., with purely austenitic microstructure, failed at $N = 2 \times 10^5$ under the same loading conditions. Furthermore, an increase in Sz by a factor of 5 for the MSL_t compared to

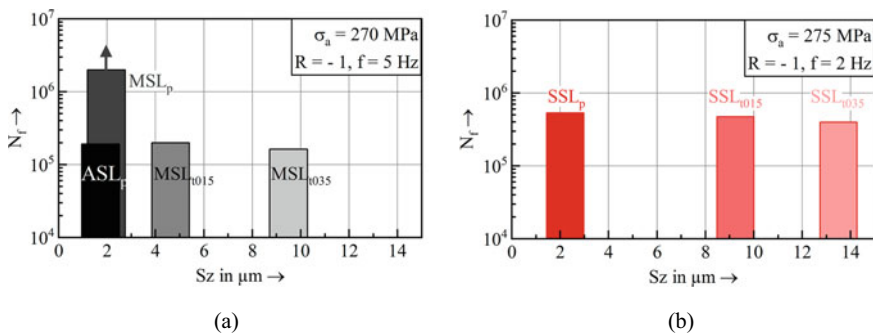


Fig. 21 Number of cycles to failure versus roughness of specimens with different surface morphologies of AISI 347^{1FP} (a), and AISI 904L^{2FP} (b)

the ASL_p specimen had no significant influence on the fatigue life, since both specimens achieved $N_f \approx 10^5$. Therefore, the negative influence of the surface roughness on fatigue life can be compensated by the martensitic surface layers. It must be mentioned here that the polished surface is practically barely used in technical applications, due to the high production time and costs. The compensation of the negative influence of the surface roughness by cryogenic turning-induced martensitic surface layers hence offers new perspectives to improve the fatigue life of metastable ASSs. Considering that no martensite formation occurred during both cryogenic turning and cyclic loading in the stable AISI 904L^{2FP}, the higher surface roughness after turning reduced the fatigue life of the stable ASSs (Fig. 21b).

6.1.3 VHCF Regime

Investigations of ASSs up to the VHCF regime showed different fatigue behavior depending on their degrees of metastability [33]. In the stable ASSs, no classical fatigue limits up to a load cycle of $N = 10^7$ existed. Crack initiation occurred at the surface in all specimens. For metastable ASSs, a true fatigue limit was detected which is associated with α' -martensite formation, i.e., specimen failure of AISI 304L only occurs below $N = 1 \times 10^6$ load cycles [44]. Since specimen failure in the VHCF regime of ASSs only occurred in case of the stable austenite, and crack initiation occurred mostly on the surface, the surface modification seems to be one possibility to increase the fatigue strength, even in the VHCF regime. Note that due to the highly transient material behavior of metastable ASSs, ultrasonic fatigue testing of this materials class is very challenging. Even a slight increase of the α' -martensitic phase leads to a pronounced change in the displacement amplitude as well as the pulse shape (Fig. 22b).

Figure 22b shows representative pulses with a constant pulse time of 60 ms for three different fatigue states: at the beginning of the test where a fully austenitic

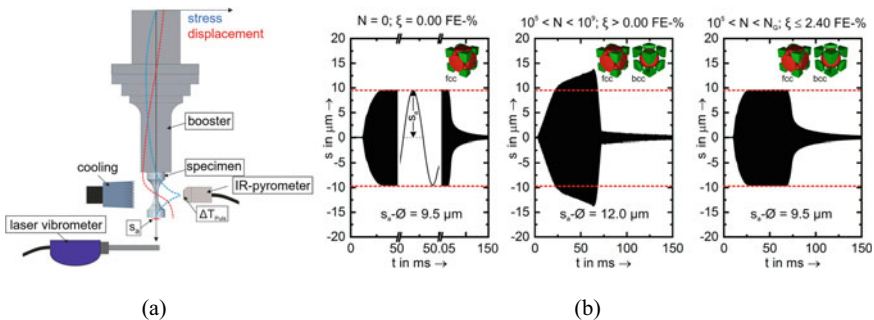


Fig. 22 Schematic view of the operating principle of the ultrasonic fatigue testing (a), and the change in load pulse as well as after adjustments of the control parameters (b) of metastable ASSs [45]

microstructure was present, at $N = 10^7$ cycles where the specimen had a mixed austenitic/ α' -martensitic microstructure without adjusting the control parameters and at the same cycle number but after successive adjustments of the control parameters. In the first case, i.e., for a fully austenitic sample, the desired amplitude was reached within a few ms, remained constant during the stationary phase of the pulse, and dropped rapidly at the end of the pulse. Within the pulse sequence, perfectly sinusoidal vibrations can be seen in the changed scale of the time axis. In the stationary phase of this pulse, a constant displacement amplitude of $9.5 \mu\text{m}$ was achieved. In contrast, the second exemplarily shown pulse showed a change in shape due to deformation-induced α' -martensite formation during cyclic loading which resulted in a considerable variation of the oscillation amplitude in the stationary load period. Consequently, a constant amplitude fatigue test was not possible in this manner. After adjusting the proportional and integral parameters of the load unit's control circuit, a nearly ideal pulse shape with constant displacement amplitude was recovered, even if further deformation-induced phase transformation occurred. Consequently, to perform VHCF tests on the metastable austenite from $N = 0$ up to the ultimate number of cycles, e.g., $N_u = 2 \times 10^9$ in the USFT system, a continuous adjustment of the control parameters must be performed. Further details on this issue are given in [45].

The influence of the metastability on the VHCF behavior can be clearly seen by comparison of the S-N curves of both ASSs (Fig. 23a). The stable AISI 904L^{2FP} specimens with the morphology SSL_p failed both in the HCF and in the VHCF regimes. With decreasing stress amplitude, the number of cycles to failure increased until the ultimate number of cycles is reached. Hence, no classical fatigue limit exists. A similar fatigue behavior was also observed by Carstensen *et al.* in fatigue tests at thin tubular specimens from AISI 904L [46]. At a stress amplitude of $\sigma_a = 306 \text{ MPa}$, the tested sample with morphology SSL_p reached the ultimate number of cycles without failure. All cryogenically turned specimens exhibited earlier failures than the spec-

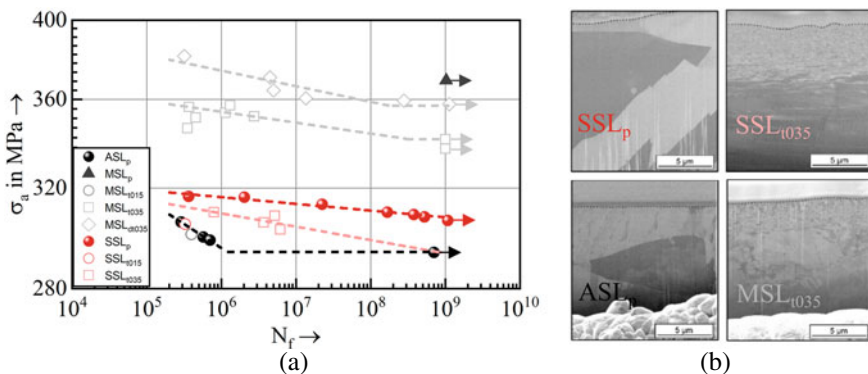


Fig. 23 S-N curves up to VHCF regime of specimens with different surface morphologies and volume fraction of α' -martensite (a), and near-surface microstructure of stable and metastable ASSs in reference state and after cryogenic turning (b) [33]

imens with morphology SSL_p at the same stress amplitude, where the sample with the SSL_{r015} morphology had the lowest lifetime. Specimen failure occurred only at the specimen surfaces due to the high roughness of $Sz = 9.2 \mu\text{m}$ (SSL_{r015}) and $Sz = 14.0 \mu\text{m}$ (SSL_{r035}). The influence of the surface roughness and the high tensile residual stresses seems to be predominant compared to the positive influence from the nanocrystalline structure (Fig. 23b), which in general reduces the plastic deformation in the specimen [24]. Accordingly, no increase in fatigue life was achieved by cryogenic turning of stable ASS. The FeritscopeTM measurements confirmed that no phase transformation occurred during these fatigue tests. Fractographic investigations of the failed specimens with SSL_p showed that for $N_f > 1 \times 10^8$ the crack initiation changes from the surface to the volume [29]. Opposed to that, the metastable AISI 347^{2FP} specimens with purely austenitic microstructure in the initial state and with different surface morphologies only failed in the HCF regime at $N < 10^7$. In the VHCF regime no specimen failure occurred, which shows that a true fatigue limit exists for this metastable austenite. During cyclic loading, the metastable AISI 347^{2FP} partially transformed from paramagnetic γ -austenite to ferromagnetic α' -martensite, which was confirmed by FeritscopeTM measurements. Hence, the surface morphology influences the fatigue behavior of metastable AISI 347^{2FP} in completely different manner compared to the stable AISI 904L^{2FP}. The specimens with morphology MSL_{r035} , which exhibited nanocrystalline and martensitic layers showed a higher fatigue strength, despite many disadvantageous factors, e.g., higher roughness values and tensile residual stresses, than the conventionally turned and polished specimens with the ASL_p morphology, which had lower roughness and compressive residual stresses. The fatigue strength of these specimens increased after cryogenic turning by about 50 MPa. The scatter of MSL_{r035} specimens failed in the HCF regime was higher than that of the ASL_p variant, which is caused by irregularities such as chip formation and chip breaking in cryogenic turning. The results showed that the martensitic surface layer in combination with the nanocrystalline structure had a very positive effect on the fatigue behavior in VHCF regime, whereas only the nanocrystalline structure did not lead to a higher fatigue life as shown for the stable AISI 904L^{2FP}. Additionally, pre-deformed AISI 347^{2FP} specimens that were finally cryogenic turned with $f = 0.35 \text{ mm/rev}$ (MSL_{dr035}) were investigated. The pre-deformation was performed to generate a specimen condition with a high content of α' -martensite in the volume. For this, the austenitic samples were pre-cooled in liquid nitrogen and finally pre-deformed by a tensile test to achieve 40 vol% α' -martensite. Generally, an increase in fatigue strength was achieved, however, failure of the specimen in the VHCF regime took place and a drop in the S-N diagram exists. Such behavior could also be observed in a metastable austenite with an α' -martensite content of 54 vol% achieved by pre-deformation and polished after conventional turning [29]. The best fatigue properties were achieved for specimens with surfaces polished after cryogenic turning of metastable AISI 347^{2FP}, which results from the low roughness, the martensitic surface layer, and the compressive residual stresses on the specimen surface [33].

6.2 Bending Fatigue

Besides the uniaxial tension–compression loading (cf. Sect. 6.1), the influence of surface morphology on the fatigue life was investigated under four-point bending condition, whereby the maximal stresses exist on the specimen surface. Single step tests at stress amplitude $\sigma_a = 405$ MPa with load ratio $R = 0.1$ and load frequency $f = 10$ Hz were performed with specimens taken from three ASSs with different metastabilities, i.e., two metastable AISI 347^{3FP} and AISI 316Ti^{3FP} and one stable AISI 904L^{3FP} (see Table 1) with three different surface morphologies: (i) reference after milling and (ii) after micro-shot peening and ultrasonic modification (cf. Fig. 17). In all cases, the maximum temperature on the sample surface was lower than 30 °C during these tests. Hence, an influence of the specimen temperature on the fatigue behavior can be excluded.

The three ASSs show different fatigue life in the reference state. The highest number of cycles to failure (N_f) was achieved by AISI 904L^{3FP} ($N_f = 4.2 \times 10^5$), followed by AISI 316Ti^{3FP} ($N_f = 2.3 \times 10^5$) and AISI 347^{3FP} ($N_f = 1.4 \times 10^5$). After MSP, similar changes in surface roughness and residual stress were confirmed for all three investigated materials, see Table 3. However, the fatigue life of metastable 347^{3FP} was improved by 54%, while a decrease of 6% and 45% was determined for the less metastable 316Ti^{3FP} and stable 904L^{3FP}, respectively. Similar to the fatigue behavior of cryogenic turned specimens (cf. Sect. 6.1), this significant difference can be well explained by X-ray phase analysis, since the DIM can only be detected in metastable 347^{3FP} after MSP. Obviously, the negative influence of the high surface roughness of $S_z = 6.6$ μm was compensated by the DIM. For the USM, due to the advantageous loading conditions, a higher DIM content was successfully achieved on both metastable ASSs: AISI 347^{3FP} and AISI 316Ti^{3FP}. However, the fatigue life was strongly reduced (around 90%) by the geometric notches since the coupling surface contour of the applied sonotrode, which consists of small pyramid units with a height of 0.4 mm, led to a surface containing evenly distributed imprints with a maximum depth of 120 μm . During the fatigue tests, these imprints caused local stress

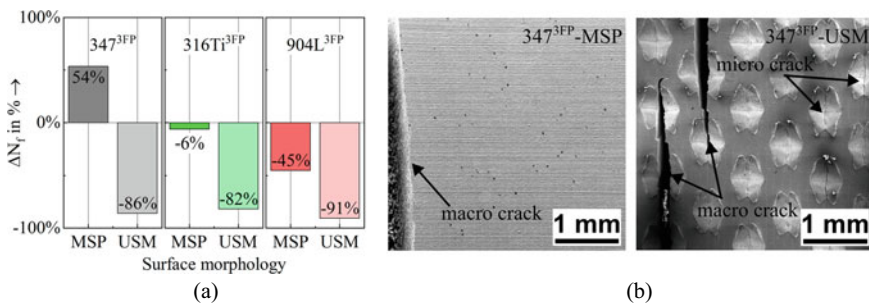


Fig. 24 Influence on the fatigue life after surface modification in investigated ASSs (a), and SEM image of fatigue cracks in AISI 347 after surface modifications (b)

concentration, which led to crack initiation and failure (Fig. 24b). Hence, further research should aim at a compromise between the profile height of the sonotrode surface necessary for sufficient ultrasonic power transmission into the sample surface and minimum notch effect.

7 Summary

As a unique material property of austenitic stainless steels, the metastability was proven to have a strong influence on the surface morphology and consequently fatigue behavior. On an atomistic scale, the austenite–martensite phase transformation behavior was studied using the Meyer–Entel potential available for iron. The influence of temperature and strain–stress state on the phase transformation during nanoindentation tests was studied by molecular dynamics simulation. Furthermore, thermophysical data of the interface structure and energetics were provided, which can be used as input parameters for the microscopic models in phase field simulation. The phase field modeling of martensitic transformations was achieved using the Allen–Cahn-type model. In order to take the plastic effects into account, the phase field model was coupled with a crystal plasticity model. To reduce the numerical effort, only one phase field variable for austenite and the two martensitic orientation variants are considered. That model was used to explain the depth distribution of martensite during cryogenic turning. A comprehensive manufacturing–morphology–property relationship study in several commercial austenitic stainless steels with surface morphologies generated by different manufacturing processes, e.g., cryogenic turning, micro-shot peening, and ultrasonic surface modification, was presented in this chapter. The surface hardening due to deformation-induced martensite formation in metastable austenitic stainless steels was able to improve the fatigue life in the whole fatigue regime from low cycle fatigue regime to very high cycle fatigue regime. The positive effect of the deformation-induced martensite provides new perspectives for the mechanical processing and application of metastable austenite.

References

1. Deutsche Institut für Normung e.V (2005) Nichtrostende Stähle - Teil 1: Verzeichnis der nichtrostenden Stähle; Deutsche Fassung EN 10088-1:2005. Berlin
2. McGuire MF (2008) Stainless steels for design engineers. ASM International, Materials Park, Ohio
3. Brooks JA, Thompson AW (1991) Microstructural development and solidification cracking susceptibility of austenitic stainless steel welds. *Int Mater Rev* 36(1):16–44. ISSN: 0950-6608
4. Lu J, Hultman L, Holmström E, Antonsson KH, Grehk M, Li W, Vitos L, Golpayegani A (2016) Stacking fault energies in austenitic stainless steels. *Acta Mater* 111:39–46. ISSN: 13596454. <https://doi.org/10.1016/j.actamat.2016.03.042>

5. Meric de Bellefon G, van Duysen JC, Sridharan K (2017) Compositiondependence of stacking fault energy in austenitic stainless steels through linear regression with random intercepts. *J Nucl Mater* 492:227–230. ISSN: 00223115. <https://doi.org/10.1016/j.jnucmat.2017.05.037>
6. Angel T (1954) Formation of martensite in austenitic stainless steels. *J Iron Steel Inst* 177:165–174
7. Smaga M, Boemke A, Daniel T, Klein MW (2018) Metastability and fatigue behavior of austenitic stainless steels. *MATEC Web Conf* 165:04010. <https://doi.org/10.1051/mateconf/201816504010>
8. Meyer R, Entel P (1998) Martensite-austenite transition and phonon dispersion curves of $\text{Fe}_{1-x}\text{Ni}_x$ studied by molecular-dynamics simulations. *Phys Rev B* 57:5140. <https://doi.org/10.1103/PhysRevB.57.5140>
9. Meiser J, Urbassek HM (2020) $\alpha \leftrightarrow \gamma$ phase transformation in iron: comparative study of the influence of the interatomic interaction potential. *Modell Simul Mater Sci Eng* 28:055011. <https://doi.org/10.1088/1361-651x/ab8f21>
10. Sandoval L, Urbassek HM, Entel P (2009) The Bain versus Nishiyama-Wassermaann path in the martensitic transformation of Fe. *New J Phys* 11:103027. <https://doi.org/10.1088/1367-2630/11/10/103027>
11. Maresca F, Curtin WA (2017) The austenite/lath martensite interface in steels: structure, athermal motion, and in-situ transformation strain revealed by simulation and theory. *Acta Mat* 134:302–323. <https://doi.org/10.1016/j.actamat.2017.05.044>
12. Wang B, Urbassek HM (2013) Phase transitions in an Fe system containing a bcc/fcc phase boundary: an atomistic study. *Phys Rev B* 87:104108. <https://doi.org/10.1103/PhysRevB.87.104108>
13. Meiser J, Urbassek HM (2018) Influence of the crystal surface on the austenitic and martensitic phase transition in pure iron. *Crystals* 8(12):469. <https://doi.org/10.3390/cryst8120469>
14. Meiser J, Urbassek HM (2019) Influence of grain boundaries on the austenitic and martensitic phase transitions in iron. *Eur Phys J B* 92:47. <https://doi.org/10.1140/epjb/e2019-90576-1>
15. Meiser J, Urbassek HM (2019) Dislocations help initiate the u-w phase transformation in iron—an atomistic study. *Metals* 9:90. <https://doi.org/10.3390/met9010090>
16. Meiser J, Alabd Alhafez I, Beck T, Smaga M, Müller R, Urbassek HM (2019) Nanoindentation into a metastable austenite triggers a martensitic phase transformation—An atomistic study. *AIP Adv* 9(1): 015228. <https://doi.org/10.1063/1.5081496>
17. Schmitt R, Müller R, Kuhn C, Urbassek HM (2013) A phase field approach for multivariant martensitic transformations of stable and metastable phases. *Arch Appl Mech* 83(6):849–859. <https://doi.org/10.1007/s00419-012-0721-6>
18. Schmidt S, Dornisch W, Müller R (2017) A phase field model for martensitic transformation coupled with the heat equation. *GAMM-Mitteilungen* 40(2):138–153. <https://doi.org/10.1002/gamm.201720005>
19. Schmidt S, Plate C, Müller R, Müller R, Meiser J, Urbassek HM (2016) A phase field model for martensitic transformations with a temperaturedependent separation potential. *PAMM* 16(1):481–482. <https://doi.org/10.1002/pamm.201610229>
20. Schmitt R, Kuhn C, Müller R (2017) On a phase field approach for martensitic transformations in a crystal plastic material at a loaded surface. *Contin Mech Thermodyn* 29(4):957–968. <https://doi.org/10.1007/s00161-015-0446-1>
21. Schmitt R, Kuhn C, Müller R, Bhattacharya K (2014) Crystal plasticity and martensitic transformations: a phase field approach. *Technische Mechanik-Eur J Eng Mech* 34(1):23–38. <https://doi.org/10.24352/UB.OVGU-2017-051>
22. Aurich JC, Mayer P, Kirsch B, Eifler D, Smaga M, Skorupski R (2014) Characterization of deformation induced surface hardening during cryogenic turning of AISI 347. *CIRP Ann* 63(1):65–68. ISSN: 0007-8506. <https://doi.org/10.1016/j.cirp.2014.03.079>
23. Graf M, Kuntz M, Autenrieth H, Diewald F, Müller R (2021) Simulation of martensitic microstructures in a low-alloy steel. *Arch Appl Mech* 91(4):1641–1668. <https://doi.org/10.1007/s00419-020-01845-6>

24. Smaga M, Skorupski R, Eifler D, Beck T (2017) Microstructural characterization of cyclic deformation behavior of metastable austenitic stainless steel AISI 347 with different surface morphology. *J Mater Res* 32(23):4452–4460. ISSN: 0884-2914. <https://doi.org/10.1557/jmr.2017.318>
25. Hotz H, Kirsch B, Mayer P, Becker S, von Harbou E, Boemke A, Skorupski R, Smaga M, Müller R, Beck T, Aurich CJ (2017) Surface integrity of cryogenic turned austenitic stainless steels AISI 347 and AISI 904L. In: *Production at the leading edge of technology - proceedings of the 7th congress of the German Academic Association for Production Technology (WGP)*, pp 473–480
26. Smaga M, Skorupski R, Mayer P, Kirsch B, Aurich JC, Raid I, Seewig J, Man J, Eifler D, Beck T (2017) Influence of surface morphology on fatigue behavior of metastable austenitic stainless steel AISI 347 at ambient temperature and 300°C. *Procedia Struct Integr* 5:989–996. <https://doi.org/10.1016/j.prostr.2017.07.150>
27. Mayer P, Kirsch B, Müller C, Hotz H, Müller R, Becker S, von Harbou E, Skorupski R, Boemke A, Smaga M, Eifler D, Beck T, Aurich JC (2018) Deformation induced hardening when cryogenic turning. *CIRP J Manuf Sci Technol* 23:6–19. ISSN: 17555817. <https://doi.org/10.1016/j.cirpj.2018.10.003>
28. Skorupski R, Smaga M, Eifler D (2014) Influence of surface morphology on the fatigue behavior of metastable austenitic steel. *Adv. Mater. Res.* 891–892:464–469. <https://doi.org/10.4028/www.scientific.net/AMR.891-892.464>
29. Boemke A, Smaga M, Beck T (2018) Influence of surface morphology on the very high cycle fatigue behavior of metastable and stable austenitic Cr-Ni steels. *MATEC Web Conf* 165:20008. <https://doi.org/10.1051/mateconf/201816520008>
30. Frölich D, Magyar B, Sauer B, Mayer P, Kirsch B, Aurich JC, Skorupski R, Smaga M, Beck T, Eifler D (2015) Investigation of wear resistance of dry and cryogenic turned metastable austenitic steel shafts and dry turned and ground carburized steel shafts in the radial shaft seal ring system. *Wear* 328–329:123–131. <https://doi.org/10.1016/j.wear.2015.02.004>
31. Kaladhar M, Subbaiah KV, Rao CS (2012) Machining of austenitic stainless steels - a review. *Inter J Mach Mach Mater* 12(1/2):178. ISSN: 1748-5711. <https://doi.org/10.1504/IJMMM.2012.048564>
32. Hotz H, Glatt M, Kirsch B, Aurich JC (2020) Quality protection of technical products - unique identification with a hidden fingerprint in smart materials. *Mater Lett: X* 8:100056. ISSN: 25901508. <https://doi.org/10.1016/j.mlblux.2020.100056>
33. Smaga M, Boemke A, Eifler D, Beck T (2022) Very high cycle fatigue behavior of austenitic stainless steels with different surface morphologies. *Metals* 12(11):1877. <https://doi.org/10.3390/met12111877>
34. Dureau C, Novelli M, Arzaghi M, Massion R, Bocher P, Nadot Y, Grosdidier T (2020) On the influence of ultrasonic surface mechanical attrition treatment (SMAT) on the fatigue behavior of the 304L austenitic stainless steel. *Metals* 10(1):100. <https://doi.org/10.3390/met10010100>
35. Liu W, Jin X, Zhang B, Yun D, Chen P (2019) A Coupled EBSD/TEM analysis of the microstructure evolution of a gradient nanostructured ferritic/martensitic steel subjected to surface mechanical attrition treatment. *Materials (Basel, Switzerland)* 12(1). <https://doi.org/10.3390/ma12010140>
36. Yasuoka M, Wang P, Zhang K, Qiu Z, Kusaka K, Pyoun Y-S, Murakami R-I (2013) Improvement of the fatigue strength of SUS304 austenite stainless steel using ultrasonic nanocrystal surface modification. *Surf Coat Technol* 218:93–98. <https://doi.org/10.1016/j.surfcoat.2012.12.033>
37. Ye C, Telang A, Gill AS, Suslov S, Idell Y, Zwiack K, Wiezorek JM, Zhou Z, Qian D, Mannava SR, Vasudevan VK (2014) Gradient nanostructure and residual stresses induced by ultrasonic nano-crystal surface modification in 304 austenitic stainless steel for high strength and high ductility. *Mater Sci Eng A* 613:274–288. <https://doi.org/10.1016/j.msea.2014.06.114>
38. Zhang KY, Pyoun YS, Cao XJ, Wu B, Murakami R (2012) Fatigue properties of SUS304 stainless steel after ultrasonic nanocrystal surface modification (UNSM). *Int J Modern Phys: Conf Ser* 06:330–335. <https://doi.org/10.1142/S201019451200339X>

39. Zhang F, Shangguan X (2017) Effect of surface ultrasonic rolling processing on fatigue properties of AISI304 austenite stainless steel. *Hot Work Technol* 46:136–140
40. Polatidis E, Šmíd M, Hsu W-N, Kubenova M, Capek J, Panzner T, van Swygenhoven H (2019) The interplay between deformation mechanisms in austenitic 304 steel during uniaxial and equibiaxial loading. *Mater Sci Eng: A* 764:138222. <https://doi.org/10.1016/j.msea.2019.138222>
41. Young RA (1993) The rietveld method. International Union of Crystallography
42. Hotz H, Kirsch B (2020) Influence of tool properties on thermomechanical load and surface morphology when cryogenically turning metastable austenitic steel AISI 347. *J Manuf Proc* 52:120–131. ISSN: 15266125. <https://doi.org/10.1016/j.jmapro.2020.01.043>
43. Chung Y-H, Chen T-C, Lee H-B, Tsay L-W (2021) Effect of micro-shot peening on the fatigue performance of AISI 304 Stainless Steel. *Metals* 11(9):1408. <https://doi.org/10.3390/met11091408>
44. Müller-Bollenhagen C, Zimmermann M, Christ H-J (2010) Very high cycle fatigue behaviour of austenitic stainless steel and the effect of strain-induced martensite. *Int J Fatigue* 32(6):936–942. ISSN: 01421123. <https://doi.org/10.1016/j.ijfatigue.2009.05.007>
45. Daniel T, Smaga M, Beck T (2022) Cyclic deformation behavior of metastable austenitic stainless steel AISI 347 in the VHCF regime at ambient temperature and 300°C. *Int J Fatigue* 156:106632. <https://doi.org/10.1016/j.ijfatigue.2021.106632>
46. Carstensen JV, Mayer H, Brøndsted P (2002) Very high cycle regime fatigue of thin walled tubes made from austenitic stainless steel. *Fatigue & Fract Eng Mater & Struct* 25(8–9):837–844

Influence of Surface Morphology on Fatigue and Tribological Behavior of TRIP/TWIP Steels



Marek Smaga, Tilmann Beck, Michael Kopnarski, Rolf Merz,
Kristin M. de Payrebrune, and Stefan Wolke

Abstract Opposite to widely used austenitic stainless steels (see Chapter “Influence of Manufacturing and Load Conditions on the Phase Transformation and Fatigue of Austenitic Stainless Steels”), high manganese Transformation Induced Plasticity (TRIP)/Twinning Induced Plasticity (TWIP) steels are not corrosion resistant. However, these steels undergo intensive research work, because of their unique combination of high strength and high ductility. First fully austenitic TWIP steels are already industrially available. Parallel to research presented elsewhere on TRIP/TWIP steels as a bulk material, the surface morphology on the micro scale was investigated in this work. The possibility to manufacture different surface morphologies as well as the change in the topography, microstructure, and mechanical properties of near-surface regions up to 10 μm depth after conventional milling, micro milling as well as lapping was investigated in detail. Based on that, the influence of different surface morphologies on the cyclic deformation behavior and fatigue life in LCF, HCF, and VHCF regime as well as tribological properties of austenitic TRIP/TWIP steels are analyzed.

1 Introduction

High manganese Transformation Induced Plasticity (TRIP)/Twinning Induced Plasticity (TWIP) steels belong to the 2nd generation of Advanced High Strength

M. Smaga (✉) · T. Beck (✉) · S. Wolke
Institute of Materials Science and Engineering, RPTU Kaiserslautern, Kaiserslautern, Germany
e-mail: m.smaga@mv.rptu.de

T. Beck
e-mail: t.beck@mv.rptu.de

M. Kopnarski · R. Merz
Institute of Surface and Thin Film Analysis (IFOS), RPTU Kaiserslautern, Kaiserslautern, Germany

K. M. de Payrebrune
Institute of Computational Physics in Engineering, RPTU Kaiserslautern, Kaiserslautern, Germany

© The Author(s), under exclusive license to Springer Nature Switzerland AG 2024
J. C. Aurich and H. Hasse (eds.), *Component Surfaces*, Springer Series in Advanced Manufacturing, https://doi.org/10.1007/978-3-031-35575-2_12

Steels (AHSSs). First generation AHSSs containing <3 wt.% manganese show a ferritic matrix with bainite and metastable retained austenite. Thus, these materials can be classified as TRIP-assisted. In contrast, the high manganese 2nd generation AHSSs have a fully austenitic microstructure. The 2nd generation AHSSs are characterized by an exceptional combination of high strength and high ductility, i.e., tensile strengths >1400 MPa and fracture strains >60 % can be achieved. Thus, the 2nd generation AHSSs have higher ductility than the 1st generation AHSSs. The aim during the development of the 3rd generation AHSSs was to reduce costs by reducing the manganese content. However, these medium Mn containing steels exhibit lower strength and ductility than the 2nd generation AHSSs [1–5].

Characteristic of high manganese steels is the eponymous mechanisms TRIP and TWIP that occur during deformation. The TRIP effect is achieved by the deformation induced martensitic transformation of the face centered cubic γ -austenitic microstructure into hexagonal close packed ε -martensite and/or body centered cubic α' -martensite. On the one hand, phase transformation of γ -austenite into ε -martensite can occur. On the other hand, transformation of γ -austenite into α' -martensite or via the $\gamma \rightarrow \varepsilon \rightarrow \alpha'$ -martensite transformation pathway has been observed. Those phase transformations result in pronounced work hardening during plastic deformation. Furthermore, the phase transformation prevents necking, which is why the TRIP effect leads to outstanding combinations of strength and ductility [3, 6, 7].

The TWIP effect is achieved by the deformation induced formation of twins, which influences the plasticity of materials in such a way that very large elongations occur in combination with considerable strain hardening. Deformation induced twins have a thickness in the range of about 100 nm in TWIP steels and are limited by large angle grain boundaries or twin boundaries. On the one hand, their formation contributes to the macroscopic deformation of the material. On the other hand, twins are strong obstacles to mobile dislocations. Hence, deformation induced twinning is also considered as a dynamic Hall-Petch effect. Furthermore, the dislocation density in these twins is high, which further contributes to strain hardening. Due to these phenomena, deformation induced twinning results in strong strain hardening and large ductility [3, 5, 6, 8, 9].

Which microstructural mechanisms occur and whether they significantly influence the deformation behavior depends on the chemical composition, the temperature as well as the strain rate. In this context, the Stacking Fault Energy (SFE) is an important parameter that can be used to narrow down the microstructural mechanisms that occur: At a SFE <20 mJ/m², it can be assumed that the TRIP effect is the dominant microstructural mechanism, while in the range from 20 mJ/m² to 60 mJ/m² the TWIP effect is the dominant one. Above 60 mJ/m², it can be assumed that dislocation generation and slip is the dominant microstructural deformation mechanism. Furthermore, TRIP and TWIP effect as well as dislocation generation and gliding can occur simultaneously. Therefore, not only TRIP or TWIP steels but also TRIP/TWIP steels exist. The mentioned limits regarding the correlation between SFE and dominant deformation mechanisms vary in the literature [3, 5, 6, 10, 11] and are only suitable for estimation [5, 6].

In high manganese steels, in addition to the SFE, the C content is also of consequence for the occurring deformation mechanisms, since independent of its influence on the SFE, higher C content promotes twinning induced plasticity. Besides Mn and C, the alloying elements Al and Si are of crucial importance for the mechanical properties of TRIP/TWIP steels. While an increase in Al content results in an increase in SFE, an increase in Si results in a decrease in SFE. Furthermore, an increase in Al content reduces the density. Moreover, high Si contents result in poor weldability of high manganese steels. In addition, due to their low Cr content, TRIP/TWIP steels are not corrosion resistant [1, 2, 5, 6].

The influence of the surface morphology on the fatigue and tribological behavior is addressed in the following sections. Section 2 gives an overview of the investigated materials. In Sect. 3 the methods by which the investigated surface morphologies were produced as well as detailed microstructure analyses, topography, and X-ray diffraction (XRD) measurements of the residual stress state and the phase composition are described. In Sect. 4, the fatigue behavior in the LCF, HCF, and VHCF regime is addressed. Section 5 focuses on the influence of the surface morphology on the tribological behavior of TWIP/TRIP steel with different surface morphologies. Finally, the addressed results are summarized in Sect. 6.

2 Investigated Materials

Two high manganese TWIP steels as well as two TRIP steels were investigated. The chemical compositions as well as the SFE according to [12] are given in Table 1.

The High Strength and Ductility (HSD) TWIP steel HSD[®]600 was strip cast by Salzgitter AG and hot rolled into 5 mm thick plates. The TWIP steel 1.7401 was hot rolled by thyssenkupp Hohenlimburg GmbH, producing plates with a thickness of 6 mm. The grain structures were determined by Electron Back Scatter Diffraction (EBSD) measurements and are shown in Fig. 1. Both TWIP steels show neither preferential orientation nor grain elongations. In contrast to the investigated TWIP steels, the TRIP steel X20MnAlSi16-1-1 and X30MnAl17-1 are not produced industrially. Both materials were melted, cast, and forged in two process steps at the laboratory

Table 1 Chemical composition in wt.% and SFE

Material	C	Mn	Al	Si	Cr	SFE in mJ/m ²
TWIP/HSD [®] 600	0.36	15.29	1.8	2.29	0.12	27.8
TWIP/1.7401	0.36	19.64	1.16	0.31	1.63	26.38
TRIP/ X20MnAlSi16-1-1	0.20	16.26	1.05	0.89	0	9.50
TRIP/X30MnAl17-1	0.3	17	1	1	0	10.70

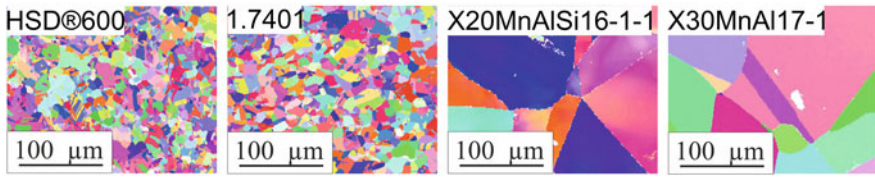


Fig. 1 Grain structure in initial state measured using EBSD techniques

Table 2 Milling parameters applied during the generation of different surface morphologies using various milling processes

Diameter	Number of teeth	Feed/tooth f_z in mm	Rotational speed in rpm	Width of cut in mm	Depth of cut in mm
10 mm	4	0.025	5091	0.1	5

of Institut für Eisenhüttenkunde of RWTH University Aachen, Germany. After the last forging step, the material was cooled in still air. The second TRIP steel investigated, X30MnAl17-1, was annealed for 0.5 h at 1050 °C and then quenched in water. To achieve defined variations in surface morphology, specimens of TRIP steel X20MnAlSi16-1-1 were first sawed and then conventionally down milled, using the parameters given in Table 2.

The reference surface condition was realized by electrolytic polishing of the milled specimens. On top of that, specimens of the TWIP steels HSD®600 and 1.7401 were first waterjet cut and afterward up and down milled, respectively. Analogous to the procedure for the TRIP steel, the reference surface condition was established by electrolytic polishing of previously up milled specimens. For surface generation by lapping, the 1.7401 as well as the X40MnAlSi16-1-1 steel were sawed and ground at room temperature (1.7401) or approximately 100 °C (X20MnAlSi16-1-1) as well as mechanically polished. This was followed by the modified lapping process, which is described and discussed in Sect. 3.3. Furthermore, both the TRIP and TWIP effect offer the potential to look in detail at local microstructural changes during micromachining using EBSD techniques. Therefore, specimens made of TWIP steel HSD®600 and TRIP steel X30MnAl17-1 were also sawed, ground, and polished before micromachining.

3 Surface Morphology

Considering the service behavior of technical components, their surfaces are of decisive importance for the fatigue and wear properties. The production route, especially the final machining processes, significantly influence the surface morphology.

For the understanding of the relationships between surface generation and resulting properties, a detailed characterization of the surface morphology is indispensable. In this work, the near-surface grain structure was analyzed using Focused Ion Beam (FIB) techniques, Electron Contrast Channeling Imaging (ECCI), Scanning Transmission Electron Microscopy (STEM), and Transmission Electron Microscopy (TEM). Thereby, the FIB-cut was generated perpendicular to the surface and the near-surface microstructure was documented by ion beam imaging. Additionally, confocal microscopy was used to measure the surface topographies. Besides the near-surface grain structure and topography, the residual stress state as well as the phase composition in the near-surface layer was determined via X-ray diffraction.

3.1 Reference Surface Morphology of TWIP Steels

The reference surfaces made of TWIP steels HSD[®]600 and 1.7401 were produced by electrolytic polishing after waterjet cutting and milling in order to obtain the geometry shown in Fig. 2 with the parameters given in Table 2.

The images of FIB-cuts shown in Fig. 3 indicate no differences in terms of grain structure between the surface and the interior of the material.

Regarding topography, the electrolytic polishing resulted in a surface with a maximum roughness height $S_z = 2.6\ \mu\text{m}$ and an arithmetical mean height $S_a = 0.3\ \mu\text{m}$ in case of the HSD[®]600 and $S_z = 4.3\ \mu\text{m}$ and $S_a = 0.3\ \mu\text{m}$ for the 1.7401. Thus, the 1.7401 exhibits a higher S_z -value than the HSD[®]600 but comparable S_a values. Differences in the topography after electrolytic polishing can be due to the initial surface topography and chemical composition of the removed material.

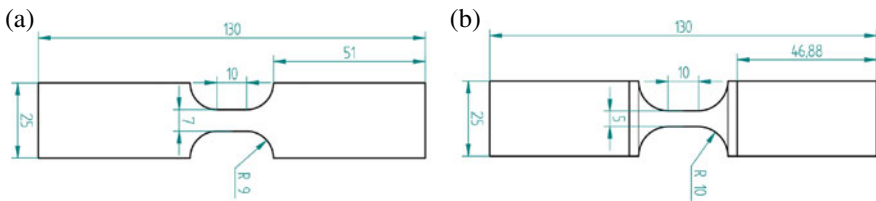


Fig. 2 Specimen geometry for fatigue investigations before milling **a** and after milling **b**

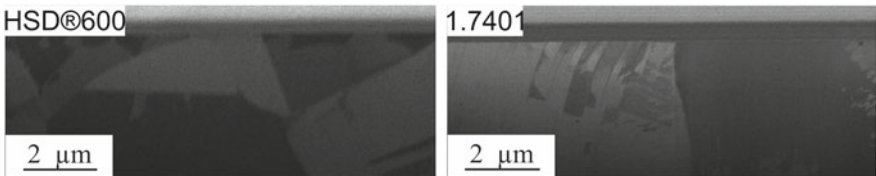


Fig. 3 Near surface microstructure after electrolytical polishing

Table 3 Phase content and residual stress in loading direction after electrolytical polishing

Material	γ -austenite in vol.%	ε -martensite in vol.%	α' -martensite in vol.%	Residual stress in MPa
HSD [®] 600	99	1	0	-120 ± 47
1.7401	100	0	0	-311 ± 15

In order to investigate the phase composition and residual stress in the near-surface region, XRD analysis was carried out. Therefore, scans were performed with CuK_α radiation, 40 kV source voltage and 40 mA source current. The spot size was approximately $2 \text{ mm} \times 2 \text{ mm}$ at the diffraction angle $2\Theta = 40^\circ$. For Rietveld-analysis, diffraction angles from $2\Theta = 40^\circ$ to $2\Theta = 100^\circ$ were realized. Afterward, a database for austenitic stainless steel was used for quantitative phase analysis. For residual stress analysis, diffraction angles from $2\Theta = 73.2^\circ$ to $2\Theta = 76.2^\circ$ were measured in order to determine the diffraction angle of the $(022)_\gamma$ peak precisely. Based on this data, residual stresses were calculated using the $\sin^2\psi$ -method. These procedures were identical for morphologies unless further information was provided.

According to Table 3, the phase composition of the electrolytically polished surfaces shows hardly any influence of surface preparation: While the surface of 1.7401 has a completely austenitic microstructure, approx. 1 vol.% of ε -martensite is present in HSD[®]600.

Both TWIP steels show compressive residual stresses, but those of 1.7401 are noteworthy higher than those of HSD[®]600.

3.2 Surface Morphology After Milling

Specimens made of HSD[®]600 and 1.7401 were waterjet cut and then conventionally up and down milled, respectively, along the gauge length according to Fig. 2 using the parameters given in Table 2. In Fig. 4, a nanocrystalline grain structure can be seen near the surface of the conventionally milled specimens of HSD[®]600 and 1.7401, in contrast to the electrolytically polished reference condition (Fig. 3). In case of the milled surface, up from a depth of approximately $1 \mu\text{m}$, the grain size increases discontinuously, so that up from a depth of about $2 \mu\text{m}$ no difference can be detected between the grain structure of the milled and electrolytically polished sample. Furthermore, there is no substantial difference in the grain structure of the up and down milled samples. As mentioned in Sect. 3.1, STEM images comparing the up and down milled as well as the reference surface morphology are given for the HSD[®]600 in Sect. 4.1 in order to further analyze the difference between the fatigued specimens' surface morphologies.

In contrast to that, the topographies of the milled TWIP steels differ despite the use of identical milling parameters according to Table 4. Furthermore, the S_z - and

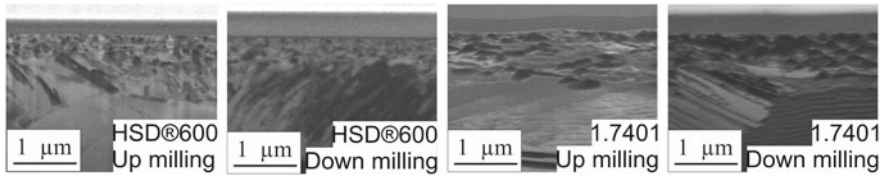


Fig. 4 Near surface microstructure after milling

Table 4 Surface roughness in μm

Manufacturing process	S_z		S_a	
	HSD®600	1.7401	HSD®600	1.7401
Up milling	3.2	3.0	0.4	0.3
Down milling	2.1	3.4	0.2	0.3

Table 5 Phase composition as well as residual stress in feed and loading direction within the up and down milled surfaces made of HSD®600 and 1.7401

Material	Surface morphology	Phase fraction in vol.%			Residual stress in MPa
		γ -austenite	ϵ -martensite	α' -martensite	
HSD®600	Up milled	99	1	0	-826 ± 37
	Down milled	96	4	0	-579 ± 20
1.7401	Up milled	100	0	0	267 ± 54
	Down milled	100	0	0	117 ± 30

S_a -values are comparable to those of the reference surface morphology described in Sect. 3.1. Nevertheless, a qualitative comparison of the topographies shows that the surface structures of the reference surface morphology are significantly smoother than those of the surface morphology after milling. This comparison is further detailed and illustrated by Fig. 8 in Sect. 4.1 for those specimens, which were investigated regarding fatigue properties.

The surface morphologies produced by up and down milling of HSD®600 differ according to Table 5 not only in terms of topography, but also with respect to their phase fractions: The down-milled sample shows the highest ϵ -martensite content of 4 vol.%, while the up milled sample shows only 1 vol.% of ϵ -martensite, just like the polished sample. The milled samples of 1.7401 are completely austenitic and, thus, do not differ from the polished samples in their phase composition. Furthermore, no α' -martensite was detected after both, up and down milling.

On top of that, significant differences can be observed in the residual stresses of the milled specimens made of HSD®600 and 1.7401. While the surfaces of HSD®600

show compressive residual stresses, the 1.7401 shows tensile residual stresses. Furthermore, the residual stresses measured in the near-surface of the milled HSD[®]600 are more than two times higher in magnitude than those measured in the 1.7401. On top of that, the residual stresses are higher in magnitude for both materials after up milling. Furthermore, the near-surface residual stresses of the 1.7401 after up milling show similar absolute values as the polished specimens, but with the opposite sign.

3.3 Surface Morphology After Modified Lapping

Both investigated specimens were processed in a modified lapping process using a tribometer, more precisely a modified lapping machine. The modeling of such processes is addressed in Chapter “Interactions Between Particles and Surfaces”. The used mechanically polished chamfered flat specimens are made of TWIP steel 1.7401 and TRIP steel X20MnAlSi16-1 with a cross-sectional area of 20 mm × 30 mm. Weights are used to press the specimens against the rotating disc of the lapping machine, which is made of steel 1.0110, so that the mean normal force is $F_N \approx 18\text{ N}$. The specimen is fixed horizontally and to compensate for any parallelism errors between the specimen surface and the lapping disc, the only rotational degree of freedom that is prevented is the rotation about the vertical axis. The center of the specimen has a distance $r = 100\text{ mm}$ from the center of rotation of the disc. By rotating, the disc moves underneath the specimen center with a velocity of $v = 120\text{ mm/s}$ and moves a distance of $s = 5.1\text{ m}$ relative to the specimen. Before each experiment, the lapping disc was covered with a mixture of $m_p \approx 1.31\text{ g}$ SiC particles of grit size F180 ($d \approx 81\text{ }\mu\text{m}$) and $m_{fl} \approx 3.35\text{ g}$ lapping oil OL 20 (sold by Stähli Lapp-Technik GmbH) on track of $r_{\min} = 80\text{ mm}$ to $r_{\max} = 120\text{ mm}$.

Figure 5 shows the grain structure of the near-surface layer established by the modified lapping process. The cross sections show that only a part of the surface is deformed by particles during the modified lapping. The areas which were deformed by modified lapping differ regarding the particles penetration depth and as a result, how strongly the near-surface material volume is deformed. In addition, grain refinement can be seen in the material that is sufficiently deformed during modified lapping. Here, a finer grain structure is produced with increasing particle penetration depth. In areas that have been less deformed, grain refinement cannot be stated and consequently no difference to the material near the polished surface can be seen in terms

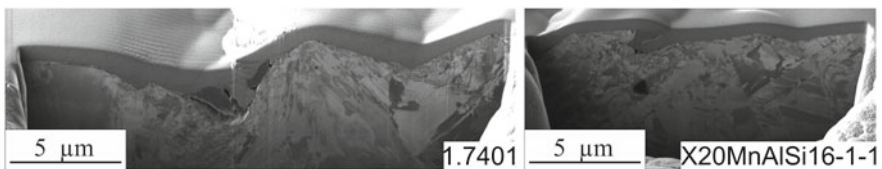


Fig. 5 Near surface layer after modified lapping process

Table 6 Surface roughness and residual stress of lapped specimens

Material	S_z in μm	S_a in μm	Residual stress in MPa
TWIP/1.7401	14.1	0.788	-434 ± 46
TRIP/ X20MnAlSi16-1-1	15.7	0.858	-616 ± 53

of grain structure. Furthermore, in the center of the cross section for the 1.7401, a micro-crack can be seen.

The topography of the TWIP steel 1.7401 and the TRIP steel X20MnAlSi16-1-1 given in Table 6 do not show significant differences. Both materials show residual compressive stresses after the modified lapping process.

The phase compositions of the surfaces structured by modified lapping were analyzed by X-ray diffraction in the initial state after mechanical polishing and after modified lapping. Here, data bases for austenitic stainless steel were used as a reference. Figure 6a shows absolute scans for a sample made of TWIP steel 1.7401 and Fig. 6b X20MnAlSi16-1-1 shows wobble scans for a sample made of TRIP steel in the initial state (mechanically polished) and after the modified lapping. For the TWIP steel all peaks of the absolute scan can be assigned to the austenitic phase revealing that no phase transformation occurred during the modified lapping process. Note that the difference between reference and measured peak position is $< 1^\circ$ for all peaks.

In contrast to the absolute scan of TWIP steel 1.7401, the analysis is less distinct for the TRIP steel, even though wobble scans were performed: In case of the polished sample, the $(111)_\gamma$, $(002)_\gamma$, $(113)_\gamma$ and $(222)_\gamma$ peaks verify an austenitic phase. In addition, it can be assumed that a superposition of the $(111)_\gamma$ and the $(001)_\epsilon$ peak leads to an asymmetry of the $(111)_\gamma$ peak. Furthermore, a peak is located at approximately $2\theta = 83^\circ$ and thus at a diffraction angle which is about $\approx 1^\circ$ greater than the expected $(112)_{\alpha'}$ peak. On top of that, this peak is comparatively broad and asymmetric. In addition to the peaks already discussed, further peaks were measured

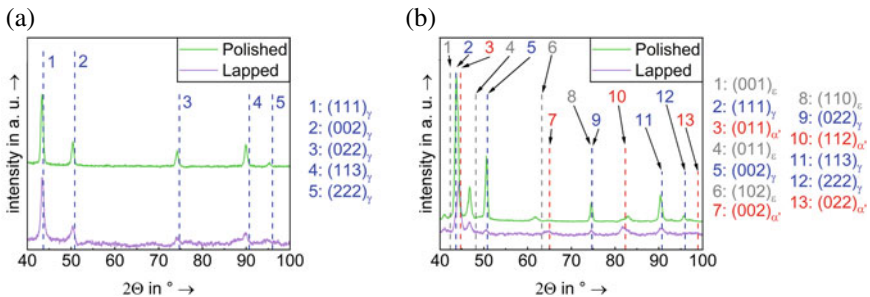


Fig. 6 Absolute scans of the TWIP steel 1.7401 **a** and wobble scan of the TRIP steel X20MnAlSi16-1-1 **b** with polished surface morphology and after modified lapping

at diffraction angles which are from approximately $\Delta 2\theta = 1^\circ$ up to 2.5° too small to be clearly assigned to the $(001)_\epsilon$, $(011)_\epsilon$ and $(012)_\epsilon$ peaks. Furthermore, based on the chemical composition, these peaks do not suggest the existence of another phase.

The wobble scan for the surface morphology after the modified lapping process differs from the polished one in a way that the $(011)_{\alpha'}$ peak can be detected. This peak shows an asymmetry that can be explained by a superposition of the $(111)_\gamma$ peak. In addition, no $(222)_\gamma$ peak can be detected after modified lapping. Accordingly, a decrease of the austenitic phase fraction and an increase of the α' -martensite content can be stated. In addition, there is no longer a peak near the $(102)_\epsilon$ peak but a $(022)_{\alpha'}$ peak instead. Furthermore, the processed wobble scan shows a peak at about $<1^\circ$ lower diffraction angle than the expected $(022)_{\alpha'}$ peak. On top of that, the measured peak is comparatively broad and asymmetric which was detected for the polished surface morphology as well. Due to these phenomena, no quantitative phase analysis was performed. Nevertheless, a significant phase transformation from austenite to α' -martensite during modified lapping was detected for the TRIP steel X20MnAlSi16-1-1, whereas no phase transformation was stated for the TWIP steel 1.7401.

3.4 Surface Morphology after Micro Milling of TRIP Steel

A successive reduction of the machining tool dimensions, and further development of micro machining systems allows manufacturing of local surface morphologies on the μm -scale (see Chapter “Creating Surface Morphologies by Micromilling and Microgrinding”) [13]. If the diameter of the milling cutter is in the order of magnitude or smaller than the diameter of the machined grains, the grain orientation has a decisive effect on the material behavior during machining [14, 15]. Furthermore, due to the high metastability of the TRIP steel, local phase transformations can be realized without cryogenic cooling [16]. The tools used in this study were single edged micro end mills with a diameter of $50\mu\text{m}$, made of cemented carbide (WC+Doping 91 %, Co 9 %, grain size $0.2\mu\text{m}$). Using these tools, surface slots were milled with a spindle speed of $45,000\text{ min}^{-1}$, a feed rate of 11.25 mm/min and a depth of cut of $5\mu\text{m}$. The total feed travel was $100\mu\text{m}$ resulting in a total slot length of $150\mu\text{m}$. No metalworking fluid was used. To obtain a suitable surface condition for EBSD investigations at the micro machined slots (Fig. 7a), it was necessary to additionally prepare the specimens. The requirement for this specimen preparation was an improvement of the surface condition with removing only a very small portion of the material influenced by micro machining. To avoid preparation induced phase transformations as far as possible, the specimens were mechanically polished with diamond suspension with a grit size of $0.02\mu\text{m}$ and a cotton polishing disc for 2 min. During this treatment, the depth of the slot was approximately halved, but its bottom was nearly unaffected. Additionally, to prepare the bottoms of the slots, the specimens were electrolytically polished for a few seconds. Afterward, the slots appear in a smooth surface condition which was suitable for EBSD investigations (Fig. 7b).

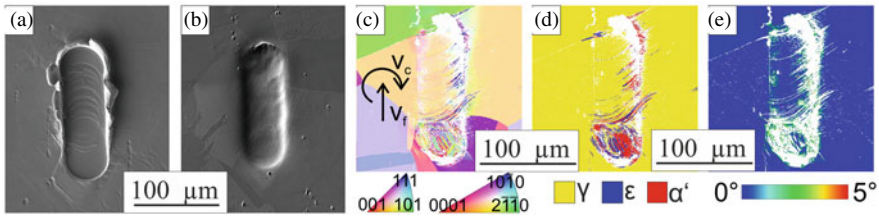


Fig. 7 Micro milled slot before **a** and after **b** the surface preparation for EBSD investigations regarding grain orientation **(c)**, phase composition **(d)** and misorientation **(e)** of TRIP steel X30MnAl17-1

The microstructure in the micro milled slots contains deformation induced ε -martensite as well as α' -martensite. The α' -martensite is mainly located inside the ε -martensite islands, indicating that the transformation path was primarily $\gamma \rightarrow \varepsilon \rightarrow \alpha'$, i.e., the ε acts as nucleation site for α' . The machining induced changes in microstructure are most pronounced at the plunging point of the micro milling tool (Fig. 7c). Besides the plunging point of the milling tool, the microstructure of the slot appears very asymmetric, i.e., the changes in grain orientations, misorientations as well as the phase transformations appear significantly more pronounced at the down milling side of the slot (Fig. 7d). Note that both sides of the slot are located in grains with the same initial orientation. Hence, a local influence of the initial grain orientation can be excluded.

4 Fatigue Behavior of TWIP Steel with Different Surface Morphologies

To characterize the cyclic deformation and fatigue lifetime behavior of TWIP steel with different surface morphologies, uniaxial fully reversed tension-compression single step tests in the Low Cycle Fatigue (LCF) and High Cycle Fatigue (HCF) regime were performed on flat specimens. Furthermore, Very High Cycle Fatigue (VHCF) tests were performed under 4 point bending conditions. The investigated material was the TWIP steel HSD®600.

4.1 LCF Regime

The LCF tests were performed under total-strain control with a frequency of $f = 0.2\text{Hz}$ using the experimental setup presented in [17]. In addition to the results shown in Sects. 4.1 and 4.2, Fig. 8a shows qualitatively the effects of polishing, (b) down milling and (c) up milling on the surface topography. Despite similar S_z and S_a values of all topographies, the polished surface morphology lets expect the highest

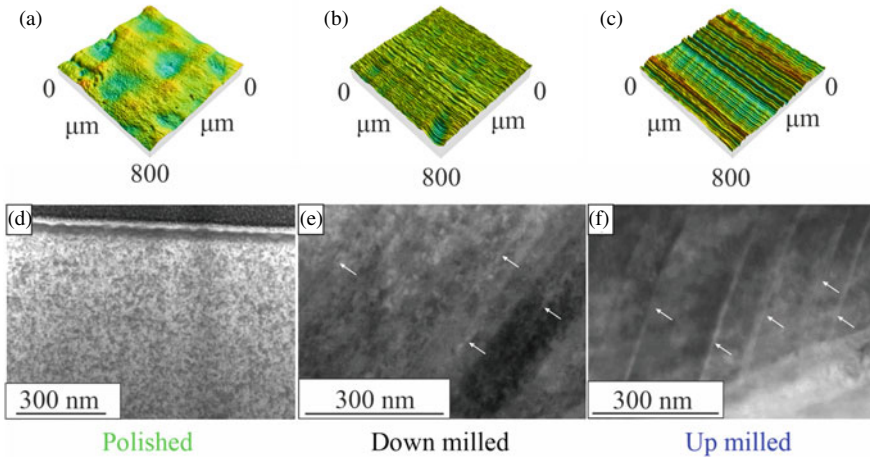


Fig. 8 Surface topography (a), (b), (c) and near-surface microstructure (d), (e), (f) of specimens' surface morphologies before fatigue in the LCF, HCF, and VHCF regime

fatigue strength, due to very smooth transitions from the maximum to the minimal height of the roughness profile. Using STEM on FIB lamellas taken directly from the specimen surface, a fine-grained microstructure is observed directly underneath the machined surfaces for the down and up milled morphologies (Fig. 8e and f). The sub-surface microstructure of the polished one has the microstructure of the bulk material according to Fig. 8d.

Figure 9a shows the cyclic deformation and Fig. 9b fatigue lifetime behavior of the TWIP steel with different morphologies as well as a change in the microstructure due to cyclic loading in the LCF regime. In general, an initial cyclic hardening within the first few load cycles, followed by cyclic softening can be observed. After approximately 10^3 cycles, a secondary cyclic hardening occurs. Since the influence of the surface morphology on the cyclic deformation behavior in the LCF regime is marginal, the results can be compared with investigations on mechanically [18, 19] or electro-polished [20, 21] as well as electro-discharge machined specimens [22]. The cyclic deformation behavior of steel with a manganese content of 12 and 13 wt.% was investigated in the LCF range by Schilke et al. [18]. The authors found a softening material behavior after an initial hardening. These results agree with the study of Rüsing et al. [22] who performed fatigue tests on a high manganese steel. Wu et al. [19] and Shao et al. [20] also investigated a high manganese steel and they observed a saturation state after initial cyclic hardening before cyclic softening starts. In another study by Shao et al. [21], initial cyclic hardening is observed, followed by cyclic softening and subsequent secondary cyclic hardening which is in perfect agreement with the work presented here. Even though the cyclic deformation behavior is qualitatively similar for the specimens with all investigated morphologies, the specimens with polished surfaces reach the highest numbers of cycles to failure

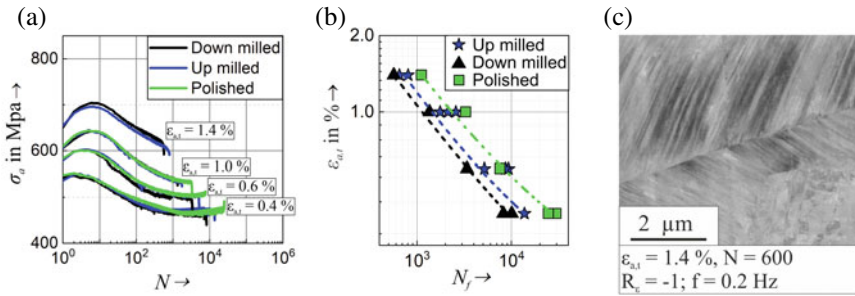


Fig. 9 Cyclic deformation (a) and fatigue life (b) curves of HSD[®]600 with different surface morphologies as well as ECCI micrograph (c) with twins after cyclic loading [25]

at the same load amplitude (see $S - N$ curve in Fig. 9b). The lowest fatigue life was observed for specimens with the down milled surface morphology. Apart from these results, it is very hard to find further work in the literature, that addresses the influence of surface morphology on fatigue life in the LCF regime of TRIP/TWIP steels. However, Shao et al. [21] show in agreement with Rüsing et al. [23] an increased fatigue strength due to grain refinement in bulk material. Furthermore, Niendorf et al. [24] showed that monotonic pre-deformation of TWIP steel leads to the formation of twins, resulting in a higher fatigue strength and a cyclically stable deformation response. Nevertheless, the deformation and grain refinement in the near-surface material due to milling results in a reduced fatigue life compared to the polished specimens.

The fatigue induced change in the microstructure is shown exemplary using ECCI (Fig. 9c). The respective specimen with polished surface was loaded with a relatively high total-strain amplitude of $\epsilon_{a,t} = 1.4\%$ up to 50% of average fatigue life for this amplitude. In the ECCI micrograph line-like structures can be detected within the individual grains. The morphology of these lines indicates twins, which contribute to strengthening of the material since they act as impassable barriers for dislocations. The twin formation requires high shear stresses (τ_T) in the individual grains. The τ_T in terms of the uniaxial stress can be calculated by $\tau_T = 6.14 \times (\text{SFE}/b_p)$, where the average Schmid factor is 0.326. Hence, the uniaxial stress for twinning is a function of SFE and the magnitude of the Burgers vector of partial dislocation (b_p) as well as of grain orientation [26]. Using the experimentally determined b_p value of 0.1478 nm and $\text{SFE} = 27.7 \text{ mJ/m}^2$ for the investigated TWIP steel [27] the critical nominal shear stress is in the range of 1150 MPa for the average Schmid factor. However, if the Schmid factor in individual grains assumes the highest possible value of 0.5, the nominal stress for the twin formation is reduced to 750 MPa. Therefore, the fatigue induced twins were only detected in isolated grains after cyclic loading in the LCF regime, predominantly in specimens loaded with high total-strain amplitudes.

4.2 HCF Regime

The HCF tests were performed under stress-control with different frequencies of $f = 5, 2$ and 1 Hz using the experimental setup presented in [10]. To obtain the ultimate's number of cycles $N_U = 2 \times 10^6$ in reliable experimental time, usually HCF tests are realized with frequencies ≥ 5 Hz. However, the development of cyclic plasticity induced specimen temperature must be taken in the consideration, especially for metastable austenitic steels, because an increase of temperature leads to an increase of the SFE and consequently to changes in the microstructure deformation mechanism. The results shown in Fig. 10 underline the importance of choosing appropriate load frequencies for fatigue tests on TWIP steels. To visualize the specimen temperature during cyclic loading, infrared camera images are shown in Fig. 10b and d. While the stress amplitude of $\sigma_a = 450$ MPa leads to an increase of the temperature in the specimen's center up to 200°C , in the fatigue test with $f = 5$ Hz, the specimen's temperature was limited to 40°C with $f = 2$ Hz. Consequently, in the test with $f = 5$ Hz pronounced cyclic softening takes place and significantly shorter fatigue life was achieved in comparison to fatigue test with $f = 2$ Hz. Because the temperature significantly influences the SFE and consequently the microstructural mechanisms in TWIP steels, the development of the cyclic plasticity induced specimen temperature was kept in all tests under 40°C .

Figure 11 shows the influence of surface morphology on the cyclic deformation and fatigue lifetime behavior as well as characteristic microstructures of fatigued specimen in the HCF regime. By analyzing the cyclic deformation behavior at the stress amplitude $\sigma_a = 480$ MPa and frequency $f = 2$ Hz, it is recognizable, that the specimen with polished surface shows significantly higher plastic strain amplitudes ($\epsilon_{a,p}$) and reaches a maximum plastic strain amplitude of $\epsilon_{a,p} = 1 \times 10^{-3}$ after approximately 10^4 cycles, while the plastic strain amplitudes of the specimens with milled surface morphologies do not exceed $\epsilon_{a,p} = 0.75 \times 10^{-3}$. The polished specimen shows significant cyclic softening and a short period of cyclic saturation before it fails, while the milled specimens show cyclic hardening after cyclic softening and reach higher fatigue lifetimes. In summary, the milled, work hardened surface mor-

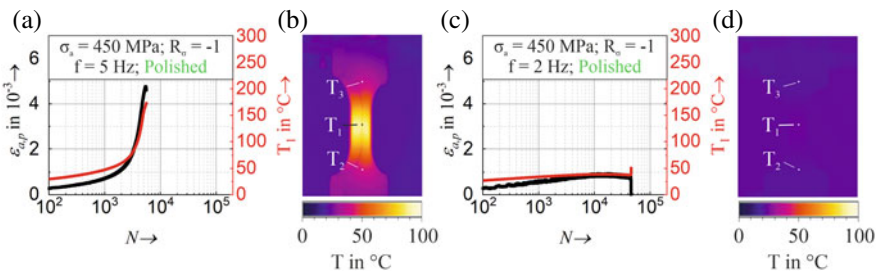


Fig. 10 Development of plastic strain amplitude and temperature during the HCF loading with $\sigma_a = 450$ MPa and two frequencies of 5 Hz (a), (b) and 2 Hz (c), (d)

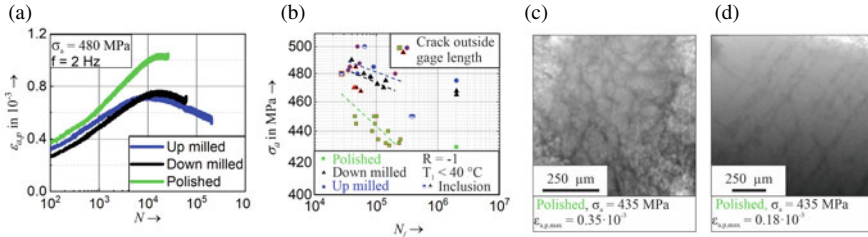


Fig. 11 Cyclic deformation (a) and fatigue lifetime (b) curves of HSD[®] 600 with different surface morphologies as well as STEM micrographs (c), (d) after cyclic loading

phologies lead to decreased plastic strain amplitude, associated with higher fatigue lifetimes.

In general, the $S - N$ curves are shifted for specimens with milled surfaces to approximately 40 MPa higher stress amplitudes although the surface of the polished specimens is the smoothest (Fig. 8b). Hence, the decreased cyclic plastic deformations at least contribute to that shift of the $S - N$ curve to higher stress amplitudes for the specimens with milled surface morphologies. Obviously, these decreased plastic deformations are caused by the work hardened surface of the milled specimens which, hence, leads to an improved fatigue strength. Furthermore, it is known, that compressive residual stresses can positively influence the fatigue life especially in the HCF regime. In interrupted single steep tests, the stability of the σ_{rs} in the up and down milled surfaces was investigated. The stress amplitude $\sigma_a = 475$ MPa leads to a reduction of the initial $\sigma_{rs} = -350$ MPa to -150 MPa after 10^4 cycles in specimens with down milled surface morphologies and in specimens with up milled surfaces, $\sigma_a = 480$ MPa only leads to slight reduction of the initial $\sigma_{rs} = -500$ MPa to -450 MPa after the same number of cycles. These results show that even after cyclic loading in HCF regime a certain amount of compressive residual stresses still exists in specimen surface, which positively influences the fatigue life especially of specimens with the up milled surface morphology.

To characterize the microstructural changes during HCF, STEM investigations were performed (Fig. 11c and d). Due to too small local shear stresses in individual grains, no development of twins during cyclic loading could be detected. Furthermore, different dislocation structures can be related with a remarkable scatter in the cyclic deformation behavior in fatigue tests with identical control parameters. Higher plastic deformations are correlated with cell-like dislocation structures while lower plastic deformations are accompanied with planar dislocation structures [27]. This indicates local differences in the stacking fault energy which leads to different dislocation structures and, in consequence, to the observed scatter in cyclic deformation behavior. To clarify this hypothesis in detail, more research is needed. Besides the results described in this chapter and in [10], no results have been published regarding the inference of the surface morphology of high manganese steel on fatigue life. However, Hamada et al. [28–30] investigated the fatigue strength of high manganese TWIP steel in the HCF range performing cyclic bending tests. No influence of the Mn

content varying between 16 and 22 wt.% was found. In contrast, an increase in fatigue strength by grain refinement was realized for a TWIP steel with 0.6 wt.% C and 22 wt.% Mn. This is in good agreement with the results presented here and in [10], since the milled surfaces show among other phenomena a grain refined near the surface associated with higher fatigue life than the polished specimens. Furthermore, Hamada et al. [28–30] found in agreement with Seo et al. [31] neither deformation induced twinning nor ε -martensite formation. Crack initiation was found at the intersections of slip bands, grain boundaries, and annealing twins. Most of the crack propagation occurred transgranularly. During uniaxial fatigue testing, Seo et al. [31] further found grain boundary cracking associated with crack initiation.

4.3 VHCF Regime

The influence of the surface morphology on the very high cyclic fatigue behavior was investigated using 4-point bending fatigue tests on flat specimens with the dimensions 50 mm \times 4 mm \times 3.5 mm and a test frequency of 100 Hz as well as a load ratio $R = 0.1$ (Fig. 12). Due to this load condition, and the relatively small specimen dimensions, the maximum temperature on the specimen was below 40° during all VHCF tests. The same three surface morphologies (see Fig. 8) as for uniaxial loading were used for the VHCF tests.

The analysis of $S - N$ data for $N < 10^7$ leads to the same behavior as observed in HCF experiments e.g., the best fatigue properties showed specimens with the milled surface. Interestingly, in the VHCF regime the specimens with polished surface achieved the ultimate number of cycles $N_u = 10^8$ without failure and the specimens with milled surface failed. A possible reason for this behavior can be the smoother transit from the peaks to the valleys within the polished specimen's surface profile in addition to the higher cyclic hardening potential $|e^{II}|$, determined using cyclic indentation tests [10]. Hence, on the one hand the higher stresses at the micro notches in milled specimens lead to more frequent crack initiation than in the polished spec-

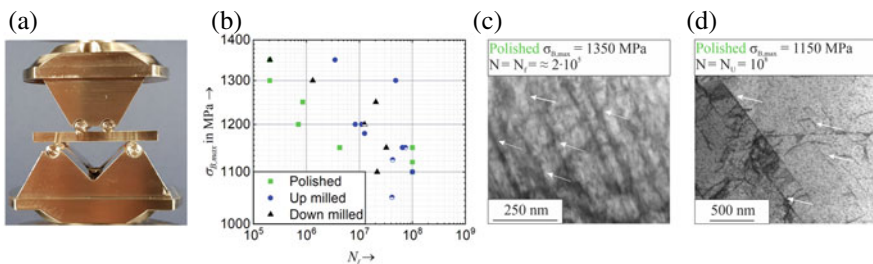


Fig. 12 Experimental setup for 4 point bending testing (a), fatigue life curve (b) and STEM micrographs (c), (d) with the near-surface microstructure after fatigue loading

imens. On the other hand, the local plasticity on the micro-crack tip in the milled surface is lower and consequently local stress relaxation is less pronounced.

Figure 12c and d show STEM micrographs of fatigued specimen with polished surfaces after failure with the high stress in the HCF regime and without failure at lower stress in the VHCF regime. The comparison of both shows that in both cases twinning occurred, which is more pronounced at higher loading amplitudes. In general, in the performed 4-point bending tests, the stresses in the specimen's surface were estimated based on an elastic material's behavior to be higher than 1000 MPa. At maximum stresses above 1000 MPa, the probability to achieve the critical shear stress for the twin formation is high and increases with the increase of the load. How this process influences the fatigue life of specimens with different surface morphologies at higher number of cycles, e.g., $10^9 - 10^{10}$ is still an open question. Hereunto an ultrasonic fatigue testing system with the load frequency of 20 kHz must be used, however, the fatigue of metastable austenites at these frequencies is not trivial [32].

5 Tribological Behavior

In engineering applications, friction is a phenomenon that causes wear, i.e., removal of material at the surface. Therefore, the surface morphology of the material strongly influences its tribological behavior. In metastable materials, other microstructural mechanisms besides the change in topography, residuals stresses, grain sizes and dislocation density like formation of twins or/and new phases can be activated [33–35]. Hence, the TWIP and TRIP effect can additionally influence the tribological and wear behavior. While the fatigue properties of high manganese TWIP steels have been intensively investigated, the tribological behavior of these materials was hardly investigated. However studies on stable and metastable austenitic stainless steels have been carried out [36–40], which reported a positive influence of metastability on the tribological behavior.

In the investigations described below, representative of typical loading scenarios under severe wear, only the tribological behavior of the new materials was investigated during iterative scratching with a sharp-edged diamond counter-body under dry running conditions without lubricant.

5.1 TRIP Steel

The tribological behavior of the TRIP steel X20MnAlSi16-1-1 during cyclic tribological load in linear reciprocating configuration was investigated using a standard diamond Vickers tip. As described by Alhafez et al. [41] the tribological behavior of such a real indenter is governed by the rounded bottommost part of its tip, considering its realistic indentation depth in the counterpart. The authors confirm by MD simula-

Table 7 Martens hardness and cyclic hardening coefficient of down milled and polished surfaces

Surface morphology	HM116 0.1	$ e^{II} $
TRIP X20MnAlSi16-1-1 down milled	2003 ± 41	0.283 ± 0.009
TRIP X20MnAlSi16-1-1 polished	4124 ± 208	0.337 ± 0.032

tion an early result of Boden and Tabor [42], which estimates the friction coefficient for a single scratch as ratio of its cross-sectional (A_T) and real bearing area (A_N) assuming nearly identical hardness in transversal (H_T) and normal (H_N) direction as $\mu = A_T/A_N \cdot H_T/H_N$. Considering the low indentation depth of the Vickers indenter, which is in the micron range, during a single scratch in the used TRIP steel at a normal force of $F_N = 5$ N, the ratio A_T/A_N was calculated according to the exact geometry of the indenter's rounded bottommost tip for this indentation depth. So realistic friction coefficients of $\mu \approx 0.06$ were received, significantly differing from $\mu \approx 0.2$ of an ideal Vickers tip with self-similar geometry and infinitely fine tip.

The tribological behavior of TRIP steel with down milled surfaces using the parameters given in Table 2 and surfaces that were electrolytically polished after down milling were investigated. The mechanical properties of the surface morphologies were determined by cyclic indentation testing with a Vickers tip, a maximum force of $F = 1$ N and a frequency of $f = 1/12$ Hz according to [10]. During the first cycle of these tests, a more than two times higher Martens hardness was measured for the down milled surface compared to the polished one. Furthermore, the cyclic hardening exponent $|e^{II}|$ given in Table 7 was determined based on the cyclic indentation tests according to the PhyBaL_{CHT} method [10, 43]. The milled surfaces show significantly lower $|e^{II}|$ -values than the polished one, which suggests in combination with the Martens hardness that the near-surface material volume was strengthened during milling.

After 150 cycles of tribological loading, the cross section of wear tracks compared in Fig. 13 were observed. Since the wear track of the polished surfaces is two times deeper than for the milled one, strengthening by milling leads to lower material removal. Besides the wear track's depth, the friction coefficient was measured.

For precise interpretation, the wear track geometries were analyzed to estimate the influence of the rounded tip. At the bottom of the wear tracks of both surface morphologies, the shapes resemble the rounded tip geometry. Following the pure geometrical argumentation for this rounded indenter shape, a higher indentation depth results in a higher friction coefficient according to the increased influence of the indenter's correct Vickers shape at its shaft. In contrast to that, the milled surfaces show lower indentation depth but slightly higher friction coefficients than the milled surfaces. On top of that, the influence of the surface morphology on the friction coefficients decreases with increasing number of cycles so that they approach asymptotically. Thus, the reason for the observed influence of the surface morphology on the friction coefficient is not the difference in indentation depth and rounded

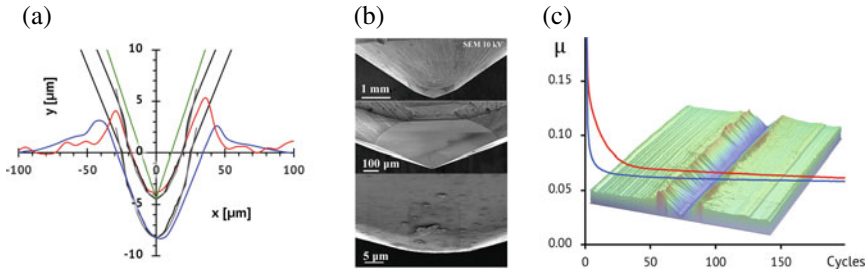


Fig. 13 Comparison of wear tracks and friction coefficients (μ) for (a) TRIP steel (X20MnAlSi16-1-1) with electro-polished (blue) and conventionally down milled (red) surface after 150 cycles of furrowing with a diamond Vickers tip in linear reciprocating configuration. Cross sections of the wear tracks (blue/red), measured by optical profilometry, the real tip geometry (black), measured in SEM pictures (b) and an ideal Vickers shape (green) are shown in (a). The corresponding friction coefficients (μ) in front of a 3D representation of the wear track as background can be taken from (c)

indenter shape. In fact, the results suggest that work hardening during milling results in a gradient of hardness from the surface to the bulk material. Consequently, the hardness ratio H_T/H_N deviates from one, which superimposes the influence of the rounded indenter shape. With increasing number of cycles and penetration depth, the influence of work hardening on the measured friction coefficient decreases resulting in decreasing discrepancies between both surfaces and similar friction coefficients.

A first comparative FIB preparation and EBSD analysis of the X20MnAlSi16-1-1 TRIP steel suggested the occurrence of a phase transformation, triggered by gallium implantation, like observed by Basa et al. [44] even for a highly stable austenite phase in a super duplex stainless steel after FIB milling, which prevented further material analysis of the wear track.

5.2 TWIP Steel

The tribological behavior of the TWIP steel HSD[®]600 was investigated analogously to the investigations on the TRIP steel X20MnAlSi16-1-1 described previously (Sect. 5.1). The determination of the friction coefficient as a function of the number of cycles during cyclic tribological loading in linear reciprocating configuration was described in Chapter “Indentation and Scratching on the Nanoscale”. Thus, the present chapter focusses on the microstructural changes during cyclic tribological loading. Since the HSD[®]600 possesses a noteworthy higher SFE than the TRIP steel X20MnAlSi16-1-1, FIB preparation without phase transformation is possible.

The tribologically induced changes in the microstructure of a specimen’s surface of TWIP steel HSD[®]600 after tribological loading is shown in Fig. 14. For details regarding the experimental setup, see [35]. The tribologically induced near-surface morphology is divided in a two-layer structure appearing with an extremely fine-

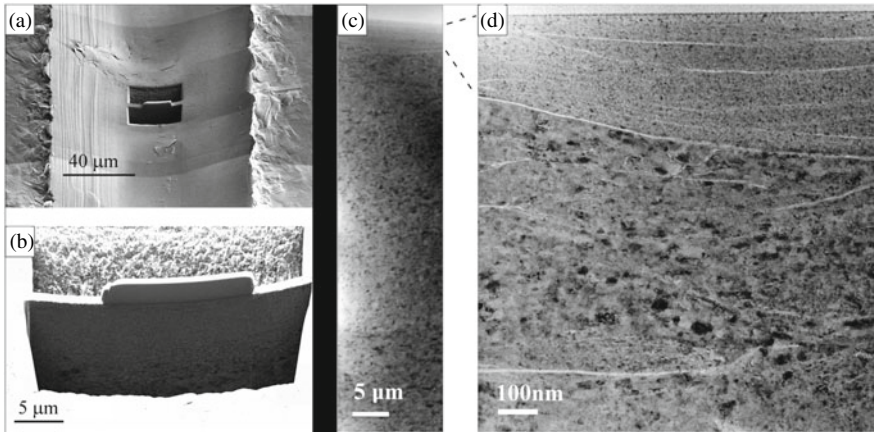


Fig. 14 Overview of the surface after tribological loading with FIB-cut (a), (b) and TEM investigation of near-surface morphology incl. phase analysis (c), (d)

grained (grain size 3 – 5 nm) surface layer of 500 – 900 nm thickness and a sub-surface layer, where the grain size gradually increases from approximately 10 nm at a sharp interface between the two layers to approximately 50 – 60 nm at a depth of 7 μm under the groove surface. The surface layer contained many cracks/fissures, which were sometimes observable within the adjacent upper part of the sub-surface layer, whereas no cracks/fissures were observed in deeper regions of the sub-surface layer ($\geq 1 \mu\text{m}$). The surface layer was partly oxidized ($\approx 28 \text{ vol.}\%$ of metal oxides) in contrast to the sub-surface one, where no significant oxidation was detected. In the investigated TWIP steel, grain refinement due to sliding was accompanied and accelerated by the phase transformation from γ -austenite to ε - and α' -martensite.

According to Fig. 15, the surface layer consists of α' -martensite with barely detectable traces of ε -martensite, whereas only approximately one third of the austenite has been transformed to martensite in the upper part of the sub-surface layer. Note, that no phase transformation from γ -austenite to α' -martensite was observed in other test configurations like monotonic or fatigue loading of the investigated TWIP steel. The kinetic of this phase transformation is still unclear and must be investigated in future research work.

6 Summary

Different Surface morphologies were produced by electrolytic polishing, milling, and modified lapping of high manganese TRIP/TWIP steel. These exhibit significant differences in terms of their grain structure, residual stresses, phase composition, and topography. A generally valid description of the surfaces produced by the var-

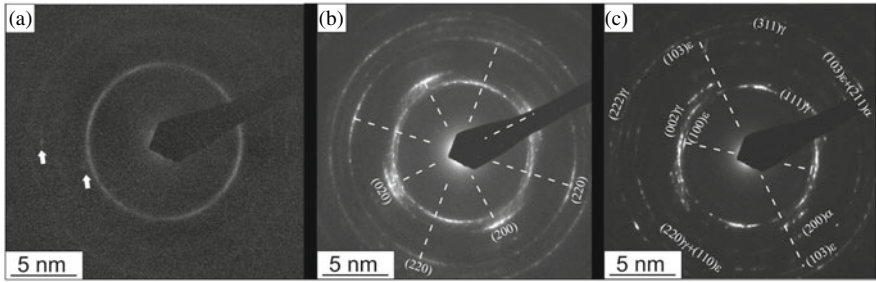


Fig. 15 Selected area diffraction patterns (SADP) of the lamella shown in Fig. 11.14 after lift-off preparation, at three different distances to the surface: Immediate uppermost and extremely fine-grained surface layer (a). Upper region of the sub-surface layer (b). Bottom region of the sub-surface layer with assignment of the Debye-circles to corresponding lattice planes (c). The most concise broad circle belongs presumably to the strongest oxide lines

ious processes is not possible, hence, all surfaces were analyzed individually with regard to their specific properties. In contrast to the macroscopic surface generation, micromachining of the TRIP steel X30MnAlSi17-1 enables the observation of phase transformation along the path γ -austenite \rightarrow ϵ -martensite \rightarrow α' -martensite on a small scale in selected grains.

The surface morphologies do not affect the cyclic deformation behavior of the TWIP steel HSD[®]600 in the LCF regime at $R_\epsilon = -1$. Nevertheless, the surface morphology affects fatigue life. In contrast to the LCF regime, the surface morphology affects the cyclic deformation behavior in the HCF regime at a stress ratio of $R_\sigma = -1$: The electrolytically polished specimens show higher plastic strain amplitudes than the milled ones. For all surface morphologies, cyclic softening occurs during the first cycles. In case of the electrolytically polished specimens, this is followed by a short saturation state before failure, whereas cyclic hardening occurs after initial cyclic softening for the milled specimens. In addition, the milled specimens show significantly longer fatigue life than the electrolytically polished ones. In contrast, the milled specimens fail in 4-point bending tests with $R_\sigma = 0.1$ in the VHCF regime between 10^7 and 10^8 load cycles, while no failure occurs in this range in the case of the polished specimens.

An influence of the surface morphology can also be observed during cyclic tribological loading of the TRIP steel X20MnAlSi16-1-1: The resulting wear track is in case of the down milled surface half as deep as in case of the electrolytically polished reference. In addition, the friction coefficient is greater for the down milled specimens than for the electrolytically polished ones, especially during the first few cycles. Moreover, during cyclic tribological loading of the HSD[®]600, in addition to grain refinement, a phase transformation occurs which cannot be observed during cyclic loading.

In summary, various machining methods applied to TRIP/TWIP steel lead to surface morphologies with highly different characteristics. For component design,

it needs to be considered that, the generated surface morphologies are of decisive importance for the fatigue and tribological behavior.

References

1. Elliott R, Coley K, Mostaghel S, Barati M (2018) Review of manganese processing for production of TRIP/TWIP steels, part 1: current practice and processing fundamentals. *JOM* 70(5):680–690. ISSN: 1047-4838. <https://doi.org/10.1007/s11837-018-2769-4>
2. Cai ZH, Ding H, Xue X, Xin QB (2013) Microstructural evolution and mechanical properties of hot-rolled 11% manganese TRIP steel. *Mater Sci Eng A* 560:388–395. ISSN: 09215093. <https://doi.org/10.1016/j.msea.2012.09.083>
3. Bouaziz O, Allain S, Scott CP, Cugy P, Barbier D (2011) High manganese austenitic twinning induced plasticity steels: a review of the microstructure properties relationships. *Curr Opin Solid State Mater Sci* 15(4):141–168. <https://doi.org/10.1016/j.cossms.2011.04.002>
4. Bleck W, Brühl F, Ma Y, Sasse C (2019) Materials and processes for the third-generation advanced high-strength steels. *BHM Berg-und Hüttenmännische Monatshefte* 164(11):466–474. <https://doi.org/10.1007/s00501-019-00904-y>
5. de Cooman BC, Kwon O, Chin K-G (2012) State-of-the-knowledge on TWIP steel. *Mater Sci Technol* 28(5):513–527. ISSN: 0267-0836. <https://doi.org/10.1179/1743284711Y.0000000095>
6. Grässel O, Krüger L, Frommeyer G, Meyer L (2000) High strength Fe-Mn-(Al, Si) TRIP/TWIP steels development—properties—application. *International Journal of Plasticity* 16(10–11):1391–1409. ISSN: 07496419. [https://doi.org/10.1016/S0749-6419\(00\)00015-2](https://doi.org/10.1016/S0749-6419(00)00015-2)
7. Grässel O, Frommeyer G, Derder C, Hofmann H (1997) Phase Transformations and Mechanical Properties of Fe-Mn-Si-Al TRIP-Steels”. In: *Le Journal de Physique IV* 07(C5):C5-383–C5-388. ISSN: 1155-4339. <https://doi.org/10.1051/jp4:1997560>
8. Bouaziz O, Allain S, Scott C (2008) Effect of grain and twin boundaries on the hardening mechanisms of twinning-induced plasticity steels. *Scr Mater* 58(6):484–487. <https://doi.org/10.1016/j.scriptamat.2007.10.050>
9. Gil Sevillano J, de las Cuevas F (2012) Internal stresses and the mechanism of work hardening in twinning-induced plasticity steels. *Scr Mater* 66(12):978–981. ISSN: 13596462. <https://doi.org/10.1016/j.scriptamat.2012.02.019>
10. Klein MW, Blinn B, Smaga M, Beck T (2020) High cycle fatigue behavior of high-Mn TWIP steel with different surface morphologies. *Int J Fatigue* 134:105499. ISSN: 01421123. <https://doi.org/10.1016/j.ijfatigue.2020.105499>
11. Tian YZ, Bai Y, Zhao LJ, Gao S, Yang HK, Shibata A, Zhang ZF, Tsuji N (2017) A novel ultrafine-grained Fe 22Mn 0.6C TWIP steel with superior strength and ductility. *Mater Charact* 126:74–80. ISSN: 10445803. <https://doi.org/10.1016/j.matchar.2016.12.026>
12. Curtze S, Kuokkala V-T, Oikari A, Talonen J, Hänninen H (2011) Thermodynamic modeling of the stacking fault energy of austenitic steels. *Acta Mater* 59(3):1068–1076. ISSN: 13596454. <https://doi.org/10.1016/j.actamat.2010.10.037>
13. Smaga M, Beck T, Arrabiyeh P, Reichenbach I, Kirsch B, Aurich JC (2015) Characterization of micro machined surface from TRIP/TWIP steels. *MATEC Web Conf* 33:07004. <https://doi.org/10.1051/mateconf/20153307004>
14. Dornfeld D, Min S, Takeuchi Y (2006) Recent advances in mechanical micromilling. *CIRP Annals* 55(2):745–768. <https://doi.org/10.1016/j.cirp.2006.10.006>
15. Kieren-Ehses S, Böhme L, Morales-Rivas L, Löscher J, Kirsch B, Kersch E, Kopnarski M, Aurich JC (2021) The influence of the crystallographic orientation when micro machining commercially pure titanium: a size effect. *Precis Eng* 72:158–171. <https://doi.org/10.1016/j.precisioneng.2021.04.007>

16. Klein M, Smaga M, Beck T (2018) Surface morphology and its influence on cyclic deformation behavior of high-Mn TWIP steel. *Metals* 8:832. <https://doi.org/10.3390/met8100832>
17. Klein M, Smaga M, Beck T (2018) Surface morphology and its influence on cyclic deformation behavior of high-Mn TWIP steel. *Metals* 8(10):832. <https://doi.org/10.3390/met8100832>
18. Schilke M, Ahlström J, Karlsson B (2010) Low cycle fatigue and deformation behaviour of austenitic manganese steel in rolled and in as-cast conditions. *Procedia Eng* 2(1):623–628. ISSN: 18777058. <https://doi.org/10.1016/j.proeng.2010.03.067>
19. Wu Y, Tang D, Jiang H, Mi Z, Xue Y, Wu H, Wu Y-X, Tang D, Jiang H-T, Mi Z-I, Xue Y, Wu H-P (2014) Low cycle fatigue behavior and deformation mechanism of TWIP steel. *J Iron Steel Res Int* 21(3):352–358. ISSN: 1006-706X. [https://doi.org/10.1016/S1006-706X\(14\)60054-6](https://doi.org/10.1016/S1006-706X(14)60054-6)
20. Shao CW, Zhang P, Liu R, Zhang ZJ, Pang JC, Zhang ZF (2016) Low-cycle and extremely-low-cycle fatigue behaviors of high-Mn austenitic TRIP/TWIP alloys: property evaluation, damage mechanisms and life prediction. *Acta Mater* 103:781–795. ISSN: 13596454. <https://doi.org/10.1016/j.actamat.2015.11.015>
21. Shao CW, Zhang P, Zhu YK, Zhang ZJ, Pang JC, Zhang ZF (2017) Improvement of low-cycle fatigue resistance in TWIP steel by regulating the grain size and distribution. *Acta Mater* 134:128–142. ISSN: 13596454. <https://doi.org/10.1016/j.actamat.2017.05.004>
22. Rüsing CJ, Lambers H-G, Lackmann J, Frehn A, Nagel M, Schaper M, Maier HJ, Niendorf T (2015) Property optimization for TWIP steels—effect of pre-deformation temperature on fatigue properties. *Mater Today Proc* 2:S681–S685. ISSN: 22147853. <https://doi.org/10.1016/j.matpr.2015.07.375>
23. Rüsing CJ, Niendorf T, Frehn A, Maier HJ, Rüsing CJ, Niendorf T, Frehn A, Maier HJ (2014) Low-cycle fatigue behavior of TWIP steel—effect of grain size. *Adv Mater Res* 891–892:1603–1608. <https://doi.org/10.4028/www.scientific.net/AMR.891-892.1603>
24. Niendorf T, Lotze C, Canadinc D, Frehn A, Maier HJ (2009) The role of monotonic pre-deformation on the fatigue performance of a high-manganese austenitic TWIP steel. *Mater Sci Eng A* 499(1–2):518–524. ISSN: 09215093. <https://doi.org/10.1016/j.msea.2008.09.033>
25. Klein MW, Smaga M, Beck T, Klein MW, Smaga M, Beck T (2018) Influence of the surface morphology on the cyclic deformation behavior of HSDr 600 steel. *MATEC Web Conf* 165:06010. <https://doi.org/10.1051/mateconf/201816506010>
26. Byun TS (2003) On the stress dependence of partial dislocation separation and deformation microstructure in austenitic stainless steels. *Acta Mater* 51(11):3063–3071. [https://doi.org/10.1016/S1359-6454\(03\)00117-4](https://doi.org/10.1016/S1359-6454(03)00117-4)
27. Klein MW (2022) Einfluss der Oberflächenmorphologie auf das Verformungs- und Schädigungsverhalten von hochmanganhaltigem TWIP Stahl. PhD thesis, Kaiserslautern: TU Kaiserslautern
28. Hamada AS, Karjalainen LP (2010) High-cycle fatigue behavior of ultrafinegrained austenitic stainless and TWIP steels. *Mater Sci Eng A* 527(21–22):5715–5722. ISSN: 09215093. <https://doi.org/10.1016/j.msea.2010.05.035>
29. Hamada AS, Karjalainen LP, Puustinen J (2009) Fatigue behavior of high-Mn TWIP steels. *Mater Sci Eng A* 517(1–2):68–77. ISSN: 09215093. <https://doi.org/10.1016/j.msea.2009.03.039>
30. Hamada AS, Karjalainen LP, Ferraiuolo A, Hamada AS, Karjalainen LP, Ferraiuolo A, Gil Sevillano J, de las Cuevas F, Pratolongo G, Reis M (2010) Hamada fatigue behavior of four high-Mn twinning induced plasticity effect steels fatigue behavior of four high-Mn twinning induced plasticity effect steels. *Metall Mater Trans A* 41(5):1102–1108. ISSN: 1073-5623. <https://doi.org/10.1007/s11661-010-0193-7>
31. Seo W, Jeong D, Sung H, Kim S (2017) Tensile and high cycle fatigue behaviors of high-Mn steels at 298 and 110K. *Mater Charact* 124:65–72. ISSN: 10445803. <https://doi.org/10.1016/j.matchar.2016.12.001>
32. Daniel T, Smaga M, Beck T (2022) Cyclic deformation behavior of metastable austenitic stainless steel AISI 347 in the VHCF regime at ambient temperature and 300°C. *Int J Fatigue* 156:106632. <https://doi.org/10.1016/j.ijfatigue.2021.106632>

33. Jost N, Schmidt I (1986) Friction-induced martensitic transformation in austenitic manganese steels. *Wear* 111:377–389. [https://doi.org/10.1016/0043-1648\(86\)90134-1](https://doi.org/10.1016/0043-1648(86)90134-1)
34. Schmidt I, Wilhelm M (1987) Friction-induced martensitic transformation of hot-rolled austenitic Mn-steels. *Int J Mater Res* 78:127–130. [https://doi.org/10.1016/0043-1648\(86\)90134-1](https://doi.org/10.1016/0043-1648(86)90134-1)
35. Brodyanski A, Klein MW, Merz R, Smaga M, Beck T, Kopnarski M (2020) Microstructural changes caused by friction loading in high manganese TWIP steel and case-hardened 16MnCr5. *Mater Charact* 163:110231. <https://doi.org/10.1016/j.matchar.2020.110231>
36. Rainforth WM, Stevens R, Nutting J (1992) Deformation structures induced by sliding contact. *Philos Mag A* 66(4):621–641. ISSN: 0141-8610. <https://doi.org/10.1080/01418619208201580>
37. Rivière JP, Brin C, Villain JP (2003) Structure and topography modifications of austenitic steel surfaces after friction in sliding contact. *Appl Phys Mater Sci & Process* 76(2):277–283. ISSN: 0947-8396. <https://doi.org/10.1007/s00339-002-1481-x>
38. Fargas G, Roa JJ, Mateo A (2016) Influence of pre-existing martensite on the wear resistance of metastable austenitic stainless steels. *Wear* 364-365:40–47. ISSN: 00431648. <https://doi.org/10.1016/j.wear.2016.06.018>
39. Kim Y-S, Kim S-D, Kim S-J (2007) Effect of phase transformation on wear of high-nitrogen austenitic 18Cr-18Mn-2Mo-0.9N steel. *Mater Sci Eng A* 449-451:1075–1078. ISSN: 09215093. <https://doi.org/10.1016/j.msea.2006.02.294>
40. Hua M, Xicheng W, Jian L (2008) Friction and wear behavior of SUS 304 austenitic stainless steel against Al₂O₃ ceramic ball under relative high load. *Wear* 265(5–6):799–810. ISSN: 00431648. <https://doi.org/10.1016/j.wear.2008.01.017>
41. Alabd Alhafez I, Brodyanski A, Kopnarski M, Urbassek HM (2017) Influence of tip geometry on nanoscratching. *Tribol Lett* 65:1. <https://doi.org/10.1007/s11249-016-0804-6>
42. Bowden FP, Tabor D (1967) Friction, lubrication and wear: a survey of work during the last decade. *Wear* 10(3):245. [https://doi.org/10.1016/0043-1648\(67\)90008-7](https://doi.org/10.1016/0043-1648(67)90008-7)
43. Kramer HS, Starke P, Klein M, Eifler D (2014) Cyclic hardness test PHYBALCHT—Short-time procedure to evaluate fatigue properties of metallic materials. *Int J Fatigue* 63:78–84. ISSN: 01421123. <https://doi.org/10.1016/j.ijfatigue.2014.01.009>
44. Basa A, Thaulow C, Barnoush A (2014) Chemically induced phase transformation in austenite by focused ion beam. *Metall Mater Trans A* 45(3):1189–1198. <https://doi.org/10.1007/s11661-013-2101-4>

Applications

Manufacturing of Areal Material Measures



Jörg Seewig, Georg von Freymann, Jan C. Aurich, Matthias Eifler, Julian Hering-Stratemeier, and Katja Klauer-Dobrowolski

Abstract Whereas the profile-based measurement and the calibration of the corresponding measuring instruments has been applied for a long time, the discipline of areal surface topography measuring instrument calibration still faces challenges. In the CRC 926, the design of corresponding material measures which can map the metrological characteristics to be considered in areal surface topography measurement just as well as the manufacturing of areal material measures using micro-milling and direct laser writing were examined. The results of different parameter studies for the design and manufacturing are presented in the following.

1 Areal Calibration of Measuring Instruments

1.1 Introduction

Profile surface texture measurement $z(x)$ has been applied for a long time and there is a lot of industrial experience. When complex, deterministic surfaces with individual features are of interest, an areal measurement, which is often also referenced as “2.5D” measurement since it leads to a topography height map $z(x, y)$ of the surface as a function of two lateral axes, is often beneficial. Areal surface texture measurement is comparatively young and the results of the first two key European projects on areal surface texture measurement were achieved starting in the 1990’s and published in the so-called “Blue Book” [1] which proposed the “Birmingham 14” parameter set and the “Green Book” [2] which extended the knowledge in areal

J. Seewig (✉) · M. Eifler

Institute of Measurement and Sensor Technology, RPTU Kaiserslautern, Kaiserslautern, Germany
e-mail: j.seewig@mv.rptu.de

G. von Freymann · J. Hering-Stratemeier

Institute of Optical Technologies and Photonics, RPTU Kaiserslautern, Kaiserslautern, Germany

J. C. Aurich · K. Klauer-Dobrowolski

Institute of Manufacturing Technology and Production Systems, RPTU Kaiserslautern, Kaiserslautern, Germany

characterization. After these first scientific results in areal surface texture measurement were published, Working Group 16 “Areal and profile surface texture” of the ISO Technical Committee 213 was formed in 2003 [3]. Since then, the ISO 25178 series of standards “Geometrical Product Specification: Surface Texture: Areal” has been developed to achieve a comprehensive standardization of the areal surface texture measurement and the standard ISO 25178 part 2 which describes the relevant surface texture parameters was first published in 2012 [4]. The industrial application of areal surface texture measurement is relatively young and still today, profile surface texture measurement remains the most common form of characterization in industrial application, even though a growing incidence of areal measurement has been observed since the work on the standardization has commenced [5]. Due to the otherwise extensive measurement time, areal surface texture measurement is most often also an optical measurement which means that with the emergence of areal surface texture evaluation not only the mathematical representation of the data changed, but also the physical principle of the measurement, introducing new challenges and an increased modeling complexity when compared to stylus instruments [6].

One topic of interest is the calibration of the surface topography measuring instruments which “establishes a relation between the quantity values with measurement uncertainties provided by measurement standards and corresponding indications with associated measurement uncertainties” [7]. This means that the measurement of “measurement standards,” in geometric applications also referenced as “material measures” enables a calibration and subsequently an adjustment of the measuring instrument and also allows a traceability with regard to the basic unit of length as e.g. described by Leach et al. [8]. Thus, the process of calibration is essential for the industrial application of surface topography measuring instruments. The ISO calibration framework generally consists of three different aspects: (i) the material measures to map defined characteristics, (ii) the definition of these characteristics and (iii) the routines and evaluations for the actual calibration.

For profile applications, there is a lot of experience and all different aspects have been standardized: the material measures are described in ISO 5436-1 [9], the properties and calibration routines for stylus instruments in ISO 12179 [10] and also many international comparison measurements have been conducted [11].

Due to the additional axis of the instrument, areal calibration is more complex than profile calibration and in the past decades, extensive research was dedicated to this topic resulting in the current status of the standardization: The material measures to allow a determination of the properties to be calibrated are standardized in ISO 25178-70 [12]. The properties to be calibrated are referenced as the metrological characteristics and are described in the standard series ISO 25178-60x [13]. The calibration itself is described in the ISO 25178-70x series [14]. Parts –600 and –700 address the basic metrological characteristics and their calibration, parts –601 ff. and –701 ff. the characteristics that are specific for different measurement principles. Figure 1 summarizes the current state of standardization.

	Surface texture: Profile method	Surface texture: Areal
geometries for calibration	Material measures ISO 5436	Material measures ISO 25178-70
properties to be calibrated	Calibration of contact (stylus) instruments ISO 12179	Metrological characteristics ISO 25178-60x
calibration routines		Calibration and verification ISO 25178-70x

Fig. 1 The ISO standardization of calibration contains of the applied material measures, the properties to be calibrated and the calibration routines. Modified from [11]

1.2 Challenges

Since areal calibration is a relatively young scientific discipline, there are still many challenges that need to be addressed. The following main challenges can be currently identified:

(i) Definitions and standardization are under dispute

One challenge is the previously mentioned standardization has neither reached a final state nor has been broadly established in the industrial application. The first standards and guidelines, like the VDI VDI 2655 [15, 16], were based on the previously available approaches used in profile stylus measurement before the approaches that are specifically applicable for an areal calibration as described in the previous section were developed. However, the corresponding definitions and standardization are still young and many terms and approaches are still under discussion within the scientific community.

(ii) Design of areal material measures

Since new, areal properties like the x - y mapping deviation have been introduced within the calibration process, also corresponding material measures that can map the corresponding characteristics need to be designed. Some suggestions have been already made in the “Green Book” [2] and have been standardized in the standard ISO 25178-70 [12]. However, the design process of e.g. the areal irregular material measure which is the areal equivalent to the profile roughness material measure, has been examined in different studies, e.g. in [17] and depending on the application needs to be customized with regard to the examined areal surface texture parameter or the measurement application [18].

(iii) Manufacturing of areal material measures

Ultra-precision turning is a common process for the manufacturing of profile material measures [19, 20] just as well as etching [21] and grinding [22, 23]. Since different surface topographies are required to calibrate the metrological characteristics of areal surface topography measuring instruments, also new challenges for their

manufacturing arise. To manufacture areal material measures that feature a defined roughness, e.g. the process of lapping has been examined [24, 25]. Other researchers have examined chipping processes like micro-milling to manufacture deterministic rough surfaces that feature defined stochastic characteristics [17] or combined this process with an electroforming for replication [26]. Also, Focused Ion Beam (FIB) [27], electron beam lithography [28, 29] and direct laser writing have been applied [30].

(iv) Concepts for areal traceability

Ideally, properties need to be established that allow an areal traceability independent from the measuring principle. One corresponding characteristic is the topography fidelity which can be applied for both tactile and optical surface topography measuring instruments [31].

1.3 Metrological Characteristics According to ISO 25178-600

The basic metrological characteristics as defined in ISO 25178-600 are the amplification coefficients, linearity deviations, flatness deviation, measurement noise, topographic spatial resolution, x - y -mapping deviation and topography fidelity [13]. A first, comprehensive approach for the determination of the basic metrological characteristics was described by Giusca, Leach et al. [32–34] and recently a review of the developments in the field of the basic metrological characteristics was presented by Leach et al. [35]. The basic metrological characteristics directly contribute to the measurement uncertainty of the applied surface topography measuring instrument and are defined as “characteristic of measuring equipment, which can influence the results of measurement” [13].

The individual characteristics are defined as follows:

The amplification coefficients and the linearity deviations are obtained from the response functions of the x -, y - and z -axis as illustrated in Fig. 2. Different, known values for the coordinate of a certain axis are measured as exemplary illustrated for the height axis. Subsequently, the measured height values are imaged as a function of the actual height values. An ideal transfer behavior would therefore represent a straight line with a slope of 1. The amplification coefficient is the slope which is obtained when a regression function is fitted into the response function and the linearity deviation equals the maximum local difference between this fit and the original data [13]. Both parameters can thus be determined for each axis x , y , z .

The flatness deviation is defined as “deviation of the measured topography from an ideal plane” [13] and the measurement noise is the noise which is added to the topography dataset by the measuring instrument when it is applied in a typical measurement task [13].

The topographic spatial resolution is generally defined as “metrological characteristic describing the ability of a surface topography measuring instrument to

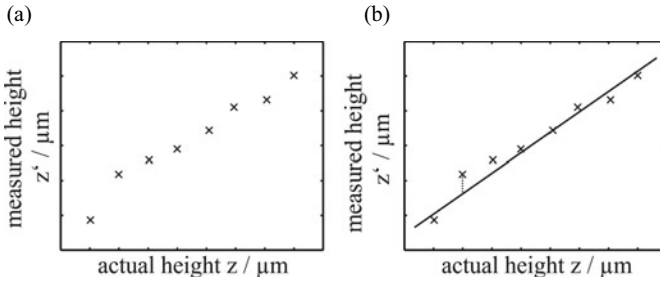


Fig. 2 **a** The response curve of the height axis can be determined by measuring multiple height values and subsequently plotting the measured height as a function of the actual height. **b** A straight line fit of the response curve leads to the value of the amplification coefficient and linearity deviation. Modified from [3]

distinguish closely spaced surface features” [13] and is in practice most often implemented similar to the cut-off wavelength of a filter by setting a threshold value of a 50% transmission [34].

Another metrological characteristic that is associated to the resolution capabilities of a surface topography measuring instrument is the topography fidelity, which describes the “closeness of agreement between a measured surface profile or measured topography and one whose uncertainties are insignificant by comparison” [13]. An associated definition that is often applied is the small-scale fidelity limit which describes the “smallest lateral surface feature for which the reported topography parameters deviate from accepted values by less than specified amounts” [13]. A first implementation of this criterion was described by Seewig et al. in 2014 based on the application of a chirp material measure [31].

A criterion that solely addresses the lateral axes of the surface topography measuring instrument is the x-y mapping deviation, a “gridded image of x- and y- deviations of actual coordinate positions on a surface from their nominal positions” [13] which can thus describe the local image distortion in the measured plane.

The described set of basic metrological characteristics provides the base for the comprehensive calibration of areal surface topography measuring instruments. Associated calibration processes are standardized in the ISO 25178-70x series which will be introduced subsequently.

1.4 Calibration According to ISO 25178-700

The ISO 25178-700 [14] standard defines methods for the calibration of the metrological characteristics of areal surface topography measuring instruments as briefly described in Sect. 1.3. The term calibration is defined in the International Vocabulary of Metrology [7] as follows:

- Establish a relationship between a quantity value provided by a measurement standard (material measure) and the corresponding indication of the measuring instrument (including uncertainties of the measurement standard and the measurement);
- use this information to establish a relation for obtaining a measurement result from an indication.

With the information provided by the calibration procedure an adjustment of a measuring instrument can be carried out, for example to correct a linearity deviation. Calibration of a measuring instrument is therefore mandatory in order to obtain reliable measurement results. In ISO 25178-700, calibration methods are defined for noise, flatness deviation, amplification, linearity deviation and x - y mapping deviations. For each of these metrological characteristics a default method for the determination of its value is defined. For example, the instrument noise is determined as follows: Measure a smooth and flat surface twice at the same location. The time interval between the two measurements shall be short as possible. Subtract both measurements from each other and if needed, subtract a plane from the difference data set. Calculate the standard deviation S_q according to [36] and divide S_q by $\sqrt{2}$. Similarly defined are the methods for the other metrological characteristics described in ISO 25178-600. The material measures required for calibration are standardized in ISO 25178-70 [12] (see also Sect. 1.5). ISO 25178-700 states, that the material measure shall be selected by taking into account the characteristics of the surface to be measured, i.e., to be as close as possible to the measuring task. Most of the standardized material measures do not fulfil this requirement. For example, calibration of the measurement noise on a flat surface says nothing about the measurement noise that occurs measuring a real surface component. A mathematical method to design realistic material measures that are closely related to the actual measurement task is introduced in Sect. 2.1.

1.5 Material Measures According to ISO 25178-70

The standard ISO 25178-70 defines various types of material measures for the calibration of surface topography measuring instruments. Since the profile method using stylus instruments has been commonly applied for a long time, there is a lot of experience with the associated calibration routines. The profile material measures defined in ISO 5436-1 are also included in ISO 25178-70 and are summarized in Fig. 3. The following types can be distinguished:

- Type PPS (Periodic Sinus Structure): This material measure is commonly available and also included in the profile standard ISO 5436-1 as type C1 [9]. When the wavelength of the sine wave is varied, the chirp material measure results [19, 37], which can be applied to characterize the transfer behavior of a surface topography measuring instrument and to determine the topography fidelity [31]. The most common manufacturing principles for chirp material measures are ultra-precision turning processes [19].

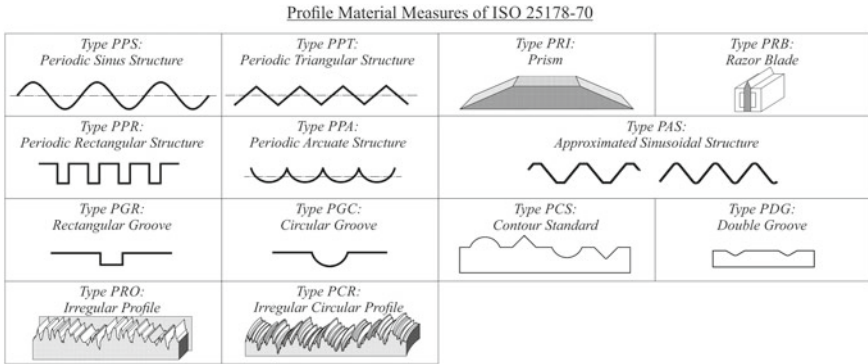


Fig. 3 The types of material measures featuring a profile geometry is summarized. Modified from [51]

- Type PPT (Periodic Triangular Structure): Also this periodic geometry is commonly used for the calibration of the lateral axes and also described as type B2 material measure in the profile standard [9]. Frühauf and Krönert describes a possible manufacturing process based on etching [21].
- Type PPR (Periodic Rectangular Structure): Material measures with a rectangular grating can also be used for a resolution determination as previously investigated in [38] and can be as well manufactured with the aid of etching [39].
- Type PPA (Periodic Arcuate Structure): Also this periodic structure can be manufactured with the aid of etching processes [39].
- Type PGR (Rectangular Groove): These material measures are commonly known as step height standards, included as type A1 in ISO 5436-1 [9], usually machined by ultra-precision turning [40], and applied for the calibration of the height axis. For this application, also various comparison measurements have been conducted [41]. In practice, most often either a set of step height material measures or an almost step-less calibration of the height axis are applied [42–44].
- Type PGC (Circular Groove): This material measure is not only included in ISO 25178-70, but also defined as type A2 in ISO 5436-1 [9]. Its round-shaped groove is more suitable for an application with optical measuring instruments [15].
- Type PRO (Irregular Profile) & Type PCR (Irregular Circular Profile): These profile material measures are also often referenced as roughness material measures, are type D1 and D2 of ISO 5436-1 and typically map defined values of profile surface texture parameters like R_a and R_q [20, 22, 23, 45–47]. There are different methods to generate a defined, rough profile surface texture like ultra-precision turning [20, 44], grinding [23] or nanogrinding [47].
- Type PRI (Prism): this material measure that can be used to calibrate the definition of the coordinate system and is also a part of ISO 5436-1 as type E2 [9].
- Type PRB (Razor Blade): This material measure known as type B3 of ISO 5436-1 is most commonly used for the calibration of stylus instruments and allows a characterization of the state of a tip [48].

Areal Material Measures of ISO 25178-70

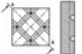





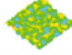
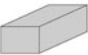



<i>Type AGP:</i> <i>Perpendicular Grooves</i> 	<i>Type AGC:</i> <i>Circular Groove</i> 	<i>Type ARS:</i> <i>Radial Sinusoidal</i> 	<i>Type ASG:</i> <i>Star-shaped Grooves</i> 
<i>Type ASP:</i> <i>Sphere</i> 	<i>Type APS:</i> <i>Plane-Sphere</i> 	<i>Type AIR:</i> <i>Irregular Surface</i> 	<i>Type AFL:</i> <i>Plane Surface</i> 
<i>Type ACG:</i> <i>Cross-Grating</i> 	<i>Type ACS:</i> <i>Cross-Grating Sinusoidal</i> 	<i>Type APC:</i> <i>Photochrome Pattern</i> 	

Fig. 4 The types of areal material measures as defined in ISO 25178-70, featuring an areal geometry is summarized. Modified from [51]

- Type PAS (Approximated Sinusoidal Structure): The material measure is available with various parameter values and is another periodic geometry allowing the calibration of the lateral axes [13].
- Type PCS (Contour Standard): This geometry features different contours and was described and examined for the calibration of tactile and optical Coordinate-measuring machines by the PTB [49].
- Type PDG (Double Groove): This geometry addresses different instrument axes and was described by Ville [50].

The second set of material measures defined in ISO 25178-70 are areal material measures and the different basic types are summarized in Fig. 4:

- Type AGP (Perpendicular Grooves) and Type AGC (Circular Grooves): These two types of material measure define areal versions of grooves and were already mentioned in the “green book” [50].
- Type ASP (Sphere): This material measure is also defined in ISO 5436-1 as type E1 and can be used for a calibration of contour measuring instruments [52, 53].
- Type APS (Plane-Sphere): the calibration abilities of this combined material measure were described by Ville [50].
- Type ACG (Cross-Grating): This type of material measure features a grid of dales and can be used for a simultaneous calibration of both lateral axes of areal surface topography measuring instruments [12, 33].
- Type ACS (Cross-Grating Sinusoidal) and Type ARS (Radial Sinusoidal): Not only rectangular, but also sinusoidal areal gratings are defined in the standard which can for example serve to characterize the overall instrument behavior by mapping a defined value of areal surface texture parameters like S_a and S_q [12].
- Type ASG (Star-shaped Grooves): This material measure is also known as “Siemens Star” and used to determine the topographic spatial resolution as for example described in previous investigations [5, 34, 54].
- Type AIR (Irregular Surface): This type of material measure is applied similar to the profile roughness material measures and maps defined values of the areal

surface texture parameters [12]. Since the fabrication of an irregular, areal surface topography is challenging, different manufacturing principles like lapping [24], micro-milling—which can also be combined with a subsequent electroforming [17, 26], focused ion beam (FIB) [27], electron beam lithography [28, 29] and direct laser writing [30] have been examined for their manufacturing.

- Type AFL (Plane Surface): The flatness material measure is used to determine both the flatness deviation and the measurement noise [32, 55, 56].
- Type APC (Photochromatic Pattern): This type of material measure does not feature a defined surface topography and is used to calibrate the determination of intensity distributions [12].

2 Model Based Design of Material Measures

The key issue of the model based design of material measures is the mathematical description of a so-called signal chain consisting of all steps required to manufacture the material measures, i.e., starting with the control data set for a suitable manufacturing process up to the target topography to be manufactured with defined geometrical properties (see Fig. 5). Afterwards, the unknown control data set for the manufacturing process has to be calculated from a known target topography. For this, an inverse problem must be solved.

The model based design of material measures starts with a reference topography with specific geometrical properties and the specification of the target parameter values, e.g. defined values for the surface texture parameters S_a , S_q , S_z , S_k , S_{pk} , S_{vk} or any possible parameter or parameter combination. The target topography can be calculated, for example, using the design technique described in Sect. 2.1. Three main operations are performed between the control data set for manufacturing and the target topography: The first operation simulates the manufacturing process, for example a turning process which can be performed by a morphological erosion using the geometry of the turning tool as the structuring element (see also Sect. 2.2). The second operation simulates the measuring process. In case of a tactile system, for example, a mathematical morphological dilatation is applied where the structuring element has the geometry of the stylus tip used for the sampling process. When optical surface topography measuring instruments are used, an estimation of their

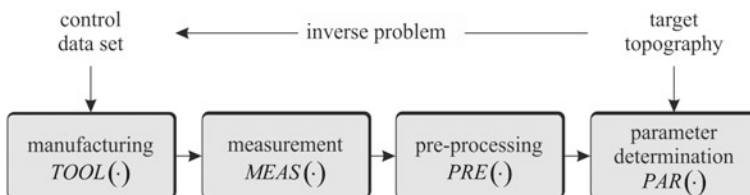


Fig. 5 Signal chain for the design of material measures

transfer function can be applied for the prediction of the measured surface topography (see Sect. 2.2). The third operation is a signal pre-processing step, which consists for example of an F-operation (see Chap. 2) and/or a combination of a high-pass filter (L-filter) and low-pass filter (S-filter). After processing the various steps, the target topography must be satisfied.

A mathematically challenging step is to invert the signal chain to calculate the unknown control data set from the known target topography. The formalism required for this depends on the individual mathematical description of the transmission blocks of the given signal chain. As an example, a high-pass filtering operator is considered. A high-pass is often implemented in such a way that in a first step the input signal is low-pass filtered by the operator flt and in a second step the low-pass filtered input signal is subtracted from the input signal itself. In our case the high-pass filtered signal z_{tar} is assumed to be known and the corresponding input signal $z_{src} = z_{tar} + \Delta z_{src}$ has to be calculated.

$$z_{tar} = z_{tar} + \Delta z_{src} - flt(z_{tar} + \Delta z_{src}). \quad (1)$$

The unknown deviation Δz_{src} can be calculated iteratively using the steepest gradient method [57]. Let Δz_{src}^i the i^{th} iteration step. The algorithm starts with $\Delta z_{src}^0 = 0$. The iterative algorithm is given by

$$\Delta z_{src}^{i+1} = \Delta z_{src}^i + \lambda (\Delta z_{src}^i - flt(z_{tar} + \Delta z_{src}^i)) \quad (2)$$

where $0 < \lambda < 1$ is a damping factor which should be chosen carefully. The iteration stops if the residuals $\Delta z_{src}^{i+1} - \Delta z_{src}^i$ are sufficiently small. This gives the result $z_{src} = z_{tar} + \Delta z_{src}^{i+1}$.

In summary, a model-based design of a material measure is carried out as follows:

- Select appropriate surface texture parameters,
- measure a real surface or simulate a surface with a specified texture,
- choose a suitable manufacturing process for the material measure,
- describe the signal chain from the control data set up to the target topography,
- solve the inverse problem to determine the control data set for the manufacturing process.

2.1 Mathematical Design of Material Measures

Material measures according to ISO 25178-70 often represent a deterministic, non-realistic surface topography in order to calibrate a specific metrological characteristic of a measuring instrument. For the characterization of a component surface, it is crucial that the calibration is performed with a material measure whose surface texture is as similar as possible to the surface texture to be tested. In particular, the surface texture parameters should also be of a similar order of magnitude. For this purpose,

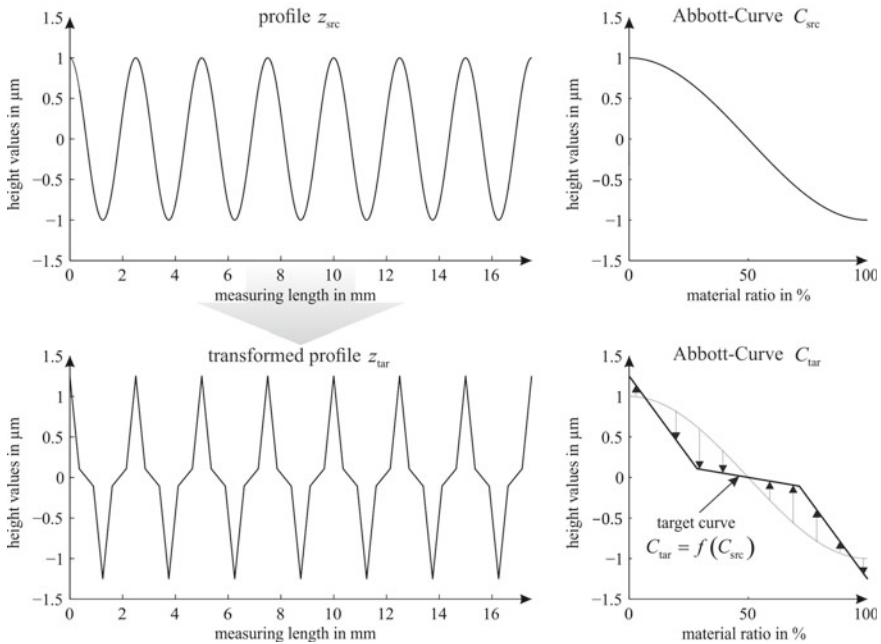


Fig. 6 Transformation of a sinusoidal profile into a piece-wise linear profile

a special method was developed to transform a map of a real surface topography in such a way that a predefined Abbott-Curve is obtained. This method is described in detail in [58] and is briefly outlined in the following. For simplicity the method is discussed for a profile trace. Consider the Abbott-Curve C_{src} of a profile trace z_{src} of a sinusoidal surface (see Fig. 6). One way to calculate the Abbott-Curve is to sort the profile values in descending order. In this case, each value z_{src} corresponds to a certain position $C_{src,k}$ within the Abbott-Curve C_{src} . Define a mapping $C_{tar} = f(C_{src})$ such that a target Abbott-Curve C_{tar} results (see Fig. 6). The corresponding target profile z_{tar} can be reconstructed from C_{tar} by using the origin positions from $z_{src,k}$.

This approach enables the design of arbitrary profile characteristics. Geometrical features like hills and dales of the original profile trace z_{src} are preserved because the position of the profile values has not changed as a result of the transformation process. To show this, a profile of a plateau-honed surface is considered in Fig. 7. The mapping $C_{tar} = f(C_{src})$ is designed as follows: both the peak area and the core roughness of the profile are increased and the grooves are decreased. The transformed profile is shown in Fig. 7. As mentioned before, the geometrical profile characteristics are preserved.

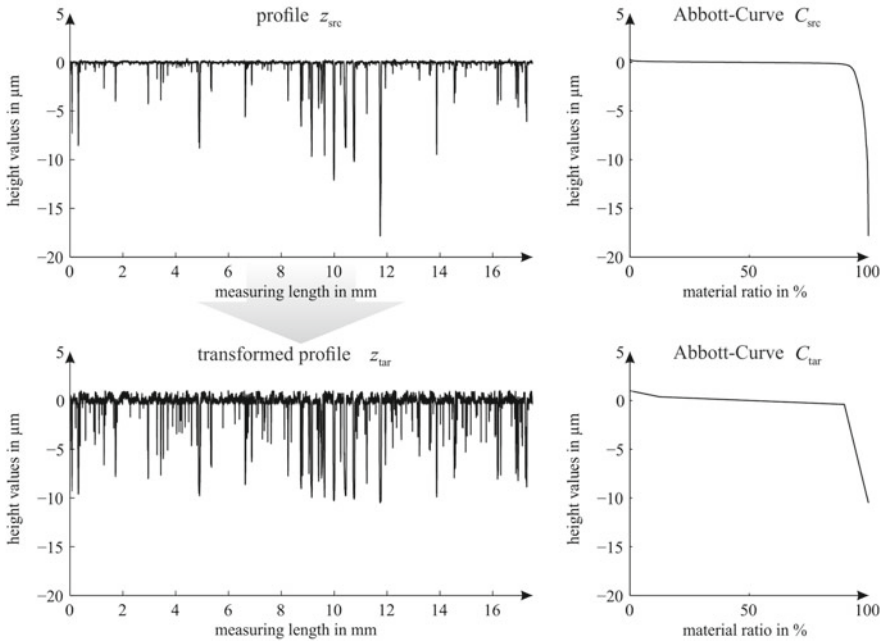


Fig. 7 Transformation of a plateau-honed surface profile

2.2 Modeling

For the implementation of the described approach of a model-based design of material measures, a modeling of the individual steps of the signal chain is required which includes both the manufacturing and the measuring process. The manufacturing process has been described as operator $TOOL(\cdot)$ in Fig. 5. As a first manufacturing process for areal material measures, ball end micro-milling was chosen and a corresponding model was implemented [18]. In previous studies of profile material measures, the process of ultra-precision turning, a process which can be simulated by a morphological filtering with the tool's geometry, was applied [44]. This general principle is illustrated in Fig. 8a. For micro-milling, an areal morphological filtering was used for the modeling of the process. As a structuring element, a sphere featuring the diameter of the milling tool was applied. Descriptively, the process applies a filter that removes structures that could not be manufactured with the dimensions of the applied tool from the areal surface topography of the material measure. Other physical considerations of the manufacturing process like kinematics and physics are not taken into account, this integral approach solely considers geometrical aspects with the aid of a common method originating from signal processing [44]. The result is that the modeling of the manufacturing process can be implemented with a significantly reduced computational effort in comparison to a comprehensive, physical

(a) Turning modeled by morphological filtering (b) Micro milling - morphological approach

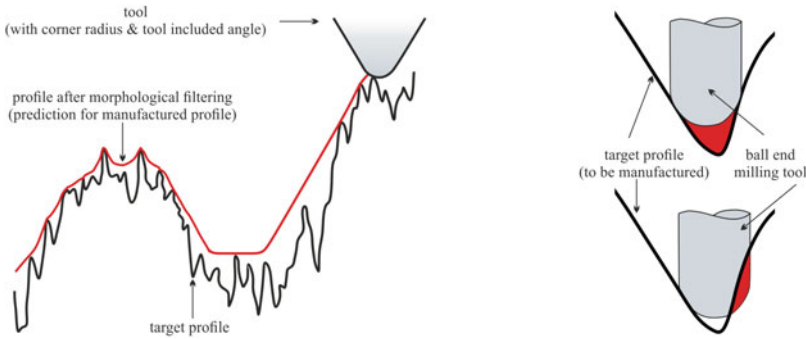


Fig. 8 Virtual manufacturing with morphological filtering. Both ultra-precision turning and micro-milling can be approximated with morphological filtering. Modified from [59]

modeling of the machining. As the virtual manufacturing is repetitively performed during the iteration of the design process described above, a computationally efficient implementation is important. The process of morphological filtering for the modeling of micro-milling is illustrated in Fig. 8b.

For the implementation, the areal morphological filtering similar to the profile-based description as defined in the standard ISO 16610-41 was used to perform a segmentation of surface texture elements that can be manufactured with the applied tool geometry [60]. Mathematically, the virtually manufactured surface topography Z_{man} is defined as a morphological closure of the designed surface topography Z_{t1} after the transformation with the structuring element, the tool geometry Z_{SE} consisting of an dilatation followed by an erosion:

$$Z_{man} = TOOL(Z_{t1}) = (Z_{t1} \otimes Z_{SE}) \odot Z_{SE}. \tag{3}$$

The procedure can be adapted to various tool geometries and radii that have been applied during different studies described below in order to map a desired range of spatial frequencies in the resulting material measures [44].

For the modeling of the measurement process, a model developed in previous work was applied [61]. This approach uses an auto-regressive moving average (ARMA) filter which is fitted to determine the transfer function of a surface topography measuring instrument and is first described for a profile-based approach [61]. In doing so, a known geometry of a profile material measure $u(x)$ is used as input quantity and the measured surface topography $z(x)$ as the output quantity. The conversion from the nominal to the measured data set can be described by the transfer function of the instrument. When an ARMA filter is selected as an approach, the conversion, i.e., the filter behavior in the frequency domain can be described based on a set of coefficients $AK[k]$ and $MA[l]$ [61]:

$$v(\Omega) = \frac{\mathbf{Z}(\Omega)}{\mathbf{U}(\Omega)} = \frac{\sum_{l=0}^q MA[l] \cdot e^{-i \cdot \Omega \cdot l}}{1 + \sum_{k=1}^p AR[k] \cdot e^{-i \cdot \Omega \cdot k}} \quad (4)$$

A determination of the coefficients is for example possible with the well-known Yule-Walker equations. The general working principle just as well as transfer functions of different measuring principles that were determined using the approach are summarized in Fig. 9a (exemplary for $q = 2$ and $p = 2$). In previous work it has been shown that with the determination of a digital filter as a linear approximation

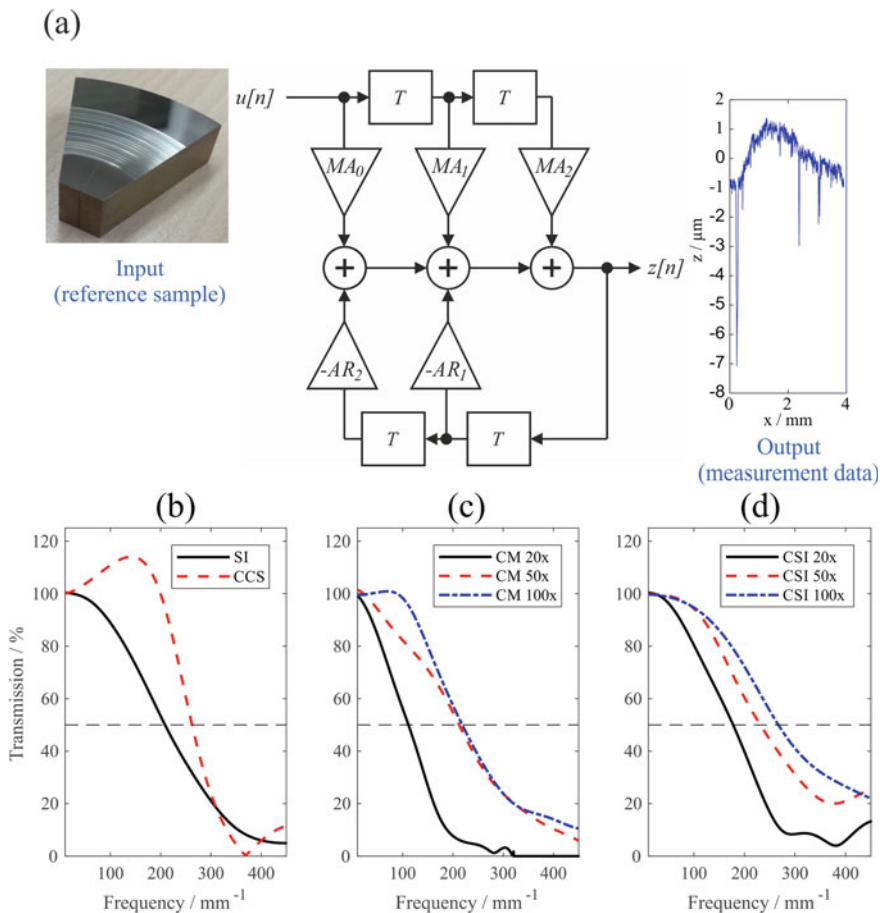


Fig. 9 Virtual measurement. The figure summarizes different transfer functions that were obtained by fitting an ARMA filter to approximate the behavior of surface topography measuring instruments. SI—stylus instrument, CCS—chromatic confocal microscope, CM—confocal microscope, CSI—coherence scanning interferometer, modified from [61]

for the transfer behavior good results for virtual measurements can be achieved for different types of surface topography measuring instruments like stylus instruments, confocal microscopes and coherence scanning interferometers [61–64]. The determined transfer functions can serve as a base for virtual measurements, as based on the convolution theorem a multiplication in the frequency domain can be used for implementation. In doing so the discrete Fourier transform of the surface topography and the transfer function are multiplied, before an inverse discrete Fourier transform is executed to determine the virtually measured surface topography. As a linear filter behavior is assumed, the areal filtering is implemented by calculating a line-wise and column-wise filtering of all individual profiles of the areal surface topography.

Since an iterative design process is performed, also a computationally efficient implementation of the virtual measurement is essential. The measurement process has been described as operator MEAS(\cdot) in Fig. 5. The linear ARMA filter allows an estimation of the filter behavior that is caused due to the physical effects during the measurement. Wavelengths that cannot be fully transmitted by the surface topography measuring instrument are removed from the data set or reduced in amplitude. Figure 9b–d summarizes different transfer functions of surface topography measuring instruments, that were obtained with the aid of the described method, including the measurement principles of a confocal chromatic sensor (CCS), stylus instrument (SI), confocal microscope (CM) and coherence scanning interferometer (CSI) featuring different objective lenses, demonstrating the ambiguity of the approach. For the measurements of the described studies, most often a confocal microscope was applied and the virtual measurement was described using the associated transfer function resulting from the ARMA modeling approach.

3 Manufacturing of Areal Material Measures

Since a precise manufacturing of material measures is crucial for all the aforementioned calibration tasks and applications, there are very high requirements for the respective manufacturing techniques. It has to be ensured that the manufactured micro-structures correspond to their target designs as good as possible. At least the surface quality of the manufactured material measures with regard to the quantities to be calibrated must exceed the precision of the respective measuring instruments that can be derived from the identical metrological characteristics. Expressed by a simplified example: the resolution of the manufacturing method for manufacturing a resolution-calibrating structure has to be better than the resolution of the measuring instrument to be calibrated. Unfortunately, no manufacturing technique has the claim to be entirely free of deviations.

Within the Collaborative Research Centre 926, the researchers investigated and optimized two specific manufacturing techniques which allow the manufacturing of areal material measures not only in an acceptable, but outstanding and partially unique quality:

- Micro-Milling and
- Laser Lithography.

The most important scientific achievements and applications regarding both techniques during the last years will be discussed in the following sections.

3.1 Micro-milling

This section first outlines micro-milling as a manufacturing process with the corresponding advantages for the manufacturing of areal material measures. The procedure used to design the process and optimize the process parameters for the manufacturing of areal material measures with novel calibration structures designed with the aid of the approach of Sect. 2 is then described.

3.1.1 Ball End Micro-milling

Milling is an important manufacturing process because of its high flexibility and relatively low costs. For the manufacturing of free-form surfaces, numerical controlled (NC-) milling is very suitable [65]. When manufacturing those free-form surfaces [66] or concave surfaces [65, 67] ball end mills are used. However, a few special characteristics must be considered when using ball end milling tools (see Fig. 10): Between the milling tool and the work-piece a tilt angle is set so that the area of the cutting edge where the cutting speed is zero is not engaged. It is also special that the spherical cutting edge produces a crescent-shaped chip, and in some areas of the engaged cutting edge, the minimum chip thickness h_{min} is not reached. This situation is unavoidable, but leads to poorer surface qualities in the area where the material is ploughed, which is why it must be taken into account in the design of the process.

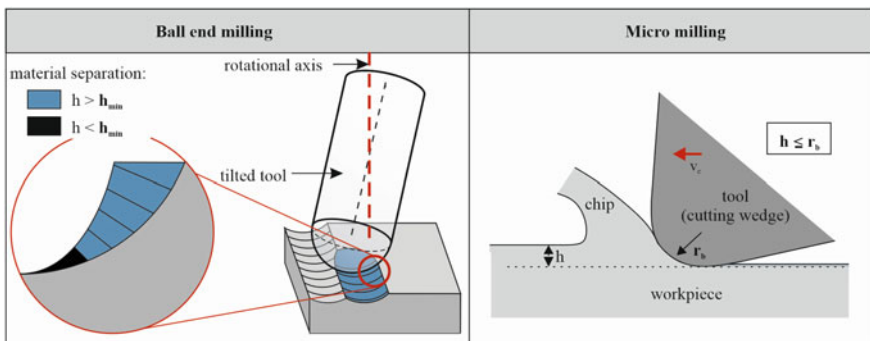


Fig. 10 Characteristics and material separation of ball end milling. Modified from [68] according to [65, 69, 70]

The influence of conventional ball end milling on the resulting surface quality of the manufactured component has already been very well studied: The main influences on the resulting surface quality are the feed per tooth, the distance between two tool paths, the cutting depth, the diameter of the milling tool and the tilt angle—see for example the results from SPP 1057 [65, 66, 69, 71, 72].

Nevertheless, the conventional ball end milling is not suitable for the manufacturing of areal material measures since the conventional ball end mills are too large to map sufficiently small structure sizes, i.e., spatial frequencies. However, the use of micro-tools and the corresponding machine tools create the possibility to manufacture structures that feature sufficiently small scales. Initial feasibility studies for the manufacturing of areal material measures by micro-milling have already been investigated. Nemoto et al. [17] and Leach et al. [26] manufactured areal material measures in NiP layers using diamond micro-milling tools with a minimum diameter of 50 μm or larger. In both cases, very promising results were obtained, but no systematic process design as well as transfer to further calibration structures followed [17, 26].

One main objective in CRC 926 was therefore the systematic investigation and design of the micro-milling process for the manufacturing of areal material measures. For this purpose, the relevant influencing variables on the surface topography first had to be investigated in order to subsequently ensure transferability to other calibration structures or even other tools. The influencing variables that were already mentioned above, which are known from conventional machining, provide a good starting point for the investigation. However, their respective influence cannot be completely transferred to micro-machining, since size effects have to be considered [73]. Basic investigations on micro-milling can also be found in Sect. 3 and [70].

3.1.2 Experimental Setup

For the experimental studies, a 5 axes micro-milling machine tool LT Ultra MMC 600 H¹ was used. This machine tool provides a Levicron ASD-80-H25¹ spindle, which allows spindle speeds of 80,000 rpm. Two different tools were used, which differ for almost all of their characteristic properties. They have different tool materials or coatings, cutting edge radii, number of cutting edges, and effective cutting edge radii (see Fig. 11). The aim of using such different tools was to identify the influence of the milling tool when varying the remaining parameters as clearly as possible. Only if the influence of the tool is known, the designed and aligned process and the knowledge about it can be transferred to new tools in further investigations.

Tool *T* 1 is a single-edged diamond tool with an effective cutter radius of 100 μm and *T* 2 is a two fluted cemented carbide tool with an effective cutter radius of 50 μm .

¹ Naming of specific manufactured is done solely for sake of completeness and does not necessarily imply an endorsement of the named companies nor that the products are necessarily the best for the purpose.

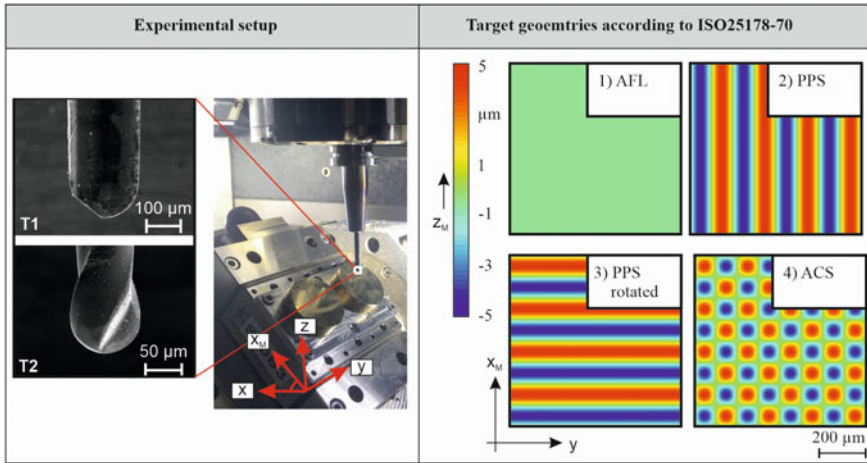


Fig. 11 Experimental setup and target geometries (areal material measures) for experimental studies. Modified from [68, 74]

The design and alignment of the micro-milling process and the investigation of the main influencing factors were carried out by manufacturing standardized areal material measures with periodic structures. Using these periodic structures, deviations from the nominal geometry can be detected more clearly. In order to investigate different target geometries with convex or concave structural details, four material measures according to ISO 25178-70 were selected [12].

Based on existing studies (see Sect. 3.1.1) on the influencing variables in ball end milling or micro-milling, it was decided which process parameters should be considered in the experimental design. Since for most influencing factors no linear influence on the quality of the resulting surfaces is assumed, the corresponding parameters have to be tested with more than two steps. This resulted in the following experimental effort (see Fig. 12): a full factorial experimental design would result in 72,000 trials. Knowing that, depending on the feed rate, the manufacturing of one material measure takes 0.5–1 h, this results in a production time of four or eight years, if the machine runs 24 h a day. Therefore, it is necessary to define an experimental design in which the number of experiments is reduced.

3.1.3 Superposition Study: Influence of Process Parameters and Process Design

A superposition study was performed (see Fig. 12). This means that certain parameters were initially examined within sub-studies, while the remaining parameters were held constant. Within these sub-studies, it was investigated which setting of the investigated parameters leads to the best surface quality. This means:

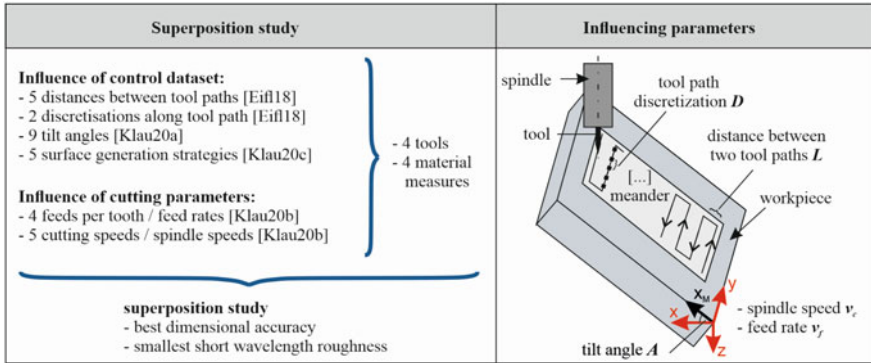


Fig. 12 Superposition study: tested parameters which influence process result. Modified from [75]

- smallest deviation from the target geometry,
- smallest short-wavelength roughness along the manufactured structure (smooth surface).

The parameter values that fulfilled the described requirements were then combined by superposition to form an overall setup. This overall setup was then again used to manufacture areal material measures, which were subsequently evaluated once more on the basis of the aforementioned criteria.

The results of the superposition study were very promising as shown in Fig. 13. The evaluation was done as described in [74, 75]: The manufactured geometries were measured four times each with the confocal microscope NanoFocus μ Surf¹. The lens features a 20x magnification, a numerical aperture of 0.6, and a field of view of $800 \mu\text{m} \times 800 \mu\text{m}$. The measured topographies were aligned with a plane fit and an evaluation area of $600 \mu\text{m} \times 600 \mu\text{m}$ was extracted. For this evaluation area, two different evaluations were performed. To investigate the dimensional accuracy of the manufactured structures, the parameters S_a and S_q were evaluated according to ISO 25178-2 [36]. For the sinusoidal structures, the wavelength and amplitude define the nominal values for S_a and S_q , which can be calculated analytically. However, for calculating the target values it was considered that for example the distance between two tool paths during micro-milling process results in slight deviations from the analytically calculated value. The target value was therefore always determined for the target topographies (the data set of the NC-code) and used as reference (see red lines in diagram in Fig. 13). As a second analysis, the very short wavelength deviations from the target geometry were also investigated. For this purpose, the wavelengths of the sinusoidal structure were removed from the measured topography by filtering [75]. The results of this superposition study can be found in detail in [76] and are summarized in Fig. 13.

In summary, the results of the superposition study show that the process design was target-oriented and that the structures can be manufactured with very small deviations from the target geometry by both tools and, moreover, that the process

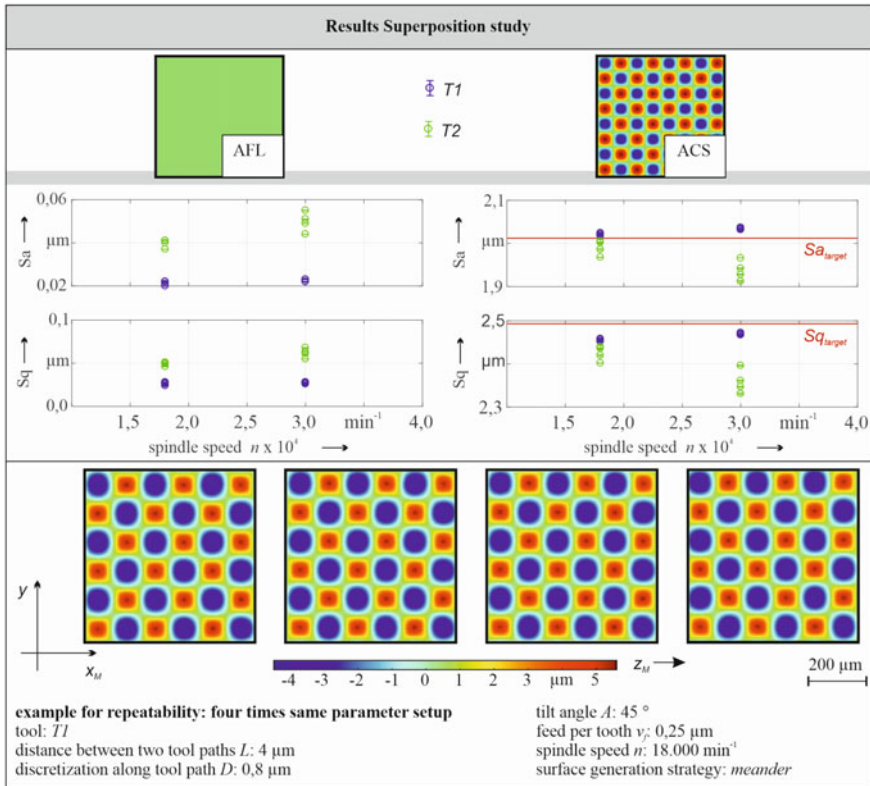


Fig. 13 Results of superposition study: dimensional accuracy (S_a - and S_q -values) and repeatability. Modified from [68] according to [76]

leads to reproducible results. The repeatability is shown by the fact that the deviations within the evaluated S_a - and S_q -values for four identical parameter setups are in the single-digit to low double-digit nanometer range. This means that stochastic influences have been almost completely eliminated by the process design and the respective influences of the process parameters are known.

In addition, the influence of tool wear was also subsequently investigated with the parameter setup from the superposition study [68]. For tool T1, it was determined that a manufacturing of 15 material measures of the mentioned size can be realized without any systematic worsening of the resulting work-piece surface quality. Tool T2 should be replaced after ten manufactured material measures, since otherwise it cannot be guaranteed that the surface quality will decline due to the resulting tool wear.

After the influence of the process parameters on the process result was known, the milling process was optimized for the application and the tool life was known, the transfer of the micro-milling process to other, more complex, target geometries, and other tools followed.

3.1.4 Manufacturing of Areal Material Measures Based on Real Component Surfaces

As already described in Sect. 2.2, areal material measures were developed and designed which are based on real component surfaces and thus allow a calibration which is closer to the subsequent measurement task. Some of the newly developed areal material measures have significantly smaller structural details, but extend over a larger area than the previously manufactured standardized material measures. However, since the effective cutter radius limits the minimum structural details that can be manufactured (see Sect. 2.2), milling tools with smaller diameters must be used for some of the newly developed areal material measures. In an experimental study, eight different areal material measures were manufactured using four different tools: four material measures each based on cylinder liners and on chain pins. The detailed description of the milling process transfer can be taken from [68, 77, 78]. In particular, the limited spindle speed of 80,000 rpm posed challenges for the transfer: lower cutting speeds had to be accepted. In addition to the two tools $T1$ and $T2$ described above, two other tools $T3$ and $T4$ were used. Both new tools were single-edged cemented carbide tools without coating. They both have the same geometry but different effective radii. $T3$ has an effective radius of 25 μm and $T4$ is even smaller and has an effective radius of 10 μm . Even for the novel areal material measures, only very small deviations occur during micro-milling (see Fig. 14 and Table 1). The material measures were designed using the model-based design approach and the above describe models for manufacturing and measurement with the constraint to feature defined values of the surface texture parameters S_k , S_{pk} , S_{vk} . The S_k parameters according to ISO 25178-2 [36] are sensitive with regard to deviations in the surface topography, but nevertheless the deviations between the manufactured topographies and the nominal topographies are only in the single-digit to low double-digit nanometer range.

The results show that the design of the micro-milling process based on simple geometries is transferable to new calibration structures and that areal material measures based on real component surfaces can be manufactured by micro-milling for different scales, surface types, and target parameter values. As long as a corresponding transformation of the desired parameter can be found and the signal chain as described can be modeled, the corresponding target values can be mapped onto a physical sample.

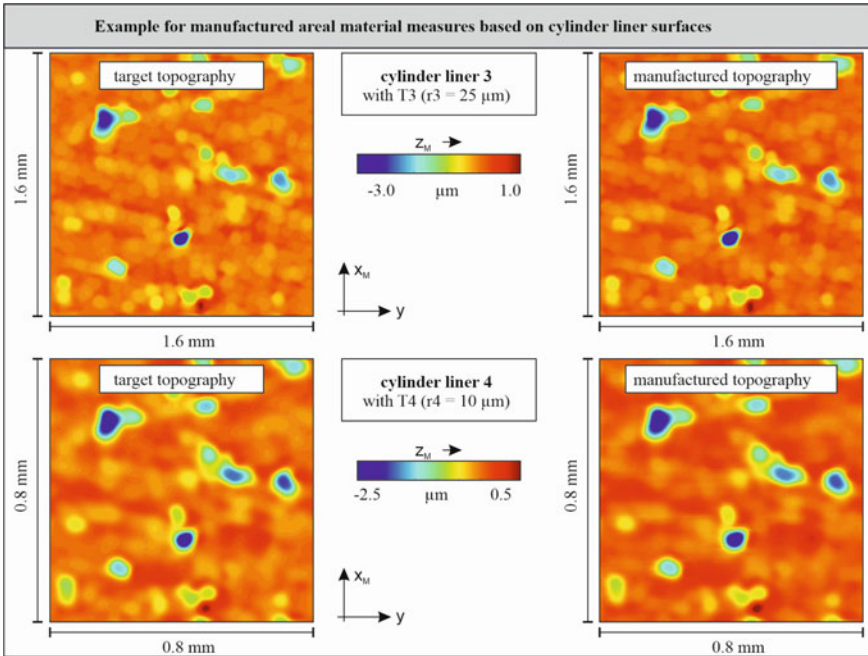


Fig. 14 Comparison of target and manufactured topography for areal material measures based on cylinder liner surfaces. Modified from [68] according to [78]

Table 1 Measured values and target values of Sk-parameters for novel areal material measures. Modified from [77]

Material measure	Sk/ μm	Spk/ μm	Svk/ μm
Cylinder liner: target values	0.4	0.2	1.0
CL1	0.430 \pm 0.001	0.213 \pm 0.003	1.015 \pm 0.001
CL2	0.426 \pm 0.002	0.195 \pm 0.000	1.012 \pm 0.004
CL3	0.419 \pm 0.001	0.191 \pm 0.000	1.067 \pm 0.004
CL4	0.419 \pm 0.001	0.183 \pm 0.000	1.061 \pm 0.001
Chain pins: target values	0.3	0.1	0.4
CP1	0.332 \pm 0.001	0.105 \pm 0.001	0.405 \pm 0.002
CP2	0.309 \pm 0.001	0.110 \pm 0.000	0.394 \pm 0.001
CP3	0.314 \pm 0.001	0.114 \pm 0.000	0.394 \pm 0.001
CP4	0.297 \pm 0.001	0.095 \pm 0.001	0.401 \pm 0.003

3.2 Laser Lithography

An alternative technology for fabricating high-quality material measures is to be found in laser lithography, alias two-photon polymerization or direct laser writing (DLW), introduced in Sect. 2. Its non-linear additive manufacturing principle allows for realizing complex 3D structures with almost arbitrary shapes, as schematically illustrated in Fig. 15.

In 1997, Maruo et al. laid the technology’s basics: typically, a femto-second pulsed laser beam radiating on the near-infrared spectrum is tightly focused into photo-sensitive materials, so-called photo resins. There, a two- or more-photon absorption process starts a polymerization on the spatial extend of the laser focus. Hence, a pre-defined relative movement of the focus with respect to the resin allows for a controlled, serial manufacturing of structures on the scale of the laser focus [79, 80].

Today, this technology is one of the most flexible and high-resolution 3D printing approaches and finds its application in a wide range of disciplines: paving the way for 4D micro-fabrication in integrated photonics [82], in life science [83], in micro-optics [84], in micro-mechanics [85] and micro-fluidics [86] or in the context of topological photonics [87, 88], to just name a few. Within this section, the focus will be on the fabrication and characterization of material measures, investigated within the funding period of CRC 926.

In 2015, the very first try of a laser lithographically realization of a mathematically modeled topography using the design scheme as described in Sect. 2.2 was performed. The resulting material measure allowed a calibration of the z -axis linearity of arbitrary optical topography measuring instruments, with a newly established design of an areal irregular roughness material measure (AIR) featuring a defined distribution of height values [89]. Its measured geometry provides a linear Abbott-curve, hence, the linearity deviation l_z as well as the amplification coefficient α_z along the height axis are determinable by many measuring points at different heights. This is in contrast to the state of the art, where typically just several step-height structures have been used and lead to a rather small amount of different height values. Due to the significant increase of evaluation data and the thus adapted evaluation routine, this new approach

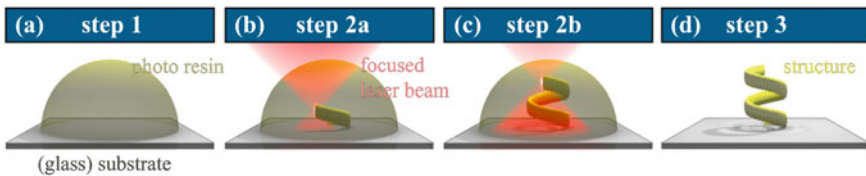


Fig. 15 **a** Step 1: application of a photo resin droplet onto a (glass) substrate, **b** step 2a: selective exposure of the photo resin by a focused near infrared laser beam, **c** step 2b: relative movement of photo resin and laser focus along a programmed trajectory, **d** step 3: removal of the uncured photo resin (development). Adapted with permission from [81]

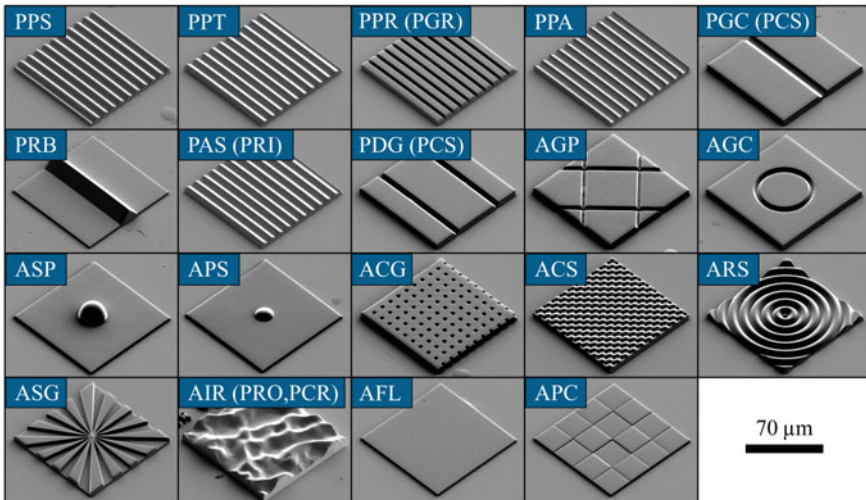


Fig. 16 SEM-images of laser lithographically fabricated material measures according to ISO 25178-70 [12]. Apparently, both, profile and areal material measures can be manufactured additively. The depictions of the material measures of types PGR, PRO, PCR, PRI, and PCS are left out due to redundancies. Adapted with permission from [51, 81]

is less prone to measuring and fabrication deviations and additionally allows for an integral calibration, based on areal surface texture parameters.

Thinking ahead, Eifler et al. published in 2018 a holistic feasibility study on fabricating material measures with direct laser writing [51]. There, they focused on the geometries given within ISO 25178-70, for the calibration of both, profile and areal surface topography measurement instruments [12]. As illustrated by the scanning electron microscope (SEM) images in Fig. 16, all relevant types of material measures can be fabricated onto only one sample, which turns out to be the unique selling point of using laser lithography. There is no need for geometry-dependent fabrication tools any longer, allowing to combine multiple material measures for various calibration tasks on just one substrate [51]. Moreover, the fabrication precision, as well as the reliability and repeatability of the printed structures, are found to exceed the respective capabilities of today's state-of-the-art optical areal measuring instruments. Having the calibration tasks in mind, this is not only reassuring but also motivates for further investigations.

For instance, one can try to reduce the great amount of different material measures within the aforementioned ISO standard down to the necessary minimum, as first realized by the so-called NPL-BentoBox in 2013 [5]. There, the most common material measures were fabricated onto five different samples, due to the different fabrication technologies needed for manufacturing. As aforementioned, laser lithography, in contrast, allows for fabricating almost arbitrary geometries, hence, all necessary ones can be fabricated onto only one single sample, greatly reducing the experimental amount of time and effort for the application of the material mea-

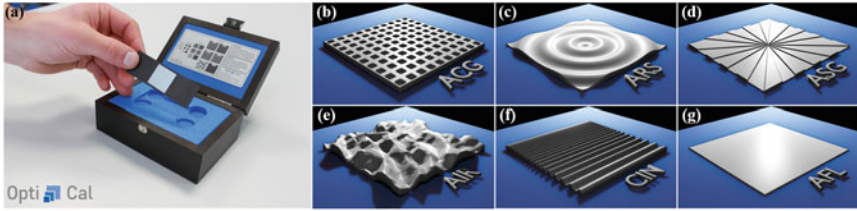


Fig. 17 Storage box and sample holder (a), accommodating the squared substrate on which the six different material measures (b–g) are applied. Adapted with permission from Opti-Cal GmbH

asures for a comprehensive calibration. This goal succeeded in 2018 by Eifler et al. for the very first time [90]: according to the ISO 25178-600 standard, there are seven so-called basic metrological characteristics to be taken into account for characterizing a measuring instrument [13] (compare Sect. 1.3). All of them can be covered by only six different material measures [90], which are illustrated in Fig. 17b–g and were mapped in different scales onto one sample, allowing a single-sample comprehensive calibration of all basic metrological characteristics. The different types of applied material measures and their capabilities for calibration are described in the following.

The areal cross grating (ACG) allows for the calibration of the x - y mapping deviations, the determination of the linearity deviations l_x, l_y , the amplification coefficients α_x, α_y as well as the perpendicularity Δ_{xy}^{per} of the axes, as suggested by Giusca et al. [32]. During the process of standardization, the metrological characteristic of the perpendicularity has been replaced by the x - y mapping deviations [13]. The areal radial sine (ARS) provides information about the arithmetic and quadratic areal surface texture parameters S_a, S_q , hence enabling an integral calibration of the overall performance of the measuring instrument. The evaluation of the Siemens Star structure (ASG) was described by Giusca et al. in 2013 [34] and deploys information about the topographic spatial resolution. The areal irregular roughness (AIR) geometry has been described above, and was designed in a way that the linearity deviation and amplification coefficient of the height axis can be calculated based on a defined distribution of height values [89], leaving a self-developed chirped topography (CIN) and the areal flatness material measure (AFL). The latter allows for calibrating the measurement noise and the flatness deviation, whereas the CIN structure was designed for the determination of the topography fidelity. Moreover, the CIN type also allows for the evaluation of a resolution parameter, named small scale fidelity ssf , corresponding to a transmission of the target amplitude of $\pm 50\%$ [31, 91]. Combining those six material measures via direct laser writing in different lateral scales onto one substrate gives the very first universal calibration artefact (Fig. 17) and enables a complete ISO-conform calibration of all basic metrological characteristics for various common microscope magnifications with a single-sample [90].

Further experiments on additively manufactured material measures show that the structures are impressively stable regarding thermal, moisture, and aging influences [90–92]. For instance, the resolution calibrating parameters topographic spatial resolution tsr and small scale fidelity ssf vary only within a more or less noisy range for the three exemplary conditions (i) 60 °C, dry, (ii) 60 °C, 70% relative humidity, and (iii) 80 °C, 30% relative humidity, evaluated by Groß et al. [92]. According to the rough “accelerated aging” estimation in Ref. [81], which is based on the Arrhenius equation [93], the investigated twelve days at 80 °C correspond to an aging of more than two years under laboratory conditions, without even taking the humidity into account. A very similar behavior can be observed for different fabrication parameters, like the discretization of the structures or the laser power, as well as for the other metrological characteristics. Hence, emphasizing once more the suitability of laser lithography for fabricating long-term stable material measures.

Moreover, completely new material measures, overcoming challenges beyond the state of the art can be thought, like for calibrating the resolution of a measuring instrument. Here, the aforementioned Siemens Star grating (ASG) is commonly used [34]: the corresponding topographic spatial resolution tsr is evaluated by extracting two profiles, one from a heightened and one from a neighbored lowered pair of pedestals. The height values are normalized to the maximum value and the spatial axis is multiplied by π/n , where n is the number of pedestals pairs of the Siemens Star. The resulting difference profile inevitably slopes towards the center of the structure, so that the resulting full width at half maximum represents the tsr . Due to the sharp edges of the Siemens Star, this routine is very prone to measurement artefacts. Furthermore, the determination of the resolution parameter is based on only two profiles of an areal material measure. Under this consideration, the chirped topography (CIN) features an advantage [31]: instead of sharp edges, the CIN topography is characterized by sequentially decreasing sine waves, being less prone to measurement artefacts. The small-scale fidelity ssf as resolution parameter is determined by fitting the extracted profile(s) and searching for the shortest wavelength whose amplitude does not deviate more than $\pm 50\%$ of the target amplitude. The disadvantages of this approach are (i) the resolution is only determined in one direction and (ii) due to the sequential sine waves, the resulting ssf tends to be discretized as well.

To overcome those issues, Dai et al. introduced a material measure being radially symmetric and consisting a continuously chirped topography (see [94] for details):

$$z(r) = \frac{H}{2} \sin \left(\Phi_0 + 2\pi r \left(f_0 - \frac{\Delta f}{2R} r \right) \right). \quad (5)$$

Scanning electron microscope images of the thus fabricated material measure are shown in Fig. 18a. Due to the linearly changing spatial frequency with respect to the position r , the evaluation routine shown in b now involves a Fourier transformation of the profiles, first. Dividing the result by the Fourier transform of the designed profile represents the so-called instrument transfer function whose logarithm times 20 results in the corresponding gain curve G . If this gain drops by more than -6 dB, less than half of the target amplitude is transferred by the measuring instrument,

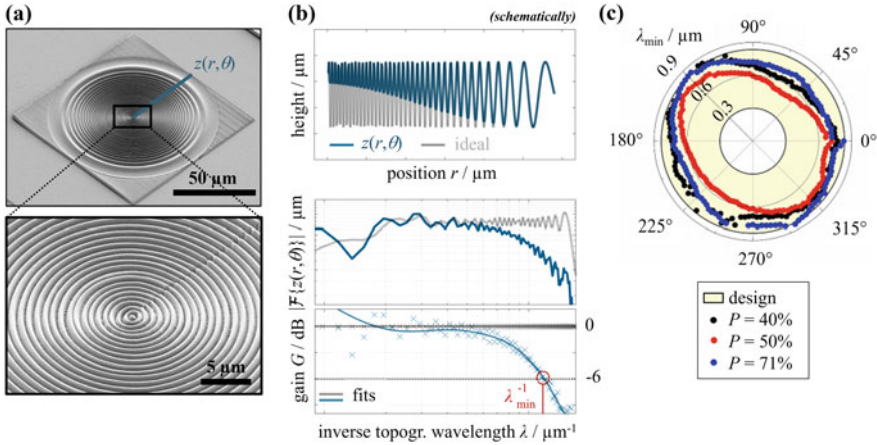


Fig. 18 Scanning electron micrograph of a direct laser written circular symmetric continuous frequency chirped topography (a). Based on height profiles at different angles $z(r, \theta)$, the smallest transferable topographic wavelength λ_{\min} can be determined (b) for all directions and different fabricating laser powers (c). Adapted with permission from [94]

hence the resolution limit λ_{\min} is found. This can be done for all orientation angles θ , providing an omni-lateral resolution calibration of the instrument. In reference [94], the authors used an atomic force microscope to exceed the fabrication resolution in the measurement procedure, hence, identifying resolution anisotropies and the influence of the fabrication laser power. This allowed for determining ideal fabrication parameters, being useful for other structures as well.

In 2021, Eifler et al. came up with a new material measure, enabling both, determining the small scale fidelity ssf based on sine fits, and determining the minimal transferable topographic wavelength λ_{\min} , based on the instrument transfer function [95]. The corresponding trapezoid CIN structure is shown in Fig. 19a as SEM image,

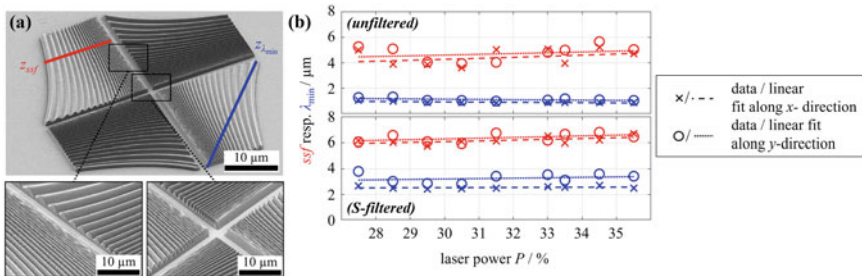


Fig. 19 Scanning electron micrograph of a direct laser written trapezoid chirped topography (a). Based on height profiles taken either orthogonal z_{ssf} or diagonal ($z_{\lambda_{\min}}$), both evaluation routines are possible: linear discrete sine fits for determining ssf in the spacial domain (red) and the gain curve drop in frequency domain (blue) for determining λ_{\min} , shown in dependence of the fabrication laser power (b). Adapted with permission from [95]

whereas the results of both evaluation routines are plotted in *b* in dependence of the fabrication laser power. Obviously, the fabrication resolution exceeds the capabilities of the confocal microscope used for the evaluation, since there is no power influence visible. In contrast, the two evaluation methods differ significantly: the resolution limit in terms of *ssf* is worse in all cases. The authors state that the frequency evaluation on the other side requires a more complex matching of the measured and nominal geometry and noise is harder to separate. Hence, both approaches have their advantages and disadvantages. Only the trapezoidal CIN material measure allows for both ways in the application and can be nicely created by laser lithography.

4 Summary

In this chapter, methods for the model-based design and the manufacturing of material measures for the calibration of surface topography measuring instruments were introduced. The topography of the material measures is developed using mathematical methods so that the metrological characteristics of the measuring Instruments can be mapped. The manufacturing processes of micro-milling and laser lithography researched in the CRC 926 enable the material measures to be manufactured with nanometer precision.

References

1. Stout K (1993) The development of methods for the characterisation of roughness in three dimensions. European Report EUR 15178N
2. Blunt L, Jiang X (2003) Advanced techniques for assessment surface topography: development of a basis for 3D surface texture standards “SURFSTAND”. Kogan Page Science, London. <https://doi.org/10.1016/B978-1-903996-11-9.X5000-2>
3. Seewig J, Eifler M (2017) Calibration of areal surface topography measuring instruments. In: Fifth international conference on optical and photonics engineering, vol 10449, Asundi AK (ed) International Society for Optics and Photonics. SPIE, p 1044911. <https://doi.org/10.1117/12.2270533>
4. ISO 25178-2 (2012) Geometrical Product Specification (GPS) — surface texture: areal — part 2: terms, definitions and surface texture parameters. Beuth Verlag, Berlin
5. Leach R (2013) Characterisation of areal surface texture. Springer. <https://doi.org/10.1007/978-3-642-36458-7>
6. Leach R (2011) Optical measurement of surface topography. Springer. <https://doi.org/10.1007/978-3-642-12012-1>
7. DIN Deutsches Institut für Normung e.V. (2010) International vocabulary of metrology - basic and general concepts and associated terms (VIM); German-English Version ISO/IEC Guide99:2007, 3rd edn. Beuth
8. Leach R, Giusca C, Haitjema H, Evans C, Jiang X (2015) Calibration and verification of areal surface texture measuring instruments. CIRP Ann 64(2):797–813. <https://doi.org/10.1016/j.cirp.2015.05.010>
9. ISO 5436-1 (2000) Geometrical product specification (GPS) — surface texture: profile method, measurement standard — part 1: material measures. Beuth Verlag, Berlin

10. ISO 12179 (2000) Geometrical product specification (GPS) — surface texture: profile method, calibration of contact (Stylus) instruments. Beuth Verlag, Berlin
11. Eifler M, Hering J, Seewig J, Leach RK, von Freymann G, Hu X, Dai G (2020) Comparison of material measures for areal surface topography measuring instrument calibration. *Surf Topogr: Metrol Prop* 8(2):025019. <https://doi.org/10.1088/2051-672x/ab92ae>
12. DIN EN ISO 25178-70 (2014) Geometrical product specification (GPS) — surface texture: areal — Part 70: material measures. Beuth Verlag, Berlin
13. DIN EN ISO 25178-600 (2019) Geometrical product specifications (GPS) — surface texture: areal — Part 600: metrological characteristics for areal topography measuring methods. Beuth Verlag, Berlin
14. ISO 25178-700 (2022) Geometrical product specifications (GPS) — Surface texture: Areal — Part 700: Calibration, adjustment and verification of areal topography measuring instruments
15. VDI 2655 Part 1.1 (2008) Optical measurement and microtopographies - calibration of interference microscopes and depth measurement standards for roughness measurement. Verein deutscher Ingenieure, Düsseldorf
16. VDI 2655 Part 1.2 (2010) Optical measurement of microtopography - calibration of confocal microscopes and depth setting standards for roughness measurement. Verein deutscher Ingenieure, Düsseldorf
17. Nemoto K, Yanagi K, Aketagawa M, Yoshida I, Uchidate M, Miyaguchi T, Maruyama H (2009) Development of a roughness measurement standard with irregular surface topography for improving 3D surface texture measurement. *Meas Sci Technol* 20(8):084023. <https://doi.org/10.1088/0957-0233/20/8/084023>
18. Eifler M, Klauer K, Kirsch B, Aurich JC, Seewig J (2021) Performance verification of areal surface texture measuring instruments with the Sk- parameters. *Measurement* 173:108550. <https://doi.org/10.1016/j.measurement.2020.108550>
19. Krüger-Sehm R, Bakucz P, Jung L, Wilhelms H (2007) Chirp-Kalibriernormale für Oberflächenmessgeräte. *tm – Technisches Messen* 74(11):572–576. <https://doi.org/10.1524/teme.2007.74.11.572>
20. Hillmann VJW, Krystek M (1997) Superfeine Rauhnormale: ... mit unregelmäßigen Profil zum Kalibrieren von mechanisch und optisch antastenden Oberflächenmeßgeräten. *qz – Qualität und Zuverlässigkeit* 42(1):76–79
21. Frühauf J, Krönert S (2005) Wet etching of silicon gratings with triangular profiles. *Microsyst Technol* 11(12):1287–1291
22. Krüger-Sehm R, Dziomba T, Dai G (2004) Profile assessment of nano roughness standards by contact and non-contact methods. In: Dietzsch M (ed) *Proceedings of the XI. International colloquium on surfaces: part II. Shaker, Aachen* (2004), pp 31–40
23. Häsing J (1965) Herstellung und Eigenschaften von Referenznormalen für das Einstellen von Oberflächenmeßgeräten. *Werkstatttechnik* 55(8):380–382
24. Frühauf J, Krüger-Sehm R, Felgner A, Dziomba T (2012) Areal roughness standards. In: *Proceedings of the 12th euspen international conference*, pp 133–136
25. Frühauf J, Gärtner E, Koenders L, Felgner A (2016) Vergleichsproben aus Silizium für die Flächenrauhheit. *tm – Technisches Messen* 83(12):681–695. <https://doi.org/10.1515/teme-2016-0025>
26. Leach R, Giusca C, Rickens K, Riemer O, Rubert P (2014) Development of material measures for performance verifying surface topography measuring instruments. *Surf Topogr: Metrol Prop* 2(2):025002. <https://doi.org/10.1088/2051-672X/2/2/025002>
27. Uchidate M, Yanagi K, Yoshida I, Shimizu T, Iwabuchi A (2011) Generation of 3D random topography datasets with periodic boundaries for surface metrology algorithms and measurement standards. *Wear* 271(3). The 12th international conference on metrology and properties of engineering surfaces, pp 565–570. <https://doi.org/10.1016/j.wear.2010.04.035>
28. Gao F, Leach RK, Petzing J, Coupland JM (2007) Surface measurement errors using commercial scanning white light interferometers. *Meas Sci Technol* 19(1):015303. <https://doi.org/10.1088/0957-0233/19/1/015303>

29. Leach R, Giusca C, Guttman M, Jakobs P-J, Rubert P (2015) Development of low-cost material measures for calibration of the metrological characteristics of areal surface texture instruments. *CIRP Ann* 64(1):545–548. <https://doi.org/10.1016/j.cirp.2015.03.002>
30. Chen Y, Zhang X, Luo T, Liu X, Huang W (2013) Fabrication and characterization of areal roughness specimens for applications in scanning probe microscopy. *Meas Sci Technol* 24(5):055402. <https://doi.org/10.1088/0957-0233/24/5/055402>
31. Seewig J, Eifler M, Wiora G (2014) Unambiguous evaluation of a chirp measurement standard. *Surf Topogr: Metrol Prop* 2(4):045003. <https://doi.org/10.1088/2051-672x/2/4/045003>
32. Giusca CL, Leach RK, Helary F, Gutauskas T, Nimishakavi L (2012) Calibration of the scales of areal surface topography measuring instruments: part 1. Measurement noise and residual flatness. *Meas Sci Technol* 23(3):035008. <https://doi.org/10.1088/0957-0233/23/3/035008>
33. Giusca CL, Leach RK, Helary F (2012) Calibration of the scales of areal surface topography measuring instruments: part 2. Amplification, linearity and squareness. *Meas Sci Technol* 23(6):065005. <https://doi.org/10.1088/0957-0233/23/6/065005>
34. Giusca CL, Leach RK (2013) Calibration of the scales of areal surface topography measuring instruments: part 3. Resolution. *Meas Sci Technol* 24(10):105010. <https://doi.org/10.1088/0957-0233/24/10/105010>
35. Leach R, Haitjema H, Su R, Thompson A (2020) Metrological characteristics for the calibration of surface topography measuring instruments: a review. *Meas Sci Technol* 32(3):032001. <https://doi.org/10.1088/1361-6501/abb54f>
36. DIN EN ISO 25178-2 (2012) Geometrische Produktspezifikation (GPS) – Oberflächenbeschaffenheit: Flächenhaft - Teil 2: Begriffe und Oberflächen-Kenngrößen. Beuth Verlag, Berlin
37. Fujii A, Suzuki H, Yanagi K (2011) Development of measurement standards for verifying functional performance of surface texture measuring instruments. *J Phys: Conf Ser* 311:012009. <https://doi.org/10.1088/1742-6596/311/1/012009>
38. Krüger-Sehm R, Frühauf J, Dziomba T (2005) Determination of the short wavelength cut-off of interferential and confocal microscopes. In: Thomas T, Rosén BG, Zahouani HH (ed) *Proceedings of metrology and properties of engineering surfaces*, pp 21–27
39. Frühauf J, Krönert S (2004) Linear silicon gratings with different profiles: trapezoidal, triangular, rectangular, arched. In: Dietzsch M (ed) *Proceedings of the XI. International colloquium on surfaces: part II*. Shaker, Aachen, pp 75–83
40. Brand U, Kleine-Besten T (2000) Development of a special CMM for dimensional metrology on microsystem components
41. Koenders L, Bergmans R, Garnæs J, Haycocks J, Korolev N, Kurosawa T, Meli F, Park BC, Peng GS, Picotto GB, Prieto E, Gao S, Smereczynska B, Vorbürger T, Wilkening G (2003) Comparison on nanometrology: nano 2–step height. *Metrologia* 40(1A):04001–04001. <https://doi.org/10.1088/0026-1394/40/1a/04001>
42. Leach R, Giusca C (2011) Calibration of optical surface topography measuring instruments. In: Leach R (ed) *Optical measurement of surface topography*. Springer, Berlin, Heidelberg, pp 49–70. https://doi.org/10.1007/978-3-642-12012-1_4
43. Kim KJ, Jung CS, Hong TE (2007) A new method for the calibration of the vertical scale of a stylus profilometer using multiple delta-layer films. *Meas Sci Technol* 18(9):2750–2754. <https://doi.org/10.1088/0957-0233/18/9/002>
44. Eifler M, Schneider F, Seewig J, Kirsch B, Aurich JC (2016) Manufacturing of new roughness standards for the linearity of the vertical axis - feasibility study optimization. *Eng Sci Technol Int J* 19(4):1993–2001. <https://doi.org/10.1016/j.jestch.2016.06.009>
45. Song J (1988) Random profile precision roughness calibration specimens. *Surf Topogr* 1:303–314
46. Kourouklis C (2007) *Entwicklung und Fertigung von Nano-Raunormalen*. PhD Dissertation, Garbsen (ed) PZH, Produktionstechnisches Zentrum
47. Gatzten HH, Kourouklis C (2001) The fabrication of nano-roughness standards for the calibration of atomic force microscopes. In: *Proceedings of the 16th ASPE annual meeting (2001)*, pp 493–496

48. Rubert P, Frenzel C (2004) The use of standard specimens to check stylus tip size in surface measuring instruments. In: Dietzsch M (ed) Proceedings of the XI. International colloquium on surfaces: part II. Shaker, Aachen, pp 129–138
49. Franke M, Jusko O, Krystek M, Neugebauer M, Neuschaefer-Rube U, Wäldele F (2004) Artefacts and test procedures for contour measuring instruments. In: Dietzsch M (ed) Proceedings of the XI. International colloquium on surfaces: part II. Shaker, Aachen, pp 102–107
50. Ville J (2003) Calibration procedures for stylus and optical instrumentation. In: Blunt L, Jiang X (ed) Advanced techniques for assessment surface topography: development of a basis for 3D surface texture standards “SURFSTAND”. Kogan Page Science, London, pp 119–174
51. Eifler M, Hering J, von Freymann G, Seewig J (2018) Manufacturing of the ISO 25178–70 material measures with direct laser writing: a feasibility study. Surf Topogr: Metrol Prop 6(2):024010. <https://doi.org/10.1088/2051-672X/aabe18>
52. Volk R, Feifel S (2014) Full scale calibration of a combined tactile contour and roughness measurement device. In: Measurement technology and intelligent instruments XI, vol 613. Key engineering materials. Trans Tech Publications Ltd, pp 94–100. <https://doi.org/10.4028/www.scientific.net/KEM.613.94>
53. Su R, Wang Y, Coupland J, Leach R (2017) On tilt and curvature dependent errors and the calibration of coherence scanning interferometry. Opt Express 25(4):3297–3310. <https://doi.org/10.1364/OE.25.003297>
54. Tan Ö (2012) Characterization of micro- and nanometer resolved technical surfaces with function-oriented parameters. Shaker, Aachen
55. Dai G, Jung L, Pohlenz F, Danzebrink H-U, Krüger-Sehm R, Hasche K, Wilkening G (2004) Measurement of micro-roughness using a metrological large range scanning force microscope. Meas Sci Technol 15(10):2039–2046. <https://doi.org/10.1088/0957-0233/15/10/013>
56. Dziomba T, Koenders L, Danzebrink H, Wilkening G (2004) Lateral & vertical calibration of scanning probe microscopes and their measurement uncertainty. In: Dietzsch M (ed) Proceedings of the XI. International colloquium on surfaces: part II. Shaker, Aachen, pp 117–128
57. Press WH, Teukolsky SA, Vetterling WT, Flannery BP (2007) Numerical recipes, 3rd edn. Cambridge University Press
58. Seewig J, Eifer M, Hüser D, Meess R (2019) Rk material measure. In: tm – Technisches Messen 2019. <https://doi.org/10.1515/teme-2019-0091>
59. Klauer K, Eifler M, Kirsch B, Böß V, Seewig J, Aurich JC (2021) Analysis of dimensional accuracy for micro-milled areal material measures with kinematic simulation. Int J Adv Manuf Technol 116(9):3087–3102. ISSN: 1433-3015. <https://doi.org/10.1007/s00170-021-07629-8>
60. ISO 16610-41 (2015) Geometrical product specification (GPS) — filtration - part 41: morphological profile filters: disk and horizontal line-segment filters (ISO 16610-41:2015). Beuth Verlag, Berlin
61. Keksel A, Lohfink AP, Eifler M, Garth C, Seewig J (2020) Virtual topography measurement with transfer functions derived by fitted time series models. Meas Sci Technol 31(5):055008. <https://doi.org/10.1088/1361-6501/ab5131>
62. Keksel A, Ströer F, Seewig J (2018) Bayesian approach for circle fitting including prior knowledge. Surf Topogr: Metrol Prop 6(3):035002. <https://doi.org/10.1088/2051-672X/aad2b4>
63. Eifler M, Keksel A, Seewig J (2019) Comparison of material measures for the determination of transfer characteristics of surface topography measuring instruments. Surf Topogr: Metrol Prop 7(1):015024. <https://doi.org/10.1088/2051-672x/ab0dc6>
64. Keksel A, Eifler M, Seewig J (2020) A model of confocal microscopy measurements combining empirical and physical properties. Meas Sci Technol 32(2):025008. <https://doi.org/10.1088/1361-6501/abbe3a>
65. Hock S (1996) Hochgeschwindigkeitsfasen im Werkzeug- und Großformenbau. Dissertation. Technische Hochschule Darmstadt
66. Urban B (2009) Kinematische und mechanische Wirkung des Kugelkopffräsens. Dissertation. Leibniz Universität Hannover
67. Tönshoff HK, Camacho JH (1987) Technologie des Mehrachsen-Hohlformfräsens. Umformtechnisches Kolloquium Hannover 12:20.1–20.14

68. Klauer K (2022) Mikrofräsen flächenhafter Kalibriernormale auf Basis realer Bauteiloberflächen. Dissertation. Technische Universität Kaiserslautern
69. Nesor D (2015) Randzonenbeeinflussung durch die Rekonturierung komplexer Investitionsgüter aus Ti-6Al-4V. Dissertation. Leibniz Universität Hannover
70. Reichenbach IG (2017) Beitrag zur Beherrschung der Mikrofräsbearbeitung von Polymethylmethacrylat. Dissertation. Technische Universität Kaiserslautern
71. Finzer T (2001) Verschleißprognose bei der Hochgeschwindigkeitsbearbeitung mit Kugelkopfwerkzeugen. Dissertation. Technische Universität Darmstadt
72. Hieu NT (2007) Modellierung des Hochgeschwindigkeitsfräsens mit Kugelkopffräsern unter besonderer Berücksichtigung der Oberflächengüte. Dissertation. Otto-von-Guericke-Universität Magdeburg
73. Vollertsen F, Biermann D, Hansen HN, Jawahir I, Kuzman K (2009) Size effects in manufacturing of metallic components. *CIRP Ann* 58(2):566–587. <https://doi.org/10.1016/j.cirp.2009.09.002>
74. Klauer K, Eifler M, Kirsch B, Seewig J, Aurich J (2020) Correlation between different cutting conditions, surface roughness and dimensional accuracy when ball end micro milling material measures with freeform surfaces. *Mach Sci Technol* 24(3):446–464. <https://doi.org/10.1080/10910344.2019.1698611>
75. Klauer K, Eifler M, Kirsch B, Seewig J, Aurich J (2020) Ball end micro milling of areal material measures: influence of the tilt angle on the resulting surface topography. *Product Eng* 14(2):239–252. <https://doi.org/10.1007/s11740-019-00943-x>
76. Klauer K, Eifler M, Kirsch B, Seewig J, Aurich JC (2019) Micro milling of areal material measures: influence of the manufacturing parameters on the surface quality. In: *Production at the leading edge of technology*. Springer, pp 259–268. <https://doi.org/10.1016/j.procir.2018.05.083>
77. Eifler M, Klauer K, Kirsch B, Aurich JC, Seewig J (2021) Performance verification of areal surface texture measuring instruments with the Sk-parameters. *Measurement* 173:108550. <https://doi.org/10.1016/j.measurement.2020.108550>
78. Eifler M, Klauer K, Seewig J, Kirsch B, Aurich J (2019) Model-based design of areal material measures with component surfaces. *Surf Topogr: Metrol Prop* 7(4):044003. <https://doi.org/10.1088/2051-672X/ab5c83>
79. Hohmann JK, Renner M, Waller EH, von Freymann G (2015) Three-dimensional μ -printing: an enabling technology. *Adv Opt Mater* 3:1488. <https://doi.org/10.1002/adom.201500328>
80. Fischer J, Wegener M (2013) Three-dimensional optical laser lithograph beyond the diffraction limit. *Laser & Photon Rev* 7(1):22–44. <https://doi.org/10.1002/lpor.201100046>
81. Hering J (2020) Von der STED inspirierten Zwei-Photonen Laserlithographie zur industriellen Metrologie. PhD thesis. Technische Universität Kaiserslautern
82. Ritacco T, Aceti DM, De Domenico G, Giocondo M, Mazzulla A, Cipparrone G, Pagliusi P (2022) Tuning cholesteric selective reflection in situ upon two-photon polymerization enables structural multicolor 4D microfabrication. *Adv Opt Mater* 2101526. <https://doi.org/10.1002/adom.202101526>
83. Babi M, Riesco R, Boyer L, Fatona A, Accardo A, Malaquin L, Moran-Mirabal J (2021) Tuning the nanoporosity and chemical functionality of 3D printed scaffolds through cellulose nanocrystal coatings. *ACS Appl Bio Mater* 4(12):8443–8455. <https://doi.org/10.1021/acsbm.1c00970>
84. Kumar A, Asadollahbaik A, Kim J, Lahlil K, Thiele S, Herkommer AM, Chormaic SN, Kim J, Gacoin T, Giessen H, Fick J (2022) Emission spectroscopy of NaYF₄: Eu Nanorods optically trapped by Fresnel lens fibers. *Photon Res* 10(2):332–339. <https://doi.org/10.1364/prj.434645>
85. Stassi S, Cooperstein I, Tortello M, Pirri CF, Magdassi S, Ricciardi C (2021) Reaching silicon-based NEMS performances with 3D printed nanomechanical resonators. *Nat Commun* 12(1):1–9. <https://doi.org/10.1038/s41467-021-26353-1>
86. Kunze FL, Henning T, Klar PJ (2021) Taking internally wetted capillary electrospray emitters to the sub-ten-micrometer scale with 3D microlithography. *AIP Adv* 11(10):105315. <https://doi.org/10.1063/5.0066619>

87. Schulz J, Vaidya S, Jörg C (2021) Topological photonics in 3D micro-printed systems. *APL Photon* 6(8):080901. <https://doi.org/10.1063/5.0058478>
88. Jörg C, Vaidya S, Noh J, Cerjan A, Augustine S, von Freymann G, Rechtsman MC (2022) Observation of quadratic (Charge-2) Weyl point splitting in near-infrared photonic crystals. *Laser & Photon Rev* 16(1):2100452. <https://doi.org/10.1002/lpor.202100452>
89. Eifler M, Seewig J, Hering J, von Freymann G (2015) Calibration of z-axis linearity for arbitrary optical topography measuring instruments. In: *Optical measurement systems for industrial inspection IX*, vol 9525. SPIE, pp 237–246. <https://doi.org/10.1117/12.2190737>
90. Eifler M, Hering J, Von Freymann G, Seewig J (2018) Calibration sample for arbitrary metrological characteristics of optical topography measuring instruments. *Optics Expr* 26(13):16609–16623. <https://doi.org/10.1364/OE.26.016609>
91. Hering J, Eifler M, Hofherr L, Ziegler C, Seewig J, von Freymann G (2018) Two-photon laser lithography in optical metrology. In: *Advanced fabrication technologies for micro/nano optics and photonics XI*, vol 10544. SPIE, pp 108–115. <https://doi.org/10.1117/12.2289900>
92. Gross K, Eifler M, Hering J, von Freymann G, Seewig J (2021) Metrological characteristics of material measures depending on manufacturing parameters in direct laser writing and external stress factors. In: *Optical measurement systems for industrial inspection XII*, vol 11782. SPIE, pp 115–127. <https://doi.org/10.1117/12.2591655>
93. Arrhenius S (1889) Über die Reaktionsgeschwindigkeit bei der Inversion von Rohrzucker durch Säuren. *Zeitschrift für physikalische Chemie* 4(1):226–248. <https://doi.org/10.1515/zpch-1889-0416>
94. Dai G, Hu X, Hering J, Eifler M, Seewig J, von Freymann G (2021) Define and measure the dimensional accuracy of two-photon laser lithography based on its instrument transfer function. *J Phys: Photon* 3:034002. <https://doi.org/10.1088/2515-7647/abfaa7>
95. Eifler M, Hering J, Keksel A, von Freymann G, Seewig J (2021) Towards a continuous frequency band chirp material measure for surface topography measuring instrument calibration. In: *Optical measurement systems for industrial inspection XII*, vol 11782. SPIE (2021), pp 99–114. <https://doi.org/10.1117/12.2591935>

Manufacturing-Morphology-Property Relationships for Rotating Shaft Sealing Systems



Stefan Thielen, Sergiy Antonyuk, Jan C. Aurich, Tilmann Beck, Hans Hasse, Michael Kopnarski, Balázs Magyar, Bernd Sauer, and Marek Smaga

Abstract In this chapter, results of the investigation of manufacturing-morphology-property (MMP) relationships for radial shaft seals, with a special focus on the shaft countersurface of the seal, are presented. This includes experimental investigations of alternative manufacturing and micro structuring processes such as turning, micro grinding, micro milling, shot- and micro peening and lapping. Furthermore, the influence of metastable austenitic shaft materials, of the rubber material and fillers and of lubricants on wear, friction and function of sealing systems with radial shaft seals was also investigated.

S. Thielen (✉) · B. Sauer
Institute of Machine Elements, Gears and Tribology, RPTU Kaiserslautern, Kaiserslautern, Germany
e-mail: stefan.thielen@rptu.de

S. Antonyuk
Institute of Particle Process Engineering, RPTU Kaiserslautern, Kaiserslautern, Germany

J. C. Aurich
Institute of Manufacturing Technology and Production Systems, RPTU Kaiserslautern, Kaiserslautern, Germany

T. Beck · M. Smaga
Institute of Materials Science and Engineering, RPTU Kaiserslautern, Kaiserslautern, Germany

H. Hasse
Institute of Engineering Thermodynamics, RPTU Kaiserslautern, Kaiserslautern, Germany

M. Kopnarski
Institute of Surface and Thin Film Analysis (IFOS), Kaiserslautern, Germany

B. Magyar
Institute of Sustainable Materials, Processes and Products, University Paderborn, Paderborn, Germany

1 Introduction

Radial shaft seals (RSS) are dynamic seals, employed for sealing rotating shafts against fluids or grease. Together, the seal, shaft and lubricant form the basic components of the sealing system (Fig. 1), and each plays an important role in its function and behavior.

During shaft rotation, an approximately $1\ \mu\text{m}$ high lubricant film partly separates the shaft and seal due to elastohydrodynamic effects between the lubricant and the micro topography ('roughness') of seal and shaft. Contrary to other machine elements, here the lubrication effect is solely based on the roughness and not on the macro geometry of the contact partners. An active reverse pumping effect in this contact area provides leak tightness despite the gap between the shaft and seal. To ensure this effect, the seal surface must be suitably rough in the contact area, and an asymmetric distortion of the sealing edge is necessary. The formation of a rough seal surface during wear processes can be influenced by adding coarse mineral fillers of sizes ranging approximately $1\text{--}25\ \mu\text{m}$ to the rubber formulation (Sect. 2.4), while the distortion pattern during rotation is ensured through choice of a suitable seal geometry and the action of a garter spring [1].

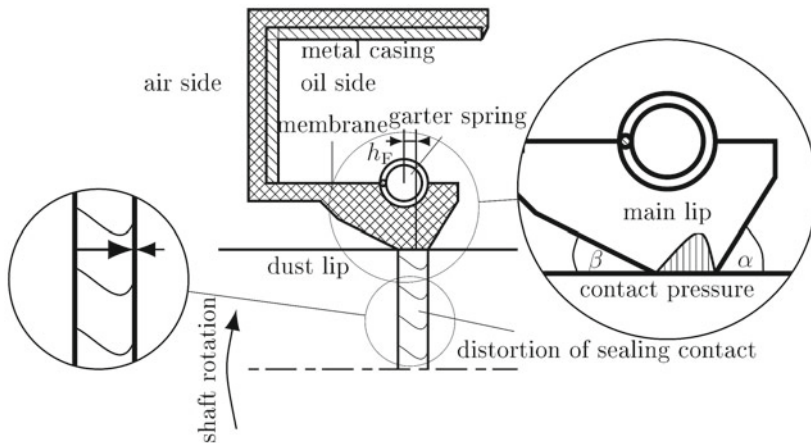


Fig. 1 Cross section of an assembled radial shaft seal

Although the axial length of the sealing contact and thereby the nominal contact area are very small, RSS exhibits a high friction torque compared to other machine elements. In many cases, the lubrication effect of the sealing contact is not strong enough to fully separate the shaft and seal, resulting in the occurrence of mixed friction and subsequently wear on the shaft and seal. Therefore, the shaft surface is required to be hardened to at least 55–60 HRC (approx. 600–700 HV) [2].

Since the sealing effect is based on the deflection of fluid through the orientation of surface roughness, the surface of the shaft can also strongly influence the sealing behavior. Therefore, the shaft countersurface of RSS is typically required to be free of any orientation of the roughness structures tilted with respect to the circumferential direction (twist). Furthermore, it must adhere to strict requirements on the surface roughness. While the latter is typically smaller than the seal roughness, standards like DIN 3760 and seal manufacturer catalogs specify permissible ranges of certain shaft surface roughness parameters [3, 4].

A twist-free surface adhering to the surface requirements is conventionally manufactured by a costly and energy-inefficient process: First, the shaft blank is pre-turned, then it is hardened and finish machined by plunge grinding to a nominal diameter. If performed correctly, this process guarantees a reliable function of the seal with respect to the shaft surface. In order to reduce manufacturing cost or friction, alternative methods of manufacturing or micro structuring the shaft surfaces are required.

In addition to the surfaces, the materials in the tribosystem play an important role for the function of the sealing system. The material of the shaft and its material state (hardness, martensite content ...) also influence the wear properties and thereby the service life. Details about this can be found in Sect. 2.3. Besides its viscosity, other lubricant properties influence friction and service life. Physical and chemical interactions between rubber and lubricant components can alter the rubber properties significantly, causing failure of the sealing system [5]. Especially with the use of low-viscosity synthetic oils, for some combinations with certain rubber types, increased shaft wear was found [6, 7]. Also, the rubber of the sealing lip influences the functional behavior, for example, through its wetting properties with regard to the lubricants [8] or its coarse mineral fillers, which can cause shaft wear [6]. Those effects are presented in more detail in Sect. 2.4.

The above-mentioned aspects and alternative manufacturing methods for shaft surfaces have been studied experimentally and simulatively. A special focus was on the relationship between the manufacturing process, the resulting surface topography and the properties and behavior of the shaft surfaces (MMP Relationships). The results will be presented in the following sections.

2 Experimental Investigations of the Influence of Materials and Different Manufacturing and Micro Structuring Processes on Friction and Wear in Radial Shaft Sealing Systems

The experimental investigations focused on the influence of surface topography on the behavior of the sealing system and on the influence of material properties on wear. Turning as an alternative manufacturing process and targeted micro structuring of shaft surfaces have been investigated.

Typical test conditions for the wear tests were 590 h test duration at 10 m/s (20.000 km sliding distance) and 70 °C oil sump temperature. Unless stated otherwise, RSS with 80 mm nominal (shaft) diameter made from fluoroelastomer (FKM) were used in combination with a polyalphaolefin (PAO) lubricant of the SAE 0W20 class ($\rho_{20} = 857.9 \text{ kg/m}^3$ and $\nu_{40} = 39.11 \text{ mm}^2/\text{s}$). The PAO was blended with a small amount of ester to achieve better solubility of the antifoam and antioxidant additives. No further additives were added.

A description of the test benches used to generate the results presented here can be found in [9].

2.1 *Micro Structuring of Shaft Surfaces (Micro Grinding, Micro Peening, Shot Peening)*

While hardening and grinding as the state-of-the-art finishing process for shaft seal counterfaces produces reliable sealing function and wear-resistant surfaces, the friction in a sealing contact with such surfaces is high.

Therefore, alternative finishing and a micro structuring process have been investigated for many decades [10–12]. Although it was shown that peening processes with steel balls or glass beads can significantly reduce friction and wear, such processes have not yet been widely adopted due to the lack of experience and the additional cost.

In simulative pre-investigations using the transient-EHL model presented in Sect. 3.3, it was shown that small indentations in the shaft surface with a depth in the range of 1 μm can significantly reduce friction [13]. Therefore, several methods (micro peening, shot peening, micro grinding) have been applied in order to create a surface micro structure with such indentations.

The micro peening process is based on the cold spray process presented in Chap. 6, using titanium particles and adapted to create small indentations in the previously ground shaft surface without particles sticking to the surface. This process was compared to state-of-the-art shot peening processes using stainless steel balls with two different parameter sets on a turned surface (Fig. 2).

Results show reduced friction (Fig. 3) and wear for all peened surfaces compared to the ground surfaces.

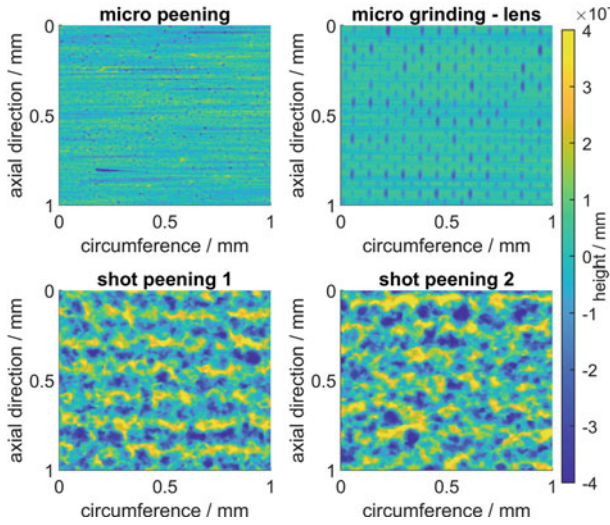
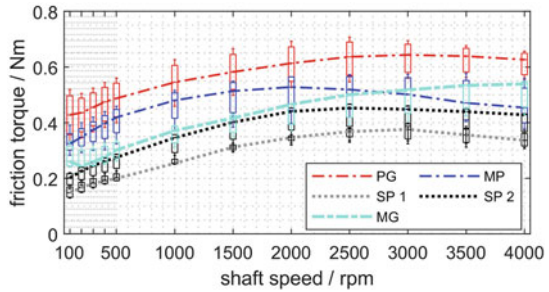


Fig. 2 Surface topography of the micro structured shafts

Fig. 3 Comparison of the friction torque of micro structured and state-of-the-art infeed ground (PG) shafts for different shaft speeds. MP: micro peening; SP1/2: shot peening; MG: micro grinding



While the lowest friction torque was found for the shot peened shafts, the micro peened surfaces had the least shaft wear [9].

While the peening processes do not allow for the generation of geometrically defined indentations, the micro grinding process (Chap. 4) can be used to create micro structures with a defined lens shape on ground shaft surfaces, which has proven to be advantageous in EHL simulations (Sect. 3.3) [13, 14]. By angling the axis of the tool with approximately 50 μm diameter with respect to the shaft surface normal direction, it is possible to create such structures with the desired structural depth of approximately 1 μm . Friction torque measurements show an average friction torque reduction compared to ground shafts of approximately 30% (Fig. 3).

The influence of those micro structures on the reverse pumping effect of the shaft has been investigated and documented in [15].

Besides those micro structured shafts, lapping (Chap. 8) has been investigated as an alternative to the grinding process. It was found that lapped surfaces show a similar performance as ground surfaces with comparable roughness.

2.2 Turning Processes

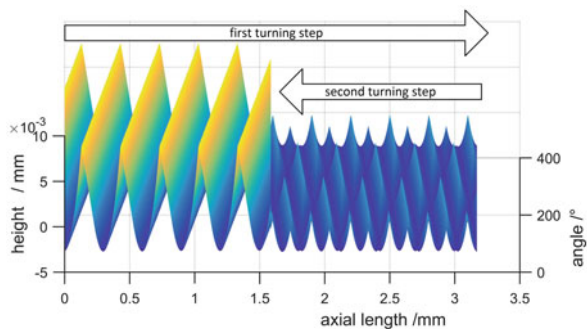
Compared to the conventional manufacturing process, the use of turning as a finish machining step of shaft countersurfaces offers a reduction of manufacturing time and thus cost. Turned shaft surfaces have been found to offer reduced friction compared to ground surfaces [11, 16]. However, conventional longitudinal turning processes create a twist structure on the shaft surface, which depends on the tool geometry, feed and depth of cut of the process [17]. Therefore, seal manufacturers recommend the use of hard turning processes only for applications where the shaft predominantly rotates in one direction. They give recommendations on the choice of machining parameters to ensure a reliable function of hard turned shaft surfaces [4].

A multiple turning process, in which the turned surface will be turned a second time with the same tool and feed, but with reversed feed direction and without additional depth of cut, was investigated. This process is intended to create two counteracting twist structures (Fig. 4) which should result in a neutral conveying effect of the shaft during rotation. Investigations have shown that for small feed values of 0.15 and 0.075 mm/rev, a leakage-free operation with reduced wear compared to conventionally turned shafts is possible [18].

Another way to improve the shaft surface in a sealing system is the use of cryogenic turning processes with metastable austenitic steel (AISI 347) shafts (Chap. 5). The cryogenic turning process induces the formation of α' -martensite in the subsurface region, increasing the wear resistance of the shaft surfaces and eliminating the need for an additional thermal hardening step.

Using a simple one-step cryogenic turning process, it could be found that shaft wear was reduced by approximately 90% compared to the state-of-the-art ground carburized shafts made of AISI 5115 [16]. An in-depth investigation of the martensite

Fig. 4 Comparison of the resulting surfaces for a simple turning step (left) and multiple turning (right) [18]



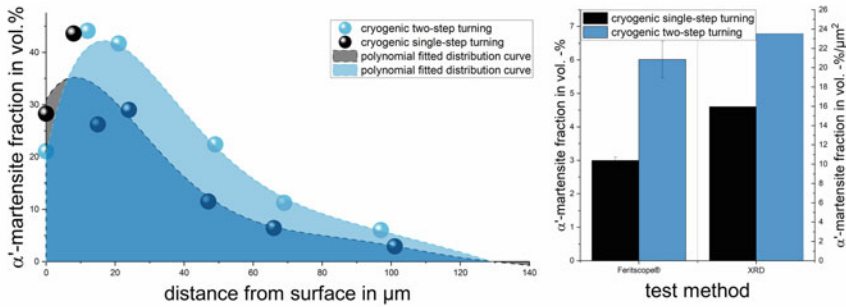


Fig. 5 **a** Polynomial fitting of the α' -martensite volume fraction according to the X-ray phase analysis, **b** Comparison of the α' -martensite volume fraction between Ferritscope measurements and integral of XRD analysis

content in the wear track revealed an increase compared to the area which was not subjected to tribological load.

In order to guarantee a functional shaft surface, both feed and depth of cut need to be low. However, those conditions are not ideal for the formation of α' -martensite. Therefore, additionally a two-step cryogenic turning process was investigated, using a first turning step designed to create high amounts of α' -martensite and a second step using machining parameters that guarantee a functional shaft surface topography. In the second step, also a small part of the surface layer resulting from the first step was removed. Magnetic FerritscopeTM measurements showed a higher overall α' -martensite content below the surface for these shafts compared to the single-step process. Surprisingly, although the wear was still much lower than for hardened and ground reference surfaces made from AISI 5115, results showed increased wear compared to the one-step cryogenic turning process. An in-depth investigation revealed that for the two-step process, the α' -martensite content in the subsurface area has its maximum approximately 20 μm below the surface, while the maximum wear depth was only 10 μm . The single-step process produced an α' -martensite maximum approximately 10 μm below the surface and also a higher α' -martensite content directly at the surface (Fig. 5).

Those results lead to the conclusion that mainly the α' -martensite content in the wear-relevant subsurface region and not the overall content determines the shaft's wear resistance in a sealing system. In order to successfully apply cryogenic turning processes to RSS-counterfaces, the machining steps and parameters should be optimized with regard to the α' -martensite content in this area.

2.3 Influence of Shaft Material and Phase Transformation on Wear

The results in Sect. 2.2 [16], as well as early results from *Otto*, who found a wear reduction when using stainless steel shafts [19], indicate an influence of the use of stainless steels as shaft material on its wear.

Therefore, the protective, purely wear-induced formation of stacking faults and/or twins and/or ϵ - and/or α' -martensite in the sealing contact of metastable austenitic steel shafts was investigated. Ground and turned shafts made from different metastable (AISI 347, AISI 303) and superstable austenitic steels (AISI 904L) were tested in staggered wear tests. As reference, shafts made from AISI 5115 were used. All shafts were turned without the application of cryogenic cooling. For each steel type, six shafts were tested for up to 590 h. Two shafts each were extracted after 10% and 50% of the test time in order to characterize the development of the wear processes during the test duration.

Investigations of martensite content and material micro structure in the close subsurface regions after the wear tests show that for metastable austenitic steels, a tribo-induced increase in α' -martensite can be found. The wear properties of the metastable austenitic steels are similar, independent of the chosen machining strategy. For AISI 347, a 10 vol% increase in α' -martensite content was found, while AISI 303 showed an increase of 6 vol% and AISI 904L showed no change. On summarizing, it could be found that the local tribo-induced changes in material micro structure, such as phase transformations and twinning, improve the wear properties of metastable austenitic steels (Fig. 6).

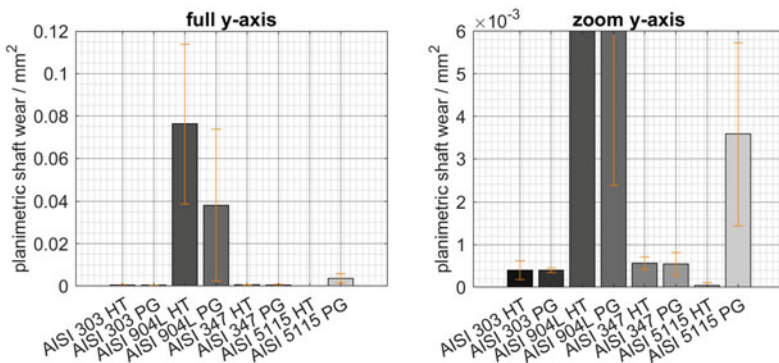


Fig. 6 Planimetric shaft wear for different turned and ground shaft surfaces made from AISI 347, AISI 303 and AISI 904L. PG: Plunge ground; HT: Hard turned

2.4 Influence of Lubricant and Rubber on Lubrication and Wear

Macroscopically, the hardness of the seal is much smaller than the hardness of the hardened shaft surface. Nevertheless, excessive shaft wear was reported by a multitude of researchers in applications with RSS, especially with FKM materials [16, 20–22]. *Frölich, Engelke* and *Kanzaki* independently found such effects in combination with synthetic lubricants [16, 23, 24]. *Schuler* and *Klaiber* identified the wetting properties of lubricants to influence shaft wear in sealing systems by diminishing the lubrication film height and thereby worsening the mixed friction conditions in the sealing contact [22, 25]. They used the penetrativity according to *Washburn* Ψ as a measure to evaluate the influence of wettability on the lubrication potential of oil in the sealing contact:

$$\Psi = \frac{\sigma_l \cos(\theta)}{2\eta} \quad (1)$$

with σ_l : surface tension oil; θ : contact angle lubricant-substrate; η : dynamic viscosity lubricant. The idea behind this is that the penetrativity describes the tendency of the lubricant to enter the small lubricated gap between the shaft and seal during shaft rotation. It thereby acts as a counter-force to the reverse pumping effect and ensures a good lubrication if its value is high enough.

A regression analysis of wear results obtained with different synthetic PAO and PG oils with the penetrativity of the oil and FKM material of the seal (Fig. 7) revealed a correlation between the values [8].

Kanzaki confirmed the influence of the presence of silica group fillers on shaft wear. Silica particles have a much higher hardness (SiC: 2,500 HV; SiO₂: 750–1,150 HV) compared to a hardened carburized steel shaft surface (600–700 HV). *Thatte* found that on a microscopic scale, the elasticity and hardness of the rubber compound vary greatly due to the presence of such filler particles [26].

Our own investigations on worn seals, amended by surface and layer analysis at the IFOS (Chap. 2), have revealed that for worn RSS, filler particles are being exposed in the sealing contact. Ion-induced secondary electron images at focused ion beam (FIB) cross section in the sealing edge of those RSS revealed sharp-edged filler particles with sizes up to 10 μm in the near-surface area (Fig. 8). The Si/O stoichiometry ratio of many of those larger filler-particles is in agreement with the stoichiometry of SiO₂.

When comparing the worn cross sections of sealing edge and shaft, similar topographies could be found on RSS and the shaft wear track (Fig. 9), indicating that shaft and seal wear are strongly coupled and influenced by local seal properties, such as micro topography and hardness. The results stipulate that exposed filler particles with sufficient size can cause abrasive wear on the shaft, if the lubrication film cannot fully separate both surfaces (which can be the case when the lubricant has bad wettability with the shaft or seal). Secondary electron microscopy analysis (SEM) of

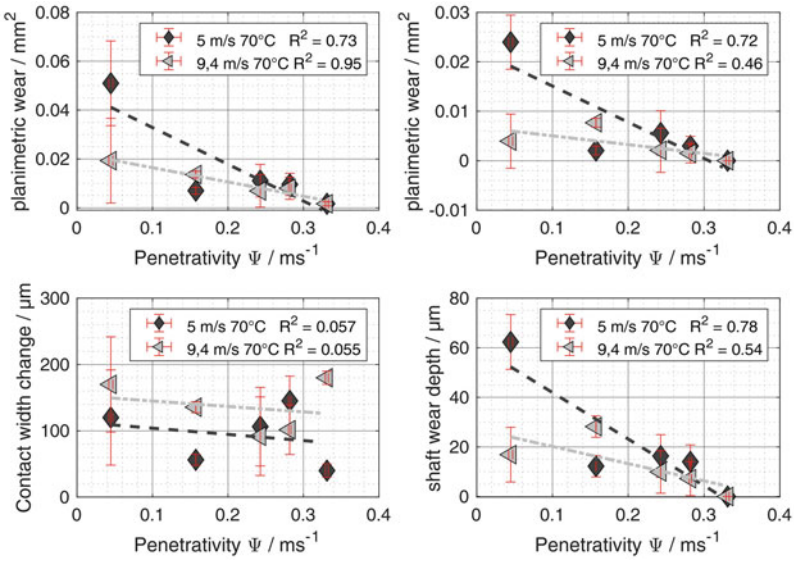


Fig. 7 Regression between penetrativity and wear quantifications on seal (l.) and shaft (r.) [8]

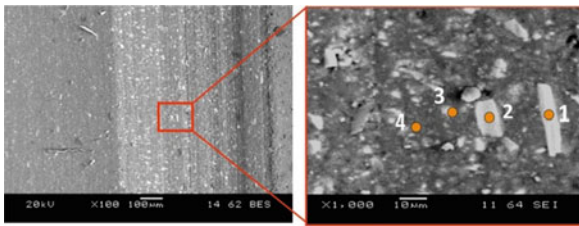


Fig. 8 SEM images of the worn surface and a FIB-cut of a sealing lip showing filler particles [7]

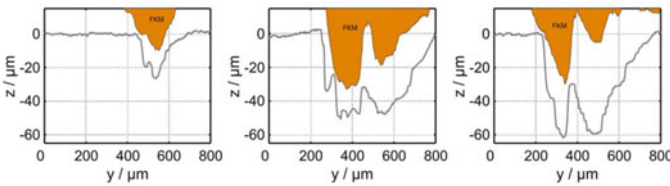


Fig. 9 Surface micro topography of seal and shaft in worn area showing good correlation between structures on seal lip and shaft wear cross section [7]

worn shaft surfaces after removal of nano scale surface layers by ion bombardment shows that in a depth between 8 and 23 nm (Ta_2O_5 -depth equivalent), a Si content of up to 30 at% can be found, confirming direct contact between the shaft and filler particles [6, 7].

3 Simulative Investigation of the Influence of Different Manufacturing and Structuring Processes on Friction and Wear in Radial Shaft Sealing Systems

Simulative investigations offer several benefits compared to experiments. After a simulation tool is set up, the cost of performing simulations is neglectable, allowing for extensive parameter variations which are often not possible experimentally. In many cases, a simulation can also be used to take into account the evolution of the object under study due to time-consuming effects, such as wear-related geometry changes. Thus, a simulation can greatly reduce the time needed to study such effects and their influence on the system behavior. Furthermore, simulations allow the investigation of properties or processes that cannot be observed experimentally or only at the cost of influencing the system.

Nevertheless, simulations cannot fully replace experiments, since the latter are necessary to determine which effects are relevant in the observed system and thus must be modeled simulatively. The necessary input data for a simulation is often determined empirically, and a model verification is commonly based on a comparison to measured data.

These facts illustrate why the investigation of radial shaft sealing systems depends on both, experimental and simulative work. While the former was already discussed in the previous section (Sect. 2), the latter shall be the topic of the following section.

Relevant simulation methods for radial shaft seals are the kinematic simulation and fractal description of shaft surface topographies, Finite Element (FE)-simulations of the RSS in contact with the shaft at the macro scale and elastohydrodynamic (EHL) simulations of the lubricated sealing contact on the micro scale.

3.1 Kinematic Simulation and Analytical Description of Turned Shaft Surfaces

Since turning involves the removal of material using a tool with defined geometry, kinematic models can be used to estimate the ideal surface topography of the resulting surface. An advanced model developed within the CRC 926 can also take into account the wear of the tool edge and vibrations or tumbling of the shaft [17].

The plastic processes during chip formation, however, cannot be reproduced with purely kinematic models. To investigate those effects, the topography of turned surfaces needs to be measured and evaluated. One example for such an evaluation is the description of the measured surface topography using *Weierstrass-Mandelbrot* fractal functions in order to characterize the surface and reproduce it (Fig. 10) with a significantly reduced amount of data compared to a point cloud representation of the measured data [27]. Such representations can then be used as input for the tribological simulations described in the following subsections.

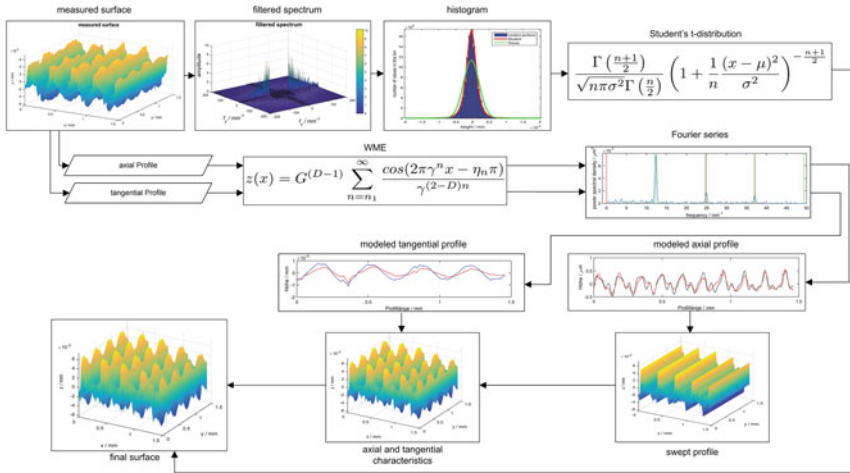


Fig. 10 Flowchart and methods used to generate a fractal reconstruction of turned shaft surfaces [27]

3.2 FE Simulation of Sealing Contacts on the Macro Scale

FE models of radial shaft seals allow for the macro scale simulation of the assembly process of the seal on the shaft. Taking into account the relevant seal and shaft geometry as well as material properties (hyper-, viscoelastic and thermal behavior of the seal), functional properties like the axial contact width between the shaft and seal or the axial pressure profile can be determined [28–30]. Special operation scenarios like a dynamic shaft run out, and the followability of the seal against this movement can also be studied directly in the FE simulation.

Together with additional information about the operation conditions of the seal (shaft speed, oil sump temperature, ...), the results of the FE simulation can then be used to calculate further tribologically relevant effects in the sealing contact in coupled calculation scripts.

Using the *Engelke* model, friction torque and contact temperate of the seal can be determined [28, 31]. The friction model is based on a semi-empirical approach and calculates the friction torque from a boundary friction term and a viscous friction term. For the calculation of the latter term, a constant gap height in the contact area is assumed and set to the sum of the maximum profile peak height R_p of the shaft and seal. For the calculation of the contact temperature, a linear behavior between the areal friction power and the overtemperature in relation to the oil sump is assumed. Since the friction and contact temperature term are coupled through the friction power dependence of the temperature and temperature dependence of the lubricant viscosity, both equations are usually solved iteratively. Although these are rather simple approaches, good results can be achieved since many parameters are determined based on empirical data from friction torque and contact temperature measurements.

Another method for calculating the temperatures in the seal and its environment is given by thermal networks. By discretizing the system in a small number of discrete, interconnected nodes and using a simple thermal-electrical analogy, the temperature can be easily determined based on the friction losses and heat sinks of the system [29, 32, 32, 33].

Furthermore, using either the pressure-based Archard [34] or the friction energy-based *Fleischer* wear model [35], the local wear of the shaft and seal in the contact zone can be calculated.

Through iterative updates of the FE model, a feedback-based coupling between the FE model and these calculation scripts is possible, allowing for the investigations of the various cross-influences (Fig. 11) [28, 36].

This model was applied to turned shaft surfaces generated with the kinematic model described in Sect. 3.1. The results show that the localization of the shaft wear in the simulation (Fig. 12) fits the experimental results very well [29].

3.3 *TEHL Simulation of Sealing Contacts on the Micro Scale*

While the FE simulation presented in the previous subsection takes into account the macro scale (full geometry of shaft and seal) in all relevant details, the micro scale effects like the friction in the sealing contact are only calculated as global values using semi-empirical models. In order to take into account micro scale lubrication effects in detail, a Thermo Elasto Hydrodynamic Lubrication (TEHL)-simulation of the sealing contact is necessary. Such simulation tools are prerequisites for comprehensively studying the influence of the micro topography on the functional behavior of sealing systems.

While for most machine elements the lubrication is based on the macro geometry, the formation of a lubrication film in the sealing contact of RSS depends mainly on the roughness of both seal and shaft. Typically, the seal roughness is 3–10 times larger than the shaft roughness. Consequently, at least the seal roughness must be modeled when simulating the lubrication of RSS on the micro scale.

Nevertheless, the seal macro geometry (length of the seal membrane, garter spring, contact angles after assembly) also influences the micro scale contact mechanics, for example through structural stiffness effects.

A TEHL simulation requires a coupled system describing the hydrodynamics and contact mechanics (deformation) of the sealing contact. Typically, the hydrodynamics are modeled using the *Reynolds* equation, while the contact mechanics modeling is based on the half-space theory (HST). The efficient deformation calculation with the HST allows for good simulation times. However, the consideration of structural deformations (e.g. bending of the seal membrane and consequently a change on the contact angles between seal and shaft) is not possible with HST alone. Therefore, a corrective term for structural deformations based on FE simulations is necessary. Also, an integration of viscoelastic material behavior in a HST deformation calculation would greatly increase simulation times. An alternative that allows for con-

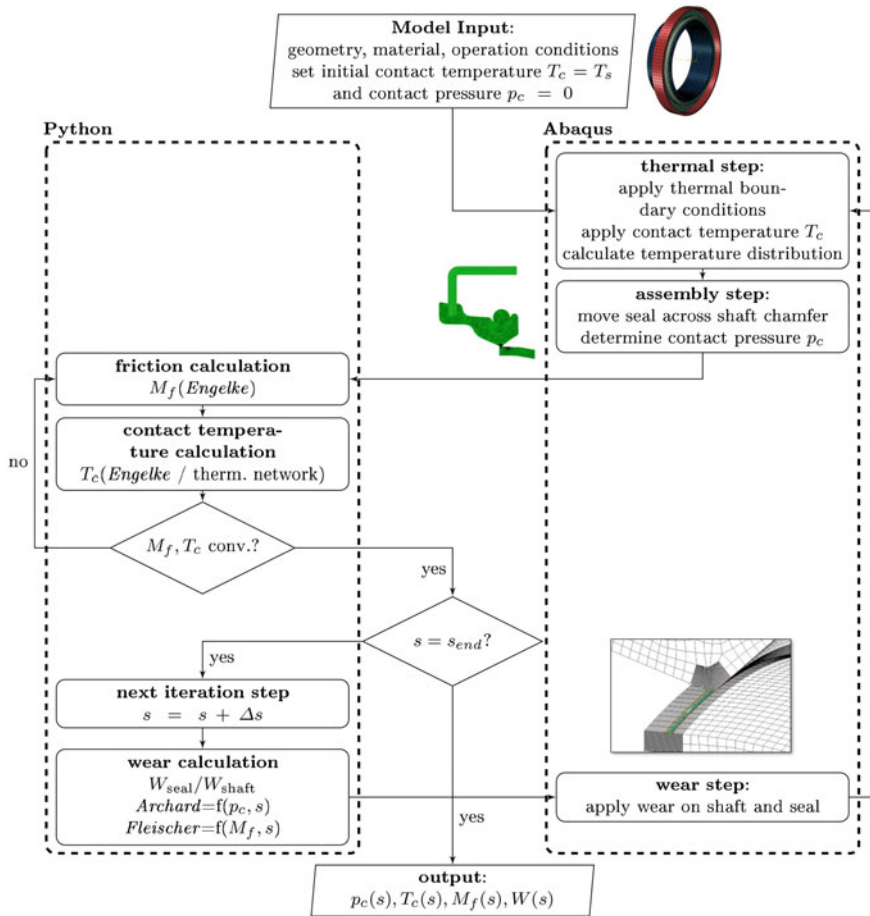


Fig. 11 Flowchart of the FE simulation on the macro scale. T_c = contact temperature, T_s = oil sump temperature, p_c = contact pressure, M_f = friction torque, s = sliding distance and $W_{\text{seal/shaft}}$ = seal/shaft wear

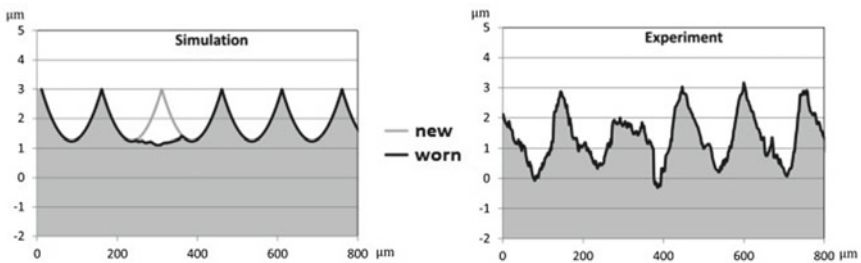


Fig. 12 Wear localization on a shaft surface turned with a feed of 0.15 mm/rev. L.: Simulation; r.: Experiment [29]

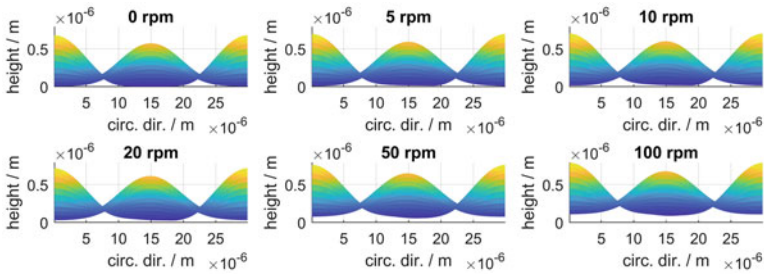


Fig. 13 Formation of a lubricating film under the asperities on the seal during start of shaft rotation [13]

sideration of the structural stiffness is the use of FE simulations either by deriving a contact stiffness matrix (fast) or by direct coupling of the hydrodynamics with the FE model (typically a lot slower).

When taking into account the local oil temperatures, an implementation of the energy equation of the lubricant and a calculation of seal and shaft temperature, e.g. with a thermal network, are necessary.

Such a TEHL model of a sealing contact has been developed. The deformation calculation used in the model was based on standalone HST models which have been developed as part of subproject C01 [37–39]. Further details about the model can be found in [13, 14, 40, 41].

Using the model, it could be shown how the lubrication film forms underneath the seal asperities as soon as the shaft starts to rotate (Fig. 13).

It was found that although the lubricant film height increases drastically from 0 to 500–1,000 rpm (shaft diameter 80 mm) before it reaches an almost constant value, mixed friction still occurs at high shaft speeds with approximately 10% of the contact force being produced from asperity contact [13, 40].

With the model, it could also be studied how the local lubricant flow was conveyed in axial direction around the single asperities on the sealing lip (Fig. 14).

The model has also been used to study the effect of a variation of surface roughness and topography direction on the system friction. The results show that a higher roughness and a longitudinal alignment of the asperities (perpendicular to the circumferential direction) on the seal and shaft reduce the friction torque [40]. However, it should be taken into account that an increase in shaft roughness is also associated with higher wear due to an increase in asperity contacts. A study of different shaft micro structures showed that a circular, lens-shaped structure with a depth of approximately 1 μm could reduce the friction torque by 18% compared to a ground shaft at 1,000 rpm (Fig. 15) [13, 14, 40, 41].

Similar to the FE model, the TEHL model was augmented with a wear calculation based on the friction energy from asperity contact (*Fleischer*) [42]. While this allows for a separation of friction torque into lubricant shearing (which does not contribute to wear) and asperity contact (which does), the determination of the wear energy density e_w (the amount of energy needed to cause a certain amount of wear) proves to be a

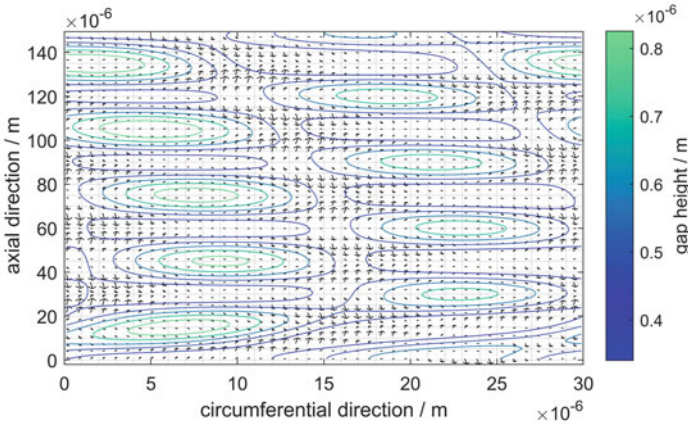


Fig. 14 Flow of the lubricant between shaft and seal around the seal micro topography [13]

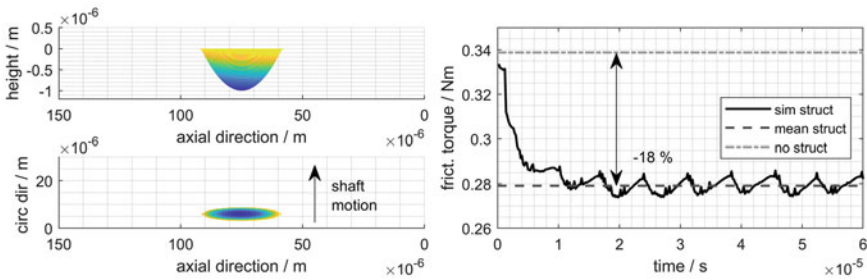


Fig. 15 Effect of a micro structured shaft on friction torque [13]. L.: Shape of the micro structure; r.: Simulation friction torque of structured shaft and comparison to unstructured shaft

complication. It needs to be determined empirically by recording the friction torque during a wear test. The torque can then be integrated over the total angle of rotation to determine the frictional energy which can then be divided by the planimetric wear of seal or shaft. This procedure however calculates e_w from the total friction torque, since it cannot be divided into a viscous and asperity contact part in the experimental measurement. In the FE simulation, this approach is feasible, since we use the total friction torque to calculate the wear energy.

For our calculations within the TEHL model, a value for e_w was estimated based on experimental results. Future work should focus on determining e_w experimentally based only on the asperity contact contribution to the frictional energy.

Results of our simulation show that the average lubricant film height does not change significantly with wear on the shaft and seal, since in soft EHL contacts, the influence of load/pressure is not as strong as for hard contact bodies [42].

Parts of the EHL approach were also used to simulate a chain joint (Chap. 16) [43, 44].

References

1. Johnston DE (1999) Design aspects of modern rotary shaft seals. Proc Inst Mech Eng Part J J Eng Tribol 213(3):203–213. <https://doi.org/10.1243/1350650991542947>
2. DIN3761 (1984) Rotary shaft lip type seals for automobile; applications. standard. withdrawn. Beuth Verlag, Berlin
3. DIN3760 (1996) Rotary shaft lip type seals. standard. Beuth Verlag, Berlin
4. Freudenberg Sealing Technologies GmbH & Co. KG (2015) Technical manual, chapter 01: simmerrings and rotary seals, vol 1
5. Bellaire D, Thielen S, Burkhart C, Münnemann K, Hasse H, Sauer B (2022) Investigation of radial shaft seal swelling using a special tribometer and magnetic resonance imaging. ACS Omega 7(14):11671–11677. <https://doi.org/10.1021/acsomega.1c06521>
6. Burkhart C, Emrich S, Kopnarski M, Sauer B (2020) Excessive shaft wear due to radial shaft seals in lubricated environment. Part II: measures against excessive shaft wear. Wear 462–463:203483. <https://doi.org/10.1016/j.wear.2020.203483>
7. Burkhart C, Emrich S, Kopnarski M, Sauer B (2020) Excessive shaft wear due to radial shaft seals in lubricated environment. Part I: analysis and mechanisms. Wear 460–461:203419. <https://doi.org/10.1016/j.wear.2020.203419>
8. Burkhart C, Heier M, Merz R, Lösch J, Wagner C, Thielen S, Sauer B, Kopnarski M, Hasse H (2021) Einfluss des Schmierstoffs auf Verschleißverhalten und-Mechanismen im System Radialwellendichtring. 62. Tribologie-Fachtagung (GfT) 2021
9. Thielen S, Breuninger P, Hotz H, Burkhart C, Schollmayer T, Sauer B, Antonyuk S, Kirsch B, Aurich JC (2021) Improving the tribological properties of radial shaft seal countersurfaces using experimental micro peening and classical shot peening processes. Tribol Int 155:106764. <https://doi.org/10.1016/j.triboint.2020.106764>
10. Heyn WO (1968) Shaft surface finish is an important part of the sealing system. J Lubr Technol 90(2):375–381. <https://doi.org/10.1115/1.3601571>
11. Johnston DE, Vogt R (1995) Rotary shaft seal friction, the influence of design, material, oil and shaft surface. In: SAE technical paper series. SAE International. <https://doi.org/10.4271/950764>
12. Vogt R, Bock E (2014) Shaft surface effects on radial shaft seals. In: Encyclopedia of lubricants and lubrication. Springer, Berlin, Heidelberg, pp 1739–1746. https://doi.org/10.1007/978-3-642-22647-2_338
13. Thielen S, Magyar B, Sauer B (2020) Thermoelastohydrodynamic lubrication simulation of radial shaft sealing rings. J Tribol 142(5). <https://doi.org/10.1115/1.4045802>
14. Thielen S, Foko FF, Magyar B, Sauer B (2018) Sealing contact shaft structure design using EHL simulation. In: Proceedings of the 17th EDF/PPRIME workshop. Green Sealing, Paris, France
15. Burkhart C, Thielen S, Sauer B (2020) Online determination of reverse pumping values of radial shaft seals and their tribologically equivalent system. Tribologie und Schmierungstechnik 67. ISSN: 07243472. <https://doi.org/10.30419/TuS-2020-0025>
16. Frölich D, Magyar B, Sauer B, Mayer P, Kirsch B, Aurich J, Skorupski R, Smaga M, Beck T, Eifler D (2015) Investigation of wear resistance of dry and cryogenic turned metastable austenitic steel shafts and dry turned and ground carburized steel shafts in the radial shaft seal ring system. Wear 328–329:123–131. <https://doi.org/10.1016/j.wear.2015.02.004>. Apr

17. Raid I, Seewig, Frölich D, Sauer B, Mayer P, Schneider F, Aurich J (2014) Kinematische Simulation gedrehter Wellenaufflächen. *wt Werkstatttechnik online* 104(5):279–287
18. Thielen S, Magyar B, Sauer B, Schneider F, Mayer P, Kirsch B, Müller R, Harbou EV, Aurich JC (2017) Functional investigation of zero lead radial shaft seal counter-surfaces turned with a special method. *Tribol Int.* <https://doi.org/10.1016/j.triboint.2017.02.002>.
19. Otto V (1988) Scene-of-the-crime—running surfaces in the sealing interface of shaft seal to shaft. In: SAE technical paper series. SAE International. <https://doi.org/10.4271/880306>
20. Padgurskas J, Rukuiza R (1998) Senkung der Verlustleistung und des Verschleißes bei der Paarung RWDR/Welle. 2. Vortrag. II. Hamburger Dichtungstechnisches Kolloquium: Dynamische Dichtungen. Hamburg. Techn. Univ
21. Hermes J, Hüttinger A, Prem E (2015) New approval process for dynamic tightness tests for gear units. *VDI-Berichte* 2255:771–782
22. Schuler P (2014) Einfluss von Grenzflächeneffekten auf den Dichtmechanismus der Radial-Wellendichtung
23. Engelke T, Poll G (2008) Prüfverfahren zur Untersuchung der Verträglichkeit von Getriebeabdichtungen und Ölen. In: Gesellschaft für Tribologie e.V., Fahrzeugtechnik, Zerspanungs- und Umformtechnik, Prüfen, Messen, Kontrollieren, Tribologische Systeme, Maschinenelemente und Antriebstechnik. Prüfen, Messen, Kontrollieren, Aachen
24. Kanzaki TKY, Kawahara Y (1989) A study of blistering phenomenon on rubber seals. In: 12th international conference on fluid sealing, pp 27–36
25. Klaiber M (2013) Betriebs- und Benetzungseigenschaften im Dichtsystem Radial-Wellendichtung am Beispiel von additivierten synthetischen Schmierölen
26. Thatte A, Salant RF (2012) Effects of multi-scale viscoelasticity of polymers on high-pressure, high-frequency sealing dynamics. *Tribol Int* 52:75–86. <https://doi.org/10.1016/j.triboint.2012.02.024>. Aug
27. Thielen S, Magyar B, Piros A (2016) Reconstruction of three-dimensional turned shaft surfaces with fractal functions. *Tribol Int* 95:349–357. <https://doi.org/10.1016/j.triboint.2015.11.028>. Mar
28. Frölich D, Magyar B, Sauer B (2014) A comprehensive model of wear, friction and contact temperature in radial shaft seals. *Wear* 311:71–80
29. Frölich D (2016) Strategien und Modelle zur Simulation des Betriebsverhaltens von Radial-Wellendichtungen. PhD thesis, Technische Universität Kaiserslautern. ISBN: 9783959740302
30. Jennewein B, Frölich D, Sauer B (2021) Simulation of the radial force of radial shaft seal rings at different temperatures and aging conditions. In: ISC Internationale Dichtungstagung, Stuttgart
31. Engelke T (2011) Einfluss der Elastomer-Schmierstoff-Kombination auf das Betriebsverhalten von Radialwellendichtungen. Dissertation, Leibniz Universität Hannover
32. Frölich D, Magyar B, Sauer B (2014) Semi-analytical model for the contact temperature calculation in radial shaft seals. In: STLE-annual meeting, Lake Buena Vista, Florida
33. Magyar B, Frölich D, Sauer B (2013) Temperaturberechnung im RWDRDichtkontakt. In: 54. Tribologie-Fachtagung, Göttingen
34. Archard JF (1953) Contact and rubbing of flat surfaces. *J Appl Phys* 24(8):981–988. <https://doi.org/10.1063/1.1721448>
35. Fleischer G (1967) Energiebilanzierung der Festkörperreibung als Grundlage zur energetischen Verschleißberechnung (Teil 1). *Schmierungstechnik* 7(8):225–230
36. Burkhart C, Weyrich D, Thielen S, Schollmayer T, Sauer B (2021) Development and optimization of a tribometer for radial shaft seals. *J Tribol* 143(4). <https://doi.org/10.1115/1.4049597>
37. Magyar BSB (2013) Contact modeling of rough surfaces. In: 5th world tribology congress, Torino, Italy
38. Magyar B, Sauer B (2016) Methods for the simulation of the pressure, stress, and temperature distribution in the contact of fractal generated rough surfaces. *Proc Inst Mech Eng Part J J Eng Tribol* 231(4):489–502. <https://doi.org/10.1177/1350650115593962>
39. Foko FF, Burkhart C, Thielen S, Sauer B (2022) Analysis of the sealing capability of radial shaft sealing rings using a semi-analytical contact model. *Tribol Online* 17(2):97–109. <https://doi.org/10.2474/trol.17.97>

40. Thielen S (2019) Entwicklung eines TEHD-Tribosimulationsmodells für Radialwellendichtringe. PhD thesis, Technische Universität Kaiserslautern. ISBN: 978-3-95974-120-0
41. Thielen S, Sauer B (2020) Thermo-Elastohydrodynamische Simulation von Radialwellendichtringen. *Tribologie und Schmierungstechnik* 67. ISSN: 07243472. <https://doi.org/10.30419/TuS-2020-0013>
42. Burkhart C (2022) Ein Beitrag zum Verständnis des Verschleißverhaltens im SystemRadialwellendichtring. PhD thesis, Technische Universität Kaiserslautern
43. Magyar B, Thielen S, Löwenstein M, Becker A, Sauer B (2018) EHD simulation eines ketten-gelenkes. *Tribol Schmierungstech* 65:40–47
44. Kamga LS, Meffert D, Magyar B, Oehler M, Sauer B (2022) Simulative investigation of the influence of surface texturing on the elastohydrodynamic lubrication in chain joints. *Tribol Int* 171:107564. <https://doi.org/10.1016/j.triboint.2022.107564>

Influence of the Surface Morphology on Rolling Bearing Life Under Mixed Lubrication



Bernd Sauer, Tilmann Beck, Bastian Blinn, Flavien Foko Foko, Pascal Ostermayer, and Lukas R uth

Abstract In the existing design guidelines for rolling bearings, there is no direct evaluation of the influence of the surface morphology on the achievable fatigue life under mixed lubrication conditions. This work focuses on the influence of different surface finishing processes, i.e., fine grinding, rough grinding, and hard turning, on the fatigue life of inner rings of radial cylindrical roller bearings. In addition to fatigue life experiments at a four-bearing test rig, detailed analyses of the finishing-induced surface morphology as well as calculations of the stress condition caused by the different surface topographies were conducted. To characterize the surface morphology, the local mechanical properties were determined using cyclic micro-indentation tests and the residual stresses were measured by X-ray diffraction. For the stress calculations, a multiscale simulation composed of a multi-body model at the macro-level and a half-space contact model at the micro-level was used. The results obtained in fatigue life experiments, surface morphology characterization, and stress calculations were combined. From this for the hard turning a high potential to increase the fatigue life of roller bearings under mixed lubrication conditions was examined.

1 Introduction

Rolling bearings are used to decouple axles, shafts, and rails in machines from the rotation of the connected structure. Their basic functions are to ensure low-friction motion, to hold the components in position and to support and transmit any forces that occur. Each time the rolling elements roll over the raceway, it is subjected to high stresses and, consequently, the demands on the purity and strength of the material as well as the existing surface conditions are relatively high. As a design according to [1] requires high-quality surface topographies and material purities, the influence

B. Sauer · F. Foko Foko · L. R uth

Institute of Machine Elements, Gears and Tribology, RPTU Kaiserslautern, Kaiserslautern, Germany

T. Beck (✉) · B. Blinn · P. Ostermayer

Institute of Materials Science and Engineering, RPTU Kaiserslautern, Kaiserslautern, Germany
e-mail: t.beck@mv.rptu.de

of the surface morphology on the fatigue life is not considered. A high potential for a reduction of the production costs of roller bearing rings is given by decreased demands on the quality of the surface topography. However, for surfaces with a more pronounced topography, existing design concepts cannot be applied. To elaborate a design concept for bearing rings with a lower quality of the surface topography, it is necessary to understand the stress conditions below the surface occurring under mixed lubrication and how they influence the rolling fatigue lifetime. Note that the influence of the surface morphology is assumed to be more pronounced under mixed lubrication, as this leads to a stronger stress concentration at the surface layer [2].

Besides the lubricant, the surface topography determines the lubricant film formation, and thus the friction condition. This is usually assessed via the viscosity ratio κ from [1] or the specific lubricant film thickness Λ according to [3, 4], which additionally includes the surface roughness of the contact partners. For mixed lubrication, the limit of the film thickness is between $\Lambda \leq 3$ [5] and $\Lambda \leq 2$ [6].

The influence of the topography and its tribological effects on rolling bearing life has been the subject of various research projects. The structure direction of roughness [7] as well as its amplitude and wavelength can be mentioned as important factors [8]. In the work of Hansen et al. [9], a modified lubricant film thickness Λ^* is presented, which considers the structure direction of the roughness. Moreover, Λ^* depends on the reduced peak height S_{pk} , the asperity height as well as the wavelength of the roughness.

As shown in [10], a specific lubricant film thickness of $\Lambda < 1.5$ leads to damages being located directly at and below the surface. According to the calculation model of [2], a lower surface roughness results in a higher fatigue lifetime. Existing empirical and deterministic fatigue life models include various factors influencing the material fatigue strength, e.g., material inhomogeneities (*Weibull's* defect model) or the occurrence of high orthogonal stresses (model of *Lundberg* and *Palmgren*) [11]. Others are based on material failure due to the cyclic stress field caused by the rolling elements [12]. The near-surface stresses caused by the roughness under mixed lubrication and their effect on the fatigue lifetime are described in [13, 14] using a micro-scale EHL (elastohydrodynamic lubrication) calculation model. This model further enables the consideration of the surface damage caused by particle indentations, which occurs more frequently under mixed lubrication [15]. By means of a continuum mechanical model, equations for the fatigue lifetime resulting from crack initiation at the surface as well as from the subsurface region were proposed [16]. In this work it was shown that the fatigue lifetime depends, among other things, on the wavelength and amplitude of the roughness, and surfaces with a low wavelength show more failure located at the surface [16].

In addition to the topography, the fatigue strength of the material plays an important role for the rolling bearing fatigue lifetime. In this context it has to be considered that the rolling contact results in multiaxial stresses with steep gradients. The strength is determined by the initial state of the material, the heat treatment, and the finishing process. As shown in [17, 18], a modification of the finishing process can lead to an increased fatigue lifetime caused by finishing-induced residual compressive stresses. In this context pronounced residual compressive stresses in hardened rolling bear-

ing steels were observed after a hard turning in [19, 20]. Moreover, combination of hard turning and deep rolling led to an experimentally proven fatigue life increase of +150% compared to conventional reference bearings, as shown in [12, 21, 22]. Hybrid machining, which combines hard turning and deep rolling in one process, has not yet been proven to be advantageous compared to pure hard turning [23, 24].

The focus of this work is to determine the influence of the finishing-induced surface morphology on the rolling bearing fatigue lifetime under mixed lubrication condition. For this, rolling bearing inner rings made of 100Cr6 (AISI 52100) were finished using three different manufacturing processes, i.e., fine grinding, rough grinding, and hard turning. Besides the experimental determination of the rolling bearing fatigue lifetimes, the different finishing-induced surface morphologies were analyzed and the stresses caused by the different surface topographies were calculated. For the characterization of the surface morphologies, cyclic indentation tests to determine the mechanical properties as well as X-ray diffraction to measure the residual stresses were used. Finally, the results obtained from fatigue tests, surface characterization, and simulation are combined to evaluate the fatigue life.

2 Experimental, Analysis Setup, and Simulation Methodology

2.1 Specimen Manufacturing

For the rolling bearing tests, inner rings were manufactured by INTERPRECISE Donath GmbH using three different finishing processes, which resulted in three different surface conditions, i.e., fine ground, rough ground, and hard turned. Note that the fine ground condition represents the state of the art and results from grinding and subsequent honing. All rings were made of 100Cr6 (AISI 52100), with a chemical composition in accordance with DIN EN ISO 683-17 [25]. The blanks of the rings, which had an outer diameter of 50.44 mm, were quenched and tempered using the parameters given in Table 1, leading to a hardness of 730 ± 7 HV30 and a retained austenite content of about 5%.

To guarantee comparable loading conditions for all rings, the raceway diameters of the original inner rings of the NU208 test bearings were measured on a 3D coordinate measuring device. The radial bearing clearance was measured manually using a dial gauge. Based on this, three tolerance classes (49.96 mm, 49.97 mm, and 49.98 mm) with a maximum diameter deviation of $\pm 5 \mu\text{m}$ were defined for manufacturing. For

Table 1 Heat treatment parameters and hardness achieved

Austenitization	Quenching	Tempering	Hardness
850 °C/45 min	180 °C/15 min	240 °C/240 min	730 ± 7 HV30

the fatigue tests, the original inner rings were replaced by the inner rings manufactured by INTERPRECISE Donath GmbH. Note that the rolling elements were guided by sheet metal cages and exhibited a logarithmic profile, while the inner rings manufactured had a cylindrical profile [1].

2.2 Bearing Test Rig

The tests were carried out on a rolling bearing life test rig, which enables a simultaneous testing of four bearings under comparable loading conditions (Fig. 1).

The radial force F_{rad} was applied via the radial force actuator at a hollow shaft containing two bearings using interposed disk springs. These two inner bearings transfer the force to the shaft, which is also connected with the two outer bearings. Due to the symmetrical arrangement of the outer and inner bearings, all bearings were loaded equally. For an axial fixture of the shaft, a deep groove ball bearing was used. Moreover, it was ensured by appropriate radial clearance that no radial forces can be carried. Between the disk springs of the radial load unit and the hollow shaft, a load cell was installed to measure the load applied.

The oil feed was realized by a circulating lubrication, which had a temperature of $80\text{ }^{\circ}\text{C}$. The temperature of the lubrication was controlled by using four heating elements, being located at the two cover sleeves. Therefore, the temperature was measured using temperature sensors of type PT100. The lubricating oil, whose flow rate was regulated, was finely filtered and injected into the contact via injection sleeves at four points around the circumference. The shaft is driven coaxially by means of a three-phase squirrel-cage motor connected via a coupling. To detect the fatigue damage at an early stage of the tests, a vibration-based condition monitoring

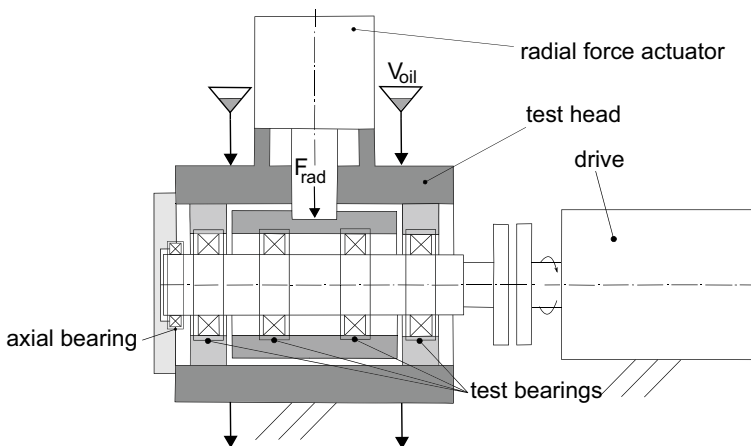


Fig. 1 Schematic illustration of the bearing test rig [26]

system of ifm electronic GmbH was used. Using this system an automatic shutdown of the test rig was enabled, whereby the acceleration of the oscillation was detected. Moreover, for the inner ring, the outer ring and the rolling elements' characteristic frequencies, which imply damages, were determined based on ordinal numbers and the rotational frequency similar to [12].

2.3 Analytcs

To determine the two-dimensional surface characteristics as well as the profiles of the inner rings, a stylus instrument of the type S3P of the company PERTHEN-MAHR was used. Moreover, the surface topography was measured by means of a confocal microscope of the type μ surf of the company NANOFOCUS. The characteristic topography values were determined in accordance with [27] using the software MountainsMap® of the supplier DIGITAL SURE.

2.3.1 X-ray Diffraction

The finishing-induced residual stresses within the subsurface volume were determined using X-ray diffraction measurements (XRD) on the peripheral surface of the roller bearing rings, as shown in Fig. 2. Using a diffractometer of type PANalytical Empyrean, the XRD measurements were conducted with Cu $K\alpha 1$ radiation at 40kV tube voltage and 40mA tube current. A scanning speed of 0.004 °/s as well as an irradiation spot size of 3 mm \times 2 mm was used. Note that ψ is defined as the

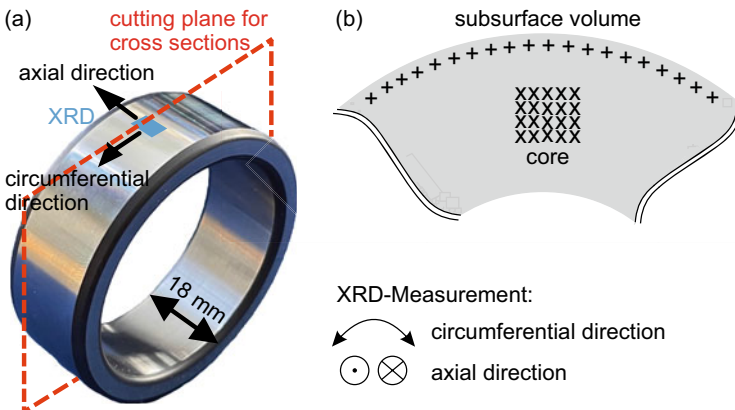


Fig. 2 a Directions and positions of the residual stress measurements by means of XRD and b cross section of the rolling bearing ring including a schematic illustration of the measurement positions used in cyclic indentation tests [29]

angle between the beam path and the normal vector of the specimen surface. The first-order residual stresses in axial and circumferential direction were determined for all specimens via the $\sin^2\psi$ method applied to the diffraction peak of the $\{211\}$ martensite lattice plane. The advantage of the $\sin^2\psi$ method is the consideration of several inclination angles ψ to determine the plane spacing. This approach enables a high accuracy of the determined residual stress state [28].

To analyze the residual stresses depending on the distance from the surface, the XRD measurements were carried out at different depths. Therefore, the material was removed by electrolytic polishing with a Struers LectroPol-5. The electrolyte was permanently cooled to temperatures between 0°C and 20°C to avoid microstructural changes during the polishing process. The changes in the residual stress state caused by electrolytic polishing can be neglected, as in relation to the geometries of the bearing rings only small areas ($20\text{ mm} \times 10\text{ mm}$) [30] as well as depths ($100\ \mu\text{m}$ to $150\ \mu\text{m}$) [31] were removed. Thus, no mathematical compensation of the residual stresses is required for the presented results.

2.3.2 Cyclic Indentation Tests

To investigate the influence of the different finishing processes and cyclic loadings on the cyclic properties of the subsurface volume of the roller bearing rings, the short-time procedure PhyBaL_{CHT} was used, which is based on instrumented cyclic indentation tests (CIT) and is explained in detail in previously published work [32–34]. The CIT were performed using a Fischerscope® of type HM2000 (Helmut Fischer GmbH, Sindelfingen, Germany), which is equipped with a Vickers indenter and enables a continuous detection of the indentation depth h and the indentation force F .

From the second cycle on, an F - h hysteresis can be obtained, which is schematically shown in Fig. 3. Similar to the plastic strain amplitude $\varepsilon_{a,p}$ obtained from a stress–strain hysteresis, the half width of the F - h hysteresis at mean loading ($0.5 F_{\max}$) is defined as the plastic indentation depth amplitude $h_{a,p}$, which is a characteristic value of the plastic deformation that occurs in the indentation cycle. By analyzing the change in $h_{a,p}$ during the CIT, which is represented by the $h_{a,p}$ - N curve, the cyclic deformation behavior of the material can be analyzed (see Fig. 3). The $h_{a,p}$ - N curve reveals a stabilized slope from the fifth cycle on, which indicates a saturation of macro-plastic deformation and that microplasticity dominates the cyclic deformation behavior. Thus, this regime of the $h_{a,p}$ - N curve is used to characterize the cyclic properties and can further be described mathematically by using the power law function $h_{a,p\text{II}}$ see Eq. (1), in which the cyclic hardening exponent CHT e_{II} represents the slope of the $h_{a,p}$ - N curve in this regime. As a steeper slope of the $h_{a,p}$ - N curve results from a more pronounced cyclic hardening, higher $|e_{\text{II}}|$ correlate with a greater cyclic hardening potential of the material [32].

$$h_{a,p\text{II}} = a_{\text{II}} \cdot N^{e_{\text{II}}}. \quad (1)$$

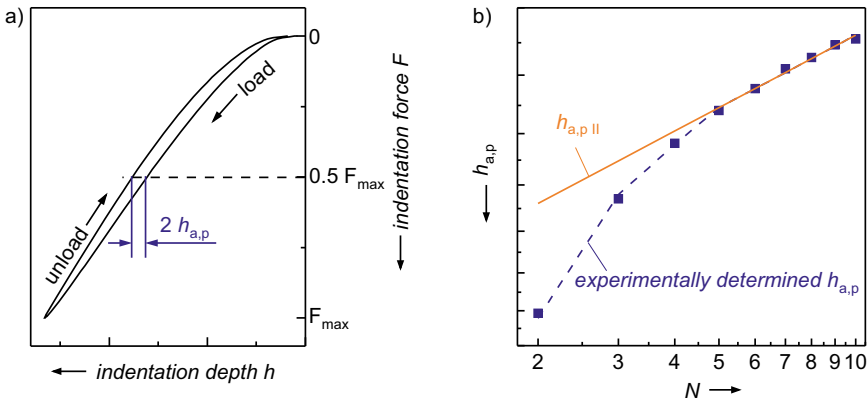


Fig. 3 Schematic description of the PhyBaL_{CHT} procedure: **a** F - h hysteresis and **b** $h_{a,p}$ - N curve

Moreover, the $h_{a,p}$ - N curve can be used to describe the cyclic plasticity of the material. Since higher $h_{a,p}$ are associated with a wider hysteresis and, accordingly, indicate a stronger plastic deformation, the vertical position of the $h_{a,p}$ - N curve can be related to the cyclic plasticity. By comparing the position of the $h_{a,p}$ - N curves of different material conditions, the amount of cyclic hardening, and thus cyclic hardening exponent_{CHT} e_{II} , as well as the absolute value of the indentation depth h have to be considered, because these values influence the absolute value of $h_{a,p}$. However, if different conditions show comparable absolute indentation depths and cyclic hardening, the $h_{a,p}$ - N curves can be used for a sufficient assessment of the cyclic plasticity [29].

In addition to the analysis of the cyclic properties, the indentation depth obtained from the first cycle can be used to determine the microhardness (Marten’s hardness, HM) of the material.

As shown schematically in Fig. 2, the CIT were performed on cross sections of the roller bearing rings in a distance from the edge of $40 \mu\text{m}$, representing the subsurface volume, as well as 2.5 mm apart from the surface to determine the properties of the core material as a reference. In the CIT, the material was loaded for ten cycles with a sinusoidal load function with a maximum indentation force $F_{max} = 500 \text{ mN}$ and a frequency of $1/12 \text{ Hz}$. To obtain statistically reliable results, a minimum of 40 CIT were performed on two cutting planes per measurement area, i.e., the subsurface volume and the core material. To produce a high surface quality, which is required for micro-indentation testing, the specimens were mechanically polished with small forces to avoid microstructural changes and preparation-induced residual stresses. Due to the maximum indentation diagonal of about $12 \mu\text{m}$, the distance from the surface of $40 \mu\text{m}$ and the point-to-point distance of $100 \mu\text{m}$ were chosen to exclude interference effects to the boundary layer or between the measuring points, which is in accordance with the DIN EN ISO 14577 [35]. Note that based on the results

of Sadrabadi et al. [36], the plastically deformed volume beneath the indenter can roughly be estimated with a factor 3 of the indent diagonal.

2.4 Modeling Strategy

To calculate the stresses occurring during the fatigue tests in the subsurface volume, all components of the bearing rings have to be modeled, i.e., the outer ring, the inner ring, the rolling element, and the cage. Using a multi-body simulation (MBS) model built with the commercial software Simpack, which was coupled with self-developed calculation routines of cylindrical roller bearings described in [37–39] the applied loads were calculated in the first simulation level. The existing solvers from Simpack are used to solve the differential equations of motion. In-house calculation routines programmed in Fortran extend the model to represent the dynamic processes in the rolling contacts with the required precision. The solver calculates the state variables in the form of positions, velocities, and accelerations of the individual bodies. Then the forces, pressures, and friction are determined in the calculation routines, which are then returned to the software as forces and moments for calculating iteratively the equilibrium state. In this way, external influencing variables can be considered as boundary conditions in the calculation. For example, the bearing clearance and the profile of the contact partners can be mapped. From the dynamic simulation on the first level (see Fig. 4a), the contact forces in the rolling element-bearing ring contact are transferred to the semi-analytical contact model on the second simulation level.

Based on the calculated loads, the stresses were determined on a microscopic scale using a semi-analytical (SA) contact model implemented in MATLAB. In the SA contact model, the contact between the rolling element and the inner ring raceway (see Fig. 4b) is elastically solved. The raceway topographies in the unloaded state and after 10^7 revolutions (see Fig. 11) are used in the contact model to determine the stresses in the surface-near area. An identical computational domain was defined with dimensions 0.6 mm, 0.6 mm, and 0.3 mm, discretized into 194, 194, and 129

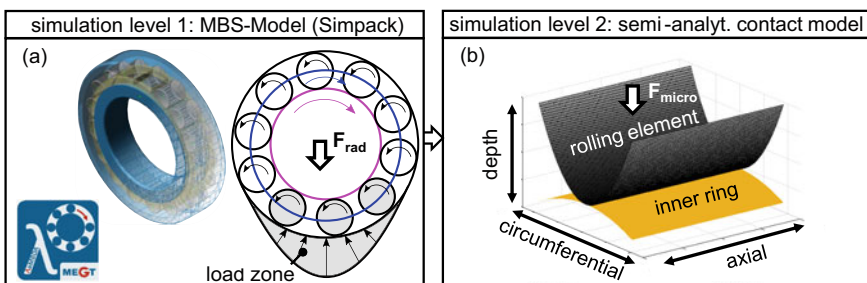


Fig. 4 Illustration of the contact models used in the two simulation levels, macro-scale MBS model (a) and micro-scale half-space model (b)

elements in the axial (x), circumferential (y), and depth (z) directions, respectively. The applied microforce is 310 N and corresponds to a maximum contact pressure of 2.4 GPa with an ideally smooth inner ring surface topography.

The implemented semi-analytical contact model is based on the half-space theory [40–42] where the contact bodies are considered as a half-space. In continuum mechanics, a half-space describes a semi-infinite space limited in one direction by a plane. Only at this plane external forces can be applied on the half-space. In this modeling approach, the solution of a contact problem mainly requires the areas of the contact partners and the stiffness at the contact, which can be derived from so-called influence functions [43, 44].

The functions for determining the stresses can be taken from the literature [45]. Note that these solutions are only valid for a point load and lead to a singularity at the coordinate origin ($x=y=z=0$). The numerical solution of the contact problem requires a discretization of the entire half-space, resulting in surface and volume elements at the surface and the inner part. Consequently, valid solutions for surface loads are required, which was proposed by Love [46] for a surface load being constant on a rectangular surface.

3 Results and Discussion

3.1 Determination of the Fatigue Lifetimes

To determine the fatigue lifetimes of the different variants, the sudden death method was used for the rolling bearing fatigue tests. Thus, the tests were performed until the first bearing failed. As for each variant six failures were obtained, in total 24 bearing rings were tested, respectively. The statistical evaluation of the fatigue lifetimes observed was based on the two-parameter Weibull distribution according to [47] and [48], which is commonly used for rolling bearing lifetime calculations [49]. Using this method, the failure probability based on the bearing rings failed in the fatigue tests can be quantified. Moreover, this approach enables to consider the bearing rings, which did not fail in the fatigue tests. This results in a higher number of specimens considered in the statistical evaluation, and thus increases the statistical validity. In the presented work, for each variant the failure probability was determined based on the 90% confidence interval and only crack initiation from the surface-near areas, which led to pitting after fatigue crack propagation, was observed. The resulting Weibull distributions of the different variants are shown in Fig. 5, while in Table 2 an overview of the corresponding theoretically ($L_{10,\Delta}$) and experimentally (B_{10}) determined fatigue lifetimes as well as the slopes of the Weibull curve β are given. Note that β further represents a measure for the lifetime scatter observed in the fatigue tests, being highest for the hard turned variant. The vertical lines in Fig. 5 represent the B_{10} values.

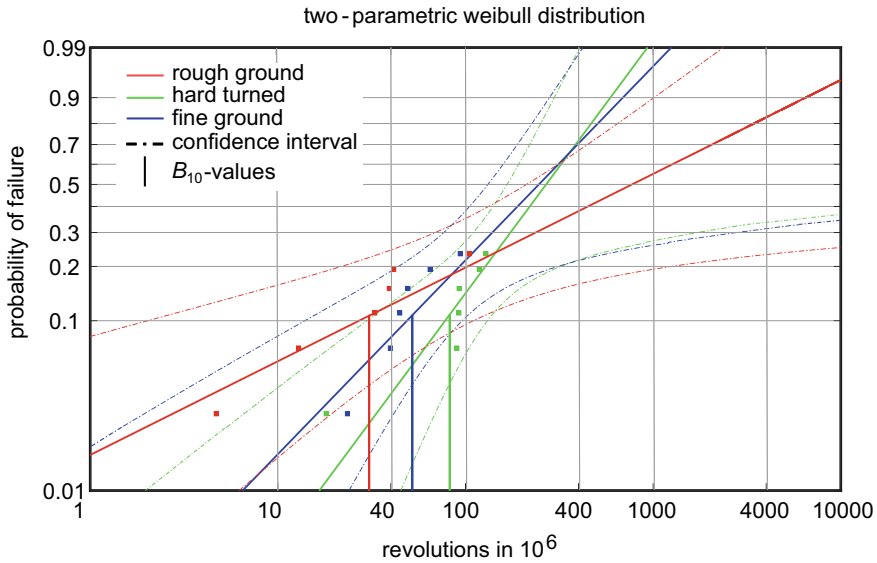


Fig. 5 Experimentally determined fatigue lifetimes as well as the resulting Weibull curves including the 90% confidence interval determined for the different variants [26]

Table 2 Test overview with the corresponding theoretically ($L_{10,\Lambda}$) and experimentally (B_{10}) determined fatigue lifetimes as well as the slopes of the Weibull curve β

	$L_{10,\Lambda}$ in 10^6 revolutions	β	B_{10} in 10^6 revolutions
Rough ground	23.7	0.56	27.1
Hard tuned	26.7	1.52	78
Fine ground	28.9	1.16	49.0

$L_{10,\Lambda}$ was calculated in accordance with [1], whereby the specific lubricant film height Λ and thus the lubrication conditions were considered. Therefore, the viscosity ratio κ was used as given in Eq. (2). Consequently, $L_{10,\Lambda}$ represents the theoretical reference lifetime that can be expected for the loading conditions applied, and thus near-surface fatigue failure.

$$\kappa = \Lambda^{1.3} \tag{2}$$

The experimentally determined B_{10} show an extension of the fatigue lifetime between a factor of 1.2 and 2.9, when compared to the theoretically determined $L_{10,\Lambda}$. This deviation might be explained by the fact that in the theoretical calculation the residual stresses in the surface-near area are not considered. In this context, compressive residual stresses at the surface and subsurface regions can substantially increase the fatigue lifetime [12].

Comparing the B_{10} obtained for the different variants in Fig. 5, the hard turned condition shows the highest fatigue lifetimes, while the rough ground condition exhibits the lowest B_{10} . Thereby, the fatigue lifetime obtained for the hard turned rings is 2.9 times higher than B_{10} of the rough ground condition.

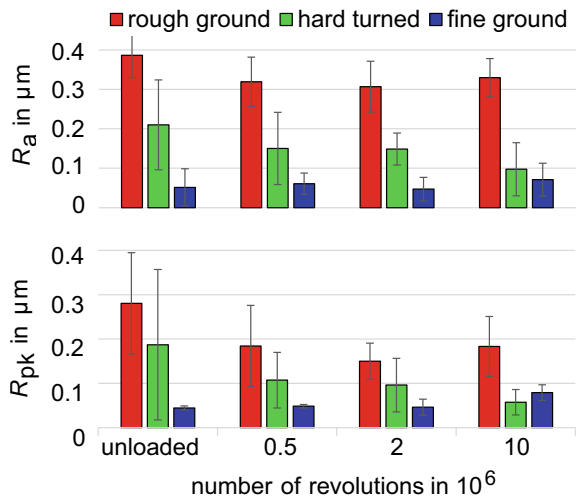
Considering the confidence intervals, large regions of intersection can be observed, which is, among other things, caused by the relatively low number of failed specimens, increasing the confidence intervals. Thus, the observed differences can only be interpreted qualitatively and no significant influence of the finishing processes on the fatigue rolling bearing lifetime can be concluded. For such conclusions, a broader database is required. However, in the experiments the hard turned variant tends to yield slightly higher fatigue lifetimes. To analyze this tendency observed, interrupted fatigue tests and investigations of the surface morphology were performed, which are presented in the following.

3.2 Interrupted Rolling Bearing Fatigue Tests

To analyze the changes in the surface topography caused by the cyclic rolling contact, interrupted fatigue tests were performed. In Fig. 6, the roughness profiles are measured tactilely in the test interruptions, and thus the evolution of the surface roughness is illustrated. Therefore, in addition to the conventional center roughness value R_a , the reduced peak height R_{pk} from the Abbot curve is shown, as these values are suitable for assessing the functional properties of the roughness peaks [50].

As shown in Fig. 6, the rough ground variant shows a significantly higher roughness in relation to the other variants, while the fine ground condition exhibits, as

Fig. 6 Evolution of the surface roughness in the form of the center roughness value R_a and the reduced peak height R_{pk} of the differently finished bearing rings obtained in the interrupted fatigue tests



expected, the smallest roughness peaks. However, while the fine ground variant shows no significant changes in roughness caused by cyclic loading, for the hard turned and rough ground variants a pronounced smoothing of the roughness peaks can be observed. This roughness peak smoothing is most pronounced in the first interval $0.5 \cdot 10^6$ revolutions, and thus at the beginning of the fatigue tests. For the remaining lifetime, the surface roughness remains nearly constant for all variants. However, from $2 \cdot 10^6$ to 10^7 revolutions the hard turned variant shows a slight decrease in surface roughness. This results in a nearly similar surface roughness for the hard turned variant in relation to the fine ground condition after 10^7 revolutions. Moreover, the relative difference in surface roughness between the hard turned and rough ground variants becomes higher, and thus a more pronounced smoothening effect can be concluded for the hard turned variant.

The higher roughness of the rough ground variant might explain the slightly lower fatigue lifetime determined experimentally. However, the hard turned variant shows a higher surface roughness than the fine ground condition but also higher fatigue lifetimes. Thus, the surface roughness cannot solely explain the differences observed in fatigue experiments. Consequently, a detailed analysis of the finishing-induced surface morphology as well as its changes during the fatigue test were conducted, which is shown in Section 3.3 and Section 3.4.

3.3 Residual Stresses at Defined Distances from the Surface

As shown in [51], finishing-induced residual stresses in the surface-near area can have a substantial influence on the fatigue lifetime of rolling bearings. Thus, the finishing-induced residual stresses in axial and circumferential direction at the surface and within the subsurface were determined for all variants and shown in Fig. 7. Moreover, the change in the residual stress state caused by the cyclic contact loading was determined, which is also given in Fig. 7. Note that the data points shown in the diagrams are the values measured by XRD, while the regression lines are based on a B-spline interpolation. These regression lines are only a rough approximation of the real distribution of the residual stresses and the measured data points show slight deviations to the calculated curves.

In the unloaded state, the rough ground variant shows in axial direction only compressive residual stresses, which are highest directly at the surface (about -500 MPa) and are relieved nearly to 0 at a depth of approximately $30 \mu\text{m}$. After the cyclic loading, the compressive residual stresses are increased significantly being also maximum directly at the surface (-1200 MPa). In the loaded state, the residual stresses are nearly resolved at a depth of $80 \mu\text{m}$ and for the loaded condition a stronger gradient in residual stresses occurs. Although the compressive residual stresses in circumferential direction are lower and are relieved at slightly smaller depth in the unloaded state, the residual stresses measured in axial and circumferential direction are qualitatively comparable.

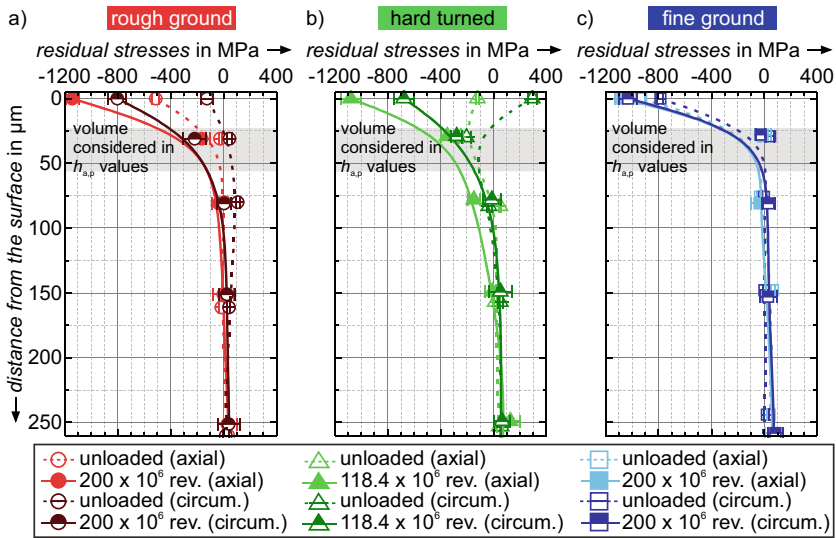


Fig. 7 Residual stresses in axial and circumferential (circum.) direction of **a** rough ground, **b** hard turned, and **c** fine ground roller bearing rings in the unloaded [29] and loaded state

Compared to the rough ground condition, the compressive residual stresses at the surface of the fine ground bearing rings are significantly higher. However, for the fine ground condition no pronounced changes in residual stresses occur due to the cyclic loading. This leads to similar residual stress at the surface of the fine and rough ground variants after $200 \cdot 10^6$ revolutions (see Fig. 7a and c). However, at the fine ground variant the residual stresses are relieved at $30 \mu\text{m}$, and thus are less pronounced in the depth of the subsurface volume when compared to the rough ground bearing ring. Comparing the residual stresses in the axial and circumferential direction, no significant changes are observed for the fine ground condition.

In contrast to the ground bearing rings, the unloaded, hard turned variant exhibits only small compressive residual stresses at the surface, which increase to a maximum in the subsurface volume (-250 MPa) until the residual stresses are relieved at $80 \mu\text{m}$ below the surface. After loading, the residual stress distribution is qualitatively similar with the ground variants. However, the residual stresses in the loaded hard turned bearing ring are relieved at approximately $15 \mu\text{m}$, which is significantly deeper in relation to the other variants (see Fig. 7b). Comparing the residual stresses measured in axial and circumferential direction, substantial differences are obtained in the unloaded state, while in the loaded state the residual stress distributions are qualitatively comparable and are only slightly smaller in circumferential direction. In contrast to the axial direction, tensile residual stresses can be observed in the circumferential direction of the unloaded bearing ring. However, in the subsurface volume nearly similar compressive residual stresses are observed for the two directions considered. Note that the hard turned roller bearing ring was only loaded with

$118.4 \cdot 10^6$ revolutions. However, it is assumed that the residual stresses will not change even at a higher running time.

The XRD analyses reveal a significant influence of the finishing process on the residual stresses in the subsurface volume. Although the fine ground variant exhibits more pronounced compressive residual stresses at the surface than the hard turned variant, the latter achieves slightly higher fatigue lifetimes. Considering the influence of the cyclic loading, all variants show comparable levels of compressive residual stresses at the surface, which is caused by the increase of compressive residual stresses of the hard turned and rough ground variant. However, the hard turned variant shows the compressive residual stresses that are more extended into the subsurface volume. This might explain the slightly higher fatigue lifetime of this variant. To further analyze the differences in surface morphology, also the mechanical properties of the subsurface volume were investigated by means of indentation testing, which is presented in Section 3.4.

3.4 Mechanical Properties Obtained in Cyclic Indentation Tests

To investigate the mechanical properties, CIT were performed at the unloaded and loaded roller bearing rings. The microhardnesses obtained from CIT show no significant differences between the subsurface volume and the core of the differently finished roller bearing rings. Moreover, the unloaded and loaded states show very similar results. Thus, an averaged value for the microhardness of the investigated specimens can be determined, which is about 6.0 GPa. Note that the microhardness measurements in the subsurface volume only provide information about the material volume in the region between roughly 25 and 55 μm distance from the surface. This limitation is caused by the selected indentation force of 500 mN and the application of the DIN EN ISO 14577 standard [35]. For smaller indentation forces, and thus a higher spatial resolution, a higher hardness near the outer surface is assumed, but this was not objective of the present work.

In accordance with the microhardness measurements, the cyclic hardening exponent_{CHT} e_{II} shows only small deviations between the unloaded and loaded conditions as well as between the subsurface volume and the core. The larger deviations are balanced out by the larger standard deviations of the measurement results, so that the cyclic hardening exponent_{CHT} $|e_{II}|$ of approximately 0.19 is at a similar level for all analyzed conditions (see Fig. 8). Consequently, e_{II} and HM indicate no significant influence of the finishing process or cyclic loading on the mechanical properties in the subsurface volume of the roller bearing rings.

However, the results presented in [29] indicate that the changes in residual stresses correlate with changes in the $h_{a,p}$ - N curves. As HM and e_{II} are nearly identical between the different conditions as well as in the subsurface volumes and the core material (see Fig. 8), the cyclic plasticity can be evaluated by comparing the verti-

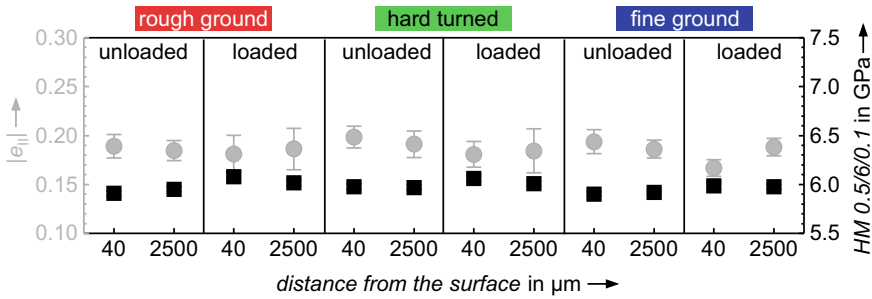


Fig. 8 Cyclic hardening exponent e_{II} and microhardness HM obtained in CIT at differently finished roller bearing rings in the unloaded (shown in [29]) and loaded states

cal positions of the $h_{a,p}-N$ curves (see Fig. 3b). Based on the results shown in [29], the $h_{a,p}-N$ curves obtained from the subsurface volume and the core material are evaluated for the different finishing processes in the unloaded and loaded states, respectively. In accordance with [29], the difference in $h_{a,p}$ at the 10th cycle between the $h_{a,p}-N$ curves obtained from the core material ($h_{a,p 10,C}$) and the subsurface volume ($h_{a,p 10,SSV}$) was determined for all conditions by means of Eq. (3). Hence, higher $\Delta h_{a,p 10}$ indicate a more pronounced increase in cyclic plasticity of the subsurface volume.

$$\Delta h_{a,p 10} = h_{a,p 10,SSV} - h_{a,p 10,C} \tag{3}$$

The differences obtained for the different conditions are given in Fig. 9, showing for all conditions $\Delta h_{a,p 10} > 0$, and thus a higher cyclic plasticity of the subsurface volume. As already shown in [29], in the unloaded condition this increase in cyclic plasticity is most pronounced for the hard turned variant.

The loaded state of the fine ground variant exhibits a slightly higher cyclic plasticity of the subsurface volume when compared to the unloaded state, while this loading-induced increase is significantly more pronounced for the rough ground variant. In contrast, the hard turned roller bearing ring reveals a smaller cyclic plasticity of the subsurface volume in the loaded condition than the unloaded state. Thus, contrary to HM and e_{II} , the $h_{a,p}-N$ curves reflect changes in the mechanical properties of the subsurface volume induced by the finishing processes and the cyclic loading, which was also observed in the residual stress analyses.

Since the previous results have shown that both, the residual stress state and the cyclic plasticity, are influenced by the different finishing processes and the cyclic loading, their correlation was analyzed. Note that the residual stresses measured at a defined distance from the surface are not one-to-one comparable to the results obtained in CIT, since the plastically deformed volume below the indenter is not exclusively the indentation point, rather a half sphere with the size of approximately three times the indent diagonal [36]. For this reason, in Fig. 7, the regions plastically deformed in CIT are depicted by gray-shaded rectangles. For this area, the $h_{a,p}-N$ curves consider a kind of integration of the plastically deformed material volume.

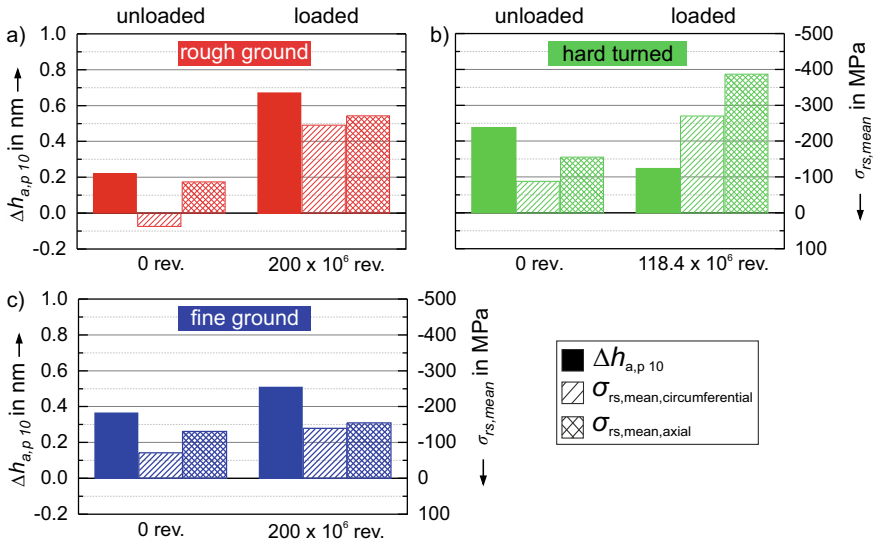


Fig. 9 Correlation between residual stresses and cyclic plasticity of unloaded [29] and loaded **a** rough ground, **b** hard turned, and **c** fine ground roller bearing rings

Note that the stress distribution below the indenter is not homogeneous, since the region immediately below the indenter has a greater influence on the $h_{a,p}$ values than the surrounding, less deformed regions [52]. In addition, the residual stresses of both directions have to be considered, since the cyclic indentation leads to a multiaxial stress state below the indenter. Due to these complex interrelations, only a qualitative comparison between the cyclic plasticity observed in $h_{a,p}-N$ curves and the residual stress state can be provided.

As a comparative value for the residual stress state, the arithmetic mean values of the plastically deformed regions were determined based on the B-spline. However, this is only a rough approximation of the residual stress state, as the stress distribution below the indenter is inhomogeneous.

In the unloaded state, $h_{a,p 10}$ correlates well with the amount of compressive residual stresses, as already shown in [29]. Nevertheless, the differently finished roller bearing rings have to be evaluated separately. The rough ground variant shows in circumferential direction small tensile residual stresses, while in axial direction compressive residual stresses exist. This extensively bigger compressive residual stress state compared to the small tensile stresses is expected to be dominating within the subsurface volume, which correlates with a slight increase in cyclic plasticity (see Fig. 9a). This assumption is confirmed by the results of the fine ground variant, since it shows compressive residual stresses in both directions, leading to a higher value of $\Delta h_{a,p 10}$. However, the highest residual compressive stresses in the range between roughly 25 and 55 μm below the surface are determined for the hard turned variant, which correlates with the highest difference in cyclic plasticity between

the subsurface volume and the core. As discussed in [29], it is assumed that the compressive residual stresses lead to more pronounced plastic deformation during indentation, since the indentation results in compressive stresses. The combination of the stresses caused by the indenter and the residual stresses leads to a higher local stress level, and thus a more pronounced plastic deformation.

Besides the results of the unloaded roller bearing rings, in Fig. 9 the correlation between the residual stresses and the cyclic plasticity of the loaded conditions is shown, respectively. While the compressive residual stresses as well as $\Delta h_{a,p 10}$ of the fine ground variant are only slightly increased after loading, a significant increase in the compressive residual stresses was observed for the rough ground variant, correlating with a pronounced increase in $\Delta h_{a,p 10}$ (see Fig. 9a and c). However, the results obtained at the loaded hard turned roller bearing ring show no correlation between the results for $\sigma_{rs,mean}$ and $\Delta h_{a,p 10}$. While the mean values for the compressive residual stresses increase, $\Delta h_{a,p 10}$ decreases (see Fig. 9b). This might be explained by the more complex microstructural changes induced by cyclic loading, which also depends on the initial microstructure. It could be assumed that the dislocation structure after hard turning is significantly different in relation to the ground variants, which might lead to differently pronounced microstructural changes caused by cyclic loading. However, this assumption has to be verified in further investigations, i.e., in high-resolution microstructural analyses.

3.5 *Simulative Results*

To analyze the contact-induced stresses for the differently finished bearing rings, fully elastic calculations were conducted. Therefore, in the simulation model the confocally measured surfaces of the inner rings were brought into contact with an ideally smooth rolling element surface using the boundary conditions described in Section 2.4. The respective surface topographies of the unloaded and loaded (after 10^7 revolutions) bearing rings are shown in Fig. 10. To illustrate the depth profile, a center section is shown additionally in the right column of the figure.

To compare the surface topographies quantitatively, the real contact areas can be evaluated, which are given in Table 3. As larger contact areas lead to a more homogenous distribution of the loading, higher local stresses can be assumed for lower A_{real} .

In the unloaded state, the fine ground and hard turned surfaces show similar real contact areas of 0.1275 mm^2 and 0.1265 mm^2 , respectively, while the rough ground surface exhibits the smallest real contact area of 0.0883 mm^2 . After 10^7 revolutions, the results of the contact simulation show an increase in the real contact area of 23%, 61%, and 49% for the rough ground, hard turned, and fine ground surfaces, respectively, as a result of the smoothing effect. This leads to a slightly higher A_{real} for the hard turned variant in relation to the fine ground condition, which is assumed to have a positive effect on the fatigue lifetime. The results of the stress calculation

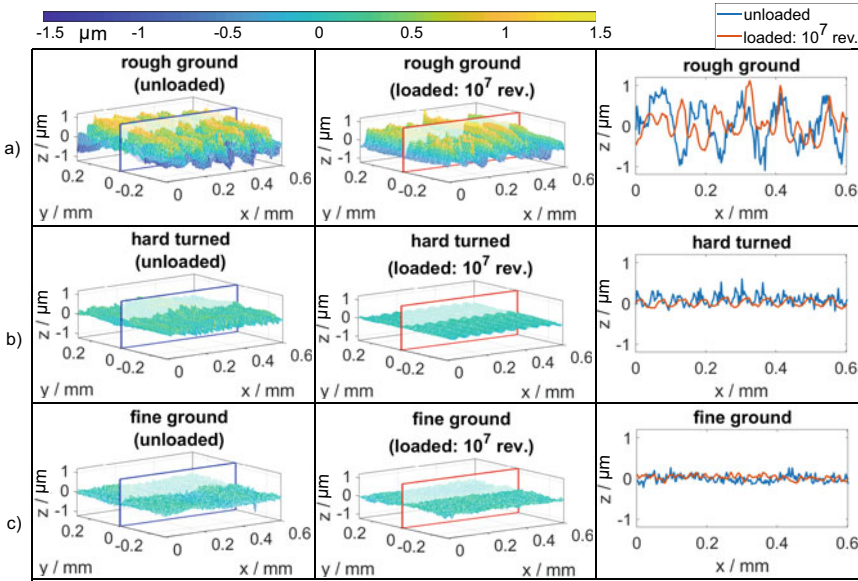


Fig. 10 3D-surface topographies determined via confocal microscope as well as the resulting 2D profile for the differently finished **a** rough ground; **b** hard turned; **c** fine ground bearing rings in the unloaded and loaded (10^7 revolutions) state

Table 3 Elastic contact simulation with real surfaces before and after loading

	Unloaded A_{real} in mm^2	Loaded (10^7 revolutions) A_{real} in mm^2
Rough ground	0.0883	0.1088
Hard tuned	0.1265	0.2037
Fine ground	0.1275	0.1896

for the differently finished bearing rings in the unloaded condition as well as after the loading are shown in Fig. 11.

Comparing the different variants, the rough ground condition exhibits in both loading states the highest stresses directly at the surface, which are significantly higher when compared to the other variants. Although the hard turned variant exhibits high maximum stresses directly at the surface in the unloaded state, after cyclic loading the maximum stress is located in the subsurface volume, which correlates to the stress distributions calculated for the fine ground variant. To further analyze the different stress distributions observed, in accordance with [53] the volume elements, which exceed stresses higher than the equivalent yield stress of 1477MPa, were determined to approximate the plastic zone beneath the rolling element (see Table 4). In correlation to the comparison of the stress distribution, the rough ground surface has the largest and the fine ground surface has the smallest theoretical plastic zone in

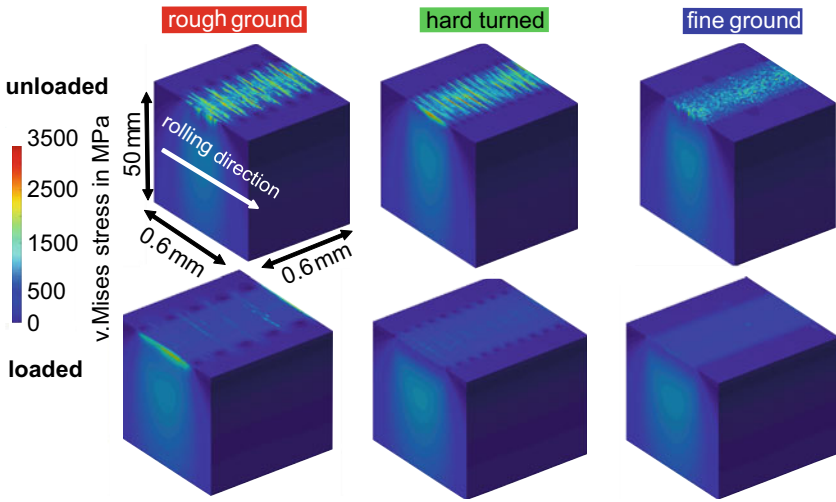


Fig. 11 Elastic v. Mises stresses for the different variants resulting from the surface topographies in the unloaded state and the surfaces caused by rolling cyclic contact for 10^7 revolutions [26]

Table 4 Approximated plastic zone, represented by the number of volume elements N_{vol} and the fraction of the analyzed volume, which was determined based on the stress calculation for the unloaded and loaded conditions of the differently finished bearing rings

	Unloaded		Loaded (10^7 revolutions)	
	N_{vol}	vol. in %	N_{vol}	vol. in %
Rough ground	434817	8.95	433501	8.92
Hard tuned	81493	1.68	477	0.0098
Fine ground	46515	0.9581	491	0.0101

the unloaded state. However, after loading, the hard turned variant yields the smallest plastically deformed volume. This further correlates with the results obtained for A_{real} , which indicate smallest stresses for the loaded condition of the hard turned variant.

Concluding the results obtained from stress calculation, the rough ground surface yields the highest stresses located directly at the surface, which corresponds to the smallest fatigue lifetime observed. For the hard turned and fine ground variants after smoothing, which is nearly completed after $0.5 \cdot 10^6$ revolutions (see Fig. 10), the stress distributions are comparable and the maximum stresses are located in the subsurface volume. As the hard turned variant shows higher compressive residual stresses in the subsurface volume than the fine ground condition, this is assumed

to cause the slightly higher fatigue lifetime of the hard turned bearing rings. Based on the presented results a high potential of hard turning for improving the fatigue lifetime of rolling bearing rings under mixed lubrication can be concluded.

4 Summary

Existing concepts to approximate the fatigue lifetime of rolling bearings contain only a very simplified consideration of the surface topography for mixed lubrication conditions [1]. Moreover, the residual stress state at the surface and within the subsurface volume, which has substantial effects on the fatigue lifetime, is not taken into account. To elaborate a data basis for an evaluation and consideration of these effects, in the present work the surface morphology and the resulting fatigue lifetime under mixed lubrication conditions of three differently manufactured rolling bearing rings were investigated. Therefore, three manufacturing processes, i.e., rough grinding, hard turning, and as a reference fine grinding, were utilized. The surface morphologies were characterized in the unloaded and loaded state for each variant. These analyses were complemented by a calculation of the stress distribution beneath the rolling contact, which results from the different surface topographies.

In the fatigue experiments, different fatigue lifetimes were obtained for the variants investigated. The hard turned variant exhibited the highest fatigue lifetime, while the rough ground condition yielded the lowest lifetimes. However, due to the high intersections of the confidence intervals these observations are only tendencies and need to be validated by a broader database.

To explain the differences in fatigue lifetime observed, detailed analyses of the surface morphology as well as its changes caused by rolling fatigue were performed. It was shown that the surface roughness of the rough ground and hard turned variants decreases due to cyclic loading. This smoothing is, however, stabilized after a short period. Although the surface roughness decreases during cyclic loading, the rough ground variant exhibits the highest surface roughness, which explains the lower fatigue lifetimes. In contrast to that the hard turned variant shows in the stabilized state a comparable roughness than the fine ground reference, which shows no fatigue-induced changes of the surface topography.

In addition to the surface topography, the mechanical properties and residual stresses of the subsurface volume were analyzed. While the mechanical properties are not significantly different to those of the core material, the subsurface volume shows differently pronounced compressive residual stresses for the three variants. Although the fine ground variant shows the highest level of compressive stresses in the unloaded condition, after cyclic loading the residual stress levels and distribution are very similar for the three conditions. However, the hard turned variant shows compressive residual stresses at significantly larger distances from the surface. Note that the differences in the residual stress states observed correlate roughly with the cyclic plasticity obtained in instrumented cyclic indentation tests, which thus will be objective of future work.

Combining the residual stress distributions with the calculations of the stresses beneath the surface, which are based on the measured surface topographies, the highest fatigue lifetime of the hard turned variant can be explained. As the smoothing leads to similar maximum stresses between the fine ground and hard turned variant, which are located in the subsurface region, the more pronounced residual stresses of the hard turned variant in the subsurface volume lead to a higher fatigue lifetime. Additionally, the numerical simulations revealed highest stresses for the rough ground variant directly at the surface, being significantly higher in relation to the stresses observed for the other variants, which corresponds to the lowest fatigue lifetime of the rough ground condition.

In summary, the presented results indicate that the influence of the surface topography, the subsurface material volume, and especially the residual stress states in the subsurface volume are of great importance for the fatigue lifetime under mixed lubrication. Thus, these effects have to be considered for a reliable design concept. Moreover, it was demonstrated that hard turning is a promising manufacturing process for increasing the fatigue lifetime of rolling bearing rings under these loading conditions and further can lead to a reduction of the production costs.

In future work, it is planned to estimate fatigue lifetime based on the model of *Fatemi-Socie* using the multi-body simulation and half-space contact simulation model presented, which will be complemented by a consideration of plasticization of the material. Therefore, an elastoplastic material model based on *Johnson-Cook* will be used.

References

1. ISO/TS 16281. ISO/TS 16281—Rolling bearings—Methods for calculating the modified reference rating life for universally loaded bearings
2. Epstein D, Keer LM, Wang QJ, Cheng HS, Zhu D (2003) Effect of surface topography on contact fatigue in mixed lubrication. *Tribol Trans* 46(4):506–513. <https://doi.org/10.1080/10402000308982657>.
3. Johnson KL, Greenwood JA, Poon S (1972) A simple theory of asperity contact in elastohydrodynamic lubrication. *Wear* 19(1):91–108. ISSN: 00431648. [https://doi.org/10.1016/0043-1648\(72\)90445-0](https://doi.org/10.1016/0043-1648(72)90445-0).
4. Tallian TE (1967) On competing failure modes in rolling contact. *ASLE Transactions* 10(4):418–439. <https://doi.org/10.1080/05698196708972201>.
5. Bartel D (2010) Simulation von Tribosystemen: Grundlagen und Anwendungen. Wissenschaft. Wiesbaden: Vieweg+Teubner. ISBN: 383489656X
6. Klocke F, Brecher C (2017) Zahnrad-und Getriebetechnik: Auslegung—Herstellung—Untersuchung—Simulation. München: Carl Hanser Verlag. ISBN: 978-3-446-43068-6
7. Wang DS, Lin JF (1991) Effect of surface roughness on elastohydrodynamic lubrication of line contacts. *Tribol Int* 24:51–62. ISSN: 0301679X. [https://doi.org/10.1016/0301-679X\(91\)90063-F](https://doi.org/10.1016/0301-679X(91)90063-F).
8. Choo JW, Olver AV, Spikes HA (2007) The influence of transverse roughness in thin film, mixed elastohydrodynamic lubrication. *Tribol Int* 40:220–232. ISSN: 0301679X. <https://doi.org/10.1016/j.triboint.2005.10.009>

9. Hansen J, Björling M, Larsson R (2021) A new film parameter for rough surface EHL contacts with anisotropic and isotropic structures. *Tribol Lett* 69. <https://doi.org/10.1007/s11249-021-01411-3>.
10. Nélias D, Dumont ML, Champiot F, Vincent A, Girodin D, Fougères R, Flamand L (1999) Role of inclusions, surface roughness and operating conditions on rolling contact fatigue. *J Tribol* 121(2):240–251. ISSN: 0742-4787. <https://doi.org/10.1115/1.2833927>.
11. Sadeghi F, Jalahamadi B, Slack TS, Raje N, Arakere NK (2009) A review of rolling contact fatigue. *J Tribol* 131(4). ISSN: 0742- 4787. <https://doi.org/10.1115/1.3209132>.
12. Neubauer T (2016) Betriebs-und Lebensdauerverhalten hartgedrehter und festgewalzter Zylinderrollenlager. Dissertation. Hannover: Gottfried Wilhelm-Leibniz-Universität
13. Morales-Espejel GE, Brizmer V, Piras E (2015) Roughness evolution in mixed lubrication condition due to mild wear. *Proc Inst Mech Eng Part J J Eng Tribol* 229(11):1330–1346. ISSN: 1350-6501. <https://doi.org/10.1177/1350650115577404>
14. Gabelli A, Morales-Espejel GE (2019) A model for hybrid bearing life with surface and subsurface survival. *Wear* 422–423:223–234. ISSN: 00431648. <https://doi.org/10.1016/j.wear.2019.01.050>.
15. Morales-Espejel GE, Gabelli A (2011) The behavior of indentation marks in rolling-sliding elastohydrodynamically lubricated contacts. *Tribol Trans* 54(4):589–606. <https://doi.org/10.1080/10402004.2011.582571>.
16. Lorenz S, Sadeghi F, Trivedi H, Rosado L, Kirsch MS, Wang C (2021) A continuum damage mechanics finite element model for investigating effects of surface roughness on rolling contact fatigue. *Int J Fatigue* 143. ISSN: 01421123. <https://doi.org/10.1016/j.ijfatigue.2020.105986>.
17. Matsumoto Y, Hashimoto F, Lahoti G (1999) Surface integrity generated by precision hard turning. *CIRP Ann Manuf Technol* 48:59–62. [https://doi.org/10.1016/S0007-8506\(07\)63131-X](https://doi.org/10.1016/S0007-8506(07)63131-X)
18. Schlicht H (2006) Die Werkstoffermüdung bei Wälzbeanspruchung-Eine Hypothese zum Mechanismus. *Materialwissenschaft und Werkstofftechnik* 37(5):383–395. ISSN: 0933-5137
19. Hashimoto F, Melkote SN, Singh R, Kalil R (2009) Effect of finishing methods on surface characteristics and performance of precision components in rolling/sliding contact. *Int J Mach Mach Mater* 6:3–15. <https://doi.org/10.1504/IJMMM.2009.026923>
20. Revel P, Jouini N, Thoquenne G, Lefebvre F (2016) High precision hard turning of AISI 52100 bearing steel. *Precis Eng* 43:24–33. ISSN: 01416359. <https://doi.org/10.1016/j.precisioneng.2015.06.006>.
21. Denkena B, Grove T, Maiss O (2016) Influence of hard turned roller bearings surface on surface integrity after deep rolling. *Procedia CIRP* 45:359–362. ISSN: 22128271. <https://doi.org/10.1016/j.procir.2016.02.047>.
22. Denkena B, Poll G, Maiß O, Pape F, Neubauer T (2016) Enhanced boundary zone rolling contact fatigue strength through hybrid machining by hard turnrolling. *Bear World Conf* 1:87–102
23. Maiß O (2019) Lebensdauererhöhung von Wälzlagern durch mechanische Bearbeitung. Dissertation. Hannover: Gottfried Wilhelm-Leibniz-Universität
24. Pape F, Coors T, Poll G (2020) Studies on the influence of residual stresses on the fatigue of rolling bearings in dependence on the production processes. *Front Mech Engineering* 6. <https://doi.org/10.3389/fmech.2020.00056>.
25. DIN EN ISO 683-17. Für eine Wärmebehandlung bestimmte Stähle, legierte Stähle und Automatenstähle - Teil 17: Wälzlagerstähle
26. Rüth L, Foko Foko F, Sauer B, Ostermayer P, Blinn B, Beck T (2022) Experimental and simulative investigations into the fatigue life of cylindrical roller bearings under mixed lubrication with differently finished inner rings. *STLE, Orlando*
27. DIN 25178-2. Geometrische Produktspezifikation (GPS) - Oberflächenbeschaffenheit: Flächenhaft - Teil 2: Begriffe und Oberflächen-Kenngrößen. 2012
28. Prevéy PS (1986) X-ray diffraction residual stress techniques. In: *Metals Handbook*. 10. Metals Park: American Society for Metals , pp. 380–392
29. Ostermayer P, Ankener W, Blinn B, Smaga M, Eifler D, Beck T (2021) Analysis of the sub-surface volume of differently finished AISI 52100 by cyclic indentation and X-ray diffraction. *Steel Res. Int.* <https://doi.org/10.1002/srin.202100253>.

30. Hornbach DJ, Prevéy PS, Mason PW (1995) X-ray diffraction characterization of the residual stress and hardness distributions in induction hardened gears. In: Proceedings: first international conference on induction hardened gears and critical components, gear research institute, Indianapolis, pp. 69–76
31. Holmberg J, Steuwer A, Stormvinter A, Kristoffersen H, Haakanen M, Berglund J (2016) Residual stress state in an induction hardened steel bar determined by synchrotron- and neutron diffraction compared to results from lab-XRD. *Mater Sci Eng A* 667:199–207. <https://doi.org/10.1016/j.msea.2016.04.075>
32. Kramer HS, Starke P, Klein M, Eifler D (2014) Cyclic hardness test PHYBALCHT—Short-time procedure to evaluate fatigue properties of metallic materials. *Int J Fatigue* 63:78–84. ISSN: 01421123. <https://doi.org/10.1016/j.ijfatigue.2014.01.009>
33. Blinn B, Klein M, Gläßer C, Smaga M, Aurich JC, Beck T (2018) An investigation of the microstructure and fatigue behavior of additively manufactured AISI 316L stainless steel with regard to the influence of heat treatment. *Metals* 8(220). <https://doi.org/10.3390/met8040220>
34. Blinn B, Görzen D, Klein M, Eifler D, Beck T (2019) PhyBaLCHT—Influence of indentation force on the results of cyclic hardness tests and investigations of comparability to uniaxial fatigue loading. *Int J Fatigue* 119:78–88. ISSN: 01421123. <https://doi.org/10.1016/j.jfatigue.2018.09.025>
35. DIN EN ISO 14577-1. Metallische Werkstoffe - Instrumentierte Eindringprüfung zur Bestimmung der Härte und anderer Werkstoffparameter - Teil 1: Prüfverfahren
36. Sadrabadi P, Durst K, Göken M (2009) Study on the indentation size effect in CaF₂: dislocation structure and hardness. *Acta Mater* 57(4):1281–1289. <https://doi.org/10.1016/j.actamat.2008.11.015>
37. Aul V (2014) Kontaktmodelle zur dynamischen Simulation vollrolliger Zylinderrollenlager. Dissertation. Kaiserslautern: TU Kaiserslautern
38. Dahiwal R (2017) Entwicklung eines Berechnungsmoduls zur Dynamiksimulation und Betriebsanalyse von Zylinderrollenlagern unter Berücksichtigung der Umgebungskonstruktion in Simpack“. In: Abschlussbericht zum FVA Vorhaben 625 II 1234
39. Kiekbusch T (2017) Strategien zur dynamischen Simulation von Wälzlagern“. Dissertation. Kaiserslautern: TU Kaiserslautern
40. Magyar B, Sauer B (2016) Methods for the simulation of the pressure, stress, and temperature distribution in the contact of fractal generated rough surfaces. *Proc Inst Mech Eng Part J J Eng Tribol* 231(4):489–502. <https://doi.org/10.1177/1350650115593962>
41. Kiekbusch T, Magyar B, Sauer B (2017) Multi-Ebenen-Simulation zur Berechnung der lokalen Lebensdauer in hochbelasteten Wälzkontakten. In: 12 VDI Fachtagung Gleit- und Wälzlager - VDI Berichte 2308:103–112. <https://doi.org/10.51202/9783181023082-103>
42. Polonsky IA, Keer LM (1999) A numerical method for solving rough contact problems based on the multi-level multi-summation and conjugate gradient techniques. *Wear* :206–219. ISSN: 00431648. [https://doi.org/10.1016/S0043-1648\(99\)00113-1](https://doi.org/10.1016/S0043-1648(99)00113-1)
43. Boussinesq J (1885) Application des potentiels a l'étude de l'équilibre et du mouvement des solides élastiques
44. Cerruti V (1882) Ricerche intorno all'equilibrio de' corpi elastici isotropi
45. Gross D, Becker W, Becker W, Gross D (2002) Mechanik elastischer Körper und Strukturen. Engineering online library. Springer, Berlin. ISBN: 978-3-642-56124-5
46. Love AEH (1929) The stress produced in a semi-infinite solid by pressure on part of the boundary. *Philos Trans R Soc Lond* 228:377–420. <https://doi.org/10.1098/rsta.1929.0009>
47. DIN 55303-7. Statistische Auswertung von Daten - Teil 7: Schätz- und Testverfahren bei zweiparametrischer Weibullverteilung. 1996
48. DIN EN 61649. Weibull Analyse
49. Seifried A (2004) Zur Statistik in der Betriebsfestigkeit. In: Materialwissenschaft und Technik 35(2). <https://doi.org/10.1002/mawe.200300722>
50. Gold PW, Loos J, Aßmann C (2001) Funktionsgerechte Oberflächenanalyse am Beispiel von Wälzlagern. In: Tribologie und Schmierungstechnik 48(6):13–20

51. Denkena B, Biermann D (2014) Cutting edge geometries. *CIRP Ann* 63(2):631–653. ISSN: 00078506. <https://doi.org/10.1016/j.cirp.2014.05.009>.
52. Feng G, Qu S, Huang Y, Nix WD (2007) An analytical expression for the stress field around an elastoplastic indentation/contact. *Acta Mater* 55(9):2929–2938. ISSN: 13596454. <https://doi.org/10.1016/j.actamat.2006.12.030>.
53. Nelias D, Boucly V, Brunet M (2005) Elastic-plastic contact between rough surfaces: proposal for a wear model. In: *World Tribology Congress III*. ASME, Washington, D.C., pp 251–252. ISBN: 0791842010. <https://doi.org/10.1115/WTC2005-63302>.

Manufacturing-Morphology-Property Relationships for Chain Joints



Manuel Oehler, Dominik Meffert, and Bernd Sauer

Abstract In this chapter, correlations between the surface morphology and the functional properties regarding friction and wear are investigated for the tribological contact between pin and bush in drive chains. Using a combination of experimental and simulative methods, influences such as surface topography, shape deviations of the components, lubricants and their contamination as well as boundary conditions with regard to load and relative velocity are determined. Friction and wear on individual chain joints are reliably determined with a single joint test rig. Essential findings are, for example, the strong dependence of wear on the inner contour of the bushings as well as the low influence of hydrodynamic effects on the friction behavior in the chain joint. Surface modifications such as micro-structuring do not bring any advantages in terms of tribological properties.

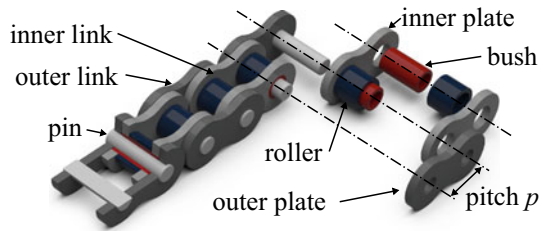
1 Introduction

Chain drives are widely used for transmitting power in drive technology. A wide variety of chain designs can be found, which differ in their use and therefore also in their structural design. Chains can be divided into three categories: Drive chains in chain transmissions, conveyor chains in conveying systems, and load chains in hoisting equipment [1]. In addition, a distinction can also be made between *simple chains without pins*, *link chains*, and *special designs* [2]. Chain drives in drive technology provide a transmission of rotary movements of parallel shafts under a constant gear ratio and can be classified between gear and belt drives with regard to the transmittable power.

Articulated chains comprise a large number of common chain designs that are characterized by a structurally integrated chain joint. Here, a pin usually forms the axis of rotation around which the chain link can move. Chain designs used in drive technology, such as sleeve, bush and roller chains, have chain links that are extended

M. Oehler (✉) · D. Meffert · B. Sauer
Institute of Machine Elements, Gears, and Tribology, RPTU Kaiserslautern, Kaiserslautern,
Germany
e-mail: manuel.oehler@rptu.de

Fig. 1 Structure of a roller chain by DIN ISO 606 [6]



by a sleeve or bush. There is no difference in the basic structure of these three chain designs, as they all consist of an alternating sequence of inner and outer links, as Fig. 1 shows. Outer links consist of outer link plates and pins press-fitted into them. Inner links have sleeves or bushings pressed firmly into the inner link plates [3, 4]. In roller chains, the inner link is supplemented by a roller rotatably mounted on the bush, which is intended to reduce acoustic behavior as well as friction and wear in the contact between chain and sprocket [5].

The outer surface of the roller is in contact with the teeth of the sprocket. Further contacts with relative movement of the contact partners involved are found between roller and bush and between pin and bush. The pin-bush contact (PBC) in particular is of great tribological relevance, since wear on the contact partners involved manifests itself as elongation of the entire chain.

Due to limited installation space within the chains, it is often not possible to implement design changes to the chain components to optimize fatigue strength and wear behavior. The focus is therefore on the further development of materials and component manufacturing. Various manufacturing processes for chain components lead not only to varying degrees of deviation in shape from the desired target geometry (for example, deviation of the inner contour of the sleeve or the outer contour of the pin from the ideal cylindrical shape), but also to different surface structures. Further development of chain components is primarily carried out by optimizing the tribological system of the chain link, since wear and friction have a direct effect on the service life of the chain. For this reason, the following section will also focus on the pin and sleeve components.

Pins are usually made from wire or bar material, from which the individual pins are cut to length. Case-hardened steels such as 16MnCr5 or quenched and tempered steels such as C60E are used [7, 8]. In order to maintain tight dimensional and form tolerances as well as to meet high demands on surface quality, chain pins are often ground. Vibratory grinding (also called barrel finishing) or centerless grinding are used for this purpose. Cold extruded pins can also be found. In addition, heat treatment is of great importance, as pins are usually case-hardened. Wear-resistant surface layers with hardness up to 2000 HV are achieved, while the core remains comparatively ductile at 400 to 500 HV. Alternatively, various coatings with triboactive or hard elements are applied to the pin surfaces [9].

With their internal concave surface, bushes form the mating surface to the pin surface in the tribological system chain joint. They are either produced from wound

strip material, which creates an edge joint and thus no continuous surface, or they are also produced with seamless geometry by means of cold extrusion. Case hardening achieves surface layers with a hardness of 500 to 800 HV [7]. Bushes, together with the inner plates, form the inner links. For this purpose, the bushes are pressed into the link plate holes. This press fit results in deformation of the bush geometry, and the inner functional surface of the bush undergoes constriction at the edge areas with reduced diameter. To reduce this effect, various design and manufacturing techniques are used, such as pre-widening, tapered ends, or pressing through a steel ball in the assembled state [7, 10, 11].

The pin-bush contact considered here forms the actual chain joint. In contrast to similarly structured tribological systems such as journal bearings, oscillating movements with a comparatively small angle of rotation occur in chain joints. This results in relative movements under load (joint oscillations in the load strand) as well as unloaded. Due to the contact conditions with high contact pressure and subordinate relative movement, boundary friction prevails in the chain joint, since hydrodynamic effects are negligibly small. Shape deviations of the chain components as well as the bending of the pin due to the tensile load of the chain lead to a concentration of the load on the edge areas of the contact, which is why the contact conditions are further negatively influenced [12]. For chain joints, coefficients of friction greater than 0.05 [13] up to 0.15 [12] can be found.

Wear on the two contact partners of the chain joint leads to an increase in the joint clearance and thus to a change in the chain pitch, which defines the distance between the chain joints and thus the chain length. In this way, the service life of a chain is also defined as a function of wear. The maximum pitch changes depending on the chain rotation speed as well as the drive layout. For slow-running chain drives with adjustable shaft distance, pitch changes of up to 3% are acceptable [14]. For timing drives in internal combustion engines, the wear limit is only 0.3–0.5% due to the mandatory timing requirements [15]. The contact area affected by wear differs for pins and bushes. The wear area of the bush is extended by the swivel or pitch angle, i.e., the amplitude of the movement in the chain joint, compared to the pin [12]. Excessive joint wear leads to incorrect seating of the chain on the sprocket, resulting in altered load application points when the chain enters the sprocket and excessive chain sag, which can cause the chain to jump over to the next sprocket tooth, resulting in severe dynamic loads. This often results in chain breakage [12, 14]. The continuous course of chain elongation can be divided into three phases, as shown in Fig. 2 [16]. The first phase, the degressive running-in wear, is characterized by a high initial intensity. With increasing wear, the contact partners align with each other and with increasingly homogeneous pressure distribution, the wear intensity decreases until it assumes a constant value. This is referred to as steady-state operational wear, which forms the second phase. Once hard surface layers of the chain components have been completely removed, the wear intensity increases. The progressive final wear that occurs defines the end of the service life.

In this chapter, a summary of the work in the field of chain drives carried out within the frame of the collaborative research center CRC 926 “Microscale morphology of component surfaces (MICOS)” is presented. First, all the test equipment

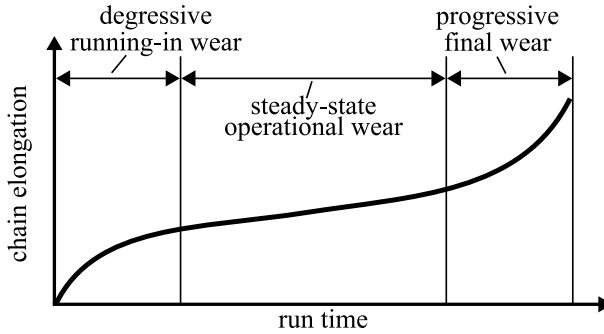


Fig. 2 Schematic wear progression over the runtime based on [12]

and methods used are presented. The results of intensive research on Manufacturing-Morphology-Property (MMP) Relationships are shown using the example of the chain joint. Essentially, the investigations and findings relate to tribological issues around friction, wear, and lubrication. The basic prerequisite for understanding these phenomena is knowledge of the conditions in the tribological contact (contact pressure, relative velocity, sliding distance, etc.).

2 Methods

2.1 Test Rigs

2.1.1 Chain Wear Test Rig

Usually, wear tests on drive chains are carried out on tension test stands. The basic principle of this type of test stands is that two chain tracks are tensioned to each other via a mechanical tensioning coupling (back-to-back test rig), as can be seen in Fig. 3. The tensioning coupling applies the load torque in both chains. This operating principle means that the electric drive motor only has to compensate for the losses in the bearings, seals and the chain drives themselves. A disadvantage of the tensioning coupling principle is that it is not possible to adjust the tensioning torque during operation. In [8, 17] a chain wear test rig using the principle described is used. Within these works an adjustment device for the tensioning torque was integrated into the test rig. This allows the two bearing blocks of the shafts to be moved and thus the tensioning torque to be adjusted by $\pm 15\%$. The test stand is designed for drive speeds of up to 3000 rpm, chain speeds of up to 30 m/s, and a maximum chain tensile force of 1400 N. Due to the system, different drive layouts are produced at the two chain tracks, with the slack strand being at the top for the left-hand chain and at the bottom for the right-hand chain. When the test rig is running, an oil unit supplies both

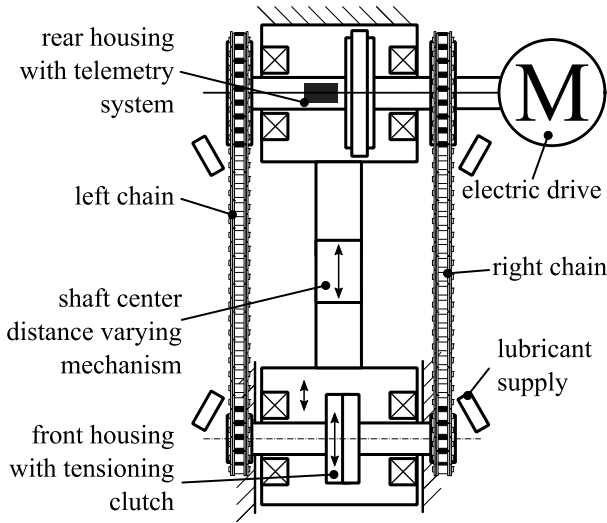


Fig. 3 Schematic structure of the chain wear test rig at MEGT [18]

chain strands with tempered oil, to which carbon black can also be added. During test rig operation, measured variables such as bearing temperature, oil temperature, rotational speed, tensioning torque, and oil flow rate are continuously monitored. In addition, these parameters are measured, in particular in order to use the collected data in the subsequent evaluation of the wear test.

2.1.2 Chain Joint Tribometer

With the use of a single component test device, called the chain joint tribometer, friction and wear within single chain joints can be investigated. The tribometer can be used to apply predefined swivel angle and tensile force curves to a single chain link. The chain link is not modified prior to the test to ensure that the load application is identical to the real behavior of the pin-bush contact in chain drives in circulating operation. To make the test environment as real as possible, the operating temperature can be adjusted by heating elements. In addition, the chain link can be lubricated, according to the test setup, by a lubricant supply during the test or initially in advance. The basic principle is shown in Fig. 4. The wear of the chain joint can be determined during the tests by means of displacement sensors. A total of three test cells are available at the test bench described in [13, 18, 19]. Two test cells have a linear motor with a maximum tensile force of 7.7 kN, the third up to 11 kN. These maximum tensile forces allow reasonable testing of chains with pitches up to 19.05 mm or 3/4” (chain 12B according to ISO 606 [5]). The tensile force is applied via the linear motor. A second motor provides the swiveling movement. The resulting frictional force is measured by a 3-axis force sensor, which is positioned between the chain

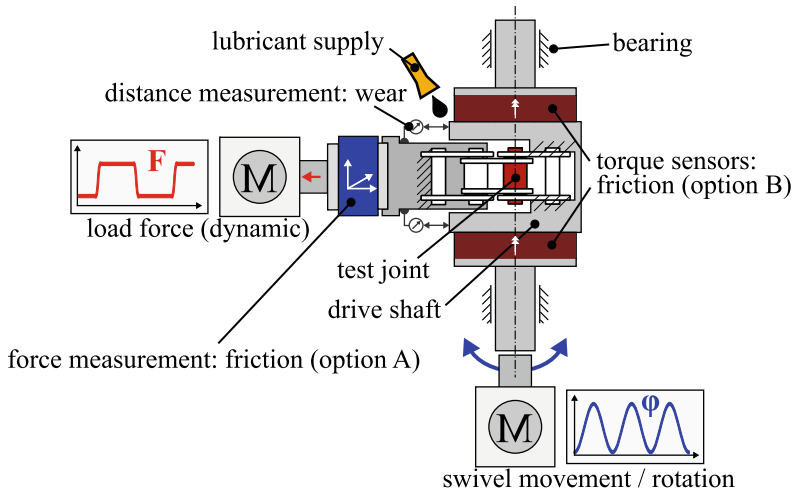


Fig. 4 Structure of a single test cell of the chain joint tribometer [6]

segment and the linear motor. In addition, two torque sensors are integrated into the drive shaft to determine the total resistance to movement at the moving part of the chain segment from the difference in sensor data. In addition to high-frequency swiveling movements in sinusoidal form with a frequency of up to 100 Hz, freely configurable movement sequences with high dynamics can also be realized. For friction measurement, the maximum possible swiveling frequency is greatly reduced, since the installed torque sensors place very strict restrictions on the permissible rotational accelerations.

2.2 Characterization of Test Specimens

2.2.1 Chain Length Measurement

One way of measuring wear is to measure the elongation of the chain. The device for the elongation measurement used in [8, 18, 20] is based on the DIN ISO 606 standard [5]. The device, which is made of steel and aluminum profiles, offers the possibility of measuring the length of chains without having to cut them open. This gives the possibility to measure the chains before and after the performed tests. The chain is clamped in the area of a section of a length defined in the standard and loaded in tension by a defined test weight. The chain is mounted on the fixture at the upper end by a positioning pin. The lower end of the chain is also held by a positioning pin, which is mounted on a vertically movable carriage. The carriage is loaded by the test weight. Before each new chain measurement, a calibration gauge with a defined length is installed and the dial gauge is locked. Here, the nominal pitch of the chain

segment to be measured is set. Afterward, the chain is installed. The difference between the chain length and the reference length can now be determined with the dial gauge. The chains are initially measured in new condition and after defined running times on the test rigs. This allows the chain elongation to be determined, which provides information on wear. The average joint wear can be calculated from the number of joints contained in the measured segment.

2.2.2 Clearance and Stiffness Measurement Devices

In addition to the chain elongation, the clearance and stiffness in individual chain joints can also be determined. For this purpose, the entire, unseparated chain is clamped in a device. One chain link is firmly clamped on the base body. Another chain link is mounted on a movable carriage. First, the links located between the clamping are compressed and then subjected to tensile stress again by means of hydraulic actuators. To prevent the chain from buckling, it is held in position by a hold-down device. Eddy current sensors record the relative movement, allowing the clearance as well as the elastic deformation to be determined. A force sensor records the chain tensile force, from which, together with the displacement measurement, the stiffness can be derived. Four joints are measured at a time. This setup achieves a repeatability of $<1 \mu\text{m}$ [8, 17].

2.2.3 Contour and Roundness Measurement

In [20], a Taylor Hobson Talyrond 365 roundness measuring device is used to measure the wear or the resulting form deviations on the bolts and bushes. The measuring principle is a tactile method in which a stationary probe scans the surface of a rotating object. For measurement, the pins and bushes are clamped in special holders, via which the components are fixed on the rotary and leveling table. At the beginning of the measurement, the device performs some reference measurements on the top and bottom level of the components. The reference measurements are used to align the components exactly. To do this, the leveling table automatically compensates for the eccentricity and misalignment of the components. Since the measuring device cannot record absolute radii, but only radius changes, a reference diameter must be recorded to accurately determine the absolute component radius. The radius is determined with an accuracy of $\pm 0.7 \mu\text{m}$. The actual form measurement is performed fully automatically on planes distributed uniformly along the longitudinal axis. The results can be used to determine wear parameters such as the wear volume.

2.2.4 Surface Characterization

The tribological behavior of the pin-bush contact is influenced not only by the external shape, but also to a decisive extent by the surface of the pin and bush. In [19], a

confocal microscope (Nanofocus μ Surf Explorer) is used to record the surface topography. An objective with 50x magnification is used for the measurements. For each measurement, a measuring area is composed of 2x2 measuring fields. The microscope takes four individual measurements and the measuring software composes a large measuring field of 470x470 μm from them. The subsequent analysis of the measurements is carried out with the surface analysis software Mountainsmap from Digital Surf. During the analysis, the cylindrical shape of the samples as well as any tilt is corrected, resulting in a flat representation of the surface.

To enable the surface measurement of the bush, it must either be cut in the longitudinal direction or the inner contour must be molded. Cutting the bush would render it unusable for subsequent examinations with other measuring instruments. For this reason, if necessary, an impression of the sleeve surface is made using silicone-based dental impression material.

3 Contact Mechanics and Kinematics

3.1 Multi-body Simulation

A chain joint is subject to dynamic forces and movements in the rotating operation of the chain. The operating behavior cannot be calculated analytically, which is why methods such as multi-body simulation (MBS) are used for this purpose. The MBS model of the chain wear test stands described in [8] (cf. Sect. 2.1.1)) is implemented in the commercial MBS software RecurDyn using the integrated chain toolkit. Corresponding to the real structure, the model includes the two chain tracks incl. sprockets, the front and rear shafts, the tensioning coupling, and the tensioning torque adjuster. Furthermore, all relevant masses, inertias, and stiffnesses are implemented. To achieve the best possible correlation between experiment and simulation, two different validation methods are used. At standstill, an adjustment against the sag of the slack strand is performed for tensioned chains. In steady-state operation, a method is used in which the chain track is photographed during test rig operation at different load points. After image processing, the visualized chain track is compared with the track calculated using MBS [8, 21]. As a result of the multi-body simulation, the relative motions and contact forces in the chain joint are available, among other things. For the simulated chain drive, the load collective can be seen in Fig. 5. The chain link under observation starts in the slack strand and initially runs onto the large sprocket (1a–1b). The contact forces are at the idle run level during this angular process. When the sprocket overruns, the load in the chain link increases and reaches the full load run force when it runs out into the load strand (2a–2b). When running into the small sprocket (3a–3b), the contact force drops sharply during the angular process and reaches slack strand level (4a–4b) by the time it runs out of the sprocket [19].

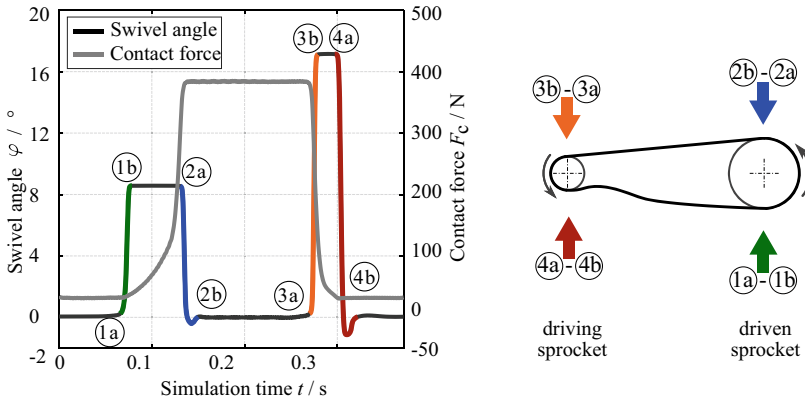


Fig. 5 Progress of swivel angle and contact force in a chain link as a result of MBS for one revolution of the chain wear test rig (left), schematic representation of the different swivel movements within one revolution (right)

3.2 Contact Pressure Distribution

When designing and dimensioning chain drives, the average pressure in the PBC can be estimated using the chain tensile force in the load strand, which is then related to the nominal contact area (diameter of the pin multiplied by the width of the bush) in the joint. This idealized assumption does not correspond to the real conditions in the PBC, since the shape deviations of the bush inner contour described in Sect. 1 have an impact on the surface deformation and the structural deformation such as pin bending and link plate deformation influence the contact pressure as well. In the new condition, the reduced bush diameter in the edge areas results in the entire chain tensile force being carried on a reduced contact area at the bush ends in the area of the press fits of the link plates. The pin bending within the bush additionally leads to lifting of the pin surface in the central area of the bush [10, 17].

The pressure distribution in the PBC depends not only on the axial position of the constrictions but also on their amplitude. For chains with a pitch of 5/8", radial deviations of up to 0.09 mm are found in conventional chains. Even comparatively small radial deviations of 0.02 mm result in a large deviation compared to a homogeneous pressure distribution. In [10], radial deviations between 0.01 and 0.07 mm are measured on chains with a pitch of 1/2". To determine the effects of this shape deviation on the contact pressure distribution in the chain joint, a simulation model using finite element analysis (FEA) was developed. The model was constructed analogously to [22] but takes into account the real shape deviations of the inner contour of the sleeve. Figure 6 shows the comparison of an idealized and a real inner bush contour for an applied tensile force of 2400 N (only half contact area shown due to symmetric assembly). Results of the FEA show, that the significantly reduced contact area actually present in the PBC leads accordingly to an increased mean contact

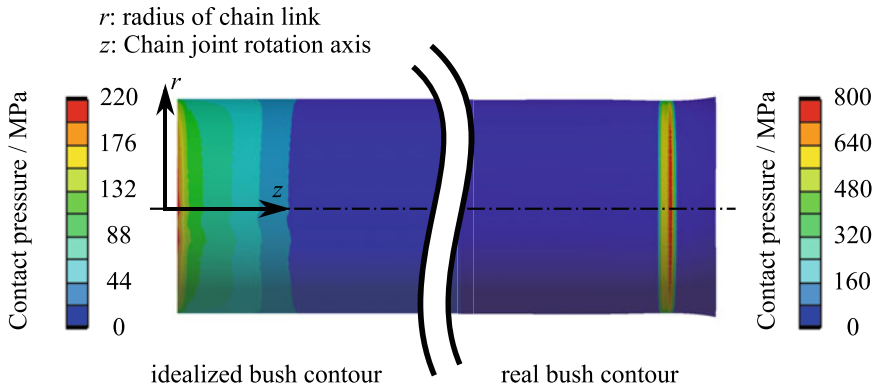


Fig. 6 Influence of the inner bush contour on the contact pressure: idealized bush (left) with larger contact area and lower maximum of pressure compared to a real bush contour (right) for an applied tensile force of 2400 N; specimen: roller chain, size ANSI 50 ($p = 5/8''$)

pressure. As the tensile load on the chain increases, the difference between nominal and local contact pressure decreases slightly, due to the overall elastic deformation of the chain components and the resulting alignment. Nevertheless, only surface areas of 25–40% of the idealized available contact area are in contact. Regarding an ideal bush inner contour, only bending of the pin is responsible for a shift of higher pressures toward the bush ends. The results correspond very well with the findings of the study on contact conditions and hydrodynamic lubrication in PBC shown in [23].

4 Lubrication

4.1 Surface Interaction

In tribological systems, the interaction between the two solid contact partners and the surrounding medium (air or lubricant) is of great importance. To understand the processes taking place in the contact, it is necessary to consider the direct surface interaction. From calculations carried out using elasto-hydrodynamic lubrication (EHL) simulation (see Sect. 4.2), it is clear that hydrodynamic effects are almost negligible in the chain joint. The reason for this is the contact conditions, which are unfavorable for the formation of a surface-separating lubricating film. Short-term, discontinuous relative motion with only small hydrodynamic velocities as well as an inhomogeneous pressure distribution caused by shape deviations of the contact partners characterize the PBC. Due to the dominant solid fraction of the pressure distribution, it results in a classification in the boundary lubrication regime for relative motion in the chain joint. The direct interaction of the contact surfaces requires consideration of real, rough surfaces in order to shed more light on the processes

inside the tribological contact. The inner contact surface of the bush cannot simply be brought to a reduced roughness by processes such as grinding, as is the case with the outer surface of the pin. Contact simulations of different surface topographies show that sub-surface and contact stress are strongly depending on the surface topography. The assumption that a smoother surface generally leads to lower mechanical stress than a rougher one does not necessarily apply. This finding is also important regarding the surfaces on components of drive chains [24].

In the counterface of shaft seals, microstructured surfaces have shown a positive effect on friction behavior as a result of increased hydrodynamic behavior [25]. These are also used as lubricant reservoirs in tribological contacts. However, contact simulations of functional surfaces provided with geometrically defined structures, such as can be introduced by micro-machining [26], show that hydrodynamic effects in the chain joint cannot be forced by this. In fact, reduced lubricant film heights and thus an increase in the solid pressure fraction in the PBC are shown. Accordingly, no optimization of the friction conditions and thus of the wear behavior can be expected [27].

4.2 *Elasto-hydrodynamic Lubrication of Chain Joints*

In [27–29], an elasto-hydrodynamic lubrication (EHL) simulation is set up to analyze the lubrication conditions in chain joints. The simulation makes use of the analogy to hydrodynamic radial journal bearings. Although the kinematic conditions in the two systems are fundamentally different (continuous vs. discontinuous movement), structural parallels can be identified. In addition to the real measured component contours of pin and bush (see Sect. 2.2.3) on the macroscopic scale, the real component surface determined with the aid of the confocal microscope (see Sect. 2.2.4) is also integrated into the simulation model for the chain joint. Mixed friction, a mass conserving cavitation algorithm, and the structural deformation such as pin bending are integrated into the EHL simulation. The load and motion data introduced are taken from MBS simulations of the chain drive to be mapped (cf. Sect. 3.1). The calculated contact pressure can be divided into the solid pressure (asperity contact) and the hydrodynamic pressure, as Fig. 7 shows. It is also possible to integrate microstructured surfaces into the contact simulation, as they are used in other technical applications to optimize tribological conditions [25]. These can be introduced into the component surface by micro-machining, for example [26]. The enhancement of hydrodynamic effects in the tribological system chain joint is investigated in [27]. The results don't show any benefit from surface texturing.

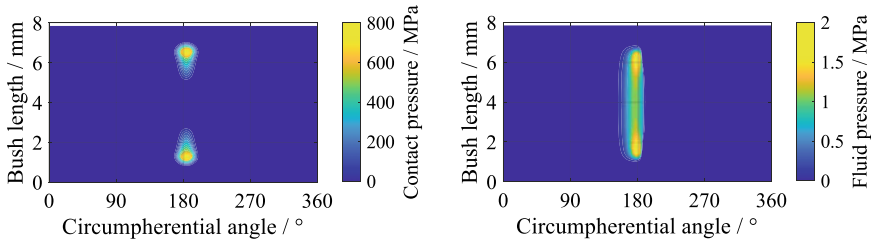


Fig. 7 Pressure distribution inside of the pin-bush contact of a chain joint: proportion of the solid pressure (left) and the hydrodynamic pressure (right) [27]

5 Friction in Chain Joints

Friction losses reduce the efficiency of technical systems. Friction within the PBC is responsible for the greatest share of the total power loss in chain drives. Nevertheless, values of over 96% for the efficiency of chain drives can be assumed. The lubricant used can influence the friction in the chain joint. Investigations on the chain joint tribometer (see Sect. 2.1.2) show that the coefficient of friction is strongly dependent on the chain design and that chains from different manufacturers of the same size differ in their initial state. Clear statements on how parameters such as component surface or component contours affect friction cannot be made yet [13]. Increasing relative velocity in the PBC leads to a decrease in the coefficient of friction. Intensive experiments on the chain joint tribometer using motorcycle drive chains with a pitch of 5/8" showed that coefficients of friction in the range between 0.05 and 0.15 are achieved depending on the lubricant used. The use of the same lubricants for different chains shows that the chain is more influential than the lubricant. The chain joints of motorcycle chains are often protected against the ingress of dirt and water by sealing rings between the chain plates. As a result, the chain links exhibit increased resistance to movement. Therefore, a tensile load-independent part resulting from the seal can be detected here. In the case of size 525 chains (pitch 5/8"), the frictional torque measured on the chain joint tribometer can be increased between 20 and 200% depending on the applied load and speed.

The influence of particles in the PBC on the friction behavior depends very much on the type of particle. Tribometer tests have shown that carbon black particles in the lubricant can even reduce friction [30]. Dirt particles, as found in operating conditions typical of chain drives such as in agricultural and construction machinery, can lead to an increase in the coefficient of friction in the PBC of up to 40%. Similar but less pronounced effects can be considered for the tribological contact between bush and roller.

The coefficient of friction for the PBC is not constant over the operating time. It increases as the contact partners become increasingly similar. This is confirmed by tribometer tests [30] and tests on chain joints under real operating conditions [6].

6 Wear in Chain Joints

6.1 Experimental Wear Investigation

The service life of chain drives is defined by the wear in the joints. Wear can be reduced by design or manufacturing modifications as well as lubricants adapted to the application. Before real system tests, tribometer tests are often carried out first. They are used to detect interrelationships and interactions at a fundamental level, such as with materials and lubricants. Experimental tests with chain components on a pin-on-disc tribometer in linearly reciprocating mode show that the results are transferable due to similar wear intensities with the results from experiments using whole chains [30]. The presence of anti-wear additives (zinc dialkyldithiophosphates ZDDP) within the lubricant leads to significantly less pronounced wear during the tribometer tests. The addition of carbon black particles to the lubricant, similar to the combustion residues in lubricants of internal combustion engines, leads to increased wear. The component surface, which is influenced by wear mechanisms, becomes rougher when a non-additivated lubricant is used. Carbon black particles in the lubricant have similar effects on the components' surfaces. Carbon black particles lead to roughening of smooth surfaces, but also to leveling of very rough initial surfaces. Anti-wear additives, for example, ZDDP, hardly affect the surface roughness or level the surface [30].

The above findings are similar for whole chain drives, as a more pronounced wear formation due to the addition of carbon black particles can be seen. However, joint wear also depends on the operating and drive layout parameters. The higher the chain tensile force in the load strand, the higher the contact pressure in the PBC [8, 31]. This manifests itself in intensified wear behavior. This behavior is also very clear in investigations of single chain joints on a chain joint tribometer [19] (see Fig. 8). It is also clear from these investigations that there is a very good correlation between the

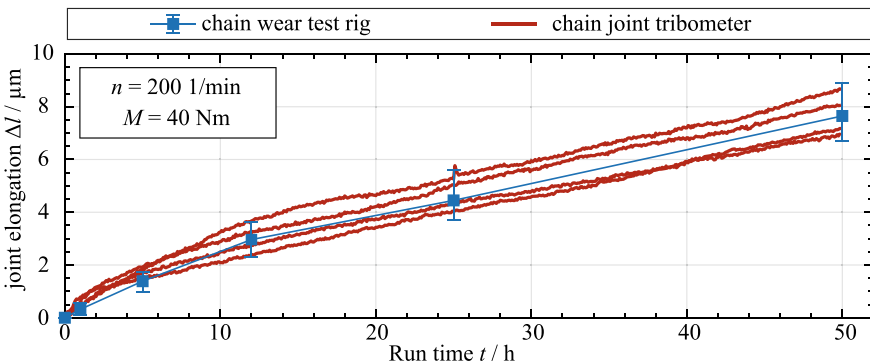


Fig. 8 Comparison of the wear progression in the chain joint between whole chains tested in the chain wear test rig and single chain joints on the chain joint tribometer (in accordance to [19])

tests on a back-to-back test rig and the chain link tribometer. The relative velocity in the PBC, which results from the chain rotation speed and the drive layout, also influences joint wear. Here, an increase in relative velocity leads to a decrease in the steady-state wear rate, which is also evident in the results of both test rig designs. In model tests with a stationary rotating bolt, this effect is very clearly visible. As a result of wear, the component surface undergoes severe roughening, which manifests itself as grooves in the direction of the sliding motion. Comparative investigations of two chains with different pin surface finishes (A: case-hardened, edge hardness 850–900 HV; B: inchromed, edge hardness: >1250 HV; bushes (identical): case-hardened, edge hardness 920–1000 HV) reveal a different distribution of wear on the joint components. While with chain A the pins show significantly more intensive material wear, the bush with chain B undergoes almost all of the joint wear. However, the wear volumes on the bushes of both chain variants are comparable for the same load conditions. In addition, the chromium plating of the pin leads to the formation of smoother component surfaces in the wear area [19].

The running-in wear behavior is primarily determined by the shape deviations of the bush. This is shown not only by experimental results but also by simulations. The matching of the contours of both joint components leads to strongly pronounced degressive run-in wear, which corresponds to the magnitude of the amount of radial constriction of the bush. Thus, the macroscopic shape overrides the wear behavior, which is determined by roughness. The contact pressure and velocity dependence are also evident in the simulative investigations presented in [6].

6.2 Analytical Wear Calculation

Since the relative movement between the bush and pin and the deformation of the individual components under load result in a contact situation in the chain joint that changes with progressive wear, an analytical calculation model for calculating wear in the chain joint was developed [8, 17, 32]. This model can be used to calculate the wear-related material removal at the bush as well as at the pin and thus the change in the component contours. For this purpose, a single chain joint is modeled, which is subjected to a constant swivel angle and a constant load. The components of the chain joint are transferred to a disk model, which reproduces the contours of the components with different diameters. In a first step, the contact between pin and bush is calculated. This includes the calculation of the pin bending as a function of the bush inner contour as well as the force distribution along the pin axis. The contact pressure distribution can be determined based on that. The wear model according to Archard [16] is used to calculate the material removal via the surface pressure and from this the new contact geometry. The calculation approach is based on experimentally determined data such as the wear volume of the contact partners, the load in the contact, the hardness of the surfaces, the sliding distance in the tribosystem, and a wear coefficient which must be determined for each tribosystem. The analytical wear

calculation shows results for both the wear volume on the pin and bush and for the local distribution of material removal that agree very well with the tests [8].

6.3 Friction-Energy-Based Wear Calculation

Based on the EHL simulation (see Sect. 4.2), a wear calculation model for chain joints was developed which takes into account the frictional energy introduced into the PBC. The wear model is based on the wear calculation approach according to *Fleischer* [33]. Considering the real component contours and surfaces and the resulting contact pressure distribution, the local wear intensity is determined for each point of the calculation grid. The contact pressure depends on the state of the component alignment due to wear, where advanced wear leads to more homogeneous contact pressure distributions (see Fig. 9). In addition to the local contact pressure, wear also depends on the friction energy introduced. The relationship between the frictional energy introduced and the material removed is described by the friction energy density. This parameter can be determined from experiments carried out on the chain joint tribometer taking into account the wear volume, the sliding distance, and the coefficient of friction prevailing in the PBC. The model is suitable for analyzing the running-in wear behavior as well as describing the steady-state operating wear. The advantage of the calculation approach is the significantly reduced material input required for the experimental generation of the input data, since the use of the chain joint tribometer means that only single chain joints are investigated. This method is therefore suitable for investigating prototype chains manufactured in small numbers or as an aid in the chain development and design process [6].

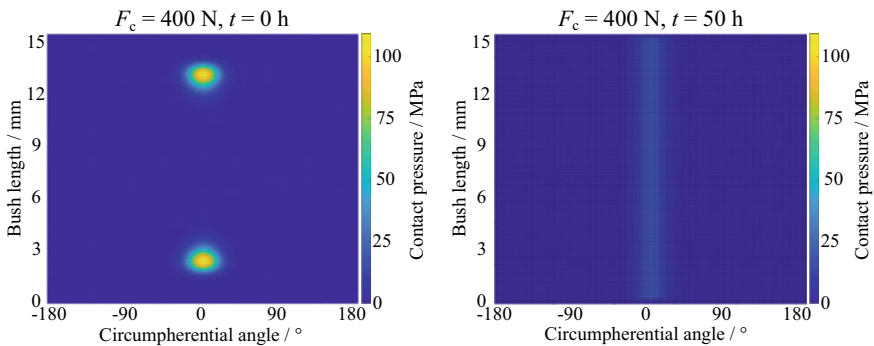


Fig. 9 Distribution of the contact pressure in the pin-bush contact in relation to wear: homogeneous pressure distribution due to matching of component contours [6]

7 Summary

Within this chapter, experiments on whole chain drives as well as tests using single chain joints are carried out to find correlations between the surface morphology and the functional properties regarding friction and wear between pin and bush in drive chains. Using a combination of experimental and simulative methods, influences such as surface topography, shape deviations of the components, lubricants and their contamination as well as boundary conditions with regard to load and relative velocity are determined. The main findings are listed in the following:

A novel test rig, the chain joint tribometer was developed. This test bench can be used to reliably determine friction and wear on individual chain joints. Based on measured parameters a friction energy-based wear simulation was set up. Experiments and simulation confirm that there is a strong dependence of wear on the inner contour of the bushings.

EHL simulation shows that hydrodynamic effects play a subordinate role and therefore, the chain joint is operating in the boundary lubrication regime. This behavior cannot be influenced using surface modifications like for example micro texturing. The coefficient of friction in the chain joint depends heavily on the lubricant used. Carbon black particles do not necessarily lead to an increase in the coefficient of friction.

Overall, it can be stated that the intensive research on the Manufacturing-Morphology-Property (MMP) Relationships has provided a better understanding of the tribological conditions in the pin-bush contact of chain drives. The research results are shown to form the basis for optimizing chain drives in terms of friction and wear in the future.

References

1. Sauer B (ed) (2018) *Konstruktionselemente des Maschinenbaus 2*. 8th edn. Springer, Berlin, Heidelberg. <https://doi.org/10.1007/978-3-642-39503-1>.
2. Pfalzgraf J (2011) *Experimentelle Reibleistungsuntersuchungen an Kettentrieben im Verbrennungsmotor*. PhD thesis, Technische Universität München
3. DIN 8154: Buchsenketten mit Vollbolzen. Berlin: DIN, Sept. (1999)
4. DIN 8164: Buchsenketten. Berlin: DIN, Mar. (2019)
5. DIN ISO 606: Kurzgliedrige Präzisions-Rollen- und Buchsenketten, Anbauteile und zugehörige Kettenräder. Berlin: DIN, Feb. (2018)
6. Meffert D, Rank M, Oehler M, Ostermann L, Kamga LS, Koch O (2022) Friction-energy-based wear calculation approach for chain joints. In: *Nordic Tribology Symposium (NordTrib)*. Nordic Tribology Symposium. Ålesund, Norway
7. Bauer P (2013) *Kettensteuertriebe : Stand der Technik, Anwendungen, Entwicklung und Herstellung*. Landsberg/Lech: Verl. Moderne Industrie. ISBN: 978- 3-86236-049-9
8. Sappok D (2016) *Experimentelle und simulative Methoden zur Untersuchung der Verschleißvorgänge im Kettengelenk von Antriebs- und Steuerketten*. PhD thesis, Technische Universität Kaiserslautern. ISBN: 978-3-959740-33-3

9. Bobzin K, Brögelmann T, Kalscheuer C (2020) Arc PVD (Cr,Al,Mo)N and (Cr,Al,Cu)N coatings for mobility applications. *Surf Coat Technol* 384:125046. <https://doi.org/10.1016/j.surfcoat.2019.125046>.
10. Binz H (1985) Untersuchungen des Einlaufverhaltens von Rollenketten unter besonderer Berücksichtigung der Buchse-Lasche-Pressverbindung. PhD thesis, Technische Hochschule Darmstadt
11. Renold Power Transmission. Renold—Rollenkettenkatalog. Version REN1/DE/07.10. Renold Power Transmission (2010)
12. Coenen W (1984) Einfluss der Schmierung auf das Verschleissverhalten von Rollenketten. PhD thesis, Technische Hochschule Aachen
13. Meffert D, Oehler M, Sauer B (2021) Precise friction measurement in drive chains using a chain joint tribometer. *Tribol Online* 16(3):151–158. <https://doi.org/10.2474/trol.16.151>.
14. Deters L, Mücke W (2018) "Zugmittelgetriebe". In: *Konstruktionselemente des Maschinenbaus 2: Grundlagen von Maschinenelementen für Antriebsaufgaben*. In: Sauer B (ed), 8th edn. Springer, Berlin, Heidelberg, pp 549–613. ISBN: 978-3-642-39503-1. https://doi.org/10.1007/978-3-642-39503-1_7.
15. Fink T, Hirschmann V (2001) Kettentriebe für den Einsatz in modernen Verbrennungsmotoren. *MTZ—Motortechnische Zeitschrift* 62(10):796–806. <https://doi.org/10.1007/BF03227087>.
16. Czichos H, Habig K-H (2020) *Tribologie-Handbuch*, 5th edn. Springer, Wiesbaden, Fachmedien. <https://doi.org/10.1007/978-3-658-29484-7>
17. Gummer A (2013) Analytische Untersuchung des Geometrieinflusses auf das Verschleißverhalten von Antriebsketten. PhD thesis, Technische Universität Kaiserslautern. ISBN: 978-3-943995-23-7
18. Becker A, Meffert D, Sauer B (2018) Friction and wear investigations on single chain joints. *Forschung im Ingenieurwesen* 83(1):53–63. <https://doi.org/10.1007/s10010-019-00297-x>.
19. Becker A (2020) Entwicklung einer Prüfmethodik für Verschleißuntersuchungen an Kettengelenken von Antriebs- und Steuerketten. PhD thesis, Technische Universität Kaiserslautern
20. Sappok D, Sauer B (2015) Wear measurement on chain joint components using a roundness instrument. *Period Polytech Mech Eng* 59(2):51–59. <https://doi.org/10.3311/PPme.7780>.
21. Becker S, Kohns M, Urbassek HM, Horsch M, Hasse H (2017) Static and dynamic wetting behavior of drops on impregnated structured walls by molecular dynamics simulation. *J Phys Chem C* 121(23):12669–12683. <https://doi.org/10.1021/acs.jpcc.6b12741>.
22. Tandler R, Bohn N, Gabbert U, Woschke E (2020) Analytical wear model and its application for the wear simulation in automotive bush chain drive systems. *Wear* :446–447, p. 203193. <https://doi.org/10.1016/j.wear.2020.203193>
23. Zhang M, Wang J, Yang P, Shang Z, Liu Y, Dai L (2020) A thermal EHL investigation for size effect of finite line contact on bush-pin hinge pairs in industrial chains. *Ind Lubr Tribol* 72(5):695–701. <https://doi.org/10.1108/ILT-10-2019-0448>.
24. Magyar B, Sauer B (2017) Methods for the simulation of the pressure, stress, and temperature distribution in the contact of fractal generated rough surfaces. *Proc Inst Mech Eng Part J J Eng Tribol* 231(4):489–502. <https://doi.org/10.1177/1350650115593962>.
25. Thielen S, Breuninger P, Hotz H, Burkhart C, Schollmayer T, Sauer B, Antonyuk S, Kirsch B, Aurich JC (2021) Improving the tribological properties of radial shaft seal countersurfaces using experimental micro peening and classical shot peening processes. *Tribol Int* 155:106764. <https://doi.org/10.1016/j.triboint.2020.106764>.
26. Kirsch B, Bohley M, Arrabiyeh P, Aurich J (2017) Application of ultra-small micro grinding and micro milling tools: possibilities and limitations. *Micromachines* 8(9):261. <https://doi.org/10.3390/mi8090261>.
27. Simo Kanga L, Meffert D, Magyar B, Oehler M, Sauer B (2022) Simulative investigation of the influence of surface texturing on the elastohydrodynamic lubrication in chain joints. *Tribol Int* :107564. <https://doi.org/10.1016/j.triboint.2022.107564>.
28. Magyar B, Thielen S, Foko Foko F, Becker A, Sauer B (2017) EHL simulation of the timing chain drive. In: 6th world tribology congress (WTC). Peking

29. Magyar B, Thielen S, Löwenstein M, Becker A, Sauer B (2018) EHD Simulation eines Kettengelenkes. *Tribologie und Schmierungstechnik* 66(3):40–55
30. Sappok D, Merz R, Sauer B, Kopnarski M (2015) Surface analysis of chain joint components after tribological load and usage of antiwear additives. *Conf Pap Sci* 2015:1–12. <https://doi.org/10.1155/2015/407048>
31. Becker A, Sauer B (2017) Experimental and analytical investigations of chain joint wear. In: 6th world tribology congress (WTC). Peking
32. Krupp F, Sappok D, Sauer B (2014) Experimentelle und simulative Untersuchungen des Wirkungsgrades und des Verschleißes von Steuerkettentrieben". In: 3. Györer Tribologie Tagung. 3. Györer Tribologie Tagung. Győr, Hungary, pp 93–108. ISBN: 978-615-5298-35-6
33. Fleischer G, Größer H, Thum H (1980) *Verschleiß und Zuverlässigkeit*, vol 1. VEB Verlag Technik, Berlin

Manufacturing-Morphology-Property Relationships for Biofilms



Roland Ulber, Sergiy Antonyuk, Jan C. Aurich, Tilmann Beck, Mustafa Bozoglu, Georg von Freymann, Sonja Kieren-Ehse, Christine Müller-Renno, Kai Muffler, Andrea Schmeckebeier, Clarissa Schönecker, Jörg Seewig, Marek Smaga, Judith Stiefelmaier, Dorina Strieth, Ahmed Zayed, Christiane Ziegler, and Sebastian Zimmermann

Abstract Prokaryotic and eukaryotic biofilm-forming microorganisms offer a wide spectrum of various biotechnological interesting products, which makes them promising cultivation organisms for industry, as biotechnological processes can be made simpler and more efficient. The biggest challenge is the cultivation since standard bioreactors like airlift or stirred tank reactors are not suitable for the cultivation of biofilms. Here, special biofilm bioreactors have been developed in recent years that

R. Ulber (✉) · A. Schmeckebeier · J. Stiefelmaier · D. Strieth (✉) · A. Zayed
Institute of Bioprocess Engineering, RPTU Kaiserslautern, Kaiserslautern, Germany
e-mail: roland.ulber@mv.rptu.de

D. Strieth
e-mail: dorina.strieth@mv.rptu.de

S. Antonyuk · M. Bozoglu
Institute of Particle Process Engineering, RPTU Kaiserslautern, Kaiserslautern, Germany

J. C. Aurich · S. Kieren-Ehse
Institute of Manufacturing Technology and Production Systems, RPTU Kaiserslautern, Kaiserslautern, Germany

T. Beck · M. Smaga
Institute of Materials Science and Engineering, RPTU Kaiserslautern, Kaiserslautern, Germany

G. von Freymann
Institute of Optical Technologies and Photonics, RPTU Kaiserslautern, Kaiserslautern, Germany

C. Müller-Renno · C. Ziegler
Institute of Physics and Biophysics of Complex Interfaces, RPTU Kaiserslautern, Kaiserslautern, Germany

K. Muffler
Bingen University of Applied Sciences, Bingen, Germany

C. Schönecker · S. Zimmermann
Institute of Micro Fluid Mechanics, RPTU Kaiserslautern, Kaiserslautern, Germany

J. Seewig
Institute of Measurement and Sensor Technology, RPTU Kaiserslautern, Kaiserslautern, Germany

© The Author(s), under exclusive license to Springer Nature Switzerland AG 2024
J. C. Aurich and H. Hasse (eds.), *Component Surfaces*, Springer Series in Advanced Manufacturing, https://doi.org/10.1007/978-3-031-35575-2_17

imitate the natural habitat of biofilms. The choice of the surface plays an important role in the initial adhesion of the cells that form the basis for the subsequent biofilm formation and productivity. To enhance initial adhesion different materials were microstructured and used as a surface for the cultivation of different biofilms. It could be shown, that initial adhesion can positively be influenced by designing flow-breaker structures. Furthermore, pH and ionic strength have an impact on initial adhesion. In summary, it can be said that microstructured surfaces have an impact on biofilm thickness and structure, biomass formation, and productivity of valuable products.

1 Introduction

About 80% of all living prokaryotes grow adherently on surfaces [1] and live embedded in a self-produced matrix of extracellular polymeric substances (EPS) as a biofilm. The EPS hold the cells together and protect against erosion as well as against fluctuating environmental conditions. Biofilms in general offer a wide spectrum of various interesting biotechnological products [2–4]. This makes them promising cultivation organisms for industry, as biotechnological processes can be made simpler and more efficient. Among other things, this is because the product purification of secreted substances is facilitated by immobilized cells [2]. Furthermore, higher productivity can be achieved in continuous processes with stable biofilms, as the growth rate can be decoupled from the dilution rate. An advantage of biofilm formers is that the cells naturally adhere to surfaces and thus no chemicals (harmful to humans) are required for immobilization [5]. Since standard bioreactors like airlift or stirred tank reactors are not suitable for the cultivation of biofilms [2], special biofilm bioreactors have been developed in recent years that imitate the natural habitat of biofilms [6]. The choice of the surface plays an important role in the adhesion of the cells and basic knowledge has to be generated to understand which microstructure is suitable for optimal cell adhesion. In this chapter different microstructured surfaces were designed and manufactured and cell adhesion as well as the productivity of different biofilm formers including (phototrophic) prokaryotes and eukaryotes were investigated.

2 Structuring Surfaces in Microbial Dimensions

2.1 Structuring of Surfaces via Micro-Milling

Micro-milling is one of the most flexible mechanical micro production processes, as a large range of workpiece materials can be utilized and a great variety of geometries can be produced [7]. Detailed information on micro-milling can be found in Chap. 4. The flexibility of the micro-milling process allows the production of various sample

geometries for the study of the manufacturing-morphology-property relationships for biofilms. The production and geometry of the two sample types used for the investigations are described in more detail below.

The samples were manufactured on three-axis desktop machine tools or an LT Ultra MMC-600. They are glued onto a sample holder and mounted onto the machining table. All samples were face milled with a 3 mm two-fluted end mill before micro-milling. This was followed by further machining of the samples by micro-milling. For micro-milling, single-edged micro end mills ($d=50\ \mu\text{m}$ and $d=100\ \mu\text{m}$ (see Fig. 1a) made of cemented carbide (FBK) as well as double-edged tools with diameters of $300\ \mu\text{m}$ and $500\ \mu\text{m}$ (Kemmer Präzision) were used. The microstructure is characterized by parallel slots with defined slot widths and depths and bar widths (see Fig. 1b). Single-edged micro end mills with a diameter of $50\ \mu\text{m}$ were used. For micro-milling, a spindle speed of 30,000 rpm, a feed per tooth of $1\ \mu\text{m}$, and a depth of cut of $5\ \mu\text{m}$ were applied. The $50\ \mu\text{m}$ wide slots were milled parallel to each other at different distances so that bar widths between $50\ \mu\text{m}$ and $500\ \mu\text{m}$ were realized. The material of this sample was commercially pure titanium grade 2. With the second specimen type, the groove width, groove depth, bar widths, and machining direction were varied (see Fig. 1c). The variation of the slot width was realized by using different micro end mills ($d=50\ \mu\text{m}$, $100\ \mu\text{m}$, $300\ \mu\text{m}$ and $500\ \mu\text{m}$). Two different groove depths ($10\ \mu\text{m}$ and $20\ \mu\text{m}$), as well as different slot distances and the milling direction, were adjusted via machine control. For micro-milling, a spindle speed of 30,000 rpm, a feed per tooth of $1\ \mu\text{m}$, and a depth of cut of $5\ \mu\text{m}$ were applied. The material of this sample was polycarbonate.

2.2 *Microstructuring of Biofilm Reactor Surfaces by Cold Spraying*

The microstructuring of surfaces with fine particles for biofilm growth experiments were conducted by a low pressure cold spray system described in Sect. 5. Titanium (grade 2, $156\times 25\times 2\ \text{mm}$) was used as the surface material. The samples were grounded and polished to an average roughness of $S_A \leq 100\ \text{nm}$. The surfaces were fixed on a 2D linear axis with a standoff distance of 5 mm from the nozzle outlet. The traverse speed was set to 10 mm/s with a line distance of $100\ \mu\text{m}$. To investigate the influence of the morphology two different surface morphologies were prepared: crater and particle-structured surfaces. To obtain crater-structured surfaces, titanium particles ($d_{P,Median} = 15\ \mu\text{m}$, grade 2, Eckart GmbH) were used as feedstock material. The nozzle temperature and pressure were set to $440\ ^\circ\text{C}$ and 7.5 bar, respectively. For the creation of surface morphology structured by deposited particles, TiO_2 particles ($d_{P,Median} = 0.65\ \mu\text{m}$, 99.9%, Sigma Aldrich) were used. Here, the nozzle temperature was set to $490\ ^\circ\text{C}$ and the pressure to 9.5 bar. The process parameters were adjusted so that the impact velocity would cause the TiO_2 particles to bind to the surface. In the case of titanium particles, a rebound at the surface occurs. For the

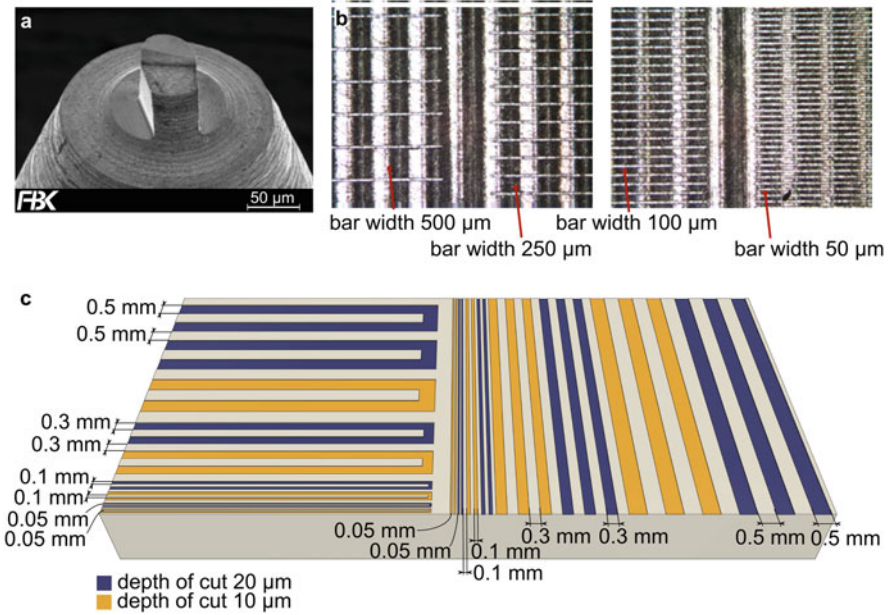


Fig. 1 a SEM image of a micro end mill $d=50\mu\text{m}$ b light microscope images of the first sample type with slot widths between $50\mu\text{m}$ and $500\mu\text{m}$ c schematic image of the second sample type with varying slot widths and slot depths

preparation of the biofilm growth experiments, the microstructured samples were cleaned by immersion in acetone, isopropanol, and distilled water. Each cleaning step was done for 10 m. After the cleaning procedure the samples were treated in an oxygen plasma for 5 m (50 W, 20% sccm O_2) [8].

2.3 Additive Manufacturing for Biofilm Growth

One key aspect of manufacturing-morphology-property relationships for biofilms is the feature size achievable for the surface in contact with the biofilm. Interaction between the biofilm and the surface depends on the characteristic features and the size of the active bacteria involved in the biofilm. From cell-growth studies, it is known that surface features matching the size of the cells foster proliferation and, thus, support efficient growth [9]. Additive manufacturing on the micron-scale as provided by three-dimensional laser lithography based on two-photon polymerization allows for feature size down to 50 nm and distances between features, i.e. resolution, of down to 500 nm (see Sect. 7.2 for technical details of the method). Hence, typical size scales of bacteria (diameters roughly 1 micron) and cells (diameters roughly 10 microns) involved in the studies are accessible.

Another advantage of this approach is the possibility to combine additive manufacturing with conventional techniques, which allows for the preparation of the mostly metallic surface via conventional micro-structuring techniques (see for example Sect. 2.1) before adding the finer structures via additive manufacturing.

Fabricating surface morphologies for biofilms in flow reactors also has to take into account the flow of the fluid inside the reactor. It is expected that biofilms preferably form in regions of reduced flow. Hence, so-called flow-breaker-structures have been designed, which allow for reduced flow velocity in the vicinity of the structures, while keeping the size scale compatible with the bacteria (see Sect. 3 for corresponding flow calculations and structure designs).

For characterization purposes, it is beneficial to use transparent materials instead of opaque metals as biofilm growth can thus be studied via, e.g., fluorescence detection. However, to study only the influence of the surface topography and not the influence due to different materials, it is important to keep the chemical environment the same as compared to the bare surface [10]. This can be achieved by coating the additively manufactured sample with a thin layer of the material the surface is made of. In this study, titanium is often used as a surface. In contact with ambient air a thin oxide layer forms on the surface. Transparent structures are fabricated from acrylate-based materials with high transparency in the visible spectral region. Surfaces and structures are subsequently coated with titanium (TiO_2) with atomic-layer-deposition, thus realizing an identical chemical environment allowing for studying the influence of the surface topography.

Exemplary for the whole structuring process Fig. 2 depicts a typical titan inset for a biofilm flow reactor $2 \times 1 \text{ cm}^2$ in size. On roughly one square centimeter a set of flow-breaker structures has been added, seen as faint white lines. One single flow-breaker structure is depicted in the center electron micrograph. The structure is roughly $10 \mu\text{m}$ high and the overarching part is $10 \mu\text{m}$ wide. The resulting surface roughness of the titan surface due to mechanical polishing is visible and substantially higher than the surface roughness of the additively manufactured part. The resulting biofilm growth predominantly close to the flow-breaker can be seen in the rightmost electron micrograph. Here, bacteria (*Lactococcus lactis*) seem to grow especially

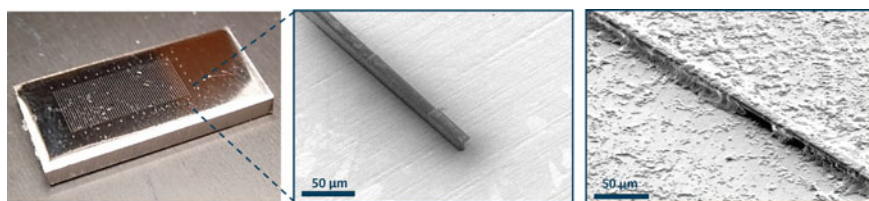


Fig. 2 Left: photograph of a structured titanium surface for cultivation of biofilms in flow reactors. Center: electron micrograph of one single flow-breaker structure after manufacturing. Right: Similar structure after biofilm growth in the flow reactor. In the zone underneath the flow-breaker increased biofilm growth is visible

in the zone of reduced flow underneath the overarching part of the structure. thus, demonstrating the expected effect of the flow-breaker structures on biofilm growth.

3 Characterization of Particle Loaded Fluid Flow over Microstructured Surfaces

A requirement for particle deposition on a (microstructured) surface is particle transport to the structure with subsequent wall contact. Local flows near the surface decisively influence this transport and are significantly determined by the topography of the microstructure. This microstructure generally serves several functions in the context of particle separation:

- can promote particle transport to the wall by influencing fluid flow,
- provides surface area for deposition and
- leads to eddy formation and flow-calmed areas.

Fluid flow can be characterized by the dimensionless Reynolds number, which describes the ratio of inertial to viscous forces within a fluid

$$\text{Re} = \frac{\rho \cdot \bar{v} \cdot L}{\mu} \quad (1)$$

with the dynamic viscosity μ and the density ρ of the fluid as well as the mean flow velocity \bar{v} . L denotes the characteristic length of the reference system, the structural distance in this case. For microstructures, this distance is of the order of 10^{-6} m with the consequence that $Re \ll 1$. The flow is consequently laminar, the viscous forces dominate the inertial forces. Such flow regimes are called Stokes flow (also creeping flow) and are mathematically described by the Stokes equations (assuming incompressible flow):

$$\mu \Delta \mathbf{v} = \nabla p \quad (2)$$

with the velocity vector \mathbf{v} , the Laplace operator Δ and the pressure gradient ∇p . As a result of negligible inertial forces, the Stokes flow essentially follows the structure topography (Fig. 3a). Laminar vortices form within and around these structures, which are largely decoupled from the outer main flow as illustrated in Fig. 3b). In analogy to fluid flow, the Reynolds number also characterizes the flow around particles. ρ denotes the particle density, \bar{v} the mean inflow velocity and μ the dynamic viscosity of the fluid. Under the simplifying assumption of spherical particles, the particle diameter is taken as the characteristic unit length. The Reynolds number for microparticles in a Stokes flow is then also less than one. Interception of particles by deflection/inertia at the surface is therefore not possible. The particles follow the streamlines that travel around the structures. Consequently, only less effective

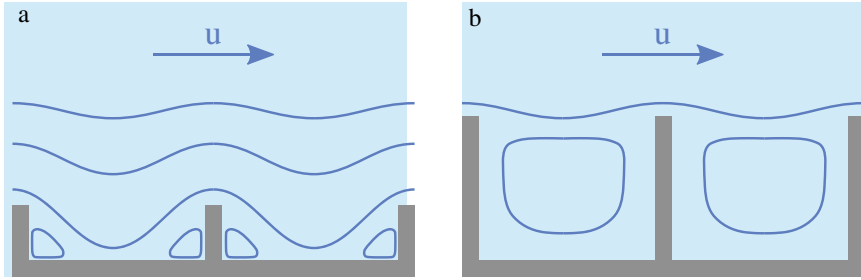


Fig. 3 Streamlines of Stokes flow over microstructured surfaces. **a** Streamlines penetrate between the relatively small vertical structures and form laminar vortices before and after them. **b** The outer main flow does not penetrate between the larger structures. Consequences are central laminar vortices within the structure gaps

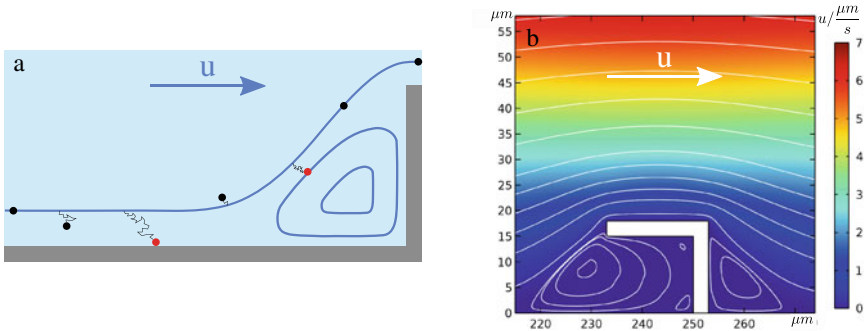


Fig. 4 a Brownian motion of particles (black dots) with subsequent potential wall separation or transportation towards eddies and dead spaces (red dots). **b** CFD-Simulation (COMSOL Multiphysics©) of transversal laminar flow over the exemplary microstructured surface with eddies forming around the structure

mechanisms such as gravity or Brownian motion remain for particle transport to the surface or into eddies and dead spaces.

The Brownian motion refers to the undirected random particle motion in liquids as a result of irregular collisions with atoms and molecules. The result is a so-called “random walk” of the particle. This allows transport between the streamlines, which can potentially lead to wall contact and thus particle separation, see Fig. 4. Brownian motion is significant for particles $< 1 \mu m$.

4 Single-Cell Behavior on Structured Surfaces

Single Cell Characterization

The formation of bacterial biofilms has been investigated extensively in previous literature with five main stages, including adsorption, adhesion, microcolony formation, biofilm maturation, and dispersion [11]. Thus, it starts with a physical single bacterial cell attachment to a solid surface in an unspecific and reversible manner usually governed partly by Van-der-Waals forces and electrostatic interactions. Such forces can be monitored and measured by scanning atomic force microscopy (AFM), which requires a single bacterium to attach to a cantilever, and force-distance curves are traced [12].

4.1 *The Importance of Bacteria Surface Interaction for Further Biofilm Development*

The adhesion of the biofilm and, thus, the adhesion of the bacteria is essential for the operation of a biofilm reactor. Ultimately, the initial layer of the biofilm determines how well it adheres to the reactor wall and thus withstands external influences such as shear stress. It is, therefore, essential to clarify where bacterial adhesion is weak and where it is strong. In addition, it is of interest which parameters promote or worsen bacterial adhesion. From these findings, measures can then be taken to improve bacterial adhesion and thus the 3D biofilm growth and its stability. Here, we describe the interaction behavior of the gram-negative sea-water bacterium *Paracoccus seriniphilus* (non-motile, non-spore-forming, aerobic), an L-serine-dehydratase-producing coccus isolated from the marine bryozoan *Bugula plumosa* [13]. In addition, *P. seriniphilus* is a biofilm-building bacterium [13].

In the following, the mechanical properties of the bacterial cell for different pH values and ionic strengths are presented first. The adhesion behavior is then described as a function of the parameters ionic strength, pH value, pre-conditioning, surface material, and surface structuring. Finally, the influence of lateral shear stress is presented, particularly regarding the material used for the reactor walls and their structuring, as well as the pH value.

4.2 *Properties of the Bacterial Cells for Different Ionic Strengths and pH Values*

Bacterial cells show different properties depending on the environmental conditions. These are reflected in particular in the charge respectively the stiffness of the cells. Therefore, the properties of the *P. seriniphilus* cells were characterized under the

influence of the parameters pH and ionic strength, the last by changing the sodium chloride (NaCl) concentration. As *P. seriniphilus* is a sea-water bacterium, it needs NaCl for growth 3%.

Changing the ionic strength changes the turgor pressure (hydrostatic pressure in excess of ambient atmospheric pressure which can build up in cells) in the cell as well as the charge of the outer cell membrane. Figure 5 left shows stiffer cell behavior (shown as turgor pressure/spring constant of the cell) at lower ionic strength [14]. If the ionic strength outside of the cell changes from isotonic solution to hypotonic solution, water rushes through the membrane into the cell and increases the inner cell volume. Although the isotonic ionic strength of *P. seriniphilus* is not known, it has the best growth rate at around 3% NaCl [15] which corresponds to the salinity of average sea-water (NaCl content of around 3%). Scanning force microscopy images (height image 3D) of bacteria in 0.9% NaCl solution and the same bacteria after

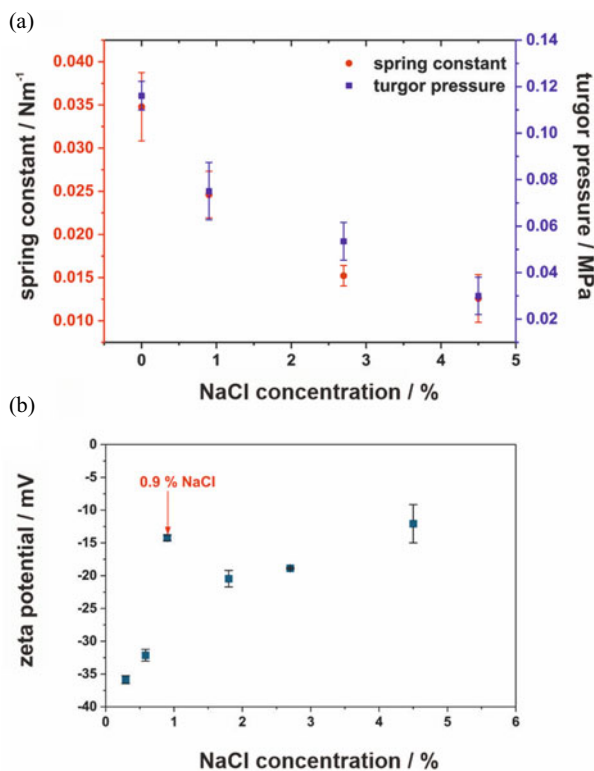
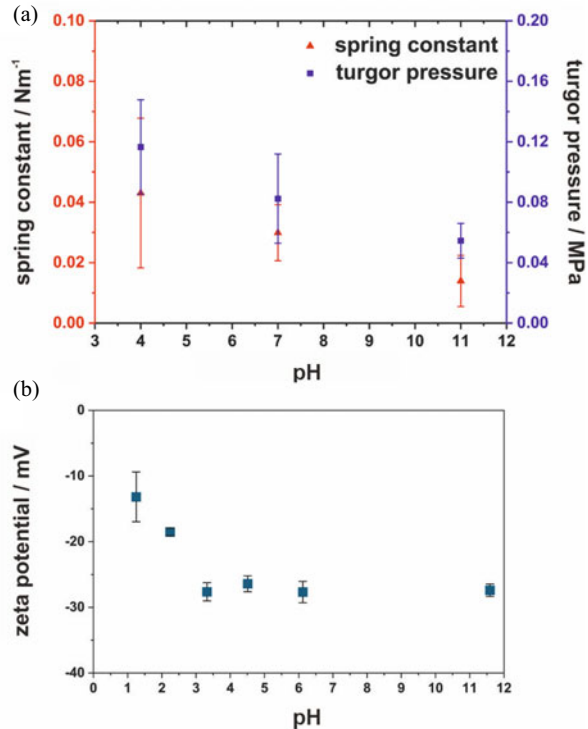


Fig. 5 Stiffness **a** and zeta-potential **b** of the *Paracoccus seriniphilus* cells as a function of the ionic strength. **a**: Reproduced from Davoudi et al. Nanomechanical properties of the sea-water bacterium *P. seriniphilus*—A scanning force microscopy approach. *Biointerphases* 10, 019004 (2015) with the permission of AIP Publishing. **b**: Reproduced from Davoudi et al. Adhesion forces of the sea-water bacterium *P. seriniphilus* on titanium: Influence of microstructures and environmental conditions. *Biointerphases* 12, 05G606 (2017) with the permission of AIP Publishing

Fig. 6 Stiffness **a** and zeta-potential **b** of the *Paracoccus seriniphilus* cells as a function of pH. **a**: Reproduced from Davoudi et al. Nanomechanical properties of the sea-water bacterium *P. seriniphilus*-A scanning force microscopy approach. *Biointerphases* 10, 019004 (2015) with the permission of AIP Publishing. **b**: Reproduced from Davoudi et al. Adhesion forces of the sea-water bacterium *P. seriniphilus* on titanium: Influence of microstructures and environmental conditions. *Biointerphases* 12, 05G606 (2017) with the permission of AIP Publishing



being incubated in deionized (DI) water for 7 h at 30 °C (0% NaCl) show that also the volume is increased [14]. In addition, the charge of the outer cell membrane differs as a function of the ionic strength. Figure 5 right shows the zeta-potential (the electric potential in the interfacial double layer (DL) at the location of the slipping plane relative to a point in the bulk fluid away from the interface) measured for *P. seriniphilus* [12].

As described above, the pH value was changed as a further parameter. Figure 6 shows the correlation between bacterial spring constants and turgor pressures of the bacteria as a function of pH (pH 4, 7, and 11) [14]. A pH value increase leads to a reduced rigidity of the cell (a three times decrease from pH 4 to pH 11, which is comparable to reported results [15]). However, one must note that the addition of HCl and NaOH also slightly changes the ionic strength and thus, the turgor pressure should also change toward softer behavior. This observation holds for pH 11, but not for pH 4. An influx of water due to higher concentrations of either protons or chloride seems to be the case at pH 4. This indicates that there are either specific ion channels or chemoreceptors that allow the influx of water. This mechanism is nearly reversible. Concerning the zeta potential of the cells, the pH value influences the charge of the outer cell membrane for very acidic pH values but not for the pH values described here [12].

4.3 Adhesion Behavior as a Function of pH, Ionic Strength, Pre-conditioning, Surface Material, and Surface Structure

As mentioned above, the initial bacterial layer plays a key role in the biofilm formation and the steadfastness of the biofilm. The initial attachment is governed by adhesion forces that act between the bacterium and the surface. These forces were measured by single-Cell force spectroscopy, where a single bacterium is attached to a cantilever of a scanning force microscope, and force-distance curves are measured [12, 16, 17].

To assess whether parameters like pH and ionic strength could increase the bacterial adhesion to a surface, multiple force-distance curves between a single cell probe [12, 16, 17] and polished titanium (cp-titanium) as a model surface were recorded. Figure 7 presents an average of the adhesion forces of *P. seriniphilus* bacteria as a function of pH value with a sequence of pH 7, 4, 7, 11, and 7 and another sequence of pH 7, 11, 7, 4, and 7. pH 7 represents a reference value between the measurements [12].

An increase in the pH value (from pH 4 to 7 to 11) decreases the adhesion forces independent of the measurement order, i.e., whether the measurement starts at pH 11 and changes then to pH 4 or vice versa. Slight changes in the ionic strength due to the addition of acid respectively base are negligible at the high ionic strengths that are used for the measurements. The trend seen in the adhesion force is directly the effect of the pH value of the surrounding solution and not of the ionic strength. The bacterium carries a negative charge over the complete measured pH range (see Fig. 5 right) [12]. At pH 4, the used titanium surface carried a positive charge resulting in an electrostatic attraction (see [12]). At pH 7 and 11 the electrostatic repulsion increases, resulting in reduced adhesion from pH 4 to pH 7 to pH 11.

Changes in the ionic strength from 0 to 0.06, 0.3, 0.6, 0.9, 1.8, 2.7, 4.5% NaCl, lead to adhesion forces consistent with the electrical double layer theory (see Fig. 7 right) [12]. The adhesion forces increase from 0% NaCl to higher ionic strength values with an outstandingly high value at 0.9% NaCl. The reason for the increased adhesion force lies in the reduced zeta-potential respectively charge of the bacteria at 0.9% NaCl (see Fig. 5, probably due to rearrangements at the outer cell surface).

Nevertheless, the influence of bacterial hardness, as described above (Sect. 4.1), must be considered. As published in Davoudi et al. [14] and shown in Fig. 5, respectively, Fig. 6 *P. seriniphilus* shows different stiffness depending on the ionic strength and the pH value. Lower ionic strength yielded harder cells due to the turgor pressure, and the adhesion forces are weaker as compared with higher ionic strength.

Another possibility to control and optimize the initial bacterial colonization is the choice of surface material. As known from the literature, hydrophilicity and hydrophobicity (wetting behavior) of the surface material plays an important role in the interaction forces [18–20]. The wetting behavior of the surface material is inversely correlated with the surface energy: hydrophobic surfaces show low surface energy, and hydrophilic surfaces have high surface energy. Therefore, materials

Fig. 7 Adhesion forces of *Paracoccus seriniphilus* as a function of pH value **a** and ionic strength **b**. Both reproduced from Davoudi et al. Adhesion forces of the sea-water bacterium *P. seriniphilus* on titanium: Influence of microstructures and environmental conditions. Biointerphases 12, 05G606 (2017) with the permission of AIP Publishing

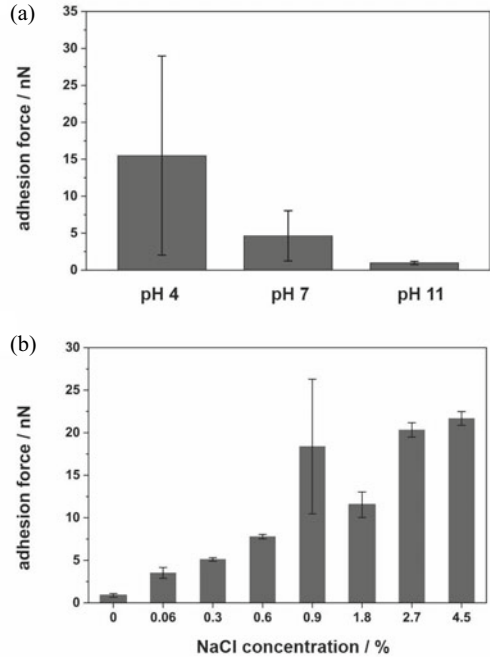
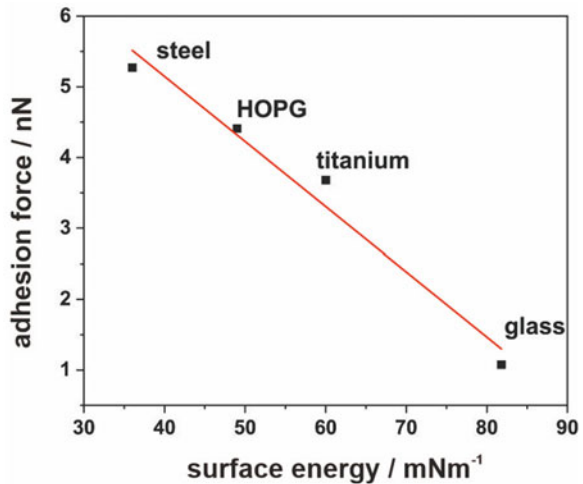


Fig. 8 Adhesion force shows a linearly decreasing relationship with increasing surface energy



across the full wetting spectrum were tested for *P. seriniphilus* adhesion. Interestingly, the adhesion forces show a linearly decreasing relationship with increasing surface energy (Fig. 8).

Another possibility to further strengthen bacterial adhesion and thus make the biofilm more resistant is the use of structured surfaces. In addition, the substructures

due to the structuring process allow the bacteria to adhere more homogeneously. For this purpose, titanium surfaces with different milled structures (as delivered, in microstructured trenches, pre-milled, between trenches which corresponds to the pre-milled state in Huttenlochner et al. [8] were examined. The different structures lead to different adhesion forces. In sum, the microstructured trenches deliver very homogeneous adhesion forces while the unstructured material (as delivered) shows a high variation in the adhesion forces. Due to that fact, the structuring favors the biofilm growth because it offers homogeneous adhesion conditions and should result in a more stable biofilm.

After the initial layer is formed, the biofilm can begin to grow into the third dimension. The basis for understanding the biofilm growth in three dimensions and the thickness of the biofilm is the contact between a single cell and preadsorbed molecules as an initial layer on the surface (e.g., from the culture medium) and/or preattached bacteria. In a later stage, already present biofilm (bacteria plus EPS) has to be taken into account. Adhesion measurements on conditioning films produced in the laboratory (surfaces pre-covered by culture medium and its components (sea salt, bacto peptone, L-serin, yeast extract) as well as model EPS (extracellular polymeric substances) components (BSA)) as well as on real biofilm reveal a passivating effect on the further cell adhesion [12]. In addition, single-Cell-cell interaction was determined and showed quite high adhesion forces, comparably high to uncovered surfaces.

4.4 Lateral Detachment Behavior as a Function of pH, Surface Material, and Surface Structuring

A requirement for bacterial attachment to a surface is that the bacterial cell and the surface get in contact. A flow and herewith a shear influence this interaction, respectively, the chance of contact. On the one side, a not attached bacterial cell can be hindered to get in contact; on the other side, an already attached bacterial cell or a biofilm experiences some shear forces and can be detached.

To get an overview of how bacteria can resist the shear forces in a flow reactor and how a flow could change the bacteria surface interaction, we determined the dislodgement forces of single *P. seriniphilus* bacteria using lateral force microscopy (LFM) [8]. The force with which the cantilever hits the bacterium laterally simulates the shear force caused by a flow. As already described for the adhesion forces, pH, surface material and structured surfaces can be a guide to make the biofilm and bacterial adhesion less sensitive to the influence of shear forces.

First results give the impression that the pH value affects the lateral dislodgement of the cells within one surface material, but further results have to be obtained. In addition, it could be shown that the more hydrophobic the surface, the more bacteria can offer resistance to shearing off, in line with a lower number of moving bacteria. Interestingly, there is a linear correlation between surface energy and moved

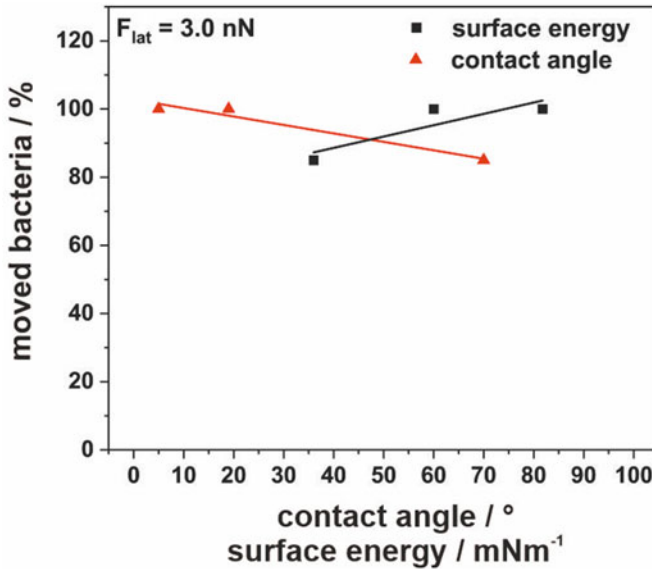


Fig. 9 Linear correlation between surface energy and moved bacteria respectively contact angle on oxide-covered surfaces (surface energy in increasing order: steel, titanium, glass). Reproduced with permission from Huttenlocher et al. [8]

bacteria on oxide-covered surfaces [8]. On these surfaces, the dislodgement forces are correlated with the initial adhesion forces to the surfaces. Electrostatics plays a minor role in dislodgement tests if different materials are taken into account (Fig. 9).

The lateral dislodgement force is increased by any structuring of the surface because it increases the resistance of the bacteria against shear forces (see Fig. 10). Any structuring in comparison with polished samples reduces the number of moving bacteria and favors the resistance against the dislodgement process. The reason is the larger surface area and more favorable sites for attachment offered by the surface structures (see Fig. 10).

4.5 Conclusion

The initial adhesion of bacterial cells plays a key role in biofilm formation. Only a stable connected initial layer is a sound basis for the formation of a thicker biofilm. Therefore, the early colonizing of bacteria to solid surfaces of a biofilm flow reactor starts at areas where these cells are protected against lateral shear stress. This fact gives the cells adequate time to change from the reversible adhered state to the irreversible adhered state. Structured surfaces per se show an increased surface area, which then increases the absolute number of adhering cells. Concerning the material

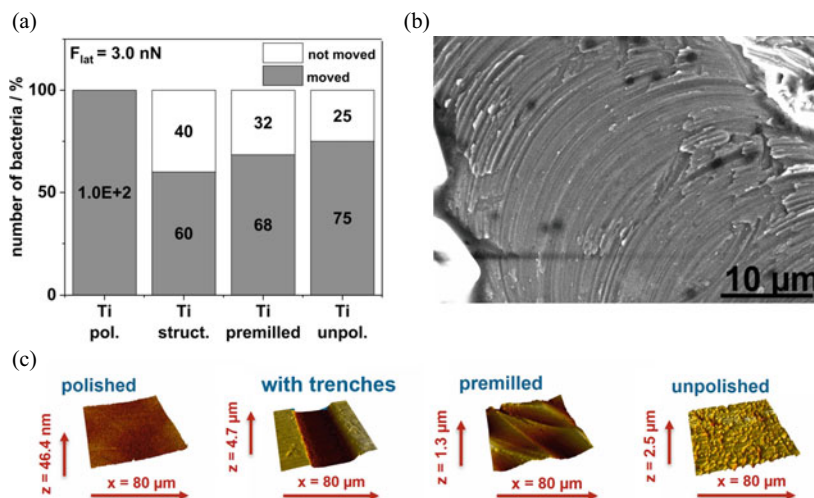


Fig. 10 Lateral dislodgement force influenced by the structuring of the surface **a**, which increases the resistance of bacteria against shear forces. The typical structures seen on the structured and pre-milled surface **b**. SFM images of the investigated structured samples in comparison to polished and unpolished surfaces **c**. A and B reproduced with permission from Huttenlocher et al. [8]

to be chosen, surface energy has a major impact on the attachment of bacterial cells. In general, hydrophobic surfaces enhance bacterial adhesion. Concerning the environmental parameters, the surface charge affects the binding forces of the bacteria to the surface. Either the surrounding pH in the biofilm reactor can be chosen as favorable to start cultivation, followed by a switch to the optimized pH for culturing. Or the best material can be chosen by comparing the adhesion forces governed by the electrostatics as a function of the pH value. In addition, the bacteria should have the opportunity to attach themselves to the surface before a conditioning film (from the components in the culture medium) is formed. This can be achieved by delaying the addition of culture medium. This initial layer should be ideally as dense as possible because the adhesion force between cells is high compared to medium-covered surfaces (low adhesion). Both the lateral and the adhesive forces benefit from a structured surface. The bacteria can use the enlarged surface for interaction and thus optimize the cell-surface interaction.

In summary, steel would be the material of choice. It shows a high water contact angle, hence low surface energy. In addition, it is non-corrosive and inexpensive. Combined with ideal conditions in terms of pH, ionic strength, and appropriate structuring, the formation of the initial layer can be influenced positively and represents the optimal basis for further 3D biofilm growth.

5 From Single Cells on Structured Surfaces to Productive Biofilms

The term ‘biofilm’ in general describes a non-specific ‘biomaterial on a surface’ [4, 21]. However, natural biofilms are a syntrophic consortium of different microorganisms. They can include a mixture of different bacteria, archae, microalgae and fungi living in a self-produced matrix of extracellular polymeric substances (EPS) that holds the cells together and acts among other things as a protection barrier against biotic and abiotic conditions [22]. Multiple layers of biofilms form microbial mats that can be up to several centimeters high [23]. The cultivation of microorganisms in their natural form as biofilm can make biotechnological processes easier. The interested reader is referred to Muffler et al. that summarize the advantages and disadvantages of cultivation of biofilms [24]. In general, biofilms offer a wide range of biotechnological interesting products as summarized in the reviews of Strieth et al., Zayed et al. and Schmeckebeier et al. [2–4]. Here, different biofilms are presented resulting in different interesting products like *Pseudomonas fluorescens* and *Lactobacillus delbrueckii* subsp. *lactis* (LAB) for the production of nisin, cyanobacterial, phototrophic biofilms (*Nostoc spec.*) for the production of antimicrobial substances, plant cells for the production of oleanolic and ursolic acids, and *Aspergillus niger* for the production of citric acid. To optimize the growth and the productivity and to investigate the influence of different growth parameters and surfaces a deeper understanding of the complex structure of biofilms is mandatory. Therefore, methods for single-cell as well as invasive and non-invasive methods for biofilm characterization are summarized and presented in the following section.

Biofilm Characterization

Then, the biofilm transforms into a more mechanically stabilized and irreversible molecular and cellular phase, where certain physiological changes with the simultaneous production of adhesive EPS result in cells adhesion and fixation [4, 25]. Interestingly, Muffler et al. revealed that several parameters affect cell adhesion and consequent biofilm formation related to the bacterial environment, surface characters, and microorganism itself [24].

Biofilms can be characterized non-invasively (without disturbing the biofilm) and invasively (after cultivation or harvesting the biofilm). With non-invasive methods the growth of the biofilm can be detected using for example a reflected light microscope, optical coherence tomography (OCT), confocal laser scanning microscope (CLSM) or a pulse amplitude modulated (PAM) fluorometry. With a reflected light microscope, the surface structure and roughness of biofilm can be determined. Mutual shading and high amounts of pigments do not allow a deeper insight into the biofilm. For detection of biofilm thickness and 3D structure OCT can be used. OCT can be separated in time-domain and frequency domain (FD) method. The methods differ in their imaging quality and applicability, due to the use of different components. Liu and Brezinski give a comprehensive overview of the different types of OCTs [26]. OCT can be used to determine the vertical growth of phototrophic and heterotrophic

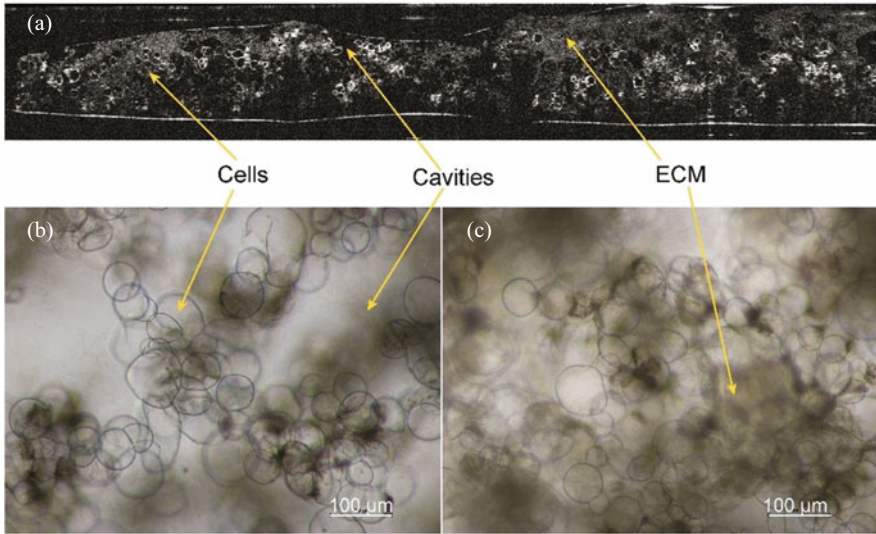


Fig. 11 Biomass of *O. sanctum* Rama grown on a structured glass surface analysed by **a** optical coherence tomography (OCT) and (B+C) microscopy. Highlighted are aggregated cells, cavities between the cells and non-cellular structures, which are assumed as extra cellular matrix (ECM)

biofilms over time [27]. Whereby, it has to be said that biofilm thickness does not correlate with biomass formation. Biofilm thickness can increase with simultaneous stagnation of the biomass due to the formation of EPS. Beside biofilm thickness also mushroom structures can be monitored. Mushroom formation and structure are strain-dependent and depend on cultivation conditions like flow, surface material and nutrient availability [28]. So, the structure of the biofilm can give information about the adaption to cultivation conditions.

For surface associated plant cell culture, the characterization with OCT and microscopy revealed different structures in the adherent cell aggregates (Fig. 11). This points towards another advantage of adherent cultivation of plant cells: By cultivation on surfaces instead of in suspension cultures, plant cells get the possibility to mimic structures present in natural tissues. Cavities between cell agglomerates might improve diffusion for cells in deeper agglomerate layers or can store water and medium components, which has already been described for microbial biofilms [29, 30]. The extracellular matrix (ECM) of plant cells is only researched little so far. It is defined as a dynamic structure starting from the cell wall, which has protective, structural and regulating functions as well as a role in cell-cell interactions [31–33]. Thus, especially in surface-associated plant cell culture its further analysis concerning impact on surface adhesion and other functions similar to EPS of microbial biofilms are of future interest.

Similar to the OCT digital microscopes are suitable for a macroscopic overview of the biofilm on different surfaces whereby the digital microscope is not the best

option to determine biofilm thickness but is suitable to determine the with biofilm overgrown area. Additional to biofilm thickness both methods allow the visualisation and determination of biofilm roughness. An increase in biofilm roughness can be for example caused by nutrient starvation [34]. An OCT is suitable for a macroscopic overview of the biofilm, if single cells are of interest CLSM would be more target-orientated. The application strongly depends on the expected biofilm thickness and the conclusions to be drawn from this. Using a CLSM, the biofilm can be stained e.g. to distinguish the phototrophic cells (chlorophyll a) from the EPS (stained e.g. with Fluorescein isothiocyanate (FITC) conjugated Concanavalin A). This method can also be used for other microorganisms by adapting the dyes. Beside the non-invasive characterization of biofilms, the product formation and different indicator components of the cells, and the EPS can reflect the vitality and productivity of the cells. Here, a combined method to extract and characterize biomass, EPS/ECM, and pigments from only one sample is described by Strieth et al. [35] and Strieth et al. [36]. This method allows a comprehensive characterization of phototrophic biofilms from only one sample. Additionally, the resazurin assay can be used to determine the vitality of all types of cells [37]. These methods allow a comprehensive characterization of phototrophic biofilms and can be transferred to other microbial communities.

5.1 Behavior of Prokaryotic Biofilms

Approx. 80% in all kinds of natural habitats of prokaryotic organisms (e.g., bacteria and archaea) were found to grow on surfaces forming biofilms [1]. Biofilms have been reported to be associated with microorganisms' environmental adaptation, pathogenicity, and antimicrobial resistance through various mechanisms resulting in life-threatening public health issues [11, 38]. For investigating the behavior of prokaryotic biofilms, various systems were developed with *P. fluorescens* and *L. delbrueckii* subsp. *lactis* (LAB), including the flow reactor system and with regard to growth surfaces, upscaling, and parallelization of the flow through the system under laminar or turbulent flow profiles, Fig. 12. The transparent design of the flow reactor system allowed a full investigation of biofilm growth using the non-invasive confocal laser scanning microscopy (CLSM) [39], while cryo-scanning electron and atomic force microscopy (AFM) were applied for structural and mechanical investigations of the cell assembly and its surrounding EPS on the different investigated cultivation surfaces. Regarding biofilm thickness, the results showed a 17-fold increase in biofilm thickness of *P. fluorescens* following cultivation on micro-structured cp-titanium (cp-Ti; grade 2, type 3.7035/34) surfaces compared to statistically shaped references. However, only 1.8-fold thicker biofilm was detected on a martensitic stainless steel (V4.A, type 1.4571) than the austenitic counterpart. This is probably due to the increased number of grain boundaries found in V4. A compared to austenite type. Such findings proved the superiority of cp-Ti microstructured surfaces for thicker biofilm formation in the case of *P. fluorescens*. Additionally, cryo-scanning

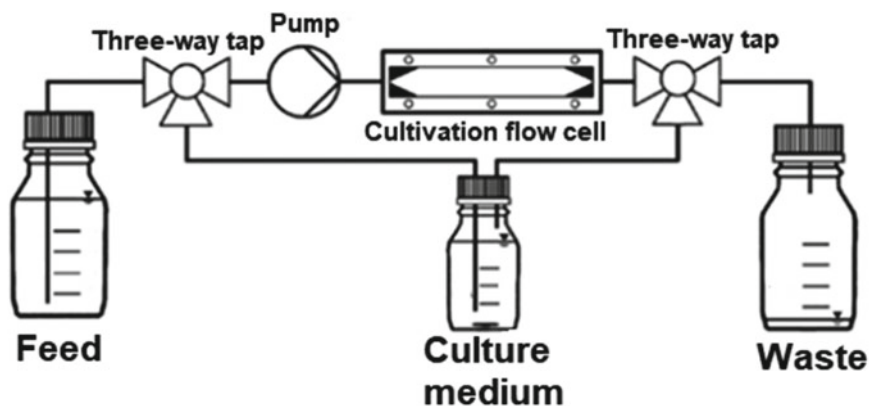


Fig. 12 The design of the flow reactor system used for biofilm cultivation of *Pseudomonas fluorescens* and *L. delbrueckii* subsp. *lactis* (LAB) in a batch and continuous processes. The flow channel (volume of 8.75 mL, $16 \times 2 \times 150$ mm in width (W), height (H), and length (L)) with cone-shaped in-and-outlet zones. The samples can be taken at the three-way tap (valve) for substrate/product analysis or collection

electron microscopy showed that a spongy structure of cells could be observed on cp-Ti surfaces with a higher cell density and a more compact structure compared to the growth on agar plates. Additionally, the mechanical properties studied by AFM showed increased elasticity with biofilm maturation. Nevertheless, further investigations in combination with the CLSM should be performed to show whether this is due to the different levels of EPS or other factors contributed. Raman microscopy and X-ray tomography, for example, may be of particular interest for future work measuring the cultures in 3D and differentiation of biofilm components.

The effect of different surface roughness ($R_a = 0.2 - 7 \mu\text{m}$) on EPS production and composition was further studied particularly with *P. fluorescens*. The results showed several findings, where biofilms of *P. fluorescens* produced less EPS with a reduced proportion of polysaccharides compared to the classical cultivation in agar cultures. This can be attributed to less drought stress in the biofilms formed in the flow reactor system. Concurrently, this polysaccharide portion was found to be rich in uronic acid indicating a higher degree of cross-linking and more stabilization. Additionally, less rough metallic surfaces resulted in low EPS characterized by high protein content. Interestingly, a higher polysaccharide content was detected in EPS for *P. fluorescens* cultivated on rough cp-Ti with a larger proportion of rhamnolipids compared with a rough V4.A surface that showed overall lower biomass also. These findings require a more in-depth analysis. In addition, there was no clear connection between the EPS composition of the main components and the total biofilm mass with the material or the roughness of the substratum. This situation was also similar to the cultures of LAB.

Furthermore, the impact of microstructured metallic surfaces (e.g., cp-Ti and V4.A) on the biofilm productivity of lactic acid from LAB was investigated in a

flow reactor system in batch and continuous cultivation process. The results showed that the surface material and microstructures were not critical for lactic acid production averaging around $6\text{--}7\text{ g (L h)}^{-1}$ [40]. Nevertheless, flow rate and pH variations affected the diffusional behavior, where the biofilm exhibited a slower diffusion rate at a higher flow rate, and a fast growth rate with increasing the cultivation medium pH values compared to the reference cultivation [41].

The production of the antimicrobial compounds, (e.g., nisin) using LAB biofilm in a custom-built flow reactor system was also performed. Nisin is a polycyclic antibacterial peptide used commonly in food industries as a preservative (E234). For its production, investigation of different surfaces for biofilm development and cultivation included V4.A, cp-Ti, metastable austenite (influence phase), polished, micro-milled, and particle-structured. All surface structures were characterized *via* optical profilometry. Besides, biofilm morphology was analyzed *via* optical coherence tomography (OCT), while relative gene expression levels were related to nisin by the real-time quantitative reverse transcription PCR (qRT-PCR).

The results showed that the surface of the substratum influenced the heterogeneity (e.g., thickness as well as mushroom count) of the biofilm and thus nisin production, Fig. 13. In addition, the expression levels of nisin-associated genes (e.g., *nisA* and *nisP*) were significantly increased in morphologically different biofilm sections, especially in the mushroom-rich biofilm section. The nisin productivity averaged 98 IU ml^{-1} using micro-milled structured surfaces, as shown in Fig. 13. mRNA levels cannot directly be linked to the microbial product titers, but it is a worthy tool investigating different behaviors of biofilm sections on the transcriptional level [42].

Therefore, the cultivation of LAB on micromilled structured surfaces, particularly in mushroom-rich biofilm, resulted in higher average thickness, and improved nisin biosynthesis.

5.2 Behavior of Eukaryotic Biofilms

Not only prokaryotic organisms but also eukaryotic organisms can be used as productive biofilms in the context of white biotechnology [4]. Therefore, various plant cell cultures of the genus *Ocimum*, among others, were investigated as potential productive biofilms. These plant cells are of interest because of their secondary metabolites oleanolic and ursolic acids, which have various pharmaceutically interesting properties. The plant cells used were established and cultivated as described in Mehring et al. [43]. To study the biofilm formation of the plant cells, the different plant cells were cultured on different surfaces, Table 1. For this purpose, the surfaces were fixed in petri dishes to prevent them from slipping. The plant cells were then cultured on the surfaces at $28\text{ }^{\circ}\text{C}$ for 16 to 28 days at $0/50\text{ rpm}$ in a shaking incubator.

Unfortunately, no successful immobilization and thus biofilm cultivation of the plant cells on the different surfaces could be achieved (Table 1). Neither the material nor the structuring had any influence. Therefore, a new surface design was developed

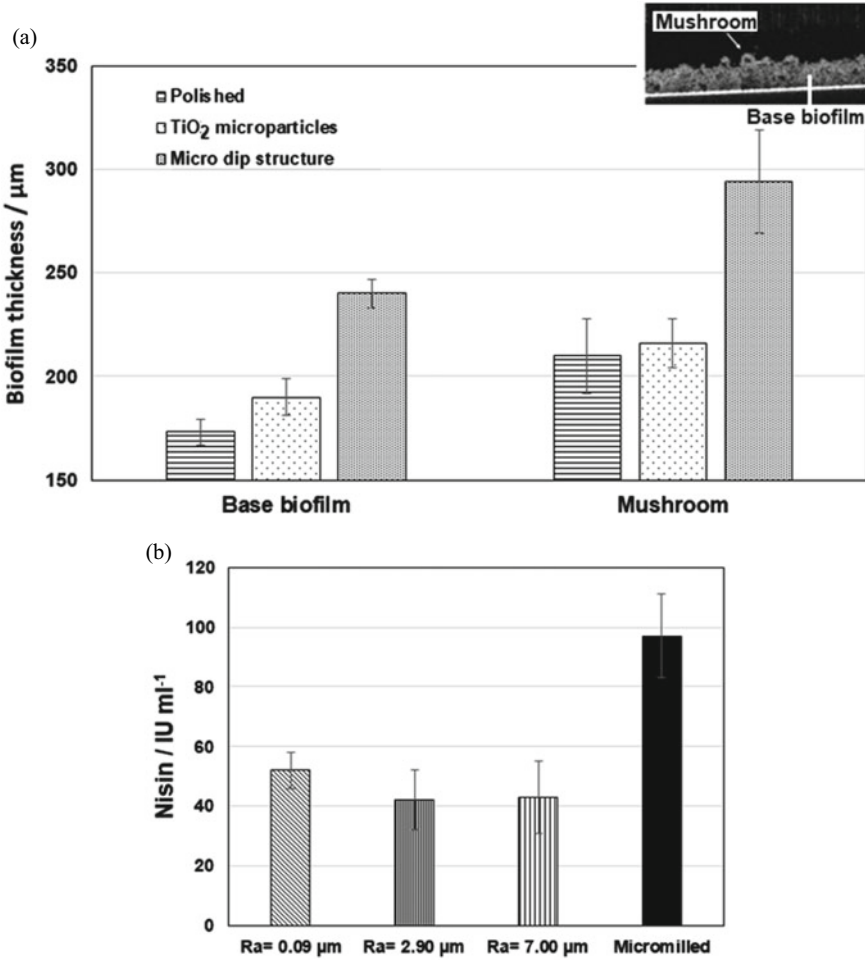


Fig. 13 Investigation of *Lactobacillus delbrueckii* subsp. *lactis* (LAB) biofilm in flow reactor system for nisin production. **a** The biofilm thickness in μm on different substrata in base and mushroom-rich biofilm sections as investigated by optical coherence tomography (OCT), **b** Nisin production in (IU ml^{-1}) in relation to different substrata roughness

to support the immobilized growth of the plant cells in order to enable biofilm cultivation of the plant cells. The design of the new surface therefore has microstructures on the scale of plant cells. The CMC cells are in an average size range of $58 \mu\text{m}$ (min. 21 , max. $134 \mu\text{m}$) [43]. Therefore, the groove widths were chosen between 50 , 100 , 300 and $500 \mu\text{m}$ to allow the cells to adhere to the grooves and thus generate biofilm cultivation. However, even here, no biofilm growth could be induced by the custom surface design. Therefore, an adhesion measurement by atomic force microscopy (see Sect. 5) of a single *Ocimum basilicum* CMC cell on a glass slide

Table 1 various plant cells and surfaces used for cultivation of biofilms

Plant Cell	Surface (Material, Structure)
CMC	
<i>Ocimum basilicum</i>	Glass, sandblasted Glass petri dish Polymethylmethacrylate (PMMA), Roughed Cp-Titanium (grade 2), longitudinally parallel milled grooves, bridges 50–250 μm Polycarbonate, microstructured groove width 50, 100, 300, and 500 μm
Callus	
<i>Ocimum basilicum</i>	Glass, sandblasted
<i>Ocimum americanum</i>	Glass petri dish
<i>Ocimum sanctum</i> Rama	
<i>Ocimum sanctum</i> Tulsi	
<i>Ocimum sanctum</i> Krishna	
<i>Ocimum citridorum</i>	

was performed. Adhesion of the single cell was measured to be very low compared to its cell size, confirming the lack of biofilm formation in the previously performed experiments.

Thus, the studies were extended to another eukaryotic system. The filamentous fungus *Aspergillus niger* is known as a biofilm former and produces citric acid as a possible valuable substance. Due to its filamentous growth behavior, it is not possible to use the biofilm flow reactor system already described in Sect. 5.1 to cultivate *A. niger* on the surfaces. Therefore, an aerosol-based reactor system for the cultivation of terrestrial cyanobacteria [44] was adapted to realize the cultivation on the component surfaces, Fig. 14.

The medium is pumped via a peristaltic pump into the aerosol generator with an ultrasonic nebulizer unit, where the medium is converted into aerosol. The aerosol is then fed into the cultivation unit via compressed air. Three component surfaces with a size of $15 \times 2 \text{ cm}$ can be vertically fixed in the cultivation unit so that the biofilm on the surfaces is supplied with the required nutrients by the aerosol. The coalesced medium is then returned to the medium receiver. Since the adaptation of the aerosol based reactor system was successfully carried out, the biofilm was cultured for 6 days on stainless steel and cp-titanium with different roughness at 30°C , Fig. 15. Both stainless steel and titanium are suitable as support materials for biofilms in a wide variety of applications due to their mechanical properties and resistance to corrosion. Biofilm thickness was analysed via optical coherence tomography (OCT).

The stainless steel surfaces (V4.A) had a roughness of $R_a = 0.2 \mu\text{m}$, $R_a = 1.7 \mu\text{m}$, $R_a = 2.4 \mu\text{m}$, and the cp-Titanium (grade 2) surfaces of $R_a = 0.5 \mu\text{m}$, $R_a = 2.9 \mu\text{m}$, $R_a = 7.0 \mu\text{m}$. After cultivating the biofilm on stainless steel at the different

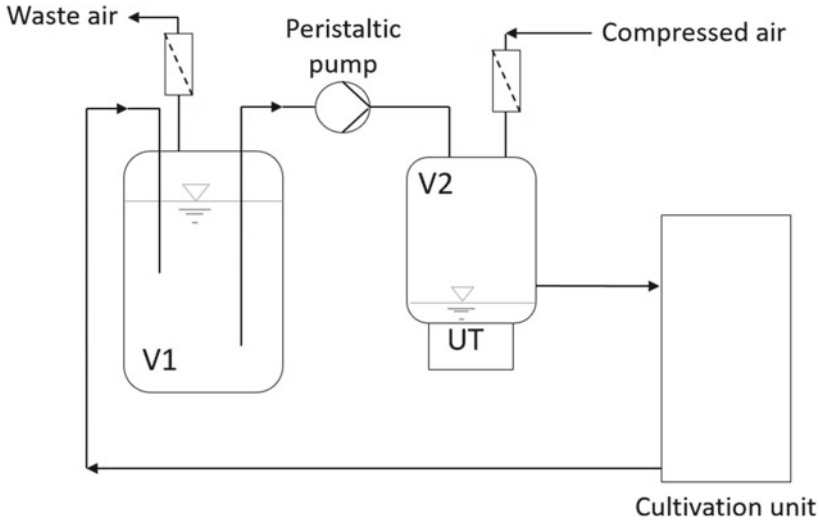


Fig. 14 Aerosol-based reactor system for the cultivation of *Aspergillus niger* on component surfaces. V1: Medium Receiver, V2: Aerosol generator with ultrasonic transducer (UT)

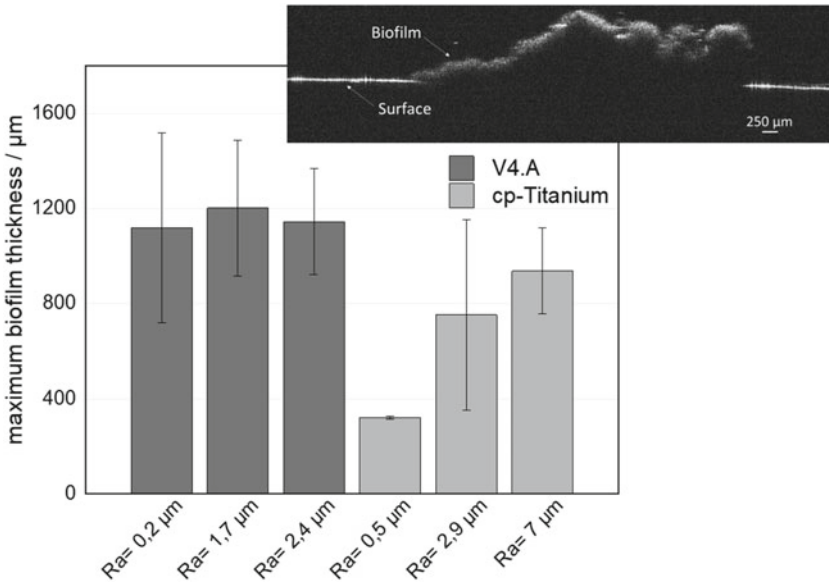


Fig. 15 Maximum biofilm thickness of *Aspergillus niger* after 6 days of cultivation in aerosol based reactor system at 30 °C stainless steel (V4.A) and cp-Titanium (grade 2) with different roughness, n=3

roughness, no effect of roughness on the maximum biofilm thickness was observed. The maximum biofilm thickness was approx. $1150\ \mu\text{m}$ regardless of the roughness. In contrast, when cultivating on cp-titanium (grade 2), a clear influence of roughness on the maximum biofilm thickness was observed. For example, the maximum biofilm thickness at a roughness of $R_a=0.5\ \mu\text{m}$ was approx. $300\ \mu\text{m}$, at $R_a=2.9\ \mu\text{m}$ $750\ \mu\text{m}$, while at a roughness of $R_a=7.0\ \mu\text{m}$ the maximum biofilm thickness was approx. $900\ \mu\text{m}$. Irrespective of the roughness, however, an influence of the material can also be seen here. For example, the maximum biofilm thickness is lower on cp-titanium (grade 2) than on stainless steel. Nevertheless, with regard to the influence of roughness, it should be noted that a significantly higher roughness of $R_a=7.0\ \mu\text{m}$ was investigated for cp-titanium compared to stainless steel. In the investigation of bacterial biofilms with thermo-resistant streptococci on stainless steel, no influence of the roughness of the material ($R_a = 0.5 - 3.3\ \mu\text{m}$) could be detected [45]. Titanium, on the other hand, is known to have material properties that do not support bacterial adhesion well, so this material is often used as an implant in medicine [46, 47]. It has also been found that the bacterial biofilm coverage of unpolished titanium is significantly higher than that of polished titanium [48]. In contrast, the antimicrobial effect of titanium dioxide was not found to be significant in the case of spore-forming bacteria such as *A. niger* [49].

Thus, successful biofilm cultivation of the eukaryotic organism *A. niger* in the aerosol-based reactor system on component surfaces was realized. In addition, first results of the influence of the surfaces on the biofilm formation could already be investigated. In future experiments, the cultivation of the *A. niger* biofilm on different microstructured surfaces should be realized in order to investigate the influence of the surfaces on the morphology and to positively influence the productivity of the biofilm.

5.3 Behavior of Phototrophic Biofilms

Phototrophic biofilms have a broad spectrum of interesting biotechnological products are thus interesting biofilm-forming organisms for industry [2, 50, 51]. Similar to Sect. 5.1 different terrestrial cyanobacteria were cultivated on microstructured surfaces in the developed flow-through chamber by simply adding a light source above the chamber. The terrestrial cyanobacteria did not show significant biofilm formation, which can be explained by their nature of growing air-exposed [6]. Therefore, different surfaces were placed in an aerosol-based photobioreactor, and area time yields were determined (Fig. 16).

It could be shown that *Nostoc spec.* grows similarly on polypropylene, borosilicate glass, PMMA, and silicone. Growth was inhibited by coating the surfaces of polypropylene and titanium with TiO_2 . This was suspected since TiO_2 damages cell surfaces whereby the selectivity and permeability functions of the cells are disturbed [52]. It could be shown that surface roughness has no impact on biomass formation, but on EPS production [53]. Since different antimicrobial substances are described

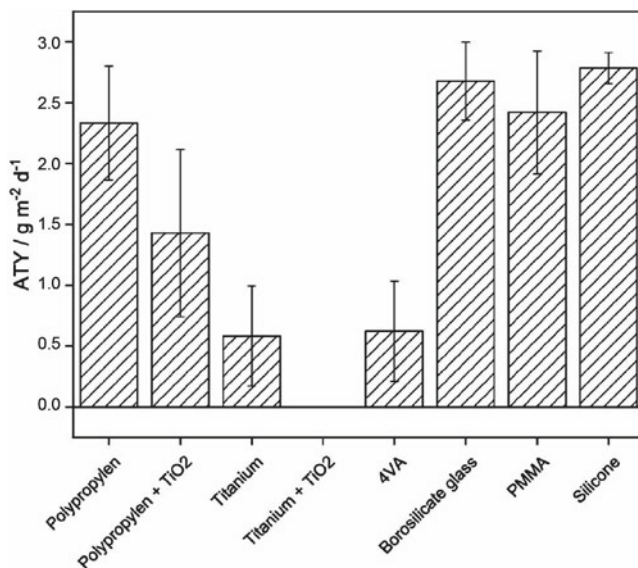


Fig. 16 Area time yield (ATY) of the terrestrial cyanobacterium *Nostoc spec.* on different surfaces in the aerosol-based photobioreactor. Rq: borosilicate glass: $1.17 \pm 0.36 \mu\text{m}$; PMMA (Poly(methyl methacrylate)) = $0.33 \pm 0.09 \mu\text{m}$; silicone = $0.25 \pm 0.08 \mu\text{m}$. Cultivation parameters: 30°C , $100 \mu\text{mol}_{\text{photones}} \text{m}^{-2} \text{s}^{-1}$, day-night rhythm: 14/8h, 24h of aerosol based on BG-11, $N_b = 3$

to be secreted in the EPS, *Nostoc spec.* was cultivated on roughened borosilicate glass in the aerosol-based photobioreactor by changing the amount of aerosol per day. The dry phases during the cultivation procedure increased the EPS production by 35% compared to continuous supply with aerosol [54]. In the next step, a semi-continuous process was developed with three phases that can be repeated over and over again: (i) a growth phase with continuous aerosol supply, (ii) followed by a dry phase without any aerosol supply, and (iii) an extraction phase. In the extraction phase, the whole reactor is flushed with an extraction solution to extract the outer layer EPS from the biofilm without detaching the biofilm from the surfaces. Afterward, the extraction solution is freeze-dried and the antimicrobial activity of EPS was tested. Through this process, the EPS production could be increased (32 times higher compared to standard cultivation) and minimal inhibitory concentration of EPS against *E. coli* could be decreased from 7.975 mg ml^{-1} (submerged cultivation in shaking flasks without any additional surfaces) to 3.75 mg ml^{-1} [55].

5.4 Segmentation of Biofilms in OCT Images

In biofilm characterization, parameters describing structural properties of biofilms, such as volumetric porosity, are of utmost interest [56]. Thus, biofilm must be evaluated volumetrically. Optical Coherence Tomography (OCT) distinguishes itself from other measurement methods characterizing biofilms, such as confocal laser scanning microscopy, by a combination of advantages given in [56]: OCT techniques provide:

- sufficient measuring volume and adequate penetration depth,
- cost-effective and compact design of the measuring device and
- simple operability of the measuring device.

However, for a robust characterization of the structural properties of a biofilm, it must be detected and segmented first in obtained OCT images.

Measurement Principle

In OCT, a light beam is split into two partial beams. One partial beam is directed onto the sample and the other onto a reference mirror. The reflection from the reference mirror and the reflection from the sample are superimposed afterward. Depending on the phase shift of the two superimposed partial beams relative to each other, constructive or destructive interferences occur. Thus, major reflections from the top surface as well as from inner boundary layers are indicated in the raw signal as intensity peaks resulting from mentioned coherent interferences. If depth measurements are taken at a single point of the sample, a so-called amplitude scan (A-scan) is generated, which represents the layers inside the sample in a spatially resolved way. If scanning is performed along a straight line additionally and thus several A-scans are lined up, this results in a brightness scan (B-scan). This B-scan can be visualized as a cross-sectional image. Similarly, a volumetric scan is created by lining up several B-scans. Further literature on OCT is provided in [57].

Biofilm Segmentation

The biofilms under investigation are cultivated on metallic surfaces. In OCT measurements, the metallic surfaces are strongly visible due to their strong reflectivity, whereas the biofilm is weaker in contrast.

To perform the biofilm segmentation, the following signal processing procedure is carried out:

1. The measured B-Scan images are converted into grayscale images (shown in Fig. 17).
2. The contour of the biofilm is determined with the help of the morphological filtering. The area detected by this technique is superimposed with the original image. For morphological filtering it is necessary to define a structuring element in shape and size. Afterwards, a marker image is created that identifies high intensity objects in the image using morphological erosion. Then, a morphological opening is performed on the mask image. This uses the marker image to identify

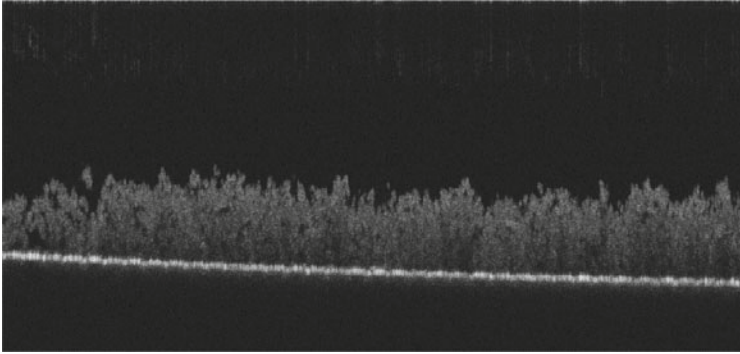


Fig. 17 Representation of the measurement of the biofilm as a B-scan. The biofilm on the metallic base, which stands out in the image, can be seen

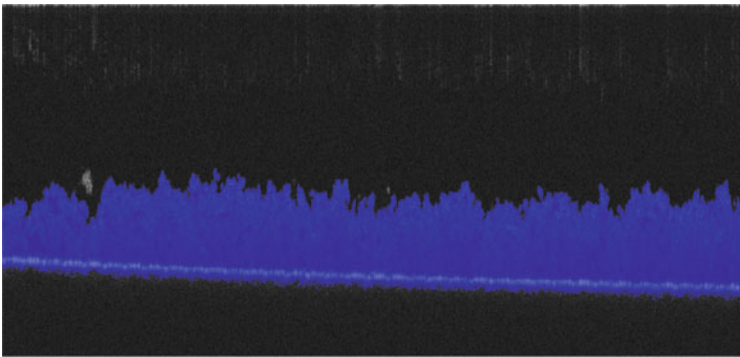


Fig. 18 The detected area of biofilm by morphological filtering overlaid to the origin image

objects with high intensity in the mask. As a result, a detected area is obtained. Morphological dilation is then performed to connect structures in the detected area and fill holes. After that, a morphological reconstruction is performed and the resulting area is overlaid on the original image (shown in Fig. 18).

3. An edge detection algorithm is used to detect the metallic surface, which is strongly highlighted in the image due to its strong reflectivity. Threshold values are used to separate the metallic surface and a straight line is fitted. The detected metallic surface is removed from the detected area in the step before (shown in Fig. 19).

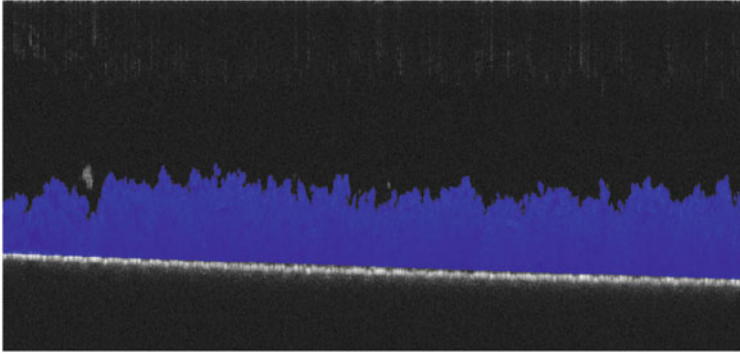


Fig. 19 The detected area of biofilm minus the metallic surface overlaid to the origin image

6 Conclusions

Various different surfaces were structured via micro-milling to enhance the immobilization of biofilms by designing flow-breaker structures with reduced flow. Different biofilms including (phototrophic) prokaryotes and eukaryotes were investigated. The initial adhesion of bacterial cells plays a key role in biofilm formation since a stable connected layer is the basis for biofilm formation. Therefore, in a first step the adhesion force of microorganisms on different surfaces was investigated resulting in a linearly decreased relationship with increasing surface energy. It could be shown that microstructured surfaces lead to an increase in the absolute number of adhering cells and the cultivation parameters like pH and ionic strength have an impact on the initial adhesion of the cells. In general, microstructured stainless steel showed the best results, because it has a high water contact angle, hence low surface energy. Furthermore, it is non-corrosive and inexpensive. To investigate the biofilm growth after the initial adhesion of the cells various non-invasive methods were established for an all-embracing characterization. It could be shown that surface roughness has an impact on biofilm thickness as well as on the formation of mushrooms. Phototrophic biofilms for example showed thicker biofilms on hydrophobic surfaces compared to hydrophilic surfaces. Different surfaces including different roughness had an impact on area time yield and productivity of antimicrobial substances of phototrophic biofilms. Also, the EPS content could be influenced by changing the water contact angle of the used surfaces. Furthermore, the production of nisin by *L. delbrueckii* subsp. *lactis* could be increased using micro-milled surfaces. Besides prokaryotic organisms, the cultivation of eukaryotic organisms was successful.

References

1. Bar-On YM, Milo R (2019) Towards a quantitative view of the global ubiquity of biofilms. *Nat Rev Microbiol* 17(4):199–200. <https://doi.org/10.1038/s41579-019-0162-0>.
2. Strieth D, Ulber R, Muffler K (2018) Application of phototrophic biofilms: from fundamentals to processes. *Bioprocess Biosyst Eng* 41(3):295–312. <https://doi.org/10.1007/s00449-017-1870-3>.
3. Zayed A, Mansour MK, Sedeek MS, Habib MH, Ulber R, Farag MA (2022) Rediscovering bacterial exopolysaccharides of terrestrial and marine origins: novel insights on their distribution, biosynthesis, biotechnological production, and future perspectives. *Crit Rev Biotechnol* 42(4):597–617. <https://doi.org/10.1080/07388551.2021.1942779>.
4. Schmeckebier A, Zayed A, Ulber R (2022) Productive biofilms: from prokaryotic to eukaryotic systems. *J Chem Technol & Biotechnol*. <https://doi.org/10.1002/jctb.7208>.
5. Garrett TR, Bhakoo M, Zhang Z (2008) Bacterial adhesion and biofilms on surfaces. *Prog Nat Sci* 18(9):1049–1056. <https://doi.org/10.1016/j.pnsc.2008.04.001>.
6. Lakatos M, Strieth D (2017) Terrestrial microalgae: novel concepts for biotechnology and applications. *Progress in botany*, vol 79. Springer, pp 269–312. https://doi.org/10.1007/124_2017_10.
7. Thepsonthi T (2014) Modeling and optimization of micro-end milling process for micro-manufacturing. Graduate School—New Brunswick Electronic Theses and Dissertations. <https://doi.org/10.7282/T35B00SD>
8. Huttenlochner K, Davoudi N, Schlegel C, Bohley M, Müller-Renno C, Aurich JC, Ulber R, Ziegler C (2018) *Paracoccus seriniphilus* adhered on surfaces: resistance of a seawater bacterium against shear forces under the influence of roughness, surface energy, and zeta potential of the surfaces. *Biointerphases* 13(5):051003. <https://doi.org/10.1116/1.5049226>.
9. Hohmann JK, Renner M, Waller EH, von Freymann G (2015) Three-dimensional 3D-printing: an enabling technology. *Adv Optical Mater* 3:1488. <https://doi.org/10.1002/adom.201500328>.
10. Hohmann J, von Freymann G (2014) Influence of direct laser written 3D topographies on proliferation and differentiation of Osteoblast-like cells: towards improved implant surfaces. *Adv Funct Mater* 24:6573. <https://doi.org/10.1002/adfm.201401390>.
11. Costa-Orlandi CB, Sardi JC, Pitangui NS, De Oliveira HC, Scorzoni L, Galeane MC, Medina-Alarcón KP, Melo WC, Marcelino MY, Braz JD et al (2017) Fungal biofilms and polymicrobial diseases. *J Fungi* 3(2):22. <https://doi.org/10.3390/jof3020022>.
12. Davoudi N, Huttenlochner K, Chodorski J, Schlegel C, Bohley M, Müller-Renno C, Aurich JC, Ulber R, Ziegler C (2017) Adhesion forces of the sea-water bacterium *Paracoccus seriniphilus* on titanium: Influence of microstructures and environmental conditions. *Biointerphases* 12(5):05G606. <https://doi.org/10.1116/1.5002676>.
13. Pukall R, Laroche M, Kroppenstedt RM, Schumann P, Stackebrandt E, Ulber R (2003) *Paracoccus seriniphilus* sp. nov., an L-serine-dehydratase-producing coccus isolated from the marine bryozoan *Bugula plumosa*. *Int J Syst Evol Microbiol* 53(2):443–447. <https://doi.org/10.1099/ijs.0.02352-0>.
14. Davoudi N, Müller-Renno C, Ziegler C, Raid I, Seewig J, Schlegel C, Muffler K, Ulber R (2015) Nanomechanical properties of the sea-water bacterium *Paracoccus seriniphilus*-A scanning force microscopy approach. *Biointerphases* 10(1):019004. <https://doi.org/10.1116/1.4906862>.
15. Laroche M, Pukall R, Ulber R (2003) Gewinnung und Charakterisierung einer L-Serindehydratase aus dem marinen Bakterium *Paracoccus seriniphilus* zum Aufbau bioanalytischer Systeme. *Chemie Ingenieur Technik* 75(1–2):146–149. <https://doi.org/10.1002/cite.200390012>.
16. Hofherr L, Chodorski J, Müller-Renno C, Ulber R, Ziegler C (2018) Comparison of versatile immobilization methods for gram-positive bacteria on a silicon cantilever. *Phys Status Solidi(a)* 215(15):1700846. <https://doi.org/10.1002/pssa.201700846>.
17. Hofherr L, Müller-Renno C, Ziegler C (2020) FluidFM as a tool to study adhesion forces of bacteria-optimization of parameters and comparison to conventional bacterial probe scanning force spectroscopy. *PLoS One* 15(7):e0227395. <https://doi.org/10.1371/journal.pone.0227395>.

18. Dou X-Q, Zhang D, Feng C, Jiang L (2015) Bioinspired hierarchical surface structures with tunable wettability for regulating bacteria adhesion. *ACS nano* 9(11):10664–10672. <https://doi.org/10.1021/acsnano.5b04231>.
19. Spriano S, Chandra VS, Cochis A, Uberti F, Rimondini L, Bertone E, Vitale A, Scolaro C, Ferrari M, Cirisano F et al (2017) How do wettability, zeta potential and hydroxylation degree affect the biological response of biomaterials? *Mater Sci Eng C* 74:542–555. <https://doi.org/10.1016/j.msec.2016.12.107>
20. Gittens RA, Scheideler L, Rupp F, Hyzy SL, Geis-Gerstorf J, Schwartz Z, Boyan BD (2014) A review on the wettability of dental implant surfaces II: biological and clinical aspects. *Acta Biomater* 10(7): 2907–2918. <https://doi.org/10.1016/j.actbio.2014.03.032>.
21. Flemming H-C, Baveye P, Neu TR, Stoodley P, Szewzyk U, Wingender J, Wuertz S (2021) Who put the film in biofilm? The migration of a term from wastewater engineering to medicine and beyond. *npj Biofilms Microbiomes* 7(1):1–5. <https://doi.org/10.1038/s41522-020-00183-3>.
22. Flemming H-C, Wingender J (2010) The biofilm matrix. *Nat Rev Microbiol* 8(9):623–633. <https://doi.org/10.1038/nrmicro2415>.
23. Prieto-Barajas CM, Valencia-Cantero E, Santoyo G (2018) Microbial mat ecosystems: structure types, functional diversity, and biotechnological application. *Electron J Biotechnol* 31:48–56. <https://doi.org/10.1016/j.ejbt.2017.11.001>
24. Muffler K, Lakatos M, Schlegel C, Strieth D, Kuhne S, Ulber R (2014) Application of biofilm bioreactors in white biotechnology. *Prod Biofilms* :123–161. https://doi.org/10.1007/10_2013_267.
25. Greer HM, Overton K, Ferguson MA, Spain EM, Darling LE, Núñez ME, Volle CB (2021) Extracellular polymeric substance protects some cells in an *Escherichia coli* biofilm from the biomechanical consequences of treatment with magainin 2. *Microorg* 9(5):976. <https://doi.org/10.3390/microorganisms9050976>.
26. Liu B, Brezinski ME (2007) Theoretical and practical considerations on detection performance of time domain, fourier domain, and swept source optical coherence tomography. *J Biomed Opt* 12(4):044007. <https://doi.org/10.1117/1.2753410>.
27. Stiefelmaier J, Strieth D, Di Nonno S, Erdmann N, Muffler K, Ulber R (2020) Characterization of terrestrial phototrophic biofilms of cyanobacterial species. *Algal Res* 50:101996. <https://doi.org/10.1016/j.algal.2020.101996>.
28. Sauer K, Stoodley P, Goeres DM, Hall-Stoodley L, Burmølle M, Stewart PS, Bjarnsholt T (2022) The biofilm life cycle: expanding the conceptual model of biofilm formation. *Nat Rev Microbiol* :1–13. <https://doi.org/10.1038/s41579-022-00767-0>.
29. Wilking JN, Zaburdaev V, De Volder M, Losick R, Brenner MP, Weitz DA (2013) Liquid transport facilitated by channels in *Bacillus subtilis* biofilms. *Proc Natl Acad Sci* 110(3):848–852. <https://doi.org/10.1073/pnas.1216376110>.
30. Rosenthal AF, Griffin JS, Wagner M, Packman AI, Balogun O, Wells GF (2018) Morphological analysis of pore size and connectivity in a thick mixed-culture biofilm. *Biotechnol Bioeng* 115(9):2268–2279. <https://doi.org/10.1002/bit.26729>.
31. Roberts K (1994) The plant extracellular matrix: in a new expansive mood. *Curr Opin Cell Biol* 6(5):688–694. [https://doi.org/10.1016/0955-0674\(94\)90095-7](https://doi.org/10.1016/0955-0674(94)90095-7)
32. Baluska F, Sámaj J, Wojtaszek P, Volkman D, Menzel D (2003) Cytoskeleton-plasma membrane-cell wall continuum in plants. Emerging links revisited. *Plant Physiol* 133(2):482–491. <https://doi.org/10.1104/pp.103.027250>
33. Popielarska-Konieczna M, Bohdanowicz J, Starnawska E (2010) Extracellular matrix of plant callus tissue visualized by ESEM and SEM. *Protoplasma* 247(1):121–125. <https://doi.org/10.1007/s00709-010-0149-1>.
34. Krsmanovic M, Biswas D, Ali H, Kumar A, Ghosh R, Dickerson AK (2021) Hydrodynamics and surface properties influence biofilm proliferation. *Adv Colloid Interface Sci* 288:102336. <https://doi.org/10.1016/j.cis.2020.102336>.
35. Strieth D, Stiefelmaier J, Wrabl B, Schwing J, Schmeckebier A, Di Nonno S, Muffler K, Ulber R (2020) A new strategy for a combined isolation of EPS and pigments from cyanobacteria. *J Appl Phycol* 32(3):1729–1740. <https://doi.org/10.1007/s10811-020-02063-x>.

36. Strieth D, Schwarz A, Stiefelmaier J, Erdmann N, Muffler K, Ulber R (2021) New procedure for separation and analysis of the main components of cyanobacterial EPS. *J Biotechnol* 328:78–86. <https://doi.org/10.1016/j.jbiotec.2021.01.007>
37. Mehring A, Erdmann N, Walther J, Stiefelmaier J, Strieth D, Ulber R (2021) A simple and low-cost resazurin assay for vitality assessment across species. *J Biotechnol* 333:63–66. <https://doi.org/10.1016/j.jbiotec.2021.04.010>
38. Uruén C, Chopo-Escuin G, Tommassen J, Mainar-Jaime RC, Arenas J (2020) Biofilms as promoters of bacterial antibiotic resistance and tolerance. *Antibiotics* 10(1):3. <https://doi.org/10.3390/antibiotics10010003>.
39. Zhang W, Sileika TS, Chen C, Liu Y, Lee J, Packman AI (2011) A novel planar flow cell for studies of biofilm heterogeneity and flow-biofilm interactions. *Biotechnol Bioeng* 108(11):2571–2582. <https://doi.org/10.1002/bit.23234>.
40. Schlegel C, Chodorski J, Huster M, Davoudi N, Huttenlochner K, Bohley M, Reichenbach I, Buhl S, Breuninger P, Müller-Renno C et al (2017) Analyzing the influence of microstructured surfaces on the lactic acid production of *Lactobacillus delbrueckii lactis* in a flow-through cell system. *Eng Life Sci* 17(8):865–873. <https://doi.org/10.1002/elsc.201700045>.
41. Chodorski J, Hauth J, Strieth D, Wirsén A, Ulber R (2021) Diffusion profiles in *L. lactis* biofilms under different conditions. *Eng Life Sci* 21(1–2):29–36. <https://doi.org/10.1002/elsc.202000059>.
42. KleineD, Breuninger P, Maus A-L, Antonyuk S, Ulber R (2020) Structural differences of biofilms. Tech. rep. Copernicus meetings. <https://doi.org/10.5194/biofilms9-109>
43. Mehring A, Haffelder J, Chodorski J, Stiefelmaier J, Strieth D, Ulber R (2020) Establishment and triterpenoid production of *Ocimum basilicum* cambial meristematic cells. *Plant Cell Tissue Organ Cult (PCTOC)* 143(3):573–581. <https://doi.org/10.1007/s11240-020-01942-y>.
44. Stiefelmaier J, Strieth D, Scherer K, Wahl M, Ulber R (2018) Kultivierung terrestrischer Cyanobakterien in emersen Photobioreaktoren. *Chemie Ingenieur Technik* 90(9):1256–1256. <https://doi.org/10.1002/cite.201855272>
45. Flint S, Brooks J, Bremer P (2000) Properties of the stainless steel substrate, influencing the adhesion of thermo-resistant streptococci. *J Food Eng* 43(4):235–242. [https://doi.org/10.1016/S0260-8774\(99\)00157-0](https://doi.org/10.1016/S0260-8774(99)00157-0).
46. Quinn J, McFadden R, Chan C-W, Carson L (2020) Titanium for orthopaedic applications: an overview of surface modification to improve biocompatibility and prevent bacterial biofilm formation. *IScience* 23(11):101745. <https://doi.org/10.1016/j.isci.2020.101745>.
47. Yue C, Yang B (2014) Bioactive titanium surfaces with the effect of inhibiting biofilm formation. *J Bionic Eng* 11(4):589–599. [https://doi.org/10.1016/S1672-6529\(14\)60070-6](https://doi.org/10.1016/S1672-6529(14)60070-6).
48. Nobre CM, Pütz N, König B, Ruff S, Hannig M (2020) Modification of in situ biofilm formation on titanium by a hydroxyapatite nanoparticlebased solution. *Front Bioeng Biotechnol* 8:598311. <https://doi.org/10.3389/fbioe.2020.598311>.
49. Muranyi P, Schraml C, Wunderlich J (2010) Antimicrobial efficiency of titanium dioxide-coated surfaces. *J Appl Microbiol* 108(6):1966–1973. <https://doi.org/10.1111/j.1365-2672.2009.04594.x>.
50. Wang C, Tan Y, Zhu L, Zhou C, Yan X, Xu Q, Ruan R, Cheng P (2022) The intrinsic characteristics of microalgae biofilm and their potential applications in pollutants removal-a review. *Algal Res* :102849. <https://doi.org/10.1016/j.algal.2022.102849>.
51. Greenman J, Walter XA, Gajda I, You J, Mendis A, Ieropoulos IA (2022) Phototrophic microbial fuel cells. In: *3rd Generation Biofuels* :699–727. <https://doi.org/10.1016/B978-0-323-90971-6.00007-3>.
52. Lu R, Liu P, Chen X (2015) Study the toxicity to *Microcystis aeruginosa* induced by TiO2 nanoparticles photocatalysis under UV light. *Bull Environ Contam Toxicol* 94(4):484–489. <https://doi.org/10.1007/s00128-015-1492-x>.
53. Strieth D, Weber A, Robert J, Stiefelmaier J, Kollmen J, Volkmar M, Lakatos M, Jordan V, Muffler K, Ulber R (2021) Characterization of an aerosolbased photobioreactor for cultivation of phototrophic biofilms. *Life* 11(10):1046. <https://doi.org/10.3390/life11101046>.

54. Kuhne S, Strieth D, Lakatos M, Muffler K, Ulber R (2014) A new photobioreactor concept enabling the production of desiccation induced biotechnological products using terrestrial cyanobacteria. *J Biotechnol* 192:28–33. <https://doi.org/10.1016/j.jbiotec.2014.10.002>.
55. Strieth D, Schwing J, Kuhne S, Lakatos M, Muffler K, Ulber R (2017) A semi-continuous process based on an ePBR for the production of EPS using *Trichocoleus sociatus*. *J Biotechnol* 256:6–12. <https://doi.org/10.1016/j.jbiotec.2017.06.1205>
56. Wagner M, Taberzadeh D, Haisch C, Horn H (2010) Investigation of the mesoscale structure and volumetric features of biofilms using optical coherence tomography. *Biotechnol Bioeng* 107(5):844–853. <https://doi.org/10.1002/bit.22864>.
57. Drexler W, Fujimoto JG et al (2015) *Optical coherence tomography: technology and applications*, vol 2. Springer. ISBN: 978-3-319-06419-2